INVESTIGATION OF PERFLUOROCARBONS AS POTENTIAL PHYSICAL SOLVENTS FOR FLUE GAS CLEANING

by

Marc Mulamba Tshibangu
BScEng (Chemical)
University of Lubumbashi, D R Congo
MScEng (Chemical)
University of KwaZulu-Natal, South Africa

Submitted in fulfilment of the academic requirements for the degree of Doctor of Philosophy in the School of Engineering, Discipline of Chemical Engineering,

University of KwaZulu-Natal

Supervisors: Professor D. Ramjugernath, Professor C. Coquelet and Dr C. Narasigadu

January 2017

DECLARATION

I, Marc Mulamba Tshibangu, declare that:

(i) The research in this report, except where otherwise indicated, is my original work.

(ii) This report has not been submitted for any degree or examination at any university.

(iii) This report does not contain other person's data, pictures, graphs or other information, unless specifically acknowledged as being sourced from other persons.

(iv) This report does not contain other person's writing, unless specifically acknowledged as being sourced from other researchers. Where other written sources have been quoted then:

a) Their words have been re-written but the general information attributed to them has been referenced;

b) Where their exact words have been used, their writing has been placed inside quotation marks, and referenced.

(v) Where I have reproduced a publication of which I am an author or co-author I have indicated in detail which part of the publication was actually written by myself alone and have fully referenced such publications:

(vi) This report does not contain text, graphics or tables copied and pasted from the internet, unless specifically acknowledged, and the source are detailed in the report and in the references sections.

_____ _____

MM Tshibangu (candidate) Date

As the candidate's supervisor I agree/ do not agree to the submission of this thesis

Prof. D. Ramjugernath Date

As the candidate's co-supervisor I agree/ do not agree to the submission of this thesis

Prof. C. Coquelet Date

As the candidate's co-supervisor I agree/ do not agree to the submission of this thesis

Dr. C. Narasigadu Date

COLLEGE OF AGRICULTURE, ENGINEERING AND SCIENCE

DETAILS OF CONTRIBUTION TO PUBLICATIONS that form part and/or include research presented in this thesis (include publications in preparation, submitted, *in press* and published and give details of the contributions of each author to the experimental work and writing of each publication).

Publication 1

Title: "Isothermal Vapour-Liquid Equilibrium Data and Thermodynamic Modeling for Binary Systems of Perfluorobutane (R610) + (Methane or Hydrogen Sulphide) at (293, 313 and 333) K", *J. Chem. Eng. Data*, 2014, 59 (9), pp 2865-2871.

Authors: Mulamba Marc Tshibangu (Experimental measurements and modelling of data, main write-up, formatting and editing)

Alain Valtz (Technical assistance during experimental measurement)

Caleb Narasigadu as the candidate's co-supervisor (Formatting and editing)

Christophe Coquelet as the candidate's co-supervisor (Formatting and editing)

Deresh Ramjugernath as the project conceptualizer and candidate's supervisor (Formatting and editing)

Publication 2

Title: "Vapour-Liquid Equilibrium (VLE) Data and Thermodynamic Modelling for Binary Systems Containing Perfluorobutane (R610) with Carbon Monoxide or Nitric Oxide at (293, 313 and 333) K", *J. Chem. Eng. Data*, 2014, 59 (2), pp 346-354.

Authors: Mulamba Marc Tshibangu (Experimental measurements and modelling of data, main write-up, formatting and editing)

Alain Valtz (Technical assistance during experimental measurement)

Caleb Narasigadu as the candidate's co-supervisor (Formatting and editing)

Christophe Coquelet as the candidate's co-supervisor (Formatting and editing)

Deresh Ramjugernath as the project conceptualizer and candidate's supervisor (Formatting and editing)

Publication 3

Title: "Isothermal Vapour-Liquid Equilibrium (VLE) and Vapour-Liquid-Liquid Equilibrium (VLLE) Data for two Binary Systems Containing Perfluorohexane with Carbon Monoxide or Hydrogen Sulphide at (293, 313 and 333) K*"* Submitted to *J. Chem. Eng. Data.*

Authors: Mulamba Marc Tshibangu (Experimental measurements and modelling of data, main write-up, formatting and editing)

Alain Valtz (Technical assistance during experimental measurement)

Alain Valtz (Technical assistance during experimental measurement)

Caleb Narasigadu as the candidate's co-supervisor (Formatting and editing)

Christophe Coquelet as the candidate's co-supervisor (Formatting and editing)

Deresh Ramjugernath as the project conceptualizer and candidate's supervisor (Formatting and editing)

Signed

_____

Mr Mulamba Marc Tshibangu

_____

Prof. Deresh Ramjugernath

_____

Prof. Christophe Coquelet

_____

Dr. Caleb Narasigadu

ACKNOWLEDGEMENTS

The following are acknowledged for their invaluable contribution to this study:

First and foremost, Jesus-Christ, my Lord and Saviour for his faithfulness. Lord, I am forever thankful and to You be the glory!

My supervisors, Professor D. Ramjugernath and Doctor C. Narasigadu of the University of KwaZulu-Natal, Durban, South Africa and Professor C. Coquelet of MINES ParisTech, Fontainebleau, France, for their guidance and support.

The technical staff of the Thermodynamics Research Unit at the University of KwaZulu-Natal and Centre Thermodynamics of Process at MINES ParisTech for their technical assistance during experimental measurement: A. Valtz, P. Theveneau, H. Legendre, L. Augustine, L. Mkhize and A. Kanyile.

Professor J. Rarey and Mr K. Moodley for provision of the sigma profiles.

Dr. B. Satola and Mr. W. Van Wassenhove for their assistance in using Aspen Plus®

My colleagues: Dr. K. Tumba, Dr. A. Lebouvier, Dr. K. Osman and Dr. S. Iwarere.

My Friends and church members: Christian and Helen Mulol, Andreas and Paulette Coutsoudis, Samuel Ikabu, Babbis Kashironge, Jim Chiyen, Serge Mapan and Joseph Kapuku.

South African Research Chair Initiative (SARChI) for financial support.

My parents, Kayembe Tshikala and Ngalula Tshizanga, for their unconditional love and their endless support and encouragement.

My parents-in-law, Professor Tshimpaka Yanga and Masengu Mubenga, for their words of encouragement and prayers.

Last but not least, to the love of my life, my wife Grace Ngomba Tshimpaka Tshibangu for her love, understanding, patience and support. I love you!

ABSTRACT

There has been a gradual increase in the average temperature of the Earth in the past century. This rise in temperature is principally attributed to the effect of climate change resulting from the emission of greenhouse gases (GHG) into the atmosphere. Greenhouse gases such as CO_2, CH_4 and NO_x, which are major contributors to climate change, are mainly produced by combustion of fossil fuels in power generation facilities. Research conducted by the International Energy Agency has shown that over 80% of the world's energy is currently supplied by fossil fuels and this will continue for the foreseeable future. Thus, concentrations of GHG could potentially increase. While a number of solutions have been proposed, including, renewable energies, nuclear power, and flue gas capture technologies; it is the capture of flue gas that is the topic of this study. More specifically, it is the design and analysis of technology to capture flue gas from a power station using a perfluorocarbon solvent.

Flue gas capture technologies have been developed in order to mitigate the emission of GHG from fossil fuels while they are still in use. The absorption process method of flue gas capture technologies, which has garnered research interest, utilizes solvents for absorption. Two types of solvent are generally used for absorption: chemical and physical solvents. The main deciding factor resides in finding the most suitable and cost-effective solvent for the specific task at hand.

An 'ideal' solvent is generally considered to possess the following characteristics: high capacity and selectivity for the particular flue gas, low vapour pressure to contain the solvent in the liquid phase, high chemical and thermal stability, low viscosity for easy mass transfer, environmentally benign, availability, and low cost. Unfortunately, there is no one solvent that has met all of the criteria, and consequently there is much potential for research and development in this field, which lead us to the purpose of this study: The use of perfluorocarbons as potential physical solvents for flue gas cleaning.

This study set out to investigate two perfluorocarbons, namely, perfluorobutane and perfluorohexane, as potential physical solvents to selectively clean CO_2, H_2S, CH_4 and CO in advanced power generation facilities, and specifically, one using an integrated gasification combined cycle (IGCC). To this end, phase equilibrium data measurement and thermodynamic

modelling were undertaken for C_4F_{10} and C_6F_{14} with common flue gas components such as CO_2, H_2S, CH_4, CO, etc. Thereafter, design of gas absorption systems using perfluorobutane and perfluorohexane as physical solvents was undertaken as an illustration that the phase equilibrium data measured could be used in the design of gas absorption systems.

It is due to the exceptional behaviour of fluorochemicals that the Thermodynamics Research Unit at the University of KwaZulu-Natal (South Africa), the Centre Thermodynamics of Processes (CTP) at MINES ParisTech (France) along with some chemical industries, have initiated research into the use of perfluorocarbons as potential enhancing agents in separation processes. This is the academic context of the study.

In order to use perfluorocarbons in separation processes, it was first necessary to design and simulate such an operation. A core component in the process design and simulation of any unit operation is accurate phase equilibrium data. However, in preliminary process designs, predicted phase equilibrium data is acceptable in the absence of accurate measurements. Vapour-liquid equilibrium data for systems containing perfluorocarbons with common flue gas components are rare to non-existent. Consequently, phase equilibrium data measurements for binary systems containing either perfluorobutane or perfluorohexane with common flue gas components were undertaken using two static-analytic apparatuses. One apparatus was designed for hazardous chemicals and the other for non-hazardous chemicals.

Using the first experimental apparatus, the ethane + perfluorobutane system was measured as a test system to demonstrate the capability of the experimental apparatus and thus verify the accuracy of the experimental procedure.

Isothermal vapour-liquid equilibrium (VLE) data measurements for binary systems containing perfluorobutane or perfluorohexane with common flue gas components were undertaken, which include:

Perfluorobutane (C_4F_{10}) with CO, NO, H_2S, CH_4, O_2, N_2 or H_2 and;

Perfluorohexane (C_6F_{14}) with CO, H_2S, CH_4 or C_2H_6.

The remainder of the binary systems, required to fully describe the gas absorption systems, could not be measured due to time constraints and, consequently, were predicted using either the

modified UNIversal Functional Activity Coefficient (UNIFAC) (Dortmund) or the Conductor-like Screening Model – Segment Activity Coefficient (COSMO – SAC) implemented into the predictive Soave-Redlich-Kwong (PSRK) property method using Aspen Properties®.

The measured and predicted data were thereafter correlated, via the direct method, using various combinations of models, which included: the Peng-Robinson or Soave-Redlich-Kwong equation of state, incorporating the Mathias-Copeman or Stryjek-Vera alpha function, with the Wong-Sandler, Huron-Vidal, predictive Soave-Redlich-Kwong, modified Huron-Vidal 1 or 2 mixing rule utilizing the non-random two liquid activity coefficient model. The combined models represented satisfactorily 80% of the measured and predicted VLE data, and their corresponding binary interaction parameters were obtained. However, for design purposes, the best-performing combination model, which was found to provide a global representation of all the binary systems under investigation, was selected. This was the Peng-Robinson equation of state, incorporating the Mathias-Copeman alpha function and the Wong-Sandler mixing rule utilizing the non-random two liquid activity coefficient model, abbreviated as PR-MC-WS-NRTL.

Once the binary interaction parameters were obtained through modelling, they were then used in the design of gas absorption systems using the Aspen Plus® V8.0 engineering suite developed by ASpenTech. More specifically, the RadFrac column model using the equilibrium method was selected for the design of the absorption and stripping columns. The optimum number of stages, operating temperature and pressure, and the solvent flow rates for the absorbers were determined as 10 or 13 stages, 260.15 K, 6.890 MPa, 8000 or 10000 kmol/h, respectively. The optimum conditions for the absorbers were determined following a sensitivity analysis. The optimum temperature was made to be within the operating temperature ranges of current commercial physical solvents, such as dimethyl ethers of polyethylene glycol (DEPG); N-methyl-2-pyrrolidone (NMP) and propylene carbonate (PC).

Under these conditions, it was found that the perfluorocarbon solvents have poor selectivity for CO_2, H_2S, CH_4 and CO, but they have high absorption capacity for these gases, increasing with carbon chain length. However, the associated high vapour pressures of the perfluorocarbon solvents at the operating conditions constitute a major drawback due to the fact that some of the solvents were lost to the atmosphere. In comparison, the current commercial solvents, DEPG,

NMP and PC, generally exhibited high gas absorption for the flue gas of interest, with much lower emissions into the atmosphere.

The principal idea is to use perfluorocarbons as potential physical solvents for flue gas cleaning while minimizing their emissions into the atmosphere due to their high global warming potentials.

In an attempt to improve the efficiency of the process, the operating temperature was reduced to 220.15 K for the perfluorocarbon absorption processes. This generally resulted in higher absorption of the flue gas of interest, but the emission of perfluorocarbons into the atmosphere was still greater than that of the DEPG, NMP and PC absorption processes. The solvent molar flow rate was then increased from 8000 to 10000 kmol/h, which resulted in even higher gas absorption and lower emissions. But the emissions into the atmosphere were still higher than trace amounts. Consequently, the two perfluorocarbons tested are not recommended for gas absorption. However, there are indications that PFC solvents with longer carbon chain length could constitute viable solvents, and are worthy of further study.

In addition to testing the solvent capacity, a solvent regeneration section, containing a series of three flash drums coupled with a stripping column, was added to both the perfluorobutane and perfluorohexane absorption processes. This resulted in less emission of the perfluorocarbon solvents into the atmosphere. However, with the new features, the perfluorocarbon solvents could not be recycled as it was impossible to strip off water vapour in the two gas absorption systems. Further processing would be required before the recycling took place.

A preliminary cost estimation was undertaken for the gas absorption systems using the perfluorobutane, perfluorohexane, DEPG and NMP solvents. This estimation revealed that the costs for both the perfluorobutane and perfluorohexane gas absorption systems were exorbitant, with the former being the most costly. These elevated costs were primarily attributed to the physical properties and the market prices of the perfluorocarbons.

A solution to the elevated costs associated with the PFC solvents, and their limited availability, could be the use of blended PFC solvents. The production of blended solvents can be cheaper because their separation during the manufacturing process is not as stringent as for pure solvents.

Following the results obtained for the C_4F_{10} and C_6F_{10} absorption processes and that of Heintz et al. (2008), PFC compounds with long carbon chain are recommended for further investigation as they promise to better meet the ‘ideal’ solvent criteria.

TABLE OF CONTENTS

LIST OF FIGURES

LIST OF TABLES

NOMENCLATURE

Symbols

a	Parameter, cubic equation of state
a_i	Activity
a_{ij}	Temperature-dependent parameter in NRTL
A	Parameter, empirical equations
b	Parameter, cubic equation of state
b_{ij}	Temperature-independent parameter in the NRTL
C_i	Adjustable parameters (Mathias-Copeman)
f_i	Fugacity, pure species i
G	Molar or specific Gibbs free energy
l_{ij}	Binary interaction parameter
k	Coverage factor
k_{ij}	Binary interaction parameter
n	Number of moles
n_i	Number of moles, species i
P	Absolute pressure
q_1, q_2	Constant in the MHV1 and MHV2 mixing rules

R	Universal gas constant
T	Absolute temperature
V	Molar or specific volume
x_i	Mole fraction, species i, liquid phase
y_i	Mole fraction, species i, liquid phase
z	Co-ordination number
Z	Compressibility factor

Greek letters

α	Function, cubic equation of state
α_{ij}	The non-random parameter in the NRTL liquid-phase model
Γ_i	Integration factor
γ_i	Activity coefficient, species i in solution
μ_i	Chemical potential, species i
τ_{ij}	Adjustable parameter in the NRTL liquid-phase model
Φ_i	Ratio of fugacity coefficients and Poynting correction factor
ϕ_i	Fugacity coefficient, pure species i
ω	Acentric factor

Superscripts

comb	Combinatorial
id	Denotes value for an ideal solution

l	Denotes liquid phase
res	Residual
sat	Property evaluated at the Saturation pressure of the component
v	Denotes vapour phase

Subscripts

c	Critical property
$calib$	Calibration
$corr$	Correlation
exp	Denotes an experimental value
i, j	Component identification
ij	Interaction between components i and j
r	Reduced property
rep	Repeatability

Overbars

¯	Partial molar property
^	Property of a component in a mixture

Abbreviations

AAD	Average Absolute Deviation
ASOG	Analytical solution of groups
CFCs	Chlorofluorocarbons

COSMO	Conductor-like Screening Model
COSMO-SAC	Conductor-like Screening Model-Segment –Activity Coefficient
COSMO-RS	Conductor-like Screening Model-Real Solvation
DDB	Dortmund Data Bank
DDBSP	Dortmund Data Bank Software Package
DEPG	Dimethyl ether of polyethylene glycol
EoS	Equation of state
FEI	Fluorochemical Expansion Initiative
GC	Gas chromatograph
GWP	Global Warming Potential
HPVLE	High-Pressure Vapour-Liquid Equilibrium
LLE	Liquid-Liquid Equilibrium
MC	Mathias-Copeman
MHV1	Modified first order Huron-Vidal mixing rule
MHV2	Modified second order Huron-Vidal mixing rule
NMP	N-Methyl-2-pyrrolidone
NRTL	Non-Random Two-Liquid activity coefficient model
PC	Propylene carbonate
PFCs	Perfluorocarbons
PR	Peng-Robinson
PSRK	Predictive Soave-Redlich-Kwong

ROLSI	Rapid Online Sampler Injector
SRK	Soave-Redlich-Kwong
SS	Stainless Steel
SV	Stryjek Vera alpha function
TCD	Thermal conductivity detector
UNIQUAC	Universal QUasi-Chemical Activity coefficient model
UNIFAC	UNIQUAC functional-group activity coefficient model
VLE	Vapour-liquid equilibrium
VLLE	Vapour-liquid-liquid equilibrium
WS	Wong and Sandler mixing rule

1

CHAPTER ONE

INTRODUCTION

The global demand for energy provision to meet social and economic development has been increasing since the steam engine launched the industrial revolution. This rise in global energy demand is primarily attributed to population growth and improvement to the standard of living. In many societies, energy provides services to meet basic human needs (e.g., lighting, water, cooking, heating and cooling, education, transportation, recreation and communication) and to serve productive processes. Since approximately 1850, fossil fuel (coal, oil and gas) usage has significantly increased to dominate energy sources, leading to high emissions of greenhouse gases which contribute to climate change (IPCC, 2011).

Greenhouse gas (GHG) emissions, resulting from the provision of energy services, have contributed significantly to historic anthropogenic GHG emissions (~75%) (IPCC, 2011), increasing, in part, the global average temperature of the earth. This rise in temperature is mainly driven by emissions of carbon dioxide (CO_2) but other greenhouse gases, such as methane (CH_4), nitrous oxides (NO_x) and fluorinated gases, also play a part (IPCC, 2011). Their global warming potential (GWP) are listed in Table 1.1.

Research conducted by the International Energy Agency (IEA) reveals that fossil fuels currently account for over 80% of the world's primary energy and this could probably remain so for some time (Gale et al., 2007). Consequently, global concentration of GHGs can grow unless significant changes are made to energy policies and practices.

Table 1.1: The GWP values and the lifetime of GHG that contribute significantly to the rise of the global average temperature [data taken from IPCC/TEAP (2005)]

			Global Warming Potential for Given Time Horizon		
Chemical Name	Chemical Formula	Lifetime (years)	20 -yr	100-yr	500-yr
Carbon dioxide	CO_2	see below[a]	1	1	1
Methane[b]	CH_4	12[b]	72	25	7.6
Nitrous Oxide	N_2O	114	289	298	153

[a] The CO_2 response function used in this report is based on the revised version of the Bern Carbon Cycle model (Joos et al. 2001) using a background CO_2 concentration value of 378 ppm. [b] The perturbation lifetime for methane is 12 years as in the IPCC third assessment report (TAR). The GWP for methane includes indirect effects from amelioration of ozone and stratospheric water vapour.

Efforts to address the issue of climate change, due to current energy practices, have resulted in the development of a number of mitigation options: control of energy consumption, fossil fuel switching, renewable energy, nuclear power, and flue gas capture technologies. A review of the mitigation options reveals the following (IPCC, 2011):

- control of energy consumption has been satisfactory but efficiency on its own is enough to achieve significant reduction in emissions of GHGs;
- switching from high-carbon to low-carbon fossil fuels is a viable option but is restricted to availability of the fuels;
- nuclear energy is feasible and provides up to 6% of the world's energy, but the need for safe disposal of radioactive wastes from nuclear reactors is a serious unresolved problem; and
- wider use of renewable energy has shown substantial potential, but the world has not yet learned to use efficiently the endless "free" energy from the sun, tides, winds etc. In addition, there are not nearly enough dams or waterfalls to provide sufficient hydroelectric power to meet the world's primary energy needs (Felder and Rousseau, 2005).

This demonstrates that current energy practices will continue for the foreseeable future and that while fossil fuels are still the primary source of the world's energy, flue gas capture technologies, geared to minimize environmental damage, can be considered as a near to medium term mitigation option.

Flue gas capture technologies involve capturing environmentally unfriendly gases emitted by power generation facilities as a result of the combustion/gasification of fossil fuels, or from natural-gas processing from fossil fuels. The gases are captured via a flue prior to their exit into the atmosphere and thereafter, the environmentally unfriendly ones are selectively removed via gas absorption systems. The captured gases are thereafter separated and used in different applications (Speight, 2002). Appendix A, Table A.1 lists the common flue gas components and their industrial applications.

The three most commonly-used modes for capturing flue gases produced by fossil fuels are the pre-combustion, oxy-fuel, and post-combustion methods. The pre-combustion method for capturing flue gas from advanced power generation facilities using the integrated gasification combined cycle (IGCC) has gained much attention. Here, the flue gas contains high concentrations of CO_2 and CH_4, which contribute to the increased global average temperature. Numerous technologies have been developed for pre-combustion capture. The most commonly used technologies include absorption processes, adsorption processes, membrane gas separation processes, cryogenic fractionations and gas hydrates (Li et al., 2011).

Absorption processing is the most favoured technology available for flue gas capture and can be categorized based on the solvent used, i.e. physical, chemical and mixed chemical/physical solvent. The chemical absorption process generally involves the use of amine-based solvents, such as monoethanolamine (MEA), diethanolamine (DEA) and methyldiethanolamine (MDEA) (Kohl and Riesenfeld, 1985), whilst the physical absorption process uses solvents such as methanol (Rectisol®), propylene carbonate (Fluor solvent ™) or *N*-Methyl-2-pyrrolidone (Purisol®) (Gielen, 2003). A comparison between chemical and physical solvents shows that the chemical reactions taking place in a chemical solvent are responsible for raising the overall absorption rate (Riesenfeld, 1970). Chemical solvents also contribute to corrosiveness and a high energy requirement for solvent regeneration. One should also note that a chemical solvent is efficient only if a chemical reaction takes place. In a physical process, however, absorption

entails a rearrangement of the molecules of the solvent to accommodate flue gas molecules, and no chemical reaction is involved.

Physical solvents are favoured over chemical solvents for a high pressure concentrated flue gas stream. Physical solvents are not efficient at low partial pressures because the compression of gas for physical absorption is expensive. However, if the gas is available at high pressure, physical solvents can be a better choice than chemical solvents. The composition of the feed gas also plays an essential role in the choice of the best absorption solvent. If the concentration of heavy hydrocarbons, such as pentanes, is high in the feed gas, a physical solvent may not be the best option due to high co-absorption of hydrocarbons. The use of physical solvents, in general, is recommended for synthesis gas (syngas) treatment, since it does not contain significant amounts of hydrocarbons, and syngas is generally available at high pressure.

This study sets out to consider some physical-solvent processes for flue gas capture. Physical solvents possess features such as high loadings at high flue gas partial pressures, stability, and generally, a lower energy requirement for solvent regeneration. However, when one considers an 'ideal' solvent for physical absorption, the following solvent properties are sought after: high capacity, high selectivity for environmentally unfriendly gases, low vapour pressures to prevent solvent loss, low viscosity to allow easy mass transfer, high chemical and thermal stability, zero environmental impact and availability at low cost (Korens et al., 2002). Unfortunately, no solvent has yet been identified that meets all these criteria, and therefore it has been a case of finding the best possible combination of features available among the current solvents for the specific task at hand. In addition, there is scope for exploring new alternative physical solvents that may provide more of the desired attributes; and this is how the current study was initiated: to investigate the use of perfluorocarbons (PFCs) as potential physical solvents for flue cleaning.

In the Thermodynamics Research Unit at the University of KwaZulu-Natal (South Africa), potential uses for fluorochemicals has attracted considerable interest, in collaboration with the Centre Thermodynamics of Processes (CTP) at MINES ParisTech (France), and with some chemical industries. These fluids present a very interesting class of chemicals because of their atypical properties. Perfluorocarbons find applications in various domains. They are used as surfactants, blood substitutes, and anaesthetics in the medical sector; as substitutes for chlorofluorocarbons (CFCs) and hydrochlorofluorocarbons (HCFCs) in the refrigeration

industry; and as solvents in the chemical industry. In this instance, the focus is on their use as potential enhancing agents in separation processes.

The present study was initiated to investigate the use of perfluorocarbons (PFCs) as potential physical solvents for flue gas cleaning of environmentally unfriendly gases in an advanced power generation facility using an integrated gasification combined cycle (IGCC). It is significant that flue gas from IGCC is available at high pressure and generally contains CO_2, CO, H_2, H_2O, N_2, Ar, CH_4, NH_3 and H_2S, and therefore, the focus is not only on capturing CO_2 and CH_4 but it is also on other gases, such as: H_2S and CO. In sum, this study focuses on capturing CO_2, CH_4, H_2S and CO selectively from the flue gas. One should note that CO_2 and H_2S are acid gases as in mixture with water, they form acidic solutions. Common flue gas components from coal-fired power generation facilities such as NO, O_2 and light hydrocarbons would require future investigation.

Accurate phase equilibrium data are essential to process design and simulations. However, vapour-liquid equilibrium data for systems involving perfluorocarbons and common flue gas components are virtually non-existent.

Consequently, the objectives assigned to this study include:

- A comprehensive literature review on perfluorocarbon compounds and current commercial physical solvents in flue gas capture;
- Measurement of isothermal phase equilibrium data for binary systems containing two perfluorocarbons, perfluorobutane (C_4F_{10}) or perfluorohexane (C_6F_{14}), with common flue gas content such as: light hydrocarbons, CO_2, CO, O_2, H_2, N_2 and H_2S, etc.;
- Modelling of experimental phase equilibrium data to obtain binary interaction parameters that can be used in chemical process optimization software;
- Proposal of a physical solvent separation process for the treatment of flue gas;
- Simulations of the proposed separation process using the binary interactions mentioned above; and
- Bench-marking of the proposed separation process against current commercial processes.

One should note that the primary focus of this study is phase equilibrium data measurement and thermodynamic modelling for binary systems composed of C_4F_{10} and C_6F_{14} with flue gas components such as CO_2, H_2S, CH_4, CO, NO, O_2, H_2, N_2, etc. The results obtained will then be used, for illustration purpose, in the design of gas absorption systems using C_4F_{10} and C_6F_{14} as physical solvents.

To this end, isothermal phase equilibrium data measurements were undertaken using two experimental apparatuses based on the static analytic method. The measured binary systems include:

- Perfluorobutane (C_4F_{10}) with CO, NO, H_2S, CH_4, O_2, N_2 or H_2
- Perfluorohexane (C_6F_{14}) with CO, H_2S, CH_4 or C_2H_6

Phase equilibrium data for binary systems such as C_4F_{10} with C_2H_6, or CO_2 and CO_2 + C_6F_{14} were taken from reliable literature sources (El Ahmar et al., 2010; Valtz et al., 2011; Gomes and Pádua, 2003). Phase equilibrium data for binary systems such as C_4F_{10} or C_6F_{14} with H_2O, COS, NH_3, Ar, H_2, O_2 and N_2 were predicted using the predictive Soave-Redlich-Kwong model in conjunction with either the Conductor-like Screening Model – Segment Activity Coefficient (COSMO – SAC) (Lin and Sandler, 2002), with the sigma profile taken from the consortium version of the Dortmund Data Bank, or with the Dortmund modified UNIversal Functional Activity Coefficient (UNIFAC) (Gmehling and Schiller, 1993).

The measured, the predicted, and the literature-derived phase equilibrium data, were all modelled via the direct method using various combinations of thermodynamic models, including: the Peng-Robinson (PR) (Peng and Robinson, 1976) or Soave-Redlich-Kwong (SRK) (Soave, 1972) equation of state with the Mathias-Copeman (MC) (Mathias and Copeman, 1983) or Stryjek-Vera (SV) (Stryjek and Vera, 1986) alpha function and the Wong-Sandler (WS) (Wong and Sandler, 1992), modified Huron-Vidal 1 and 2 (MHV1 and MHV2) (Michelsen, 1990b and Dahl and Michelsen, 1990) or predictive Soave-Redlich-Kwong (PSRK) (Holderbaum and Gmehling, 1991) mixing rule utilizing the non-random two-liquid (NRTL) (Renon and Prausnitz, 1968) activity coefficient model, thereby obtaining the binary interactions parameters.

It is notable that although only binary systems were measured in this study, the NRTL activity coefficient model based in a semi-empirical way on the two-liquid theory of Scott, can be extended to multicomponent mixtures. The computer programmes used to obtain the NRTL parameters for binary mixtures by fitting vapour-liquid equilibrium data and to predict multicomponent vapour-liquid equilibrium data can be found in Appendix K of Renon (1966).

The binary interaction parameters obtained from the correlation of the experimental and predicted data were utilized in the design of the gas absorption systems using the perfluorobutane or perfluorohexane solvent. The design was undertaken in the Aspen Plus® V8.0. The gas absorption results obtained were, thereafter, bench-marked against that of current commercial physical solvents such as the Dimethyl Ether of Polyethylene Glycol (DEPG), *N*-Methyl-2-Pyrrolidone (NMP) and Propylene Carbonate (PC).

2

CHAPTER TWO

LITERATURE REVIEW

2.1 Introduction

This study investigates the use of perfluorocarbons as potential physical solvents for flue gas cleaning in power generation facilities that expel gases under high pressure as it is the case with the integrated gas combined cycle (IGCC). As a result, this chapter begins with a brief review on the operating conditions of two main types of coal power plants, i.e. pulverised coal-fired and integrated gasification combined cycle (IGCC) plants, followed by their flue gas capture modes. Thereafter, a discussion is provided on general features of gas absorption processes, such as current commercial physical solvent absorption processes, to provide some background for a detailed description of a perfluorocarbon absorption process. This discussion presents the design variables that must be taken into consideration in designing a process for flue gas removal.

As briefly explained in Chapter 1, by 2004 fossil fuels (coal, oil and gas) accounted for over 80% of the world's primary energy, and these fuels will continue to be the primary energy source for at least the next few decades (IEA, 2006b).

Fossil fuels, such as coal, are a reliable source of energy for generating electricity worldwide. On an international level, the use of coal is widespread, accounting for nearly 36 % of the world's electricity production. Numerous processes have been developed to convert solid coal into a liquid or gaseous form for use as fuel in the production of electricity. These include: combustion and gasification. As a result, there are presently two principal types of coal power plants. The pulverised coal-fired plants and the integrated gasification combined cycle (IGCC) plants.

2.2 Pulverised coal-fired power plants

In a pulverised coal-fired power plant, as illustrated in Figure 2.1, raw coal is transported on conveyor belts to a pulveriser where it is ground to fine powder for efficient combustion. The coal is, thereafter, burnt with air in a steam generator (e.g. boiler) by means of high temperature oxidation reactions. The resulting high pressure energy (steam) flows through a series of steam turbines, which spin an electrical generator to produce electricity. One should note that the steam that drives the turbines is cooled and condensed in cooling towers for easy pumping and recycling to the steam generator.

The gases released during the coal combustion process are generally treated by means of filtration, to remove ash, with the remaining gases emitted via a flue gas stack into the atmosphere.

However, depending on the quality of coal, the combustion process may produce a significant concentration of pollutants such as NOx, SOx and particulates, which are environmentally unfriendly. Hence, cleaning processes such as desulphurisation or denitrification are employed prior to any emissions.

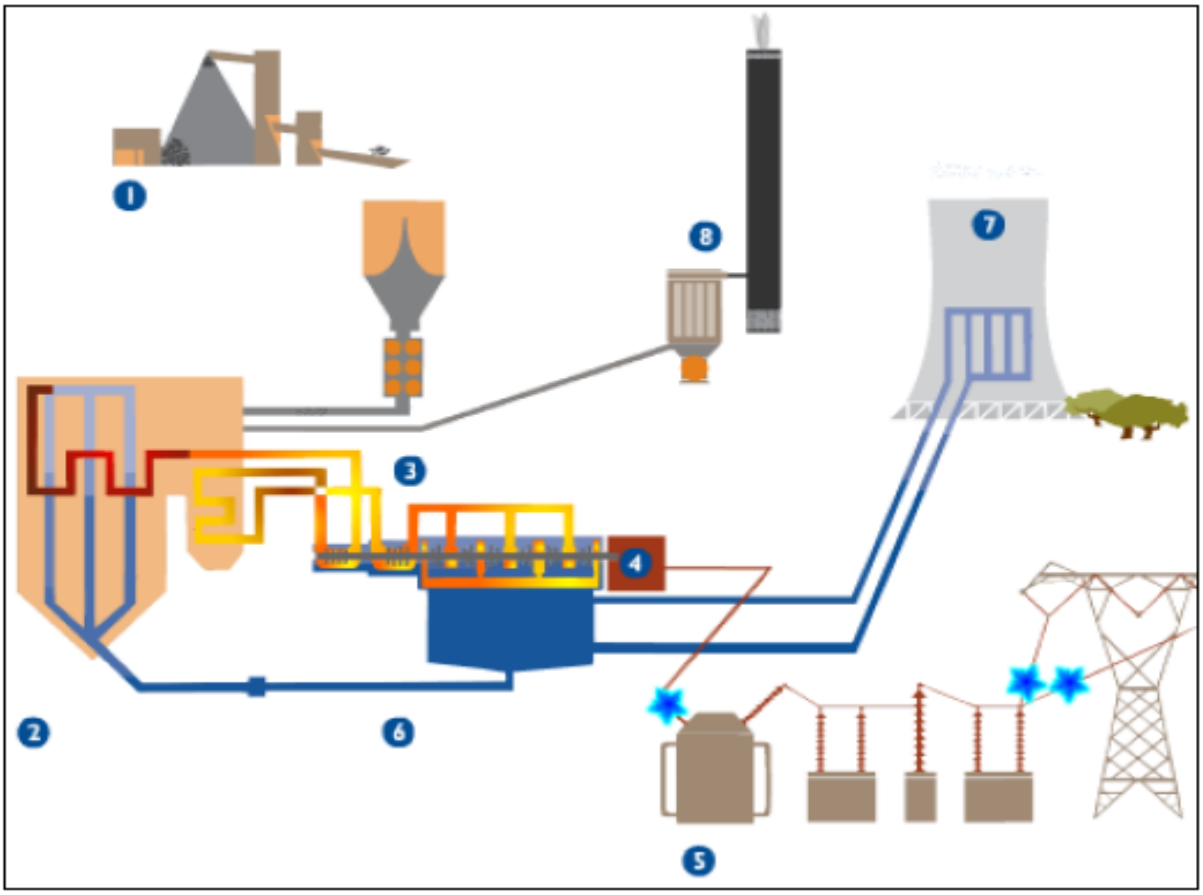

Figure 2.1: Eskom pulverised coal-fired power plant as taken from (Eskom, 2011). 1. Coal mine; 2. Boiler; 3. Superheated steam in turbines; 4. Generator rotor; 5. Transmission lines; 6. Condensed water; 7. Cooling towers; 8. Chimney.

The pulverised coal-fired power plants are by far the most established and abundant power plants. They account for more than 90 % of all coal-fired stations currently in operation (Breeze, 2014). One should note that coal-fired power plants supply approximately 41 % of global electrical energy, whilst in some countries a much higher percentage is reported (WCA, 2012). However, their inefficiency is still of great concern as combustion of large quantity of coal is required to generate electricity, which results in a higher emission of environmentally unfriendly gases.

The typical flue gas composition at the Eskom 650MW Highveld coal-fired power plant, as given by Ebrahim Patel (production engineer Integration Coal/ Air Pollution Control, Eskom), can be found in Table 2.1.

Table 2.1 Flue gas composition (typical at 650MW Highveld Power Plant) at Eskom

Flue gas details (Typical at 650MW Highveld Power Plant)	
Temperature (K)	414 - 416
Pressure (kPa)	84
Flow gas rate (Kg/s)	+/-950
Component	mole %
CO_2	12 - 15 %
H_2O	5 -8 %
O_2	5 - 7 %
CO	< 100 ppm
NOx (NO2)	450 - 1275 ppm
SO_2	700 - 1400 ppm
N_2	balance

2.3 Integrated gasification combined cycle (IGCC) power plants

Integrated gasification combined cycle (IGCC) power plants have been developed to improve the efficiency and environmental performance of coal-fired power generation. In IGCC power plants, as illustrated in Figure 2.2, coal is initially dried and fed into a gasifier, where thermal decomposition of coal takes place in an oxidant environment (air or pure oxygen) with a controlled carbon/oxygen ratio to maintain the reduction conditions of the global process, which results in synthesis gas or syngas (a fuel gas mixture consisting mainly of carbon monoxide, hydrogen, carbon dioxide and water). The syngas is subsequently treated for particulate removal, cooled down (not shown in Figure 2.2), as required for the shift reaction, and thereafter stripped of environmentally unfriendly gases using processes such as sulfur and nitrogen removal (depending on their concentration), carbon capture and storage, etc. The remaining gas, which is mainly hydrogen, is thereafter burnt to generate high pressure steam which is used in a gas turbine combined cycle plant to generate electricity.

One should note that the electricity generated is not just for commercial use but to heat the steam for the gasifier and the shift convector as well. In addition, it can also be used to achieve the necessary pressure and temperature for the air separation unit.

Table 2.2 shows a typical flue gas composition from the gasification of Illinois No. 6 bituminous coal (Doctor et al., 1994).

.

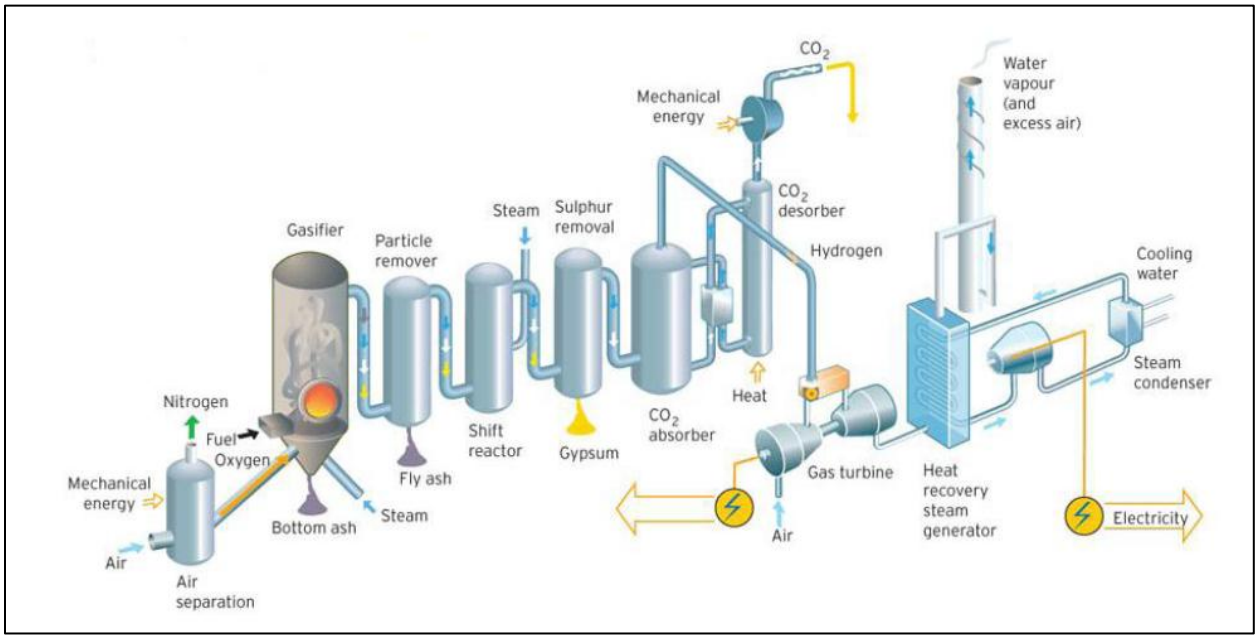

Figure 2.2: Integrated Gasification Combined Cycle (IGCC) power plant with a CO_2 capture unit (Arshad, 2009).

Table 2.2: Details of the flue gas from the gasification of Illinois No. 6 bituminous coal (Doctor et al., 1994) as taken from Aspen Plus® V 8.0.

temperature (K)	293.24
pressure (MPa)	6.881
flow rate (kmol/h)	7990
Component	composition (mole %)
CO	0.439
CO_2	24.62
H_2	31.86
H_2O	0.352
N_2	41.48
Ar	0.503
CH_4	0.731
NH_3	0.017
H_2S	0.002

2.4 Comparison between PC and IGCC power plants

This section presents the performance and cost measures for the PC and IGCC new plants, ranging from 300 to 800 MW in terms of CO_2 capture, as summarised by the Intergovernmental Panel on Climate Change and presented in Table 2.3. One should note that this study does not focus only on the capture of CO_2 but also on other environmental unfriendly gases. However, CO_2 has been given considerable attention due to its global warming potential. This has led to the existence of extensive documentation on CO_2 in relation to that of the other environmentally unfriendly gases.

Table 2.3: Summary of new PC and IGCC plants performance and CO_2 capture based on current technology (IPCC, 2005)

Performance and Cost Measures	New PC plant			New IGCC		
	Range		Rep. Value	Range		Rep. Value
	low	high		low	high	
Emission rate without capture (kg CO_2 MWh^{-1})	736	811	762	682	846	773
Emission rate with capture (kg CO_2 MWh^{-1})	92	145	112	65	152	108
Percent CO_2 reduction per kWh (%)	81	88	85	81	91	86
Plant efficiency with capture LHV basis (%)	30	35	33	31	40	35
Capture energy requirement (% more input MWh^{-1})	24	40	31	14	25	19
Total capital requirement without capture (US$ kW^{-1})	1161	1486	1286	1169	1565	1326
Total capital requirement with capture (US$ kW^{-1})	1894	2578	2096	1414	2270	1825
Percent increase in capital cost with capture (%)	44	74	63	19	66	37
Cost of electricity without capture (US$ MWh^{-1})	43	52	46	41	61	47
Cost of electricity with capture (US$ MWh^{-1})	62	86	73	54	79	62
Increase in cost of electricity with capture (%)	18	34	27	9	22	16
Percent increase in cost of electricity with capture (%)	42	66	57	20	55	33
Cost of CO_2 captured (US$/t$CO_2$)	23	35	29	11	32	20
Cost of CO_2 avoided (US$/t$CO_2$)	29	51	41	13	37	23

Analysis of Table 2.3 reveals that the CO_2 emission rate without capture from an IGCC plant may be higher than that of a PC plant. However, if coupled with a CO_2 capture method, less CO_2 emission rate can take place in an IGCC plant than in a PC plant. One should also note that the capture energy is higher for a PC plant as opposed to that of an IGCC plant.

Analysis of Table 2.3 also shows that the total capital requirement of an IGCC plant with CO_2 capture is slightly lower than that of a PC plant with CO_2 capture. Whereas the total capital requirement of an IGCC plant without CO_2 capture is slightly higher than that of a PC plant without CO_2 capture. This is due to the fact that CO_2 capture is expensive when fitted or retrofitted in PC plants, as the flue gas to be treated is generally emitted at low CO_2 partial pressure and high temperature, which do not favour low cost operations.

IPCC (2005) reported that for a modern coal-fired power plant fitted with CO_2 capture, using an amine-based absorber, increases the cost of electricity generation by between 40 and 70%, while reducing the CO_2 emission rate (KWh) by approximately 80%. However, in an IGGC system using a shift reactor followed by a physical absorption system, while the CO_2 emission rate is similar to the previous method, the cost of electricity generation increases by approximately 20 to 50 %. This is largely due to that fact that the flue gas to be treated is generally at high CO_2 partial pressure which requires less energy for the capture process as opposed to the combustion-based systems.

One should note that in IGCC plants there is a high energy requirement in the air separation unit for the production of pure oxygen to feed the gasifier. To overcome this challenge, Jones et al. (2011) summarised various methods aiming at optimizing the cryogenic air separation unit, which includes finding the ideal operating temperatures, gas and liquid handling and gas turbine operating pressures.

In light of the above, while most industries consider the modification of existing PC plants as a promising mid-term option, it is commonplace that the IGCC system is considered the better longer-term option for new coal power plants.

2.5 Capture methods

The increasing generation of greenhouse gases from coal power plants, which affect the climate, has been of great concern worldwide. Efforts to address this concern have led to greenhouse gas capture technologies as a near to medium term mitigation option. Depending on the source of flue gas, several capture methods have been suggested and implemented, but a few have gained acceptance from industrial, political and societal standpoints. Three methods for flue gas capture that are generally accepted as suitable for commercial deployment in the near to medium term are:

- pre-combustion capture for gasification (coal) or reforming (natural gas);
- post-combustion capture for existing facilities; and
- oxy-fuel combustion capture sometimes referred to as oxy-firing or oxy-combustion capture.

The three methods for CO_2 capture are schematically illustrated in Figure 2.3 as taken from Rackley (2010). Oxy-fuel capture is still at an early stage of development whilst post-combustion and pre-combustion captures are economically feasible under specific conditions (Rackley, 2010).

Pre-combustion capture refers to the removal or separation of CO_2 from fossil fuels before the combustion process. This capture method is used in the manufacturing of fertilisers, chemical gaseous fuel and coal power generation facilities (IPCC, 2005). Pre-combustion capture related to IGCC plants is shown in Figure 2.2, where the fossil fuel is converted into a mixture of H_2 and CO_2 via gasification and shift reaction.

The separation of CO_2 and H_2 can be achieved using numerous technologies. In Figure 2.2, CO_2 capture is achieved, after the shift reaction, via a gas absorption system containing an absorber and a stripper. In this process approximately 90% of CO_2 can be captured. It is notable that in the pre-combustion capture method, the flue gas is available at high pressure. This condition is desirable as many capture methods are efficient only at high pressures. Currently, commercially available pre-combustion capture technologies are used to capture CO_2 in several industrial applications. The same technologies used for pre-combustion capture in integrated gasification

combined cycle (IGCC) plants are employed in large-scale production of hydrogen (IPCC, 2005).

Despite its efficiency, however, pre-combustion capture technology requires either significant costly modifications of existing power generation facilities or construction of new ones.

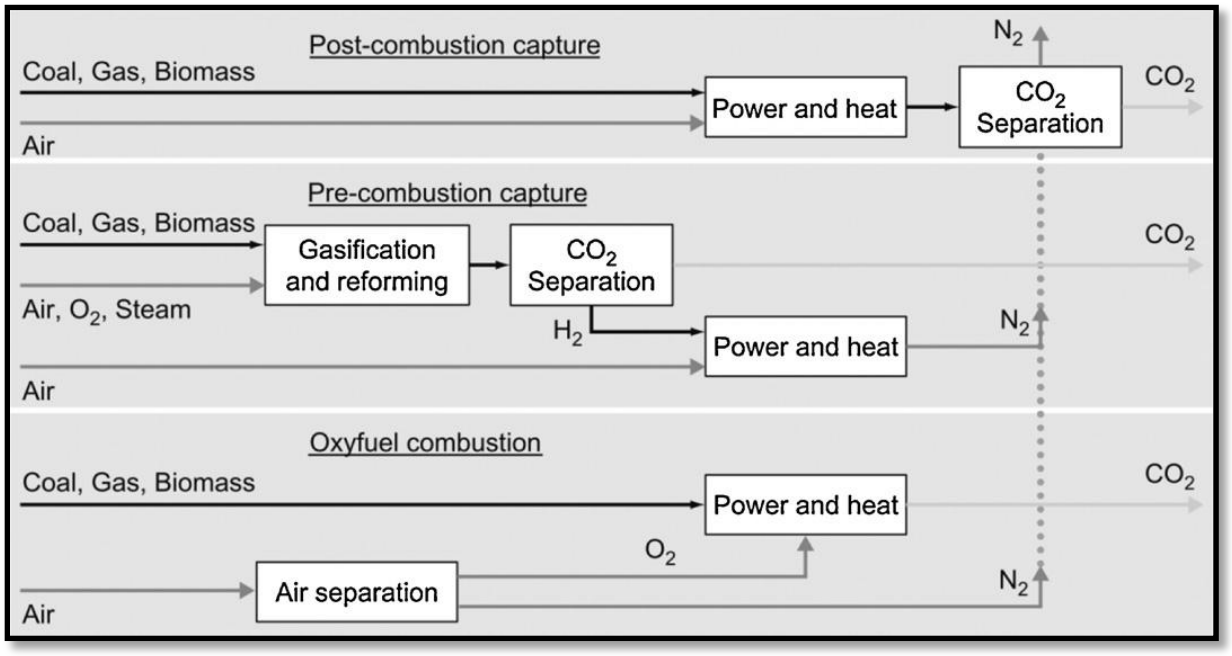

Figure 2.3: Three methods for CO_2 capture from power generation facilities as taken from (Rackley, 2010).

An oxy-fuel combustion system uses a physical separation process. This is due to the fact that in oxy-fuel combustion, nearly pure oxygen is used in lieu of air, thereby eliminating the presence of nitrogen oxides (NO_x) in the flue gas. The flue gas is then composed mainly of a high CO_2 concentration (greater than 80% by volume) and H_2O, and is easily purified. The water is thereafter separated from the CO_2 by cooling and compressing the gas stream. The main drawback to this method is the stringent requirement of using pure oxygen, which is usually obtained by means of conventional cryogenic air separation. This contributes to the high cost of the oxy-fuel combustion capture method.

In post-combustion capture, one component, or more, from a gas mixture is/are selectively captured from the exhaust of a combustion process prior to emission into the atmosphere. This

method can be retrofitted to most of the existing power generation facilities or fitted to new ones. Post-combustion capture methods have been commercially deployed for the removal of minor contaminants such as Hg, SOx or NOx gas, but materials for the separation of a gas such as CO_2 have not yet been satisfactorily developed (Li et al., 2011).

A comparison between pre-combustion and post-combustion capture methods, based on PC and IGCC power plants, reveals that there is no clear preference, since both approaches make sense in different circumstances. For retrofit applications, post-combustion is preferred.

However, in this study, the pre-combustion capture method applied to an IGCC plant is the subject of research interest mainly due to the availability of flue gas at high pressure, which provides a necessary condition for the use of physical solvent in an absorption process.

Figure 2.4 schematically illustrates the most commonly used technologies for the capture of flue gases at high pressure, which are by means of the following:

- absorption;
- cryogenics;
- membrane;
- microbial/algae; and
- adsorption.

Absorption is the most commonly used, and established, technology for flue gas capture. In absorption (also known as gas absorption or gas scrubbing), a gas mixture is put in contact with either a liquid or a gas (the absorbent or solvent) in order to selectively dissolve one component or more of the gas mixture (the solute or absorbate). In absorption, chemical and physical solvents, or a mixture of these, are commonly used.

Chemical absorption involves the reaction of one or more components of the flue gas with a chemical solvent to form complexes or chemical compounds. The regeneration of the chemical solvent is achieved by means of the application of heat to the solution. In general, chemical absorption uses alkaline solutions such as carbonates and amines (monoethanolamine (MEA), diethanolamine (DEA) and methyldiethanolamine (MDEA)) (Kohl and Riesenfeld, 1985).

However, based on both the composition and the operating conditions of the feed gas, different amines and carbonates can be chosen to meet the product gas specification.

Figure 2.4 shows a schematic diagram of the most commonly used technologies with their associated materials for CO_2 capture as taken from (Li et al., 2011).

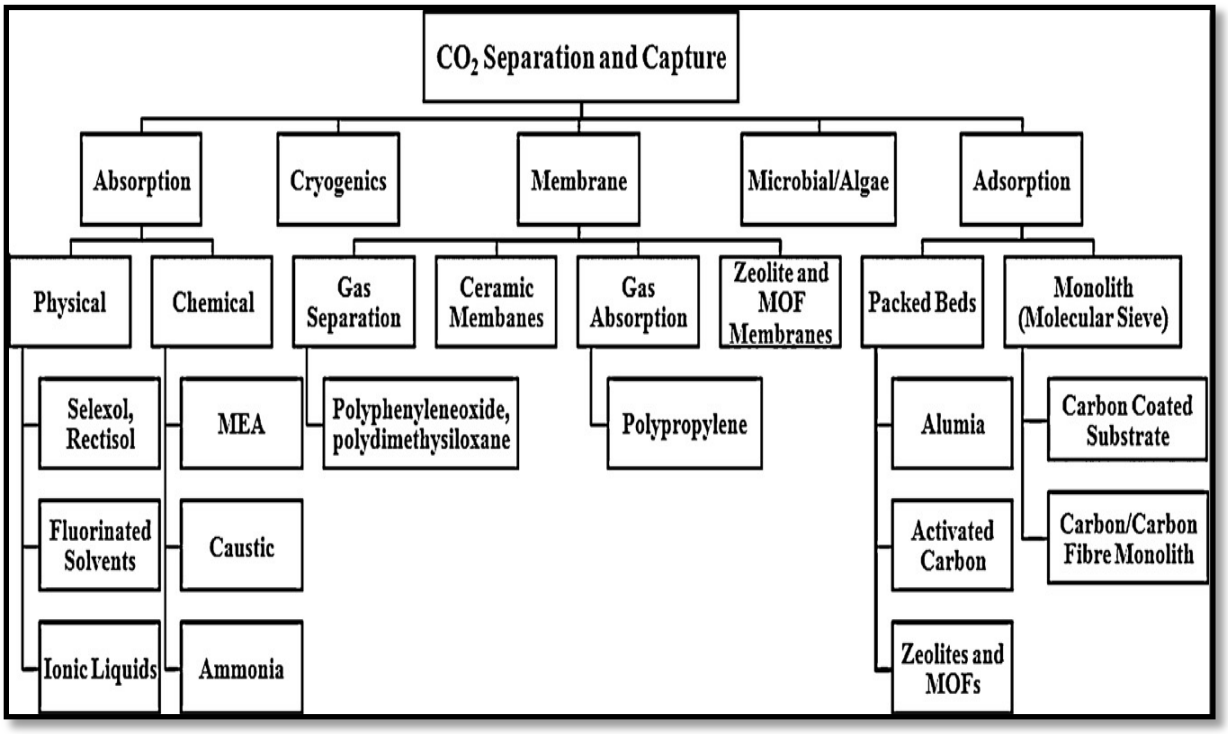

Figure 2.4: Most commonly used technologies with associated materials for CO_2 capture as taken from (Li et al., 2011).

In physical absorption, there is no reaction taking place but a mere rearrangement of the solvent molecules to accommodate flue gas molecules. Hence, the solvent regeneration is generally achieved by a pressure swing step (also known as pressure reduction), using a series of flash drums or application of heat, in some cases, where the flash drum desorption is inadequate. The heat required for solvent regeneration in physical absorption is less than that required in chemical absorption. Typical physical solvents include Selexol (dimethyl ether of polyethylene glycol or DEPG), Rectisol® (methanol) and Purisol® (N-methyl-2-pyrrolidone or NMP). A comprehensive list of commercial physical solvents can be found in gas purification (Kohl and Riesenfeld, 1985).

One should note that the term acid gas refers to any gas mixture that forms an acidic solution when mixed with water, i.e. hydrogen sulphide and carbon dioxide. In some cases, a mixture of both physical and chemical solvents is used for acid gas removal. The most commonly used examples are Sulfinol which is a mixture of sulfonate and the amines MDEA or DIPA, and Amisol, a mixture of methanol and secondary amines (Bullin, 2003). These blends take advantage of the properties of particular constituents under specific conditions.

Cryogenic separation has been used in liquid separation for a number of years. This technology utilises the difference in boiling points of components in a mixture to enable separation by distillation under cryogenic conditions. Cryogenic separation can also be used for flue gas capture; but high energy is required for practical applications, which increases costs. Nevertheless, this technology can be used in oxy-fuel combustion as it is effective for flue gas containing high concentration of CO_2 (Li et al., 2011).

Membrane separation processing of flue gas is achieved by means of pressure-driven mass transfer through a semipermeable membrane, allowing one component or more to move faster than the other. Membrane separation has been extensively used in nitrogen separation from air, CO_2 recovery in natural gas processing, and hydrogen recovery in ammonia synthesis, but it has not yet been commercially used for CO_2 recovery from flue gas. However, the membranes used for the aforementioned applications could, in principle, be used for flue gas capture. These processes offer the advantages of being less energy intensive, environmentally friendly, reliable and simple, but their development and industrial implementation lag far behind those of absorption processes.

Microbial/algae as a production source of biofuel have generated interest in a number of research groups worldwide. These microorganisms are generally cultivated in large open ponds of seawater where CO_2 is used as a carbon source during their photosynthesis. Yusuf (2007) reported that microalgae cells contain about 50% carbon, in which 1.8 kg of CO_2 are captured or fixed by producing 1kg of microalgae biomass. Consequently, research has been diverted to using CO_2 as a carbon source to cultivate microalgae.

Tang et al. (2011) reported positive result from growing microalgae using either pure CO_2 or flue gas, aiming at carbon fixation and biomass production. However, using industrial flue gas to

grow microalgae is challenging as some of the microalgae trains are sensitive to the contaminants and the temperature of flue gas. Furthermore, the low solubility of CO_2 in water should be considered, as concentrated CO_2 could be released into the atmosphere prior to reaching the microalgae. Possible solutions to this challenge could be the use of microbubble technology or membrane sparged photobioreactor technology. These methods create tiny bubbles which ameliorate dissolution of CO_2 in water (Lam et al., 2012).

Adsorption is a physico-chemical phenomenon where components from a gas or liquid stream (adsorbate) diffuse to the surface of a solid (adsorbent) to which they bond or are held by weak intermolecular forces (Keller and Staudt, 2005). This feature allows an adsorbent regeneration by the application of heat (temperature swing) or by pressure reduction in some cases. To achieve a very large surface area for adsorption per unit volume, highly porous solid materials are required. Carbon is usually used as the adsorbing medium (Speight, 1993 and 1999). However current adsorption processes suffer from low adsorption capacity which constitutes a major barrier for its application in large scale power plant flue gas treatment.

A comparison between the most commonly used techniques for flue gas capture indicates that there is still potential for significant progress in each technology. Despite the advantages of each flue gas capture techniques aforementioned, the absorption process remains the most promising solution for flue gas capture, and is the process selected for this study. Thus, the rest of this chapter will provide a review of the absorption processes.

2.6 Absorption processes

2.6.1 Process description

The process flow diagram for an absorption process, in the main, consists of two distinct operations, namely, absorption and desorption. As can be seen in Figure 2.5, a gas mixture and a solvent stream are both introduced into the absorber, which contains either packing materials or trays, at levels corresponding to the bottom and the top, respectively. The gas mixture, flowing upwards, meets the solvent stream flowing downwards. The counter-current contact of the two streams enriches the solvent with one component or more of the gas mixture, referred to as the solute. The clean gas leaves through the top of the absorber whilst the rich solvent leaves through the bottom of the absorber.

The solvent regeneration procedure may vary depending on the type of solvent used. For a chemical solvent, regeneration is achieved by application of heat in a stripping unit. However, for a physical solvent, the rich solvent passes through a series of flash drums at successively lower pressures to achieve solvent regeneration. The top product of the first flash drum contains most of the dissolved non-acidic gases, which can be either re-compressed and mixed with the fresh gas feed to minimise their loss, or be routed to other facilities. The bottom product of each flash drum serves as a feed to the next flash drum until it yields lean solvent of sufficient purity for recycling.

Further purification can be achieved by vacuum flashing, by stripping with an inert gas or air, or by stripping with heat (thermal regeneration). The bottom product from either the last flash unit or the stripping unit together, with the make-up stream of fresh solvent is compressed and re-introduced into the absorber.

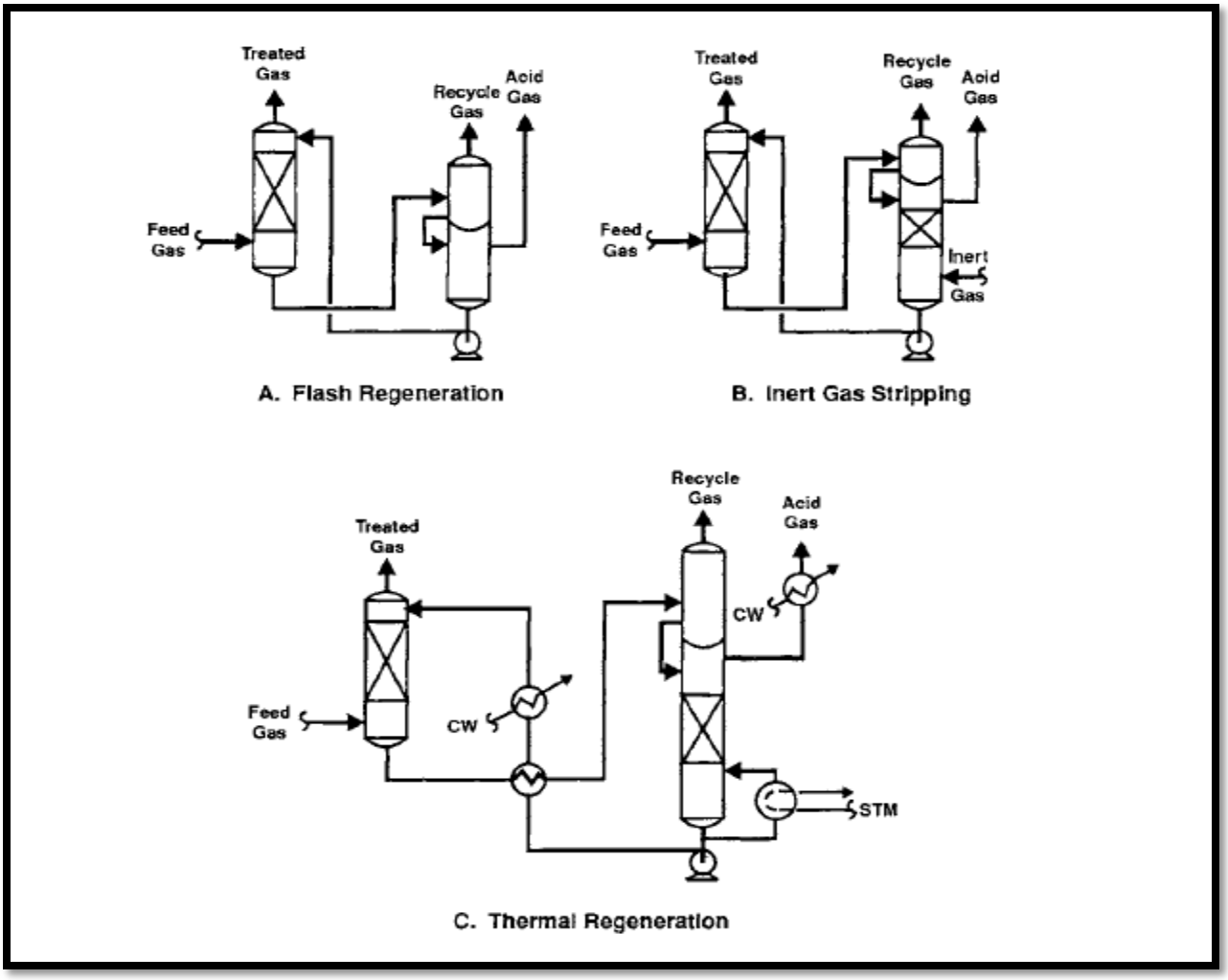

Figure 2.5: Simplified flow diagrams of physical absorption processes showing basic methods for solvent regeneration as taken from (Kohl and Nielson, 1997).

2.6.2 Solvent selection

This study focuses on using PFC solvents for the selective removal of CO_2, H_2S, CO and CH_4 from flue gas from the gasification of Illinois No. 6 bituminous coal (Doctor et al., 1994) as taken from Aspen Plus® V 8.0. This type of flue gas was chosen because it is available at high pressure and the concentration of flue gas of interest is high. These conditions are favourable for a physical absorption process.

There are various solvents used for flue gas removal. They are required to exhibit certain characteristics to render them suitable as solvents. According to Korens et al. (2002) and Letcher (2007), the key characteristics for consideration are: (1) capacity and selectivity, (2) vapour

pressure, (3) viscosity, (4) boiling point, (5) chemical and thermal stability, (6) environmental impact and (7) availability and cost.

Consequently, in this study, an 'ideal'solvent should enjoy the characteristics listed in Table 2.4.

Table 2.4: Characteristics of an 'ideal' solvent

Property	comment
Solubility	High solubility, high selectivity and high capacity for the target solutes (CO_2, H_2S, CH_4 and CO in this study) over other components in the gas mixture at reasonable operating conditions. Selectivity is useful in the preliminary selection of a solvent, whereas capacity reveals the quantity of a solvent used during the separation process. Hence, a solvent with a large capacity and high selectivity will require only a small quantity to be effective.
Vapour pressure	Low vapour pressure values at operating conditions to avoid solvent loss due to vapourisation.
Viscosity	Low viscosity as it leads to faster mass transfer and higher heat transfer rates and a decreased load in terms of pumping duties for the solvent (Mangers and Ponter, 1980).
Boiling point	A large boiling point difference between the solvent and the solutes (CO_2, H_2S, CH_4 and CO) is desirable for better separation and complete regeneration of the solvent through extractive distillation or stripping process (lei et al., 2003).

Table 2.4: Continued

Property	comment
Chemical and thermal stability	These characteristics are important as they improve the economy of the separation process. The occurrence of chemical and thermal instability may induce polymerization or decomposition reactions which will result in a loss of solvent regeneration potential (Letcher, 2007).
Environmentally benign	A solvent should be non-toxic for human health and environmental constraints, non-flammable and non-corrosive for handling and processing.
Availability	Last but not least, a solvent should be available at high purity at reasonable cost.

As outlined in Section 2.5, solvents are classified as chemical or physical. A chemical solvent reacts to form a chemical bond with one or more of the constituents of the gas mixture, whilst a physical solvent forms weaker interactions with the constituents of the gas mixture. This distinction governs procedures required for their regeneration.

A comparison between a physical and chemical solvent reveals that a chemical solvent is only efficient if a reaction can indeed take place whereas a physical solvent is generally preferred over a chemical solvent when the pressure for solutes of interest is high. This is due to the fact that the concentration gradient or the partial pressure difference between the solutes of interest, and the physical solvent constitute the driving force behind the acid gas removal process.

For CO_2 capture, the use of physical solvents is impractical at low partial pressures because the compression of gas for physical absorption is expensive. However, if the gas is available at high pressure, the use of physical solvents might be a better choice than chemical solvents. But if the

concentration of heavy hydrocarbons, such as pentanes, is high in the feed gas, physical solvent may not be the best option due to the high co-absorption of hydrocarbons.

In general, the use of physical solvents is recommended for synthesis gas (syngas) treatment, since they do not contain significant amounts of hydrocarbons and are generally available at high pressures.

Because of its corrosive tendency on equipment and degradation of the solvent, the presence of O_2 in a gas stream is not desirable in the case of chemical absorption. As a result, some processes use O_2 scavengers or inhibitors to counteract the oxygen activity. In addition, for chemical absorptions that use amine-based solvent, flue gas must contain very low levels of nitrogen and sulphur oxides. This is because SO_x and NO_x react with the amine-based solvent to produce stable salts, causing a steady loss of the solvent. An up-stream denitrification and desulfurization are therefore required. In contrast to chemical solvents, physical solvents are generally non-degradable and non-corrosive. However, one should note that some of the physical solvents may be toxic.

Despite the shortcomings associated with physical solvents, their advantages over chemical solvents, under certain conditions, have generated interest in their further development, which is the case in this study. To this end, a discussion on the potential of current commercial physical solvents will first be provided, followed by an in depth investigation of the perfluorocarbons that will be the main focus of interest.

2.6.3 Commercial physical solvent processes

Several physical absorption processes have been developed for acid gas removal. Those commonly used include Selexol (Dimethyl Ether of Polyethylene Glycol or DEPG), Rectisol® (methanol), Purisol® (N-methyl-2-pyrrolidone or NMP) and Fluor solvent processes. Table 2.5 lists properties related to these solvents.

Table 2.5: Commercial physical solvent properties (Bucklin and Schendel, 1985)

Commercial designation	Selexol	Purisol®	Rectisol®	Fluor solvent
Solvent	Dimethyl Ether Polyethylene Glycol (DEPG)	N-Methyl-2-Pyrrolidone (NMP)	Methanol	Propylene carbonate (PC)
Chemical formula	$(CH_3O(CH_2CH_2O)_xCH_3)$	C_5H_9NO	CH_3OH	$C_4H_6O_3$
Licence	Dow Chemical	Lurgi	Linde and Lurgi	Fluor Daniel
Maximum T (K)	448.15	—	—	338.00
Vapour pressure at 298.15 K (kPa)	9.730×10^{-05}	0.050	16.67	0.011
Dynamic viscosity at 298.15 K (Pa·s)	0.00580	0.00165	0.00060	0.00300
Normal boiling point (K)	548.00	477.44	337.85	514.85
Freezing point (K)	247.60	249.15	175.47	224.85
Molecular weight ($g \cdot mol^{-1}$)	280.00	99.130	32.042	102.09

2.6.3.1 Methanol (Rectisol Process)

There are numerous methanol-based processes for acid gas removal, e.g., the Rectisol process developed by Linde and Lurgi, and the Ifpexol process developed by Prosenat. The Rectisol process is one of the earliest physical absorption processes developed, and has been used for hydrate inhibition, dehydration, and for treating natural and synthesis gas streams (Hochgesand, 1970; and Kohl and Nielson, 1997). However, this process was originally designed and applied together with the Lurgi coal gasification process, mainly for the removal of acid gas, e.g., ammonia, gas naphtha, and cyanides, together with CO_2 and sulphur compounds. The absorption capacity of methanol, for these unwanted components made it the natural solvent of choice. As of 1996, it was reported that more than 100 Rectisol units were in operation or under construction (Lurgi and Linde, 1996).

Methanol has very low viscosity, which allows low operating temperatures for the Rectisol process, generally ranging between 273.15 K and 200.15 K. The low temperatures prevent high solvent loss due to vaporisation as a result of high vapour pressures. Under these operating

conditions, both H_2S and CO_2 are highly soluble in methanol, with the solubility of H_2S exceeding that of CO_2 by a factor of 5-6 (Hochgesand, 1970). This feature may lead to an off-gas rich in H_2S, even from gas mixtures containing low concentrations of H_2S. For this reason, the Rectisol process can attain concentrated H_2S streams suitable for the Claus plant feed.

On the other hand, low temperatures require deep refrigeration, which makes the Rectisol process energy intensive, leading to high capital and operating costs. However, this drawback can be outweighed by significant reduction of the solvent flow rate for CO_2 removal, as compared to other physical solvent processes. Methanol has low surface tensions and therefore does not foam. This solvent can be recovered from off-gas streams by backwashing with small amounts of water, followed by a simple distillation to separate the solvent/water mixture.

In conclusion, Methanol is chemically and thermally stable, but not at higher temperatures where acid oxidation occurs. Methanol is non-corrosive, and does not degrade. It is produced in large quantities and is availability at a reasonable cost.

2.6.3.2 Dimethyl Ethers of Polyethylene Glycol (DEPG) (Selexol Process)

The Selexol process utilises a mixture of Dimethyl Ethers of Polyethylene Glycol which has a chemical formula of $CH_3(CH_2CH_2O)_nCH_3$, where n is an integer ranging from 3 to 9. The Selexol process is mainly used for the removal of H_2S, CO_2 and mercaptans in natural and synthetic gas streams. The Selexol solvent has the advantage of selectively dissolving sulphur compounds over CO_2, which makes it desirable for partial oxidation processes. One should also note that the solvent will dehydrate natural gas if water is removed in the regeneration process.

In 1992, Union Carbide reported that 53 Selexol units had been installed, including 10 for CO_2 removal from synthesis gas, 12 for CO_2 removal from natural gas, 15 for selective H_2S removal, 8 for desulfurization of synthesis gas, and for landfill gas purification. The Selexol process has been extensively described in literature (Sweny, 1973; Valentine, 1974; Hegwer and Harris, 1970; Judd, 1978).

DEPG has low vapour pressure values and is suitable for operating temperatures ranging from 255.15 K to 448.15 K. At low temperatures, DEPG has higher viscosity values which reduce mass and heat transfer properties. This property may constitute a disadvantage since it is

sometimes desirable to reduce temperature in order to increase gas solubility. In addition, it is a drawback of the Selexol process that heavy hydrocarbons are absorbed, which, in turn, reduces its overall absorption capacity.

2.6.3.3 N-Methyl-2-Pyrolidone (NMP) (Purisol Process)

The Purisol process, which is licensed by Lurgi GmbH of Frankfurt (Germany), utilises N-methyl-2-pyrolidone as a physical solvent for acid gas removal. The process was first applied for natural gas sweetening. However, new trends in synthesis gas production have revealed its potential, as an efficient method for the purification of high pressure hydrogen.

NMP has a high boiling point which facilitates its application for treating high pressure gases, with high acid gas concentrations, at ambient temperatures. In addition, NMP is used as a solvent under the BASF license for the recovery and concentration of acetylene and butadiene. The Lurgi Arosolvan and Distapex processes also use NMP solvent for the extractive recovery of pure aromatics. As of 1996, seven Purisol processes were in operation or under construction (Lurgi, 1996).

The Purisol process for acid gas removal operates at both ambient (~298.15K) and sub-ambient temperatures (~258.15 K). The licensor recommends water washing of the treated gas and the rejected acid gases, which indicates that NMP cannot be used for simultaneous gas dehydration. One should, however, note that NMP recovery using water is not necessary when the Purisol process is achieved at sub-ambient temperatures.

The key advantage of the Purisol process is the high boiling characteristics of NMP, which results in a high solubility for H_2S. NMP also shows high selectivity for H_2S over CO_2, which explains its suitability for the purification of high pressure, high CO_2 synthesis gas for gas turbine integrated gasification combined cycle (IGCC) systems. Other advantages include chemical and physical stability, no degradation, and availability in large quantities at reasonable costs. An extensive literature review on the Purisol process is available (Kriebel, 1989; Lurgi, 1988, Hochgesand, 1970).

2.6.3.4 Propylene Carbonate (PC) (Fluor Solvent Process)

The Fluor solvent process uses propylene carbonate (PC) as a physical solvent for the removal of CO_2 and H_2S from natural and synthesis gas streams. This process has been licensed by Fluor Daniel since 1960 and was one of the first solvents to use a simple process to treat natural gas primarily containing CO_2. Propylene carbonate is also well suited for the removal of COS, CS_2 and SO_2, H_2O from natural and synthesis gas streams. The process has been applied in 14 commercial installations, 5 for synthesis gas treatment and 9 for natural gas treatment (Kohl and Nielson, 1997 and Buckingham, 1964).

Propylene carbonate features the following characteristics: high solubility for CO_2 and other gases, low heat of solution for CO_2, low vapour pressure at operating condition, low solubility for light hydrocarbon, low viscosity, chemical inertness towards natural gas components, noncorrosive towards common metals, biodegradable and, readily available in large quantities. The combination of these characteristics yields both low heat and pumping requirements, and minimal solvent loss. The solvent is generally kept at sub-ambient temperatures to increase the solubility of the acid gas, thereby decreasing the solvent circulation rates. In addition, propylene carbonate does not become too viscous at low temperatures, but it does become unstable at high temperatures. One should note that the operating temperature for PC is ranged from 255.37 to 338.15 K.

2.6.4 Comparison of commercial physical solvents

Table 2.1 lists significant properties of the most commonly used commercial physical solvents. An examination of these solvents reveals differences in their properties: properties such as molecular weights and densities. Thus, a comparison of solvents based, for instance, on mole fraction or weight of solute in the solvent, at saturation, will not reflect the true absorption capacity of the solvent for acid gas removal. However, Bucklin and Schendel (1985) indicate that the volume of solute expressed as vapour, at the reference condition, per unit volume of solvent, can be used as a significant tool for solvents' comparison.

Most of the solvent processes considered here operate between 253.15 K and 303.15 K except the Rectisol process which operates at lower temperatures to prevent solvent loss due to

vaporisation. Table 2.6 compares solubility of various gases in (DEPG, PC and NMP) solvents relative to CO_2 at ambient temperature (298.15 K) and atmospheric pressure (100 kPa).

Table 2.6: Gas Solubility data for Selexol, Purisol and Fluor Solvent Process Absorbents. Volume Gas/Volume at 298.15 K and 100 kPa (Bucklin and Schendel, 1985)

Gas	**Selexol**	**Purisol**	**Fluor Solvent**
H_2	0.047	0.020	0.027
N_2	—	—	0.03
CO	0.100	0.075	0.072
C_1	0.24	0.26	0.13
C_2	1.52	1.36	0.58
CO_2	3.63	3.57	3.41
C_3	3.70	3.82	1.74
iC_4	6.79	7.89	3.85
nC_4	8.46	12.4	5.97
COS	8.46	9.73	6.41
iC_5	16.2	—	11.9
NH_3	17.7	—	—
nC_5	20.1	—	17.0
H_2S	32.4	36.4	11.2
nC_6	39.9	—	46.0
CH_3SH	82.4	121	92.7

The comparative solubility data in Table 2.6 shows that sulphur compounds such as carbonyl sulphide, carbon disulphide, and mercaptans are quite soluble in all the selected physical solvents. These components are removed along with the acid gas, to a large extent. However, the solubility data for H_2S at 298.15 K in DEPG and NMP is about three times higher than in PC. In other words, DEPG and NMP would be preferable for a gas mixture containing a substantial amount of H_2S, or processes targeting selective H_2S removal. However, PC has a significant advantage over DEPG and NMP in cases where CO_2 removal governs the process. This is evidenced by gas mixtures containing little or no H_2S, and light hydrocarbons, whose components are less soluble in PC.

The effect of water in the feed gas can be analysed using solubility data. Buckingham (1964) reported that NMP and Selexol are totally miscible in water, whilst PC has limited water solubility. This implies that PC requires another solvent for hydrate control during feed gas chill-down. In addition, at high temperatures (~388.15 K), PC reacts irreversibly in the presence of water and CO_2, and therefore becomes unstable (Bucklin and Schendel, 1985). This drawback disqualifies PC for water-controlled atmospheric distillation (Texaco Chemical company, 1960). Literature indicates that for design purposes, water content for various solvents should range from 1 to 6 % by weight, to prevent impairing the solvent absorption capacity for CO_2 and H_2S. However, the significant penalty associated with water content control is the pumping cost of removing the extra water.

Solvent regeneration is another aspect worthy of comparison between commercial physical solvents. As stated in Section 2.2.1, the optimum choice for a solvent regeneration method depends upon the purity required for the treated gas. The solvent regeneration methods, covered in Section 2.2.1 and shown in Figure 2.3, are generally similar for the Selexol and Rectisol processes, but not for the Purisol process.

Lurgi (1978) proposes three different scenarios for acid gas removal using the Purisol process, each with their associated solvent regeneration methods. For bulk removal of H_2S from natural gas, solvent regeneration is achieved by successive flashing at three different pressures, whilst for selective H_2S removal from natural gas, flashing and thermal regeneration with reboiling are employed. For complete CO_2 removal from high pressure gas mixtures, solvent regeneration by flashing and inert-gas stripping are used.

Several authors have discussed in detail the solvent regeneration methods for the Selexol process (Deraerschot and Valentine, 1976; Sweny, 1980). These authors report that only if a plant is properly designed can sulphur compounds be removed at concentrations as low as a few parts per million with low co-absorption of CO_2.

The Fluor solvent process utilises the solvent regeneration method described in Section 2.2.1 and shown in Figure 2.3 (A). In this process, loss of hydrocarbons has often been reported (Buckingham, 1961). Freireich and Tennyson (1977) modified the conventional Fluor solvent process in order to reduce the loss of hydrocarbons. The modification is mainly centred on the solvent regeneration method, where the top product from the second intermediate flash unit is washed with solvent in a separated small absorber. The overhead from the small absorber is recompressed and mixed with the main absorber feed gas. It is claimed that the value of the hydrocarbon gases recovered compensates for the cost of the additional equipment. Thermal solvent regeneration cannot be applied in the Fluor solvent process due to the instability of PC at elevated temperatures.

Other key process parameters worthy of comparison include solvent circulation, heating duty, air cooling, and power. Burr and Lyddon (2008) compared four physical solvents (methanol, NMP, PC and DEPG) for acid gas removal on the basis of these parameters. The comparison was achieved using the process simulator ProMax ® 2.0., and the feed gas composition was that of the basic non-selective Rectisol Wash example presented by Ranke and Mohr (1985), listed in Table 2.7. Some of the parameters such as solvent (methanol) flow rate are not available in the reference and therefore were estimated. For comparison purposes, parameters for the other solvents were adjusted to meet the treated gas composition obtained in the methanol simulation (1.75% CO_2, 0.36 ppm H_2S and 0.077 ppm COS). The simulation results for the selected four solvents are available in Burr and Lyddon (2008).

Table 2.7: Feed gas specification for physical solvent comparison as taken from Ranke (1985)

Component	**Mole %**
Hydrogen	54.7
Nitrogen	0.20
Argon	0.40
Carbon monoxide	0.40
Methane	2.00
Carbon dioxide	42.2
Hydrogen sulphide	0.05
Carbonyl sulphide	0.05
Temperature / K	298.15
Pressure / MPa	3.199

The simulation results reveal that all of the four selected solvents are able to meet the CO_2 treated gas specifications (1.75%). Three of the solvents, with the exception of PC, are able to meet H_2S and COS treated gas specifications. As discussed in Section 2.2.2, this is true because PC is not a suitable solvent for feed gas containing high concentrations of H_2S. However, the removal of H_2S and COS could be improved with additional stripping gases.

A comparison of physical solvents, based upon equipment required shows that methanol requires the most equipment, whilst PC requires the least equipment. However, equipment required by methanol, such as heat exchangers and compressor sizes, is smaller relative to that required by other solvents (Burr and Lyddon (2008).

The heat exchanger duty, pump and compressor power requirements are significantly smaller for the refrigerated NMP and DEPG processes compared to unrefrigerated ones. This is true because of the low circulation rate of the former. Low temperatures are also beneficial for methanol, since they result in both the lowest circulation rate and lowest net power requirement.

The PC process has the highest net power requirement compared to the other solvents due to the fact that it uses a vacuum compressor for the flash drums. However the total heat exchanger duty relative to PC is lower than that of the other solvents due to a lower refrigeration duty and also

due to the absence of a reboiler and a condenser. Burr and Lyddon (2008) reported significant solvent loss for methanol and unrefrigerated NMP, but this could be prevented using a water wash.

Other physical solvent comparisons have been made by several authors. Bucklin and Schendel (1985) compared PC and Selexol processes and found the Selexol process to be better in applications involving H_2S and CO_2 removal from hydrocarbon systems. Doctor et al. (1994) compared Selexol and Rectisol processes for an IGCC application and found the Selexol process less costly than the Rectisol process as far as the fuel-cycle CO_2 sequestration is concerned. Mak et al. (2003) compared Selexol and Fluor solvent processes and found that the Fluor solvent process is suitable for treating natural gas predominantly rich in CO_2. In this case, Fluor solvent has the advantage of operating at lower temperatures than the Selexol processes without becoming too viscous.

One should note that the major economic factors in absorption processes are usually determined by the solvent circulation rate and solvent losses. This is due to the fact that solvent circulation rate affects sizing and operation parameters of the process and that solvents are generally expensive, and the most costly part of a gas absorption system is associated with the solvent regeneration section.

In light of the above, a preliminary check of the solvent characteristics can help disqualify those that do not meet the chief criteria for a particular application. Considerable weight should be given to existing and proven performance processes. Innovative technologies are encouraged but the associated high costs of testing and that of commercialization constitute both a barrier to development and an incentive to stick to old technologies if they have proven to be satisfactory. Unfortunately, none of the tested solvents meet all of the "ideal" solvent criteria and there is therefore a compromise required regarding overall suitability. This provides an incentive to search for suitable physical solvents relative to particular applications.

The Thermodynamics Research Unit of the School of Engineering at the University of KwaZulu-Natal in collaboration with the Centre Thermodynamics of Processes (CTP) at MINES-ParisTech and some industry partners have therefore initiated research into the use of fluorochemicals as potential enhancing agents in separation processes. Fluorochemicals such as

perfluorocarbons (PFCs) possess remarkable absorption capability with regard to gases (Heintz et al., 2008).

2.7 Perfluorocarbons

Fluorocarbons, frequently referred to as perfluorocarbons (PFCs), are organofluorine compounds consisting wholly of carbon and fluorine connected together in strong carbon-fluorine bonds. In other words, PFCs are hydrocarbons in which hydrogen atoms are replaced with fluorine atoms. Their molecular formula is C_nF_{2n+2}. Figure 2.6 shows the C-F bonds in the molecular structure of perfluorohexane.

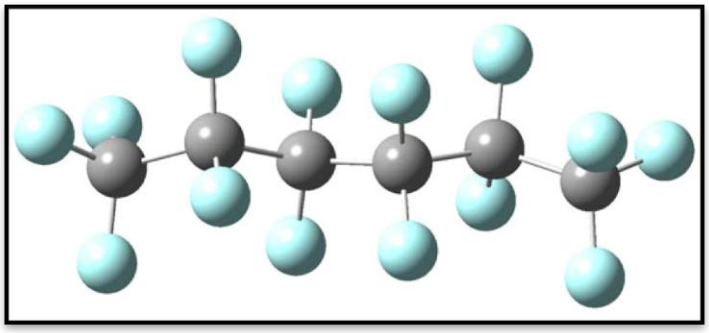

Figure 2.6: Molecular structure of perfluorohexane

2.7.1 Properties

The nature of the carbon-fluorine (C-F) and carbon-carbon (C-C) bonds in PFCs results in a high degree of thermal and chemical stability. However, the thermal stability is limited by the strength of the C-C bonds, which decreases with the increase of chain length. However, although PFCs with more carbon atoms are less thermally stable, temperatures higher than 1000 °C are required for their destruction.

PFCs are generally inert, non-toxic and non-flammable. In addition, the strength of C-F bonds in PFCs resides in the electronegativity of fluorine which takes on a partially ionic character through partial charges in the carbon and fluorine atoms. The multiple C-F bonds present in any PFC compound inductively strengthen the C-C bonds. However, the high electronegativity relative to fluorine diminishes the polarizability of the atom, which results in low intermolecular forces, lipophobicity, hydrophobicity and non-polarity of fluorocarbon compounds. One should

note that the non-polar property of PFCs is an important element in the selection of the thermodynamics models, which will be discussed in Chapter 3.

The number of carbon atoms in PFCs defines most of their physical properties. The greater the number of carbon atoms, the higher the boiling point, the higher the density, the higher the surface tension, the higher the critical properties, the higher the refractive indices and the lower the vapour pressure. The physical properties of PFCs ranging from C_4 to C_8 listed in Tables 2.8 and 2.9 are compiled by Smart and Tatlow (1994).

In general, PFCs have a higher density (almost twice as dense as water), and higher compressibility, than their corresponding alkanes. However, saturated PFCs have lower surface tensions, lower viscosities, lower heat of vaporisation and a lower dielectric constant than saturated alkanes, which reveals their non-polar character and low polarizability. Furthermore, van der Waal interactions are revealed in PFCs, which lead to low cohesive energies in liquids. This property explains the high gas solubility of PFCs. Spiess (2010) reports the absorption capability of PFCs for gases such as CO_2, N_2 and O_2. PFCs are immiscible with many common organic solvents, but are miscible with some hydrocarbons. More details on the properties of PFCs are available in the literature (Smart and Tatlow, 1994 and Houghman, 2002).

Table 2.8: Typical properties for a gaseous PFC (C_4F_{10}) as taken from Smart and Tatlow (1994)

Property	C_4F_{10}
Molecular weight ($g.mol^{-1}$)	283.02
Boiling point (K) at 101.325 kPa	270.95
Freezing point (K) at 101.325 kPa	144.95
Specific volume at 294.25 K and 101.325 kPa ($m^3.kg^{-1}$)	0.101
Density of gas at bp ($kg.m^3$) at 293.15 K	24.60
Density of liquid ($kg.m^{-3}$) at 293.15 K	1517
Critical temperature (K)	113.20
Critical pressure (kPa)	2323
Critical density ($kg.m^3$)	629.0
Latent heat of vaporization at bp ($kJ.mol^{-1}$)	340.26
Latent heat of fusion at mp ($kJ.kg^{-1}$)	—

Table 2.9: Typical physical properties for liquid PFCs ranging from C_5 to C_8 as taken from Smart and Tatlow (1994)

Property	C_5F_{12}	C_6F_{14}	C_7F_{16}	C_8F_{18}
Molecular weight ($g.mol^{-1}$)	288	338	350	400
Density ($kg.m^{-3}$)	1604	1682	1788	1828
Boiling point (K)	302.15	330.15	349.15	375.15
Pour point (K)	153.15	183.15	243.15	203.15
Viscosity (kinematic) ($mm^2.s^{-1}$)	0.29	0.39	0.87	1.06
Viscosity (dynamic)(mPa. s)	0.465	0.656	1.561	1.919
Surface tension ($mN.m^{-1}$)	9.4	11.1	15.4	16.6
Vapour pressure (kPa)	86.2	29.4	14.1	4.8
Heat of vaporization at boiling point ($kJ.mol^{-1}$)	315.28	252.96	245.43	207.25
Specific heat ($kJ.kg^{-1}.K^{-1}$)	1.05	1.09	0.963	0.963
Critical temperature (K)	421.85	451.05	485.95	514.65
Critical pressure (kPa)	2048	1834	2019	1881
Critical volume ($liter.kg^{-1}$)	1.626	1.582	1.522	1.52
Thermal conductivity ($mW.m^{-1}.K^{-1}$)	64.0	65.3	59.9	60.4
Coefficient of expansion at 273.15 K	0.00189	0.00159	0.00138	0.00123
Refractive index n_D^{20} at 298.15 K	1.2383	1.2509	1.2781	1.2895

2.7.2 Uses

Fluorochemicals have attracted considerable interest from both industry and academia because of their exceptional behaviour. Fluorochemicals find application in a number of different areas. They are used as blood substitutes, surfactants and anaesthetics in the medical sector; as substitutes for ozone-depleting substances such as chlorofluorocarbons (CFCs) and hydrochlorofluorocarbons (HCFCs) in refrigeration industries; as etching agents and dielectric fluids in the semiconductor sector, and as solvents in chemical industries, to name just a few applications (Heintz et al., 2008).

2.7.3 Environmental impact

PFCs are included in fluorine-containing gases, the so called "F-Gases" [Hydrofluorocarbons (HFCs), perfluorocarbons (PFCs) and sulphur hexafluoride (SF_6)]. These are industrial gases recently used in a number of different applications. However, they are very potent climate gases with a warming potential of up to 23000 times stronger than CO_2, and their emission is increasing significantly. Due to their high global warming potential (GWP) and long atmospheric lifetimes, several member states have already adopted legislation to monitor, control or phase out some of them (Sekiya and Misaki, 2000), namely PFCs ranging from C_1 to C_4. The sources of high emission of PFCs include: aluminum smelting, semiconductor manufacturing, fire extinguishing, refrigeration and air-conditioning. Table 2.10 lists the GWP values and the lifetime of PFCs ranging from C_1 to C_6.

In principle, PFCs should not make considerable impact on global warming because of the small volumes expected to be emitted in different areas where they find application. Nevertheless, it is desirable to reduce their emissions to as low as possible for both economic and environmental reasons as their GWP, coupled with a long atmospheric lifetime, lead to their increase in the atmosphere.

Several factors contribute to a low emission rate of PFCs. Firstly, the physical properties of PFCs compared to CFCs and other halogenated solvents. PFCs have lower heats of vaporization, lower diffusivities and higher (vapour) densities compared to those of CFCs. Some of these properties account for an easier containment. Secondly, the improvement of containment technologies has lowered the emission rate of PFCs compared to CFCs, which is typically 5 to 10 times less in industrial practice (Houghman, 2002). Finally, improvement of containment and recovery technologies promise to further reduce PFC emission.

Table 2.10: The GWP values and the lifetime of PFCs ranging from C_1 to C_6 [data taken from IPCC/TEAP (2005)]

		Global Warming Potential for Given Time Horizon		
Chemical formula	Lifetime (years)	20-yr	100-yr	500-yr
CF_4	50000	5210	7390	11200
C_2F_6	10000	8630	12200	18200
C_3F_8	2600	6310	8830	12500
C_4F_{10}	2600	6330	8860	12500
C_5F_{12}	4100	6510	9160	13300
C_6F_{14}	3200	6600	9300	13300

2.7.4 Regulations of F-Gases

One should note that, in this study, the regulations of F-Gases is not specific to a particular group of gases in the F-Gases, it rather refers to the ensemble, unless otherwise stated.

As mentioned in section 2.3.3, emission of F-Gases is increasing, and it is reported to have risen by 60% since 1990. Consequently, several member states and non-governmental organizations have taken regulatory actions to control F-Gases as part of combatting climate change. In 2006, the European Union (EU) adopted its first F-Gases regulation (EC: No. 842/2006), which focused on containment technologies, recovery of the F-Gases and imposing regulations on reporting, training and labeling, on those using the F-Gases. It is reported to have stabilized the EU emissions at 2010 levels.

In 2012, a new regulation was proposed to come into effect from the 01 January 2015, aimed at strengthening the existing measures and introducing a number of changes. Change such as replacing F-Gases with energy-efficient alternatives with less impact on the climate system. The regulation is projected to cut, by 2030, the EU's emissions of F-Gases by two-thirds, in comparison to the 2010 levels, at low cost. However, one should note that some stakeholders have indicated the difficulties associated with marketing greener technology. On the other hand, in a country such as Denmark, where F-Gases regulations are strictly applied, start-ups have

successfully developed and new green technologies have been marketed (European Commission, 2012).

In 2009, 2010, 2011 and 2012, numerous parties of the Montreal Protocol requested at phase down of the supply and consumption of the HFCs worldwide. However, little development has taken place as countries such as China, Brazil and India. Other countries have refused, under the Montreal Protocol, to discuss the request. One should note that the United Nations Conference on Sustainable Development (UNCSD) has recently shown support for a gradual phase-down of the consumption and production of the HFCs (UNCSD, 2012).

In South Africa, the regulation of the F-Gases was only announced in the Goldstream News Gazette in May 2014 (GNG451, 2014). This was for the phasing out of the HCFCs as ozone-depleting substances, by 2040. Consequently, South Africa could potentially be a dumping ground for HFC products emanating from EU, as their F-gases regulations are strictly reinforced.

2.7.5 PFCs as physical Solvents

As explained in Sections 2.3.1 and 2.3.3, liquid or higher carbon chain length PFCs, in general, may possess, the necessary properties to behave as an 'ideal' solvent. The large solubility of gases in perfluorocarbons, mainly liquid, is justified by the ease cavity formation within them to accommodate the solute molecule (Swinton, 1978). Hence, gas solubility data can provide necessary information on the properties and structure of solutions (Scott, 1970). Dias et al. (2003) investigated the solubility of oxygen both in *n*-C_6F_{14} and n-C_6H_{14}.The results obtained reveal that the solubility of O_2 in *n*-C_6F_{14} was twice that in *n*-C_6H_{14}, and an increase in temperature decreases the oxygen solubility in both liquids. Furthermore, Costa Gomes et al. (2003) measured the solubility of O_2 and CO_2 in the same liquids (*n*-C_6F_{14} and *n*-C_6H_{14}). The results obtained show a remarkable improvement, almost 100 % for the solubility of O_2 in *n*-C_6F_{14} when compared to that in *n*-C_6H_{14}. For CO_2, the solubility increase is not as significant. However, one should note that *n*-C_6F_{14} dissolved between 2-20 times more CO_2 than O_2 depending upon the temperature.

Recently, El Ahmar et al. (2010) and Valtz et al. (2011) investigated the absorption capabilities of C_4F_{10} with regard to C_2H_6 and CO_2. Phase equilibria measurements and modeling were

undertaken for the C_2H_6 + C_4F_{10} and CO_2 + C_4F_{10} systems. The results obtained reveal that the solubility of both C_2H_6 and CO_2 in C_4F_{10} increases with a decrease in temperature.

Heintz et al. (2008) investigated carbon dioxide capture from fuel gas streams under elevated pressures and temperatures using three PFCs, namely perfluoroperhydrofluorene ($C_{13}F_{22}$), perfluoro-perhydrophenanthrene ($C_{14}F_{24}$), and perfluoro-cyclohexylmethyldecalin ($C_{17}F_{30}$). Phase equilibria measurements were undertaken for N_2 and CO_2 with each of the perfluorocarbons. The measured data were modelled using the Peng-Robinson property method in Aspen Plus®, and thereafter a conceptual design of a gas absorption system was performed. The final results reveal that CO_2 solubility was higher in $C_{17}F_{30}$ than in the other two PFCs. Therefore, the authors investigated $C_{17}F_{30}$ as a potential physical solvent. In the simulation, the shifted gas flow rate in the absorption system was 1938 kmol/h and the $C_{17}F_{30}$ solvent flow rate 55038.08 kmol/h. The capture process was carried out at 500 K and 3 MPa and the solvent was able to retain 56.10 % of CO_2, 51.00 % of CH_4 and 67.19 % of H_2S but 0.36 % of $C_{17}F_{30}$ was lost in the vapour phase, leaving the top of the absorber. The results obtained reveal the high vapour pressure for $C_{17}F_{30}$ at 500 K resulting in solvent loss, and the low solubility of $C_{17}F_{30}$ for CO_2 at 500 K.

In light of the above findings and considering the definition of an ‘ideal’ solvent in this study, it can be said that not all PFCs meet the criteria. The major drawback for PFCs with shorter chain lengths (C_1 to C_4), resides in their high vapour pressure as opposed to that of commercial physical solvents, and their high cost, starting from 2940 USD/ kg for 100 % pure C_4F_{10}. Following the results obtained by Heintz et al., (2008), PFCs with longer carbon chains, ranging from C_{15} upwards, at low temperatures, have the potential to behave as ‘ideal’ solvents. And, to reduce the price of PFCs, blends of PFCs could be investigated as their production does not generally require stringent separation processes.

Consequently, the use of perfluorocarbons as potential physical solvents requires one to minimize its emission into the atmosphere due to its associated GWP. To achieve this, one can either reduce the gas absorption operating temperature or use a PFC compound with a longer carbon chain since the longer the PFC carbon chain length the lower the vapor pressures. However, one should ensure that the viscosity of the solvent at lower temperatures or that of the PFC with a longer carbon chain does not significantly reduce mass transfer between components

involved in the gas absorption system. Otherwise, a PFC with higher viscosity may result in poor absorption and increased pumping cost.

One should note that at the time of this study, only two PFCs (C_4F_{10} and C_6F_{14}) were available in the laboratories of both the Centre Thermodynamics of Processes in Fontainebleau (France) and the Thermodynamic Research Unit in Durban (South Africa). Due to the fact that C_4F_{10} and C_6F_{14} do not meet the criteria of an 'ideal solvent', this study focused mainly on the measurement and thermodynamic modelling of VLE data for C_4F_{10} and C_6F_{14} with flue gas components. The results obtained were then used in the design of gas absorption systems for illustration purpose. In other words, this practice was undertaken to show that with measured VLE data, it was possible to design gas absorption systems.

Phase equilibrium data measurements and thermodynamic modeling for the systems under investigation are essential data required to design a unit operation. In case of an equilibrium based absorption process, phase equilibrium data can give ample information about the behaviour of each system under investigation. These data are measured and thereafter correlated using appropriate thermodynamic models to obtain binary interaction parameters which are then used in simulators such as Aspen plus, ChemCad, Hysim and Prosim, etc., for design purpose. In the absence of experimental phase equilibrium data, predicted data can be used in the preliminary stage of a design process.

Consequently, the next chapter will focus on important notions of theoretical treatment of phase equilibrium data.

3

CHAPTER THREE

THEORETICAL TREATMENT OF PHASE EQUILIBRIUM DATA

3.1 Introduction

Thermodynamic data are important in numerous industries, for both the design of separation equipment and processes. Accurate knowledge of thermodynamic data plays an important role in cost-effective design of chemical plants. For design of both separation equipment and processes, the issue of accuracy is acute as often more than 40 % of the cost of the process is related to the separation units Tsonopoulos et al., 1986)".

The petroleum, chemical and pharmaceutical industries have for many years been traditional users of thermodynamic data, especially phase equilibrium data. The design of separation processes, such as distillation and absorption, requires accurate vapour-liquid equilibrium (VLE) data and in some cases vapour-liquid-liquid equilibrium (VLLE) data. These data are regarded as being amongst the most important types of information for the successful design of the separation processes aforementioned.

Over the years, in the field of thermodynamics of phase equilibria, there has been a concentration of effort on the development of thermodynamic models. To date, several models have been developed, but there is a question still whether enough data and/or suitable models are available for a particular process or need. For the purpose of this study, the following aspects need to be addressed:

(i) Are there existing thermodynamic models that are suitable to represent experimental high pressure phase equilibrium data containing perfluorocarbons with common flue gas content;

(ii) Are the thermodynamic models able to predict data at conditions beyond the measurement conditions?

To this end, it is the purpose of this chapter to discuss a few representative models dealing with VLE data relative to this study. This involves theoretical methods (thermodynamic models) for representation and prediction of VLE data. Kontogeorgis and Folas (2009) provide further details on thermodynamic models for industrial applications.

3.2 Equilibrium and chemical potential

Equilibrium is a static condition in which no changes occur in the macroscopic properties of a system with time. This implies a balance of all potentials that may cause change (Smith et al., 2005).

According to Smith et al. (2005), multiple phases at the same temperature *T* and pressure *P* are in equilibrium when the chemical potential (μ_i) of each constituent species is the same in all phases. Mathematically, this is expressed as follows:

$$\mu_i^{\alpha} = \mu_i^{\beta} = ... = \mu_i^{\pi} \tag{3.1}$$

where μ_i is the chemical potential of species i, with $i = 1,2,...,N$, α, β and π are the phases

The development of the criterion for phase equilibria is covered by Raal and Mühlbauer (1998); Praustnitz et al. (1999) and Smith et al. (2005).

3.3 Fugacity and fugacity coefficients

Praustnitz et al. (1980) state that chemical potential is defined in terms of immeasurable quantities where absolute values are not known. Since chemical potential serves as a fundamental criterion for phase equilibria, it is desirable to express it in terms of measurable quantities such as temperature and pressure. For these reasons, Lewis (1980) introduced the concept of fugacity which has more physical meaning and could be related to chemical potential:

$$\overline{G_i} = \Gamma_i(T) + RT \ln f_i \tag{3.2}$$

where $\overline{G_i}$ is the partial molar Gibbs energy, $\Gamma_i(T)$ is the integration constant at temperature T, and f_i is the fugacity, with units of pressure.

The partial molar Gibbs energy is defined as follows:

$$\overline{G_i} = \left[\frac{\partial(nG)}{\partial n_i}\right]_{T,P,n_j} \tag{3.3}$$

Equation (3.4) derives from the development of the criterion of phase equilibria.

$$\mu_i = \overline{G_i} \tag{3.4}$$

Comparison of Equations (3.2) and (3.4) leads to Equation (3.5)

$$\mu_i = \Gamma_i(T) + RT \ln f_i \tag{3.5}$$

Substitution of Equation (3.5) into Equation (3.1) leads to Equation (3.6), which is the phase equilibrium criterion based on fugacities.

$$f_i^{\alpha} = f_i^{\beta} = \ldots = f_i^{\pi} \qquad \text{with } i = 1, 2, \ldots, N \tag{3.6}$$

where N is the number of components.

For a species in solution, Equations (3.5) and (3.6) become (3.7) and (3.8), respectively.

$$\mu_i = \Gamma_i(T) + RT \ln \hat{f}_i \tag{3.7}$$

$$\hat{f}_i^{\alpha} = \hat{f}_i^{\beta} = \ldots = \hat{f}_i^{\pi} \tag{3.8}$$

For a closed system where vapour and liquid are in equilibrium, Equation (3.8) becomes:

$$\hat{f}_i^{v} = \hat{f}_i^{l} \text{ with } i = 1,2, \ldots, N \tag{3.9}$$

where N is the number of components, and *v* and *l* are the vapour and liquid phases, respectively.

The relationship between the fugacities and the measurable properties such as temperature, pressure and phase compositions is achieved by utilizing the fugacity coefficient ϕ, the activity coefficient γ, and the liquid standard-state fugacity f^{OL}. The terms activity coefficient and liquid standard-state fugacity are explained further in this chapter.

Fugacity coefficient is defined as:

$$\phi = \left(\frac{f}{P} \right) \tag{3.10}$$

For binary VLE, Equation (3.10) becomes:

In the vapour phase:

$$\hat{\phi}_i^V = \frac{\hat{f}_i^V}{y_i P} \tag{3.11}$$

and in the liquid phase:

$$\hat{\phi}_i^L = \frac{\hat{f}_i^L}{x_i P} \tag{3.12}$$

where the fugacity coefficient can be calculated from any of the equivalent equations below:

$$RT \ln \hat{\phi}_i = RT \ln \frac{\hat{f}_i}{y_i P} = \int_V^\infty \left[\left(\frac{\partial P}{\partial n_i} \right)_{T,V,n_j} - \frac{RT}{V} \right] dV - RT \ln \left(\frac{PV}{RT} \right) \tag{3.13}$$

$$RT \ln \hat{\phi}_i = RT \ln \frac{\hat{f}_i}{y_i P} = \int_0^P \left(\bar{V}_i - \frac{RT}{P} \right) dP \tag{3.14}$$

In principle, Equations (3.13) and (3.14) are suitable for all types of fluid phase, conditions (*T*, *P*, phase compositions) and mixtures of any number of components.

For the liquid phase, the activity coefficient γ (introduced in Section 3.6) relates to the liquid phase fugacity $\hat{f}_i^L$ to the mole fraction x_i and to a standard-state fugacity f_i^{OL}. This is expressed as follows:

$$\gamma_i = \frac{\hat{f}_i^L}{x_i f_i^{OL}} \tag{3.15}$$

From Equation (3.9), taking into account Equations (3.11) and (3.12), the equation for equilibrium for any component i can be expressed as follows:

$$\hat{f}_i^V = \hat{\phi}_i^V y_i P = \hat{f}_i^L = \gamma_i x_i f_i^{OL} = \hat{\phi}_i^L x_i P \tag{3.16}$$

3.4 Fugacity coefficients from cubic equations of state

Numerous methods have been developed and are readily available to determine the fugacity coefficients of species. One of these methods is the use of cubic equations of state. The most popular cubic EoS includes the Van der Waals (vdW) (1873), Redlich-Kwong (RK) (1949), Soave-Redlich-Kwong (SRK) (1972) and the Peng-Robinson (PR) (1976) equations. Table 3.1 shows these cubic EoS together with the typical expressions often used for estimating their parameters.

The van der Waals (1873) equation of state was the first attempt to give qualitative description of vapour-liquid coexistence and phase transitions, but was not accurate for critical properties and phase equilibrium calculations (Van Konynenburg and Scott, 1980). Later, the Redlich-Kwong (RK) (1949) equation of state improved the accuracy of the van der Waals equation by introducing temperature-dependence and different volume dependence in the attraction term. Soave (1972) suggested replacing the term $a/T^{0.5}$ in the RK EoS by the term $a(T)$ which has more temperature-dependence. In 1976, Peng and Robinson (1976) proposed additional modifications which result in accurate prediction of saturation pressure and liquid molar volume. The Soave-Redlich-Kwong (SRK) and the Peng-Robinson (PR) EoS are currently the primary choice of models in the petroleum and chemical industries. Hence, they were chosen as EoS in this study. They are therefore discussed in more detail in the next section.

Table 3.1: The most popular cubic EoS and the classical way of estimating their parameters (based on the critical properties and vapour pressures) (Kontogeorgis and Folas, 2010)

EoS	Equation	a and b	Z_c
vdW	$P = \frac{RT}{V-b} - \frac{a}{V^2}$	$a = \frac{27}{64}\frac{(RT_c)^2}{P_c}$ $b = \frac{1}{8}\frac{RT_c}{Pc}$	$Z_c = 0.375$
RK	$P = \frac{RT}{V-b} - \frac{a}{T^{0.5}[V(V+b)]}$	$a = 0.42748\frac{(R^2T_c^{2.5})}{P_c}$ $b = 0.08664\frac{RT_c}{P_c}$	$Z_c = 0.333$
SRK	$P = \frac{RT}{V-b} - \frac{a(T)}{V(V+b)}$	$a = 0.42748\frac{(RT_c)^2}{P_c}$ $b = 0.08664\frac{RT_c}{P_c}$ $a(T) = a[1+m(1-\sqrt{T_r})]^2$ $m = 0.48 + 1.574\omega - 0.176\omega^2$	$Z_c = 0.333$
PR	$P = \frac{PV}{V-b} - \frac{a(T)}{V(V+b)+b(V-b)}$	$a = 0.45724\frac{(RT_c)^2}{P_c}$ $b = 0.7780\frac{(RT_c)^2}{P_c}$ $a(T) = a[1+m(1-\sqrt{T_r})]$ $m = 0.37464 + 1.54226\omega - 0.26992\omega^2$	$z_c = 0.307$

3.4.1 Soave-Redlich-Kwong Equation of State

The Soave-Redlich-Kwong cubic EoS was developed to improve the calculation of VLE data using the cubic EoS of Redlich and Kwong (1949) in modifying the attractive term $a/T^{0.5}$ to account for the temperature dependency. The proposed SRK EoS is:

$$P = \frac{RT}{(V-b)} - \frac{a(T)}{V(V+b)} \tag{3.17}$$

The constant a is related to the intermolecular attraction force of molecules whilst the constant b accounts for the molecular size. Expressions related to constants a and b are defined in Table 3.1.

For computational calculation purposes, Equation (3.17) can be expressed in terms of the compressibility factor (Z) for a mixture:

$$Z^3 - Z^2 + Z\left(A - B - B^2\right) - AB = 0 \tag{3.18}$$

where

$$A = \frac{a(T)P}{R^2T^2} \tag{3.19}$$

$$B = \frac{bP}{RT} \tag{3.20}$$

$$Z = \frac{PV}{RT} \tag{3.21}$$

The solution of Equation (3.18) can produce either one or three real roots. For a binary system and if the solution yields three real roots, the largest real root corresponds to the vapour phase compressibility factor and the smallest real root corresponds to that of the liquid phase compressibility factor.

The pure component fugacity coefficient using the SRK EoS is then found from:

$$\ln\phi = Z - 1 - \ln(Z-B) - \frac{A}{B}\ln\left(\frac{Z+B}{Z}\right) \tag{3.22}$$

In comparison with the RK EoS, The SRK EoS provides better calculations of vapour pressures for several hydrocarbons and correlation of phase equilibria behaviour for systems containing non-polar and slightly polar fluids.

3.4.2 Peng-Robinson Equation of State

The cubic EoS developed by Peng and Robinson in 1976 aimed to address the difficulties encountered in utilizing the Soave-Redlich-Kwong EoS. The main difficulties were found in the representation of liquid phase densities and accuracy of the equation of state near the critical region (Peng and Robinson, 1976). The proposed Peng-Robinson EoS is:

$$P = \frac{RT}{V-b} - \frac{a(T)}{V(V+b)+b(V-b)} \tag{3.23}$$

The constants a and b are defined in Table 3.1.

Equation (3.23) is expressed in terms of the compressibility factors as follows:

$$Z^3 - (1-B)Z^2 + Z(A-3B-2B^2) - (AB-B^2-B^3) = 0 \tag{3.24}$$

Similar to the SRK EoS, the largest real root of Equation (3.24) corresponds to the vapour compressibility factor while the smallest real root corresponds to the liquid compressibility factor.

The pure component fugacity coefficient using the PR EoS becomes:

$$\ln\phi = Z - 1 - \ln(Z-B) - \frac{A}{2\sqrt{2B}}\ln\left(\frac{Z+\left(1+\sqrt{2}\right)B}{Z+\left(1-\sqrt{2}\right)B}\right) \tag{3.25}$$

The Peng-Robinson EoS has been tested to predict the vapour pressure and volumetric behaviour from pure components to multiple systems and confirmed that it can be used for accurate prediction of vapour pressures and phase equilibria (Latini et al., 2006). As for the SRK EoS, the PR EoS suffers from inaccuracy in the critical region and poor liquid density calculations.

The Peng-Robinson and Soave-Redlich-Kwong EoS are typically employed in petroleum and chemical industries. These equations can correlate phase behaviour from binary to

multicomponent systems. Furthermore, the PR and the SRK EoS only require little input information such as critical properties and acentric factors for generalized parameters. Additional discussion on the advantages and disadvantages of the PR and SRK EoS are available in literature (Martin, 1979; and Wei and Sadus, 2000).

3.4.2.1 The Alpha function

As aforementioned, a cubic EoS such as the PR and SRK EoS have found widespread use in industrial applications for their simplicity and accuracy in the calculations of thermodynamic properties, especially phase equilibria of mixtures. However, the accuracy in modelling phase equilibria does not just depend on the choice of a suitable equation of state or mixing rules (introduced in Section 3.4.3) but also on the attractive term known as the alpha function for the selected pure components.

Numerous alpha functions have been proposed to improve the accuracy of cubic equations of state in predicting vapour pressures. Amongst these are those developed by Redlich and Kwong (1949), Soave (1972), Mathias-Copeman (1983), Stryjek-Vera (1986) and Twu et al. (1991). However, a number of authors have used the PR EoS combined with the Mathias-Copeman alpha function for vapour pressure calculations for several compounds (Valtz et al., 2002; Coquelet et al., 2003; Ramjugernath et al., 2009).These results have led to the use of the Mathias-Copeman alpha function in this study. It is expressed as follows:

$$\alpha(T)=\left[1+C_1\left(1-\sqrt{T_r}\right)+C_2\left(1-\sqrt{T_r}\right)^2+C_3\left(1-\sqrt{T_r}\right)^3\right]^2 \text{ if } T < T_C \tag{3.26}$$

and

$$\alpha(T)=\left[1+C_1\left(1-\sqrt{T_r}\right)\right]^2 \text{ if } T > T_C \tag{3.27}$$

where C_1, C_2, C_3 are the adjustable parameters unique to each component and are obtained from the regression of experimental vapour pressures; T_r, is the reduced temperature; T_c, is the critical temperature. One should note that if the temperature is supercritical, C_2 and C_3 are set to zero.

In addition, the incorporation of the Stryjek-Vera alpha function into the Peng-Robinson EoS has significantly improved the model's accuracy by introducing an adjustable pure component

parameter and modifying the polynomial fit relative to the acentric factor (Stryjek and Vera, 1986). The Stryjek-Vera function is defined as follows:

$$\alpha = \left[1 + k\left(1 - \sqrt{T_r}\right)\right]^2 \tag{3.28}$$

where

$$k = m + \left[A + B\left(C - T_r\right)\left(1 - \sqrt{T_r}\right)\right]\left[\left(1 + \sqrt{T_r}\right)\left(0.7 - T_r\right)\right] \tag{3.29}$$

$$m = 0.378893 + 1.4897153\omega - 0.1713184\omega^2 + 0.0196554\omega^3 \tag{3.30}$$

A, *B* and *C* are the adjustable parameters unique to each component and obtained via regression of the experimental vapor pressure data; T_r, is the reduced temperature; ω, is the acentric factor.

3.4.3 Mixing rules for cubic equations of state

Mixing rules are required when cubic equations of state for pure fluids are utilized to calculate thermodynamic properties of fluid mixtures. One way to extend cubic equations of state to fluid mixtures is via the van der Waals one fluid mixing rules and the classical combining rules, which are described in Equations (3.31-32) and (3.33-34), respectively.

$$a = \sum_{i=1}^{n}\sum_{j=1}^{n} x_i x_j a_{ij} \tag{3.31}$$

$$b = \sum_{i=1}^{n}\sum_{j=1}^{n} x_i x_j b_{ij} \tag{3.32}$$

where x may express either the liquid or vapour phase composition of species i or j.

$$a_{ij} = \sqrt{a_i a_j}\left(1 - k_{ij}\right) \tag{3.33}$$

$$b_{ij} = \frac{b_i + b_j}{2}\left(1 - l_{ij}\right) \tag{3.34}$$

where k_{ij} and l_{ij} are the binary interaction parameters. In most cases $l_{ij} = 0$, Equation (3.32) becomes:

$$b = \sum_{i=1}^{n} x_i b_i \tag{3.35}$$

An examination of equations ranging from (3.31 to 3.34) reveals that mixing rules depend on phase compositions while the combining rules do not. This explains the randomness of the mixing of molecules.

In literature, researchers have used the van der Waals mixing rules and reported that its strength lies in fast calculations and accurate representation of a wide range of VLE data for mixtures involving hydrocarbons and gases such as CH_4, N_2, CO_2 and H_2S. However, its weakness lies in its representation of complex mixtures in terms of chemical structure and other types of phase equilibria such as LLE, SLE and VLLE (Kontogeorgis and Folas, 2010). A cubic EoS utilizing the van der Waals mixing rules and the classical combining rules are capable of accurately representing non-polar and slightly polar mixtures using the interaction parameter k_{ij} but their failure resides in representing highly polar and hydrogen-bonding mixtures.

The limited use of cubic EoS for mixtures has led researchers to develop alternative mixing rules. The case of EoS/g^E mixing rules for a cubic EoS will be presented in Section 3.6 after the activity coefficient models are introduced in Section 3.5.1.

3.5 Activity and activity coefficients

The activity coefficient represents the non-ideality correction of the liquid phase in phase equilibria. This can be defined as in Equation (3.15).

$$\gamma_i = \frac{\hat{f}_i}{x_i f_i} \tag{3.36}$$

In terms of the molar Gibbs energy, Equation (3.15) is written as:

$$\overline{G_i} = \Gamma_i(T) + RT \ln \hat{f}_i \tag{3.37}$$

For an ideal solution, the activity coefficient $\gamma_i = 1$ and Equation (3.15) becomes (3.38)

$$\hat{f}_i^{id} = x_i f_i \tag{3.38}$$

Therefore, for an ideal solution Equation (3.37) can be written as:

$$\overline{G}_i^{id} = \Gamma_i(T) + RT \ln x_i f_i \tag{3.39}$$

Equation (3.38), known as the Lewis/Randall rule, stipulates that the fugacity of species in an ideal solution is equal to the fugacity of pure species *i* in the same physical state as the solution and at the same temperature and pressure. Furthermore, the Lewis/Randall rule shows that the fugacity of each species in an ideal solution is proportional to its mole fraction.

Excess properties are introduced in thermodynamics to account for deviations from the behaviour of an ideal solution. They are defined as properties that are in excess of those of an ideal solution at the same temperature, pressure and composition (Praustnitz, 1999).

Considering the excess properties definition, Equation (3.37) and (3.39) become:

$$\overline{G}_i^{E} = RT \ln \gamma_i \tag{3.40}$$

The fundamental excess property is mathematically expressed as:

$$d\left(\frac{nG^E}{RT}\right) = \frac{nV^E}{RT}dP - \frac{nH^E}{RT^2}dT + \sum_i \frac{\overline{G}_i^E}{RT}dn_i \tag{3.41}$$

An alternative form of the fundamental excess property expression results from the combination of Equations (3.40) and (3.41). It is expressed as:

$$d\left(\frac{nG^E}{RT}\right) = \frac{nV^E}{RT}dP + \frac{nH^E}{RT^2}dT + \sum_i \ln \gamma_i dn_i \tag{3.42}$$

Manipulation of Equations (3.41) and (3.42) yields:

$$\ln \gamma_i = \left[\frac{\partial\left(nG^E / RT\right)}{n_i}\right]_{T,P,n_j} \tag{3.43}$$

In practice, the process is reversed and excess Gibbs energies are calculated from known activity coefficients using the summability relation. This is expressed as:

$$\frac{G^E}{RT} = \sum_i x_i \ln \gamma_i \tag{3.44}$$

For a binary system the activity coefficients can be calculated from Equation (3.44) as follows:

$$\ln \gamma_1 = \frac{G^E}{RT} + x_2 \frac{d\left(G^E / RT\right)}{dx_1} \tag{3.45}$$

$$\ln \gamma_2 = \frac{G^E}{RT} - x_1 \frac{d\left(G^E / RT\right)}{dx_2} \tag{3.46}$$

3.5.1 Activity coefficient models

The difficulties encountered in the use of the cubic EoS have led researchers to develop alternative ways, such as the use of the combined method also known as the gamma-phi ($\gamma - \phi$) method (introduced later in this chapter). In the gamma-phi method, the activity coefficients are used to describe the behaviour in the liquid phase while the fugacity coefficients are used to account for the behaviour in the vapour phase.

There are basically two types of activity coefficient models: the random-mixing models which involve the Margules and the van Laar equations, and the local composition based models such as Wilson (Wilson, 1964), NRTL (Non-Random Two Liquid) (Renon and Prausnitz, 1986) and UNIQUAC (UNIversal QUAsi-Chemical) (Abrams and Prausnitz, 1975). The Wilson and UNIQUAC models were further developed into predictive models such as the analytical solution of groups (ASOG) (Derr and Deal, 1969) and UNIFAC (Fredenslund, 1977). One should note that quantum mechanics (QM) or quantum chemistry (QC) are becoming popular in predicting phase equilibria and other thermodynamic properties. In addition, they are used as alternatives for the UNIFAC model (Kontogeorgis and Folas, 2010).

QM calculations can be used in different semi-direct or indirect approaches in thermodynamics:

1. Calculation of the intermolecular potential from QM and thereafter phase equilibria calculation using molecular simulation.
2. QM calculations to determine interaction parameters in existing thermodynamic models.

3. The continuum solvation models such as Conductor-like Screening Model – Real Solvation (COSMO-RS) (Klamt, 1995) or Conductor-like Screening Model – Segment Activity Coefficient (COSMO-SAC) (Lin and Sandler , 2002).

It is important to note that predictive models are useful tools in the preliminary design of separation processes when no data is available or when approximate values are acceptable, i.e. for a component with low priority. Models such as UNIFAC or other UNIFAC-based activity coefficient models are predictive approaches that use structural groups to estimate the interactions amongst components. If the functional groups and interaction parameters are available, the UNIFAC model is able to predict the activity coefficients.

In recent years, research has been undertaken to ameliorate the UNIFAC model to better predict VLE, heat of mixing, and LLE data over a wider range of temperature. The UNIFAC revisions and extensions include: Dortmund-modified UNIFAC (1993) which predicts VLE, LLE, heat of mixing and activity coefficient at infinite dilution (Gmehling and Schiller, 1993); Kleiber extension (1994) predicts VLE of fluorinated hydrocarbons (Kleiber, 1995); Lyngby-modified UNIFAC (1986) predicts VLE and Excess Enthalpy (Larsen et al., 1987); UNIFAC, LLE (1980) predicts LLE (Magnussen et al., 1980) and UNIFAC revision 5 (1991) predicts VLE (Hansen et al., 1991).

The COSMO-SAC model is used as an alternate prediction model for components that cannot be defined in UNIFAC.

To ensure that the aforementioned models are able to predict binary systems that cannot be measured in this study, the VLE data for the CO_2 (1) + C_4F_{14} (2) system of Valtz et al., (2011) and VLE data for CO_2 (1) + C_6F_{14} (2) system of Costa Gomes and Pádua (2003) have been predicted and compared. The results obtained are graphically presented in Figures 3.1 and 3.2.

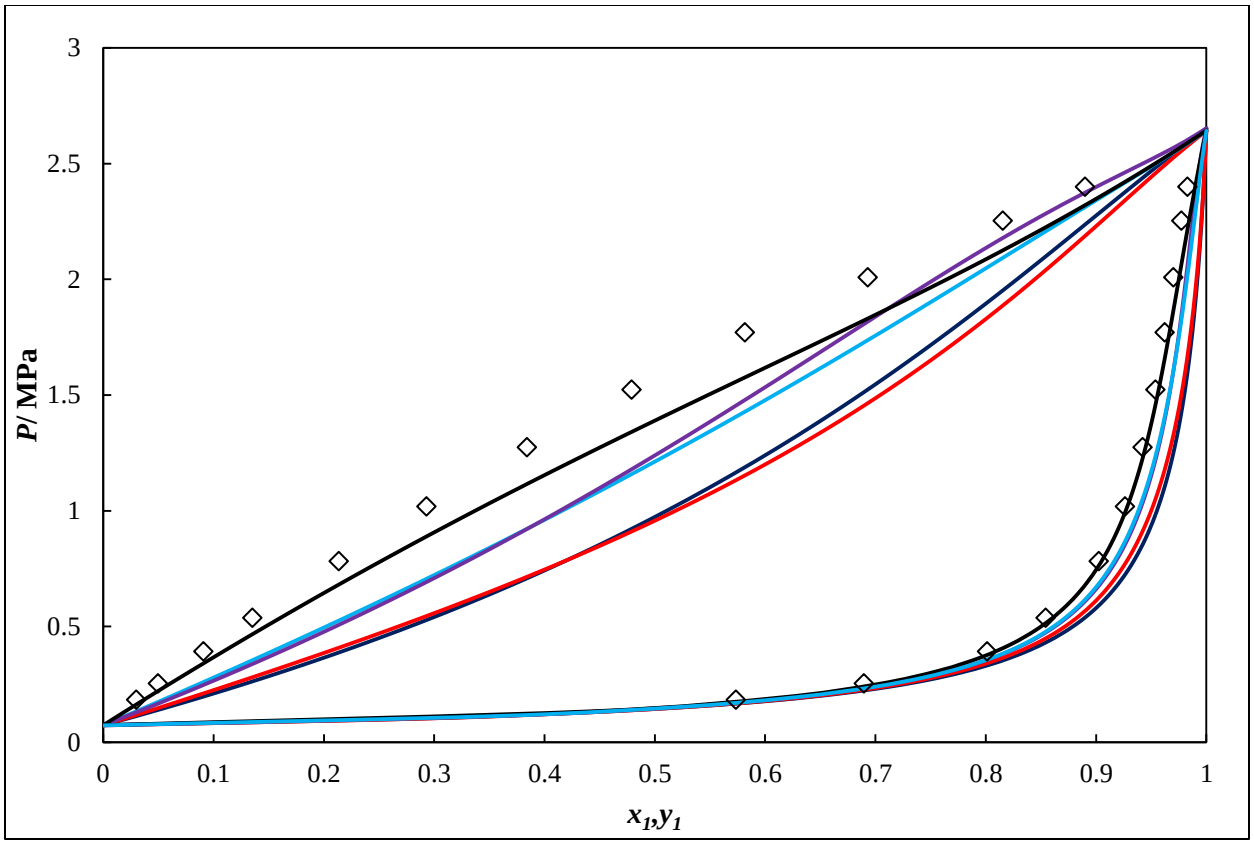

Figure 3.1: P-x-y plot for the CO_2 (1) + C_4F_{10} (2) binary system. VLE data of Valtz et al., (2011): ◊ (263.15 K); ○ (313.15 K); □ (333.15 K). Predicted data using the PSRK – COSMO-SAC model (solid black line); predicted data using the Dortmund-modified UNIFAC (solid purple line); predicted data using the PSRK-Dortmund modified UNIFAC (solid sky blue); predicted data using the UNIFAC model (solid dark blue line).

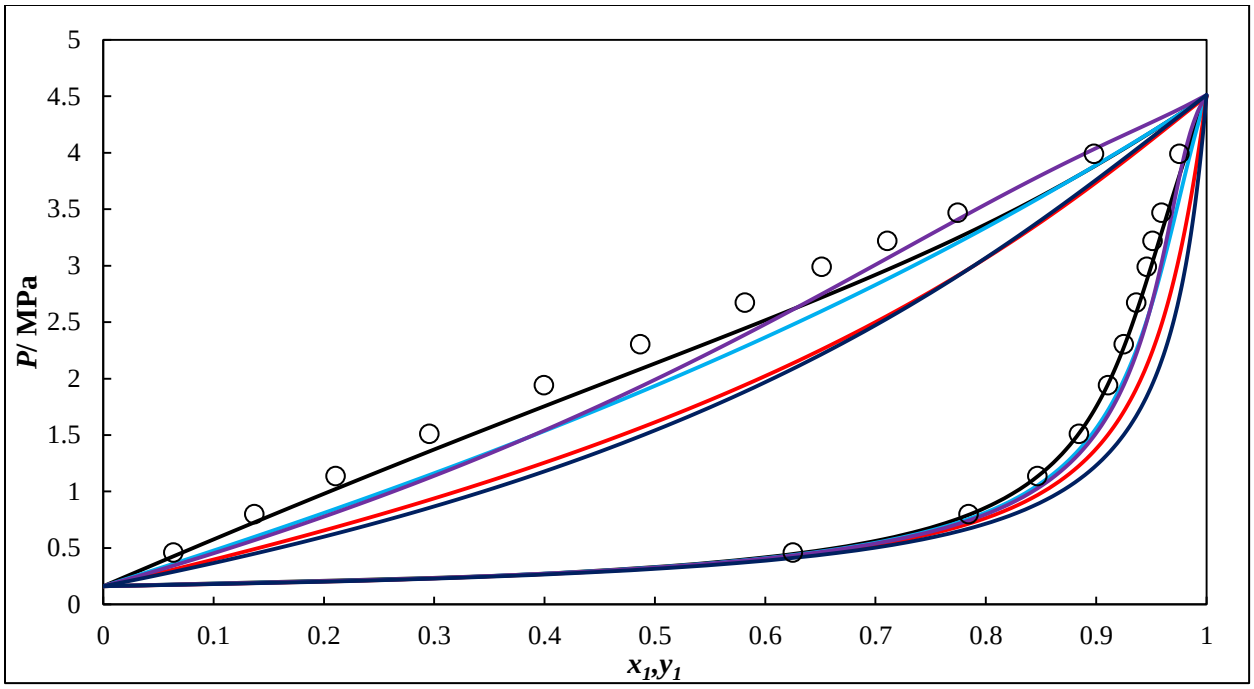

Figure 3.1: Continued.

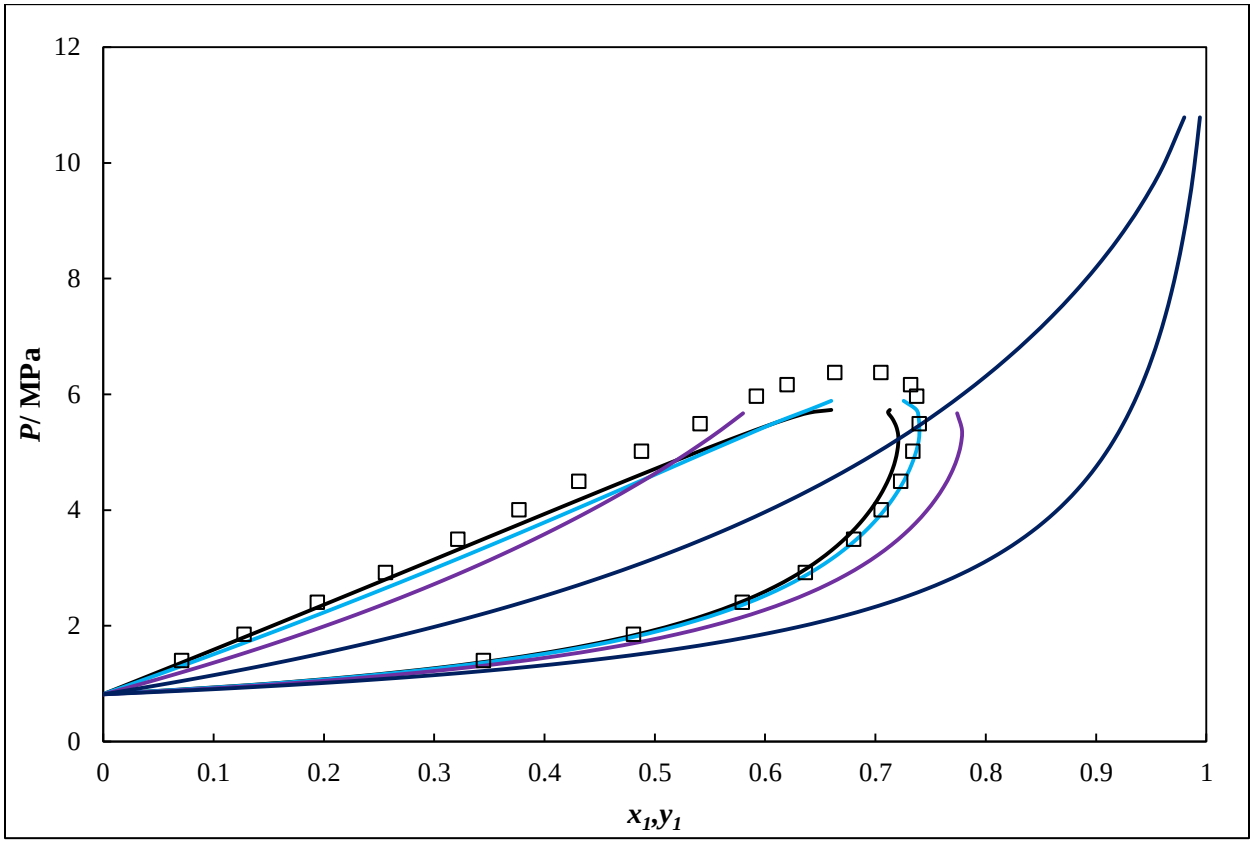

Figure 3.1: Continued.

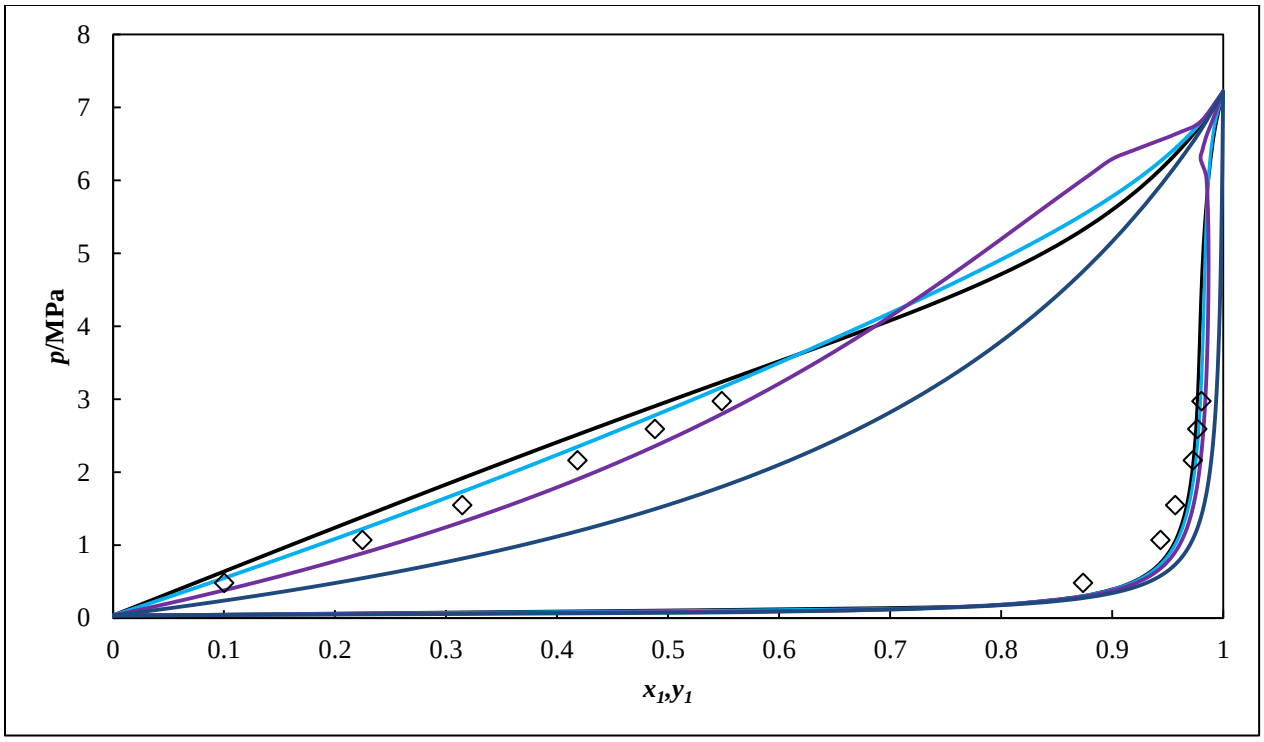

Figure 3.2: P-x-y plot for the CO_2 (1) + C_6F_{14} (2) binary system. VLE data of Costa Gomes and Pádua (2003): ◊ 303.15 K); ○ (313.15 K); □ (323.15 K). Predicted data using the PSRK – COSMO-SAC model (solid black line); predicted data using the Dortmund-modified UNIFAC (solid purple line); predicted data using the PSRK-Dortmund modified UNIFAC (solid sky blue); predicted data using the UNIFAC model (solid dark blue line).

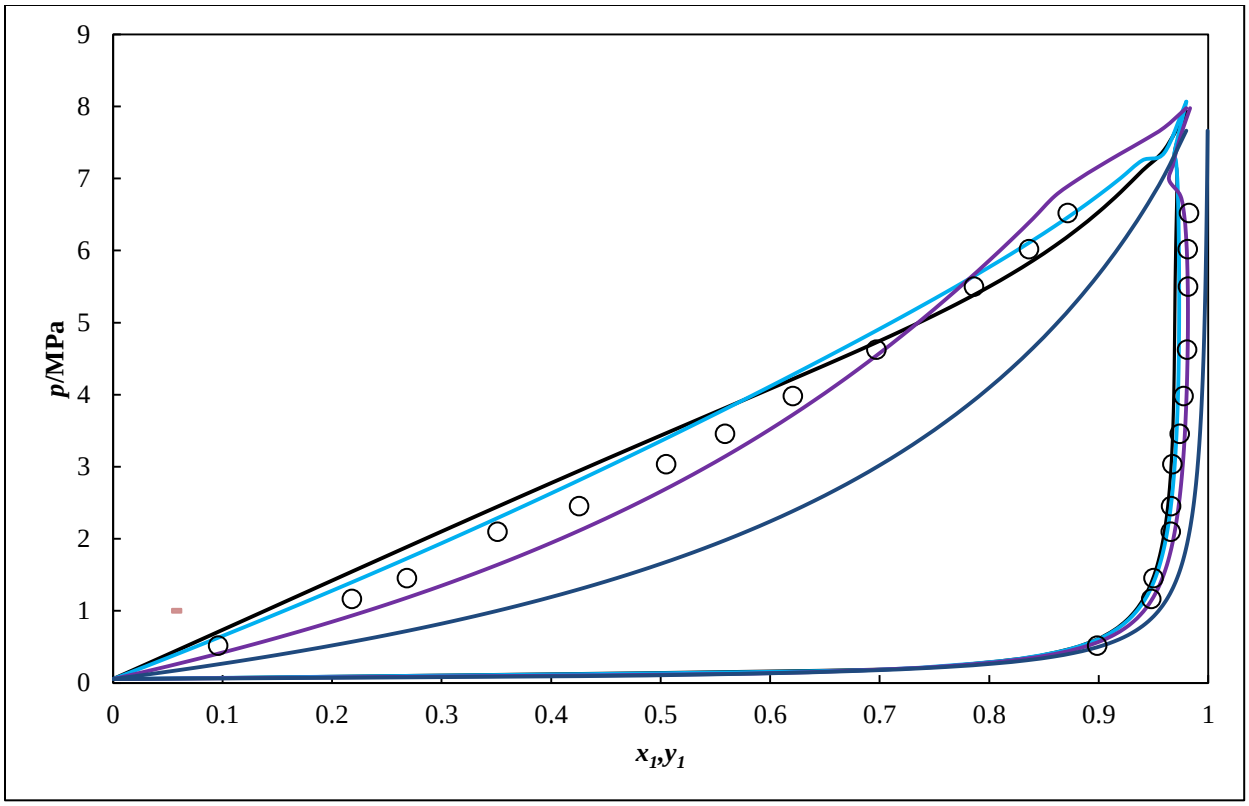

Figure 3.2: Continued.

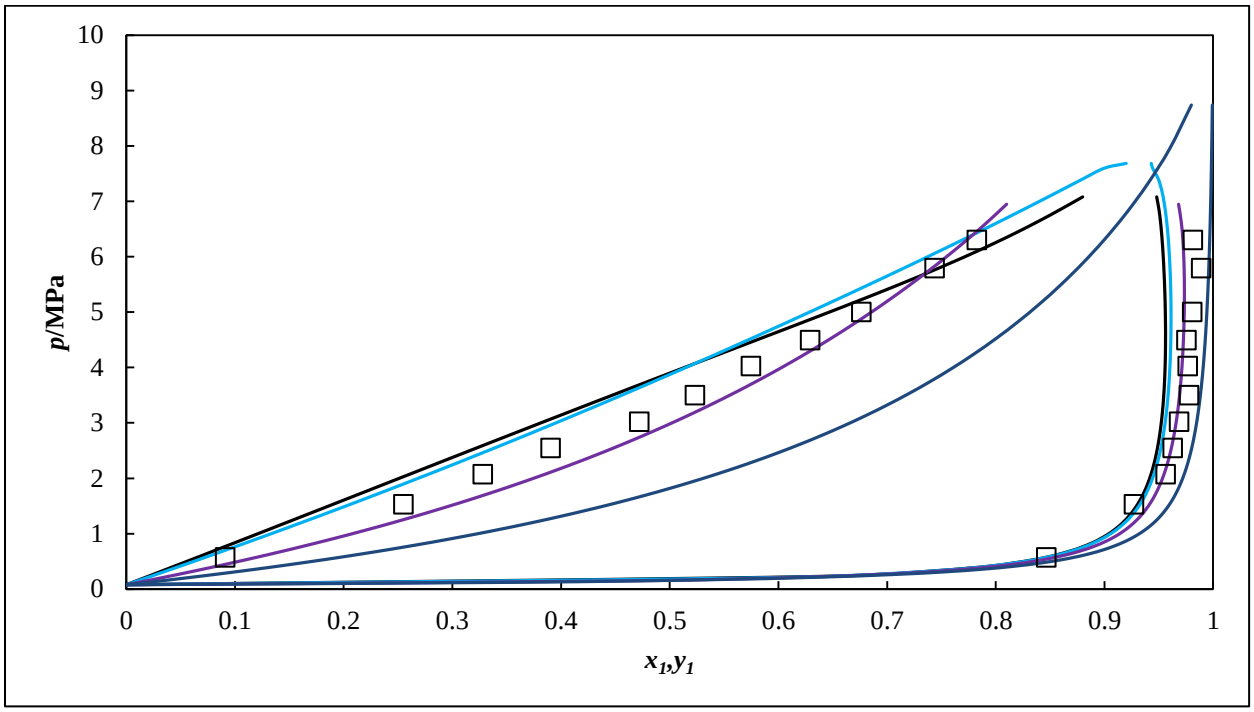

Figure 3.2: Continued.

As can be seen in Figures 3.1 and 3.2, the PSRK model combined with COSMO-SAC has outperformed the other models in predicting the VLE data much closer to the VLE data of Valtz et al., (2011) and Costa Gomes and Pádua (2003) for all the three isotherms selected. However, it is worth noting that the Dortmund-modified UNIFAC and the PSRK model, combined with modified UNIFAC, are the second best predictive models for the measured of Valtz et al., (2011) and Costa Gomes and Pádua (2003). Consequently, in this study the Dortmund-modified UNIFAC and the PSRK model combined with COSMO-SAC were used for prediction of data that could not be measured. Their descriptions are available in Appendix B.

3.5.1.1 The NRTL (Non-Random Two liquid) equation

The Margules and the van Laar equations were the first activity coefficient models developed and were widely used up to about 1965. These models use average or overall composition and are based on random mixing. Due to intermolecular forces, the mixing of molecules is never totally random. To account for the non-randomness, alternative methods for accurate description of phase behaviour were considered. The local composition based models were thus developed.

Renon and Praustnitz (1968) developed and proposed the NRTL equation based on the concept of local composition, which also accounts for non-randomness in solutions. For a binary system, the NRTL equation is expressed as follows.

$$\frac{G^E}{RT} = x_1 x_2 \left[\frac{\tau_{21} G_{21}}{x_1 + G_{21} x_2} + \frac{\tau_{21} G_{12}}{G_{12} x_1 + x_2} \right] \tag{3.47}$$

where

$$\tau_{ji} = \frac{G_{ji} - G_{ii}}{RT} = \frac{\Delta G_{ji}}{RT} \tag{3.48}$$

$$G_{ji} = \exp\left(-\alpha_{ji} \tau_{ji}\right) \tag{3.49}$$

The activity coefficients are derived as:

$$\ln \gamma_1 = x_2^2 \left[\tau_{21} \left(\frac{G_{21}}{x_1 + G_{21} x_2} \right)^2 + \frac{\tau_{12} G_{12}}{\left(G_{12} x_1 + x_2 \right)^2} \right] \tag{3.50}$$

$$\ln \gamma_2 = x_1^2 \left[\tau_{12} \left(\frac{G_{12}}{G_{12}x_1 + x_2} \right)^2 + \frac{\tau_{21} G_{21}}{(x_1 + G_{21}x_2)} \right] \tag{3.51}$$

The NRTL equation consists of three adjustable parameters: τ_{ij}, τ_{ji} and α_{ji} where τ_{ij} and τ_{ji} are the interaction parameters and α_{ji} is the non-randomness parameter. The values of α_{ji} range between 0.20 and 0.47 with zero indicating that the mixture is completely random (Renon and Praustnitz, 1986). In the absence of data the non-randomness parameter is set to 0.3 or 0.4 for non-aqueous mixtures and aqueous organic mixtures, respectively (Walas, 1985). In general, negative values and those greater than 0.5 of α_{ji} are questionable. Negative values are not in accordance with the physical meaning of the randomness parameters, although some authors have reported a value of $\alpha_{ji} = -1.0$ which yielded good results for a wide range of mixtures (Marina and Tassios, 1973). Raal and Mühlbauer (1998), on the contrary, found these guidelines inconclusive and proposed that an appropriate value of α_{ji} should be obtained from the regression of experimental data.

The NTRL model has been previously used to describe the behaviour of liquid phase for similar systems that are investigated in this study, and modelling has been found to be satisfactory (Ahmar et al., 2010 and Valtz et al., 2011).

3.6 The EoS/GE mixing rules for cubic Equations of state

The mixing rules for cubic EoS (standard van der Waals mixing rules) and the g^E models were discussed in Sections 3.4.3 and 3.5, respectively. The applicability range of cubic equations of state using the van der Waals one fluid mixing rules and the g^E models (local compositions based models) is presented in Table 3.2.

Table 3.2 shows that the strength of cubic EoS lies in their application at high pressures whilst the strength of the g^E models lies in their application to polar and non-polar mixtures. A combination of strength of both the cubic EoS and the g^E models has led to developing

alternative mixing rules, the so-called EoS/G^E mixing rules. In these mixing rules, the g^E model is incorporated into the EoS to allow the cubic EoS to also represent phase equilibria for polar compounds at high pressures.

Table 3.2: Applicability range of cubic EoS using the van der Waals one fluid mixing rules and activity coefficient models as taken from Kontogeorgis and Folas (2010)

Application	Cubic EoS	g^E activity coefficients models
Low pressures	✓	✓
High pressures	✓	
Simple mixtures (hydrocarbons gases)	✓	✓
Polar mixtures		✓
Many more properties than phase equilibria	✓	
Predictive calculations	Seldom	✓ (using the group contribution models)

Most (not all) of the EoS/G^E models developed so far derived from the following expression:

$$\left(\frac{g^E}{RT}\right)_P^{EoS} = \left(\frac{g^E}{RT}\right)_P^{model,*} \tag{3.52}$$

where P can be either the infinite pressure or the zero pressure, the superscript * refers to the specific activity coefficient model. The right hand side of Equation (3.52) is the expression of an explicit activity coefficient model whilst the left hand side is obtained from classical thermodynamics when the fugacity expression is known:

$$\frac{g^E}{RT} = \ln\phi - \sum_i x_i \ln\phi_i = \sum_i x_i \ln\gamma_i \tag{3.53}$$

$$RT\ln\gamma_i = \ln\frac{\hat{\phi}_i}{\phi_i} = \left(\frac{\partial n g^E}{\partial n_i}\right)_{T,P,n_{j\neq i}} \tag{3.54}$$

where ϕ, ϕ_i and $\hat{\phi}_i$ are the fugacity coefficients of the mixture, pure compound and of component i in the mixture, respectively.

Vidal (1978) and, Huron and Vidal (1979) developed the first EoS/G^E model which used infinite pressure as the reference pressure. The Huron and Vidal model combines flexibility with thermodynamic consistency. Although this model is useful for estimating essentially non-polar mixtures, it also offers a better correlation for mixtures consisting of polar and hydrogen bonding compounds compared to vdW1f mixing rules (Karen et al., 2014). Undovenko et al. (1972) show that a combination of SRK and the Huron-Vidal mixing rule satisfactorily describes polar mixtures at high pressures. However, the major drawback of the Huron-Vidal mixing rule is that it is incapable of handling large collections of interaction parameters of g^E models that are based on low pressure VLE data. Later, the Michelsen approach also known as the zero reference approach was introduced. This approach improved the "infinite pressure" mixing rules by allowing a direct use of interaction parameter tables, e.g. DECHEMA or UNIFAC. Furthermore, this approach has shown consistency using g^E models such as UNIFAC and UNIQUAC. The Michelsen approach for any vdW-type cubic EoS, when using equation (3.49) is:

$$\left(\frac{g^E}{RT}\right)_0^{model,*} + \sum_i x_i \ln\left(\frac{b}{b_i}\right) = q^e(\alpha) - \sum x_i q_i^e(\alpha_i) \tag{3.55}$$

where

$$\alpha = \frac{a}{bRT} \tag{3.56}$$

The $q^e(\alpha)$ term relies solely on the EoS used and is valid only for values of $\alpha > \alpha_{\lim}$. Table 3.3 lists expressions of $q^e(\alpha)$ and values of $\alpha_{\lim}$ for the SRK and PR EoS. Equation (3.55) is an implicit mixing rule for the energy parameter and, therefore requires an iterative procedure to calculate the energy parameter. Consequently, several zero reference pressure mixing rules have

been proposed to obtain a simpler or an explicit mixing rule and to address the limitation issue related to $\alpha_{\lim}$ values.

Table 3.3: The $q^e(\alpha)$ expressions and the $\alpha_{\lim}$ values in the Michelsen zero reference pressure mixing rule for two cubic EoS as taken from Kontogeorgis and Folas (2010)

EoS	$q^e(\alpha)$	$\alpha_{\lim}$
SRK	$q(\alpha) = -1 - \ln(u_0 - 1) - \alpha \ln\left(\frac{u_0 + 1}{u_0}\right)$	$3 + 2\sqrt{2}$
PR	$q(\alpha) = -1 - \ln(u_0 - 1) - \frac{\alpha}{2\sqrt{2}} \ln\left(\frac{u_0 + \left(1 + \sqrt{2}\right)}{u_0 + \left(1 - \sqrt{2}\right)}\right)$	$4 + 2\sqrt{2}$

u_0 *is the value of* V/b *at zero pressure*

Dahl and Michelsen (1990) proposed the modified Huron-Vidal first order and second order (MHV1 and MHV2) mixing rules, and Holderbaum and Gmehling (1991) proposed the predictive SRK model (PSRK), which is essentially the MHV1 mixing rule with a different value for q_1 as can be seen in Table 3.4 below. One should note that in the PSRK mixing rule, the SRK EoS is generically combined with either the original or the modified Dortmund UNIFAC versions which confer upon them the predictive capability. However, the PSRK mixing rule is not specific to any models and therefore other models, e.g., EoS and activity coefficient models can be used. Expressions of the mixing rules most well-known are listed in Table 3.4.

Examination of the MHV1, MHV2 and the PSRK mixing rules reveals that MHV1and PSRK, are simpler and explicit in their equations. The MHV1 and MHV2 mixing rules contain approximating functions that improve their correlative capabilities. However, both models do not satisfy the second virial coefficient boundary condition. The PSRK performed much better at high pressures than MHV1 and MHV2. The MHV2 mixing rule is theoretically incorrect at low pressure but the practical consequences of this drawback are minimal since equations of state are primarily used at high pressure.

Table 3.4: Expressions of the most well-known zero reference pressure mixing rules

Model	Expression
MHV1	$\alpha = \sum_i x_i \alpha_i + \frac{1}{q_1}\left[\frac{g^{E,*}}{RT} + \sum_i x_i \ln\left(\frac{b}{b_i}\right)\right]$ q_1 = -0.53 (SRK EoS) and -0.530 (PR EoS))
MHV2	$q_1\left(\alpha - \sum_i x_i \alpha_i\right) + q_2\left(\alpha^2 - \sum_i x_i \alpha_i^2\right) = \left(\frac{g^{E,*}}{RT}\right) + \sum_i x_i \ln\left(\frac{b}{b_i}\right)$ q_1 = -0.4780; q_2 =-0.0047 (SRK EoS) q_1 = -0.4347; q_2 =-0.003654 (PR EoS)
PSRK	$\alpha = \sum_i x_i \alpha_i + \frac{1}{q_1}\left[\frac{g^{E,*}}{RT} + \sum_i x_i \ln\left(\frac{b}{b_i}\right)\right]$ q_1 = -0.64663 (SRK EoS)

The main limitations of zero reference pressure models are that they cannot fully reproduce, at low pressures, the expression of activity coefficient models with which they are combined (Wertheim, 1984a). They also suffer the disadvantage of representing VLE data for size-asymmetric systems, e.g., mixtures containing either CO_2 or ethane with heavy hydrocarbons. The limitations of the EoS/G^E discussed so far have resulted in alternative models such as the Wong-Sandler mixing rule and the EoS/G^E approaches being found more suitable for asymmetric mixtures.

3.6.1 The Wong-Sandler mixing rule

Wong-Sandler (1992) developed a new EoS/G^E mixing rule somewhat different from the models discussed previously. This mixing rule derived from equating the Helmholtz energy (A^E) of a g^E model to that of an EoS at infinite pressure. The advantage of this is that the low pressure

activity coefficient model parameters can be useful because A^E does not strongly depend on pressure. As for mixing rules previously discussed, the Wong-Sandler mixing rule can be applied to any cubic EoS. In most cases, this has been used in conjunction with the PR EoS. The mixture parameters from the Wong-Sandler (1992) mixing rule are expressed as follows:

$$\frac{a_m}{RT} = Q\frac{D}{1-D} \tag{3.57}$$

$$b_m = \frac{Q}{1-D} \tag{3.58}$$

where Q and D are defined as:

$$Q = \sum\sum z_i z_j \left(b - \frac{a}{RT}\right)_{ij} \tag{3.59}$$

with

$$\left(b - \frac{a}{RT}\right)_{ij} = \frac{1}{2}\left[b_i + b_j\right] - \frac{\sqrt{a_{ii}a_{jj}}}{RT}\left(1 - k_{ij}\right) \tag{3.60}$$

$$D = \frac{A^E_{EOS}\left(T, P = \infty, x_i\right)}{\Lambda RT} + \sum_{i=1}^{n} z_i \frac{a_i}{b_i RT} \tag{3.61}$$

and $A^E_{EOS}(T, P = \infty, x_i)$ is the excess Helmholtz free energy calculated at infinite pressure and k_{ij} is the binary interaction parameter which is generally obtained from the regression of experimental VLE data. Orbey et al. (1993) developed a predictive Wong-Sandler model using the UNIFAC g^E models to calculate the binary interaction parameter k_{ij}. The modelling procedure for this can be found in their work.

The fugacity coefficients for the vapour and liquid phases calculated using the Peng-Robinson (PR) EoS is expressed as follows:

***Peng-Robinson (PR) EoS*:**

$$\ln \hat{\phi}_i = -\ln\left[\frac{P(V-b_m)}{RT}\right] + \frac{1}{b_m}\left(\frac{\partial n b_m}{\partial n_i}\right)\left(\frac{PV}{RT}-1\right) + \frac{1}{2\sqrt{2}}\left(\frac{a_m}{b_m RT}\right) \left[\frac{1}{a_m}\left(\frac{1}{n}\frac{\partial n^2 a_m}{\partial n_i}\right) - \frac{1}{b_m}\frac{\partial n b_n}{\partial n_i}\right]\ln\left[\frac{V+\left(1-\sqrt{2}\right)b_m}{V+\left(1+\sqrt{2}\right)b_m}\right] \quad (3.62)$$

The Wong and Sandler (1992) mixing rule has proven to be excellent in the correlation of phase equilibria for both simple and complex systems consisting of polar and associating species. Combined with a cubic EoS, the Wong and Sandler (WS) mixing rule can be used for a wide range of highly non-ideal systems. Despite its capabilities to predict, correlate and model various numbers of mixtures, it has been shown that the WS mixing rule with the composition-independent k_{ij} is unable to match the EoS obtained g^E expression to that of the activity coefficient model for asymmetric systems (Kontogeorgis and Folas, 2010).

Several discussions on the mixing rules have been published by Raal and Mühlbauer (1998) and Kontogeorgis and Folas (2009) which present an excellent review of their capabilities as well as their limitations.

3.7 Vapour-Liquid Equilibrium (VLE) data

Vapour-liquid equilibrium is a state or condition where both the vapour and liquid phases are in equilibrium with each other at constant temperature and pressure. In fact, an exchange of their different constituents takes place until the compositions of the two phases are stable.

VLE data are frequently represented in forms of phase diagrams. Raal and Mühlbauer (1998) present different types of phase diagrams for VLE behaviour. The common phase diagrams involve the *P*-*x*-*y* plot for isothermal conditions, the *T*-*x*-*y* plot for isobaric conditions and *x*-*y* plots either for isothermal or isobaric conditions.

To date, analytical methods have been developed for thermodynamic representation of VLE data. The most widely used methods are the $\gamma - \phi$ approach also known as the combined

method and the $\phi - \phi$ approach also known as the direct method. The combined method uses an EoS such as a van der Waals or PR EoS to describe the non-idealities of the vapour phase whilst an activity coefficient model such as the Wilson or NRTL equations are used to describe the non-idealities in the liquid phase. The direct method instead uses an EoS to describe the non-idealities of both the liquid and the vapour phases. An extensive discussion about the direct and the combined method can be found in Raal and Mühlbauer (1998). The direct method was used in this study and will be discussed later in this chapter.

The calculation procedures undertaken by both the combined and the direct method depend on the type of measurements. Three approaches are common in VLE data measurements: the dew point, the bubble point and the flash calculations. An approach is defined as the bubble point pressure calculation when for a single data point, the system temperature and the liquid phase composition are given but the pressure and the vapour phase composition are calculated. Otherwise, the approach is defined as the dew point pressure calculation. At a given pressure, these approaches are either defined as the bubble point or dew point temperature calculations depending on whether the liquid or the vapour phase composition is known. The flash calculation approach is defined when for a single data point, temperature and pressure of the system are fixed and the vapour and liquid phase compositions are calculated using thermodynamic models. In this study, the T-flash calculation was chosen for the data treatment.

3.7.1 The direct method

The direct method uses the fugacity coefficients to describe both the vapour and liquid phase non-idealities of mixture at the equilibrium condition. This is described by:

$$\hat{f}_i^V = y_i \hat{\phi}_i^V = \hat{f}_i^L = x_i \hat{\phi}_i^L \tag{3.63}$$

The fugacity coefficients are calculated using the following equations.

$$\ln \hat{\phi}_i^V = \left(\frac{1}{RT}\right) \int_V^\infty \left[\left(\frac{dP}{dn_i} \right)_{T,V,n_j} - \frac{RT}{V} \right] dV - \ln \left[\frac{PV}{RT} \right] \tag{3.64}$$

$$\ln \hat{\phi}_i^l = \frac{1}{RT} \int_v^{\infty} \left[\left(\frac{\partial P}{\partial n_i} \right)_{T,V,n_j} - \frac{RT}{V} \right] dV - \ln \left[\frac{PV}{RT} \right] \quad (j \neq i) \tag{3.65}$$

The equilibrium ratio K_i which is a measure of the tendency of a given chemical species to distribute itself preferentially between the liquid and vapour phases is often used in the direct method to simplify calculations. It is mathematically described as:

$$K_i = \frac{y_i}{x_i} \tag{3.66}$$

where x_i and y_i are the liquid and vapour mole fraction of species *i*.

Figure 3.3 illustrates a computational procedure for the temperature flash calculation using the direct method (Coquelet, 2003).

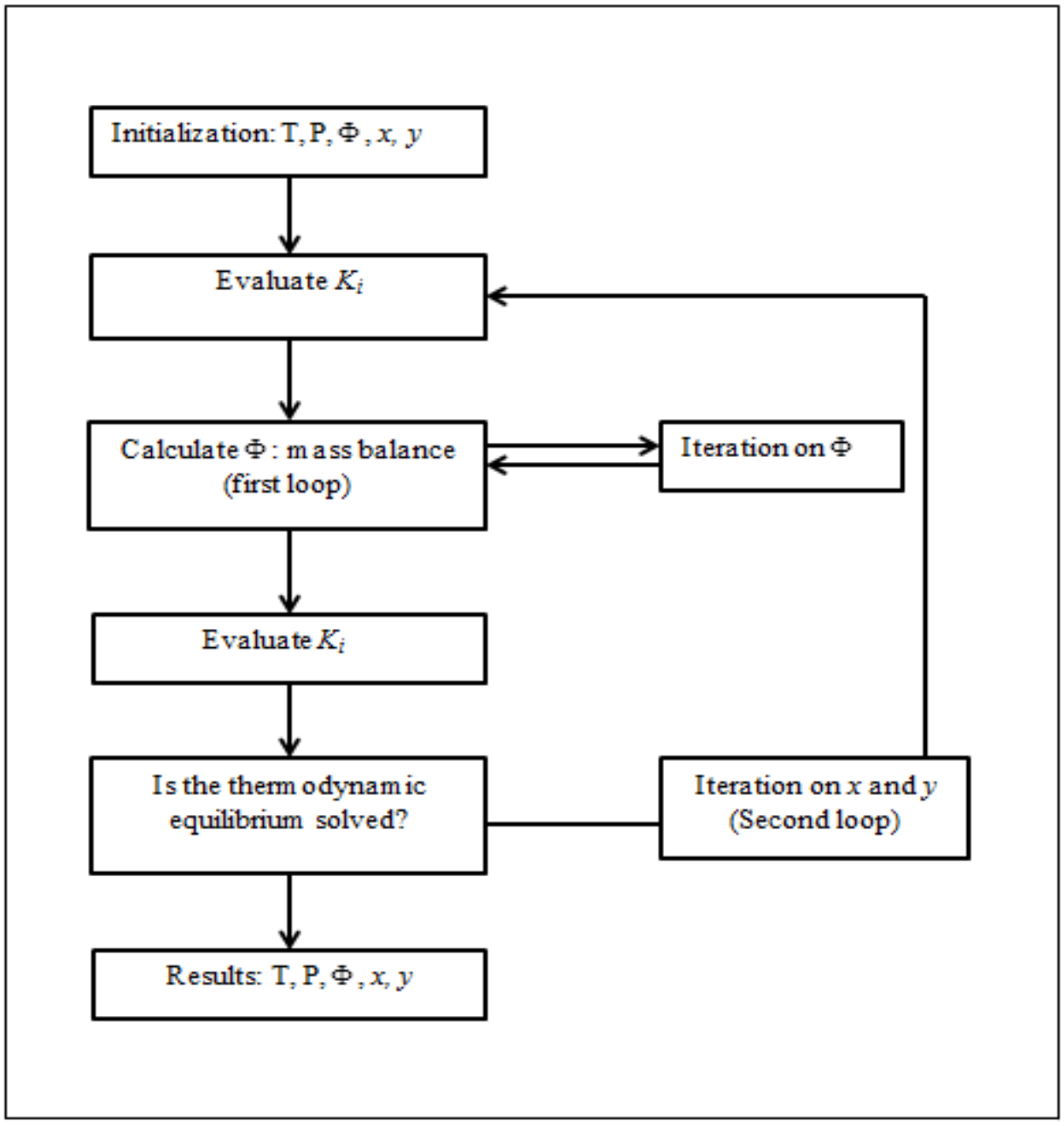

Figure 3.3: Schematic diagram of the T-flash calculation procedure using the direct method (Coquelet, 2003).

Several attempts have been made to use the direct method (T-flash calculation) to regress VLE data for systems similar to the ones investigating in this study. These authors used different EoS with different mixing rules incorporating the NRTL model (Coquelet, 2003; Ramjugernath et al., 2009; Chiyen, 2011; Tshibangu et al., 2013). The results obtained agreed favourably with the experimental data. However the main challenges using the direct method are listed from Raal et al. (1980) and, Raal and Mühlbauer (1998) as follows:

1) Selection of a suitable EoS to describe both the vapour and liquid non-idealities. Furthermore the EoS should be flexible enough to fully describe the *P*, *V*, *T* behaviour of a pure substance for both phases in the temperature and pressure range under investigation;
2) Selection of suitable mixing rules for an accurate description of an EoS to mixtures; and
3) Location of the convenient roots for liquid and vapour molar densities when an EoS higher than cubic ones is used.

3.8 Selection of thermodynamic models

The selection of thermodynamic models is of paramount importance as it could affect all subsequent tasks in a simulation process if not undertaken correctly. Consequently, a number of factors should be considered which are in accordance with a decision tree show in Figure 3.4.

1. the nature of the properties of interest;
2. the composition of the mixture;
3. the pressure and temperature range; and
4. the availability of parameters.

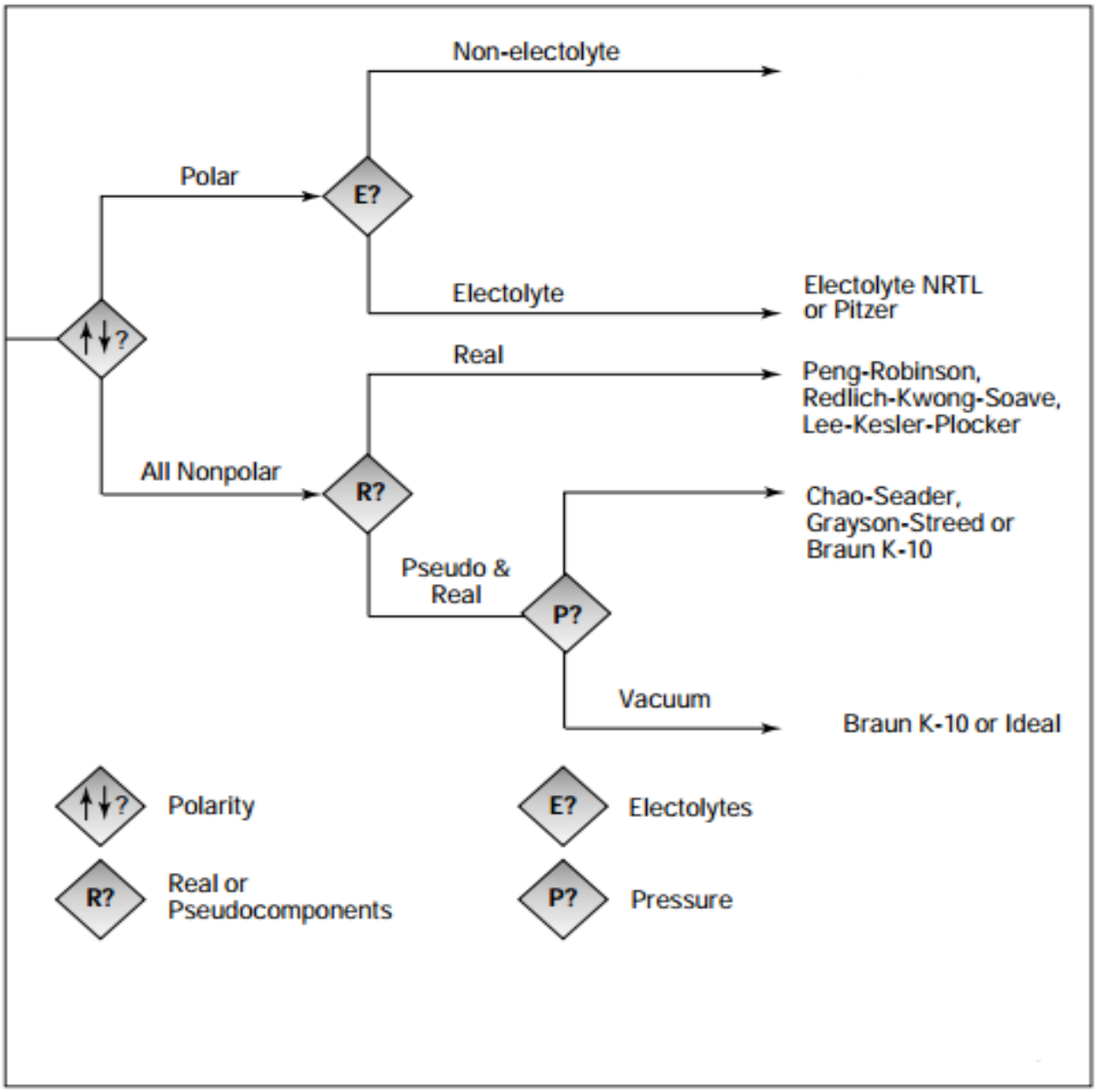

Figure 3.4: The first steps in the selection of thermodynamic models (Aspen Plus, 2008).

One should note that in Figure 3.4, pseudocomponents are referred to a grouping of mixture's constituents by a useful property such as boiling point. In this manner, a mixture of 100 constituents can be reduced to 20 or fewer. The properties of the pseudocomponents are represented by an average boiling point, molecular weight or specific gravity.

In Aspen Plus, there are two groups of methods which are based either on activity coefficient models or equations of state. These methods are defined as sets of thermodynamic models that incorporate equations of state, alpha functions, mixing rules and activity coefficient models.

For pressures less than 1 MPa, and if no components making up the mixture is near critical point, activity coefficient-based methods are recommended. These models are used in the predictions of non-ideal liquid behaviour for VLE and LLE, whereas methods based on the equations of state are known to representing data up to the critical points and above. However, if the equations of state-based methods are coupled with predictive mixing rules, the strengths of the two models will effectively combine. One should note that the equations of state based-methods incorporate the activity coefficient models in the modelling of phase behaviour. They are also recommended for higher pressure and temperature data as they were developed for this purpose.

As can be seen from Figure 3.4, for all real nonpolar systems the following property methods are recommended: Peng-Robinson, Soave-Redlich-Kwong and Lee-Kesler-Plocker.

In light of the discussion presented throughout this chapter, the following combinations of thermodynamic models were selected to correlate the experimental VLE data investigated in this study:

1) The Peng-Robinson EoS incorporating the Mathias-Copeman alpha function, with the Wong-Sandler mixing rule utilizing the non-random two-liquid activity coefficient model;
2) The Peng-Robinson EoS incorporating the Stryjek-Vera alpha function, with the Wong-Sandler mixing rule utilizing the non-random two-liquid activity coefficient model;
3) The Soave Redlich-Kwong EoS incorporating the Mathias-Copeman alpha function, with the modified Huron-Vidal 1 or 2 mixing rule utilizing the non-random two-liquid activity coefficient model; and
4) The Soave-Redlich-Kwong EoS incorporating the Mathias-Copeman alpha function, with the predictive Soave-Redlich-Kwong mixing rule utilizing the non-random two-liquid activity coefficient model.

4

CHAPTER FOUR

PHASE EQUILIBRIUM DATA MEASUREMENTS

4.1 Experimental apparatus

4.1.1 Introduction

The Thermodynamics Research Unit of the School of Engineering at the University of KwaZulu-Natal has, over the past 25 years, gained a reputation for its phase equilibrium studies. Design, construction and commissioning of experimental apparatus, covering both static and dynamic methods, has been undertaken (Ramjugernath, 2000; Naidoo, 2004; Chiyen, 2010 and Tshibangu, 2010).

The choice of experimental apparatus for phase equilibria, and thermophysical property measurements, depends on the experimental conditions and the types of applications. Although various equipment is available, particular applications can still require either equipment modification or new equipment design.

Most of the static-analytic based equipment developed in the Thermodynamics Research Unit up to 2011 featured quite large volume equilibrium cells, i.e. 60 cm^3, which therefore required significant amount of chemicals. This has been of concern because the synthesis of chemicals at high purity is expensive.

To address this particular drawback, the Thermodynamics Research Unit introduced the design, development and commissioning of static-analytic based apparatus for small volumes (~ 17.4 cm^3) as an objective (Narasigadu, 2011 and Nelson, 2012).

In this study two experimental apparatuses were selected for isothermal VLE data measurements. The experimental apparatuses have been previously described by Laugier et al. (1986) and Narasigadu (2011).

The apparatus described by Laugier et al. (1986) was mainly used for binary systems involving hazardous chemicals, and the measurements were undertaken at MINES ParisTech, CTP – Centre Thermodynamics of Processes in Fontainebleau (France). The CTP laboratories generally keep their experimental setups enclosed in fumehoods and have both built-in and portable gas detector systems. One should note that fumehoods are an excellent means of dealing with hazardous chemicals, as in the case of any chemical leakage, it is rapidly captured and vented to a safer environment.

The experimental apparatus described by Narasigadu (2011) was mainly used for binary systems involving non-hazardous chemicals and the measurements that were undertaken at the University of KwaZulu-Natal in the Thermodynamics Research Unit in Durban (South Africa).

The two experimental apparatuses present similar characteristics except for the volume of their equilibrium cells. The equilibrium cell described by Laugier et al. (1986) consists of a cylindrical cavity with two sapphire windows whilst that of Narasigadu (2011) consists of a hollow cylindrical sapphire tube. Due to their similarities, only the experimental apparatus described by Narasigadu (2011) will be presented in this chapter. However, more details pertaining to the apparatus by Laugier et al. (1986) can be found in their work or in Tshibangu et al. (2014a and 2014b).

4.1.2 Description of the experimental apparatus of Narasigadu (2011)

The experimental apparatus, previously described by Narasigadu (2011), is based on a static-analytic method. Figures 4.1 and 4.2 show the equilibrium cell and the schematic diagram illustrating the experimental setup, respectively.

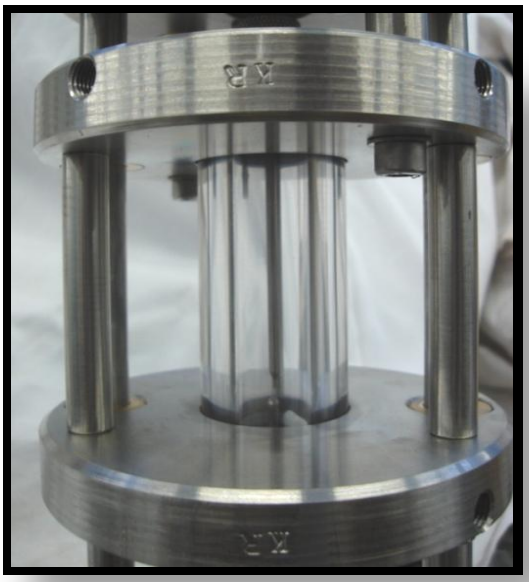

Figure 4.1: Equilibrium cell (Narasigadu, 2011)

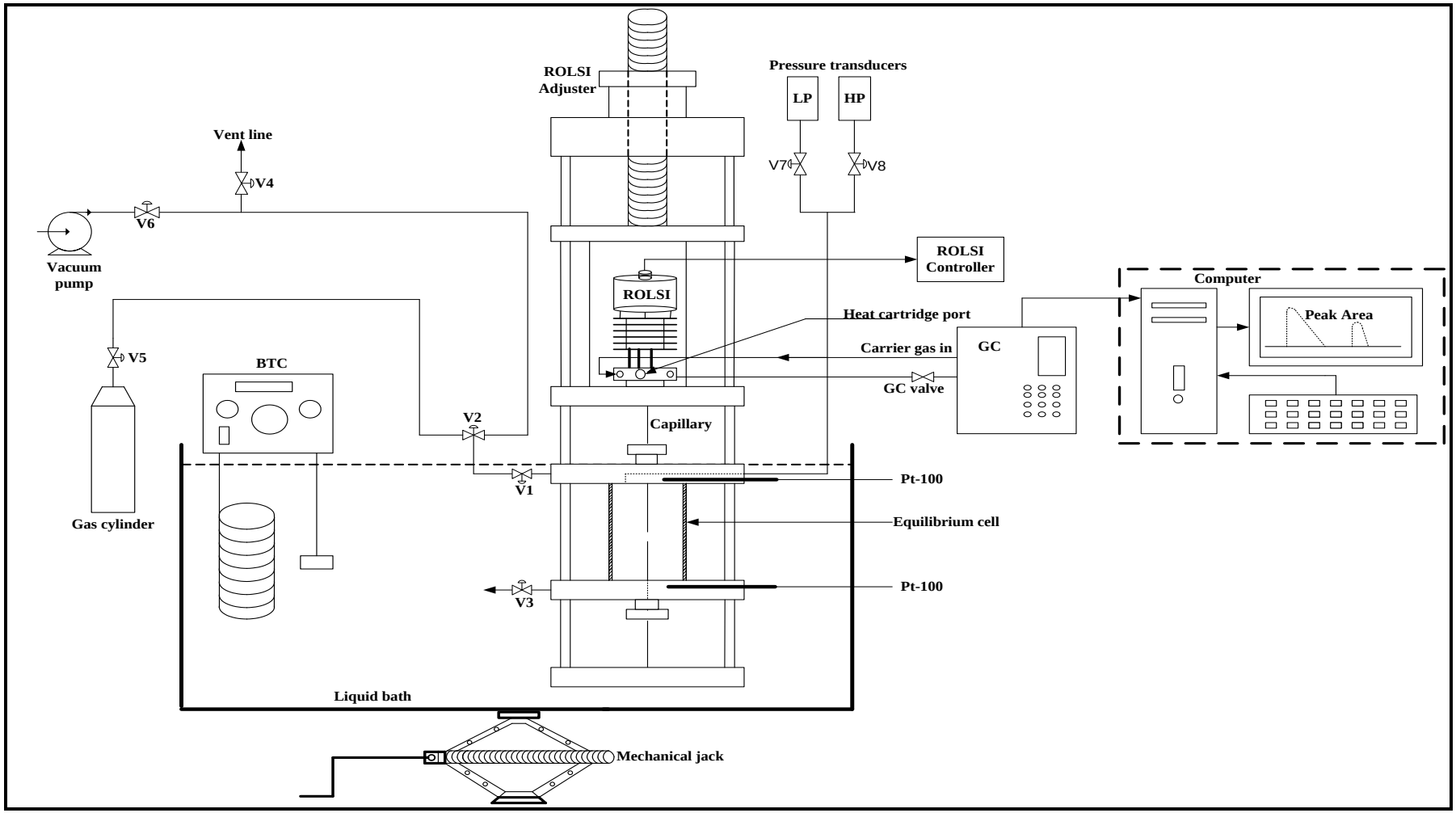

Figure 4.2: Schematic diagram of the experimental apparatus (Narasigadu, 2011)

The equilibrium cell, which is the central feature of the experimental apparatus, was fully immersed in a thermo-regulated bath filled with ethylene glycol. The equilibrium cell was constructed from a cylindrical sapphire tube (supplied by Rayotec Scientific Inc.), with an internal diameter of 17.80 mm (±0.10 mm), outer diameter of 35.60 mm (±0.05 mm) and height of 70.00 mm. This results in an internal volume of approximately 17.4 cm^3.

The sapphire equilibrium cell was designed and constructed for multiple purposes; to facilitate observation of the liquid level and viewing of the equilibrium phases, and for adjustment of the capillary of the mobile ROLSI ^{TM} sampler into either the vapor or liquid phase, during sampling.

The equilibrium cell was held between two 316 stainless steel (316 SS) flanges and three 316 SS spacer rods evenly distributed. Sealing between the equilibrium cell and the two 316 SS flanges was accomplished using two Viton O-rings. The O-rings were fitted into grooves that were cut into the top and bottom 316 SS flanges enclosing the equilibrium cell.

Each flange contains valves and fittings for the filling and evacuation of the equilibrium cell content, as well as for temperature and pressure measurements.

The internal cell pressure was measured using a 0-25 MPa absolute WIKA model type P-10 pressure transducer housed in a thermo-regulated aluminium block. The temperature of the aluminium block was monitored by means of a Shinko ACS-13A digital indicating controller, and was connected to 34970 A Agilent data acquisition unit. Calibration of the pressure transducer was periodically performed using the WIKA CPH 6000 pressure calibration unit with a 0-25 MPa gauge WIKA CPT 6000 standard pressure transducer. The calculated accuracies in the pressure measurement are estimated to be within ± 0.3 kPa.

The temperature measurement was achieved via two WIKA model REB Pt-100 Ω with class A ceramic bulb type sensor temperature probes, which were inserted inside wells drilled into each flange, i.e., the top and bottom flange. As with pressure, temperature data logging was achieved via a computer linked to a 3497A Agilent data acquisition. The temperature probes were intermittently calibrated against a WIKA type Pt-100 Ω standard probe using a WIKA type CTH 6500 bath. Accuracies in the temperature measurement are estimated to be within ± 0.02 K for both probes.

Stirring of the equilibrium cell contents was achieved through the magnetic stirrer placed inside the cell. The revolving magnet was positioned at the side of the cell and linked to the motor by means of two sprockets and a stainless steel roller chain which transmitted motion from one to the other. The stirring mechanism was designed so that the stirrer bar could efficiently rotate near the bottom of the cell therefore preventing any adverse effect on the thermodynamic equilibrium time.

Sampling of phases in equilibrium was achieved via a mobile Rapid-Online-Sampler-Injector (ROLSI ^{TM}) (Guilbot et al., 2000). The ROLSI ^{TM} was developed for sampling of high pressure fluids and the analysis of phases by gas chromatography. It allows the in situ removal of repeatable and representative samples from the cell without any contamination or disturbance to equilibrium.

Since the cell has a small internal volume (approximately 17.4 cm^3), a disturbance to the equilibrium state was expected due to the movement of the ROLSI ^{TM} capillary during the sampling process. This would cause a change in volume and therefore a pressure variation. To address this issue, a mechanism similar to the sampling process was put into place to compensate for the change in volume due to the movement of the ROLSI ^{TM} capillary. A 316 SS dowel with dimensions similar to that of the capillary of the ROLSI ^{TM} was placed and operated from the bottom. It was designed in such a way that it would move simultaneously with the capillary of the ROLSI ^{TM} thereby keeping a constant volume throughout the sampling process.

Analysis of the equilibrium phase composition was carried out using a gas chromatograph (GC) (model: Shimadzu 2010) configured with a thermal conductivity detector (TCD) connected to a computer that uses the GC solutions software. Good separation of the components was achieved using a Porapak Q packed column. Periodic calibration of the detector was achieved by repeated injection of known amounts of each pure component into the injector of the gas chromatograph using a gastight syringe. This method was undertaken for all the components investigated in this study.

4.2 Experimental procedure

4.2.1 Introduction

Accurate experimental VLE data is a difficult and time consuming task as certain measurements need to be taken manually. However, an obvious solution is a well formulated experimental procedure as well as its proper execution. The nature of chemicals to be studied should also be investigated from a safety and practical standpoint. This ensures safety for both the experimenter and those in the immediate environment.

The experimental procedure used in this work has been well documented by numerous authors (Ramjugernath, 2000; Coquelet, 2003; Tshibangu, 2010 and Narasigadu, 2011). The guidelines that they have listed as essential in successfully achieving accurate experimental measurements were employed and are presented in this chapter.

One should note that the experimental procedure for the experimental apparatuses described by Laugier et al. (1986) and Narasigadu (2011) is similar and only the experimental procedure regarding the apparatus by Narasigadu (2011) is described in this chapter.

The experimental procedure, the details for the temperature probes, pressure transducers and gas chromatograph, including the calibration units, relating to the experimental apparatus described by Laugier et al. (1986), can be found in Tshibangu et al. (2014a and 2014b).

4.2.2 Preparation of the phase equilibrium apparatus

4.2.2.1 Equipment calibration

4.2.2.1.1 Temperature probe calibration

The two Pt-100s probes allocated to the cell at levels corresponding to vapour and liquid phases ensured the absence of a temperature gradient between the top and bottom of the cell. These probes were initially calibrated against a standard 100 Ω platinum resistance using a processor calibrator CPH 6000 supplied by WIKA. The standard probe is certified accurate to within ± 0.02 K.

The three probes (the standard Pt-100 and the two Pt-100s) were immersed in a liquid bath. Vigorous stirring of the liquid medium was essential to ensure the absence of temperature gradients within the bath. The calibration procedure was achieved via increasing and decreasing the temperature monotonically to account for the hysteresis effect. Several points were measured for the same temperature and only those that correlated to within 0.1% deviation were considered to obtain an average temperature value. The calibration range of the two Pt-100s extended from 278.15 to 338.15 K and the uncertainty emanating from the temperature calibration was estimated to be within ± 0.02 K.

Temperature data logging was achieved via a computer linked to a 3497A Agilent data acquisition unit.

4.2.2.1.2 Pressure transducer calibration

Internal cell pressure measurement was achieved via a 0-25 MPa absolute WIKA model type P-10. The P-10 pressure transducer was calibrated using a WIKA CPT 6000 standard pressure transducer certified accurate to within 0.0025 %. The two pressure transducers were directly connected to the equilibrium cell and the same pressure was applied to both. The comparison between the two readings helps one to verify the accuracy of the pressure transducer under calibration. One should note that a bottle of nitrogen was used as a source of pressure. The highest pressure in a nitrogen bottle is generally about 20 MPa. Consequently, the pressure calibration range for the pressure transducer extended from 0 – 17 MPa (absolute) and the uncertainty emanating from the pressure calibration was determined to be within ± 1.5 kPa.

As for temperature, data logging was achieved via a computer linked to a 3497 A Agilent data acquisition unit.

4.2.2.1.3 Gas chromatograph detector calibration

The analysis of the equilibrium phase composition was carried out using a Shimadzu chromatograph model 2014 configured with the thermal conductivity detector (TCD) connected to a computer that uses the GC solutions software. A Poropak or 5 % Krytox carboblack B analytical column was used with either helium or nitrogen as the carrier gas depending on the

component under investigation. One should note that the nitrogen carrier gas was only used for the binary system involving hydrogen as this could not be detected using helium.

Calibration of the detector was achieved by repeated injection of known amounts of each pure component into the injector of the gas chromatograph using SGE type syringes of various volumes. For each volume, at least five samples were injected until the average absolute deviation for the corresponding peak areas were within 1% error. At the end, plots of peak area versus number of moles were generated, with polynomial regression type equations:

$$n_i = A_i P^2 + B_i P + C_i \tag{5.3}$$

where P is the peak area and n_i the number of moles of component i. A_i, B_i and C_i are the calibration coefficients. C_i corresponds to the constant at the origin and therefore it is not considered in the calculation of the number of moles of samples from the ROLSI ^{TM} sampler (the constant at the origin C_i can either be positive or negative). This is explained by the imperfection of SGE type syringes.

4.2.3 Preparation of the equilibrium cell

4.2.3.1 Leak testing

Since pressure is one of the vital variables for VLE data measurement, it is crucial to ensure that the entire experimental set-up is leak-tight, mainly the equilibrium cell and lines that convey samples to the gas chromatograph. The adverse effect of leaks would result in unreliable temperature and pressure measurements, material loss and safety hazards, to name just a few.

Consequently, leak testing was thoroughly and routinely conducted throughout the period allocated for VLE data measurement. The equilibrium cell was charged with nitrogen at a pressure in excess of the expected maximum operating pressure and monitored for leaks. 'Snoop' liquid leak detector was applied to various connections and seals in the apparatus. The existence of a leak would have been revealed in the form of bubble formations. The equipment was deemed ready for use when the pressure decrease was within a specified tolerance (~ 1.5 kPa) for a period of twenty-four hours.

The greatest challenge encountered in leak testing, was on the ROLSI ^{TM} sampler thumb screw situated on top of the upper 316 SS flange of the cell and the thumb screw for the metallic dowel located below the lower 316 SS flange. Thumb screws were fully tightened and O-rings were examined and replaced if damaged.

4.2.3.2 Cleaning of the equilibrium cell

The equilibrium cell, with its associated lines, was always cleaned before commencing with experimental measurements. The line connecting the cell to the pressure transducer was heat-traced to avoid condensation of non-volatile components. The three-way valve connected to the cell loading valve was switched to the vacuum position until an absolute vacuum was reached in the cell. The cell loading needle valve was then closed and the three-way valve switched to the "charge" position. A volume of 15 cm^3 was then charged into the cell using a syringe and the cell loading needle valve was closed.

Thereafter, with the aid of a mechanical jack, the cell was fully immersed in a temperature regulated bath set at 323 K and the stirrer switched on and adjusted to ensure vigorous stirring for a period of 30 minutes. Ethanol was then drained from the cell by opening the cell loading needle valve and switching the three-way valve to the "charge" position. The compressed air cylinder was then connected to the three-way valve and compressed air was loaded into the cell. The draining needle valve was then opened and ethanol was collected in a beaker and discarded in a hazardous waste bottle. The compressed air was then disconnected from the equilibrium cell.

The entire process was repeated at least once to ensure proper cleaning. After completion of the cleaning process, the cell was open to the atmosphere via the draining and loading needle valve to dry the ethanol residue. On several occasions, compressed air was used to accelerate the drying process. Trace amounts of ethanol were removed from the equilibrium cell with the aid of a vacuum pump and then samples were sent to the GC to confirm whether ethanol residues were still present in the cell.

The sampling lines that conveyed samples to the GC were heat-traced and flushed with helium, the carrier gas. Thereafter, these lines were evacuated using a vacuum pump for a period of 30 minutes. This process was repeated at least twice to ensure proper cleaning. In addition, samples

were sent to the GC for analysis which helped confirm whether any impurities remained in the lines.

4.2.4 Start-up procedure

The equilibrium cell, with its associated lines, was initially cleaned as outlined in Section 4.2.3.2. For binary VLE data measurements, the equilibrium cell was initially evacuated and maintained at the lowest vacuum for a period of 30 minutes. The least volatile component was then loaded into the equilibrium cell as outlined in Section 4.2.3.2.

The thermo regulated liquid bath was then elevated with the aid of a mechanical jack to fully immerse the cell in the liquid. The bath was set to a desired temperature, stirrers switched on and adjusted to a high speed and the system was left to attain thermal equilibrium. Thereafter, the component present in the cell was degassed in situ by firstly switching the three-way valve to the 'venting" position and then intermittently opening the loading needle valve. This process took about 5 minutes; it also helped position the liquid level.

During the venting process, one had to ensure that not too much liquid was removed from the cell since a low level of liquid would cause errors in the sample analysis. Once the liquid was totally degassed, samples were withdrawn using a ROLSI ^{TM} and sent to the GC. The result obtained served as an indication of the component purity. The entire process was repeated when impurities were noticed through the GC analysis.

Vapour pressure measurements were thereafter undertaken at various temperatures. For each temperature, equilibrium was deemed established when fluctuations in the measured temperature between the two probes inserted into flanges enclosing the cell were within ± 0.02 K and pressure within ± 1.5 kPa. The 34970A Agilent data acquisition unit was then used to record the temperature and pressure readings for at least 200 data points in intervals of 3 seconds.

After recording vapour pressure measurements for the heavier component, the system temperature was set on the temperature controller for an isothermal run and the liquid bath was allowed to reach the set point. Thereafter, the second component was filled directly from its cylinder into the equilibrium cell to the desired experimental pressure. This was achieved by connecting the cylinder to the cell via a three-way valve switched to the "charge" position and

slowly opening the loading needle valve. The liquid bath was then quickly lowered and raised up to position the ROLSI ^{TM} sampler in the vapour phase in preparation for sample withdrawal and the stirrer was switched on. Thereafter, the system was left to equilibrate within the cell, and the 34970A Agilent data acquisition unit switched on for temperature and pressure readings. Thermodynamic equilibrium was deemed attained when the system temperature and pressure remained unchanged to within ± 0.02 K and ± 1.5 kPa, respectively. This normally took approximately 30 minutes.

At the equilibrium condition, the stirrer was completely switched off. This helped to prevent entrainment in the ROLSI ^{TM} capillary of one phase while sampling the other.

In the meantime, the sampling lines, the ROLSI ^{TM} expansion chamber and the six-port sampling valve block were heat-traced not just to prevent condensation or vaporization of samples but also to prevent the instant vaporization of a liquid sample or the maintaining of a vapour sample at high temperature in a gaseous state. The six-port sampling valve was also switched to the sampling mode and kept in this position during the entire sampling process.

The samples were firstly withdrawn from the vapour phase as this phase requires less time for the ROLSI ^{TM} capillary cleaning process when compared to the liquid phase. The ROLSI ^{TM} sampler was connected to an online set up, a Crouzet TOP 948 electronic timer, with two timing modes where “time on” corresponds to the time between samples taking and “time off”, corresponds to the sample removal time. The ROLSI ^{TM} capillary cleaning process was achieved by setting the “time on” to 0.01 second and “time off” to 5 seconds for a period of 25 seconds. Thereafter the two times were set in such a way that the peak areas obtained fell within the GC detector calibration range for the system under investigation. At least five samples were withdrawn till the absolute average deviation of the composition was within 1% error. This ensured repeatability of the samples.

For the liquid phase sampling, the turn dial on the apparatus helped to position the capillary of the ROLSI ^{TM} into the liquid phase. During this process, the equilibrium cell pressure was monitored not to change significantly since this could disturb the equilibrium conditions. Thereafter the sampling process commenced. The sampling procedure was achieved similarly to that of the vapour phase.

The scanning of temperature and pressure readings was then stopped and the data were recorded.

A new equilibrium was then achieved by addition of the second component into the equilibrium cell. This procedure continued until the phase diagram was completed.

After completion of one isotherm, the cell was emptied and the procedure repeated for a new isotherm.

5

CHAPTER FIVE

PHASE EQUILIBRIUM DATA MEASUREMENT:

RESULTS AND DISCUSSION

5.1 Introduction

The experimental investigations were primarily based on measurement of vapour pressures and isothermal vapour-liquid equilibrium (VLE) data for binary systems.

This chapter therefore presents the experimental results obtained following the experimental procedure described in Chapter 4. The factors that affect the accuracy of the experimental results such as temperature, pressure, composition as well as chemical purity are also discussed.

Isothermal VLE data were measured for 12 binary systems using two experimental apparati based on the static analytic method. The experimental apparatus previously described by Laugier et al. (1986) was used to measure 6 binary systems, namely CO (1) + C_4F_{10} (2), NO (1) + C_4F_{10} (2), H_2S (1) + C_4F_{10} (2), CH_4 (1) + C_4F_{10} (2), CO (1) + C_6F_{14} (2) and H_2S (1) + C_6F_{14} (2) whereas the experimental apparatus previously described by Narasigadu (2011) was used to measure the remaining binary systems which include C_2H_6 (1) + C_4F_{10} (2), O_2 (1)+ C_4F_{10} (2), N_2 (1) + C_4F_{10} (2), H_2 (1) + C_4F_{10} (2), CH_4 (1) + C_6F_{10} (2) and C_2H_6 (1) + C_6F_{14} (2). One should note that numbers 1 and 2 in parenthesis next to components making up each binary system mean lighter and heavier component, respectively. The experimental apparatus described by Laugier et al. (1986) had been thoroughly validated at the CTP laboratories of the MINES ParisTech, hence there was no need for further validation.

The C_2H_6 (1) + C_4F_{10} (2) system was measured at 308.24 K using the apparatus described by Narasigadu (2011). This system was considered as a test system whereby the operation of the experimental apparatus and the reliability of the experimental procedure were checked.

The 11 remaining systems constitute novel systems. Vapour-liquid equilibrium data measurements for two systems were performed at four (292.89; 303.03; 308.03 and 317.92 K) and five (at 293.39, 303.39, 313.39, 323.41 and 333.28K) isotherms for the C_2H_6 (1) + C_6F_{14} (2) and CH_4 (1) + C_6F_{14} (2) systems, respectively. The remaining novel systems were all measured at three (293, 313 and 333 K) isotherms.

5.2 Chemical purity

The chemicals used in this study were either a gaseous or liquid state at standard conditions. The suppliers stated purities for the chemicals were confirmed by gas chromatography (GC) analysis. No significant impurities were observed and, therefore all chemicals were used without further purification, apart from in-situ degassing. Table 5.1 lists the specifications for all the chemicals used in this study.

Table 5.1: Specifications for all chemicals used in this study

compound	CAS number	Supplier	Purity[a]
perfluorobutane	355-25-9	NECSA	0.9800
perfluorohexane	355-42-0	Across Organic	0.9800
ethane	74-84-0	Air Products	0.9900
methane	98615-67-9	Afrox	0.9995
methane	98615-67-9	Air Liquide	0.9999
carbon monoxide	630-08-0	Air Liquide	0.9900
nitric oxide	10102-43-9	Air Liquide	0.9900
hydrogen sulphide	7783-06-4	Air Liquide	0.9950
hydrogen	1333-74-0	Afrox	0.9999
oxygen	7782-44-7	Afrox	0.9999
nitrogen	7727-37-9	Afrox	0.9999
helium	7440-59-7	Afrox	0.9999

[a]Supplier purity in mole fraction

5.3 Calibrations

Temperature, pressure and equilibrium phase composition are the most conveniently measured properties in phase equilibria studies. Special care is required during their measurements. Calibration was therefore undertaken for each temperature probe, pressure transducer and the GC detector used. Details regarding the calibration procedures are presented in Chapter 4.

5.3.1 Temperature

For each experimental apparatus, temperature measurement of the equilibrium cell was achieved via two sets of Pt-100s located at the top and bottom flanges of each cell. Each set of two Pt-100s was calibrated against a standard probe following the procedure outlined in Chapter 4. The temperature calibration ranges extended from 298.15 to 373.15 K and 278.15 to 338.15 K for the apparatus of Laugier et al. (1986) and Narasigadu (2011), respectively.

A correlation polynomial was used to fit a nonlinear relationship between the temperatures measured by each set of two Pt-100s and the true temperatures measured by the standard probes. The correlation polynomial model used in this project is expressed in Equation (5.1) with coefficients reported in Table 5.2. Figures 5.1 and 5.2 graphically show the errors in the temperature measurements for the two sets of Pt-100s for the apparatus of Laugier et al. (1986) and Narasigadu (2011), respectively.

$$T_{calculated}(K) = A * T_{Pt-100}^2 + B * T_{Pt-100} + C \tag{5.1}$$

Table 5.2: Correlation polynomial coefficients for the top and bottom Pt-100s

		Correlation coefficients		
Pt-100s	Temperature range (K)	A	B	C
top[a]	298.15 to 373.15	2.800×10^{-05}	0.992	0.304
bottom[a]		2.600×10^{-05}	0.994	0.364
top[b]	278.15 to 338.15	5.100×10^{-06}	0.996	-0.966
bottom[b]		-9.000×10^{-06}	0.999	-0.775

[a] Pt-100s for the apparatus described by Laugier et al. (1986).

[b] Pt-100s for the apparatus described by Narasigadu (2011).

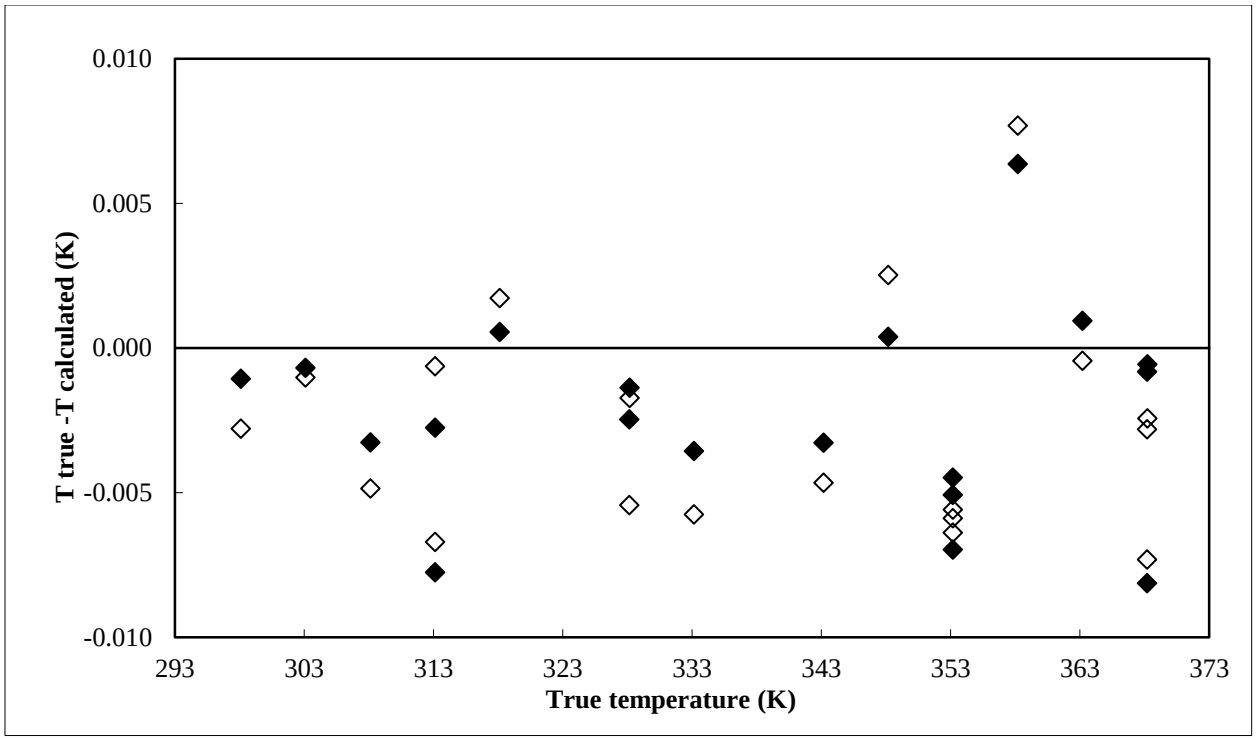

Figure 5.1: Temperature deviations for the top (◊) and bottom (♦) Pt-100s from the true temperature resulting from Eq. (5.1) for the apparatus of Laugier et al. (1986).

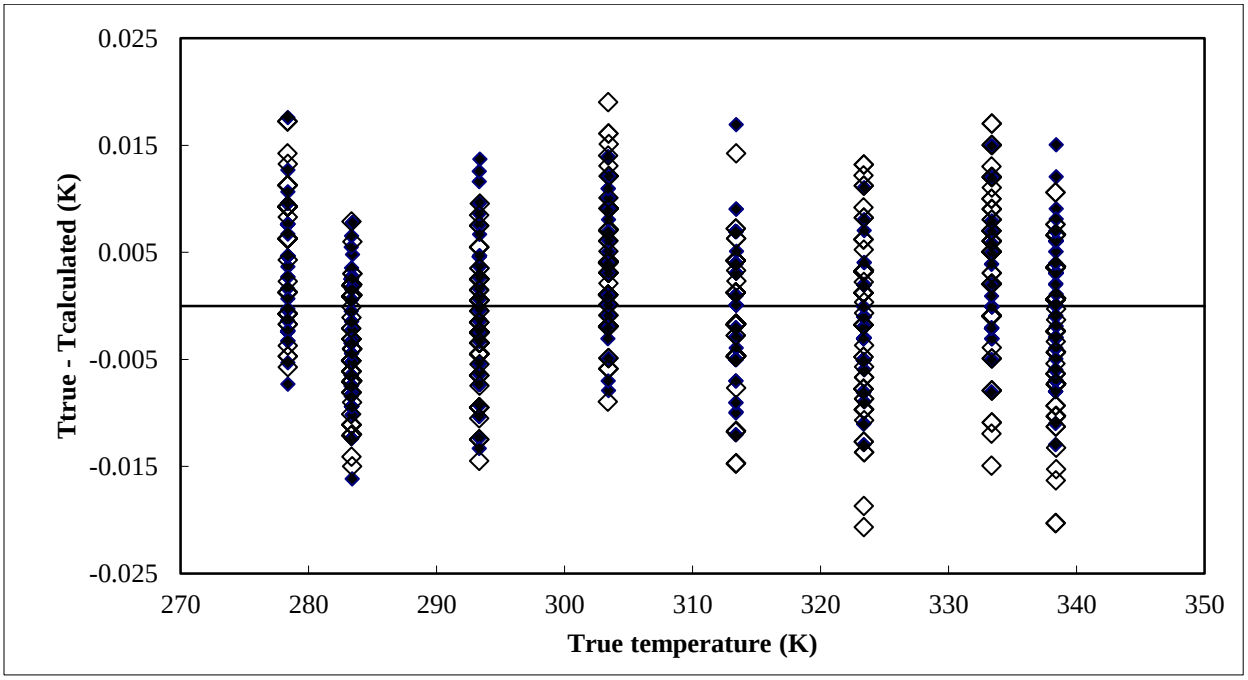

Figure 5.2: Temperature deviations for the top (◊) and bottom (♦) Pt-100s from true temperature resulting from Eq. 6.1 for the apparatus of Narasigadu (2011).

5.3.2 Pressure

As for temperature, the internal pressure measurement was achieved using two pressure transducers, namely the P-10 and PTX611 pressure transducer models. Prior to usage, the two pressure transducers were each calibrated against a standard pressure transducer following the procedure outlined in Chapter 4. The pressure calibration ranges extended from (0 to 17) and (0 to 16) MPa (absolute) for the P-10 and PTX611 pressure transducer models, respectively.

A correlation polynomial was used to fit a nonlinear relationship between values obtained from each pressure transducer and their respective standard pressure transducers. The resulting correlation polynomial model is expressed in Equation (5.2) with coefficients reported in Table 5.3. The error in the pressure measurement is graphically shown in Figures 5.3 and 5.4.

$$P_{true}(MPa) = A * T_{read}^{2} + B * T_{read} + C \tag{5.2}$$

Table 5.3: Calibration curve parameters for the P-10 pressure transducer

		Parameters		
Pressure transducer	Pressure range (MPa)	A	B	C
P-10	0 - 17	4.270×10^{-06}	1.000	-0.076
PTX611	0 - 16	1.818×10^{-06}	1.002	-0.304

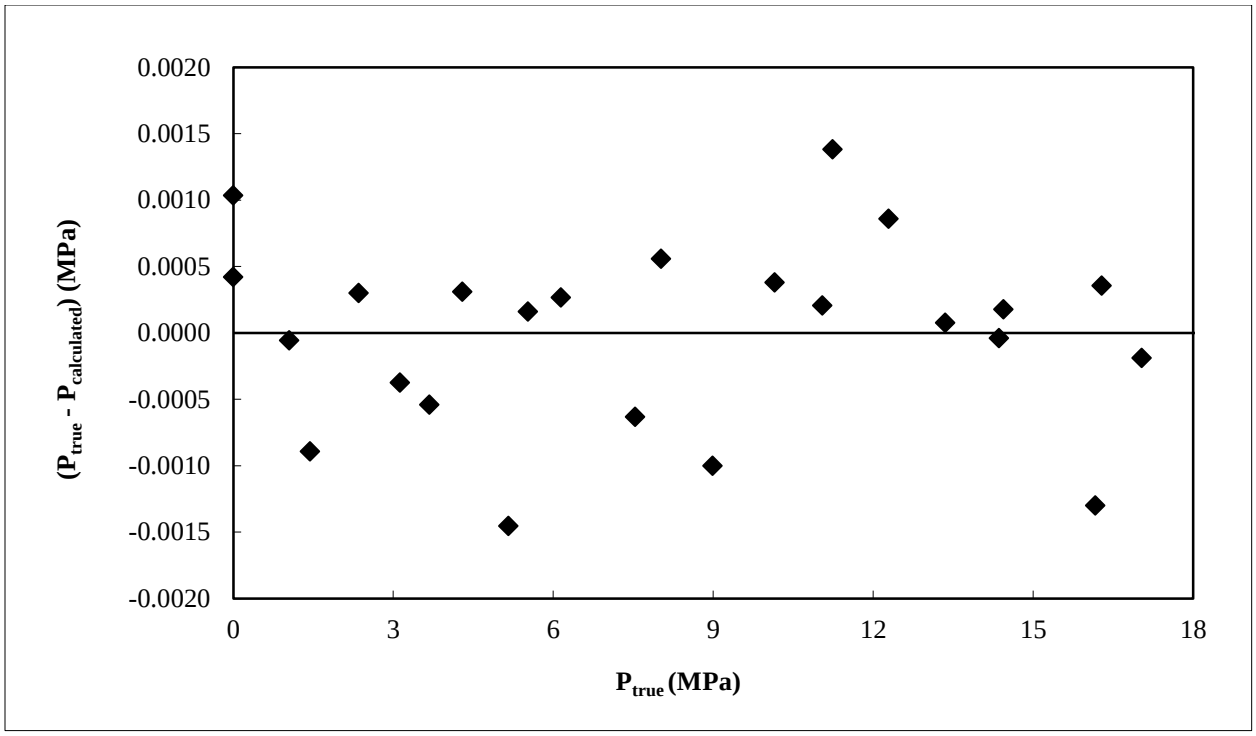

Figure 5.3: Pressure deviation for the P-10 from the true pressure resulting from Eq. (5.2).

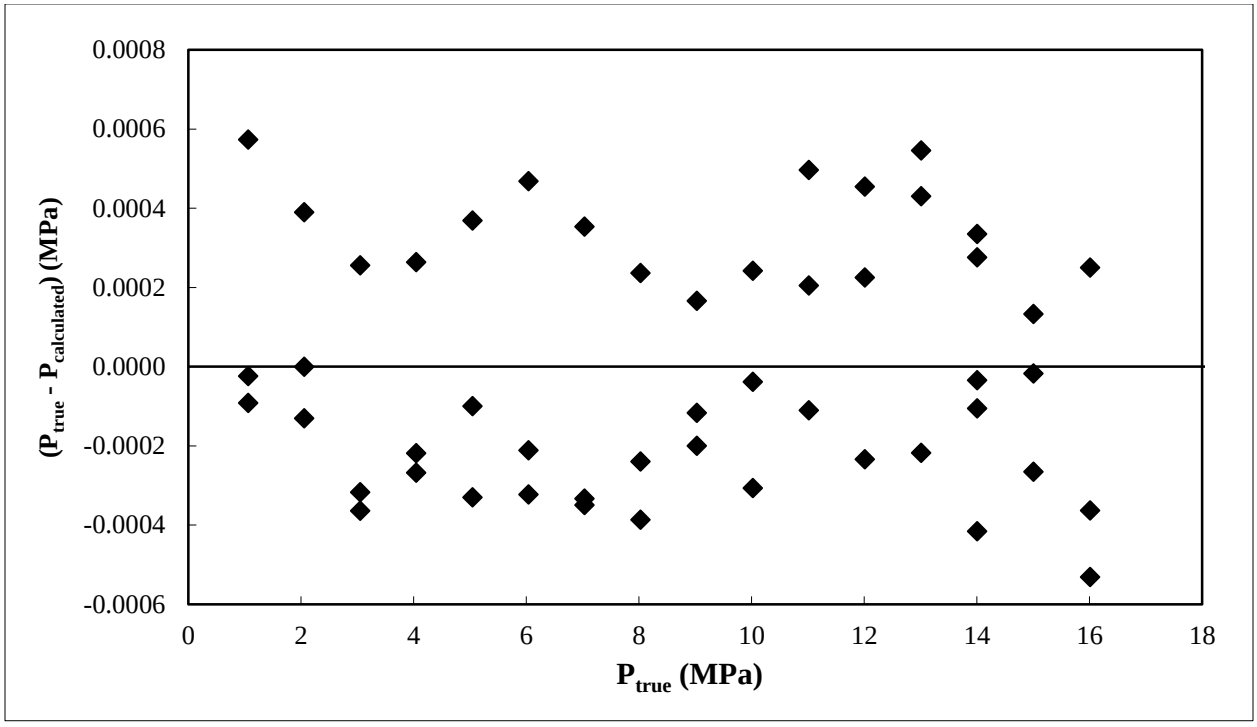

Figure 5.4: Pressure deviation for the PTX611 from the true pressure resulting from Eq. (5.2).

5.3.3 Composition

Two gas chromatographs (GC) were used for the analysis of the equilibrium phase compositions in this study, namely, the Shimadzu model 2014 and Varian CP-3800 model gas chromatographs. Both gas chromatographs are configured with a thermal conductive detector (TCD) in conjunction with either a Poropak Q or a Krytox/Carboblack B column. The GC detector calibration method is extensively discussed in Chapter 4. For each component, a plot of peak area versus number of moles injected was generated. For gaseous components, the number of moles was calculated using the ideal gas equation of state:

$$PV = nRT \tag{5.3}$$

where P is the pressure measured with a digital barometer, T is the temperature measured with a Pt-100 probe, V is the volume read as accurately as possible from the air-tight gas syringe and R is the ideal gas constant. Pressure and temperature measurements were carried out at the exit nozzle of the gas cylinder.

More accurate equations of states (i.e., the van der Waals EoS) offer only slight differences for the components studied. Thus, only the ideal gas equation was considered for the calculation of the number of moles for all the gaseous components studied.

For liquid components, TCD calibrations require an empirical model for liquid densities as a function of temperature for calculation of the number of moles:

$$\rho = \frac{n}{V} = \frac{A}{B^{\left(1+\left(1-\frac{T}{T_C}\right)^C\right)}} \tag{5.4}$$

where A, B and C are empirical constants correlated from experimental data, T is the variable temperature, T_c is the critical temperature, and V is the volume. Since the density of an incompressible liquid is a weak function of pressure, only temperature and volume are essential.

The GC operating conditions for all the binary systems studied are presented in Table 5.4. The GC calibration graphs for all the components investigated are presented in Appendix C.

Table 5.4: GC operating conditions for the binary systems investigated in this study

Binary systems	$C_2H_6 + C_4F_{10}$	$CO + C_4F_{10}$	$NO + C_4F_{10}$	$H_2S + C_4F_{10}$	$O_2 + C_4F_{10}$	$N_2 + C_4F_{10}$
Carrier gas	Helium	Helium	Helium	Helium	Helium	Helium
Column type	Poropak Q	5 % Krytox /Carboblack B	5 % Krytox /Carboblack B	5 % Krytox /Carboblack B	Poropak Q	Poropak Q
Column pressure (kPa)	168.1	200.0	200.0	200.0	168.1	168.1
Column flow (mL/min)	30	30	30	30	30	30
Column temperature (K)	393.15	333.15	333.15	333.15	393.15	393.15
Injector temperature (K)	473.15	433.15	433.15	433.15	473.15	473.15
Detector temperature (K)	473.15	433.15	433.15	433.15	473.15	473.15

Table 5.4: Continued

Binary systems	H_2 +C4F_{10}	CH_4 +C_4F_{10}	CH_4 + C_6F_{14}	C_2H_6 + C_6F_{14}	H_2S +C_6F_{14}	CO + C_6F_{14}
Carrier gas	Nitrogen	Helium	Helium	Helium	Helium	Helium
Column type	Poropak Q	Poropak Q	Poropak Q	Poropak Q	5 % Krytox /Carboblack B	5 % Krytox /Carboblack B
Column pressure (kPa)	237.8	200.0	168.1	168.1	200.0	200.0
Column flow (mL/min)	40	30	30	30	30	30
Column temperature (K)	403.15	333.15	473.15	473.15	333.15	333.15
Injector temperature (K)	473.15	433.15	473.15	473.15	433.15	433.15
Detector temperature (K)	473.15	433.15	473.15	473.15	433.15	433.15

5.4 Estimation of experimental uncertainty

Uncertainties in the temperature and pressure measurements and in the equilibrium phase composition for both the vapour and liquid mole fractions of each binary system studied were calculated and reported. The uncertainty calculations followed the method outlined by NIST (National Institute of Science and Technology) (Taylor et al., 2007). A detailed overview of the uncertainty calculation route relative to VLE data measurement is available in literature (Soo, 2011).

5.4.1 Temperature (pressure) uncertainty

The sources of uncertainties that are considered non-negligible in the temperature and pressure measurements emanate principally from the calibration imperfections and the repeated readings of a single sensor. A combination of these uncertainties referred to as the combined standard uncertainty can be expressed mathematically as follows:

$$u_c(\theta) = \pm\sqrt{u_{calib}(\theta)^2 + u_{rep}(\theta)^2} \tag{5.5}$$

where $u_c(\theta)$ is the combined standard uncertainty (in this case, θ can represent either temperature or pressure), subscripts *calib* and *rep* refer to calibration and repeatability, respectively. Considering the temperature case, the intervals of uncertainty from the temperature calibration are determined from the correlation polynomial which is illustrated graphically in Figure 5.2 and is approximated to be 0.02 K. This implies that the temperature will fall anywhere within this interval, so that a uniform or rectangular distribution is followed. Uncertainty for a rectangular distribution is expressed as follows:

$$u_{calib}(\theta) = \frac{b}{\sqrt{3}} \tag{5.6}$$

where *b* is the upper half of the interval, i.e. for temperature, b = 0.02 K in the actual case.

Isothermal VLE data experiments concern with the monitoring of temperature and pressure so that they remain constant during the sampling procedure. Oftentimes, this is not always the case because sample withdrawal results in a slight temperature change. The averaging of the repeated readings is one of the sources of uncertainty and can be expressed as follows:

$$u_{rep}(\theta) = \frac{\sigma}{\sqrt{n}} \tag{5.7}$$

where σ is the standard deviation of θ and n is the number of repeated measurements.

One should note that similar procedure is also used to estimate the pressure uncertainty.

5.4.2 Molar composition uncertainty

Two sources of non-negligible uncertainties in the determination of number of moles are the accuracy in the TCD calibration and the standard deviation from the averaging of the repeated samples. The combined expanded uncertainty relative to molar composition is similar to that of temperature and pressure:

$$u_c(x_i) = \pm\sqrt{u_{calib}(x_i)^2 + u_{rep}(x_i)^2} \tag{5.8}$$

where subscript *i* represents component *i.*

Consider the standard uncertainty arising from the TCD calibration method. For gaseous components, the number of moles calculated by the ideal gas law is governed by the pressure, temperature and volume of the gas injected into the GC. The gas constant *R* is assumed to have a value of negligible uncertainty. The standard uncertainty arising from the TCD calibration method is expressed generally as:

$$u_{calib}(x_i) = \sqrt{\left[\left(\frac{\partial x_i}{\partial n_1}\right)_{n_2} u(n_1)\right]^2 + \left[\left(\frac{\partial x_i}{\partial n_2}\right)_{n_1} u(n_2)\right]^2} \tag{5.9}$$

The calculation of $u(n_1)$ and $u(n_2)$ involves a combination of two uncertainties. For gaseous components, the two uncertainties emanate from the usage of the ideal gas law (*ig*) and the calibration polynomial (*corr*).

$$u(n_i) = \sqrt{u_{ig}(n_i)^2 + u_{corr}(n_i)^2} \tag{5.10}$$

The standard uncertainty of the number of moles, $u_{ig}(n_i)$, is expressed as follows:

$$u_{ig}(n_i) = \left\{ \left[\left(\frac{\partial n_i}{\partial P} \right)_{V,T} u(P) \right]^2 + \left[\left(\frac{\partial n_i}{\partial V} \right)_{P,T} u(V) \right]^2 + \left[\left(\frac{\partial n_i}{\partial T} \right)_{P,V} u(T) \right]^2 \right\}^{1/2} \tag{5.11}$$

where $u(P)$, $u(V)$ and $u(T)$ are the uncertainties related to the pressure, volume and temperature, which are obtained from their respective instrument specifications. The uncertainty related to the syringe is difficult to quantify, an error of 2% is considered for each volume reading. $U_{corr}(n_i)$ is determined from the maximum error observed from the calibration polynomials.

For liquid components, an empirical model for liquid densities as a function of temperature is used (i.e., Equation (5.4)). Uncertainties are governed by the temperature and volume imprecisions. Thus, Equation (6.11) is re-written as:

$$u_{id}(n_i) = \sqrt{\left[\left(\frac{\partial n_i}{\partial T} \right)_V u(T) \right]^2 + \left[\left(\frac{\partial n_i}{\partial V} \right)_T u(V) \right]^2} \tag{5.12}$$

Considering Equation (5.4) and the derivations in Equation (5.11), $u_{id}(ni)$ can be expressed as:

$$u_{id}(n_i) = n_i \sqrt{\left(\frac{C}{T_C} \ln B \left(1 - \frac{T}{T_C} \right)^{C-1} u(T) \right)^2 + \left(\frac{u(V)}{V} \right)^2} \tag{5.13}$$

Note that the assumption of 2% error in the syringe volume reading is also applied in the $u_{id}(n_i)$ calculation.

The combined standard uncertainty for the relative volatility (α_{ij}) can be calculated using the following mathematical expression:

$$u(\alpha_{ij}) = \alpha_{ij} \sqrt{\left(\frac{u(x_i)}{x_i x_j} \right)^2 + \left(\frac{u(y_i)}{y_i y_j} \right)^2} \tag{5.14}$$

where $u(x_i)$ and $u(y_i)$ are the standard uncertainties for the liquid and vapor mole fraction, respectively.

5.4.3 Reporting of uncertainty

In accordance with the NIST guidelines, the experimental uncertainty should be reported in the form of expanded uncertainty because it somehow defines an interval about the measurement result "y" within which the value of the measurand "Y" is confidently believed to lie. The expanded uncertainty is expressed as:

$$U(\theta) = k u_c(\theta) \tag{5.15}$$

where u_c is the combined standard uncertainties and k is a coverage factor.

The value of k is generally chosen based on the desired level of confidence to be associated with the interval defined by Equation (5.15). Typically, k values range from 2 to 3. Values of 2 and 3 define an interval having a level of confidence of approximately 95% and 99%, respectively. This is true if the distribution errors follow a Gaussian distribution (i.e., type A).

5.5 Phase equilibria measurement results

Uncertainties for the phase equilibrium measurements were calculated and reported following the procedure outlined in the preceding sections. Uncertainties on temperature, pressure and molar compositions emanate mainly from the calibration polynomials, with the remaining uncertainties making up approximately 1% of the final uncertainty, which can be negligible. Table 5.5 lists the averaged uncertainties for temperature, pressure and mole fraction for all systems measured.

Table 5.5: Averaged uncertainties for temperature, pressure and mole fraction for the binary systems measured

		Expanded uncertainties U(θ) with $k = 2$			
Component 1	Component 2	*U(T)* (K)	*U(P)* (kPa)	*U(x)*	*U(y)*
methane	perfluorobutane	0.04	2.00	0.01	0.01
carbon monoxide	perfluorobutane	0.04	2.00	0.03	0.02
nitric oxide	perfluorobutane	0.04	2.00	0.01	0.01
hydrogen sulphide	perfluorobutane	0.04	2.00	0.01	0.01
hydrogen	perfluorobutane	0.04	15.50	0.05	0.12
nitrogen	perfluorobutane	0.04	2.50	0.01	0.01
oxygen	perfluorobutane	0.04	3.50	0.03	0.04
ethane	perfluorohexane	0.04	2.50	0.03	0.03
methane	perfluorohexane	0.04	2.50	0.02	0.03
hydrogen sulphide	perfluorohexane	0.04	2.00	0.01	0.01
carbon monoxide	perfluorohexane	0.04	2.00	0.01	0.01

5.5.1 Vapour pressure data

Vapour pressure measurements were undertaken for some of the components investigated in this study namely, ethane and perfluorobutane.

Vapour pressures for perfluorohexane could not be measured using the available experimental setups. The perfluorohexane component has low vapour pressure values and its measurement requires equipment with a pressure transducer ranging from 0 to 500 kPa absolute. Vapour pressure data for perfluorohexane and that of H_2S were taken from the NIST data bank (Dunlap et al., 1958 and Reid et al., 1987) and fitted to either the Peng-Robinson or Soave-Redlich-Kwong EoS to obtain the correlated Mathias-Copeman alpha function parameters.

Vapour pressure measurement for methane, CO, H_2, O_2, N_2 and NO could not be undertaken since the operating temperatures were above their critical temperatures. The experimental vapour pressure data for ethane and perfluorobutane were compared with those obtained from the literature computed with Antoine coefficients obtained from Aspen Plus (2004). The measured data were also fitted to the Peng-Robinson EoS to obtain the correlated Mathias-Copeman alpha function parameters.

The experimental vapour pressures are presented in Tables 5.6 and 5.7 and graphically compared with literature (Aspen Plus, 2004) and calculated vapour pressure data in Figures 5.5 and 5.6. The Mathias-Copeman parameters for ethane and perfluorobutane are listed in Table 5.7.

Table 5.6: Experimental vapour pressure for perfluorobutane

T / K	P / kPa
293.44	238.0
298.47	277.2
303.42	319.7
308.25	374.0
313.43	428.3
318.44	491.7
323.42	562.1

Expanded uncertainty u (T, k =2) = 0.02 K; u (P, k = 2) = 2 kPa.

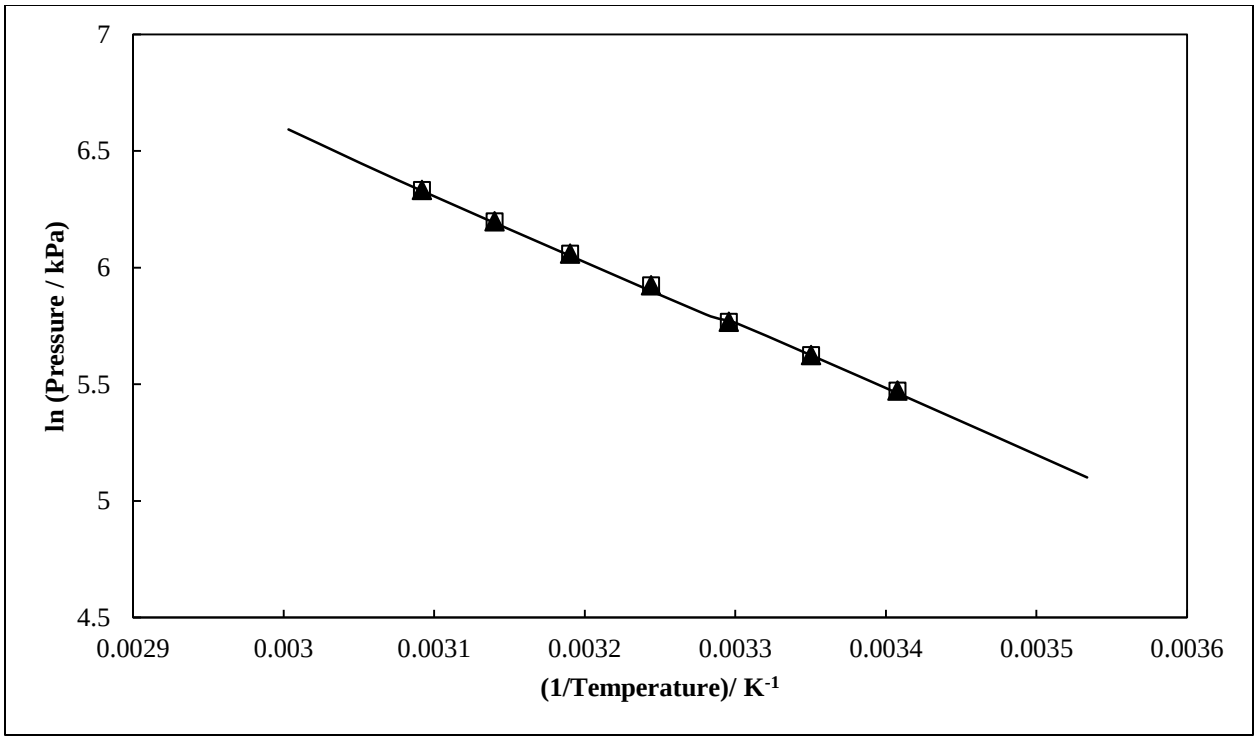

Figure 5.5: Vapour pressure graph for perfluorobutane (C_4F_{10}). Experimental: □; Model (PR-MC): ▲; Aspen Plus (2004): —.

Table 5.7: Experimental vapour pressure for ethane

T / K	P / kPa
256.53	1570
263.50	1887
273.49	2418
283.45	3051
288.43	3411
301.45	4510

Expanded uncertainty u (T, k =2) = 0.02 K; u (P, k = 2) = 2 kPa.

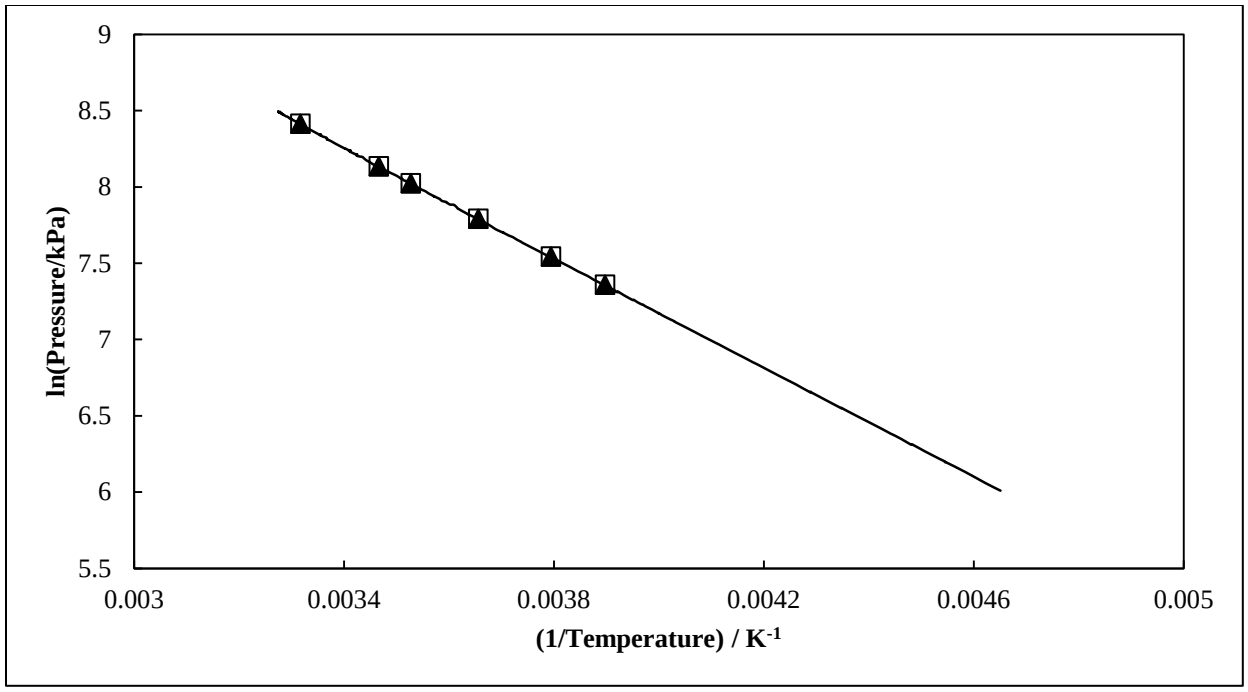

Figure 5.6: Vapour pressure graph for ethane (C_2H_6). Experimental: □; Model (PR-MC): ▲; Aspen Plus: —.

Table 5.7.1: Mathias-Copeman coefficients for ethane (C_2H_6) and perfluorobutane (C_4F_{10}) obtained by regression of the experimental vapour pressure

	Component	
Coefficient	C_2H_6	C_4F_{10}
C_1	0.544	0.925
C_2	-0.281	-0.094
C_3	0.090	2.340

Vapour pressures for pure perfluorobutane and ethane were measured at various temperatures and compared to literature data. The experimental vapour pressure data for perfluorobutane and ethane show an overall satisfactory agreement with both the literature (Aspen Plus, 2004) and correlated vapour pressure as can be seen in Figures 5.5 and 5.6.

The experimental vapour pressure data were also checked for qualitative thermodynamic consistency using the recommendations in the Design Institute for Physical Property Data (DIPPR) outlined by Daubert et al. (1990). This method consists of a graphical representation of

the vapour pressure data in the form of *ln P* versus *1/T* whereby an increase in temperature will notify a possible occurrence of decomposition or polymerization.

However, the data are considered thermodynamically consistent when the graph exhibits a linear trend as no decomposition or polymerization would have taken place. One should note that a wide range of temperature is required to reach a sound conclusion. The vapour pressure data measured for both perfluorobutane and ethane exhibit a linear trend and therefore passed the qualitative thermodynamic test within the range considered. See Figures 5.5 and 5.6.

5.5.2 Vapour-liquid equilibrium (VLE) data

Isothermal vapour-liquid equilibrium data measurements were undertaken for 11 novel binary systems, which were all correlated using the THERMOPACK version 1.10, in house software developed at CTP MINES ParisTech, previously known as CEP/TEP or Aspen Plus® version 8.0. The correlation of the measured data could not be undertaken using one software due to unavailability of some models in THERMOPACK and consequently, Aspen Plus® version 8.0 was used.

The critical parameters for each pure component investigated in this study are presented in Appendix D. The GC detector calibrations for each pure component making up each binary system investigated in this study were undertaken and their corresponding results are presented in Appendix C. The averaged uncertainties in the equilibrium phase composition for both the vapour and liquid mole fractions are presented in Table 5.5.

The experimental VLE data were modelled via the direct method using various combinations of thermodynamic models namely, the Peng-Robinson or Soave-Redlich-Kwong EoS incorporating the Mathias-Copeman or Stryjek Vera alpha function, with the Wong-Sandler, Huron-Vidal, predictive Soave-Redlich-Kwong, modified Huron-Vidal 1 or 2 mixing rule utilizing the non-random two-liquid activity coefficient model. One should note these thermodynamic models were chosen following the selection rules presented in Chapter 3. In addition, they have proven satisfactory and are widely used in the modelling for systems comprising fluorochemical + alkane components (Coquelet et al., 2009), (El Ahmar et al., 2010) and (Tshibangu, 2010). For these types of binary systems, the NRTL non randomness parameter α_{ji} was set to 0.3 as recommended by Sandler (1997) (discussed in Section 3.6.1.1). The other two NRTL parameters

(g_{ij}, g_{ji}) or (τ_{ij}, τ_{ji}) (depending on whether THERMOPACK or Aspen Plus® was used) and the Wong-Sandler parameter k_{ij}, were adjusted directly onto the measured VLE data using an objective function.

One should note that Aspen Plus was used for two combinations of thermodynamic models. The first involved the Soave-Redlich-Kwong EoS incorporating the Mathias-Copeman alpha function with the predictive Soave-Redlich-Kwong mixing rule utilizing the non-random two-liquid activity coefficient model abbreviated as SRK-MC-PSRK-NRTL. The second involved the Peng-Robinson EoS incorporating the Mathias-Copeman alpha function with the Wong-Sandler mixing rule utilizing the non-random two-liquid activity coefficient model abbreviated as PR-MC-WS-NRTL.

The SRK-MC-PSRK-NRTL combination could not be undertaken in THERMOPACK due to unavailability of the PSRK mixing rule. As one can notice, the PR-MC-WS-NRTL model was undertaken both in THERMOPACK and Aspen Plus. This allowed rational comparisons between the PR-MC-WS-NRTL and SRK-MC-PSRK-NRTL models as their data were all adjusted using the same objective function (ordinary least squares).

In THERMOPACK, the measured data were adjusted through a simplex algorithm using a flash calculation objective function (*FC*), which is expressed as follows:

$$FC = \frac{100}{N}\left[\sum_{1}^{N}\left(\frac{x_{\exp} - x_{cal}}{x_{\exp}}\right)^2 + \sum_{1}^{N}\left(\frac{y_{\exp} - y_{cal}}{y_{\exp}}\right)^2\right] \tag{5.16}$$

where F is the objective function to be minimized by data regression, N is the number of data points, x_{exp} and x_{cal} are the experimental and calculated liquid mole fractions; y_{exp} and, y_{cal} the experimental and calculated vapour mole fractions, respectively.

In Aspen Plus, the default objective function is the Maximum likelihood (Q) which is expressed as follows:

$$Q = \sum_{n=1}^{NDG} w_n \sum_{i=1}^{NP} \left[\left(\frac{T_{e,i} - T_{m,i}}{\sigma_{T,i}} \right)^2 + \left(\frac{P_{e,i} + P_{m,i}}{\sigma_{P,i}} \right)^2 + \sum_{j=1}^{NC-1} \left(\frac{x_{e,i,j} - x_{m,i,j}}{\sigma_{x,i,j}} \right)^2 + \sum_{j=1}^{NC-1} \left(\frac{y_{e,i,j} - y_{m,i,j}}{\sigma_{y,i,j}} \right)^2 \right] \quad (5.17)$$

where Q is the objective function to be minimized by data regression, NDG is the number of data groups in the regression case, W_n is the weight of data group n, NP is the number points in data group, NC is the number of components present in the data group; T, P, x and y are temperature, pressure, liquid and vapour mole fractions, respectively; e is the estimated data, m is the measured data, i is the data for data point i, j is the fraction data for component j and σ is the standard deviation of the indicated data.

The maximum likelihood objective function is a generalization of least squares methods where independent variables are assumed to be error free. One should note that the errors in the independent variables are minimized by adjusting one model parameter or more.

In Aspen Plus, the measured VLE data were adjusted using the Britt-Luecke algorithm and the ordinary least squares (OLS) objective function with the Deming method used for initialization. For isothermal VLE data, the ordinary least squares objective function minimizes pressure and vapour composition between the measured and modelled data.

In other words, all the modelled data obtained from THERMOPACK were adjusted using the flash calculation objective function whilst those obtained from Aspen Plus were adjusted using the ordinary least squares objective function. Hence, for example, experimental data modelled using the PR-MC-WS-NRTL combination, and adjusted using the flash calculation objective function, is abbreviated as PR-MC-WS-NRTL (FC). The experimental data modelled using the PR-MC-WS-NRTL, and adjusted using the ordinary least squares objective function, is abbreviated as PR-MC-WS-NRTL (OLS). One should note that experimental data and measured data are used interchangeably in this study as they have the same meaning.

Each isotherm measured for every system was individually correlated as it generally provides a better fit. Thereafter, all isotherms measured for each system were correlated simultaneously in a temperature-dependent form to facilitate phase equilibrium predictions for isotherms that were not measured, which is useful for design purposes.

In THERMOPACK, the temperature-dependence form considered is expressed as follows:

$$\Delta g_{ij} = a_{ij} + b_{ij}T \tag{5.18}$$

where Δg_{ij} is expressed in [J.mol^{-1}.K].

In Aspen Plus®, the temperature-dependence form considered is expressed as follows:

$$\tau_{ij} = a_{ij} + b_{ij}/T \tag{5.19}$$

where τ_{ij} is expressed in [K].

The temperature-independence forms for Eqs. (5.7) and (5.19) can be expressed, respectively, as follows:

$$\Delta g_{ij} = a_{ij} \tag{5.20}$$

where Δg_{ij} is expressed in [J.mol^{-1}].

$$\tau_{ij} = a_{ij} \tag{5.21}$$

where τ_{ij} is dimensionless.

Δg_{ij} and τ_{ij} are linked by the following expression:

$$\tau_{ij} = \frac{\Delta g_{12}}{RT} \tag{5.22}$$

where R, is the ideal gas constant.

One should note that, in this study, a model agrees well or favourably well with the experimental data if 80 – 100 % of these is represented.

To assess the agreement between the selected models and the experimental data, the deviations bias *U* and *AAD U*, were determined for both the liquid and vapour phase moles fractions and pressure depending on the objective function considered. The deviations are expressed as follows:

$$AAD(\%) = (100/N)\sum\left|\left(U_{cal} - U_{\exp}\right)/U_{\exp}\right| \tag{5.23}$$

$$BIASU(\%) = (100/N)\sum\left(\left(U_{\exp} - U_{cal}\right)/U_{\exp}\right) \tag{5.24}$$

where N is the number of data points and $U = x_1$ *or* y_1.

Relative volatility (α_{ij}), which is an indicator that shows the easiness or difficulty for a process to separate a more volatile component from the less volatile component in a mixture, can be calculated using the following equation:

$$\alpha_{ij} = \frac{K_i}{K_j} = \frac{y_i / x_i}{y_j / x_j} = \frac{y_i / x_i}{(1-y_i)/(1-x_i)} \tag{5.25}$$

The relative volatilities were computed for the combination of models chosen and compared to the experimental values. This also serves as a further comparison between the experimental data and the modelled data.

For VLE data measured above the critical temperature, the critical coordinates were approximated using extended laws as presented by Ungerer et al. (2005). In this method, the critical region of the *P-x-y* diagram is represented by complementing with a linear term which is expressed as:

$$y - x = \lambda_1(P_c - P) + \mu(P_c - P)^{\beta} \tag{5.26}$$

$$\frac{y+x}{2} - x_c = \lambda_2(P_c - P) \tag{5.27}$$

where y and x are the vapour and liquid mole fraction, respectively; λ_1, λ_2 and μ are adjustable coefficients regressed from a set of *P-x-y* experimental data below the critical point; β is a constant and (P_c, x_c), the critical coordinates.

5.5.2.1 Ethane (1) + perfluorobutane (2) system

The VLE data of El Ahmar et al. (2010) for the ethane (1) + perfluorobutane (2) system at 308.20 K was chosen as a test system to demonstrate the capability of the experimental apparatus to produce accurate VLE data. This system was chosen because it lies within the principal

objective of this study, which is phase equilibrium measurements for binary systems containing perfluorocarbons and common flue gas components such as CO_2, CO, H_2S, CH_4, NH_3, light hydrocarbons, etc.

Isothermal VLE data were measured at 308.24 K and are reported in Table 5.8. The measured data were thereafter modelled using the Peng-Robinson EoS incorporating the Mathias-Copeman alpha function and the Wong-Sandler mixing rule utilizing the NRTL activity coefficient model and adjusted using the flash calculation objective function abbreviated as PR-MC-WS-NRTL (FC). The results obtained from the modelling are graphically compared with the measured data in Figure 5.7. The modelled parameters for the PR-MC-WS-NRTL (FC) model are reported in Table 5.9. Relative volatilities were computed using the PR-MC-WS-NRTL (FC) model and graphically compared with the experimental values in Figure 5.8.

Table 5.8: Experimental VLE data for the ethane (1) + perfluorobutane (2) system at 308.24 K

P / MPa	n_x	x_1	δx_1	n_y	y_1	δy_1
0.374	—	0	—	—	0	—
0.493	6	0.022	0.0010	6	0.236	0.0021
0.931	5	0.106	0.0021	5	0.582	0.0010
1.335	5	0.189	0.0020	5	0.701	0.0000
1.723	7	0.272	0.0010	5	0.770	0.0020
2.217	5	0.388	0.0010	5	0.808	0.0010
2.559	5	0.467	0.0010	5	0.836	0.0000
2.964	6	0.564	0.0000	5	0.855	0.0011
3.322	6	0.643	0.0023	6	0.872	0.0000
3.602	6	0.709	0.0012	5	0.885	0.0000
3.843	6	0.771	0.0001	5	0.900	0.0000
4.165	5	0.838	0.0011	6	0.916	0.0000
4.417	7	0.886	0.0010	5	0.924	0.0000

x, y: liquid and vapour mole fraction. n_x, n_y : number of samples taken. *δx, δy*: standard deviation for *x* and *y*.

Expanded uncertainty: *u (T, k = 2)* = 0.04 K*; u (P, k = 2)* = 4.00 kPa and *u* (x_1,y_1) = 0.006.

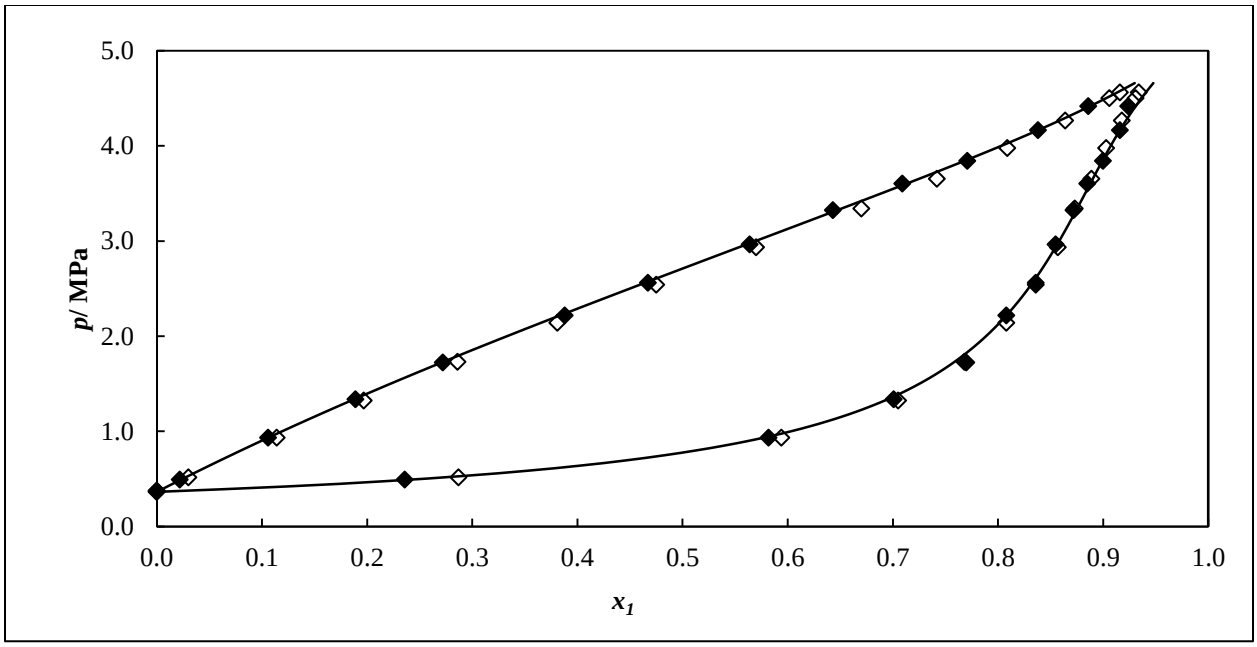

Figure 5.7: Phase diagram (*P-x-y*) for the C_2H_6 (1) + C_4F_{10} (2) system at 308.24 K. Experimental data: ♦; El Ahmar et al. (2011): ◊; Model: PR-MC-WS-NRTL (FC) (solid black line).

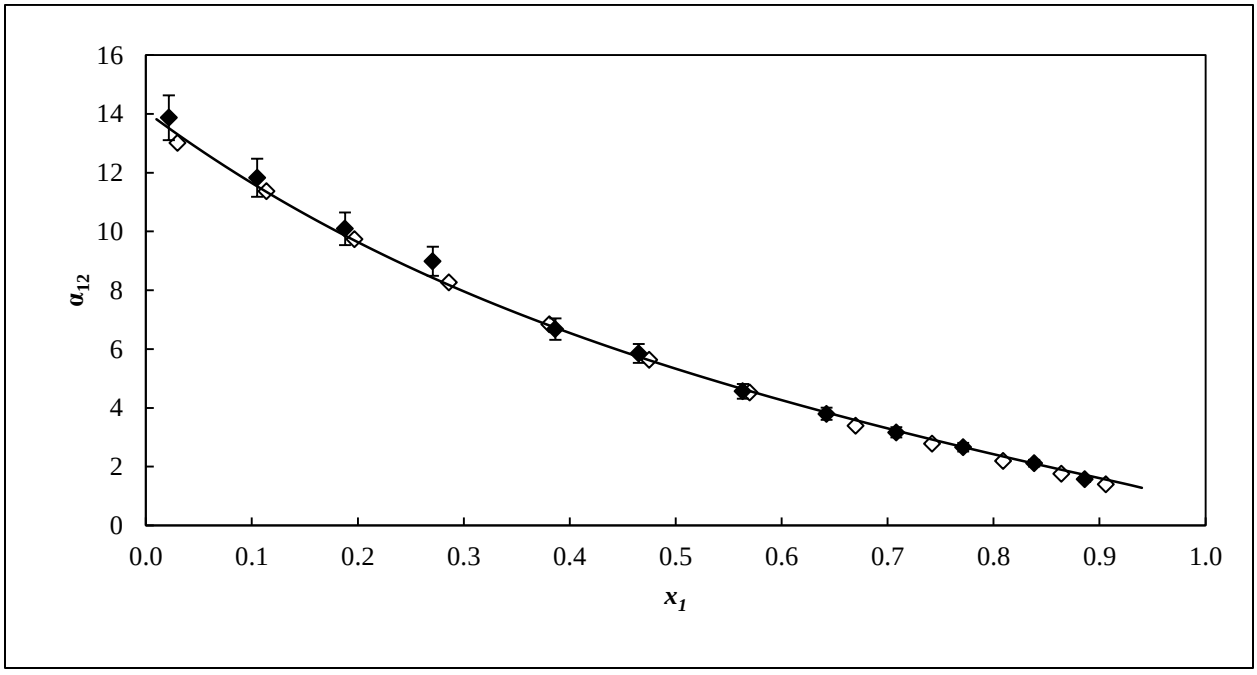

Figure 5.8: Phase diagram of the relative volatility versus the liquid mole fraction for the C_2H_6 (1) + C_4F_{10} (2) system at 308.24 K. Experimental data: ♦; El Ahmar et al. (2011): ◊; Model: PR-MC-WS-NRTL (solid black line). Error bands: shown at 5.5% for the experimental data.

Table 5.9: Model parameters for the PR-MC-WS-NRTL (FC) model for the ethane (1) + perfluorobutane (2) system at 308.24 K

Model	$(g_{12} - g_{22})^a$ / J.mol^{-1}	$(g_{21} - g_{11})^a$ / J.mol^{-1}	$k_{12}{}^b$
PR-MC-WS-NRTL (FC)	2795	471.0	0.41

[a] NRTL model parameters obtained from THERMOPACK, $\Delta g_{ij} = a_{ij}$.

[b] WS mixing rule parameter incorporated into the PR EoS obtained from THERMOPACK.

The results presented in Figure 5.7 show that the experimental VLE data agree reasonably well with the correlated data but slight deviations are observed in the liquid phase when compared to the data of El Ahmar et al. (2011).

The relative volatilities were computed for the PR-MC-WS-NRTL model and compared to the experimental data. Once again, the results exhibit a good agreement with the correlated data and slightly deviated from the data of El Ahmar et al. (2011). This can be seen graphically in Figure 5.8.

Figure 5.7 reveals slight deviations between the VLE data measured in this study and those of El Ahmar et al., (2011) for the ethane (1) + perfluorobutane (2) system at 308.24 K , the PR-MC-WS-NRTL (FC) model represents the measured data very well as opposed to those of El Ahmar et al., (2011).

The slight deviations observed between the two sets of data could be due to the different setup of experimental apparatuses as well as the techniques of measurements employed. One should note that the data of El Ahmar et al., (2011) were measured at CTP MINES ParisTech in Fontainebleau (France).

However, the results obtained demonstrated the reliability of the experimental apparatus to produce vapour-liquid equilibrium data and confirmed the accuracy of the experimental procedure. Hence experimental VLE data for novel binary systems could be undertaken. One should note that a novel binary system is regarded as a system that has not previously been measured and reported in the open literature. Consequently, the rest of the systems measured in this study are regarded as novel.

One should note that VLE data for binary systems such as C_4F_{10} with CO, NO, H_2S or CH_4 and C_6F_{14} with H_2S or CO have already been published. However, the results reported in the publications may be different to the ones reported in this thesis due to the fact that additional models have been considered for some of the VLE data.

5.5.2.2 Carbon monoxide (1) + perfluorobutane (2) system

The experimental VLE data for the carbon monoxide (1) + perfluorobutane (2) system were undertaken at three temperatures (293.48, 313.44 and 333.33 K) and are reported in Table 6.10.

The measured data were modelled using the Peng-Robinson or Soave-Redlich-Kwong EoS with the Mathias-Copeman or the Stryjek-Vera alpha functions and the Wong-Sandler or the predictive Soave-Redlich-Kwong mixing rule incorporating the NRTL activity coefficient model and adjusted using the flash calculation (FC) or ordinary least squared (OLS) objective function (OF) abbreviated as PR-MC-WS-NRTL (OF: FC), PR-MC-WS-NRTL (OF: OLS), PR-SV-WS-NRTL (OF: FC) and SRK-MC-PSRK-NRTL (OF:OLS) models, respectively. The results from the modelling are graphically compared with the experimental data in Figures 5.9 to 5.11. The modelled parameters for the three combinations of models in temperature-independent and temperature-dependent forms are reported in Tables 5.11 and 5.12, respectively.

The relative volatilities were also computed for the three sets of models and compared to the experimental data. The results obtained are graphically presented in Figure 5.10.

Deviations bias U and AAD U between the experimental and the calculated (PR-MC-WS-NRTL, PR-SV-WS-NRTL and SRK-MC-PSRK-NRTL) vapour and liquid mole fractions for the CO (1) + C_4F_{10} (2) system are reported in Table 5.13.

Table 5.10: Experimental VLE data for the carbon monoxide (1) + perfluorobutane (2) system

T/K = 293.48 K						
P/MPa	n_x	x_1	δx_1	n_y	y_1	δy_1
1.436	5	0.041	0.0005	7	0.807	0.0029
1.868	6	0.057	0.0008	5	0.829	0.0045
2.653	7	0.087	0.0015	6	0.872	0.0021
3.594	5	0.121	0.0009	6	0.889	0.0014
4.632	6	0.156	0.0012	6	0.905	0.0019
5.602	5	0.193	0.0008	6	0.911	0.0011
6.825	5	0.229	0.0013	5	0.913	0.0010
8.296	6	0.275	0.0011	5	0.916	0.0009
9.936	6	0.337	0.0013	7	0.923	0.0008
12.113	6	0.402	0.0018	5	0.902	0.0005
14.464	6	0.486	0.0021	6	0.877	0.0014
15.192	6	0.519	0.0011	6	0.862	0.0013
16.130	5	0.558	0.0009	5	0.837	0.0035

Table 5.10: Continued

T/K = 313.44 K						
P/MPa	n_x	x_1	δx_1	n_y	y_1	δy_1
0.965	6	0.021	0.0002	5	0.502	0.0012
2.010	5	0.058	0.0005	6	0.735	0.0003
3.003	6	0.091	0.0008	5	0.785	0.0002
3.994	6	0.130	0.0010	6	0.812	0.0014
4.997	5	0.163	0.0004	5	0.832	0.0002
6.004	5	0.199	0.0007	6	0.842	0.0005
8.112	5	0.276	0.0011	6	0.851	0.0004
10.132	6	0.349	0.0008	5	0.841	0.0003
11.870	5	0.414	0.0011	6	0.819	0.0008
12.523	5	0.441	0.0003	5	0.807	0.0009
12.988	5	0.461	0.0005	6	0.796	0.0008
13.661	5	0.516	0.0015	5	0.771	0.0004
14.171	5	0.593	0.0005	5	0.747	0.0002

Table 5.10: Continued

T/K = 333.02 K						
P/MPa	n_x	x_1	δx_1	n_y	y_1	δy_1
1.454	6	0.031	0.0002	6	0.434	0.0009
2.559	5	0.080	0.0004	6	0.626	0.0002
3.508	5	0.124	0.0017	5	0.701	0.0004
4.286	5	0.152	0.0002	5	0.730	0.0002
5.034	6	0.189	0.0008	6	0.748	0.0009
5.821	5	0.219	0.0015	5	0.762	0.0004
6.553	5	0.247	0.0001	5	0.770	0.0006
7.236	5	0.275	0.0004	5	0.772	0.0008
7.825	6	0.303	0.0002	5	0.772	0.0005
8.632	6	0.340	0.0002	6	0.765	0.0008
9.831	5	0.395	0.0025	6	0.748	0.0007
10.546	6	0.450	0.0004	6	0.732	0.0007
11.138	6	0.516	0.0002	6	0.684	0.0003

x_1, y_1: liquid and vapour mole fraction; n_x, n_y : number of samples taken; δx_1, δy_1: standard deviation for x_1 and y_1.

Expanded uncertainty: $u\,(T, k = 2)$ = 0.04 K; $u\,(P, k = 2)$ = 2.00 kPa; u (x_1, k = 2) = 0.03 and u (y_1, k = 2) = 0.02.

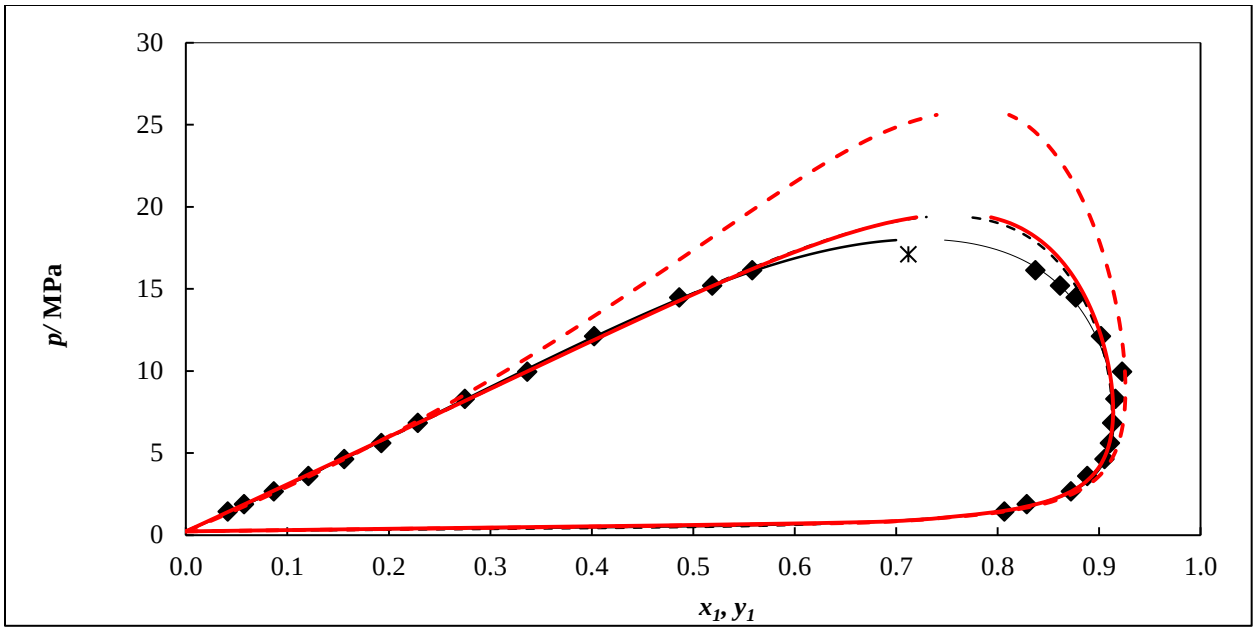

Figure 5.9: Phase diagrams (*P-x-y*) for the CO (1) + C_4F_{10} (2) system. Experimental data: ♦, 293.48 K; Models: PR-MC-WS-NRTL (OF: FC) (solid black line); PR-SV-WS-NRTL (OF: FC) (dashed black line); PR-MC-WS-NRTL (OF: OLS) (solid red line) and SRK-MC-PSRK-NRTL (OF: OLS) (dashed red line); *, mixture critical point.

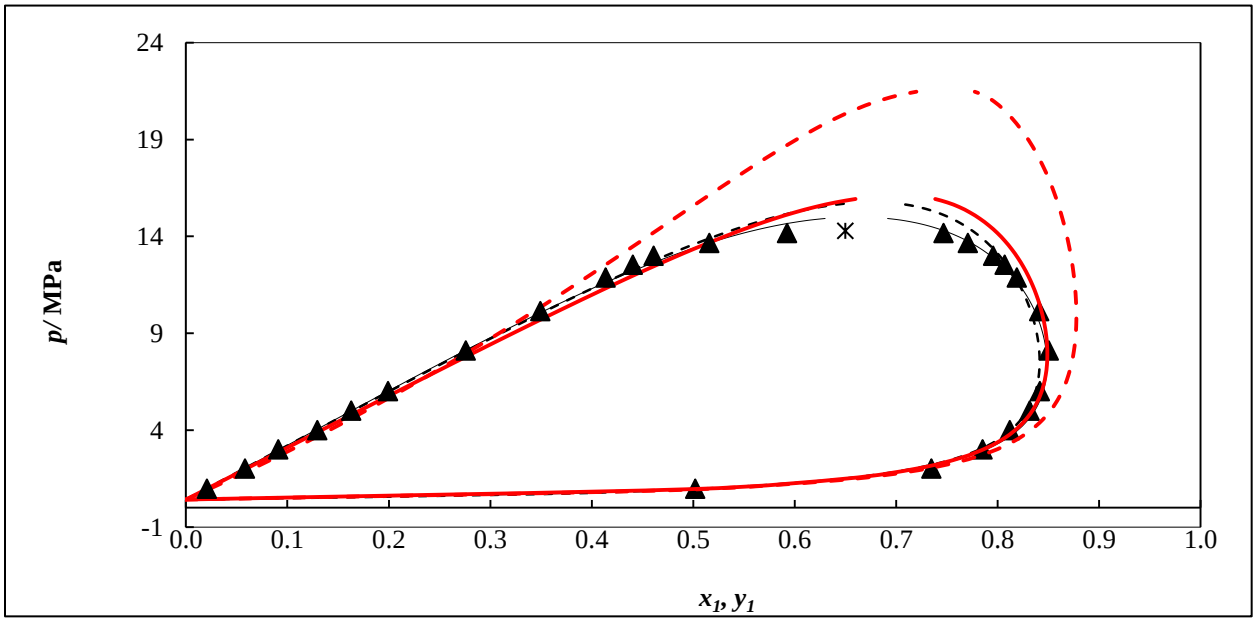

Figure 5.10: Phase diagrams (*P-x-y*) for the CO (1) + C_4F_{10} (2) system. Experimental data: ▲, 313.44 K; Models: PR-MC-WS-NRTL (OF: FC) (solid black line); PR-SV-WS-NRTL (OF: FC) (dashed black line); PR-MC-WS-NRTL (OF: OLS) (solid red line) and SRK-MC-PSRK-NRTL (OF: OLS) (dashed red line); *, mixture critical point.

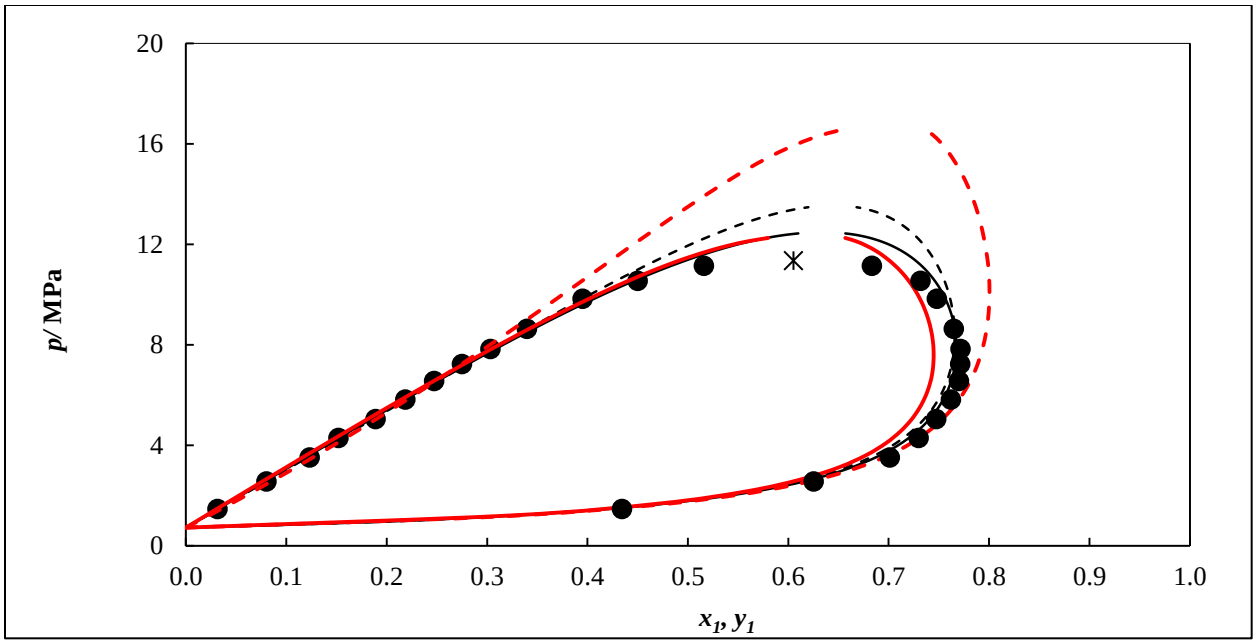

Figure 5.11: Phase diagrams (*P*-*x*-*y*) for the CO (1) + C_4F_{10} (2) system. Experimental data: ●, 333.33 K; Models: PR-MC-WS-NRTL (OF: FC) (solid black line); PR-SV-WS-NRTL (OF: FC) (dashed black line); PR-MC-WS-NRTL (OF: OLS) (solid red line) and SRK-MC-PSRK-NRTL (OF: OLS) (dashed red line); *, mixture critical point.

Table 5.11: Model parameter for the PR-MC-WS-NRTL, PR-SV-WS-NRTL and SRK-MC-PSRK-NRTL models in a temperature-independent form for the CO (1) + C_4F_{10} (2) system at 293.48, 313.44 and 333.33 K

Model	Isotherm /K	$(g_{12} - g_{22})^a$/J.mol^{-1}	$(g_{21} - g_{11})^a$/J.mol^{-1}	$k_{ij}{}^b$
objective function: flash calculation				
PR-MC-WS-NRTL	293.48	5908.0	-597.23	0.76
	313.44	5959.6	-267.66	0.76
	333.33	5457.8	-700.00	0.80
PR-SV-WS-NRTL	293.48	1366.4	-410.48	0.74
	313.44	1890.6	-430.17	0.73
	333.33	-720.85	1169.7	0.78
		$\tau_{12}{}^c$	$\tau_{21}{}^c$	$k_{ij}{}^d$
objective function: ordinary least squares				
PR-MC-WS-NRTL	293.48	85.503	-0.0507	0.75
	313.44	85.503	0.0847	0.75
	333.33	85.503	-0.0887	0.74
SRK-MC-PSRK-NRTL	293.48	85.503	-0.2200	—
	313.44	85.503	-1.6527	—
	333.33	85.503	-1.7199	—

[a] NRTL model parameters obtained from THERMOPACK, $\Delta g_{ij} = a_{ij.}$

[b, d] WS mixing rule parameter incorporated into the PR EoS correlated from THERMOPACK and Aspen Plus, respectively.

[c] NRTL model parameters obtained from Aspen Plus, $\tau_{ij} = a_{ij}$.

Table 5.12: Model parameters for the PR-MC-WS-NRTL, PR-SV-WS-NRTL and SRK-MC-PSRK-NRTL models in a temperature-dependent form for the CO (1) + C_4F_{10} (2) system for all isotherms

Model	$(g_{12} - g_{22})^a$/J.mol-1.K		$(g_{21} - g_{11})^a$/J.mol-1.K		$k_{ij}{}^b$
	a_{12}	b_{12}	a_{21}	b_{21}	
objective function: flash calculation					
PR-MC-WS-NRTL	-3986	32.93	2198.0	-9.086	0.76
PR-SV-WS-NRTL	1621	-0.935	280.60	-2.159	0.75
Model	$\tau_{12}{}^c$ / K		$\tau_{21}{}^c$ / K		$k_{ij}{}^d$
objective function: ordinary least squares					
PR-MC-WS-NRTL	21179		100.85		0.74
SRK-MC-PSRK-NRTL	21179		342.57		—

[a] NRTL model parameters obtained from THERMOPACK, $\Delta g_{ij} = a_{ij} + b_{ij}.T$

[b, d] WS mixing rule parameter incorporated into the PR EoS correlated from THERMOPACK and Aspen Plus, respectively.

[c] NRTL model parameters obtained from Aspen Plus, $\tau_{ij} = b_{ij}$.

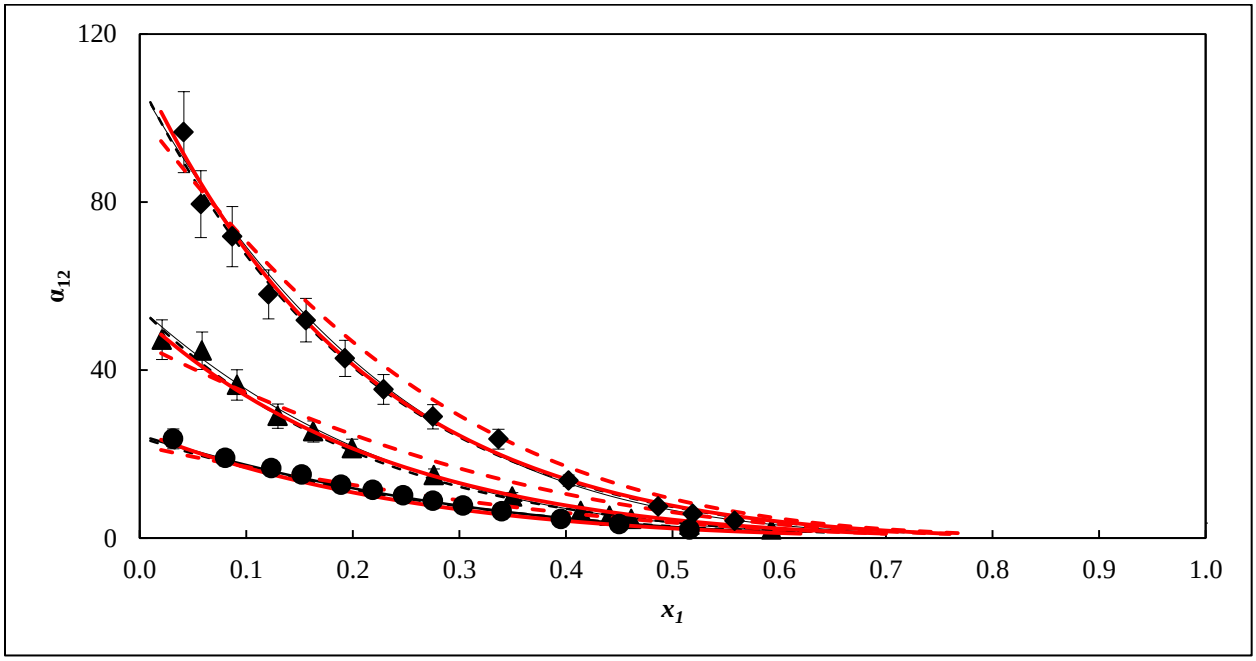

Figure 5.12: Plot of relative volatilities (α_{12}) for the CO (1) + C_4F_{10} (2) system. Experimental data: ♦, 293.48 K; ▲, 313.44 K; ●, 333.33 K. Models: PR-MC-WS-NRTL (OF: FC) (solid black line); PR-SV-WS-NRTL (OF: FC) (dashed black line); PR-MC-WS-NRTL (OF: OLS) (solid red line) and SRK-MC-PSRK-NRTL (OF: OLS) (dashed red line). Error bands: shown at 10 % for the experimental data.

Table 5.13: Deviations, Bias U and the AAD obtained in fitting experimental VLE data with the PR-MC-WS-NRTL, PR-SV-WS-NRTL and SRK-MC-PSRK-NRTL models for the CO (1) + C_4F_{10} (2) system

Model	Isotherm / K	bias x %	AAD x %	bias y %	AAD y %
objective function: flash calculation					
PR-MC-WS-NRTL	293.48	-0.08	0.23	0.05	0.45
	313.44	0.65	0.73	0.03	0.45
	333.02	0.65	0.61	0.24	1.22
PR-SV-WS-NRTL	293.48	-0.27	0.27	-0.07	0.67
	313.44	0.93	0.91	-0.09	0.85
	333.02	1.11	0.79	0.33	1.74
		bias P %	AAD P %	bias y %	AAD y %
objective function: ordinary least squares					
PR-MC-WS-NRTL	293.48	0.04	8.15	-0.55	0.84
	313.44	-0.10	21.86	-1.10	1.08
	333.02	-0.09	12.74	2.69	2.03
SRK-MC-PSRK-NRTL	293.48	-1.14	69.81	-1.14	1.64
	313.44	-0.56	70.81	-0.56	5.68
	333.02	-0.01	27.18	-0.01	3.48

A comparison between the experimental VLE and the modelled data presented in Figures 5.9-11 shows that the PR-MC-WS-NRTL (OF: FC) combination provides a better fit for the CO (1) + C_4F_{10} (2) system at 293.48 K and 313.44 K than the PR-SV-WS-NRTL (OF: FC), PR-MC-WS-NRTL (OF: OLS) and SRK-MC-PSRK-NRTL (OF: OLS) combinations. However at 333.33 K, slight deviations between the experimental VLE data and the modelled data from the PR-MC-WS-NRTL (OF: FC) model are observed in the vapour phase, with significant deviations in the vicinity of the mixture critical point. However the PR-MC-WS-NRTL (OF: OLS) and PR-SV-WS-NRTL (OF: FC) models provide a similar fit for the 293.48 K and 333.44 K isotherms with a poor fit for the 333.44 K isotherm.

The SRK-MC-PSRK-NRTL (OF: OLS) model provides a poor fit for the three isotherms with large deviations observed both in the vapour phase and the vicinity of the mixture critical points. The slight deviations observed in the vapour phase could be due to the asymmetry of the CO (1) + C_4F_{10} (2) system, whereas the deviations in the vicinity of the mixture critical point could be

attributed to the nature of the Peng-Robinson cubic EoS in the PR-MC-WS-NRTL model. One should also note that accurate VLE data measurement in the vicinity of the mixture critical point can be very challenging when the equilibrium cell is immersed in an opaque liquid bath.

Deviations bias U and AAD U between the experimental and the calculated (PR-MC-WS-NRTL (OF: FC), PR-SV-WS-NRTL (OF: FC), PR-MC-WS-NRTL (OF: OLS) and SRK-MC-PSRK-NRTL (OF: OLS) vapour and liquid mole fractions are reported in Table 5.13. The results obtained help to quantify the fit of the models to the experimental data. As can be seen from Table 6.13, a comparison of the four models taking into their objective functions reveals that the PR-MC-WS-NRTL (OF: FC) model provides a better fit than the PR-SV-WS-NRTL (OF: FC) model whilst the PR-MC-WS-NRTL (OF: OLS) model provides a better fit than the SRK-MC-WS-NRTL (OF: OLS) model.

The experimental relative volatilities for the CO (1) + C_4F_{10} (2) system and the calculated ones using the four models as shown in Figure 5.12 are in agreement with the results obtained from bias U and AAD U.

The solubility of carbon monoxide in perfluorobutane can also be examined through Figures 5.9 to 5.11. One can observe that as temperature decreases more carbon monoxide is absorbed in perfluorobutane. However, a temperature variation between 293.48 and 333.33 K has no significant influence on the solubility of CO in C_4F_{10}.

5.5.2.3 Nitric oxide (1) + perfluorobutane (2) system

The experimental VLE data for the nitric oxide (1) + perfluorobutane (2) system were undertaken at three temperatures (292.97, 312.93 and 332.97) K and are reported in Table 5.14.

The measured data were modelled using two combinations of models namely, the Peng-Robinson EoS incorporating the Mathias-Copeman alpha function and the Wong-Sandler mixing rule utilizing the NRTL activity coefficient model and adjusted using both the flash calculation and ordinary least squares objective functions abbreviated as PR-MC-WS-NRTL (OF: FC) and PR-MC-WS-NRTL (OF: OLS) models and, the Peng-Robinson EoS incorporating the Stryjek-Vera alpha function and the Wong-Sandler mixing rule utilizing the NRTL activity coefficient model and adjusted using the flash calculation objective function abbreviated as PR-SV-WS-

NRTL (OF: FC) model. The results from the modelling are graphically compared with the experimental data in Figures 5.13 to 5.15. The model parameters for both models in the temperature-independent and temperature-dependent forms are reported in Tables 5.15 and 5.16, respectively. The relative volatilities were also computed for the three models and graphically compared with the experimental values in Figure 5.16.

Table 5.14: Experimental VLE data for the nitric oxide (1) + perfluorobutane (2) system

T/K = 292.97						
P/MPa	n_x	x_1	δx_1	n_y	y_1	δy_1
1.762	5	0.073	0.0002	5	0.823	0.0006
2.300	5	0.094	0.0001	5	0.849	0.0007
3.162	5	0.130	0.0004	5	0.879	0.0006
3.645	6	0.153	0.0014	5	0.888	0.0009
4.984	5	0.204	0.0010	5	0.905	0.0006
6.480	5	0.278	0.0018	5	0.910	0.0001
8.266	5	0.352	0.0011	5	0.908	0.0006
9.561	5	0.401	0.0011	5	0.900	0.0008
10.774	5	0.445	0.0010	6	0.894	0.0004
12.048	5	0.495	0.0007	5	0.888	0.0004
13.592	5	0.572	0.0016	5	0.874	0.0009
14.894	5	0.675	0.0011	5	0.832	0.0004
15.369	5	0.730	0.0004	5	0.787	0.0015
T/K = 312.93						
P/MPa	n_x	x_1	δx_1	n_y	y_1	δy_1
1.015	5	0.033	0.0003	5	0.524	0.0012
2.083	5	0.078	0.0003	5	0.722	0.0047
3.138	7	0.126	0.0004	5	0.793	0.0021
4.137	5	0.175	0.0010	5	0.811	0.0010
5.380	5	0.229	0.0011	5	0.835	0.0011
6.758	5	0.308	0.0008	5	0.845	0.0010
8.210	5	0.360	0.0006	5	0.845	0.0009
9.705	5	0.420	0.0018	5	0.841	0.0004
11.685	5	0.507	0.0014	5	0.825	0.0011
13.265	5	0.636	0.0033	5	0.796	0.0014

Table 5.14: Continued

T/K = 332.97						
P/MPa	n_x	x_1	δx_1	n_y	y_1	δy_1
1.612	5	0.044	0.0001	5	0.447	0.0017
2.460	5	0.080	0.0004	5	0.575	0.0015
3.391	5	0.125	0.0005	5	0.652	0.0018
4.181	5	0.163	0.0011	5	0.698	0.0015
5.022	5	0.202	0.0003	5	0.719	0.0015
6.025	5	0.244	0.0008	5	0.736	0.0028
7.405	5	0.306	0.0021	5	0.745	0.0019
8.848	6	0.376	0.0024	5	0.736	0.0009
9.968	5	0.435	0.0002	5	0.721	0.0011
10.597	5	0.495	0.0015	5	0.705	0.0018

x_1, y_1: liquid and vapour mole fraction; n_x, n_y : number of samples taken; δx_1, δy_1: standard deviation for x_1 and y_1.
Expanded uncertainty: $u\ (T, k = 2)$ = 0.04 K; $u\ (P, k = 2)$ = 2.00 kPa; u (x_1, k = 2) = 0.01 and u (y_1, k = 2) = 0.01.

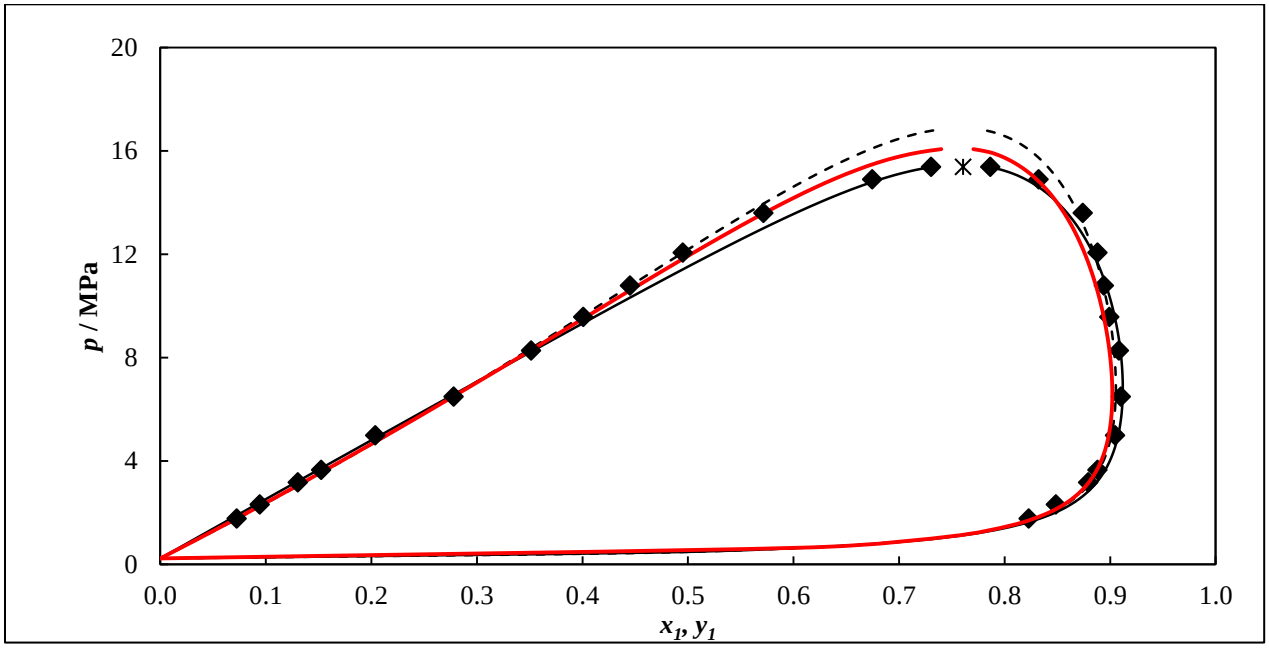

Figure 5.13: Phase diagrams (*P-x-y*) for the NO (1) + C_4F_{10} (2) system. Experimental data: ♦, 292.97 K; Models: PR-MC-WS-NRTL (OF: FC) (solid black line); PR-SV-WS-NRTL (OF: FC) (dashed black line) and PR-MC-WS-NRTL (OF: OLS) (solid red line); *, mixture critical point.

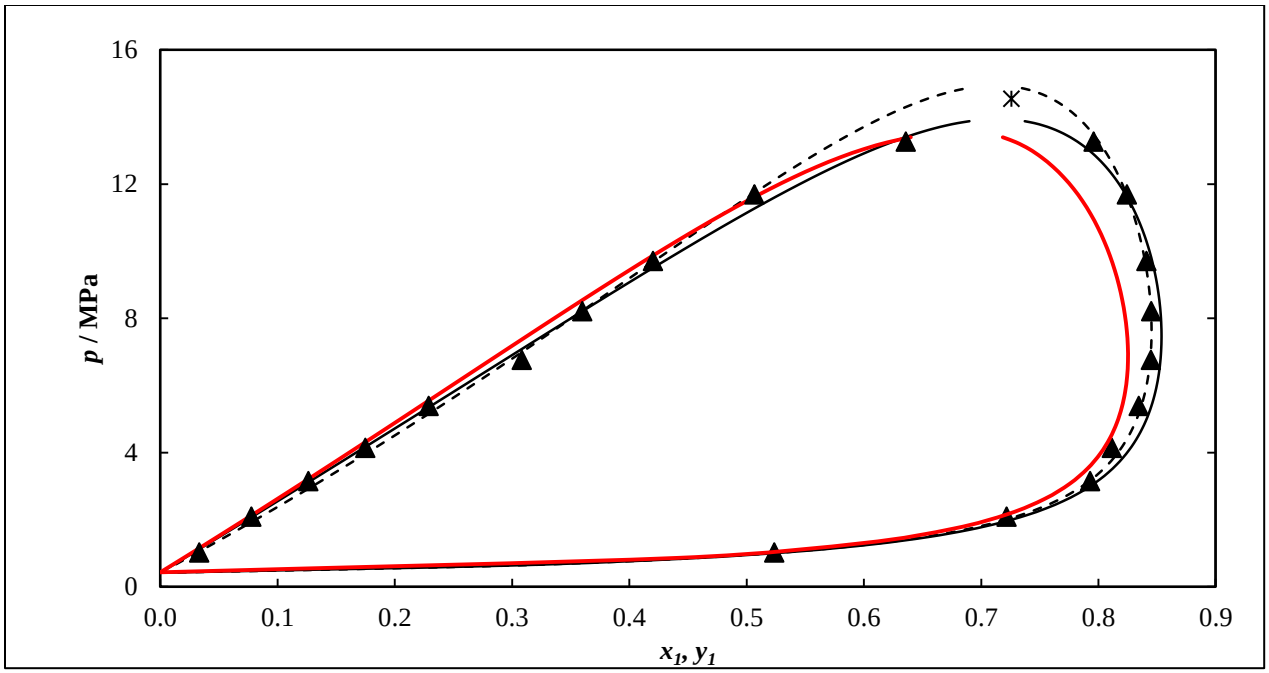

Figure 5.14: Phase diagrams (*P-x-y*) for the NO (1) + C_4F_{10} (2) system. ▲, Experimental data: 312.93 K; Models: PR-MC-WS-NRTL (OF: FC) (solid black line); PR-SV-WS-NRTL (OF: FC) (dashed black line) and PR-MC-WS-NRTL (OF: OLS) (solid red line); *, mixture critical point.

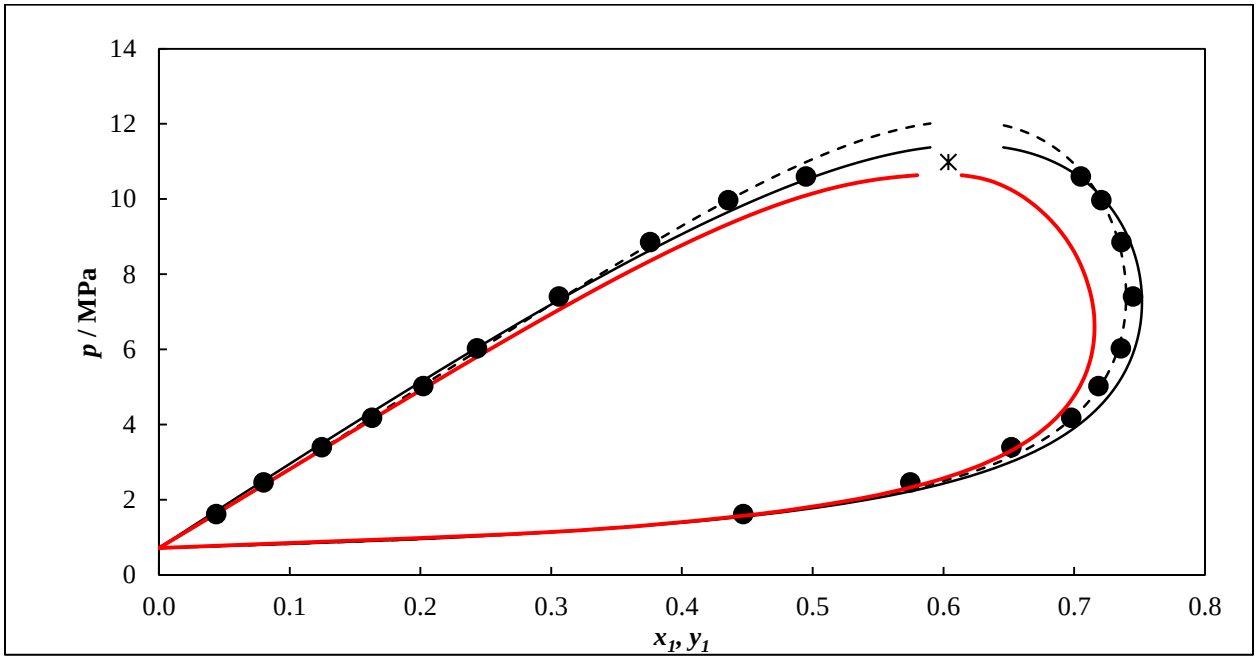

Figure 5.15: Phase diagrams (*P-x-y*) for the NO (1) + C_4F_{10} (2) system. Experimental data: ●, 332.97 K; Models: PR-MC-WS-NRTL (OF: FC) (solid black line); PR-SV-WS-NRTL (OF: FC) (dashed black line) and PR-MC-WS-NRTL (OF: OLS) (solid red line); *, mixture critical point.

Table 5.15: Model parameters for the PR-MC-WS-NRTL and PR-SV-WS-NRTL models in a temperature-independent form for the NO (1) + C_4F_{10} (2) system

Model	Isotherm /K	$(g_{12} - g_{22})^a$/J.mol^{-1}	$(g_{21} - g_{11})^a$/J.mol^{-1}	$k_{ij}{}^b$
objective function: flash calculation				
PR-MC-WS-NRTL	292.97	15847	893.84	0.72
	312.93	16117	467.82	0.73
	332.97	14544	748.78	0.76
PR-SV-WS-NRTL	292.97	1077.7	-1154.6	0.67
	312.93	2190.8	-2527.1	0.68
	332.97	2999.0	-2504.3	0.71
Model		$\tau_{12}{}^c$	$\tau_{21}{}^c$	$k_{ij}{}^d$
objective function: ordinary least squares				
PR-MC-WS-NRTL	292.97	0.4849	-0.3702	0.64
	312.93	-0.9100	1.0580	0.65
	332.97	-0.3666	0.3491	0.69

[a] NRTL model parameters obtained from THERMOPACK, $\Delta g_{ij} = a_{ij}$.

[b, d] WS mixing rule parameter incorporated into the PR EoS correlated from THERMOPACK and Aspen Plus, respectively.

[c] NRTL model parameters obtained from Aspen Plus, $\tau_{ij} = b_{ij}$.

Table 5.16: Model parameters for the PR-MC-WS-NRTL and PR-SV-WS-NRTL models in a temperature-dependent form for the NO (1) + C_4F_{10} (2) system

Model	$(g_{12} - g_{22})^a$/J.mol-1.K		$(g_{21} - g_{11})^a$/J.mol-1.K		$k_{ij}{}^b$
	a_{12}	b_{12}	a_{21}	b_{21}	
objective function: flash calculation					
PR-MC-WS-NRTL	-10811	76.569	-3092.7	10.669	0.74
PR-SV-WS-NRTL	7420.1	-24.123	-5211.8	15.872	0.68
Model	$\tau_{12}{}^c$ / K		$\tau_{21}{}^c$ / K		$k_{ij}{}^d$
objective function: ordinary least squares					
PR-MC-WS-NRTL	-57.590		115.54		0.65

[a] NRTL model parameters obtained from THERMOPACK, $\Delta g_{ij} = a_{ij} + b_{ij}$.T

[b, d] WS mixing rule parameter incorporated into the PR EoS correlated from THERMOPACK and aspen Plus, respectively.

[c] NRTL model parameters obtained from Aspen Plus, $\tau_{ij} = b_{ij}$/T

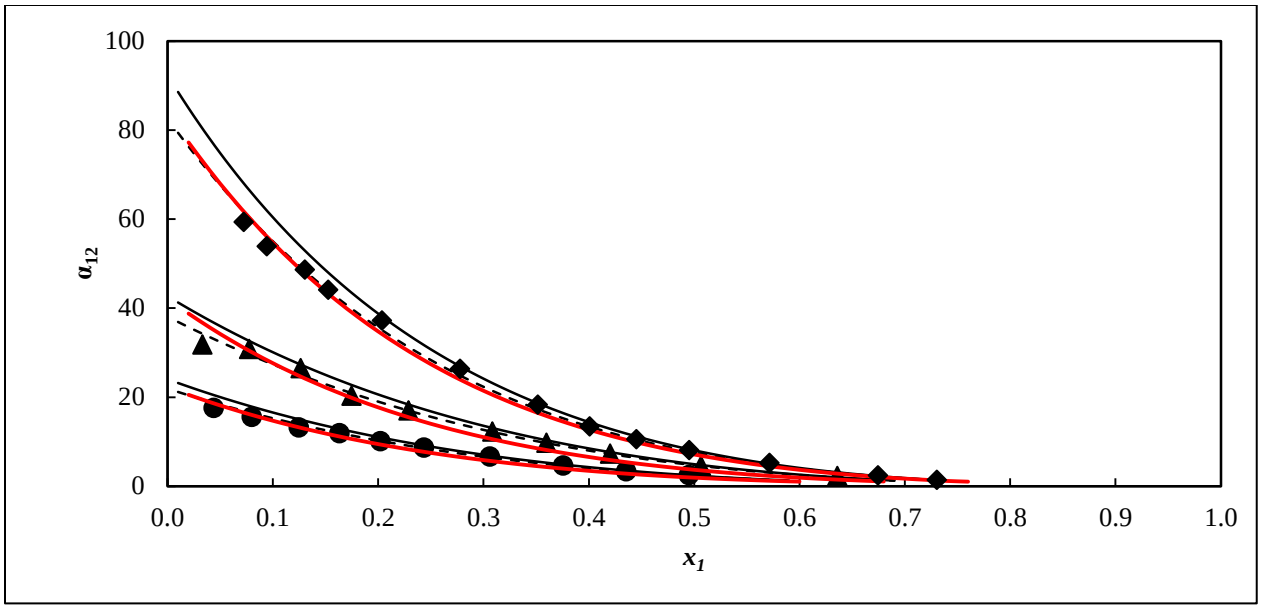

Figure 5.16: Plot of relative volatilities (α_{12}) for the NO (1) + C_4F_{10} (2) system. Experimental data: ♦, 292.97 K; ▲, 312.93 K; ●, 332.97 K. Models: PR-MC-WS-NRTL (OF: FC) (solid black line); PR-SV-WS-NRTL (OF: FC) (dashed black line) and PR-MC-WS-NRTL (OF: OLS) (solid red line). Error bands: shown at 6.0 % for the experimental data.

Table 5.17: Deviations, Bias U and the AAD U obtained in fitting experimental VLE data with the PR-SV-WS-NRTL and PR-MC-WS-NRTL model for the NO (1) + C_4F_{10} (2) system

Model	Isotherm / K	bias x %	AAD x %	bias y %	AAD y %
objective function: flash calculation					
PR-MC-WS-NRTL	292.97	-0.36	0.94	-0.18	0.64
	312.93	1.44	0.67	-0.73	0.86
	332.97	1.47	0.70	-1.91	1.21
PR-SV-WS-NRTL	292.97	0.84	1.59	-0.67	0.87
	312.93	-0.79	1.11	-0.30	0.30
	332.97	-0.01	0.41	-0.78	0.62
Model	Isotherm / K	bias P %	AAD P %	bias y %	AAD y %
objective function: ordinary least squares					
PR-MC-WS-NRTL	292.97	-0.07	12.80	1.41	1.41
	312.93	-0.25	12.74	1.53	1.90
	332.97	-0.03	7.28	-0.31	0.92

Unlike the experimental VLE data for the carbon monoxide (1) + perfluorobutane (2) system, the experimental VLE data for the nitric oxide (1) + perfluorobutane (2) agree well with the VLE data obtained from the PR-SV-WS-NRTL (OF: FC) model. However, the PR-SV-WS-NRTL (OF: FC) model still fails to represent VLE data in the vicinity of the mixture critical point well. At 292.97 and 332.97 K, The PR-MC-WS-NRTL (OF: FC) model represents the measured data globally well, except a few data points in the liquid phase that exhibit slight deviations. At 312.93 K, the PR-MC-WS-NRTL (OF: FC) model represents the measured data well with slight deviations observed in the vapour phase. The third model, PR-MC-WS-NRTL (OF: OLS), represents the measured data well at 292.97K but fails at 312.93 K and 332.97 K where large deviations are observed in the vapour phase.

Deviations BIAS U and AAD between the experimental and the modelled (PR-MC-WS-NRTL (OF: FC), PR-MC-WS-NRTL (OF: OLS) and PR-SV-WS-NRTL (OF: FC)) vapour and liquid mole fractions for the nitric oxide + perfluorobutane system were calculated and reported in Table 5.17. The results obtained help quantify the fit of the models to the experimental data. As can be seen from the table, the PR-SV-WS-NRTL (OF: FC) model shows better agreement with the measured data with $AAD_{x, y} < 1.60$ % and $Bias_{x, y} < 1.00$ %.

The relative volatilities were computed for the three combinations of models chosen and compared to the experimental values. The results obtained are presented in Figures 5.16, where the experimental relative volatilities for the NO (1) + C_4F_{10} (2) system are generally in good agreement only with those calculated using the PR-SV-WS-NRTL (OF: FC) model.

Figures 5.13 to 5.15 reveal that like the carbon monoxide (1) + perfluorobutane (2) system, temperature does not have much effect on the solubility of nitric oxide in perfluorobutane within a temperature range of 292.97 and 332.97 K. Considering the effect of temperature on the relative volatility, for an equilibrium based absorption process, one should optimize the absorption column temperature accordingly to obtain good results.

5.5.2.4 Hydrogen sulfide (1) + perfluorobutane (2) system

Isothermal VLE data measurements for the hydrogen sulfide (1) + perfluorobutane (2) system were undertaken at three temperatures from (293.08, 313.00 and 333.03) K and are reported in Table 5.18.

The experimental VLE data were modelled using the Soave-Redlich-Kwong EoS incorporating the Mathias-Copeman alpha function and the Wong-Sandler or predictive Soave-Redlich-Kwong mixing rule utilizing the NRTL activity coefficient model and adjusted using the flash calculation objective function abbreviated as SRK-MC-MHV1-NRTL (OF: FC), SRK-MC-PSRK-NRTL (OF: OLS) and PR-MC-WS-NRTL (OF: OLS) models. The results from the modelling are graphically compared with the experimental data in Figures 5.17-5.19. The model parameters in both the temperature-independent and temperature-dependent forms are reported in Tables 5.19 and 5.20, respectively. The relative volatilities were also computed for the SRK-MC-MHV1-NRTL (OF: FC), SRK-MC-PSRK-NRTL (OF: OLS) and PR-MC-WS-NRTL (OF: OLS) models. The results obtained are graphically compared with the experimental values in Figure 5.20.

Table 5.18: Experimental VLE data for the hydrogen sulfide (1) + perfluorobutane (2) system

T/K = 293.08						
P/MPa	n_x	x_1	δx_1	n_y	y_1	δy_1
0.394	5	0.027	0.0001	5	0.396	0.0023
0.533	5	0.051	0.0002	6	0.555	0.0028
0.679	5	0.081	0.0003	5	0.644	0.0018
0.834	5	0.108	0.0004	5	0.706	0.0020
0.965	5	0.131	0.0003	5	0.747	0.0014
1.120	5	0.168	0.0005	5	0.780	0.0005
1.301	5	0.213	0.0002	5	0.810	0.0004
1.426	5	0.249	0.0003	5	0.819	0.0005
1.639	5	0.319	0.0008	5	0.840	0.0008
1.844	5	0.997	0.0010	5	0.972	0.0005
1.863	5	0.433	0.0030	5	0.859	0.0010
1.906	6	0.991	0.0003	5	0.943	0.0014
1.987	6	0.982	0.0003	5	0.907	0.0016
2.010	5	0.570	0.0030	5	0.879	0.0005
2.014	5	0.683	0.0050	5	0.884	0.0001
2.014	5	0.970	0.0036	5	0.891	0.0004
2.015	5	0.718	0.0024	5	0.894	0.0059

Table 5.18: Continued

T/K = 313.00						
P/MPa	n_x	x_1	δx_1	n_y	y_1	δy_1
0.721	5	0.043	0.0001	5	0.395	0.0013
0.923	5	0.069	0.0002	5	0.508	0.0003
1.112	5	0.095	0.0003	5	0.573	0.0004
1.343	5	0.130	0.0001	5	0.635	0.0001
1.553	5	0.159	0.0002	5	0.676	0.0004
1.769	5	0.196	0.0005	5	0.715	0.0006
2.153	5	0.268	0.0001	5	0.763	0.0005
2.481	5	0.355	0.0001	5	0.796	0.0004
2.899	5	0.507	0.0012	5	0.826	0.0016
3.155	5	0.672	0.0001	5	0.853	0.0007
3.202	5	0.760	0.0004	5	0.865	0.0007
2.958	5	0.996	0.0001	5	0.981	0.0004
3.222	5	0.957	0.0002	5	0.895	0.0009
3.228	5	0.952	0.0011	5	0.890	0.0010
3.242	5	0.930	0.0005	5	0.888	0.0010
3.239	5	0.931	0.0007	5	0.883	0.0007

Table 5.18: Continued

T/K = 333.03						
P/MPa	n_x	x_1	δx_1	n_y	y_1	δy_1
1.163	5	0.052	0.0003	5	0.324	0.0004
1.487	5	0.088	0.0003	5	0.435	0.0001
1.989	5	0.149	0.0001	5	0.547	0.0005
2.464	5	0.215	0.0001	5	0.625	0.0007
2.907	5	0.284	0.0002	5	0.675	0.0006
3.303	5	0.349	0.0002	5	0.714	0.0005
3.931	5	0.479	0.0001	5	0.748	0.0008
4.203	5	0.554	0.0006	5	0.768	0.0007
4.769	5	0.771	0.0010	5	0.841	0.0006
4.602	5	0.692	0.0008	5	0.807	0.0006
4.861	5	0.915	0.0003	5	0.890	0.0004
4.874	5	0.892	0.0007	5	0.878	0.0005
4.708	5	0.976	0.0007	5	0.933	0.0009

x_1, y_1: liquid and vapour mole fraction; n_x, n_y : number of samples taken; δx_1, δy_1: standard deviation for x_1 and y_1.

Expanded uncertainty: $u\ (T, k = 2)$ = 0.04 K; $u\ (P, k = 2)$ = 2.00 kPa; u (x_1, k = 2) = 0.01 and u (y_1, k = 2) = 0.01.

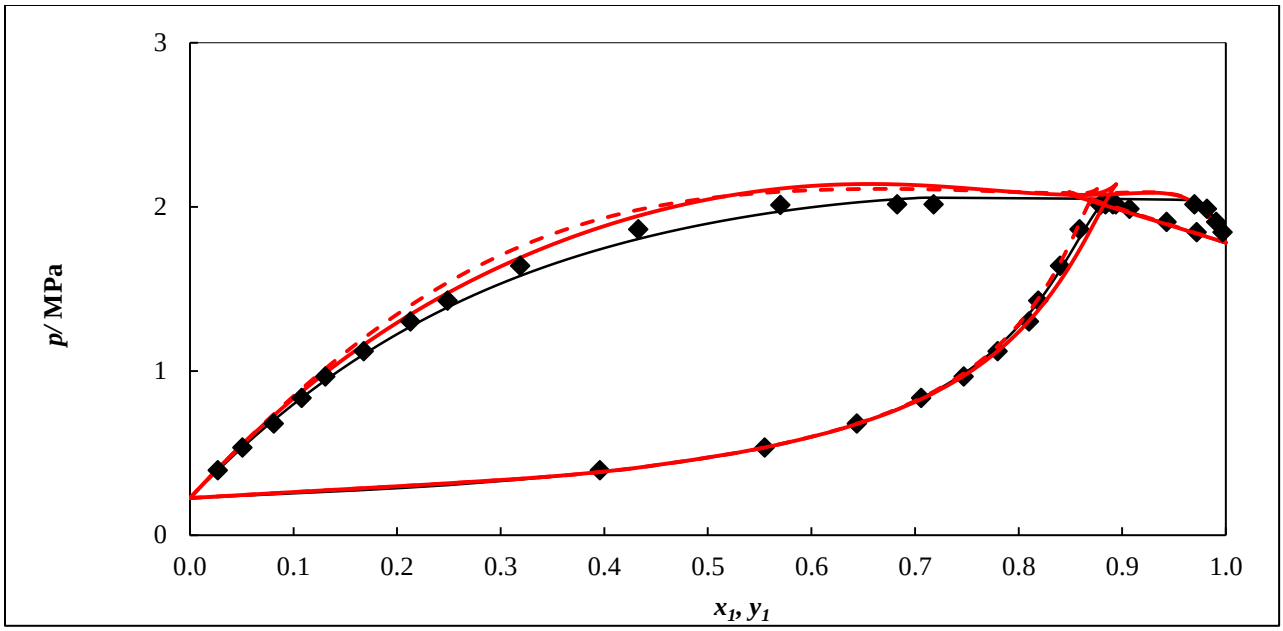

Figure 5.17: Phase diagrams (*P-x-y*) for the H_2S (1) + C_4F_{10} (2) system. Experimental data: ♦, 293.08 K; Models: SRK-MC-MHV1-NRTL (OF: FC) (solid black line); SRK-MC-PSRK-NRTL (OF: FC) (dashed red line) and PR-MC-WS-NRTL (OF: OLS) (solid red line).

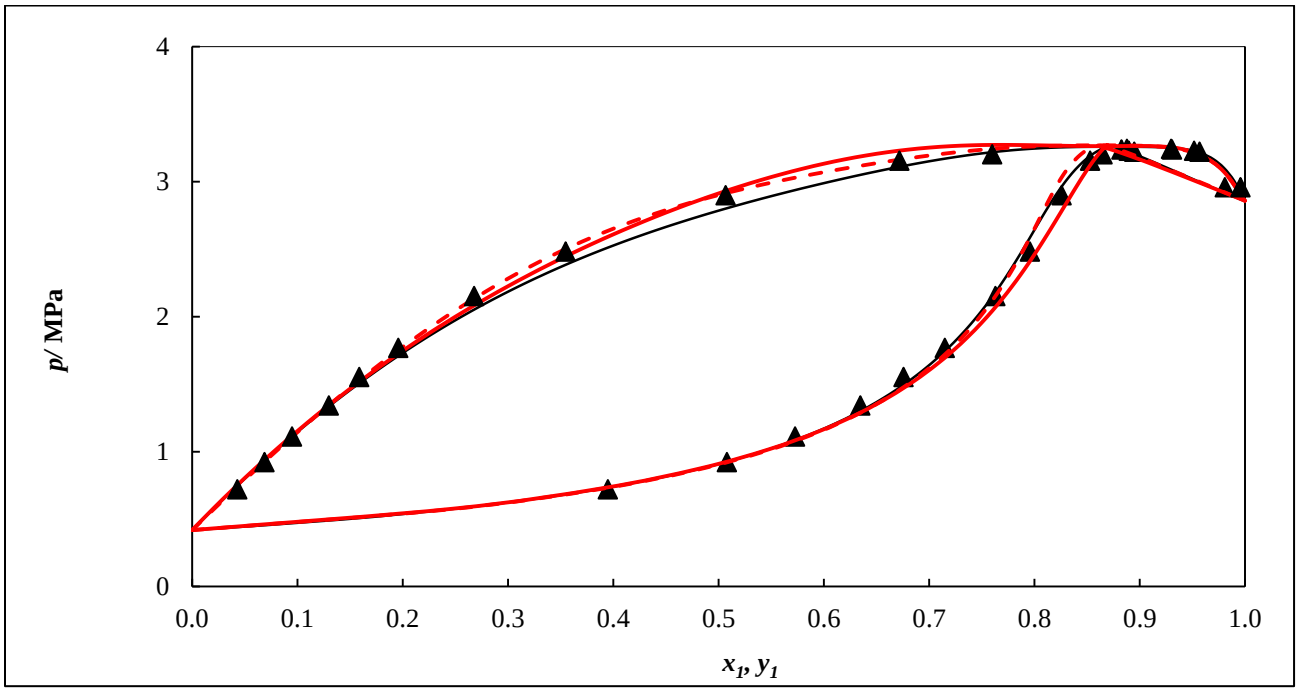

Figure 5.18: Phase diagrams (*P-x-y*) for the H_2S (1) + C_4F_{10} (2) system. Experimental data: ▲, 313.00 K; Models: SRK-MC-MHV1-NRTL (OF: FC) (solid black line); SRK-MC-PSRK-NRTL (OF: FC) (dashed red line) and PR-MC-WS-NRTL (OF: OLS) (solid red line).

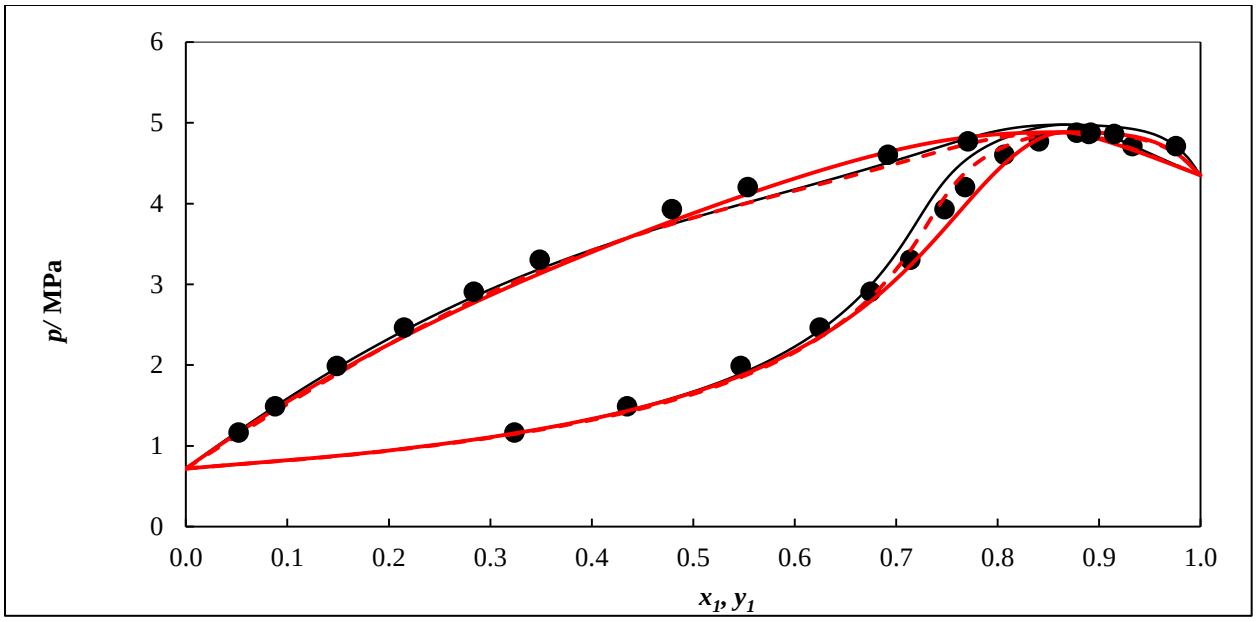

Figure 5.19: Phase diagrams (*P*-*x*-*y*) for the H_2S (1) + C_4F_{10} (2) system. Experimental data: ●, 333.03 K; Models: SRK-MC-MHV1-NRTL (OF: FC) (solid black line); SRK-MC-PSRK-NRTL (OF: FC) (dashed red line) and PR-MC-WS-NRTL (OF: OLS) (solid red line).

Table 5.19: Model parameters for the SRK-MC-MHV1-NRTL, SRK-MC-PSRK-NRTL and PR-MC-WS-NRTL models in a temperature-independent form for the H_2S (1) + C_4F_{10} (2) system

Model	Isotherm / K	$(g_{12} - g_{22})^a$/J.mol^{-1}	$(g_{21} - g_{11})^a$/J.mol^{-1}	$k_{ij}{}^b$
	objective function: flash calculation			
SRK-MC-MHV1-NRTL	293.08	10819	1106.3	—
	313.00	10467	757.49	—
	333.03	10700	494.39	—
Model		$\tau_{12}{}^c$	$\tau_{21}{}^c$	$k_{ij}{}^d$
	objective function: ordinary least function			
PR-MC-WS-NRTL	293.08	-1.4665	-1.7690	0.48
	313.00	-2.2585	-1.7885	0.55
	333.03	0.8750	-2.9881	0.53
SRK-MC-PSRK-NRTL	293.08	0.5621	-2.8246	—
	313.00	1.1376	-3.8743	—
	333.03	0.6918	-2.8706	—

[a] NRTL model parameters obtained from THERMOPACK, $\Delta g_{ij} = a_{ij}$.

[b, d] WS mixing rule parameter incorporated into the PR EoS correlated from THERMOPACK and Aspen Plus, respectively.

[c] NRTL model parameters obtained from Aspen Plus, $\tau_{ij} = a_{ij}$.

Table 5.20: Model parameters for the SRK-MC-MHV1-NRTL, SRK-MC-PSRK-NRTL and PR-MC-WS-NRTL models in a temperature-dependent form for the H_2S (1) + C_4F_{10} (2) system

Model	$(g_{12} - g_{22})^a$/J.mol-1.K		$(g_{21} - g_{11})^a$/J.mol-1.K		$k_{ij}{}^b$
	a_{12}	b_{12}	a_{21}	b_{21}	
objective function: flash calculation					
SRK-MC-PSRK-NRTL	1274.8	35.422	226.52	141.80	—
Model	**$\tau_{12}{}^c$ / K**		**$\tau_{21}{}^c$ / K**		**$k_{ij}{}^d$**
objective function: ordinary least squares					
PR-MC-WS-NRTL	2106.8		671.51		0.50
SRK-MC-PSRK-NRTL	1250.7		1053.4		—

[a] NRTL model parameters obtained from THERMOPACK, $\Delta g_{ij} = a_{ij} + b_{ij}.T$

[b, d] WS mixing rule parameter incorporated into the PR EoS correlated from THERMOPACK and Aspen Plus, respectively.

[c] NRTL model parameters obtained from Aspen Plus, $\tau_{ij} = b_{ij}/T$

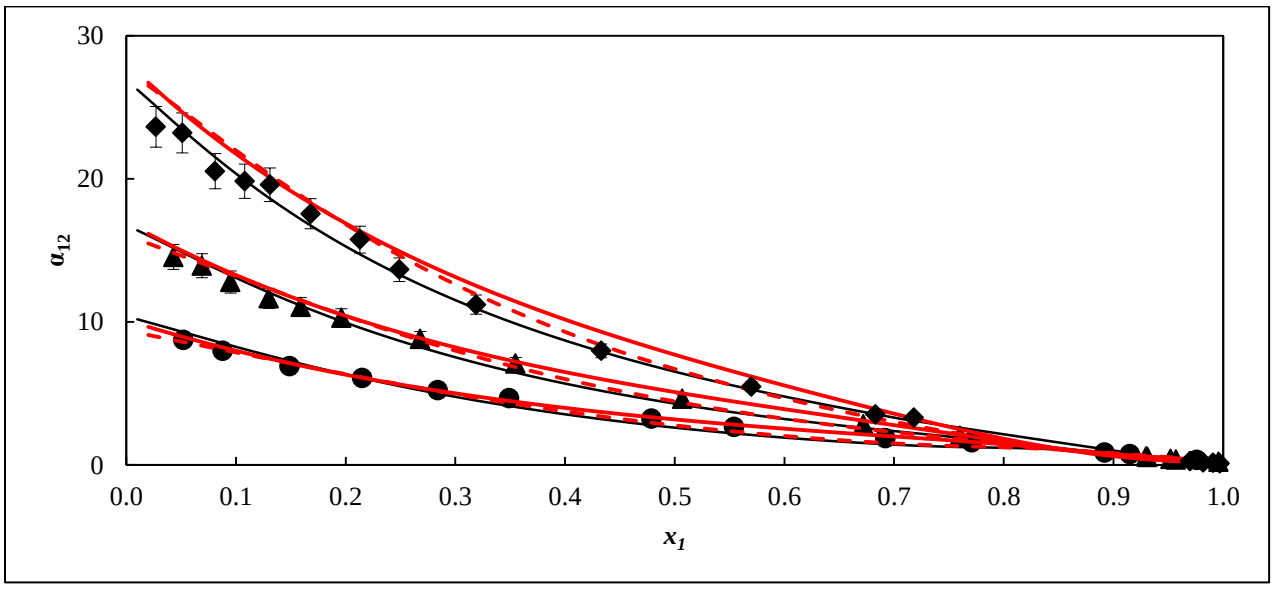

Figure 5.20: Plot of relative volatilities (α_{12}) for the H_2S (1) + C_4F_{10} (2) system. Experimental data: ♦, 293.08 K; ▲, 313.00 K; ●, 333.03 K. Models: SRK-MC-MHV1-NRTL (OF: FC) (solid black line); SRK-MC-PSRK-NRTL (OF: FC) (dashed red line) and PR-MC-WS-NRTL (OF: solid red line). Error bands: shown at 6.0 % for the experimental data.

Table 5.21: Deviation bias U and AAD U obtained in fitting experimental VLE data with the SRK-MC-MHV1-NRTL, SRK-MC-PSRK-NRTL and PR-MC-WS-NRTL models for the H_2S (1) + C_4F_{10} (2) system

Model	Isotherm / K	bias x %	AAD x %	bias y %	AAD y %
objective function: flash calculation					
SRK-MC-MHV1-NRTL	293.08	-0.73	0.13	1.82	0.46
	313.00	-2.00	0.28	1.29	0.64
	333.03	-2.85	0.53	1.66	1.51
Model	**Isotherm / K**	**bias P %**	**AAD P %**	**bias y %**	**AAD y %**
objective function: ordinary least squares					
PR-MC-WS-NRTL	293.08	-0.16	2.26	-0.17	0.54
	313.00	-0.07	3.28	-0.50	0.91
	333.03	1.65	8.44	0.19	0.54
SRK-MC-PSRK-NRTL	293.08	0.54	3.27	-0.08	0.91
	313.00	0.01	1.76	0.01	0.69
	333.03	3.39	12.76	1.25	1.10

Azeotropic behaviour was observed for both the 313.00 and 333.03 K isotherms at approximately x_1 = 0.87 and 0.86, respectively. For such isotherms conventional distillation cannot separate the mixture into high purity compounds. Alternative methods such as pressure-swing distillation should be investigated. For the 293.08 K isotherm, as pressure was increased (at approximately 1.987 MPa), the phenomenon of vapour-liquid-liquid equilibrium (VLLE) were suspected but no analysis was undertaken at these conditions due to the use of an opaque thermo-regulated liquid bath in the experimental setup. This made analysis of multiple liquid phases nearly impossible as one had to intermittently have the equilibrium cell removed from the thermo-regulated liquid bath to observe the state of phases in equilibrium. The change of the environment affected the equilibrium cell temperature, and consequently, one could see the second liquid phase disappear as the equilibrium cell temperature varied from 293.08 K to the ambient temperature (~298.15 K).

However, the data obtained from the SRK-MC-MHV1-NRTL (OF: FC), SRK-MC-PSRK-NRTL (OF: OLS) and PR-MC-WS-NRTL (OF: OLS) models did not reveal/show the existence of the VLLE for this system at 293.08 K. Consequently, further experimental investigation using a

transparent thermo-regulated liquid bath should be envisaged to confirm the immiscibility between H_2S and C_4F_{10} at 293.08 K.

The results presented in Figures 5.17, 5.18 and 5.19 show that the SRK-MC-PSRK-NRTL (OF: OLS) and PR-MC-WS-NRTL (OF: OLS) models represent the experimental data favourably well for the three isotherms. However, the modelled data obtained from the SRK-MC-MHV1-NRTL (OF: FC) and experimental data agree well at 298.08 and 313.00 K with slight deviations observed in vapour phase in the vicinity of the azeotrope at 333.03 K.

The bias U and AAD U deviations were determined between the experimental and calculated VLE data to quantify the fit of the model to the experimental data. The results obtained are reported in Table 5.21, where values of bias $_{x,y}$ are less than 3.00 % and AAD $_{x,y}$ less than 2.00 % for the SRK-MC-MHV1-NRTL (OF: FC) model. The high values of bias $_{x,y}$ and AAD $_{x,y}$ are mainly attributed to the isotherms at 313.00 and 333.03 K where the two models considered, failed to represent accurately the data in the azeotropic point region. The bias U and AAD P results obtained for the SRK-MC-WS-NRTL (OF: OLS) and PR-MC-WS-NRTL (OF: OLS) models show that the latter is better than the former as it yields lower values.

The relative volatility results graphically shown in Figure 5.20 reveal that there is a good agreement between the experimental and computed values for the three isotherms measured at 293.08, 313 and 333.03 K. At lower temperatures, the system may split into more than two liquid phases as suspected during experimentation.

For the H_2S (1) + C_4F_{10} system, temperature does not have much effect on the solubility of hydrogen sulphide in perfluorobutane. As temperature decreases from 293.08 K, one would expect the solubility of hydrogen sulphide to increase in perfluorobutane but this is not the case since this system could exhibit vapour-liquid-liquid equilibrium, with the liquid-liquid equilibrium envelop becoming larger at lower temperatures.

5.5.2.5 Methane (1) + perfluorobutane (2) system

The experimental VLE data for the methane (1) + perfluorobutane (2) system were undertaken at three temperatures from (293.05, 313.09 and 32.973) K and are reported in Table 5.22.

The experimental VLE data were modelled using the Peng-Robinson or Soave-Redlich-Kwong EoS incorporating the Mathias-Copeman alpha function and the Wong-Sandler or predictive Soave-Redlich-Kwong mixing rule utilizing the NRTL activity coefficient model and adjusted using the flash calculation and the ordinary objective functions abbreviated as PR-MC-WS-NRTL (OF: FC and OF: OLS) and SRK-MC-PSRK-NRTL (OF: OLS) models. The results from the correlation are graphically compared with the experimental VLE data in Figures 5.21 to 5.23. The model parameters in the temperature-independent and temperature-dependent forms are reported in Tables 5.23 and 5.24, respectively. The relative volatilities were also computed using the PR-MC-WS-NRTL (OF: FC or OLS) and SRK-MC-PSRK-NRTL (OF: OLS) models and compared with the experimental values in Figure 5.24.

Table 5.22: Experimental VLE data for the methane (1) + perfluorobutane (2) system

T/K = 293.05						
P/MPa	n_x	x_1	δx_1	n_y	y_1	δy_1
0.473	5	0.012	0.0000	5	0.423	0.0009
2.015	5	0.085	0.0003	5	0.803	0.0013
3.988	5	0.181	0.0003	5	0.867	0.0007
6.587	5	0.307	0.0013	5	0.875	0.0008
8.058	5	0.393	0.0002	5	0.858	0.0009
5.188	5	0.234	0.0005	5	0.875	0.0005
2.914	5	0.123	0.0006	6	0.847	0.0015
8.901	5	0.434	0.0004	5	0.846	0.0003
10.276	5	0.552	0.0020	5	0.804	0.0004
10.655	5	0.606	0.0004	5	0.773	0.0010
9.562	5	0.483	0.0003	5	0.834	0.0010

Table 5.22: Continued

T/K = 313.09						
P/MPa	n_x	x_1	δx_1	n_y	y_1	δy_1
1.052	5	0.029	0.0002	5	0.467	0.0004
1.853	5	0.061	0.0003	5	0.626	0.0005
2.687	5	0.092	0.0001	5	0.699	0.0007
3.924	5	0.149	0.0006	5	0.754	0.0020
4.788	5	0.191	0.0002	5	0.767	0.0009
5.603	5	0.226	0.0020	5	0.774	0.0008
6.459	5	0.268	0.0002	5	0.775	0.0009
7.447	5	0.318	0.0003	5	0.768	0.0004
8.432	5	0.379	0.0005	5	0.749	0.0013
9.446	5	0.467	0.0004	5	0.706	0.0013
9.837	5	0.519	0.0008	5	0.665	0.0013
T/K = 332.97						
P/MPa	n_x	x_1	δx_1	n_y	y_1	δy_1
7.753	5	0.355	0.0017	6	0.619	0.0013
1.321	6	0.029	0.0002	5	0.336	0.0012
2.168	5	0.064	0.0002	5	0.499	0.0013
2.839	5	0.094	0.0002	5	0.563	0.0011
3.704	5	0.133	0.0003	5	0.618	0.0014
4.541	5	0.169	0.0001	5	0.635	0.0010
5.301	5	0.203	0.0002	5	0.646	0.0012
6.017	5	0.239	0.0002	5	0.648	0.0004
6.743	5	0.279	0.0001	5	0.645	0.0007
7.368	5	0.316	0.0020	5	0.634	0.0019
8.466	5	0.435	0.0003	5	0.547	0.0010
8.138	5	0.380	0.0003	6	0.597	0.0016

x_1, y_1: liquid and vapour mole fraction; n_x, n_y : number of samples taken; δx_1, δy_1: standard deviation for x_1 and y_1.

Expanded uncertainty: $u\ (T, k = 2)$ = 0.04 K; $u\ (P, k = 2)$ = 2.00 kPa; u (x_1, k = 2) = 0.01 and u (y_1, k = 2) = 0.01.

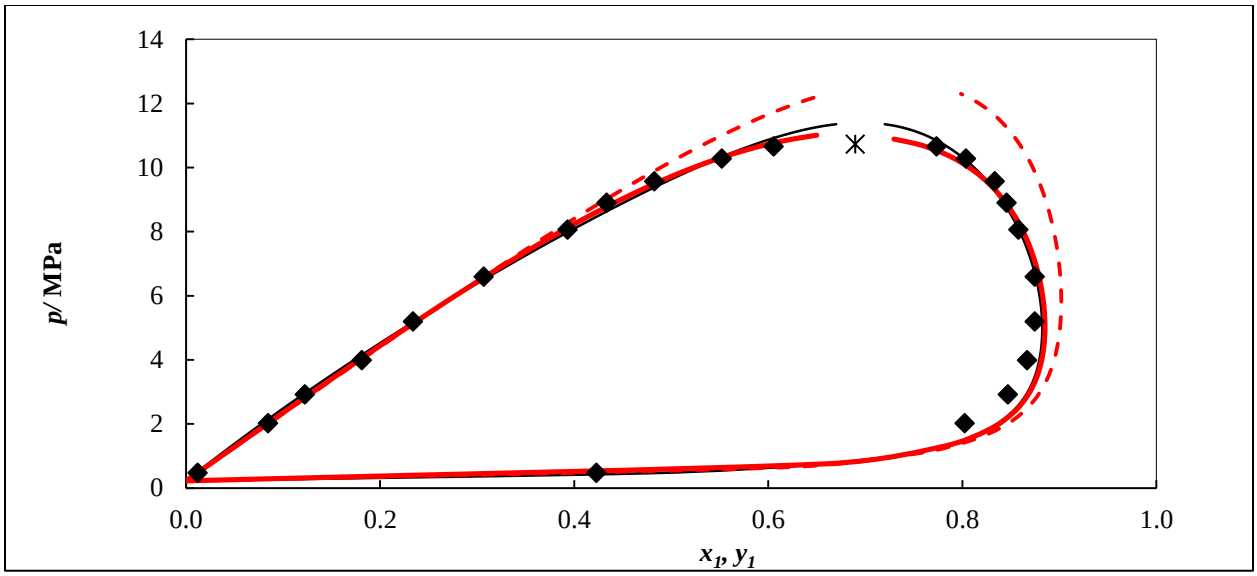

Figure 5.21: Phase diagrams (*P-x-y*) for the CH_4 (1) + C_4F_{10} (2) system. Experimental data: ♦, 293.05 K; Models: PR-MC-WS-NRTL (OF: FC) (solid black line); SRK-MC-PSRK-NRTL (OF: OLS) (dashed red line) and PR-MC-WS-NRTL (OF: OLS) (solid red line); *, mixture critical point.

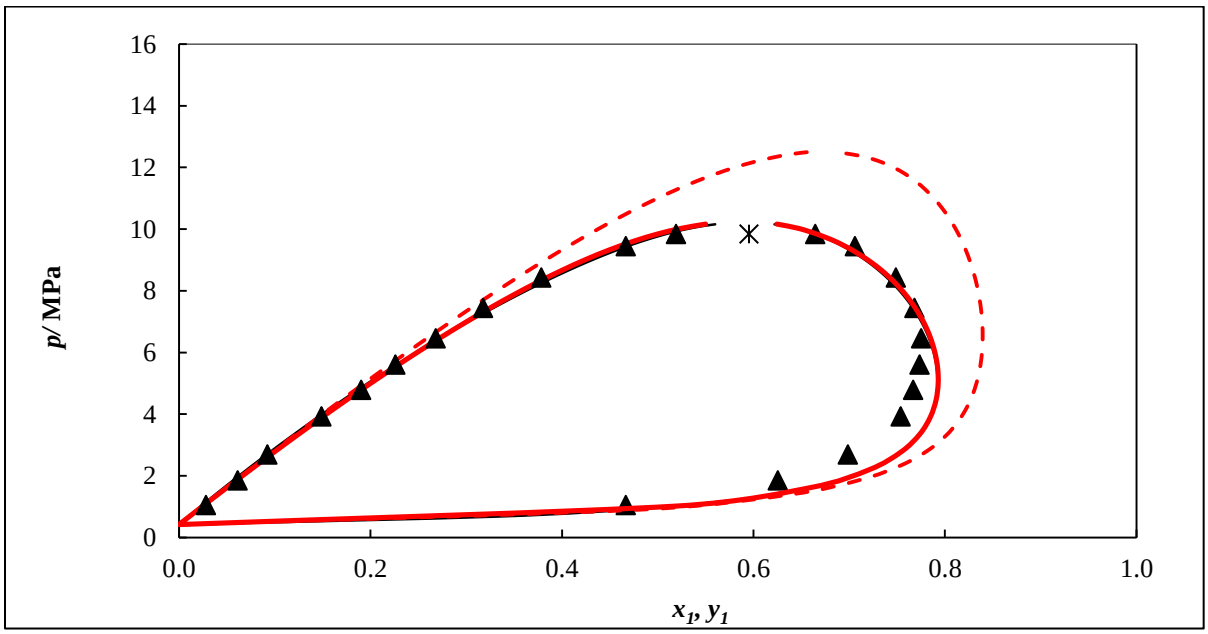

Figure 5.22: Phase diagrams (*P-x-y*) for the CH_4 (1) + C_4F_{10} (2) system. Experimental data: ▲, 313.09 K; Models: PR-MC-WS-NRTL (OF: FC) (solid black line); SRK-MC-PSRK-NRTL (OF: OLS) (dashed red line) and PR-MC-WS-NRTL (OF: OLS) (solid red line); *, mixture critical point.

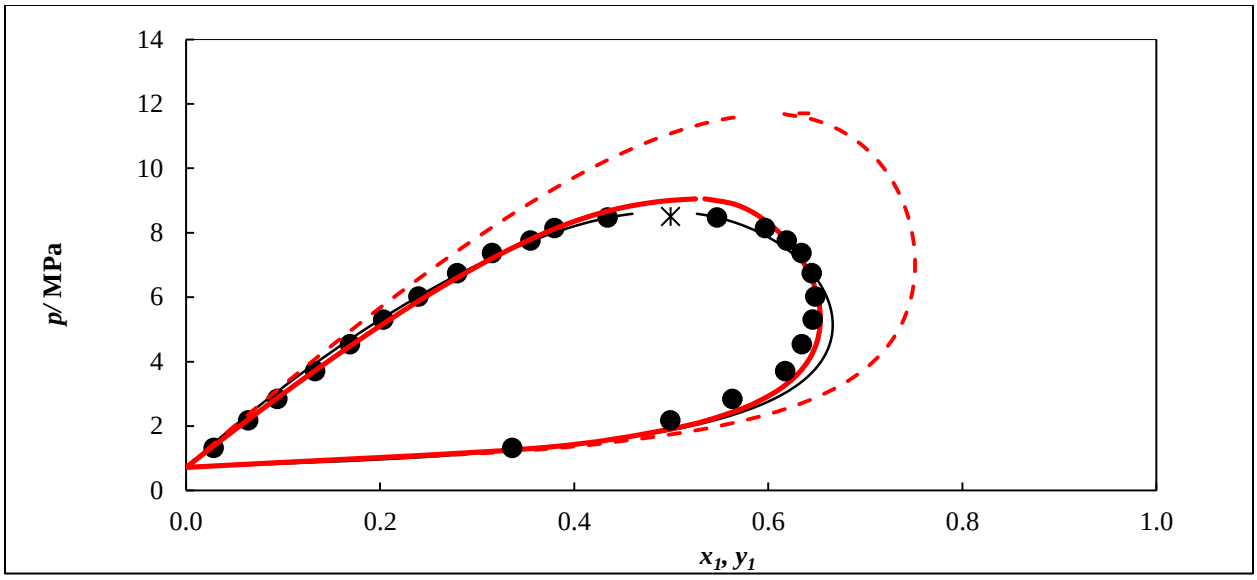

Figure 5.23: Phase diagrams (*P*-*x*-*y*) for the CH_4 (1) + C_4F_{10} (2) system. Experimental data: ●, 332.97 K; Models: PR-MC-WS-NRTL (OF: FC) (solid black line); SRK-MC-PSRK-NRTL (OF: OLS) (dashed red line) and PR-MC-WS-NRTL (OF: OLS) (solid red line); *, mixture critical point.

Table 5.23: Model parameters for the PR-MC-WS-NRTL and SRK-MC-PSRK-NRTL models in a temperature-independent form for the CH_4 (1) + C_4F_{10} (2) system

Model	Isotherm / K	$(g_{12} - g_{22})^a$/J.mol^{-1}	$(g_{21} - g_{11})^a$/J.mol^{-1}	$k_{ij}{}^b$
	objective function: flash calculation			
PR-MC-WS-NRTL	293.05	16649	1955.5	0.60
	313.09	14414	2234.7	0.60
	332.97	12164	2573.7	0.61
Model	Isotherm / K	$\tau_{12}{}^c$	$\tau_{21}{}^c$	$k_{ij}{}^d$
	objective function: ordinary least squares			
PR-MC-WS-NRTL	293.05	2.3136	-0.1603	0.60
	313.09	2.3260	0.0872	0.58
	332.97	5.4303	0.3348	0.52
SRK-MC-PSRK-NRTL	293.05	3.7614	2.2124	—
	313.09	2.8034	2.9902	—
	332.97	49.490	2.3284	—

[a] NRTL model parameters obtained from THERMOPACK, $\Delta g_{ij} = a_{ij}$.

[b, d] WS mixing rule parameter incorporated into the PR EoS correlated from THERMOPACK and Aspen Plus, respectively.

[c] NRTL model parameters obtained from Aspen Plus, $\tau_{ij} = a_{ij}$.

Table 5.24: Model parameters for the PR-MC-WS-NRTL and SRK-MC-PSRK-NRTL models in a temperature-dependent form for the CH_4 (1) + C_4F_{10} (2) system

Model	$(g_{12} - g_{22})^a$/J.mol-1.K		$(g_{21} - g_{11})^a$/J.mol-1.K		$k_{ij}{}^b$
	a_{12}	b_{12}	a_{21}	b_{21}	
	objective function: flash calculation				
PR-MC-WS-NRTL	48354	-106.61	-3079.5	17.591	0.60
Model	$\tau_{12}{}^c$ / K		$\tau_{21}{}^c$ / K		$k_{ij}{}^d$
	objective function: ordinary least squares				
PR-MC-WS-NRTL	830.11		-1057.3		0.26
SRK-MC-PSRK-NRTL	831.99		-649.51		—

[a] NRTL model parameters obtained from THERMOPACK, $\Delta g_{ij} = a_{ij} + b_{ij}$.T

[b, d] WS mixing rule parameter incorporated into the PR EoS correlated from THERMOPACK and Aspen Plus, respectively.

[c] NRTL model parameters obtained from Aspen Plus, $\tau_{ij} = b_{ij}$/T

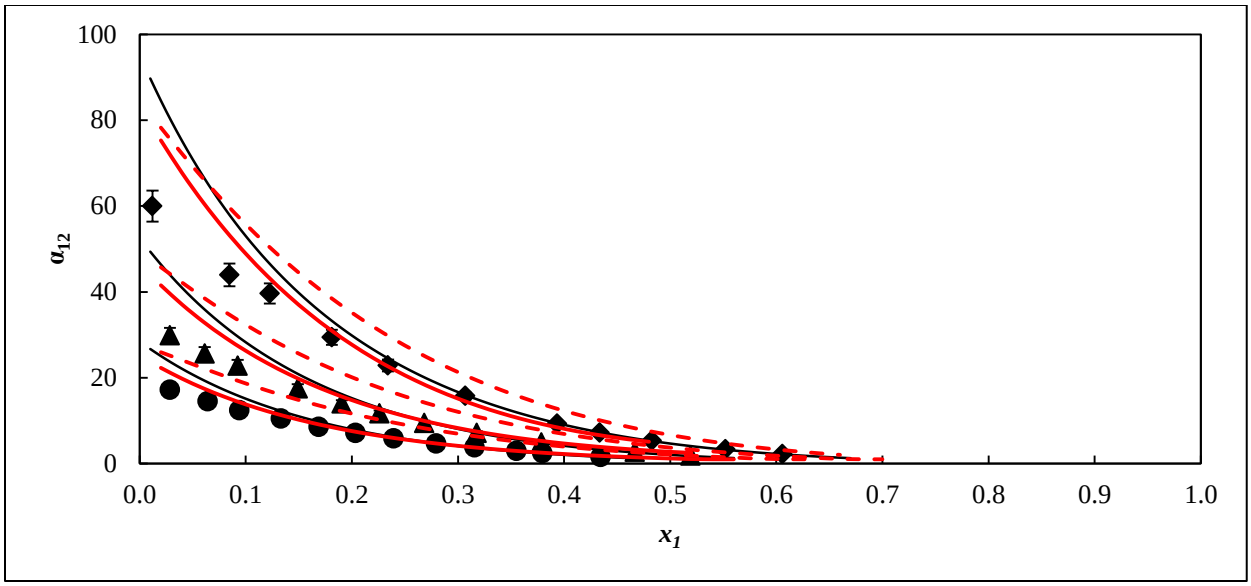

Figure 5.24: Plot of relative volatilities (α_{12}) for the CH_4 (1) + C_4F_{10} (2) system. Experimental data: ♦, 293.05 K; ▲, 313.09 K; ●, 332.97 K; Models: PR-MC-WS-NRTL (OF: FC) (solid black line); SRK-MC-PSRK-NRTL (OF: OLS) (dashed red line) and PR-MC-WS-NRTL (OF: OLS) (solid red line). Error bands: shown at 6.0 %for the experimental data.

Table 5.25: Deviations bias U and AAD U obtained in fitting experimental VLE data with the PR-MC-WS-NRTL and SRK-MC-PSRK-NRTL models for the CH_4 (1) + C_4F_{10} (2) system

Model	Isotherm / K	bias x %	AAD x %	bias y %	AAD y %
objective function: flash calculation					
PR-MC-WS-NRTL	293.05	2.12	-2.12	0.80	1.45
	313.09	1.79	-3.49	0.52	2.58
	332.97	4.10	-2.76	0.62	2.04
	Isotherm / K	bias P %	AAD P %	bias y %	AAD y %
objective function: ordinary least squares					
PR-MC-WS-NRTL	293.05	-0.03	5.32	-2.02	1.82
	313.09	-0.13	7.49	-3.75	2.97
	332.97	-0.20	9.33	-3.36	1.67
SRK-MC-PSRK-NRTL	293.05	-0.58	32.86	0.20	6.94
	313.09	-0.21	30.68	-3.92	9.52
	332.97	-1.71	63.55	0.18	13.98

Figures 5.21-5.23 reveal that the experimental VLE data measured for the three isotherms do not match the modelled data obtained from the SRK-MC-PSRK-NRTL (OF: OLS) model. However, a comparison between the modelled data from the PR-MC-WS-NRTL (OF: FC) and PR-MC-WS-NRTL (OF: OLS) models reveals that the latter provides a closer fit to the experimental data as opposed to the former, except at 313.09 K where the two models exhibit a similar behaviour. One should note that the difference between the two models resides in the objective functions employed. In addition, in the flash calculation (FC) objective function, pressure and temperature are fixed and the liquid and vapour molar compositions calculated, whereas, in the ordinary least squares (OLS) objective function, temperature and liquid molar composition are fixed and pressure and vapour molar composition, calculated. Hence, the disparity between the experimental and the modelled data from the PR-MC-WS-NRTL model at 313.09 K could be due to the imperfection in the measurement of one of the four variables (Pressure, temperature, and liquid or vapor molar composition).

Figure 5.24 shows that the relative volatilities data agree well with the PR-MC-WS-NRTL (OF: FC and OLS) model only towards the mixture critical point whereas the SRK-MC-PSRK-NRTL (OF: FC) model is completely off.

One should note that in the To assess the fit of the model to the experimental VLE data, the bias U and AAD U were calculated and reported in Table 5.25, where the highest values of AAD U and bias U relative to the PR-MC-WS-NRTL (OF: FC) model are 3.49 % and 4.10 %, respectively. A comparison between the AAD U and bias U values relative to the SRK-MC-PSRK-NRTL (OF: OLS) and PR-MC-WS-NRTL (OF: OLS) models reveals that the former model has the lowest values. These results indicate that the PR-MC-WS-NRTL (OF: OLS) is better than the SRK-MC-WS-NRTL (OF: OLS) model.

5.5.2.6 Nitrogen (1) + perfluorobutane (2) system

The experimental VLE data for the nitrogen (1) + perfluorobutane (2) system were undertaken at three temperatures from (293.37, 313.35 and 333.23) K and reported in Table 5.26.

The measured data were modelled using the Peng-Robinson or Soave-Redlich-Kwong EoS incorporating the Mathias-Copeman alpha function and the Wong-Sandler mixing or predictive Soave-Redlich-Kwong rule utilizing the NRTL activity coefficient model and adjusted using either the flash calculation or ordinary least squares objective function abbreviated as PR-MC-WS-NRTL (OF: FC or OLS) and SRK-MC-PSRK-NRTL (OF: OLS) models. The results from the modelling are graphically compared with the experimental VLE data in Figures 5.25-5.27. The model parameters in the temperature-independent and temperature-dependent forms are presented in Tables 5.27 and 5.28. The relative volatilities were also computed and graphically compared with the experimental values in Figure 5.28. The relative bias U and AAD U were calculated to quantify the fit of the models to the experimental VLE data. The results obtained are reported in Table 5.29.

Table 5.26: Experimental VLE data for the nitrogen (1) + perfluorobutane (2) system

T/K = 293.37						
P/MPa	n_x	x_1	δx_1	n_y	y_1	δy_1
1.348	6	0.047	0.0000	6	0.808	0.0006
1.917	5	0.069	0.0001	5	0.845	0.0013
2.915	5	0.107	0.0001	5	0.891	0.0005
4.841	5	0.178	0.0001	5	0.916	0.0002
7.065	5	0.259	0.0001	6	0.924	0.0002
9.001	6	0.326	0.0003	5	0.922	0.0008
10.626	5	0.378	0.0004	5	0.918	0.0002
13.544	5	0.476	0.0003	5	0.902	0.0004
15.188	5	0.536	0.0011	5	0.886	0.0013
17.014	5	0.612	0.0007	5	0.864	0.0010
T/K = 313.35						
P/MPa	n_x	x_1	δx_1	n_y	y_1	δy_1
1.268	6	0.036	0.0001	5	0.620	0.0007
1.851	6	0.060	0.0000	5	0.721	0.0006
2.606	5	0.089	0.0001	5	0.784	0.0002
3.452	5	0.125	0.0004	5	0.822	0.0003
4.463	5	0.164	0.0000	5	0.843	0.0012
6.253	6	0.232	0.0001	5	0.862	0.0002
7.892	5	0.292	0.0001	5	0.867	0.0001
10.201	5	0.377	0.0004	5	0.865	0.0021
12.226	6	0.456	0.0002	5	0.852	0.0001
13.950	5	0.533	0.0002	5	0.827	0.0009
15.008	6	0.606	0.0005	5	0.804	0.0012

Table 5.26: Continued

T/K = 333.23						
P/MPa	n_x	x_1	δx_1	n_y	y_1	δy_1
1.501	6	0.034	0.0000	5	0.452	0.0027
1.939	6	0.053	0.0001	5	0.548	0.0010
2.652	6	0.082	0.0001	5	0.637	0.0012
3.285	6	0.110	0.0002	5	0.685	0.0009
3.859	5	0.133	0.0001	5	0.715	0.0010
5.130	6	0.188	0.0001	5	0.751	0.0005
6.902	6	0.262	0.0001	5	0.772	0.0011
7.534	5	0.29	0.0002	5	0.776	0.0016
8.906	6	0.35	0.0004	5	0.770	0.0011
9.870	5	0.395	0.0007	5	0.764	0.0028
11.141	5	0.467	0.0009	5	0.737	0.0048

x_1, y_1: liquid and vapour mole fraction; n_x, n_y : number of samples taken; δx_1, δy_1: standard deviation for x_1 and y_1.

Expanded uncertainty: $u\ (T, k = 2)$ = 0.04 K; $u\ (P, k = 2)$ = 2.50 kPa; u (x_1, k = 2) = 0.01 and u (y_1, k = 2) = 0.01.

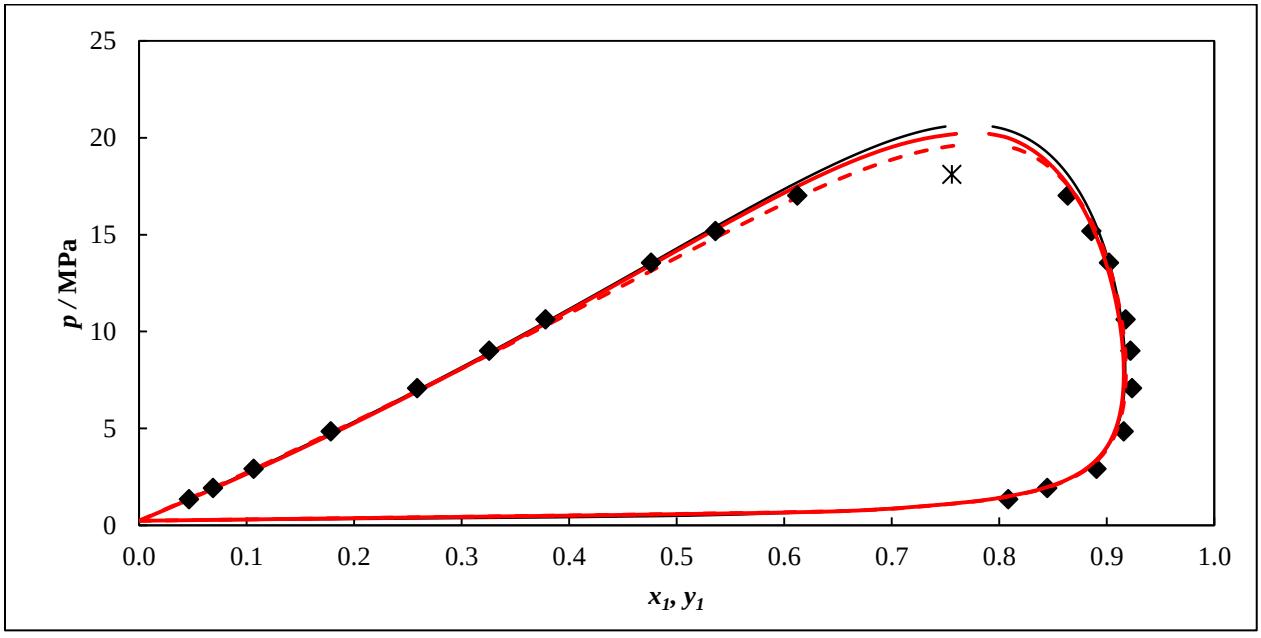

Figure 5.25: Phase diagrams (*P-x-y*) for the N_2 (1) + C_4F_{10} (2) system. Experimental data: ♦, 293.37 K; Models: PR-MC-WS-NRTL (OF: FC) (solid black line); SRK-MC-PSRK-NRTL (OF: OLS) (dashed red line) and PR-MC-WS-NRTL (OF: OLS) (solid red line); *, mixture critical point.

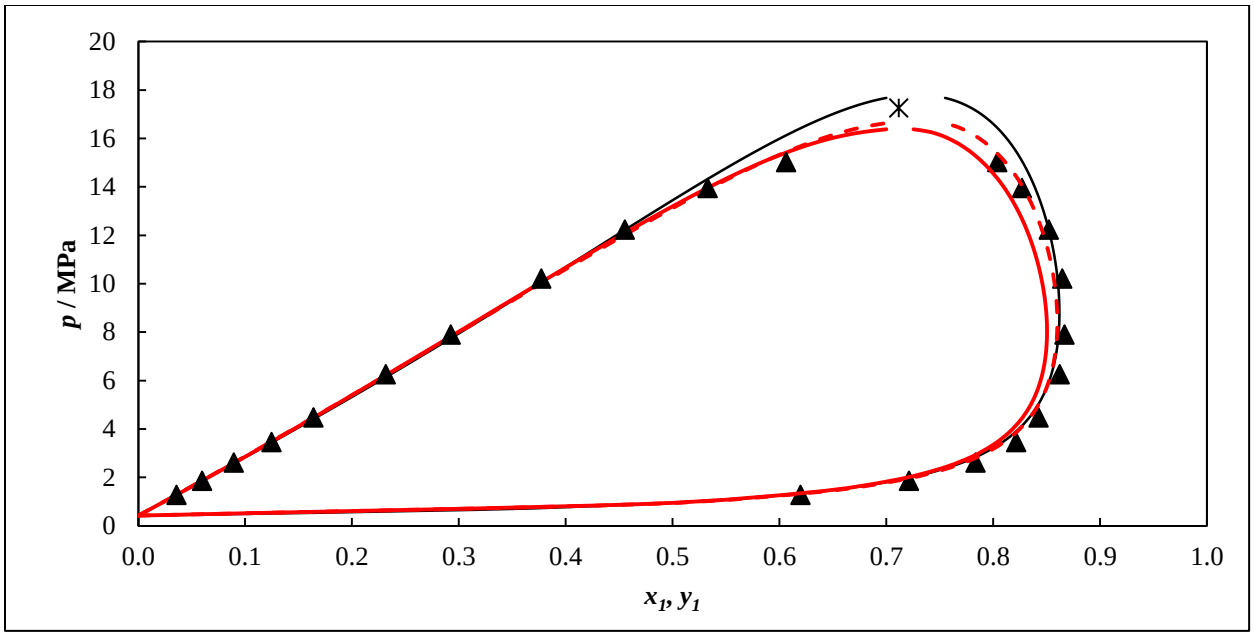

Figure 5.26: Phase diagrams (*P-x-y*) for the N_2 (1) + C_4F_{10} (2) system. Experimental data: ▲, 313.35 K; Models: PR-MC-WS-NRTL (OF: FC) (solid black line); SRK-MC-PSRK-NRTL (OF: OLS) (dashed red line) and PR-MC-WS-NRTL (OF: OLS) (solid red line); *, mixture critical point.

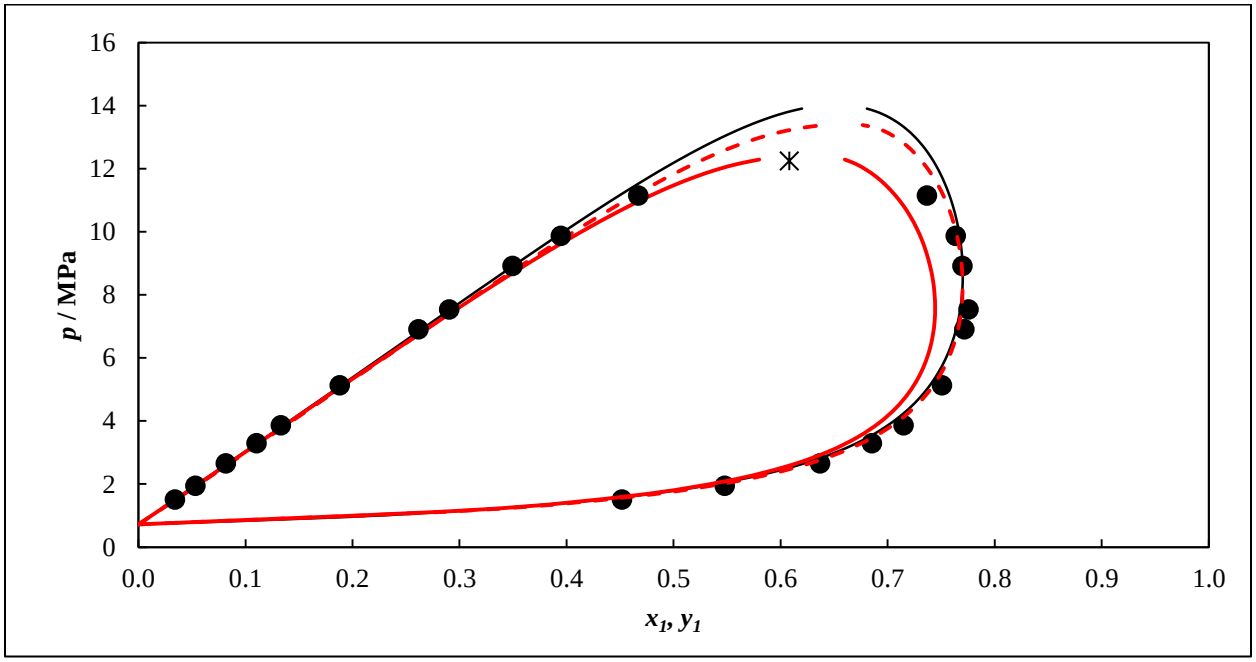

Figure 5.27: Phase diagrams (*P-x-y*) for the N_2 (1) + C_4F_{10} (2) system; Experimental data: ●, 333.23 K; Models: PR-MC-WS-NRTL (OF: FC) (solid black line); SRK-MC-PSRK-NRTL (OF: OLS) (dashed red line) and PR-MC-WS-NRTL (OF: OLS) (solid red line); *, mixture critical point.

Table 5.27: Model parameters for the PR-MC-WS-NRTL and SRK-MC-PSRK-NRTL models in a temperature-independent form for the N_2 (1) + C_4F_{10} (2) system

Model	Isotherm / K	$(g_{12} - g_{22})^a$/J.mol^{-1}	$(g_{21} - g_{11})^a$/J.mol^{-1}	$k_{ij}{}^b$
	objective function: flash calculation			
PR-MC-WS-NRTL	293.37	-2248.4	2928.4	0.74
	313.35	-2745.0	3777.0	0.76
	333.23	-2294.7	3142.8	0.79
Model	Isotherm / K	$\tau_{12}{}^c$	$\tau_{21}{}^c$	$k_{ij}{}^d$
	objective function: ordinary least squares			
PR-MC-WS-NRTL	293.37	15.671	0.2643	0.72
	313.35	1.2098	0.6335	0.73
	333.23	15.671	0.3328	0.75
SRK-MC-PSRK-NRTL	293.37	-1.6620	-0.7520	—
	313.35	-1.7412	-0.7681	—
	333.23	-2.0102	-0.7019	—

[a] NRTL model parameters obtained from THERMOPACK, $\Delta g_{ij} = a_{ij}$.

[b, d] WS mixing rule parameter incorporated into the PR EoS correlated from THERMOPACK and Aspen Plus, respectively.

[c] NRTL model parameters obtained from Aspen Plus, $\tau_{ij} = a_{ij}$.

Table 5.28: Model parameters for the PR-MC-WS-NRTL and SRK-MC-PSRK-NRTL models in a temperature-dependent form for the N_2 (1) + C_4F_{10} (2) system

Model	$(g_{12} - g_{22})^a$/J.mol-1.K		$(g_{21} - g_{11})^a$/J.mol-1.K		$k_{ij}{}^b$
	a_{12}	b_{12}	a_{21}	b_{21}	
	objective function: flash calculation				
PR-MC-WS-NRTL	-251.57	4.3119	-1833.8	2.4933	0.76
Model	$\tau_{12}{}^c$ / K		$\tau_{21}{}^c$ / K		$k_{ij}{}^d$
	objective function: ordinary least squares				
PR-MC-WS-NRTL	-327.91		-228.42		0.73
SRK-MC-PSRK-NRTL	837.93		-74.718		—

[a] NRTL model parameters correlated from THERMOPACK, $\Delta g_{ij} = a_{ij} + b_{ij}$.T

[b, d] WS mixing rule parameter incorporated into the PR EoS correlated from THERMOPACK and Aspen Plus, respectively.

[c] NRTL model parameters correlated from Aspen Plus, $\tau_{ij} = b_{ij}$/T

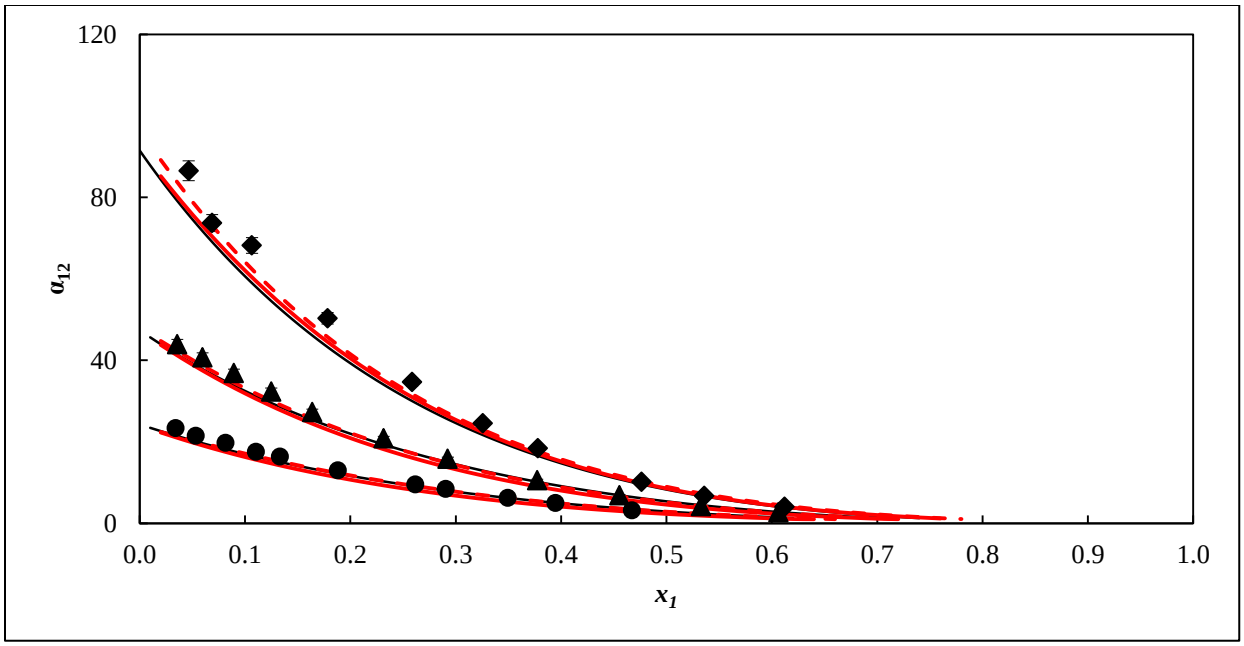

Figure 5.28: Plot of relative volatilities (α_{12}) for the N_2 (1) + C_4F_{10} (2) system; Experimental data: ♦, 293.37 K; ▲, 313.35 K; ●, 333.23 K; Models: PR-MC-WS-NRTL (OF: FC) (solid black line); SRK-MC-PSRK-NRTL (OF: OLS) (dashed red line) and PR-MC-WS-NRTL (OF: OLS) (solid red line). Error bands: shown at 2.8 % for the experimental data.

Table 5.29: Deviation bias U and AAD U obtained in fitting experimental VLE data with the SRK-MC-PSRK-NRTL and PR-MC-WS-NRTL models for the N_2 (1) + C_4F_{10} (2) system

Model	Isotherm / K	bias x %	AAD x %	bias y %	AAD y %
objective function: flash calculation					
PR-MC-WS-NRTL	293.37	-0.03	0.40	0.47	0.73
	313.35	0.32	0.62	0.73	1.10
	333.23	0.10	1.40	0.28	1.26
Model	**Isotherm / K**	**bias P %**	**AAD P %**	**bias y %**	**AAD y %**
objective function: ordinary least squares					
PR-MC-WS-NRTL	293.37	-0.10	7.15	1.03	0.91
	313.35	-0.10	7.96	2.24	1.79
	333.23	-0.08	3.41	2.62	1.74
SRK-MC-PSRK-NRTL	293.37	-0.09	8.78	0.10	0.60
	313.35	-0.10	10.09	0.91	0.75
	333.23	0.03	4.01	1.01	0.92

Figures 5.25-5.27 show an overall satisfactory agreement between the PR-MC-WS-NRTL (OF: FC or OLS) and SRK-MC-PSRK-NRTL (OF: OLS) models, and the experimental data for each isotherm measured. However, large deviations are observed in the vapour phase, increasing towards the mixture critical point for the PR-MC-WS-NRTL (OF: OLS) model at 333.23 K. The relative deviations bias U and AAD U reported in Table 5.24 show that the PR-MC-WS-NRTL (OF: FC) and SRK-MC-PSRK-NRTL (OF: OLS) models fit fairly well the experimental data. The slight deviations between the experimental data and the modelled data in the vicinity of the mixture critical points for each isotherm are not revealed through the AAD U and bias U values relative to the PR-MC-WS-NRTL (OF: FC) and SRK-MC-PSRK (OF: OLS) models because almost no data point was measured in the mixture critical point regions. One should note that accurate VLE data measurement in the vicinity of the mixture critical point is difficult if not impossible using an opaque liquid bath. As can be seen from Table 5.24, a comparison between the PR-MC-WS-NRTL (OF: OLS) and SRK-MC-WS-NRTL (OF: OLS) models based on the bias U and AAD U values shows that the SRK-MC-WS-NRTL (OF: OLS) model provides a slightly better fit.

Figure 5.28 which compares graphically the experimental and calculated values of the relative volatilities reveals an overall satisfactory agreement between three models except for the PR-MC-WS-NRTL (OF: OLS) model at 333.23 K. One should note that decreasing temperature from 333.23 to 293.37 does not favour the solubility of nitrogen in perfluorobutane, which can be clearly observed through Figures 5.25-5.27.

5.5.2.7 Oxygen (1) + perfluorobutane (2) system

The experimental VLE data for oxygen (1) + perfluorobutane (2) system were undertaken at three temperatures from (293.41, 313.42 and 333.46) K and reported in Table 5.30.

The measured data were modelled using two combination of models, the Peng-Robinson EoS incorporating the Mathias-Copeman alpha function and the Wong-Sandler mixing rule utilizing the NRTL activity coefficient model and adjusted using either the flash calculation or ordinary least squares objective functions abbreviated as PR-MC-WS-NRTL (OF: FC or OLS) model and the Soave-Redlich-Kwong incorporating the Mathias-Copeman alpha function and the predictive Soave-Redlich-Kwong mixing rule utilizing the NRTL activity coefficient model and adjusted

using the ordinary least squares objective function abbreviated as SRK-MC-PSRK-NRTL (OF: OLS) model. The results from the modelling are graphically compared with the experimental VLE data in Figures 5.29-5.31. The model parameters in the temperature-independent and temperature-dependent forms are presented in Tables 5.31 and 5.32, respectively. The relative volatilities were also computed and compared with the experimental values in Figure 5.32.

Table 5.30: Experimental VLE data for the oxygen (1) + perfluorobutane (2) system

T/K = 293.41						
P/MPa	n_x	x_1	δx_1	n_y	y_1	δy_1
2.021	7	0.089	0.0004	5	0.842	0.0014
3.737	7	0.173	0.0003	5	0.890	0.0013
5.278	5	0.239	0.0002	6	0.912	0.0018
6.534	5	0.292	0.0025	5	0.917	0.0014
7.941	5	0.347	0.0021	5	0.918	0.0005
9.299	6	0.396	0.0029	5	0.916	0.0003
11.273	12	0.469	0.0029	5	0.909	0.0001
12.967	5	0.530	0.0028	5	0.898	0.0003
14.924	5	0.609	0.0027	6	0.875	0.0017
15.788	5	0.655	0.0008	7	0.849	0.0023
16.376	5	0.722	0.0035	5	0.819	0.0021
T/K = 313.42						
P/MPa	n_x	x_1	δx_1	n_y	y_1	δy_1
2.016	5	0.079	0.0002	5	0.723	0.0014
3.047	5	0.129	0.0004	5	0.790	0.0023
4.047	5	0.175	0.0000	6	0.831	0.0051
5.220	5	0.226	0.0004	5	0.849	0.0035
6.466	5	0.277	0.0003	5	0.858	0.0036
8.648	5	0.364	0.0007	5	0.863	0.0048
9.932	5	0.415	0.0012	5	0.860	0.0041
11.222	5	0.467	0.0010	5	0.851	0.0030
12.082	6	0.507	0.0039	5	0.839	0.0012
12.682	5	0.530	0.0012	5	0.828	0.0033
13.709	6	0.585	0.0001	5	0.803	0.0010

Table 5.30: Continued

T/K = 333.46						
P/MPa	n_x	x_1	δx_1	n_y	y_1	δy_1
2.333	5	0.081	0.0003	5	0.579	0.0007
3.695	6	0.148	0.0003	6	0.693	0.0043
4.299	5	0.176	0.0001	5	0.723	0.0005
5.889	5	0.246	0.0002	6	0.756	0.0030
6.238	5	0.262	0.0004	5	0.758	0.0014
6.755	5	0.284	0.0001	6	0.765	0.0037
7.561	5	0.319	0.0004	6	0.771	0.0010
7.736	5	0.328	0.0003	5	0.769	0.0016
8.902	5	0.378	0.0000	5	0.771	0.0039
9.554	5	0.409	0.0004	5	0.768	0.0013
10.203	5	0.442	0.0005	5	0.752	0.0024
10.879	6	0.487	0.0029	5	0.732	0.0085

x_1, y_1: liquid and vapour mole fraction; n_x, n_y : number of samples taken; δx_1, δy_1: standard deviation for x_1 and y_1.

Expanded uncertainty: $u\ (T, k = 2)$ = 0.04 K; $u\ (P, k = 2)$ = 3.50 kPa; u (x_1, k = 2) = 0.02 and u (y_1, k = 2) = 0.03.

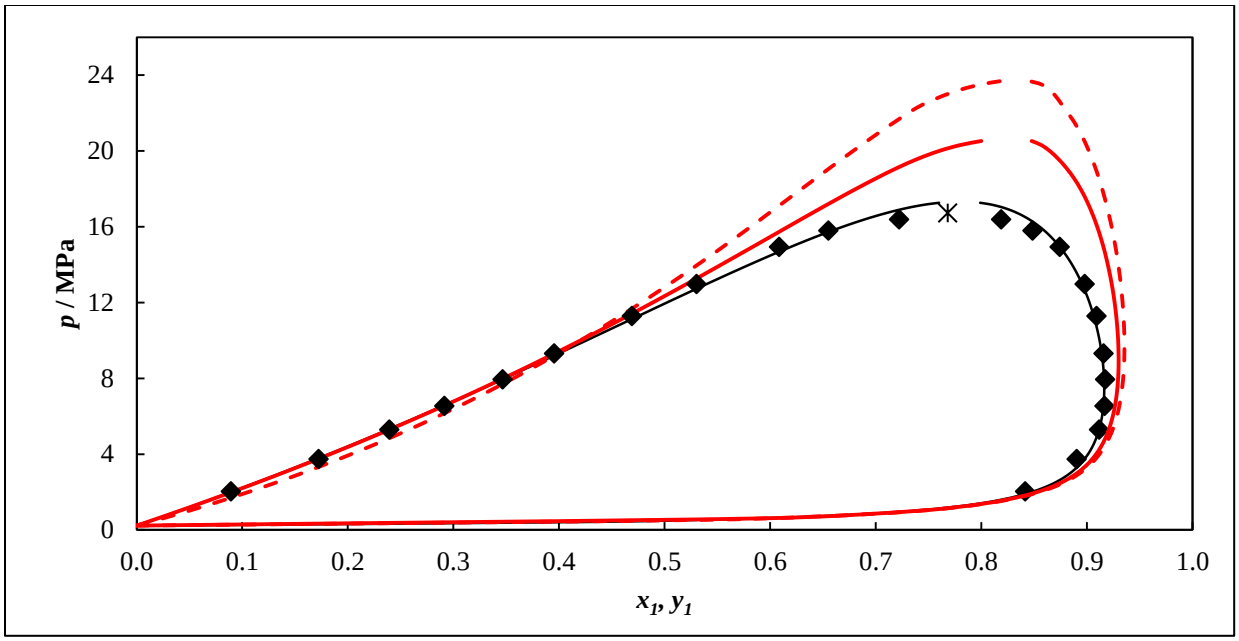

Figure 5.29: Phase diagrams (*P-x-y*) for the O_2 (1) + C_4F_{10} (2) system; Experimental data: ♦, 293.41 K; Models: PR-MC-WS-NRTL (OF: FC) (solid black line); SRK-MC-PSRK-NRTL (OF: OLS) (dashed red line) and PR-MC-WS-NRTL (OF: OLS) (solid red line); *, mixture critical point.

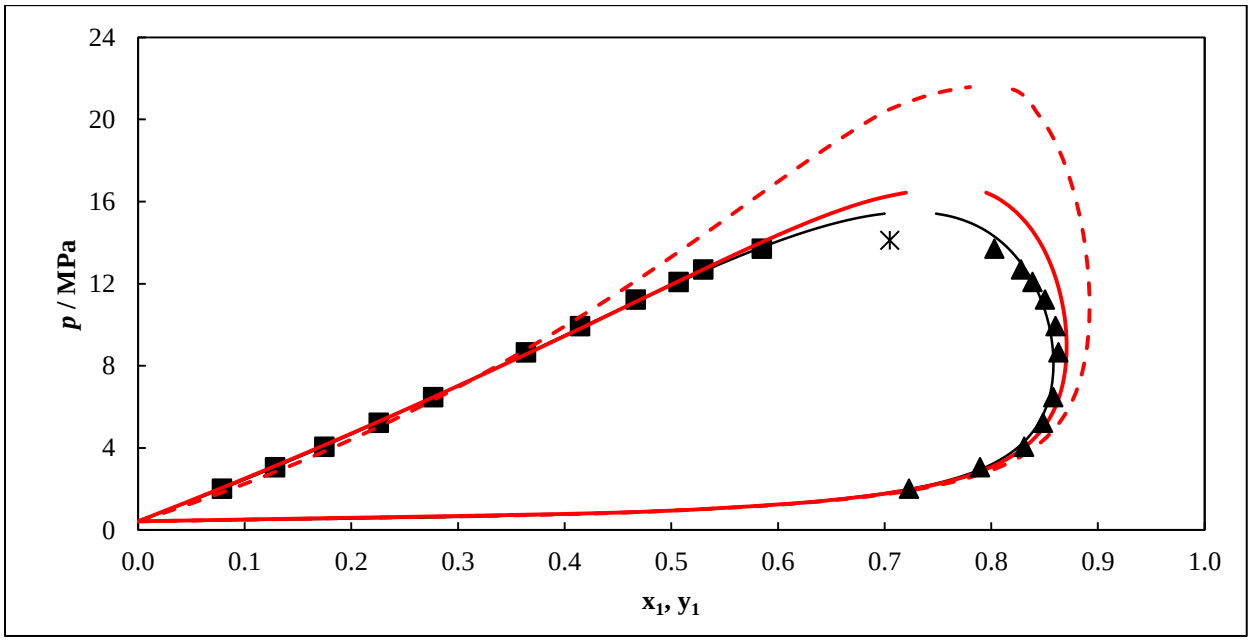

Figure 5.30: Phase diagrams (*P-x-y*) for the O_2 (1) + C_4F_{10} (2) system; Experimental data: ▲, 313.42 K; Models: PR-MC-WS-NRTL (OF: FC) (solid black line); SRK-MC-PSRK-NRTL (OF: OLS) (dashed red line) and PR-MC-WS-NRTL (OF: OLS) (solid red line); *, mixture critical point.

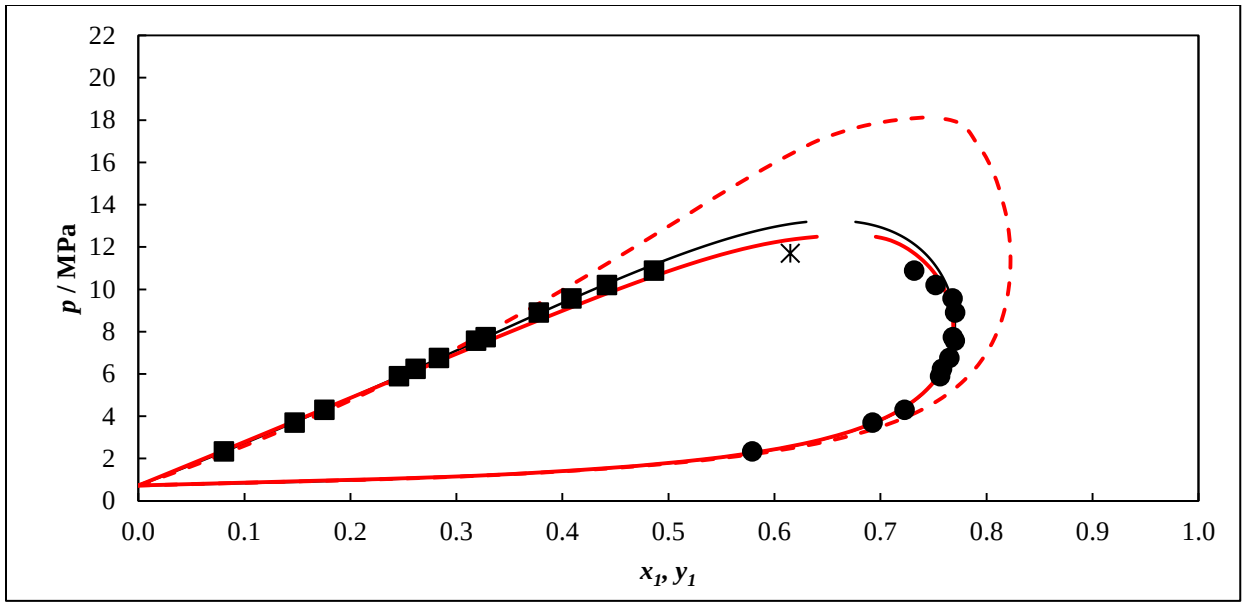

Figure 5.31: Phase diagrams (P-x-y) for the O_2 (1) + C_4F_{10} (2) system; Experimental data: ●, 333.46 K; Models: PR-MC-WS-NRTL (OF: FC) (solid black line); SRK-MC-PSRK-NRTL (OF: OLS) (dashed red line) and PR-MC-WS-NRTL (OF: OLS) (solid red line); *, mixture critical point.

Table 5.31: Model parameters for the SRK-MC-PSRK-NRTL and PR-MC-WS-NRTL models in a temperature-independent form for the O_2 (1) + C_4F_{10} (2) system

Model	Isotherm /K	$(g_{12} - g_{22})^a$/J.mol^{-1}	$(g_{21} - g_{11})^a$/J.mol^{-1}	$k_{ij}{}^b$
objective function: flash calculation				
PR-MC-WS-NRTL	293.41	4487.4	-2396.0	0.72
	313.42	5160.0	-2580.0	0.73
	333.46	6288.1	-2822.3	0.75
Model	**Isotherm /K**	**$\tau_{12}{}^c$**	**$\tau_{21}{}^c$**	**$k_{ij}{}^d$**
objective function: ordinary least squares				
PR-MC-WS-NRTL	293.41	-8.0111	1.6374	0.74
	313.42	-8.0111	1.5369	0.76
	333.46	-8.0111	1.4918	0.79
SRK-MC-PSRK-NRTL	293.41	-8.0111	-2.1038	—
	313.42	-8.0111	-1.9639	—
	333.46	-8.0111	-1.8255	—

[a] NRTL model parameters obtained from THERMOPACK, $\Delta g_{ij} = a_{ij}$.

[b, d] WS mixing rule parameter incorporated into the PR EoS correlated from THERMOPACK and Aspen Plus, respectively.

[c] NRTL model parameters obtained from Aspen Plus, $\tau_{ij} = a_{ij}$.

Table 5.32: Model parameters correlated for the SRK-MC-PSRK-NRTL and PR-MC-WS-NRTL models in a temperature-dependent form for the O_2 (1) + C_4F_{10} (2) system

Model	$(g_{12} - g_{22})^a$/J.mol-1.K		$(g_{21} - g_{11})^a$/J.mol-1.K		$k_{ij}{}^b$
	a_{12}	b_{12}	a_{21}	b_{21}	
objective function: flash calculation					
PR-MC-WS-NRTL	74469	-109.65	27644	155030	0.734
Model	**$\tau_{12}{}^c$ / K**		**$\tau_{21}{}^c$ / K**		**$k_{ij}{}^d$**
objective function: ordinary least squares					
PR-MC-WS-NRTL	52116		-590.64		0.77
SRK-MC-PSRK-NRTL	52116		-538.23		—

[a] NRTL model parameters obtained from THERMOPACK, $\Delta g_{ij} = a_{ij} + b_{ij}$.T

[b, d] WS mixing rule parameter incorporated into the PR EoS correlated from THERMOPACK and Aspen Plus, respectively. [c] NRTL model parameters obtained from Aspen Plus, $\tau_{ij} = b_{ij}$/T

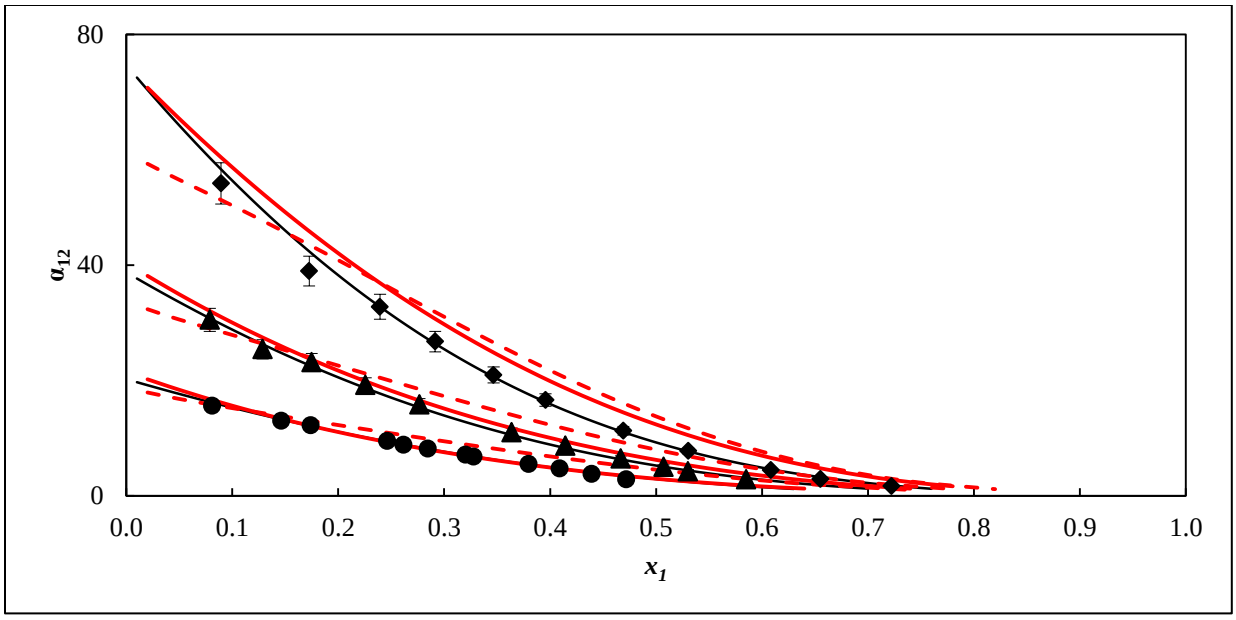

Figure 5.32: Plot of relative volatilities (α_{12}) for the O_2 (1) + C_4F_{10} (2) system; Experimental data: ♦, 293.41 K; ▲, 313.42 K; ●, 333.46 K; Models: PR-MC-WS-NRTL (OF: FC) (solid black line); SRK-MC-PSRK-NRTL (OF: OLS) (dashed red line) and PR-MC-WS-NRTL (OF: OLS) (solid red line). Error bands: shown at 7.0 % for the experimental data.

Table 5.33: Deviation bias U and AAD U obtained in fitting experimental VLE data with the SRK-MC-PSRK-NRTL and PR-MC-WS-NRTL models for the O_2 (1) + C_4F_{10} (2) system

Model	Isotherm / K	bias x %	AAD x %	bias y %	AAD y %
objective function: flash calculation					
PR-MC-WS-NRTL	293.41	0.04	0.66	-0.47	0.56
	313.42	0.05	0.21	0.04	0.48
	333.46	0.34	0.21	-0.42	0.47
Model	**Isotherm / K**	**bias P %**	**AAD P %**	**bias y %**	**AAD y %**
objective function: ordinary least squares					
PR-MC-WS-NRTL	293.41	0.16	10.95	-0.23	2.01
	313.42	0.12	9.20	-1.72	1.42
	333.46	0.06	7.36	-2.28	1.68
SRK-MC-PSRK-NRTL	293.41	-1.73	89.27	1.47	4.20
	313.42	-0.81	61.10	-0.23	4.22
	333.46	0.51	28.08	-3.79	4.47

Figures 5.29-5.31 show an overall satisfactory agreement between the PR-MC-WS-NRTL (OF: FC) model and the experimental data. However, the model fails to represent the VLE data measured in the mixture critical point regions. The deviation AAD U and bias U values reported in Table 5.33, where the highest value is less than 1.00%, indicate that the PR-MC-WS-NRTL (OF: FC) fits fairly well the experimental data. One should note that the failure of the model in the critical point regions is not revealed in the AAD U or bias U values as only one or two points were measured in these regions. The PR-MC-WS-NRTL (OF: OLS) and the SRK-MC-PSRK-NRTL (OF: OLS) models fail to represent the experimental data well, except for the isotherm measured at 333.46 K where the PR-MC-WS-NRTL (OF: OLS) model exhibits a similar fit as the PR-MC-WS-NRTL (OF: FC) model. Table 5.33 shows that PR-MC-WS-NRTL (OF: OLS) model provides a better fit than the SRK-MC-PSRK-NRTL (OF: OLS) model based on the bias U and AAD U values.

The experimental and computed relative volatility values are mostly in agreement with the representation provided by the PR-MC-WS-NRTL (OF: FC) model as can be graphically seen in Figure 5.32. Figures 5.29-5.31 reveal that varying temperature from 293.41 to 333.46 K does not have much effect on the solubility of oxygen in perfluorobutane.

5.5.2.8 Hydrogen (1) + perfluorobutane (2) system

The experimental VLE data for the hydrogen (1) + perfluorobutane (2) system were undertaken at three temperatures from (293.35, 313.34 and 333.38) K and are reported in Table 5.34.

The measured data were modelled using the Soave-Redlich-Kwong EoS incorporating the Mathias-Copeman alpha function and the Huron-Vidal or the predictive Soave-Redlich-Kwong mixing rule utilizing the NRTL activity coefficient model and adjusted using either the flash calculation or the ordinary least squares objective functions abbreviated as SRK-MC-HV-NRTL (OF: FC) and SRK-MC-PSRK-NRTL (OF: OLS) models. The measured data were also modelled using Peng-Robinson EoS incorporating the Mathias-Copeman alpha function and the Wong-Sandler mixing rule utilizing the NRTL activity coefficient model and adjusted using the ordinary least squares objective function abbreviated as PR-MC-WS-NRTL (OF: OLS). The results from the modelling are graphically compared with the experimental VLE data in Figures 5.33-5.35. The model parameters in the temperature-independent and temperature-dependent

forms are presented in Tables 5.35 and 5.36, respectively. The relative volatilities were also computed and compared with the experimental values in Figure 5.36.

Table 5.34: Experimental VLE data for the hydrogen (1) + perfluorobutane (2) system

T/K = 293.35						
P/MPa	n_x	x_1	δx_1	n_y	y_1	δy_1
2.600	6	0.032	0.0069	7	0.888	0.0056
4.386	6	0.057	0.0010	7	0.933	0.0011
6.177	5	0.080	0.0018	6	0.947	0.0029
8.083	5	0.106	0.0008	5	0.957	0.0012
9.589	5	0.121	0.0004	6	0.959	0.0014
11.057	5	0.139	0.0009	7	0.961	0.0037
12.673	6	0.155	0.0021	5	0.962	0.0009
14.363	5	0.175	0.0015	6	0.964	0.0016
15.517	6	0.188	0.0028	5	0.964	0.0016
16.918	8	0.205	0.0076	6	0.966	0.0025
T/K = 313.34						
P/MPa	n_x	x_1	δx_1	n_y	y_1	δy_1
4.022	6	0.059	0.0071	7	0.850	0.0046
6.008	8	0.087	0.0029	6	0.893	0.0027
7.615	8	0.109	0.0044	6	0.907	0.0037
8.419	5	0.121	0.0025	7	0.914	0.0020
9.403	5	0.136	0.0032	8	0.920	0.0043
10.577	6	0.152	0.0021	5	0.923	0.0036
11.551	9	0.165	0.0032	6	0.926	0.0019
13.507	6	0.192	0.0056	6	0.929	0.0021
15.693	5	0.219	0.0024	7	0.934	0.0076
17.898	5	0.248	0.0091	5	0.942	0.0006

Table 5.34: Continued

T/K = 333.38						
P/MPa	n_x	x_1	δx_1	n_y	y_1	δy_1
3.923	5	0.066	0.0005	5	0.749	0.0007
5.075	8	0.087	0.0031	6	0.795	0.0045
6.731	5	0.113	0.0036	5	0.842	0.0010
8.428	5	0.141	0.0015	5	0.860	0.0013
10.367	5	0.177	0.0017	5	0.872	0.0047
12.009	5	0.204	0.0029	8	0.88	0.0058
13.805	6	0.231	0.0023	5	0.886	0.0056
14.809	5	0.242	0.0046	7	0.889	0.0026
15.804	5	0.258	0.0052	5	0.893	0.0065
17.777	7	0.283	0.0111	5	0.898	0.0037

x_1, y_1: liquid and vapour mole fraction; n_x, n_y : number of samples taken; δx_1, δy_1: standard deviation for x_1 and y_1.

Expanded uncertainty: $u\ (T, k = 2)$ = 0.04 K; $u\ (P, k = 2)$ = 15.50 kPa; u (x_1, k = 2) = 0.05 and u (y_1, k = 2) = 0.12.

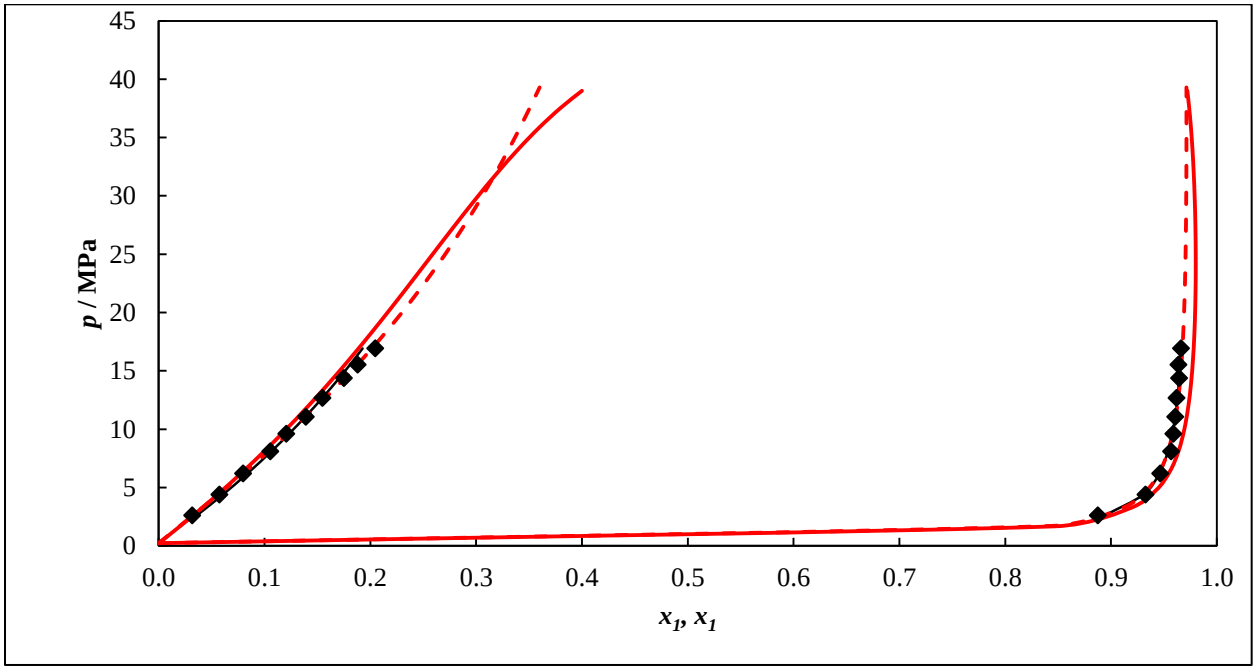

Figure 5.33: Phase diagrams (*P-x-y*) for the H_2 (1) + C_4F_{10} (2) system; Experimental data: ♦, 293.35 K; Models: SRK-MC-HV-NRTL (OF: FC) (solid black line); SRK-MC-PSRK-NRTL (OF: OLS) (dashed red line) and PR-MC-WS-NRTL (OF: OLS) (solid red line).

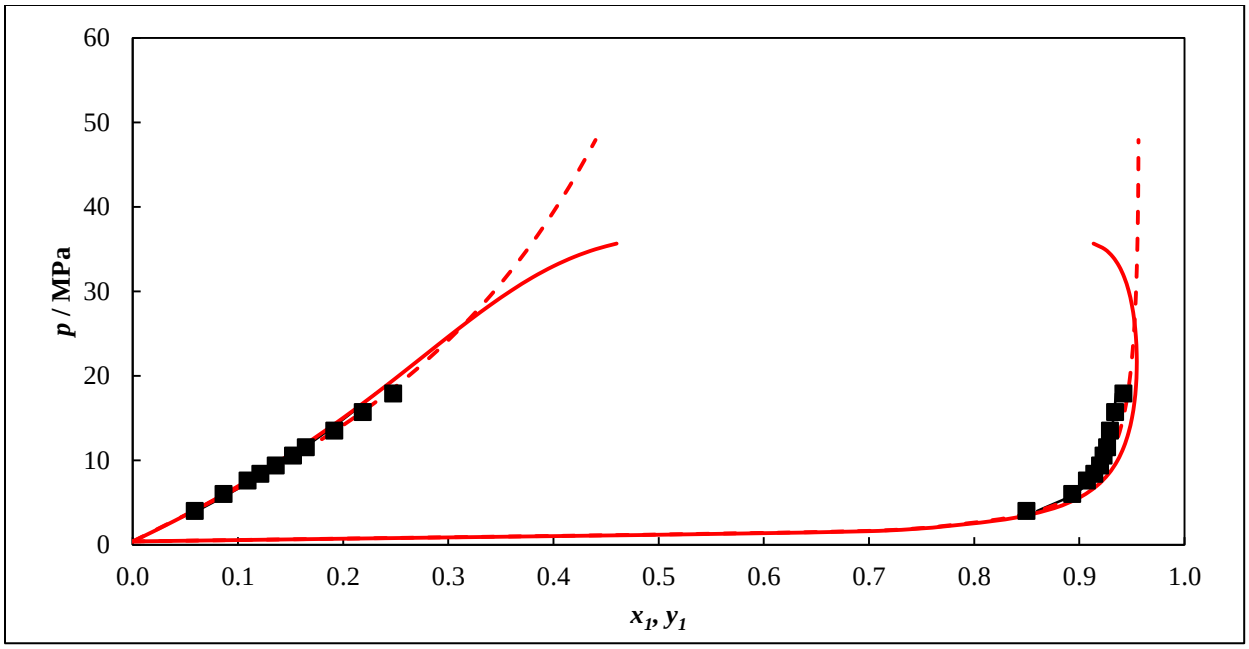

Figure 5.34: Phase diagrams (P-x-y) for the H_2 (1) + C_4F_{10} (2) system; Experimental data: ■, 313.34 K; Models: SRK-MC-HV-NRTL (OF: FC) (solid black line); SRK-MC-PSRK-NRTL (OF: OLS) (dashed red line) and PR-MC-WS-NRTL (OF: OLS) (solid red line).

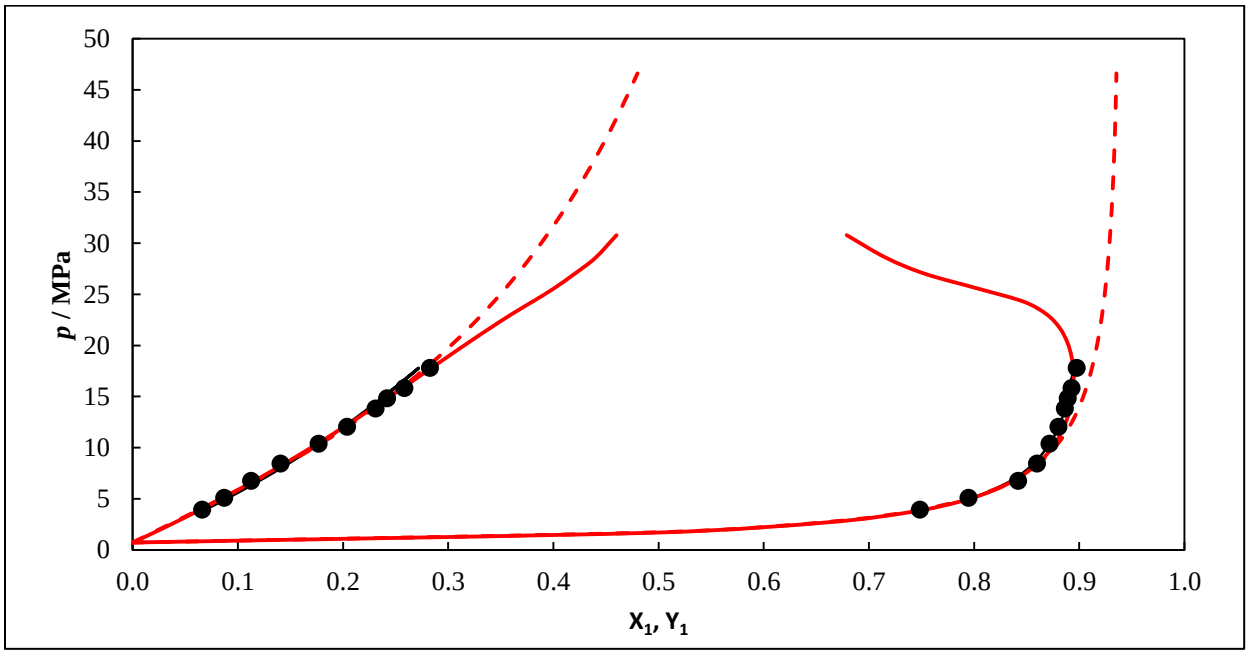

Figure 5.35: Phase diagrams (P-x-y) for the H_2 (1) + C_4F_{10} (2) system; Experimental data: ●, 333.38 K; Models: SRK-MC-HV-NRTL (OF: FC) (solid black line); SRK-MC-PSRK-NRTL (OF: OLS) (dashed red line) and PR-MC-WS-NRTL (OF: OLS) (solid red line).

Table 5.35: Model parameters for the SRK-MC-HV-NRTL, SRK-MC-PSRK-NRTL and PR-MC-WS-NRTL models in a temperature-independent form for the H_2 (1) + C_4F_{10} (2) system

Model	Isotherm /K	$(g_{12} - g_{22})^a$/J.mol^{-1}	$(g_{21} - g_{11})^a$/J.mol^{-1}	$k_{ij}{}^b$
	objective function: flash calculation			
	293.35	8585.0	-892.98	—
SRK-MC-HV-NRTL	313.34	7033.5	-850.63	—
	333.38	7318.1	-1062.1	—
Model	Isotherm /K	$\tau_{12}{}^c$	$\tau_{21}{}^c$	$k_{ij}{}^d$
	objective function: ordinary least squares			
	293.35	-4.6172	-0.1337	0.99
PR-MC-WS-NRTL	313.34	-1.4691	0.0097	0.99
	333.38	-4.5042	-0.5326	0.99
	293.35	-2.2312	3.7348	—
SRK-MC-PSRK-NRTL	313.34	-2.2451	3.8269	—
	333.38	-2.2493	3.8360	—

[a] NRTL model parameters obtained from THERMOPACK, $\Delta g_{ij} = a_{ij}$.

[b, d] WS mixing rule parameter incorporated into the PR EoS correlated from THERMOPACK and Aspen Plus, respectively.

[c] NRTL model parameters obtained from Aspen Plus, $\tau_{ij} = a_{ij}$.

Table 5.36: Model parameters correlated for the SRK-MC-HV-NRTL, SRK-MC-PSRK-NRTL and PR-MC-WS-NRTL models in a temperature-dependent form for the H_2 (1) + C_4F_{10} (2) system

Model	$(g_{12} - g_{22})^a$/J.mol^{-1}.K	$(g_{21} - g_{11})^a$/J.mol^{-1}.K	$k_{ij}{}^b$
	objective function: flash calculation		
SRK-MC-HV-NRTL	-30.21	-3.720	—
Model	$\tau_{12}{}^c$ / K	$\tau_{21}{}^c$ / K	$k_{ij}{}^d$
	objective function: ordinary least squares		
PR-MC-WS-NRTL	3232.9	337.90	0.99
SRK-MC-PSRK-NRTL	173.90	-394.50	—

[a] NRTL model parameters obtained from THERMOPACK, $\Delta g_{ij} = a_{ij} + b_{ij}$.T

[b, d] WS mixing rule parameter incorporated into the PR EoS correlated from THERMOPACK and Aspen Plus, respectively.

[c] NRTL model parameters obtained from Aspen Plus, $\tau_{ij} = b_{ij}$/T

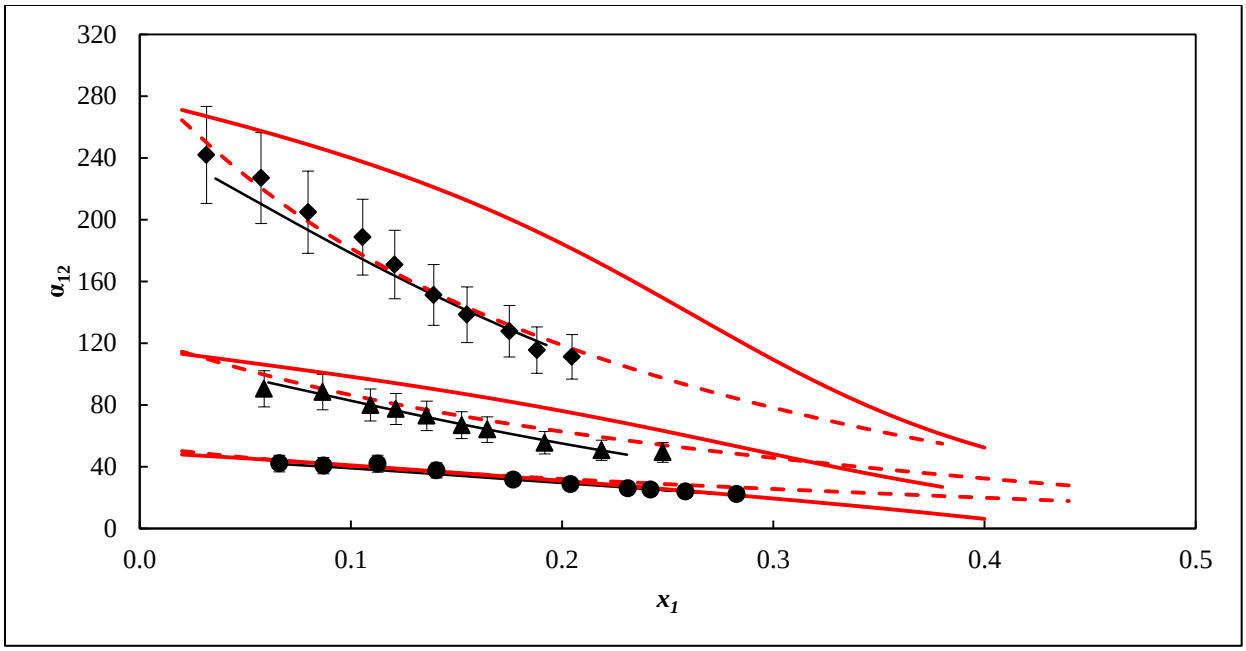

Figure 5.36: Plot of relative volatilities (α_{12}) for the H_2 (1) + C_4F_{10} (2) system. Experimental data: ♦, 293.35 K; ■, 313.34 K; ●, 333.38 K. Models: SRK-MC-HV-NRTL (OF: FC) (solid black line); SRK-MC-PSRK-NRTL (OF: OLS) (dashed red line) and PR-MC-WS-NRTL (OF: OLS) (solid red line). Error bands: shown at 13.0 % for the experimental data.

Table 5.37: Relative deviation bias U and AAD U obtained in fitting experimental VLE data with the SRK-MC-HV-NRTL, SRK-MC-PSRK-NRTL and PR-MC-WS-NRTL models for the H_2 (1) + C_4F_{10} (2) system

Model	Isotherm / K	bias x %	AAD x %	bias y %	AAD y %
	objective function: flash calculation				
	293.35	-1.26	0.39	0.00	0.16
SRK-MC-HV-NRTL	313.34	0.18	0.50	-0.08	0.24
	333.38	-0.30	0.55	0.08	0.23
Model	**Isotherm / K**	**bias P %**	**AAD P %**	**bias y %**	**AAD y %**
	objective function: ordinary least squares				
	293.35	0.00	9.05	0.03	0.11
PR-MC-WS-NRTL	313.34	-0.02	5.94	-0.13	0.22
	333.38	-0.03	13.09	-0.05	0.42
	293.35	-0.01	11.14	-0.02	0.17
SRK-MC-PSRK-NRTL	313.34	-0.02	14.86	-0.67	0.61
	333.38	-0.06	16.25	-0.68	0.91

Unlike previous systems, the experimental VLE data for the hydrogen (1) + perfluorobutane (2) system could not be represented using the SRK-MC-HV-NRTL (OF: FC) model to cover the entire phase envelop in the THERMOPACK software. Consequently, correlation was therefore undertaken only for VLE data points measured. However in Aspen Plus, the SRK-MC-PSRK-NRTL (OF: OLS) and PR-MC-WS-NRTL (OF: OLS) models were used and the modelled data covered significantly the phase envelop. One should also note that the experimental VLE data could not be undertaken at pressures above 20 MPa as this value corresponded to the highest pressure in the hydrogen bottle used.

Figures 5.33-5.35 reveal an overall satisfactory agreement between the experimental data and, the SRK-MC-HV-NRTL (OF: FC) and SRK-MC-PSRK-NRTL (OF: OLS) models except for the PR-MC-WS-NRTL (OF: OLS) model where slight deviations are observed in the vapour phase for the 293 K and 313 K isotherms. The deviation AAD U and bias U values reported in Table 5.37 indicate that the absolute highest value relative to the SRK-MC-HV-NRTL (OF: FC) model are 1.26 % implying that the model fits fairly well with the experimental data. However, the bias U and AAD U relative to the SRK-MC-PSRK-NRTL (OF: OLS) and PR-MC-WS-NRTL (OF: OLS) models show that the PR-MC-WS-NRTL (OF: OLS) provides a better fit as it has lower values. One should notice that higher values for the SRK-MC-PSRK-NRTL (OF: OLS) are observed mainly for the AAD P.

Similar agreement can also be observed in Figure 5.36, where the experimental and computed relative volatilities are graphically compared. The solubility of hydrogen in perfluorobutane is nearly independent of temperature for the three isotherms measured. This can be seen through Figures 5.33-5.35.

5.5.2.9 Hydrogen sulfide (1) + perfluorohexane (2) system

The experimental VLE data for the hydrogen sulfide (1) + perfluorohexane (2) system were undertaken at three temperatures from (293.03, 313.08 and 332.96) K and are reported in Table 5.38.

The experimental VLE data were modelled using the Soave-Redlich-Kwong EoS incorporating the Mathias-Copeman alpha function and predictive Soave-Redlich-Kwong, modified Huron Vidal 1 or 2 mixing rules utilizing the NRTL activity coefficient model and adjusted using either

the flash calculation or the ordinary least squares objective functions abbreviated as SRK-MC-PSRK-NRTL (OF: OLS), SRK-MC-MHV1-NRTL (OF: FC) and SRK-MC-MHV2-NRTL (OF: FC) models. The measured data were also modelled using the Peng-Robinson EoS incorporating the Mathias-Copeman alpha function and the Wong-Sandler mixing rule utilizing the NRTL activity coefficient model and adjusted using the ordinary least squares objective function abbreviated as PR-MC-WS-NRTL (OF: OLS). The results obtained from the modelling are graphically compared with the experimental VLE data in Figures 5.37-5.39. The model parameters in the temperature-independent and temperature-dependent forms are presented in Tables 5.39 and 5.40, respectively. The relative volatilities were also computed and graphically compared with the experimental values in Figure 5.40. The relative bias U and AAD U were calculated to quantify the fit of the models to the experimental VLE data. The results obtained are reported in Table 5.41.

Table 5.38: Experimental VLE data for the hydrogen sulfide (1) + perfluorohexane (2) system

T/K = 293.03									
P/MPa	n_x^I	x_1^I	δx_1^I	n_x^{II}	x_1^{II}	δx_1^{II}	n_y	y_1	δy_1
0.428	5	0.07	0.0004	—	—	—	5	0.943	0.0006
0.544	5	0.091	0.0001	—	—	—	5	0.951	0.0007
0.643	5	0.108	0.0002	—	—	—	5	0.955	0.0020
0.910	5	0.160	0.0003	—	—	—	5	0.967	0.0010
1.078	5	0.200	0.0002	—	—	—	5	0.975	0.0003
1.220	5	0.230	0.0002	—	—	—	5	0.976	0.0010
1.379	5	0.272	0.0002	—	—	—	6	0.98	0.0003
1.618	5	0.349	0.0002	—	—	—	5	0.981	0.0004
1.838	5	0.455	0.0008	—	—	—	5	0.986	0.0004
*1.871	5	*0.452	0.0006	5	*0.994	0.0003	5	*0.986	0.0003

Table 5.38: Continued

T/K = 313.08						
P/MPa	n_x	x_1	δx_1	n_y	y_1	δy_1
0.322	5	0.039	0.0002	5	0.825	0.0025
0.517	5	0.070	0.0003	5	0.885	0.0007
0.734	5	0.103	0.0003	5	0.918	0.0012
1.071	5	0.157	0.0003	6	0.939	0.0006
1.316	5	0.197	0.0002	5	0.950	0.0002
1.584	5	0.243	0.0002	5	0.958	0.0008
1.861	5	0.294	0.0002	5	0.962	0.0007
2.191	5	0.370	0.0001	5	0.964	0.0010
2.358	5	0.417	0.0003	5	0.968	0.0004
2.717	5	0.561	0.0005	5	0.967	0.0013
2.860	5	0.692	0.0005	5	0.974	0.0004
2.900	5	0.827	0.0008	6	0.975	0.0008

Table 5.38: Continued

T/K = 332.96						
P/MPa	n_x	x_1	δx_1	n_y	y_1	δy_1
0.332	5	0.030	0.0002	5	0.652	0.0028
0.659	5	0.073	0.0001	5	0.812	0.0003
0.983	5	0.116	0.0005	5	0.868	0.0009
1.302	5	0.156	0.0002	5	0.894	0.0006
1.660	5	0.201	0.0003	5	0.906	0.0028
2.017	5	0.253	0.0004	5	0.921	0.0011
2.519	5	0.330	0.0003	5	0.933	0.0018
3.089	5	0.435	0.0004	5	0.946	0.0008
3.502	5	0.527	0.0006	5	0.949	0.0008
3.872	5	0.638	0.0005	5	0.955	0.0006
4.055	6	0.714	0.0011	6	0.960	0.0014
4.234	5	0.819	0.0003	6	0.962	0.0006
4.235	5	0.821	0.0010	5	0.963	0.0003
4.277	5	0.851	0.0004	5	0.965	0.0006
4.309	5	0.879	0.0008	5	0.966	0.0005
4.367	5	0.939	0.0010	7	0.970	0.0009

x_1, y_1: liquid and vapour mole fraction; n_x, n_y : number of samples taken; δx_1, δy_1: standard deviation for x_1 and y_1.

Expanded uncertainty: $u\ (T, k = 2)$ = 0.04 K; $u\ (P, k = 2)$ = 2.00 kPa; u (x_1, k = 2) = 0.01 and u (y_1, k = 2) = 0.01.

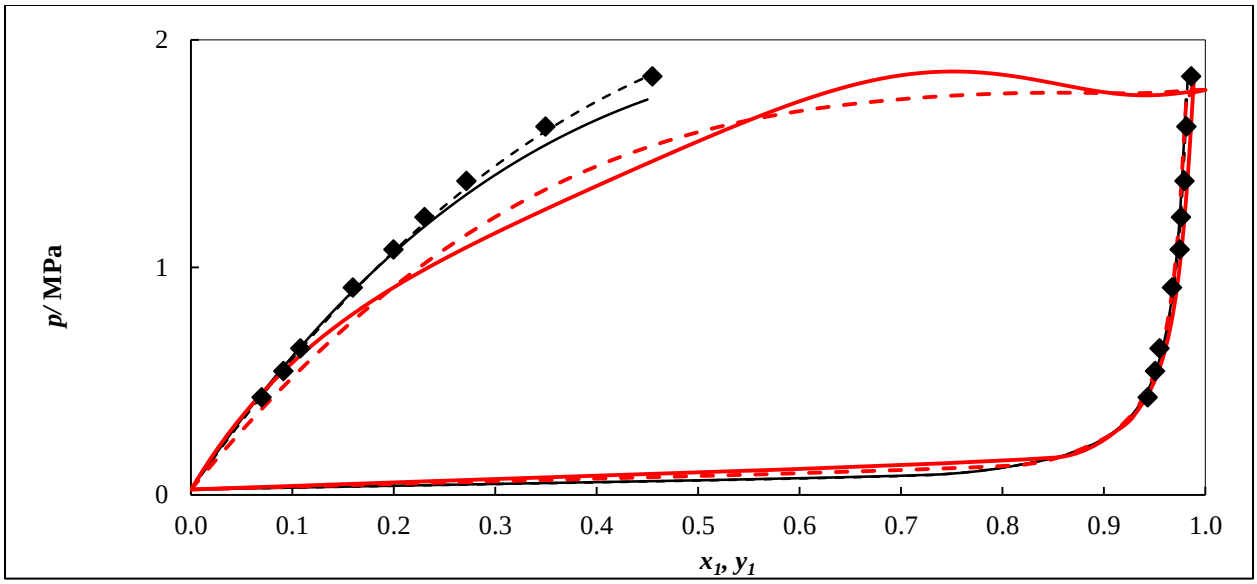

Figure 5.37: Phase diagrams (*P-x-y*) for the H_2S (1) + C_6F_{14} (2) system; Experimental data: ♦, 293.03 K; Models: SRK-MC-MHV1-NRTL (OF: FC) (solid black line); SRK-MC-MHV2-NRTL (OF:FC) (dashed black line); SRK-MC-PSRK-NRTL (OF:OLS) (dashed red line) and PR-MC-WS-NRTL (OF:OLS) (solid red line).

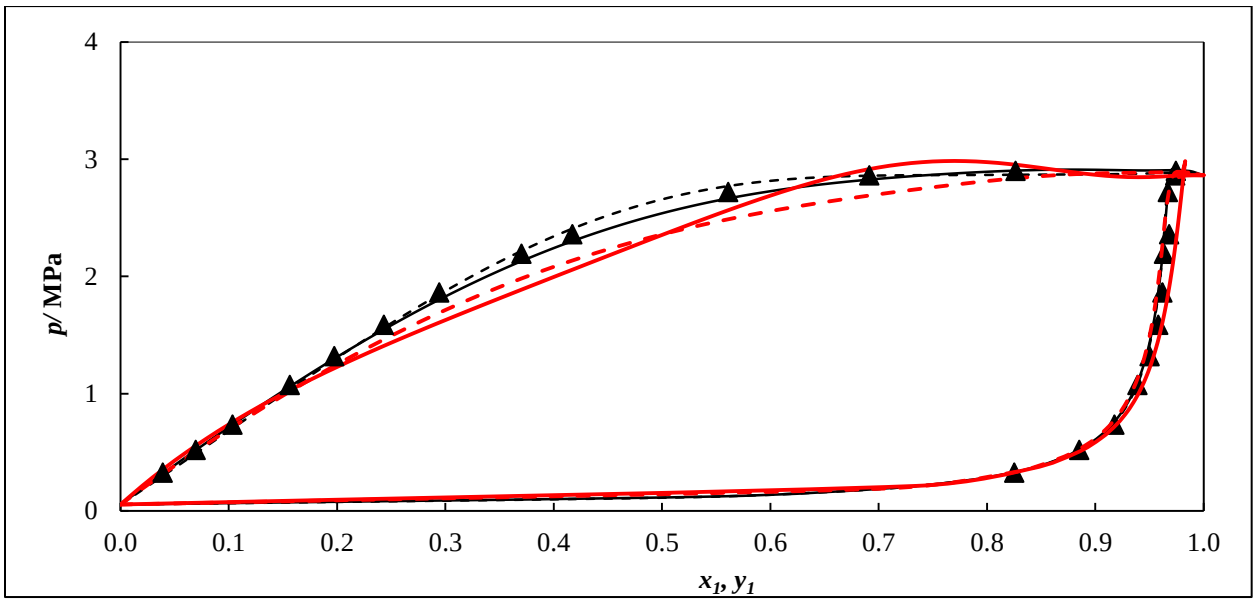

Figure 5.38: Phase diagrams (*P-x-y*) for the H_2S (1) + C_6F_{14} (2) system; Experimental data: ▲, 313.08 K; Models: SRK-MC-MHV1-NRTL (OF: FC) (solid black line); SRK-MC-MHV2-NRTL (OF:FC) (dashed black line); SRK-MC-PSRK-NRTL (OF:OLS) (dashed red line) and PR-MC-WS-NRTL (OF:OLS) (solid red line).

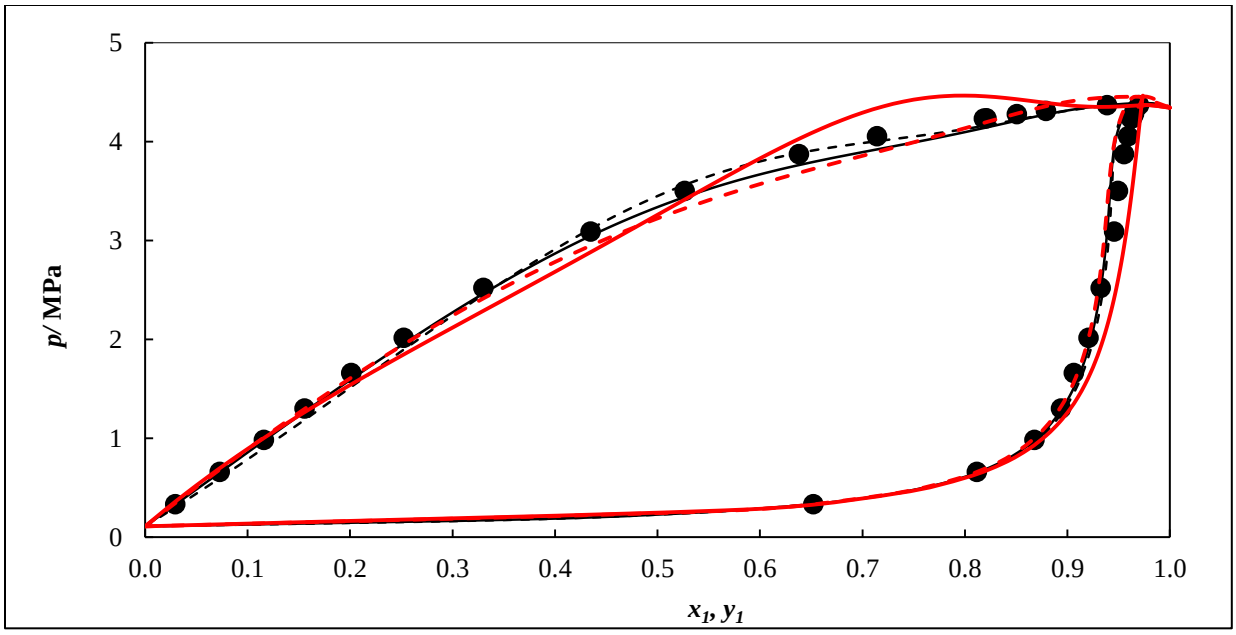

Figure 5.39: Phase diagrams (*P*-*x*-*y*) for the H_2S (1) + C_6F_{14} (2) system; Experimental data: ●, 332.96 K; Models: SRK-MC-MHV1-NRTL (OF: FC) (solid black line); SRK-MC-MHV2-NRTL (OF:FC) (dashed black line); SRK-MC-PSRK-NRTL (OF:OLS) (dashed red line) and PR-MC-WS-NRTL (OF:OLS) (solid red line).

Table 5.39: Model parameters for the SRK-MC-MHV1-NRTL, SRK-MC-MHV2-NRTL, SRK-MC-PSRK-NRTL and PR-MC-WS-NRTL models in a temperature-independent form for the H_2S (1) + C_6F_{14} (2) system

Model	Isotherm /K	$(g_{12} - g_{22})^a$/J.mol^{-1}	$(g_{21} - g_{11})^a$/J.mol^{-1}	$k_{ij}{}^b$
	Objective Function: Flash Calculation			
SRK-MC-MHV1-NRTL	293.03	15146	884.09	—
	313.08	13729	-202.42	—
	332.96	13699	899.90	—
SRK-MC-MHV2-NRTL	293.03	17797	1304.3	—
	313.08	11514	-662.66	—
	332.96	12337	-1521.3	—
Model	**Isotherm /K**	$\tau_{12}{}^c$	$\tau_{21}{}^c$	$k_{ij}{}^d$
	Objective Function: Ordinary Least Squares			
PR-MC-WS-NRTL	293.03	10.226	-3.5237	0.85
	313.08	9.7043	-3.4081	0.77
	332.96	9.4592	-3.2838	0.73
SRK-MC-PSRK-NRTL	293.03	12.771	-0.7852	—
	313.08	12.771	-0.9655	—
	332.96	12.668	-1.0765	—

[a] NRTL model parameters obtained from THERMOPACK, $\Delta g_{ij} = a_{ij}$.

[b, d] WS mixing rule parameter incorporated into the PR EoS correlated from THERMOPACK and Aspen Plus, respectively.

[c] NRTL model parameters obtained from Aspen Plus, $\tau_{ij} = a_{ij}$.

Table 5.40: Model parameters for the SRK-MC-MHV1-NRTL, SRK-MC-MHV2-NRTL, SRK-MC-PSRK-NRTL and PR-MC-WS-NRTL models in a temperature-dependent form for the H_2S (1) + C_6F_{14} (2) system

Model	$(g_{12} - g_{22})^a$/J.mol-1.K		$(g_{21} - g_{11})^a$/J.mol-1.K		$k_{ij}{}^b$
	a_{12}	b_{12}	a_{21}	b_{21}	
objective function: flash calculation					
SRK-MC-MHV1-NRTL	13310	1.3311	11946	-38.695	—
SRK-MC-MHV2-NRTL	-2204.2	43.769	13433	-44.977	—
Model	$\tau_{12}{}^c$ / K		$\tau_{21}{}^c$ / K		$k_{ij}{}^d$
objective function: ordinary least squares					
PR-MC-WS-NRTL	-1883.0		1393.3		0.78
SRK-MC-PSRK-NRTL	-2231.3		379.35		—

[a] NRTL model parameters obtained from THERMOPACK, $\Delta g_{ij} = a_{ij} + b_{ij}.T$

[b, d] WS mixing rule parameter incorporated into the PR EoS correlated from THERMOPACK and Aspen Plus, respectively. [c] NRTL model parameters obtained from Aspen Plus, $\tau_{ij} = b_{ij}/T$

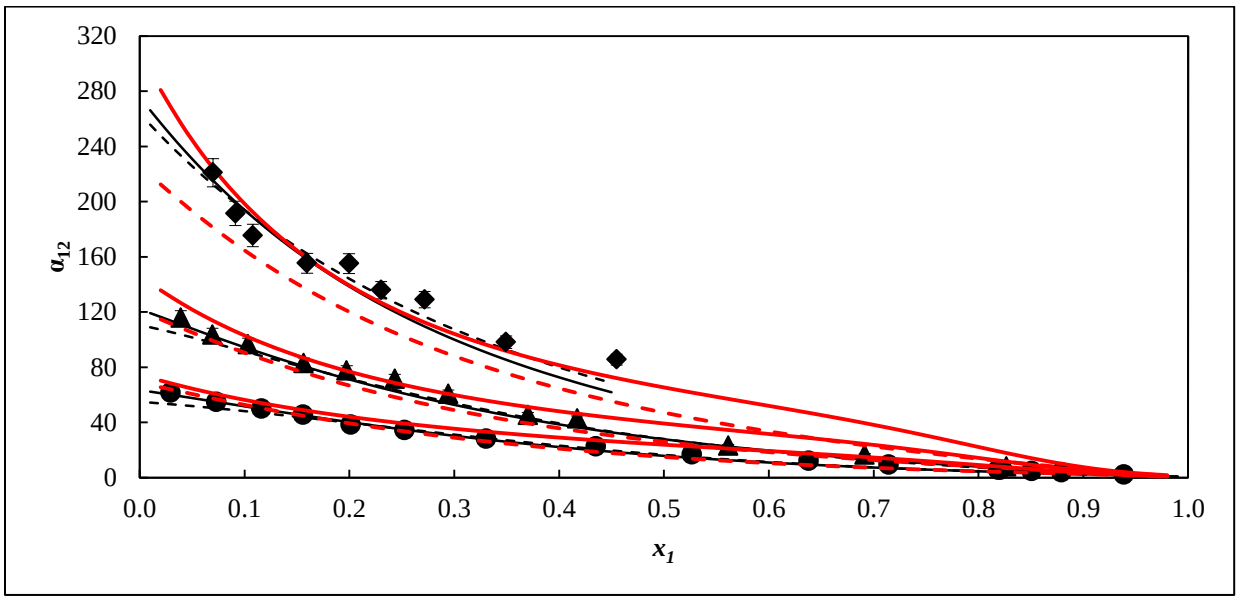

Figure 5.40: Plot of relative volatilities (α_{12}) for the H_2S (1) + C_6F_{14} (2) system; Experimental data: ♦, 293.03 K; ▲, 313.08 K; ●, 332.96 K; Models: SRK-MC-MHV1-NRTL (OF: FC) (solid black line); SRK-MC-MHV2-NRTL (OF:FC) (dashed black line); SRK-MC-PSRK-NRTL (OF:OLS) (dashed red line) and PR-MC-WS-NRTL (OF:OLS) (solid red line). Error bands: shown at 4.6 % for the experimental data.

Table 5.41: Deviation bias U and AAD U obtained in fitting experimental VLE data with the SRK-MC-MHV1-NRTL, SRK-MC-MHV2-NRTL, SRK-MC-PSRK-NRTL and PR-MC-WS-NRTL models for the H_2S (1) + C_6F_{14} (2) system

Model	Isotherm / K	bias x %	AAD x %	bias y %	AAD y %
objective function: flash calculation					
SRK-MC-MHV1-NRTL	293.03	-3.50	1.69	0.14	0.24
	313.08	-2.48	1.22	0.33	0.31
	332.96	-3.25	1.88	0.47	0.58
SRK-MC-MHV2-NRTL	293.03	-0.84	0.42	0.06	0.20
	313.08	-2.22	1.32	0.39	0.37
	332.96	-4.94	1.70	0.38	0.68
Model	Isotherm / K	bias P %	AAD P %	bias y %	AAD y %
objective function: ordinary least squares					
PR-MC-WS-NRTL	293.03	0.35	4.83	-0.49	0.48
	313.08	-0.19	11.74	-0.77	0.72
	332.96	-0.51	12.92	-1.18	1.04
SRK-MC-PSRK-NRTL	293.03	2.56	8.47	0.35	0.43
	313.08	1.81	7.68	0.44	0.49
	332.96	0.98	7.22	0.56	0.78

For the hydrogen sulphide (1) + perfluorohexane (2) system, azeotropic behaviour was observed for both the 313.08 and 332.96 K isotherms at approximately x_1 = 0.971. This implies that conventional distillation cannot separate the mixture into high purity compounds. Alternative methods such as pressure-swing distillation should be investigated. However, for the 293.03 K isotherm, as pressure was increased (at approximately 1.871 MPa), the phenomenon of vapour-liquid-liquid equilibrium was observed. Despite of the opacity of the thermo-regulated liquid bath used, the VLLE data point was measured and presented in Table 5.39.

Figures 5.37-5.39 show the agreement between the models and the experimental VLE data, where the SRK-MC-MHV2-NRTL (OF: FC), SRK-MC-MHV1-NRTL (OF: FC), SRK-MC-PSRK-NRTL (OF: OLS) and PR-MC-WS-NRTL (OF: OLS) models represent the experimental VLE data globally well for all the three isotherms. However slight deviations are observed in the liquid phase between the experimental data and the models where significant deviations are mainly observed for the PR-MC-WS-NRTL (OF: OLS) model. In addition, the four models confirm the existence of the azeotropic points in the concentrated region of H_2S at 313.08 and

332.96 K. Although, the existence of the VLLE phenomenon was observed during experimentation at 293.03 K, the four models did not predict it; instead, the SRK-MC-PSRK-NRTL (OF: OLS) and PR-MC-WS-NRTL (OF: OLS) model predicted an azeotrope. As for the H_2S (1) + C_4F_{10} (2) system, the VLE data measurements should be undertaken in a transparent thermo-regulated liquid bath to facilitate viewing of multiple phases in equilibrium.

The relative deviations bias U and AAD U were also calculated to quantify the fit of the models to the experimental VLE data. The results obtained, which are reported in Table 5.41, reveal similar values of bias U and AAD U for both the SRK-MC-MHV1 (OF: FC) and SRK-MC-MHV2 (OF: FC) models which implies that the two models provide similar fits to the experimental data. The same conclusion can also be drawn from the SRK-MC-PSRK-NRTL (OF: OLS) and PR-MC-WS-NRTL (OF: OLS) models due to the similarity in the bias U and AAD U values.

The relative volatilities were calculated for each model and compared to the experimental values. The results obtained, which are graphically presented in Figure 5.40, show a good representation for the three models, except at 293.03 K where slight deviations are observed for the SRK-MC-PSRK-NRTL (OF: OLS) and PR-MC-WS-NRTL (OF: OLS) models. The solubility of hydrogen sulfide in perfluorohexane increases with decreasing temperatures but at a lower temperature such as 293.03 K, VLLE was observed which means at much lower temperatures this system may exhibit a larger LLE envelop than VLE envelop.

5.5.2.10 Carbon monoxide (1) + perfluorohexane (2) system

The experimental VLE data for the carbon monoxide (1) + perfluorohexane (2) system were undertaken at three temperatures ranging from (293.01, 313.04 and 333.04) K and are reported in Table 5.42.

The experimental VLE data were correlated using the Peng-Robinson or Soave Redlich-Kwong EoS incorporating the Mathias-Copeman alpha function and the Wong-Sandler or predictive Soave-Redlich-Kwong mixing rule utilizing the NRTL activity coefficient model and adjusted using either the flash calculation or the ordinary least squares objective function abbreviated as PR-MC-WS-NRTL (OF: FC or OLS) and SRK-MC-PSRK-NRTL (OF: OLS) models. The results obtained from the modelling are graphically compared with the experimental VLE data in

Figures 5.41-5.43. The model parameters in both the temperature-independent and the temperature-dependent forms are reported in Tables 5.43 and 5.44, respectively. The relative volatilities which were computed using the PR-MC-WS-NRTL (OF: FC or OLS) and SRK-MC-PSRK-NRTL (OF: OLS) models are graphically compared with the experimental values in Figure 5.44. The relative deviations bias U and AAD U were also calculated and are reported in Table 5.45.

Table 5.42: Experimental VLE data for the carbon monoxide (1) + perfluorohexane (2) system

T/K = 293.01						
P/MPa	n_x	x_1	δx_1	n_y	y_1	δy_1
1.229	5	0.048	0.0003	5	0.976	0.0007
3.083	5	0.111	0.0003	5	0.985	0.0001
5.036	5	0.172	0.0006	5	0.984	0.0020
13.924	6	0.410	0.0010	5	0.983	0.0010
16.016	5	0.450	0.0009	5	0.981	0.0007
17.572	5	0.474	0.0005	5	0.978	0.0006
20.169	5	0.543	0.0009	6	0.975	0.0008
22.288	5	0.570	0.0030	5	0.969	0.0004
24.235	5	0.600	0.0003	5	0.963	0.0013
11.973	5	0.364	0.0007	5	0.986	0.0007
9.079	5	0.289	0.0006	5	0.989	0.0007
7.102	5	0.249	0.0009	5	0.985	0.0005
T/K = 313.04						
P/MPa	n_x	x_1	δx_1	n_y	y_1	δy_1
17.690	5	0.504	0.0020	5	0.963	0.0017
19.968	5	0.557	0.0011	5	0.956	0.0025
22.997	5	0.620	0.0008	5	0.941	0.0012
15.459	5	0.463	0.0002	5	0.972	0.0006
13.442	5	0.413	0.0013	5	0.975	0.0009
11.467	5	0.369	0.0006	5	0.978	0.0010
9.456	5	0.315	0.0001	5	0.980	0.0004
7.667	5	0.265	0.0005	5	0.981	0.0005
5.626	5	0.202	0.0008	5	0.980	0.0006
4.300	5	0.157	0.0010	5	0.978	0.0005
2.042	5	0.081	0.0014	5	0.966	0.0011

Table 5.42: Continued

T/K = 333.04						
P/MPa	n_x	x_1	δx_1	n_y	y_1	δy_1
2.228	5	0.088	0.0002	5	0.935	0.0009
4.013	5	0.149	0.0004	5	0.956	0.0009
6.050	5	0.220	0.0009	5	0.962	0.0010
8.998	5	0.313	0.0008	5	0.963	0.0007
11.344	5	0.382	0.0002	5	0.962	0.0007
13.311	5	0.420	0.0016	5	0.958	0.0006
15.320	5	0.483	0.0007	5	0.952	0.0013
17.314	5	0.518	0.0013	5	0.947	0.0007
19.169	5	0.583	0.0018	5	0.938	0.0006
21.232	5	0.637	0.0005	5	0.922	0.0006
23.636	5	0.742	0.0002	5	0.892	0.0012
24.497	5	0.830	0.0010	5	0.833	0.0011

x_1, y_1: liquid and vapour mole fraction; n_x, n_y : number of samples taken; δx_1, δy_1: standard deviation for x_1 and y_1.

Expanded uncertainty: $u\ (T, k = 2)$ = 0.04 K; $u\ (P, k = 2)$ = 2.00 kPa; u (x_1, k = 2) = 0.01 and u (y_1, k = 2) = 0.01.

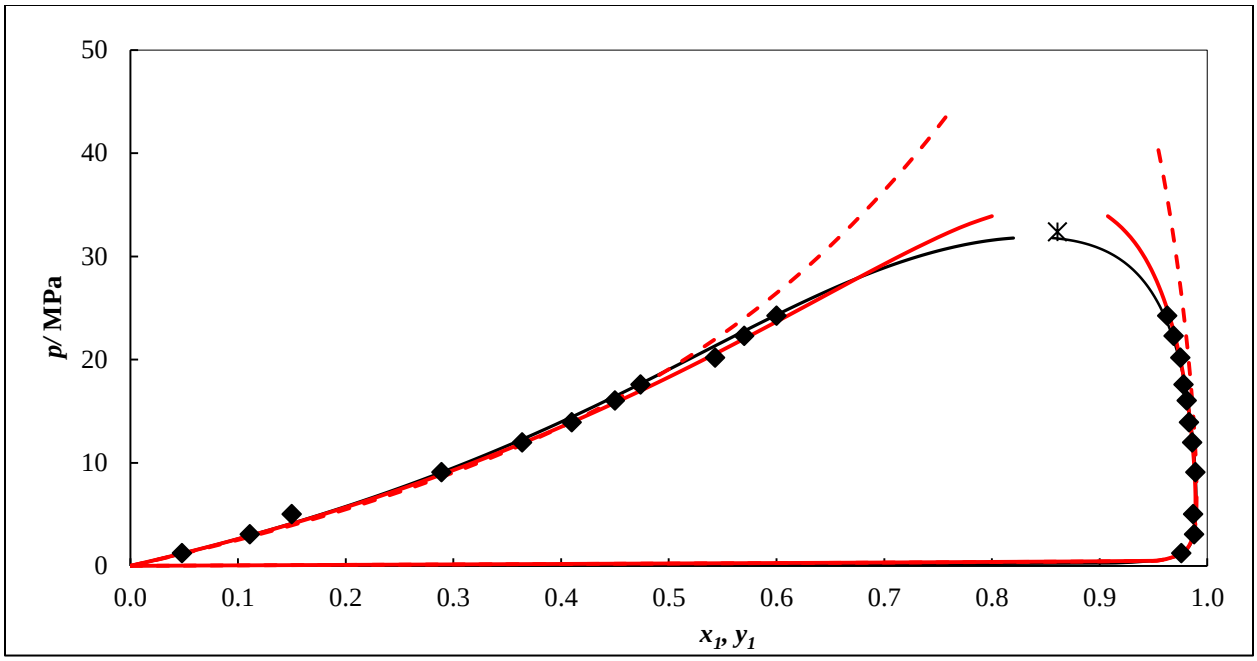

Figure 5.41: Phase diagrams (*P-x-y*) for the CO (1) + C_6F_{14} (2) system. Experimental data: ♦, 293.01 K. Models: PR-MC-WS-NRTL (OF: FC) (solid black line); SRK-MC-PSRK-NRTL (OF: OLS) (dashed red line) and PR-MC-WS-NRTL (OF: OLS) (solid red line); *, mixture critical point.

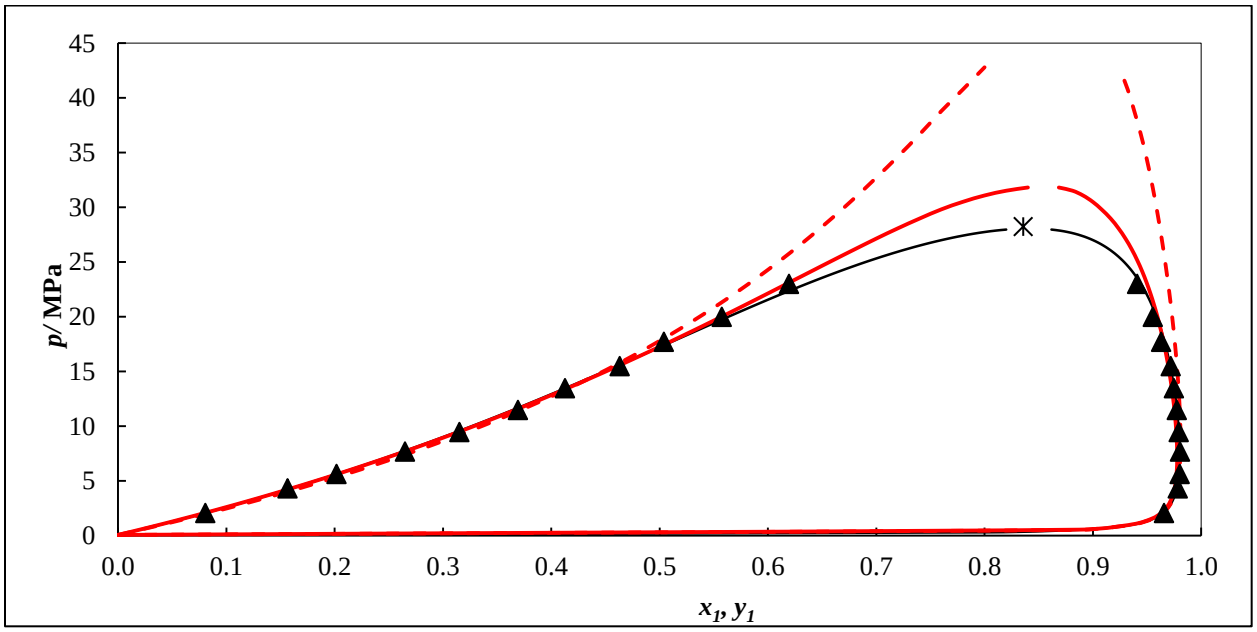

Figure 5.42: Phase diagrams (*P-x-y*) for the CO (1) + C_6F_{14} (2) system. Experimental data: ▲, 313.04 K. Models: PR-MC-WS-NRTL (OF: FC) (solid black line); SRK-MC-PSRK-NRTL (OF: OLS) (dashed red line) and PR-MC-WS-NRTL (OF: OLS) (solid red line); *, mixture critical point.

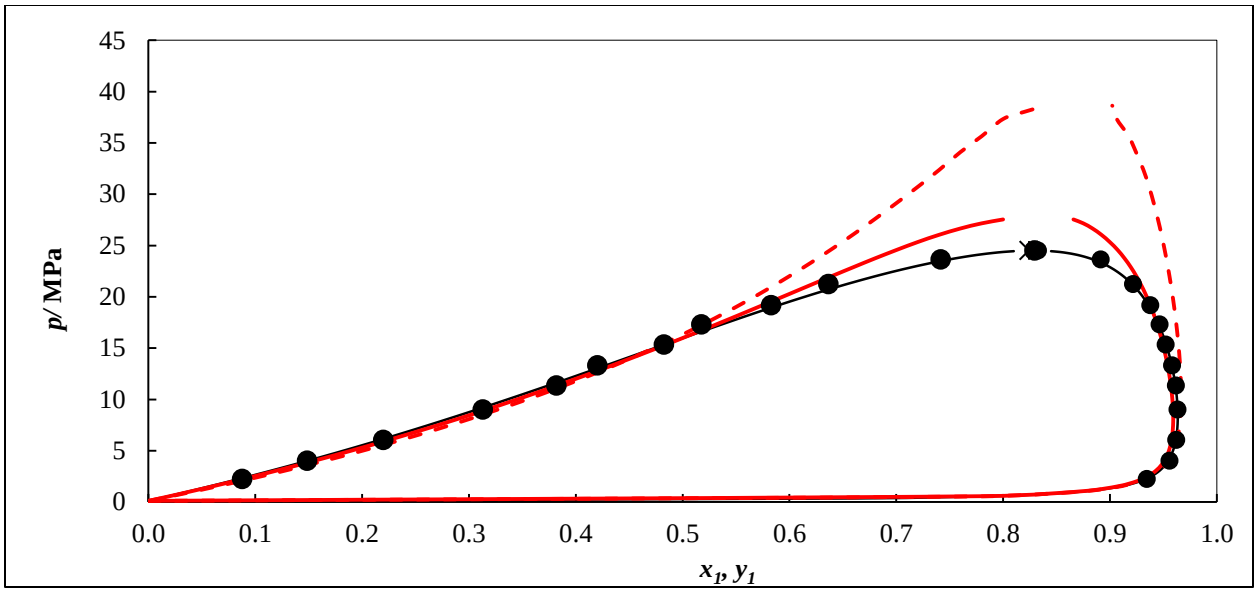

Figure 5.43: Phase diagrams (*P*-*x*-*y*) for the CO (1) + C_6F_{14} (2) system. Experimental data: ●, 333.04 K. Models: PR-MC-WS-NRTL (OF: FC) (solid black line); SRK-MC-PSRK-NRTL (OF: OLS) (dashed red line) and PR-MC-WS-NRTL (OF: OLS) (solid red line); *, mixture critical point.

Table 5.43: Model parameters for the PR-MC-WS-NRTL and SRK-MC-PSRK-NRTL models in a temperature-independent form for the CO (1) + C_6F_{14} (2) system

Model	Isotherm /K	$(g_{12} - g_{22})^a$/J.mol^{-1}	$(g_{21} - g_{11})^a$/J.mol^{-1}	$k_{ij}{}^b$
	objective function: flash calculation			
PR-MC-WS-NRTL	293.01	8020.3	-1799.7	0.83
	313.04	7897.1	-2029.4	0.84
	333.04	7584.7	-2004.4	0.85
Model	**Isotherm /K**	$\tau_{12}{}^c$	$\tau_{21}{}^c$	$k_{ij}{}^d$
	objective function: ordinary least squares			
PR-MC-WS-NRTL	293.01	-0.7492	-0.8774	0.77
	313.04	-0.6374	-1.0351	0.83
	333.04	3.8408	-2.5569	0.83
SRK-MC-PSRK-NRTL	293.01	4.6185	-3.8760	—
	313.04	4.4662	-3.8155	—
	333.04	5.4425	-4.1777	—

[a] NRTL model parameters obtained from THERMOPACK, $\Delta g_{ij} = a_{ij}$.

[b, d] WS mixing rule parameter incorporated into the PR EoS correlated from THERMOPACK and Aspen Plus, respectively.

[c] NRTL model parameter obtained from Aspen Plus, $\tau_{ij} = a_{ij}$.

Table 5.44: Model parameters for the PR-MC-WS-NRTL and SRK-MC-PSRK-NRTL models in a temperature-dependent form for the CO (1) + C_6F_{14} (2) system

Model	$(g_{12} - g_{22})^a$/J.mol-1.K		$(g_{21} - g_{11})^a$/J.mol-1.K		$k_{ij}{}^b$
	a_{12}	b_{12}	a_{21}	b_{21}	
Objective Function: flash calculation					
PR-MC-WS-NRTL	1998.9	17.149	1645.6	-10.722	0.86
Model	**$\tau_{12}{}^c$ / K**		**$\tau_{21}{}^c$ / K**		
Objective Function: ordinary least squares					
PR-MC-WS-NRTL	774.99		-39.185		0.83
SRK-MC-PSRK-NRTL	-928.76		582.50		—

[a] NRTL model parameters correlated from THERMOPACK, $\Delta g_{ij} = a_{ij} + b_{ij}.T$

[b, d] WS mixing rule parameter incorporated into the PR EoS correlated from THERMOPACK and Aspen Plus, respectively.

[c] NRTL model parameters correlated from Aspen Plus, $\tau_{ij} = b_{ij}/T$

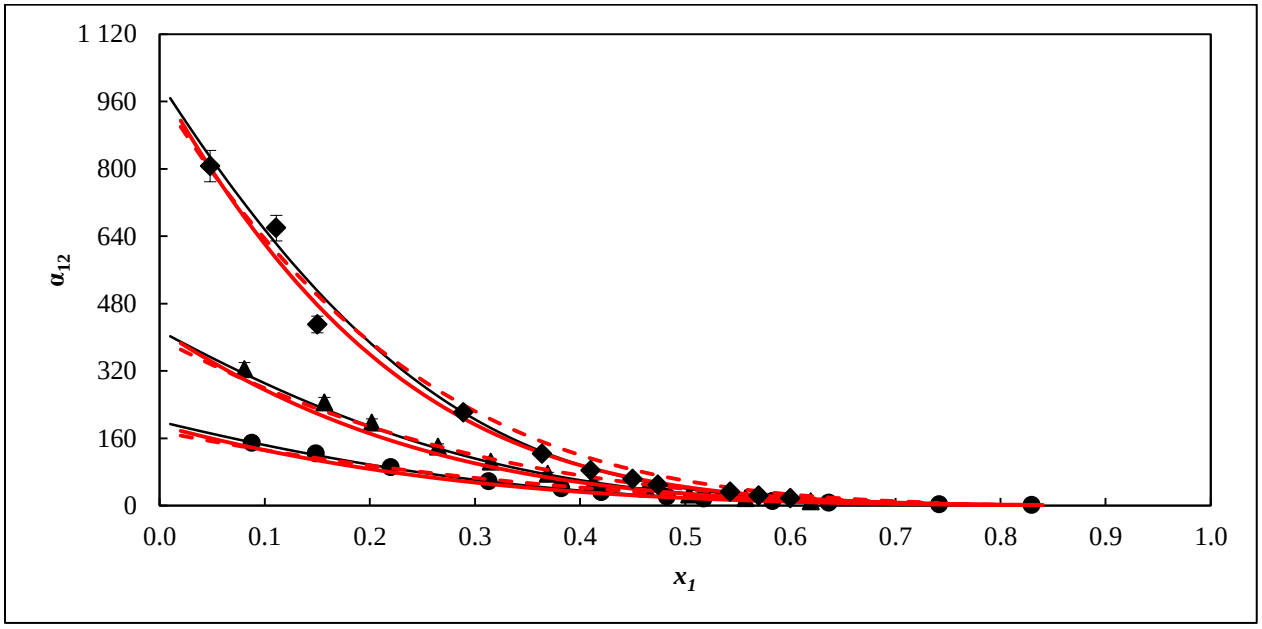

Figure 5.44: Plot of relative volatilities (α_{12}) for the CO (1) + C_6F_{14} (2) system. Experimental data: ♦, 293.01 K; ▲, 313.04 K; ●, 333.04 K. Models: PR-MC-WS-NRTL (OF: FC) (solid black line); SRK-MC-PSRK-NRTL (OF: OLS) (dashed red line) and PR-MC-WS-NRTL (OF: OLS) (solid red line).Error bands: shown at 4.6 % for the experimental data.

Table 5.45: Relative deviation bias U and AAD U obtained in fitting experimental VLE data with the PR-MC-WS-NRTL and SRK-MC-PSRK-NRTL models for the CO (1) + C_6F_{14} (2) system

Model	Isotherm / K	bias x %	AAD x %	bias y %	AAD y %
Objective Function: Flash Calculation					
PR-MC-WS-NRTL	293.01	-0.92	0.86	-0.02	0.13
	313.04	-0.21	0.42	-0.04	0.13
	333.04	-0.08	0.66	0.13	0.13
Model	Isotherm / K	bias P %	AAD P %	bias y %	AAD y %
Objective Function: Ordinary Least Squares					
PR-MC-WS-NRTL	293.01	-0.03	18.19	0.35	0.40
	313.04	-0.01	8.27	0.06	0.33
	333.04	-0.11	16.72	0.52	0.49
SRK-MC-PSRK-NRTL	293.01	0.15	60.14	-0.50	0.49
	313.04	0.11	56.24	-0.58	0.65
	333.04	0.53	32.92	0.74	2.32

As can be seen from Figures 5.41-5.43, the PR-MC-WS-NRTL (OF: FC) model agree well with the experimental VLE data for all the three isotherms whereas the SRK-MC-PSRK-NRTL (OF: OLS) and PR-MC-WS-NRTL (OF: OLS) models over represent the experimental the data as their approach the mixture critical point for each isotherm with larger deviations observed for the latter model.

The deviation bias U and AAD U between the experimental and calculated vapour and liquid mole fractions reported in Table 5.45, indicate that the PR-MC-WS-NRTL (OF: FC) model fits well the experimental VLE data for the three isotherms as its bias U and AAD U values are low (< 1.00 %). Table 5.45 also reveals that the PR-MC-WS-NRTL (OF: OLS) model is better than the SRK-MC-PSRK-NRTL (OF: OLS) model as it has lower values of bias U and AAD U.

The relative volatilities results presented graphically in Figure 5.44 show a better agreement between the experimental and the computed values obtained from the PR-MC-WS-NRTL (OF: FC or OLS) model than those obtained from the SRK-MC-PSRK-NRTL (OF: OLS) model. Examination of Figures 5.41-5.43 reveals that solubility of carbon monoxide in perfluorohexane

is favoured at lower temperatures. One should note that, for the temperature range considered, no significant influence on the solubility is observed.

5.5.2.11 Ethane (1) + perfluorohexane (2) system

The experimental VLE data for the ethane (1) + perfluorohexane (2) system were undertaken at four isotherms (292.89, 303.03, 308.03 and 317.92) K and are reported in Table 5.46.

The experimental VLE data were modelled using the Peng-Robinson or Soave-Redlich-Kwong EoS incorporating the Mathias-Copeman alpha function and the Wong-Sandler or predictive Soave-Redlich-Kwong mixing rule utilizing the NRTL activity coefficient model and adjusted using either the flash calculation or the ordinary least squares objective function abbreviated as PR-MC-WS-NRTL (OF: FC or OLS) and SRK-MC-NRTL (OF: OLS) models. The results obtained from the modelling are graphically compared with the experimental VLE data in Figures 5.45-5.48. The model parameters in the temperature-independent and temperature-dependent forms are reported in Tables 5.47 and 5.48, respectively. The relative volatilities which were computed using the PR-MC-WS-NRTL (OF: FC or OLS) and SRK-MC-PSRK-NRTL (OF: OLS) models are graphically compared with the experimental values in Figure 5.49. The relative deviations bias U and AAD are reported in Table 5.49.

Table 5.46: Experimental VLE data for the ethane (1) + perfluorohexane (2) system

T / K = 292.89						
P / MPa	n_x	x_1	δx_1	n_y	y_1	δy_1
0.513	5	0.120	0.0009	5	0.950	0.0016
0.816	6	0.196	0.0017	6	0.966	0.0014
1.269	5	0.276	0.0035	5	0.973	0.0009
1.533	5	0.352	0.0008	5	0.979	0.0003
1.888	5	0.454	0.0014	5	0.981	0.0004
2.186	5	0.563	0.0010	5	0.984	0.0017
2.469	5	0.659	0.0017	5	0.987	0.0011
2.834	5	0.814	0.0011	5	0.987	0.0006
3.060	5	0.878	0.0002	5	0.989	0.0003
3.400	5	0.936	0.0001	5	0.992	0.0002

Table 5.46: Continued

T / K = 303.03						
P / MPa	n_x	x_1	δx_1	n_y	y_1	δy_1
0.559	5	0.115	0.0010	5	0.929	0.0028
0.879	5	0.189	0.0040	5	0.951	0.0035
1.339	5	0.286	0.0007	5	0.965	0.0010
1.685	5	0.361	0.0004	5	0.970	0.0002
2.121	5	0.440	0.0010	5	0.973	0.0011
2.484	5	0.546	0.0068	5	0.977	0.0018
2.841	5	0.645	0.0007	5	0.980	0.0002
3.197	5	0.743	0.0011	5	0.980	0.0008
3.572	5	0.840	0.0010	5	0.983	0.0002
4.001	5	0.920	0.0002	5	0.984	0.0004
4.242	5	0.956	0.0013	5	0.989	0.0001
T / K = 308.03						
P / MPa	n_x	x_1	δx_1	n_y	y_1	δy_1
0.607	5	0.121	0.0006	5	0.919	0.0028
1.223	5	0.244	0.0005	5	0.947	0.0011
1.653	5	0.326	0.0035	5	0.965	0.0004
2.127	6	0.425	0.0005	5	0.970	0.0004
2.613	5	0.538	0.0014	6	0.975	0.0014
3.158	6	0.670	0.0012	5	0.977	0.0008
3.549	6	0.765	0.0007	5	0.977	0.0003
3.899	5	0.844	0.0001	5	0.976	0.0008
4.421	5	0.920	0.0003	5	0.984	0.0001

Table 5.46: Continued

T / K = 317.92						
P / MPa	n_x	x_1	δx_1	n_y	y_1	δy_1
0.559	6	0.092	0.0007	5	0.876	0.0040
1.051	5	0.174	0.0005	5	0.930	0.0001
1.547	5	0.273	0.0021	5	0.944	0.0010
1.914	5	0.319	0.0038	5	0.953	0.0002
2.421	5	0.397	0.0045	5	0.957	0.0019
2.752	5	0.481	0.0030	5	0.962	0.0010
3.153	5	0.567	0.0018	5	0.963	0.0011
3.556	5	0.653	0.0009	5	0.966	0.0014
4.054	5	0.749	0.0010	5	0.967	0.0003
4.523	5	0.837	0.0003	5	0.967	0.0001
4.913	5	0.897	0.0001	5	0.969	0.0002

x_1, y_1: liquid and vapour mole fraction; n_x, n_y : number of samples taken; δx_1, δy_1: standard deviation for x_1 and y_1.

Expanded uncertainty: $u\ (T, k = 2)$ = 0.04 K; $u\ (P, k = 2)$ = 2.50 kPa; u (x_1, k = 2) = 0.03 and u (y_1, k = 2) = 0.03.

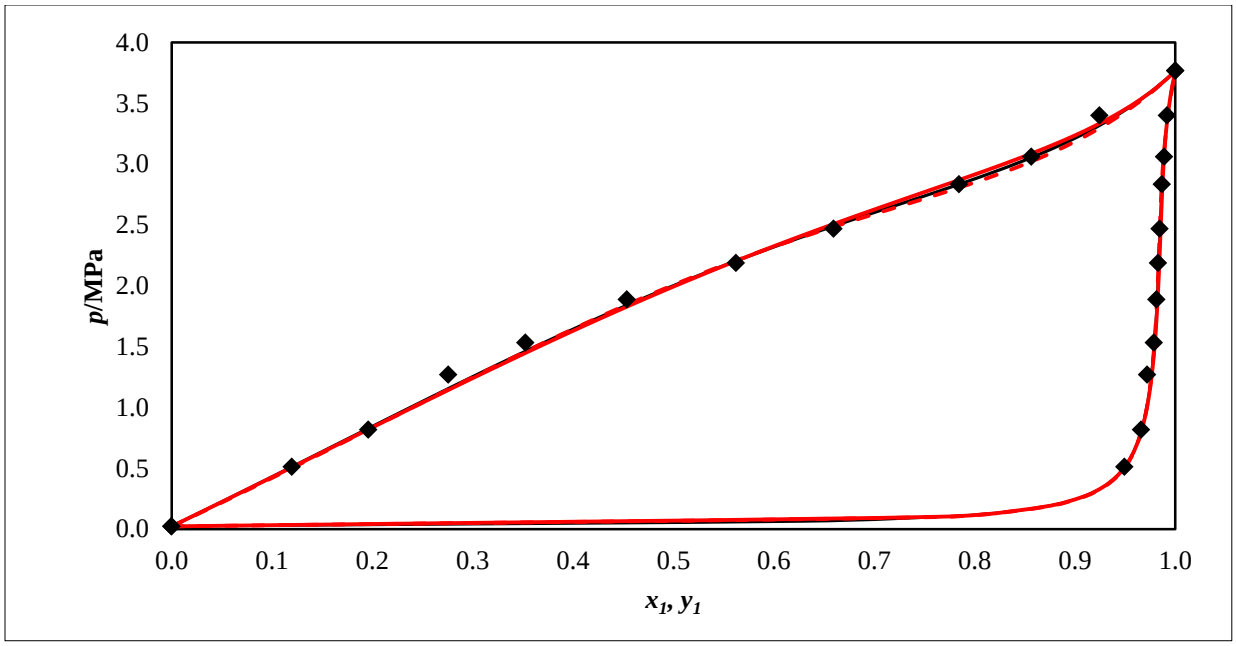

Figure 5.45: Phase diagrams (*P-x-y*) for the C_2H_6 (1) + C_6F_{14} (2) system. Experimental data: ♦, 292.89 K. Models: PR-MC-WS-NRTL (OF: FC) (solid black line); SRK-MC-PSRK-NRTL (OF: OLS) (dashed red line) and PR-MC-WS-NRTL (OF: OLS) (solid red line).

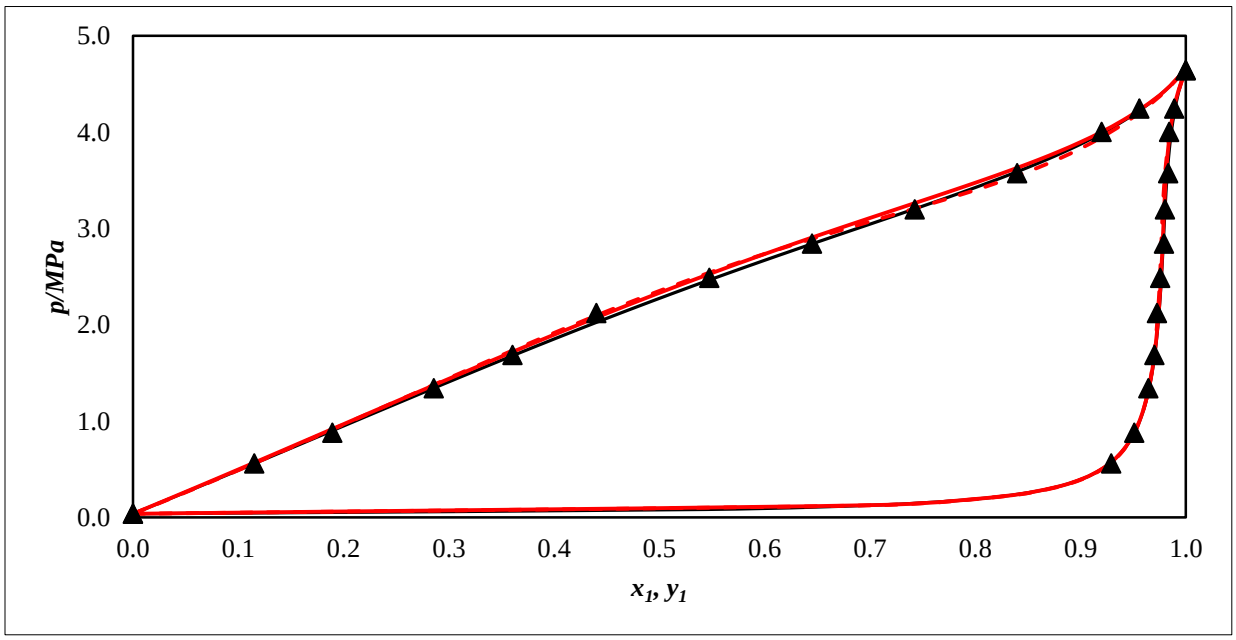

Figure 5.46: Phase diagrams (*P-x-y*) for the C_2H_6 (1) + C_6F_{14} (2) system. Experimental data: ▲, 303.03 K. Models: PR-MC-WS-NRTL (OF: FC) (solid black line); SRK-MC-PSRK-NRTL (OF: OLS) (dashed red line) and PR-MC-WS-NRTL (OF: OLS) (solid red line).

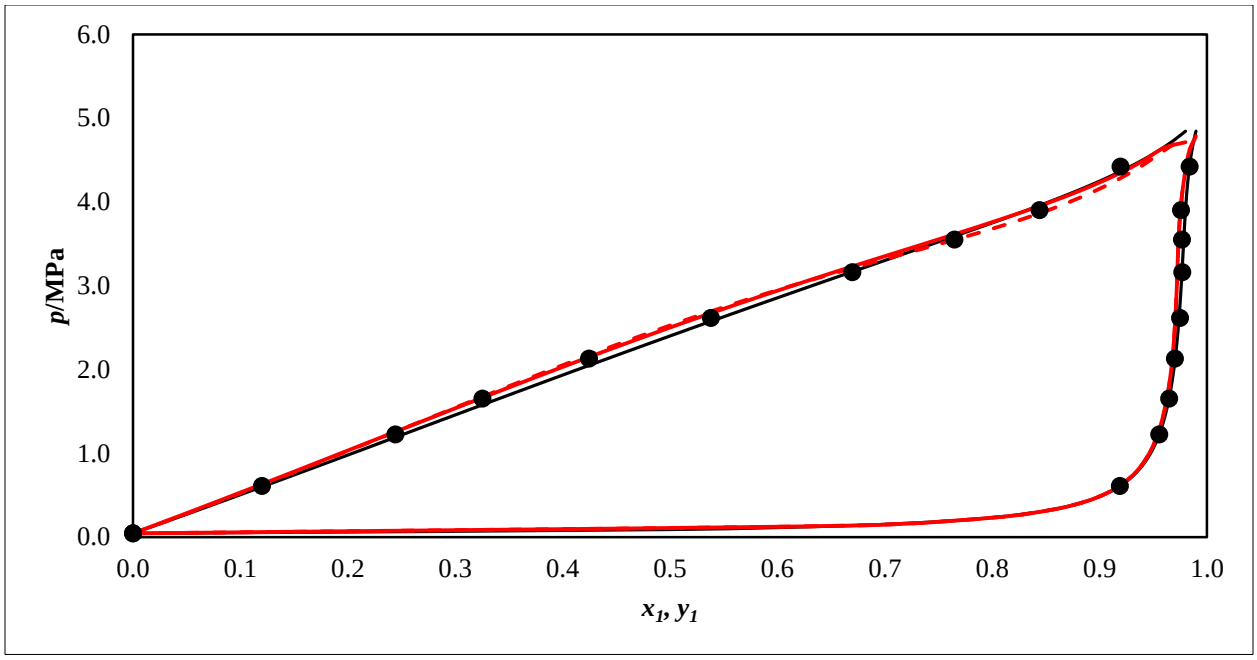

Figure 5.47: Phase diagrams (*P*-*x*-*y*) for the C_2H_6 (1) + C_6F_{14} (2) system. Experimental data: ●, 308.03 K. Models: PR-MC-WS-NRTL (OF: FC) (solid black line); SRK-MC-PSRK-NRTL (OF: OLS) (dashed red line) and PR-MC-WS-NRTL (OF: OLS) (solid red line).

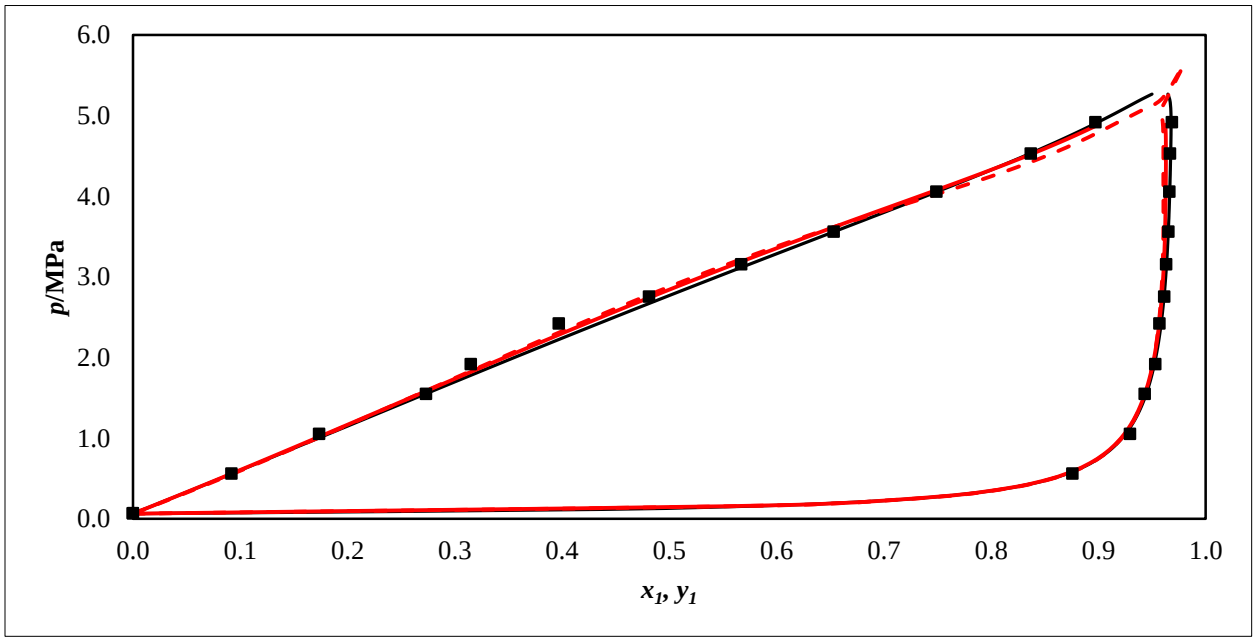

Figure 5.48: Phase diagrams (*P*-*x*-*y*) for the C_2H_6 (1) + C_6F_{14} (2) system. Experimental data: ■, 317.92 K. Models: PR-MC-WS-NRTL (OF: FC) (solid black line); SRK-MC-PSRK-NRTL (OF: OLS) (dashed red line) and PR-MC-WS-NRTL (OF: OLS) (solid red line).

Table 5.47: Model parameters for the PR-MC-WS-NRTL and SRK-MC-PSRK-NRTL models in a temperature-independent form for the C_2H_6 (1) + C_6F_{14} (2) system

Model	Isotherm /K	$(g_{12} - g_{22})^a$/J.mol^{-1}	$(g_{21} - g_{11})^a$/J.mol^{-1}	$k_{ij}{}^b$
objective function: flash calculation				
PR-MC-WS-NRTL	292.89	7689.1	-987.30	0.48
	303.03	6624.7	-1132.4	0.49
	308.03	5697.9	-1250.3	0.51
	317.92	5955.0	-1145.5	0.51
Model	**Isotherm /K**	$\tau_{12}{}^c$	$\tau_{21}{}^c$	$k_{ij}{}^d$
objective function: ordinary least squares				
PR-MC-WS-NRTL	292.89	3.6541	-0.2847	0.48
	303.03	3.0629	-0.4445	0.50
	308.03	2.8597	-0.4711	0.51
	317.92	2.8186	-0.4171	0.52
SRK-MC-PSRK-NRTL	292.89	3.2254	-1.7600	—
	303.03	3.2482	-1.8504	—
	308.03	3.2587	-1.8722	—
	317.92	3.1825	-1.8020	—

[a] NRTL model parameters obtained from THERMOPACK, $\Delta g_{ij} = a_{ij}$.

[b, d] WS mixing rule parameter incorporated into the PR EoS correlated from THERMOPACK and Aspen Plus, respectively.

[c] NRTL model parameters obtained from Aspen Plus, $\tau_{ij} = a_{ij}$.

Table 5.48: Model parameters for the PR-MC-WS-NRTL and SRK-MC-PSRK-NRTL models in a temperature-dependent form for the C_2H_6 (1) + C_6F_{14} (2) system

Model	$(g_{12} - g_{22})^a$/J.mol-1.K		$(g_{21} - g_{11})^a$/J.mol-1.K		$k_{ij}{}^b$
	a_{12}	b_{12}	a_{21}	b_{21}	
objective function: flash calculation					
PR-MC-WS-NRTL	-2233.1	28.903	8119.1	-30.452	0.50
Model	$\tau_{12}{}^c$ / K		$\tau_{21}{}^c$ / K		
objective function: ordinary least squares					
PR-MC-WS-NRTL	-217.02		223.26		0.52
SRK-MC-PSRK-NRTL	-90.814		273.61		—

[a] NRTL model parameters obtained from THERMOPACK, $\Delta g_{ij} = a_{ij} + b_{ij}.T$

[b, d] WS mixing rule parameter incorporated into the PR EoS correlated from THERMOPACK and Aspen Plus, respectively.

[c] NRTL model parameters obtained from Aspen Plus, $\tau_{ij} = b_{ij}/T$

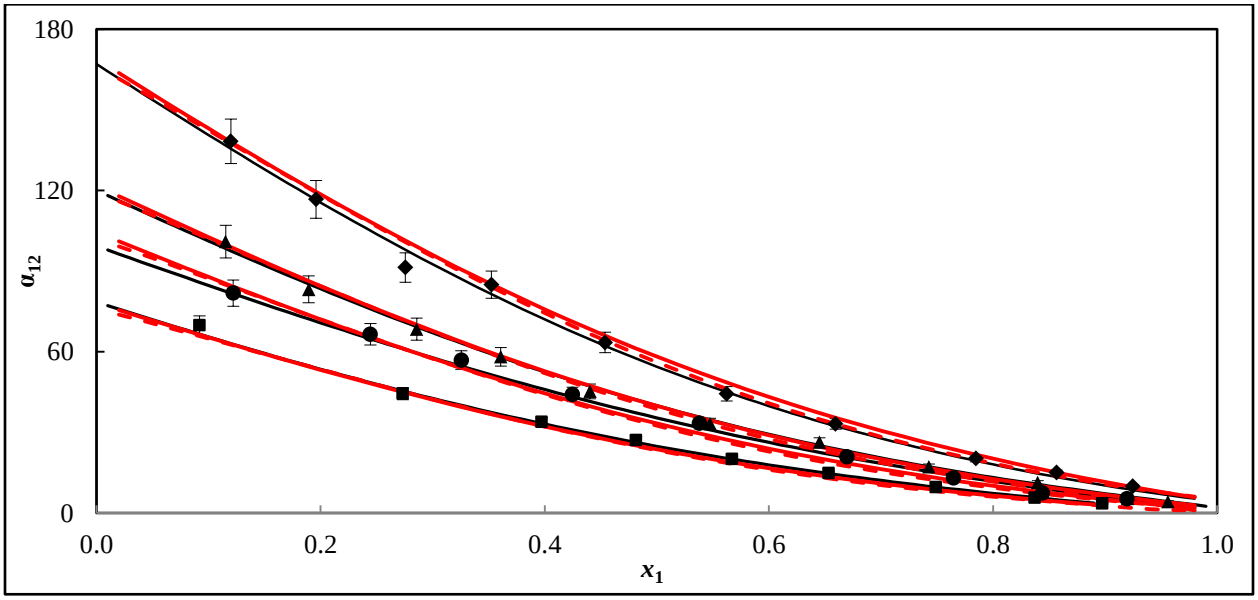

Figure 5.49: Plot of relative volatilities (α_{12}) for the C_2H_6 (1) + C_6F_{14} (2) system. Experimental data: ♦, 292.89 K; ▲, 303.03 K; ●, 308.03 K; ■, 317.92 K. Models: PR-MC-WS-NRTL (OF: FC) (solid black line); SRK-MC-PSRK-NRTL (OF: OLS) (dashed red line) and PR-MC-WS-NRTL (OF: OLS) (solid red line). Error bands: shown at 6.0 % for the experimental data.

Table 5.49: Deviations, Bias U and the AAD obtained in fitting experimental VLE data with the PR-MC-WS-NRTL and SRK-MC-PSRK-NRTL models for the C_2H_6 (1) + C_6F_{14} (2) system

Model	Isotherm / K	bias x %	AAD x %	bias y %	AAD y %
objective Function: Flash Calculation					
PR-MC-WS-NRTL	292.89	-0.18	0.98	-0.02	0.03
	303.03	0.09	0.53	0.00	0.08
	308.03	-0.27	1.23	-0.05	0.11
	317.92	-0.44	0.68	0.08	0.12
Model	Isotherm / K	bias P %	AAD P %	bias y %	AAD y %
Objective Function: Ordinary Least Squares					
PR-MC-WS-NRTL	292.89	-0.25	4.35	0.09	0.12
	303.03	0.00	2.20	0.07	0.10
	308.03	0.06	2.81	0.07	0.26
	317.92	-0.06	4.19	0.36	0.35
SRK-MC-PSRK-NRTL	292.89	-0.21	3.82	0.00	0.10
	303.03	0.29	2.74	0.08	0.12
	308.03	0.48	3.15	0.14	0.30
	317.92	0.45	6.14	0.49	0.48

As can be seen from Figures 5.45-5.48, the PR-MC-WS-NRTL (OF: FC or OLS) and the SRK-MC-PSRK-NRTL (OF: OLS) models agree well with the experimental data, except at 308.03K and 317.92 K where the SRK-MC-PSRK-NRTL (OF: OLS) model exhibit slight deviations in both the liquid and vapour phase as the data approach the mixture critical point region.

In addition, the deviations bias U and AAD U reported in Table 5.49 reveal roughly equal values for the two models implying a good fit of the models to the experimental data.

As can be seen from Figure 5.49, the experimental and calculated relative volatility for the PR-MC-WS-NRTL (OF: FC or OLS) and SRK-MC-PSRK-NRTL (OF: OLS) models are also in good agreement. One should note that increasing temperature disfavours the solubility of ethane in perfluorohexane as can be seen through Figures 5.45-5.48. However, for the three temperatures considered no significant influence on the solubility of ethane in perfluorobutane is observed.

5.5.2.12 Methane (1) + perfluorohexane (2) system

The experimental VLE data for the methane (1) + perfluorohexane (2) system were undertaken at five temperatures ranging from (293.39, 298.64, 313.39, 323.41and 333.38) K and are reported in Table 5.50.

The experimental VLE data were modelled using the Peng-Robinson or Soave-Redlich-Kwong EoS incorporating the Mathias-Copeman alpha function and the Wong-Sandler or predictive Soave-Redlich-Kwong mixing rule utilizing the NRTL activity coefficient model and adjusted using either the flash calculation or the ordinary least squares objective function abbreviated as PR-MC-WS-NRTL (OF: FC or OLS) and SRK-MC-PSRK-NRTL (OF: OLS) models. The results obtained from the modelling are graphically compared with the experimental VLE data in Figures 5.50-5.54. The model parameters in temperature-independent and temperature-dependent forms are reported in Tables 5.51 and 5.52, respectively. The relative volatilities which were computed using the PR-MC-WS-NRTL (OF: FC or OLS) and SRK-MC-PSRK-NRTL (OF: OLS) models are graphically compared with the experimental values in Figure 5.55.

Table 5.50: Experimental VLE data for the methane (1) + perfluorohexane (2) system

T / K = 293.39						
P / MPa	n_x	x_1	δx_1	n_y	y_1	δy_1
0.403	5	0.018	0.0003	6	0.921	0.0029
0.704	5	0.039	0.0002	5	0.959	0.0044
1.000	5	0.059	0.0003	5	0.970	0.0018
1.378	6	0.080	0.0006	6	0.978	0.0010
1.889	6	0.109	0.0004	5	0.982	0.0002
2.500	5	0.143	0.0008	5	0.984	0.0005
3.163	5	0.178	0.0005	5	0.986	0.0002
3.766	5	0.209	0.0006	5	0.987	0.0001
4.322	5	0.236	0.0006	5	0.988	0.0001
4.864	5	0.261	0.0001	5	0.988	0.0000
5.529	5	0.291	0.0010	5	0.987	0.0001
6.292	5	0.321	0.0018	5	0.987	0.0002
T / K = 313.39						
P / MPa	n_x	x_1	δx_1	n_y	y_1	δy_1
0.434	5	0.015	0.0001	5	0.815	0.0024
0.752	5	0.032	0.0001	5	0.895	0.0006
1.057	6	0.048	0.0006	6	0.935	0.0006
1.459	5	0.074	0.0006	6	0.948	0.0015
1.985	5	0.103	0.0005	5	0.957	0.0014
2.622	5	0.135	0.0003	5	0.974	0.0001
3.335	5	0.171	0.0010	5	0.973	0.0001
3.943	5	0.201	0.0005	5	0.975	0.0001
4.520	5	0.228	0.0009	5	0.976	0.0002
5.072	5	0.252	0.0016	5	0.975	0.0002
5.742	5	0.282	0.0006	5	0.975	0.0002
6.463	5	0.314	0.0024	5	0.975	0.0004

Table 5.50: Continued

T / K = 303.39						
P / MPa	n_x	x_1	δx_1	n_y	y_1	δy_1
0.416	6	0.015	0.0003	5	0.870	0.0009
0.723	5	0.034	0.0000	5	0.918	0.0049
1.031	6	0.053	0.0001	6	0.956	0.0005
1.417	6	0.074	0.0003	5	0.964	0.0009
1.937	5	0.101	0.0004	5	0.974	0.0003
2.556	5	0.134	0.0034	5	0.978	0.0001
3.263	6	0.172	0.0005	5	0.979	0.0003
3.853	5	0.201	0.0006	5	0.982	0.0002
4.424	5	0.228	0.0020	5	0.982	0.0002
4.970	5	0.255	0.0004	5	0.982	0.0001
5.634	5	0.284	0.0007	5	0.981	0.0002
6.409	5	0.321	0.0009	5	0.982	0.0003
T / K = 323.41						
P / MPa	n_x	x_1	δx_1	n_y	y_1	δy_1
0.457	5	0.015	0.0002	5	0.735	0.0017
0.785	5	0.030	0.0001	5	0.871	0.0003
1.089	6	0.050	0.0002	5	0.908	0.0011
1.503	6	0.072	0.0003	5	0.934	0.0009
2.088	6	0.105	0.0036	5	0.949	0.0018
2.689	5	0.135	0.0003	5	0.957	0.0001
3.423	5	0.171	0.0004	5	0.959	0.0012
4.032	5	0.201	0.0004	5	0.966	0.0004
4.616	5	0.228	0.0004	5	0.966	0.0001
5.171	5	0.252	0.0007	5	0.967	0.0003
5.845	5	0.282	0.0006	5	0.967	0.0002
6.561	5	0.311	0.0064	5	0.966	0.0004

Table 5.50: Continued

T / K = 333.38						
P / MPa	n_x	x_1	δx_1	n_y	y_1	δy_1
0.484	5	0.014	0.0001	5	0.253	0.0019
1.134	6	0.050	0.0002	5	0.674	0.0025
2.096	6	0.103	0.0008	6	0.925	0.0003
2.770	5	0.136	0.0007	5	0.940	0.0001
3.512	5	0.172	0.0006	5	0.949	0.0001
4.114	5	0.201	0.0010	5	0.954	0.0006
4.701	5	0.227	0.0016	5	0.955	0.0003
5.278	5	0.253	0.0007	5	0.956	0.0002
5.964	5	0.283	0.0007	5	0.956	0.0001
6.669	5	0.313	0.0023	5	0.955	0.0006

x_1, y_1: liquid and vapour mole fraction; n_x, n_y : number of samples taken; δx_1, δy_1: standard deviation for x_1 and y_1.

Expanded uncertainty: $u\ (T, k = 2)$ = 0.04 K; $u\ (P, k = 2)$ = 2.50 kPa; u (x_1, k = 2) = 0.02 and u (y_1, k = 2) = 0.03.

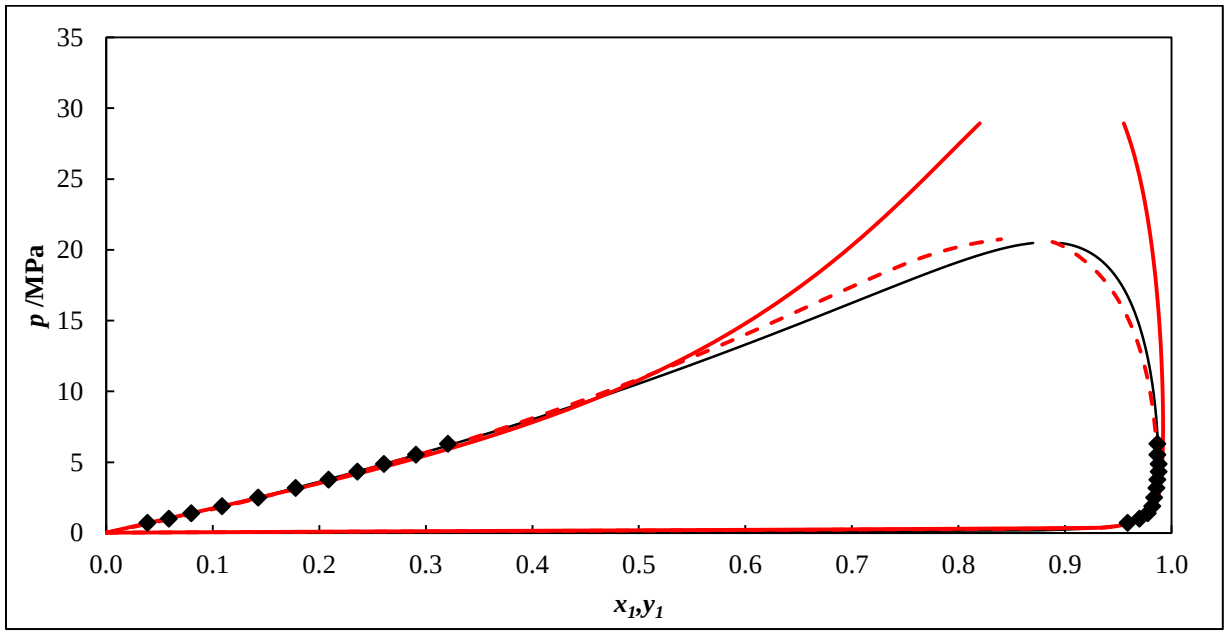

Figure 5.50: Phase diagrams (*P*-*x*-*y*) for the methane (1) + perfluorohexane (2) system. Experimental VLE data: ♦, 293.39 K. Models: PR-MC-WS-NRTL (OF: FC) (solid black line); SRK-MC-PSRK-NRTL (OF: OLS) (dashed red line) and PR-MC-WS-NRTL (OF: OLS) (solid red line).

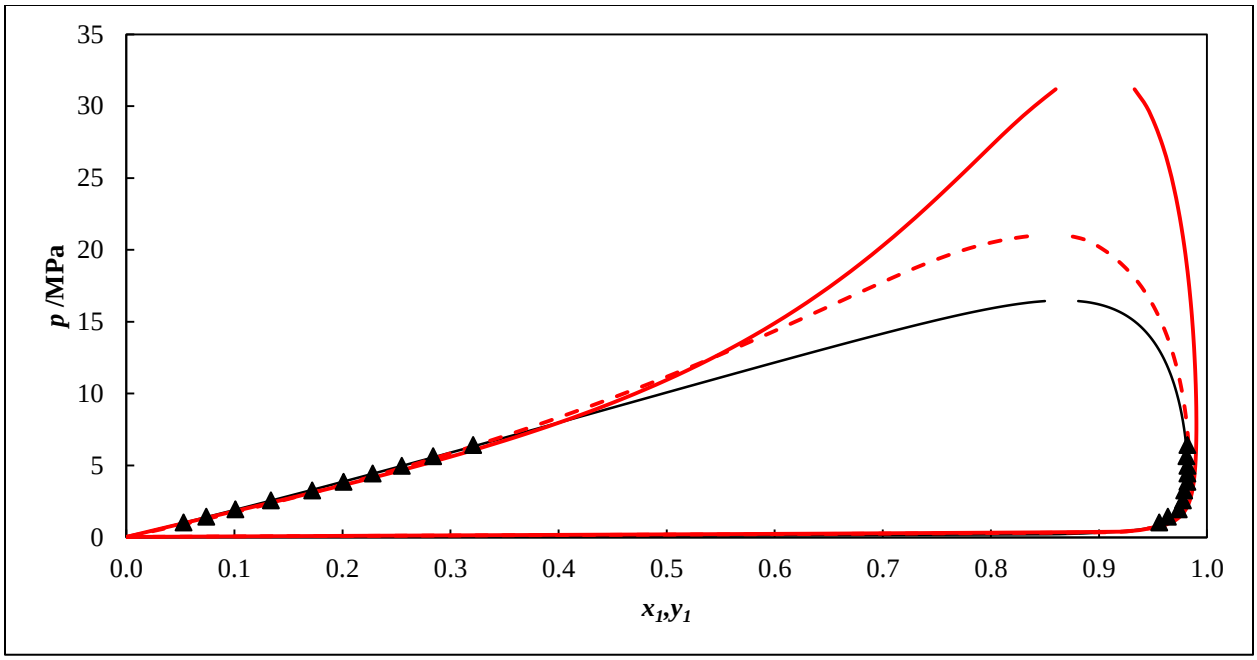

Figure 5.51: Phase diagrams (*P-x-y*) for the methane (1) + perfluorohexane (2) system. Experimental VLE data: ▲, 298.64 K. Models: PR-MC-WS-NRTL (OF: FC) (solid black line); SRK-MC-PSRK-NRTL (OF: OLS) (dashed red line) and PR-MC-WS-NRTL (OF: OLS) (solid red line).

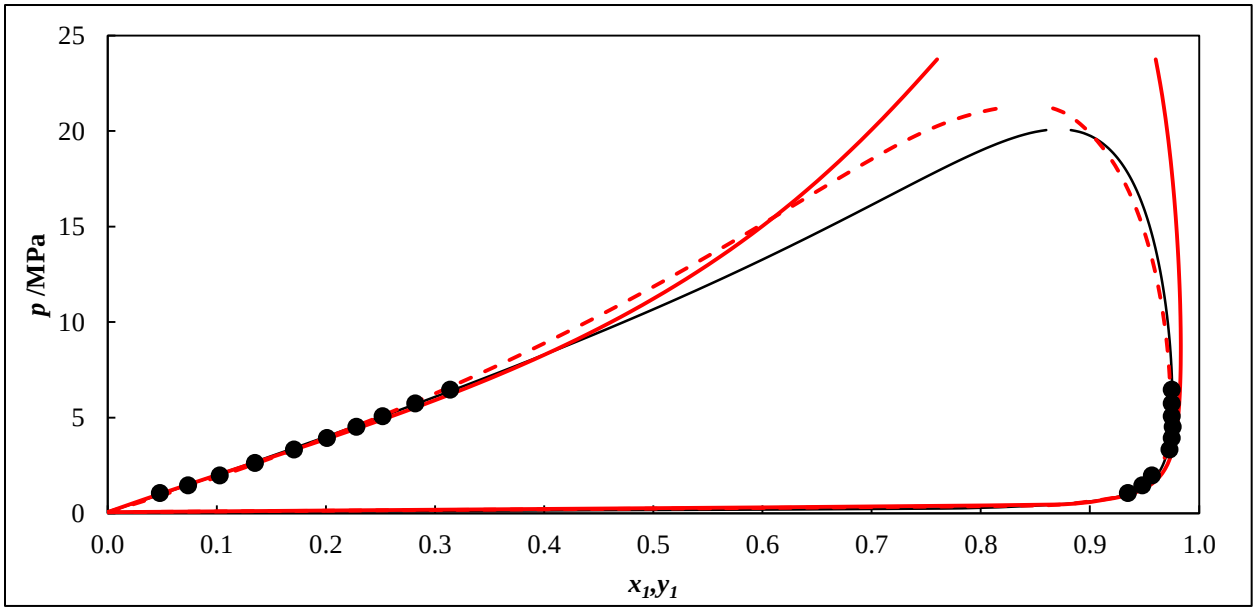

Figure 5.52: Phase diagrams (*P-x-y*) for the perfluorohexane (1) + methane (2) system. Experimental VLE data: ●, 313.39 K. Models: PR-MC-WS-NRTL (OF: FC) (solid black line); SRK-MC-PSRK-NRTL (OF: OLS) (dashed red line) and PR-MC-WS-NRTL (OF: OLS) (solid red line).

.

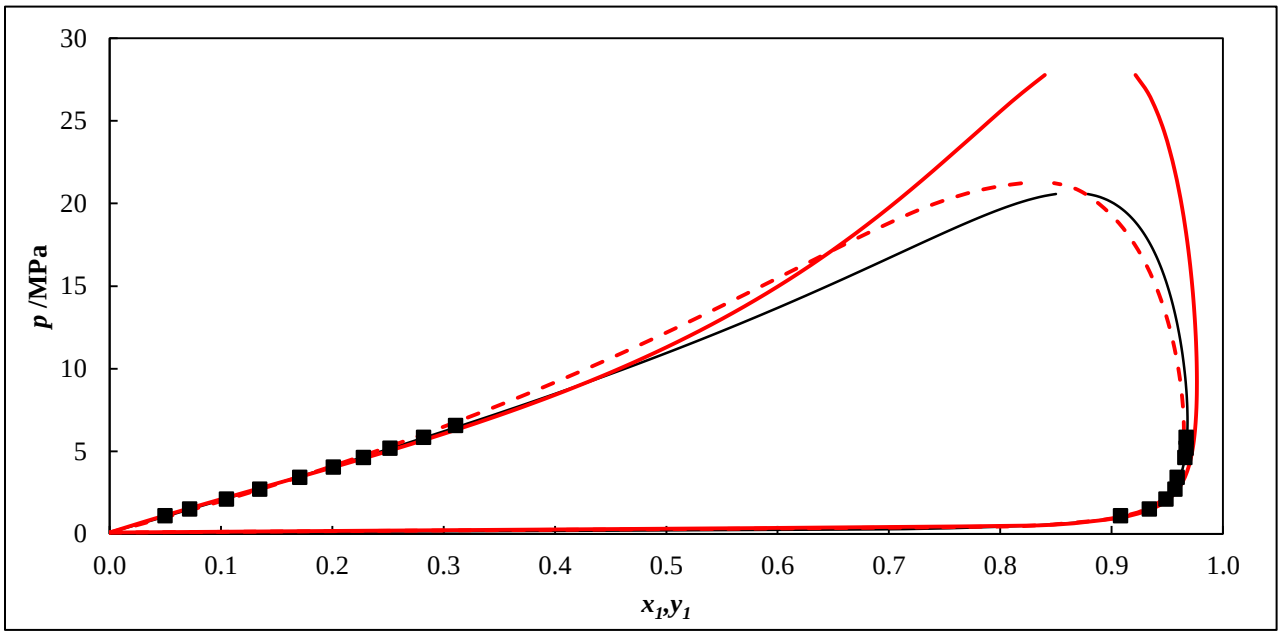

Figure 5.53: Phase diagrams (*P-x-y*) for the methane (1) + perfluorohexane (2) system. Experimental data ■, 323.41 K. Models: PR-MC-WS-NRTL (OF: FC) (solid black line); SRK-MC-PSRK-NRTL (OF: OLS) (dashed red line) and PR-MC-WS-NRTL (OF: OLS) (solid red line).

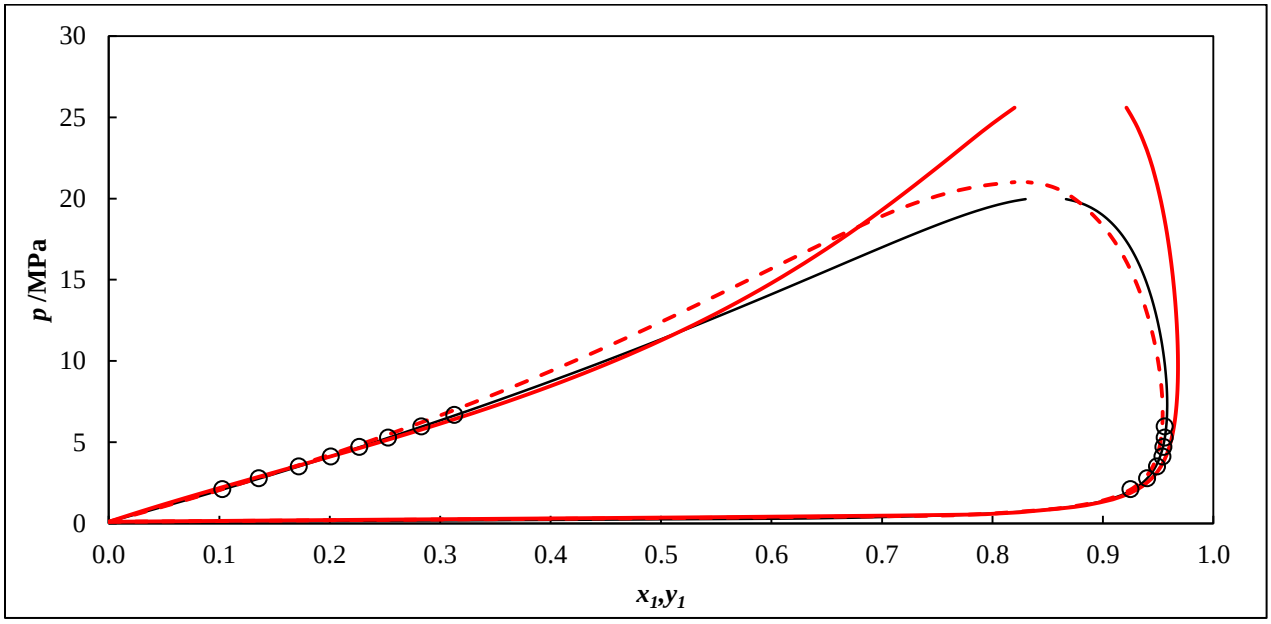

Figure 5.54: Phase diagrams (*P-x-y*) for the perfluorohexane (1) + methane (2) system. Experimental data: □, 333.38 K. Models: PR-MC-WS-NRTL (OF: FC) (solid black line); SRK-MC-PSRK-NRTL (OF: OLS) (dashed red line) and PR-MC-WS-NRTL (OF: OLS) (solid red line).

Table 5.51: Model parameters for the PR-MC-WS-NRTL and SRK-MC-PSRK-NRTL models in a temperature-independent form for the CH_4 (1) + C_6F_{14} (2) system

Model	Isotherm /K	$(g_{12} - g_{22})^a$/J.mol^{-1}	$(g_{21} - g_{11})^a$/J.mol^{-1}	$k_{ij}{}^b$
	objective function: flash calculation			
PR-MC-WS-NRTL	293.39	4385.6	-1804.9	0.76
	298.64	3702.3	-1124.5	0.72
	313.39	1783.6	-355.92	0.78
	323.41	1348.9	-142.15	0.79
	333.38	3419.8	-1574.6	0.80
Model	Isotherm /K	$\tau_{12}{}^c$	$\tau_{21}{}^c$	$k_{ij}{}^d$
	objective function: ordinary least squares			
PR-MC-WS-NRTL	293.39	-0.7742	3.4748	0.82
	298.64	-1.1157	4.0274	0.80
	313.39	-1.6458	4.5789	0.86
	323.41	-1.6458	4.5201	0.86
	333.38	-1.6458	4.4434	0.87
SRK-MC-PSRK-NRTL	293.39	0.0585	-0.5103	—
	298.64	0.0089	-0.4163	—
	313.39	0.0892	-0.5067	—
	323.41	0.1277	-0.5468	—
	333.38	0.1829	-0.6183	—

[a] NRTL model parameters obtained from THERMOPACK, $\Delta g_{ij} = a_{ij}$.

[b, d] WS mixing rule parameter incorporated into the PR EoS correlated from THERMOPACK and Aspen Plus, respectively.

[c] NRTL model parameters obtained from Aspen Plus, $\tau_{ij} = a_{ij}$.

Table 5.52: Model parameters for the PR-MC-WS-NRTL and SRK-MC-PSRK-NRTL models in a temperature-dependent form for the CH_4 (1) + C_6F_{14} (2) system

Model	$(g_{12} - g_{22})^a$/J.mol-1.K		$(g_{21} - g_{11})^a$/J.mol-1.K		$k_{ij}{}^b$
	a_{12}	b_{12}	a_{21}	b_{21}	
objective function: flash calculation					
PR-MC-WS-NRTL	-14118	65.327	1665.5	-7.6540	0.79
	$\tau_{12}{}^c$ / K		$\tau_{21}{}^c$ / K		
objective function: ordinary least squares					
PR-MC-WS-NRTL	265.41		-928.06		0.87
SRK-MC-PSRK-NRTL	297.93		-247.68		—

[a] NRTL model parameters obtained from THERMOPACK, $\Delta g_{ij} = a_{ij} + b_{ij}.T$

[b, d] WS mixing rule parameter incorporated into the PR EoS correlated from THERMOPACK and Aspen Plus, respectively.

[c] NRTL model parameters obtained from Aspen Plus, $\tau_{ij} = b_{ij}/T$

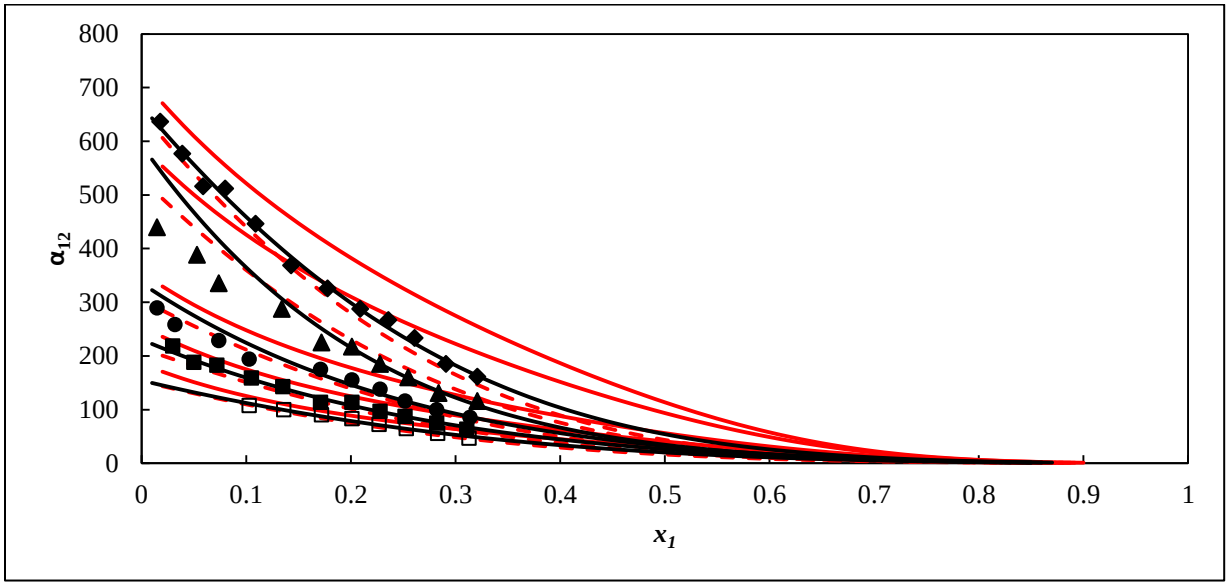

Figure 5.55: Plot of relative volatilities (α_{ij}) for the CH_4 (1) + C_6F_{14} (2) system. Experimental data: ♦, 293.39 K; ▲, 298.64 K; ●, 313.39 K; ■, 323.41 K; □, 333.38 K . Models: PR-MC-WS-NRTL (OF: FC) (solid black line); SRK-MC-PSRK-NRTL (OF: OLS) (dashed red line) and PR-MC-WS-NRTL (OF: OLS) (solid red line). Error bands: shown at 10.0 % for experimental data.

Table 5.53: Deviations, Bias U and the AAD obtained in fitting experimental VLE data with the PR-MC-WS-NRTL and SRK-MC-PSRK-NRTL models for the CH_4 (1) + C_6F_{14} (2) system

Model	Isotherm / K	bias x %	AAD x %	bias y %	AAD y %
Objective Function: Flash Calculation					
PR-MC-WS-NRTL	293.39	-0.43	-0.19	0.14	0.22
	298.64	0.25	0.00	0.27	0.23
	313.39	0.07	-0.04	0.23	0.16
	323.41	0.05	-0.03	0.03	0.14
	333.38	-0.39	-0.02	0.13	0.06
Model	Isotherm / K	bias P %	AAD P %	bias y %	AAD y %
Objective Function: Ordinary Least Squares					
PR-MC-WS-NRTL	293.39	0.06	8.26	-0.21	0.21
	298.64	0.20	11.09	-1.06	0.98
	313.39	0.16	10.21	-0.88	0.83
	323.41	0.17	10.50	-1.16	0.96
	333.38	0.48	10.41	-21.90	7.25
SRK-MC-PSRK-NRTL	293.39	-0.19	9.08	0.05	0.09
	298.64	-0.38	19.37	-0.78	0.71
	313.39	-0.22	20.56	-0.06	0.40
	323.41	-0.03	19.85	-0.07	0.48
	333.38	0.46	14.18	-19.44	6.41

The isothermal VLE data measurement for the methane (1) + perfluorohexane (2) system were undertaken at five temperatures but the data points measured for each temperature were not enough to fully cover the corresponding phase diagram envelops. The modelled data graphically presented in Figures 5.50-5.54 reveal that this system has uniform behaviour and does not incorporate any particular characteristic such as an azeotrope. As can be seen through Figures 5.50-5.54, the experimental VLE data and the modelled data show an overall satisfactory agreement except for the PR-MC-WS-NRTL (OF: OLS) model where the modelled data exhibit slight deviations in the vapor phase for all the isotherms measured. The PR-MC-WS-NRTL (OF: FC or OLS) and SRK-MC-PSRK-NRTL (OF: OLS) models disagree for the data predicted to cover the phase envelop for each isotherm. More experimental data are required to confirm the suitability of the three models.

The deviations bias U and AAD U reported in Table 5.53, which quantify the fit of the model to the experimental VLE data, show values less than 0.50 % for the PR-MC-WS-NRTL (OF: FC)

model indicating a better fit to the measured data. The bias U and AAD U values for the PR-MC-WS-NRTL (OF: OLS) and SRK-MC-PSRK-NRTL (OF: OLS) models are similar except for the AAD P values of the latter model which are higher.

Figure 5.55 which graphically compares the experimental and computed relative volatilities also confirms the agreement between the experimental data and the PR-MC-WS-NRTL (OF: FC) and SRK-MC-PSRK-NRTL (OF: OLS) models.

The solubility of methane in perfluorohexane can also be examined through Figures 5.50-5.54, where temperature seems to have no significant effect on solubility for the isotherms measured. However the 298.64 K isotherm graphically shown in Figure 5.51 exhibits a different behaviour, where methane becomes more soluble in perfluorohexane when the binary mixture contains 50 % of both components. This observation reveals that the solubility of methane in perfluorocarbon increases with decreasing temperature.

The mixture critical points for binary systems such as C_4F_{10} + (CO, NO, CH_4, O_2 and N_2) and C_6F_{14} + CO were approximated using extended scaling laws as presented by Ungerer et al (2005). As can be seen throughout the figures representing the VLE data graphically, the mixture critical points obtained are mostly in agreement with the experimental data.

For all the novel binary systems measured in this study, one can see that the two versions of the PR-MC-WS-NRTL models considered have different representations of the experimental VLE data where one version provides better fits to the experimental data as opposed to the other. This is due to the fact the two models employ different objective functions for the regression of VLE data. As mentioned earlier in this chapter, the ordinary least squares (OLS) and the flash type calculation (FC) objective functions were employed. The OLS objective function minimises the sum of squared errors of the *P* and *y* values from the data in order to provide the best fit a best fit whilst the FC objective function minimises the errors of the *x* and *y* values from the VLE data. From all the figures representing the experimental data graphically, it is obvious that the PR-MC-WS-NRTL (OF: FC) model provides better fits to the experimental data than the PR-MC-WS-NRTL (OF: OLS). This is due to the fact that the errors stemming from the *x* and *y* values are generally insignificant as opposed to those from the *P* values.

The modelling results are summarized in Table 5.54. One should note that a rational comparison can only be undertaken between the PR-MC-WS-NRTL (OLS) and SRK-MC-PSRK-NRTL (OLS) models as for these models, the measured date were adjusted using the same objective function which is the ordinary least squares. In addition, the PR-MC-WS-NRTL (OLS) and SRK-MC-PSRK-NRTL (OLS) models were employed in the modelling of all the binary systems measured in study.

Table 5.54: Summary of the modelling results (✓✓very satisfactory, ✓satisfactory and ✖ not satisfactory)

Binary system	PR-MC-WS-NRTL (FC)	PR-MC-WS-NRTL (OLS)	SRK-MC-PSRK-NRTL (OLS)	SRK-MC-MHV1-NRTL (FC)	SRK-MC-MHV2-NRTL (FC)	SRK-MC-HV-NRTL (FC)	PR-SV-WS-NRTL (FC)
$CO + C_4F_{10}$[a]	✓✓	✓✓	✓	n.d	n.d	n.d	✓✓
$NO + C_4F_{10}$	✓✓	✓	n.d	n.d	n.d	n.d	✓✓
$H_2S + C_4F_{10}$[a]	✓✓	✓✓	✓✓	✓✓	n.d	n.d	n.d
$CH_4 + C_4F_{10}$[a]	✓✓	✓	✖	n.d	n.d	n.d	n.d
$N_2 + C_4F_{10}$[a]	✓✓	✓	✓✓	n.d	n.d	n.d	n.d
$O_2 + C_4F_{10}$	✓✓	✓✓	✓	n.d	n.d	n.d	n.d
$H_2 + C_4F_{10}$[a]	n.d	✓	✓✓	n.d	n.d	✓✓	n.d
$H_2S + C_6F_{14}$[a]	n.d	✓	✓	✓✓	✓✓	n.d	n.d
$CO + C_6F_{14}$[a]	✓✓	✓✓	✓	n.d	n.d	n.d	n.d
$C_2H_6 + C_6F_{14}$	✓✓	✓✓	✓✓	n.d	n.d	n.d	n.d
$CH_4 + C_6F_{14}$[a]	✓✓	✓✓	✓✓	n.d	n.d	n.d	n.d

a: binary systems containing flue gas components considered in this study; n.d: not determined.

One should note that the criterion in Table 5.54 is subject to this study and was used to select the best overall model for binary systems containing flue gas components considered for the gas absorption systems using perfluorobutane or perfluorohexane as physical solvents, and thus, for design purpose. In Table 5.54, the model is considered very satisfactory (✓✓) if 80-100% of the experimental data are well represented; satisfactory (✓) if 50-79 % of the experimental data are well represented and not satisfactory (✖) if 0-49 % of the experimental data are well represented. However, the model is not determined (n.d) if it was not selected for modelling. As can be seen from Table 5.54, the overall best model is the PR-MC-WS-NRTL (OF: OLS) model followed by the SRK-MC-PSRK-NRTL (OF: OLS) model. One should note that a comparison could only be

undertaken between the PR-MC-WS-NRTL (OF: OLS) and SRK-MC-PSRK-NRTL (OF: OLS) models as they both adjusted the measured data using the ordinary least squares objective function.

For design purpose, the model (PR-MC-WS-NRTL: OLS) parameters in the temperature-dependent form for all the novel binary systems measured are summarised in Table 5.55.

Table 5.55: Summary of the model (PR-MC-WS-NRTL: OLS) parameters in the temperature-dependent form for all the novel binary systems measured

Binary system	τ_{12} / K	τ_{21} / K	k_{ij}
CO + C_4F_{10}[a]	21179	100.85	0.74
NO + C_4F_{10}	-57.590	115.54	0.65
H_2S + C_4F_{10}[a]	2106.8	671.51	0.50
CH_4 + C_4F_{10}[a]	-92.443	-769.99	0.60
N_2 + C_4F_{10}[a]	-327.91	-228.42	0.73
O_2 + C_4F_{10}	52116	-590.64	0.77
H_2 + C_4F_{10}[a]	3232.9	337.90	0.99
H_2S + C_6F_{14}[a]	-1883.0	1393.3	0.78
CO + C_6F_{14}[a]	774.99	-39.185	0.83
C_2H_6 + C_6F_{14}	-217.02	223.26	0.52
CH_4 + C_6F_{14}[a]	265.41	-928.06	0.87

a: binary systems containing flue gas components considered in this study; n.d: not determined.

Considering the number of the binary systems measured, an in-depth analysis was necessary to understand the behaviour exhibited between the solutes and solvents under investigation. It is worth noting that for all the binary systems measured, increasing the temperature decreased the relative volatility, which means that at higher temperatures where its values (relative volatility) are close or equal to 1, separation between the solutes and solvents considered will not be possible by conventional distillation column unless other methods of separation are considered, i.e., pressure swing distillation, extractive distillation, pervaporation or other membrane methods. One should note that the higher the relative volatility, the greater the degree of separation, i.e., the easier the separation. For a given temperature, i.e., 293.13 K, the relative volatility values for all the binary systems measured are observed to vary significantly. This could be due to the

interactions between the solute and solvent. Hence, the dielectric constant property, which provides an approximate measure of chemical polarity of a component, was investigated. The dielectric constant values of nitrogen, oxygen, hydrogen and methane obtained from Lide (1998) and the calculated relative volatility values for binary systems such as N_2 (1) + C_4F_{10} (2), O_2 (1) + C_4F_{10} (2), H_2 (1) + C_4F_{10} (2) and CH_4 (1) + C_4F_{10} (2) reported in Table 6.56 were compared at temperature and pressure of 300 K and 10 MPa, respectively.

Table 5.56: Dielectric constant versus relative volatility values for some of the flue gas components at 300 K and 10 MPa.

Component	Dielectric constant (D)[a]	α_{12}
Hydrogen	1.023	120.1
Oxygen	1.051	14.56
Nitrogen	1.053	11.46
Methane	1.095	2.654

[a]Values obtained from Lide (1998)

One should note the dielectric constant values of the aforementioned solutes were not available in the open literature at 293.13 K but 300 K. It was found that there was a strong correlation between the relative volatility and the dielectric constant as the solutes with higher constant dielectric values resulted in lower relative volatility values. This is in agreement with the work of Van der Merwe (1994) where a definite strong correlation between the relative volatility and the dielectric constant is indicated. In addition, the dielectric constant values of the 4 components selected ranged from 1.09513 to 1.02315 indicating their nonpolar characteristic. One should note that components with a dielectric constant of less than 15 are generally considered to be nonpolar (Lowry and Richardson, 1987). So, the relationship between the dielectric constant and the relative volatility shows that solutes with lower dielectric constant values can be separated with the C_4F_{10} via conventional distillation methods as opposed to the solutes with higher dielectric constant values. Furthermore, based on the like dissolves like principle, components such as O_2, N_2, H_2 and CH_4 can dissolve easily in C_4F_{10} as they are all nonpolar compounds.

The elongation of the alkyl chain of the PFC was also investigated for a given temperature and solute. The H_2S, CH_4 and CO_2 solutes were considered as they were all mixed with both C_4F_{10}

and C_6F_{14}. For the VLE data measured at 293.15 K, the relative volatilities for the selected solutes in both C_4F_{10} and C_6F_{10} exhibited higher values for the data with C_6F_{14} than C_4F_{14}. One should also note that the longer the alkyl chain of PFC compounds, the bigger the cavity within, the higher the solute absorption. Hence, solutes are highly absorbed in C_6F_{14} than C_4F_{10}. Furthermore, due to the fact that the selected solutes have higher relative volatility values in C_6F_{14} than C_4F_{10}, and they are highly absorbed in C_6F_{14} than C_4F_{10}, this means that the PFC compounds with higher absorption can exhibit easier separation by conventional distillation column as their associated relative volatility values are generally higher.

For a given temperature and PFC compound, the effect of the elongation of the alkyl chain of the solute was analysed. In this study, the two hydrocarbons considered were methane and ethane. At 293.14 K, the relative volatility values for hydrocarbon compounds in C_4F_{10} decrease with the elongation of the carbon chain length. In other words, the elongation of carbon chain in hydrocarbon reveals that the lighter the hydrocarbon, the easier the separation from C_4F_{10} will be. Considering the Henry's Law, which states that the solubility of a solute (gas) in a solvent is directly proportional to the pressure of that gas above the surface of the solution, a comparison between the VLE data for the CH_4 (1) + C_4F_{10} (2) and C_2H_6 + C_4F_{10} systems at approximately 293.15 K shows that high solubility of CH_4 in C_4F_{10} is attained at pressures that are lower than that of C_2H_6 in C_4F_{10}. One should note that the VLE data of El Ahmar et al., (2011) were considered as the VLE data for the C_2H_6 (1) + C_4F_{10} (2) system were not fully measured in this study except for the test system that was measured at 308.24 K. As for the C_4F_{10} solvent, the elongation of the alkyl chain in hydrocarbon has similar effect in C_6F_{14}.

For some of the systems measured such as CO (1) + C_4F_{10} (2), deviations between the models and the experimental data is pronounced at higher temperatures, this could be due to the Mathias-Copeman alpha function which has no thermodynamic background, and if extrapolated to higher temperatures, the vapour pressure curve tend to diverge (Ahlers, 2003). One should note that this observation was undertaken while using the PSRK model incorporating the Mathias-Copeman alpha function for the prediction of VLE data.

5.6 Selectivity of C_4F_{10} or C_6F_{14} for CO_2 relative to CO, H_2S and CH_4 investigated in this study

As mentioned in Chapter 2, selectivity is useful in the preliminary selection of a solvent whereas capacity reveals the quantity of a solvent to be used in a separation process. Thus a solvent with a large capacity will require only a small quantity to be effective if selectivity is high. In this section the selectivity of C_4F_{10} or C_6F_{14} for CO_2 relative to CO, H_2S and CH_4 is discussed using VLE data. The measured and modelled VLE data for the CO (1) + C_4F_{10} (2), H_2S (1) + C_4F_{10} (2) and CH_4 (1) + C_4F_{10} (2) systems are graphically compared with VLE data for the CO_2 (1) + C_4F_{10} (2) system of Valtz et al., (2011) predicted at (293, 313 and 333) K in Figures 5.56-5.58.

For the C_6F_{14} solvent, the measured and modelled data for the CO (1) + C_6F_{14} (2), H_2S (1) + C_6F_{14} (2) and CH_4 (1) + C_6F_{14} (2) systems are graphically compared with VLE data for the CO_2 (1) + C_6F_{14} (2) system of Costa Gomes and Pádua (2003) predicted at (293, 313 and 333) K in Figures 5.59-5.51.

One should note that the VLE data of Valtz et al., (2011) and Costa Gomes and Pádua (2003) were measured at isotherms that did not match any isotherm measured in this study. Consequently, the prediction of new isotherms was undertaken by modelling the measured VLE data to obtain binary interaction parameters in a temperature-independent form.

The comparisons shown in Figures 6.56-58 reveal that C_4F_{10} has a strong selectivity for CO_2 as opposed to CH_4 and CO whereas there is no preference between CO_2 and H_2S at (293, 313 and 333) K. At these temperatures, co-absorption of CO_2 and H_2S can occur unless there is variation in temperature, pressure and solvent concentration. Figure 6.56 shows that at pressure values higher than 5 MPa, C_4F_{10} will selectively absorb H_2S than CO_2. This reinforces the work of Tassios (1969) which acknowledges the effect of temperature, pressure and solvent concentration on the selectivity of a solvent.

As can be seen through Figures 5.58-5.61 which are relative to C_6F_{14}, the same conclusions as for the C_4F_{10} solvent can be drawn. In other words, the variation in the carbon chain length by 2 in the PFCS has no notable impact on the selectivity for CO_2 relative to CO, CH_4 and H_2S.

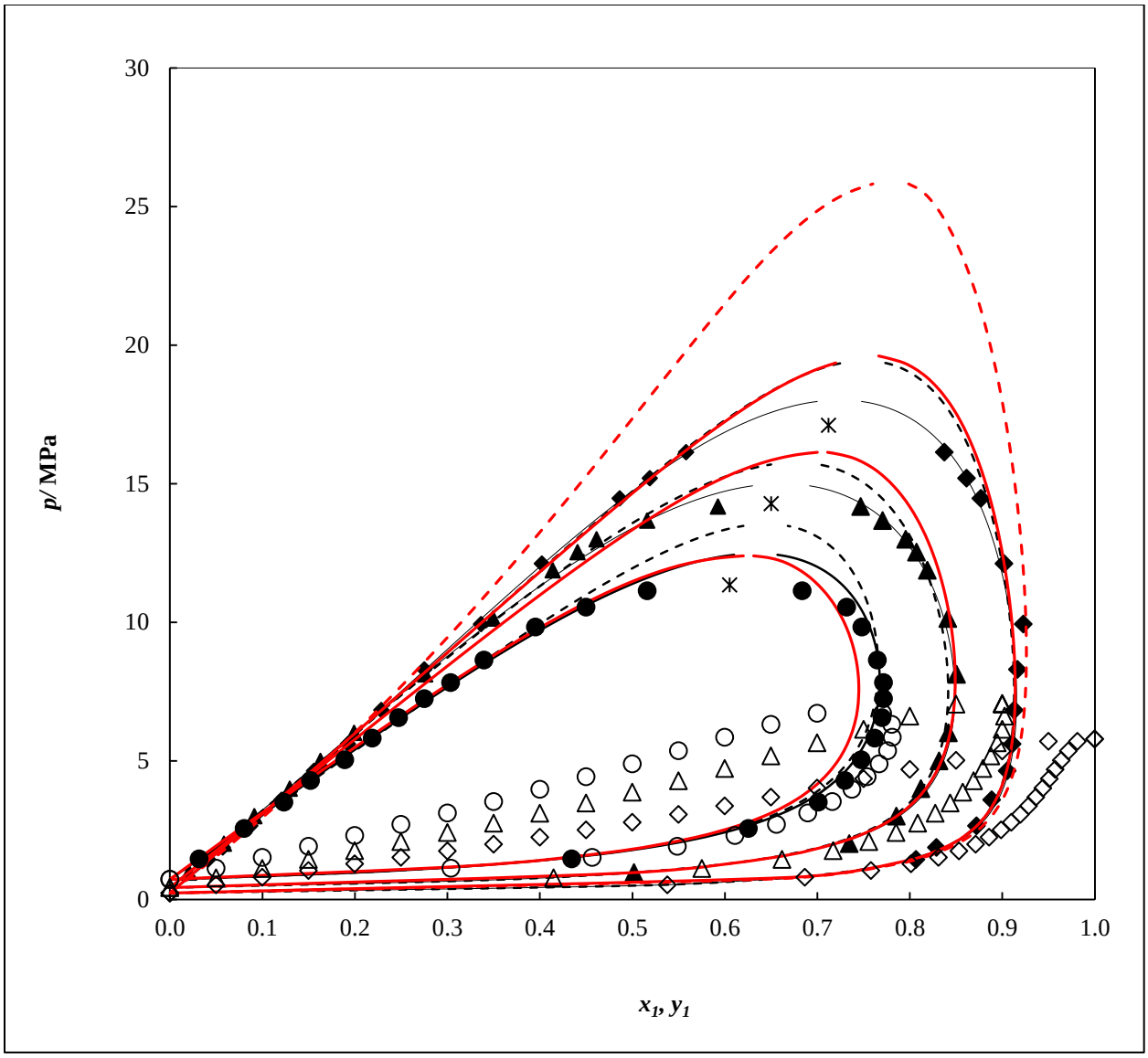

Figure 5.56: Selectivity of C_4F_{10} for CO_2 relative to CO. Phase diagrams (*P*-*x*-*y*) for the CO (1) + C_4F_{10} (2) system. (Experimental: ♦, 293.48 K; ▲, 313.44 K; ●, 333.33 K). Models: PR-MC-WS-NRTL (solid black line); PR-SV-WS-NRTL (dashed black line); SRK-MC-PSRK-NRTL (dashed red line); PR-MC-WS-NRTL (solid red line). VLE data for the CO_2 (1) + C_4F_{10} (2) system of Valtz et al. (2011) predicted at: ◊, 293.48 K; Δ, 313.44 K; ○, 333.33 K. *, mixture critical points.

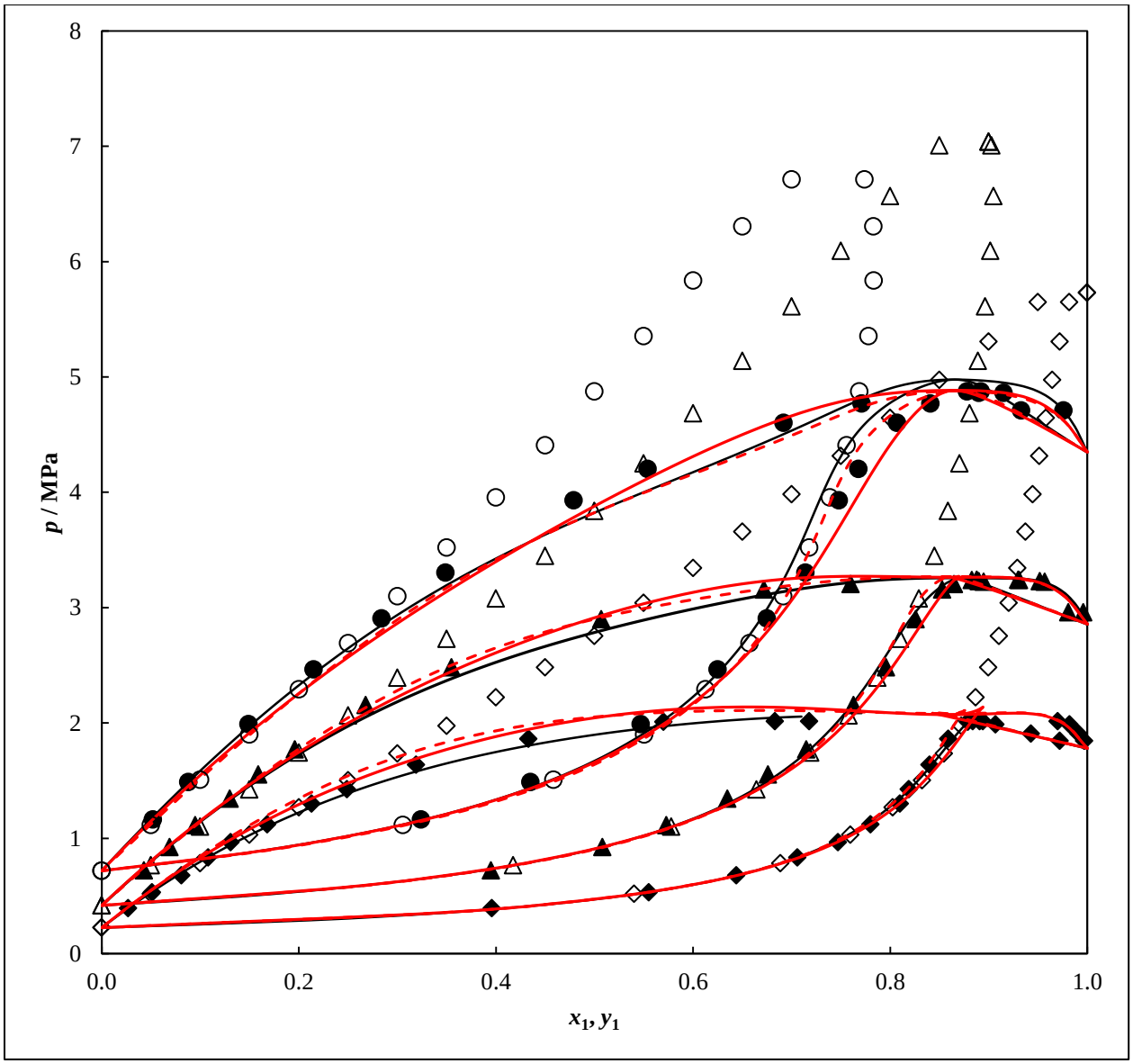

Figure 5.57: Selectivity of C_4F_{10} for CO_2 relative to H_2S. Phase diagrams (*P-x-y*) for the H_2S (1) + C_4F_{10} (2) system. (Experimental: ♦, 293.08 K; ▲, 313.00 K; ●, 333.03 K). Models: SRK-MC-MHV1-NRTL (solid black line); SRK-MC-PSRK-NRTL (dashed red line); PR-MC-WS-NRTL (solid red line). VLE data for the CO_2 (1) + C_4F_{10} (2) system of Valtz et al. (2011) predicted at: ◊, 293.08 K; Δ, 313.00 K; ○, 333.03 K.

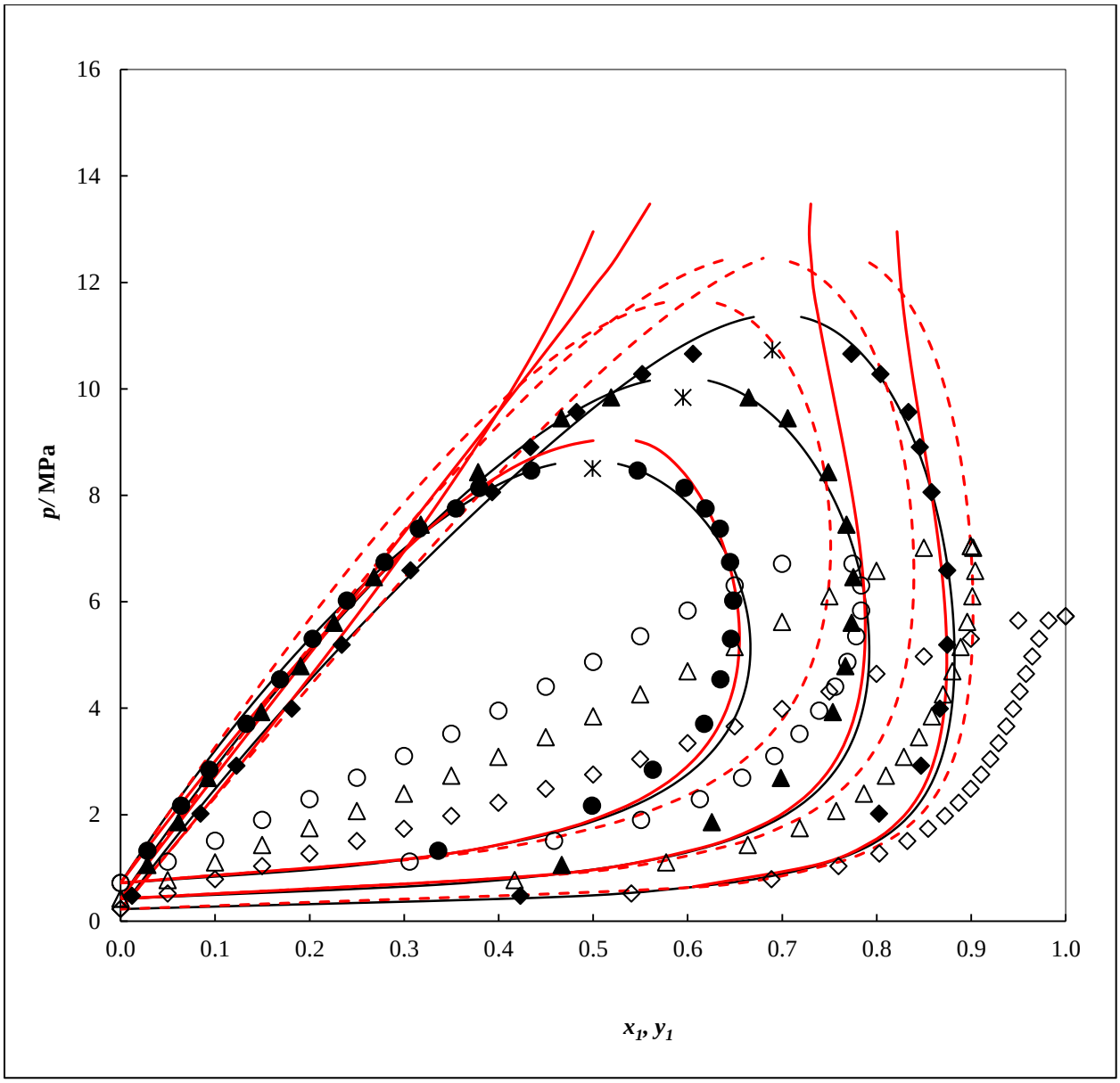

Figure 5.58: Selectivity of C_4F_{10} for CO_2 relative to CH_4. Phase diagrams (*P-x-y*) for the CH_4 (1) + C_4F_{10} (2) system. (Experimental: ♦, 293.05 K; ▲, 313.09 K; ●, 332.97 K). Models: PR-MC-WS-NRTL (OF: FC) (solid black line); SRK-MC-PSRK-NRTL (OF: OLS) (dashed red line); PR-MC-WS-NRTL (OF: OLS) (solid red line). VLE data for the CO_2 (1) + C_4F_{10} (2) system of Valtz et al. (2011) predicted at: ◊, 293.05 K; Δ, 313.09 K; ○, 332.97 K. *, mixture critical points.

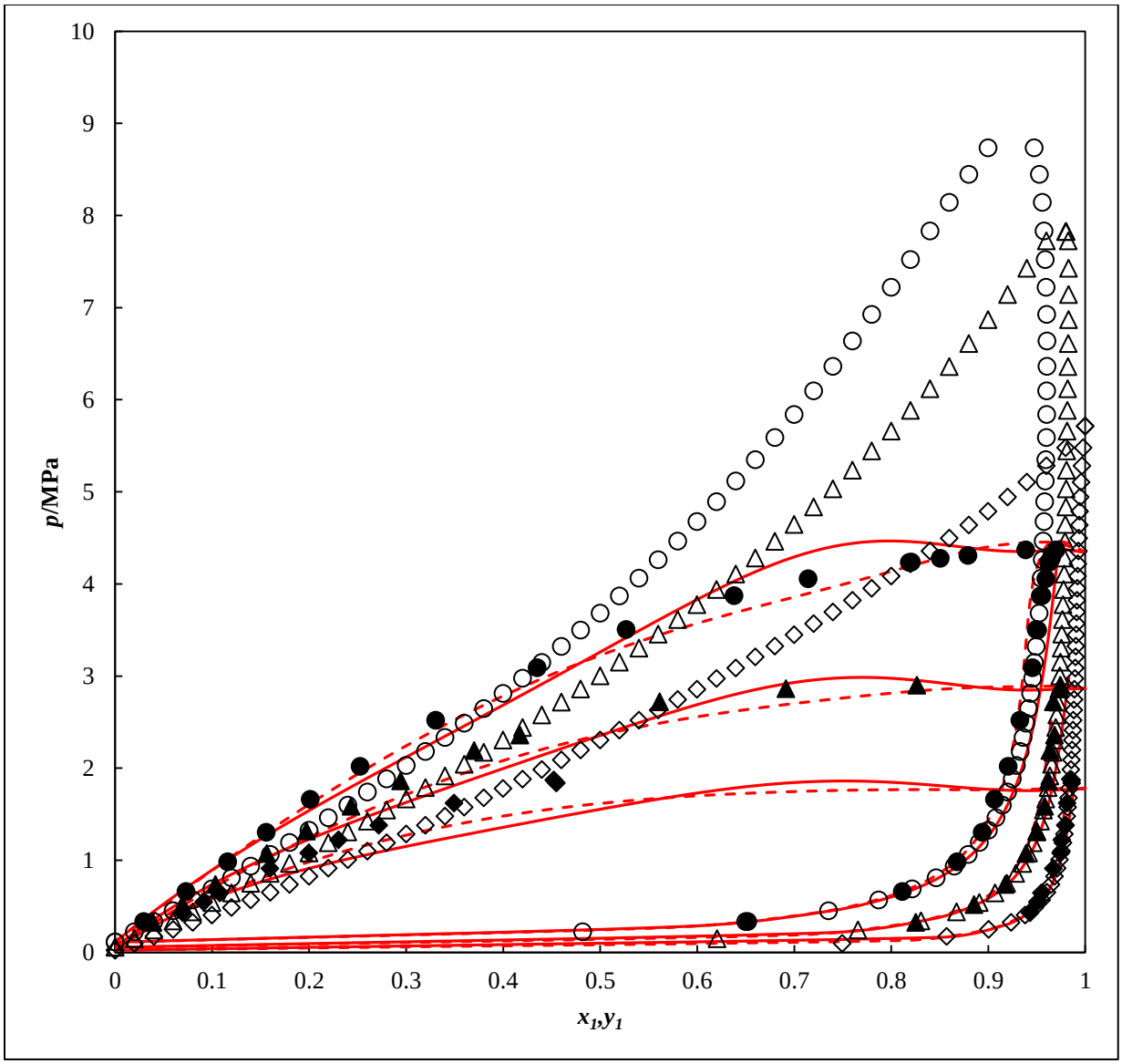

Figure 5.59: Selectivity of C_6F_{14} for CO_2 relative to H_2S. Phase diagrams (*P*-*x*-*y*) for the H_2S (1) + C_6F_{14} (2) system. (Experimental: ♦, 293.03 K; ▲, 313.08 K; ●, 332.96 K). Models: SRK-MC-PSRK-NRTL (dashed red line); PR-MC-WS-NRTL (solid red line). VLE data for the CO_2 (1) + C_4F_{10} (2) system of Costa Gomes and Pádua (2003) predicted at: ◊, 293.03 K; Δ, 313.08 K; ○, 332.96 K.

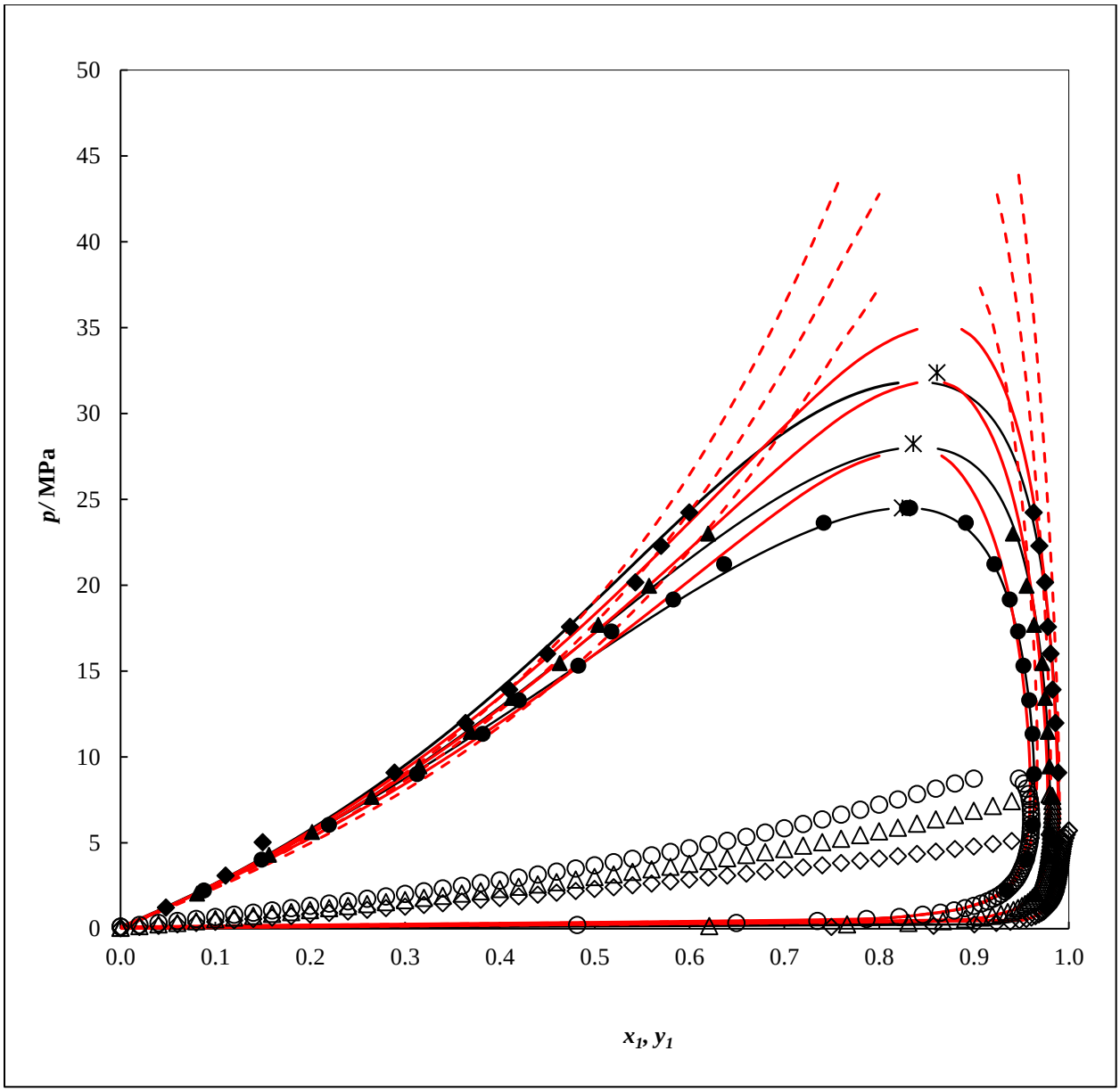

Figure 5.60: Selectivity of C_6F_{14} for CO_2 relative to CO. Phase diagrams (*P-x-y*) for the CO (1) + C_6F_{14} (2) system. (Experimental: ♦, 293.01 K; ▲, 313.04 K; ●, 333.04 K). Models: PR-MC-WS-NRTL (OF: FC) (solid black line); SRK-MC-PSRK-NRTL (OF: OLS) (dashed red line); PR-MC-WS-NRTL (OF: OLS) (solid red line). VLE data for the CO_2 (1) + C_4F_{10} (2) system of Costa Gomes and Pádua (2003) predicted at: ◊, 293.01 K; Δ, 313.04 K; ○, 333.04 K. *, mixture critical point.

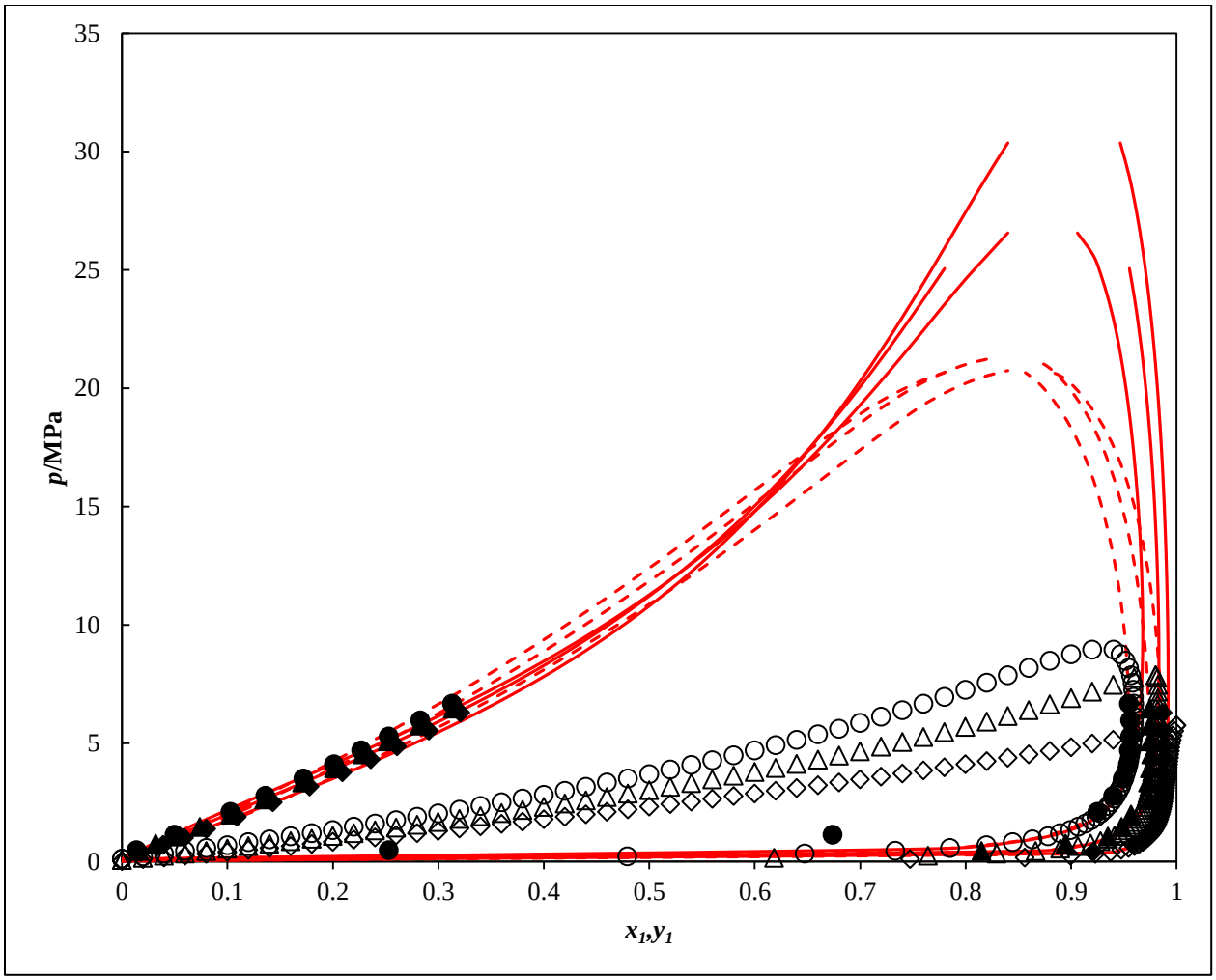

Figure 5.61: Selectivity of C_6F_{14} for CO_2 relative to CH_4. Phase diagrams (*P-x-y)* for the CH_4 (1) + C_6F_{14} (2) system. (Experimental: ♦, 293.01 K; ▲, 313.04 K; ●, 333.04 K). Models: SRK-MC-PSRK-NRTL (OF: OLS) (dashed red line); PR-MC-WS-NRTL (OF: OLS) (solid red line). VLE data for the CO_2 (1) + C_4F_{10} (2) system of Costa Gomes and Pádua (2003) predicted at: ◊, 293.01 K; Δ, 313.04 K; ○, 333.04 K.

6

CHAPTER SIX

DESIGN OF GAS ABSORPTION SYSTEMS USING PERFLUOROCARBONS AS PHYSICAL SOLVENTS

6.1 Introduction

Design is a creative activity and arguably the most rewarding and satisfying activity undertaken by an engineer. It involves the synthesis of ideas to achieve a desired purpose (Sinnott, 2005). The designer starts with a specific objective in mind and through exploring possible means to this end, he finds the best way to achieve the desired purpose. This conception finds applications in multiple engineering disciplines including electrical, chemical, mechanical, civil, etc.

Luyben (2006) states that there are basically three distinct steps in developing a successful process design. The first step is conceptual design, in which simple approximate methods are used to develop a preliminary flowsheet. The next step is preliminary design, in which rigorous simulation methods are used to evaluate both steady-state and dynamic performance of the proposed flowsheet. The final step is the detailed design, in which the hardware is specified in great detail such as types of trays, number of sieve tray holes, feed and reflux piping, pumps, heat exchanger areas, and valve sizes. One should note that conceptual and preliminary designs have the same meaning in some literature sources and are used interchangeably. In this study, only the definition given by Luyben (2006) will be considered.

One should note that the design of gas absorption systems using C_4F_{10} and C_6F_{14} as physical solvents is undertaken for illustration purpose using the results obtained from the measurements

and thermodynamic modelling of VLE data presented in Chapter 5. This is due to the fact that C_4F_{10} and C_6F_{14} do not meet the 'ideal solvent' criteria but they were the only two perfluorocarbons available during the period of this study. Hence, VLE data measurement for C_4F_{10} and C_6F_{14} with flue gas components such as CO_2, H_2S, CH_4, CO etc. was undertaken in this study.

As explained in Chapter 2, a gas absorption system is composed of an absorption section and a stripping section. One should note that the absorption capability of a solvent in terms of its capacity and selectivity for components of interest is determined in the absorption column.

In this study, the absorption capability of perfluorocarbons for flue gas in terms of their selectivity and capacity for CO_2, H_2S, CH_4 and CO will be firstly determined followed by a stripping section to complete the gas absorption system.

Given that VLE data for some of the binary systems were obtained using predictive models, a preliminary design was first undertaken. This approach is encouraged by Prausnitz et al., (1999), as predictive models, such as group contribution methods, only produce approximate VLE data. Hence, Praustnitz advised that predicted VLE data be used only for a preliminary design. In addition, he recommended that only accurate experimental data be used in order undertake a detailed design.

A preliminary design provides a connection between the conceptual design and the detailed design phase. In this task, the overall system configuration is defined, thereby laying a solid foundation upon which to build a project.

In this case, the conceptual design, upon which the preliminary design is based, consisted mainly of identifying the essential problems pertaining to gas absorption systems, searching for solutions and finally drawing a preliminary flowsheet. One should note that the conceptual design was principally achieved by means of screening potential process flow diagrams, and selecting key variables that could be judged on the basis of engineering experience and relevant literature.

Aspen Plus® V8.0 was used to design the gas absorption systems using perfluorobutane and perfluorohexane as physical solvents. In Aspen Plus®, one has to select an appropriate physical property method, which is generally a combination of thermodynamic models, such as a cubic equation of state incorporating an alpha function, with a mixing rule utilizing an activity coefficient model. Factors that are essential in selecting appropriate physical property methods are discussed in Chapter 3. The selection of appropriate physical property methods is crucial. If not done correctly, all subsequent tasks will be affected. One should note that no single property method can handle all systems and therefore there is generally a compromise in choosing the best property method for design purposes.

As can be seen from Chapter 5, the PR-MC-WS-NRTL (OF: OLS) model was chosen as the best model to represent all of the binary systems under investigation. The PR-MC-WS-NRTL (OF: OLS) model can be incorporated into Aspen Plus via the PRWS property method, which, by default, uses the Peng-Robinson (PR) EoS, incorporating the Schwartzentruber-Renon-Watanasiri (SRW) alpha function and the Wong-Sandler (PSRK) mixing rule, utilizing the UNIFAC activity coefficient model. However, the PRWS property method was modified by substituting the alpha function and activity coefficient model by Mathias-Copeman (MC) and non-random two-liquid (NRTL) model, respectively, abbreviated as PR-MC-WS-NRTL model. This property method was used for the design of the gas absorption system using both the perfluorobutane and perfluorohexane solvents.

In order to fully describe the gas absorption systems using either the perfluorobutane or perfluorohexane as physical solvents, VLE data for binary systems that could not be measured were predicted in Aspen Plus®. The predictive Soave-Redlich-Kwong (PSRK) property method was used, incorporating either the Conduct-like Screening Model - Segment Activity Coefficient (COSMO-SAC) or Dortmund modified UNIversal Functional Activity Coefficient (UNIFAC) models. One should note that sigma profiles used in the COSMO-SAC model were taken from the consortium version of the Dortmund Data Bank. The two selected predictive models were validated, in Chapter 3, using the VLE data measured for the CO_2 with C_4F_{10} or C_6F_{14} of Valtz et al., (2011). The predicted data were thereafter modelled via the direct method using the PR-MC-WS-NRTL model, in order to obtain their corresponding binary parameters. VLE data were predicted for the following binary systems:

- Argon + perfluorobutane (using Dortmund modified UNIFAC)
- Ammonia + perfluorobutane (using PSRK/COSMO-SAC)
- Water vapour + perfluorobutane (using Dortmund modified UNIFAC)
- Argon + perfluorohexane (Dortmund modified UNIFAC)
- Ammonia + perfluorohexane (using PSRK/COSMO-SAC)
- Water vapour + perfluorohexane (using Dortmund modified UNIFAC)
- Hydrogen + perfluorohexane (using PSRK/COSMO-SAC)
- Nitrogen + perfluorohexane (using PSRK/COSMO-SAC)

The graphical representations of the predicted and correlated data are available in Appendix F.

Once the physical property method was selected and the binary interaction parameters obtained, the design for a gas absorption system could commence. As discussed in the literature review in Chapter 2, most of the gas absorption systems using physical solvents include an absorption column (where the absorption capability of a solvent is determined) coupled with either a series of flash drums, or a stripping column, or a combination of both. The addition of a stripper to the gas absorption system is essential when the recycled solvent still contains significant amounts of the flue gas components. The recycled solvent should not normally contain flue gas content although trace impurities are generally acceptable.

To complete the gas absorption systems, three solvent regeneration methods were considered and their respective advantages and disadvantages are discussed based on the results obtained.

6.2 Preliminary design of a gas absorption system using perfluorobutane (C_4F_{10}) or perfluorohexane (C_6F_{14}) as physical solvents

The aim of the preliminary scheme was to design gas absorption systems geared for the use of C_4F_{10} and C_6F_{14} as physical solvents for selective removal of CO_2, H_2S, CH_4 and CO from the flue gas components emanating from the gasification of Illinois No. 6 are reported in Table 2.2 of Chapter 2. This flue gas was chosen for the experiments because it is available at high pressure, and is therefore suitable for the application of a physical absorption process.

The emission targets for gas treating in major industrial processes can be found in Cussler (1984). In a coal gas process, the following emission targets have been set for CO_2 and H_2S as <500 ppm and <0.01 ppm, respectively.

These emission targets should be considered in relation to the IPCC synthesis report on climate change of 2014, which notes that emissions scenarios leading to CO_2 concentration of 450 ppm by the year 2100 or lower can maintain the average global temperature below 2°C, over the 21st century, relative to pre-industrial levels. But Hansen and Sato (2012) suggest 350 ppm, warning that concentrations of CO_2 above this, is dangerous. To the best of our knowledge no restrictions have yet been set for CH_4 and CO. In light of the above, in this study, the emission targets for CO_2 and H_2S are set as 450 ppm and <0.01 ppm, respectively. However, emissions of CO_2 and H_2S in trace amounts will be acceptable. For CH_4 and CO, a 50 % emission reduction target has been set.

6.2.1 Absorption column section

The RadFrac column model, using the equilibrium method, was chosen for the design of the absorption columns. This model is rigorous for simulating all types of multistage vapour-liquid fractionation. It is suitable for three phase systems, narrow and wide-boiling systems, and systems exhibiting strong liquid non-ideality. In addition, RadFrac can detect and handle a free-water phase, or other second liquid phase, anywhere inside the column.

To design the absorber for a gas absorption system, one has to determine the number of stages, the temperatures of both the entering streams (the flue gas and the solvent), and the operating pressure.

The operating conditions for gas absorption systems of the flue gas from the gasification of Illinois No. 6 bituminous coal using current commercial physical solvents (DEPG, NMP and PC) available in Aspen Plus® V8.0 were considered as a starting point in this study. The operating conditions in Aspen Plus® V8.0 are summarised in Table 6.1.

The DEPG, NMP and PC data on vapour pressure, liquid density, viscosity, surface tension and thermal conductivity were used to determine the thermophysical property and transport property models. For the remaining components, the thermophysical property models were validated

using the DIPPR (Design Institute for Physical Property Data) correlations, available in Aspen Plus, for the component vapour pressure and liquid density. The property method used was the PC-SAFT (Perturbed Chain Statistical Association Fluid Theory) equation of state (Gross and Sadowski, 2001).

Table 6.1 Operating conditions for gas absorptions using current commercial physical solvents (DEPG, NMP and PC) available in Aspen Plus® V8.0

	Flue gas conditions			Solvent conditions			
Solvent	T (K)	P (MPa)	flow rate (kmol/h)	T (K)	P (MPa)	flow rate (kmol/h)	No Stage
DEPG	293.24	6.789	7990.0	272.04	6.890	3182.2	10
NMP	293.22	1.621	7990.0	272.04	1.723	10612	12
PC	293.22	1.621	7990.0	272.04	1.723	10612	12

As can be seen from Table 6.1, the pressure values for both the NMP and PC processes are lower than that of the DEPG process. To facilitate comparisons between the solvents, their pressure and flow rate values were adjusted to be equal to that of the DEPG process. As mentioned in Chapter 2, physical absorption is favoured when the partial pressure of the flue gas of interest is high.

Figure 6.1 illustrates a simple absorption process which was used to compare the absorption capability of all the solvents investigated in this study. One should note that the absorption capability of a solvent is referred to the amount of the targeted gases that a solvent is able to absorb as well as its selectivity for the targeted gas as opposed to the other flue gas component. In this absorption process, the outlet streams are one vapour phase and one liquid phase denoted as ABS-GAS and ABS-LIQ, respectively.

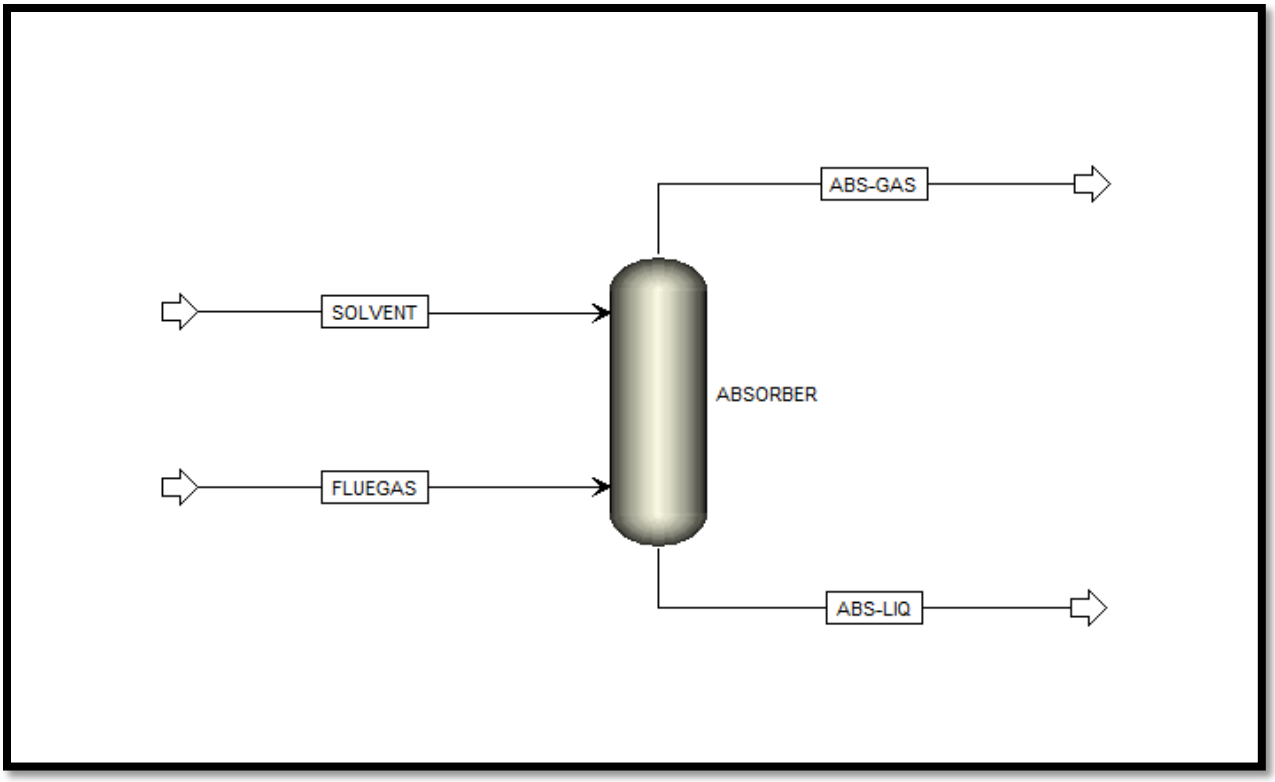

Figure 6.1: Absorption process using Aspen Plus

At the adjusted operating conditions, the results obtained reveal that 82.58 %, 38.74 % and 33.00 % of CO_2 is absorbed in the DEPG, NMP and PC solvent processes, respectively, which corresponds to 395.00 kmol/h, 1599.0 kmol/h and 1371.0 kmol/h of CO_2 emitted into the atmosphere. CH_4 is poorly absorbed in all the three solvents with more than 90 % emitted into the atmosphere, whereas H_2S is fully absorbed in the DEPG and NMP solvent processes, with their trace amounts emitted into the atmosphere. In the PC solvent process, 4.95 % of H_2S is emitted into the atmosphere which corresponds to 0.010 kmol/h. It is obvious from the results obtained that the gas absorption systems using the adjusted operating conditions do not meet the emission targets of 450 ppm for CO_2, 0.01 ppm for H_2S and 50 % emission reduction of $CH_4$and CO.

Consequently, sensitivity analysis was necessary to verify if the solution to meeting the design targets lay within the range of the manipulated variables such as the number of stages, solvent flow rate and temperature of the current commercial physical solvents. The optimum parameters obtained for each commercial physical solvent were thereafter used in the gas absorption system

based on the C_4F_{10} solvent. One should note that the benchmarking between the PFC solvents and the commercial physical solvents will be undertaken individually as they have different characteristics.

6.2.1.1 Dimethyl Ether of Polyethylene Glycol versus perfluorobutane (C_4F_{10}) or perfluorohexane (C_6F_{14}) solvents

A sensitivity analysis was firstly undertaken for the number of stages, while keeping the flow rate and temperature of the solvent constant. One should note that the flue gas conditions were kept constant throughout all the simulations. The results obtained for the sensitivity analysis, based on the number of stages, are presented in Figure 6.2 (a, b and c), where the number of stages range from 6 to 20.

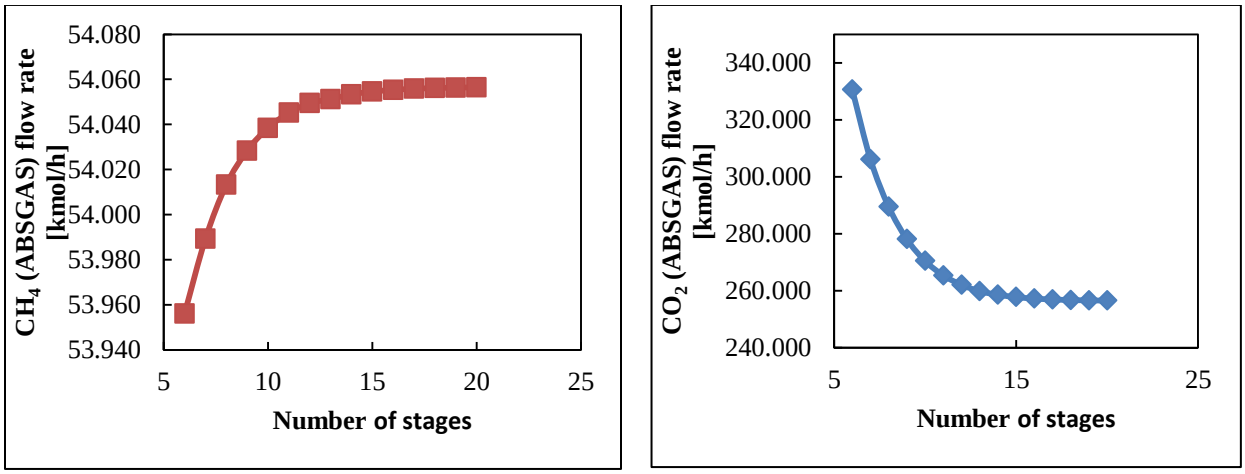

Figure 6.2 (a): Sensitivity analysis relative to the number of stages versus the amount in [kmol/h] of CH_4 (left) and CO_2 (right) emitted into the atmosphere via the ABSGAS stream for the DEPG process.

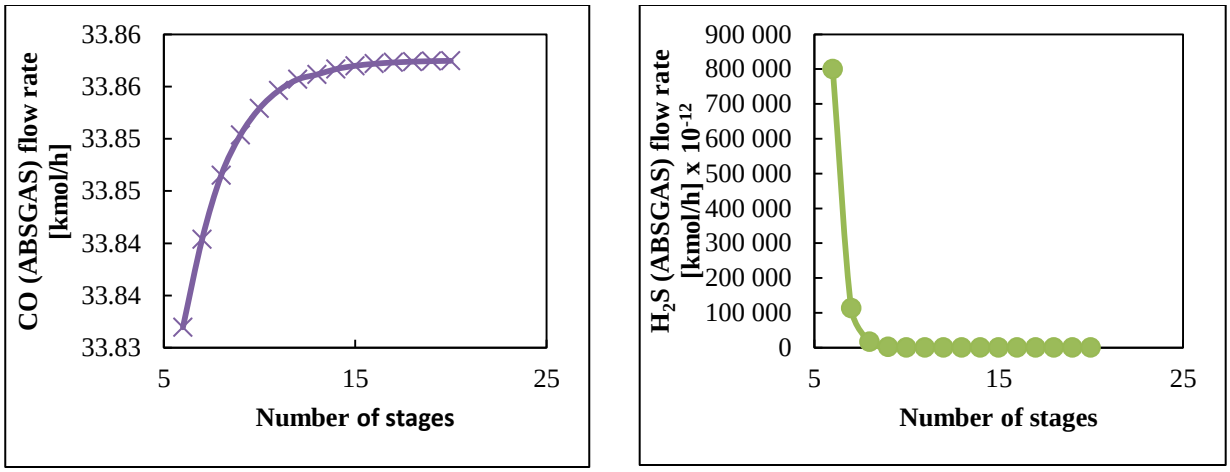

Figure 6.2 (b): Sensitivity analysis relative to the number of stages versus the amount in [kmol/h] of CO (left) and H_2S (right) emitted into the atmosphere via the ABSGAS stream for the DEPG process.

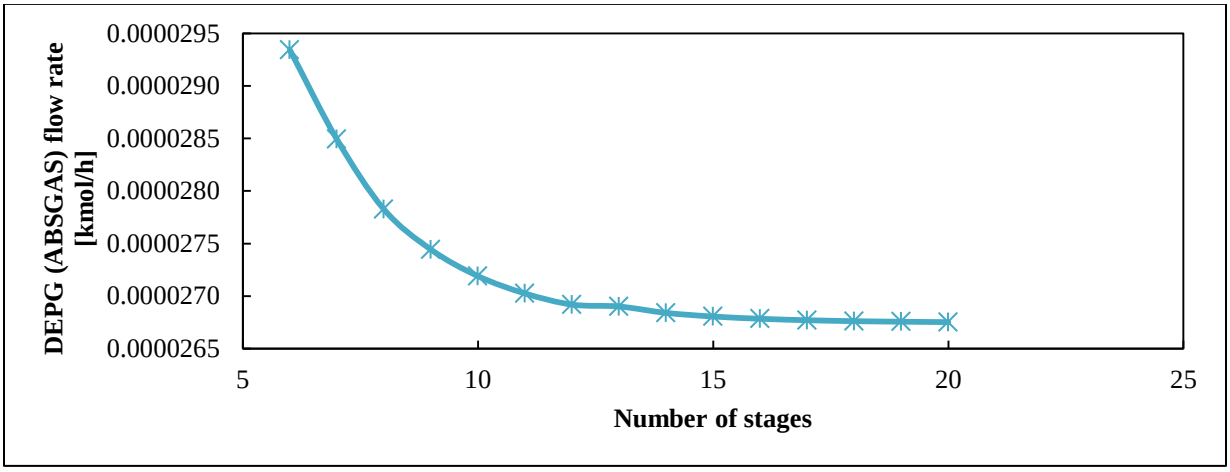

Figure 6.2 (c): Sensitivity analysis relative to the number of stages versus the amount in [kmol/h] of DEPG emitted into the atmosphere via the ABSGAS stream for the DEPG process.

As can be seen in Figure 6.2 (a,b and c), an increase in the number of stages from 6 to 20 resulted in more CH_4 and CO being emitted into the atmosphere, with their flow rates ranging from 53.960 to 54.060 kmol/h and 33.800 to 33.86 kmol/h, respectively. However, an opposite trend is observed for CO_2, H_2S and DEPG, where increasing the number of stages decreased their emissions into the atmosphere via the ABSGAS stream. One should note that the change in the number of stages did not result in a significant change for DEPG, as its emission was only reduced from 0.0000293 to 0.0000268 kmol/h. For H_2S, it is observed that trace amounts are emitted into the atmosphere from stage 6 to 20. The CO_2 component reacted positively to the

variation of the number of stages as its flow rate in the ABSGAS stream decreased from 330.50 to 256.60 kmol/h. However, significant changes are observed from stage 6 to 13 where the flow rate decreased from 330.540 to 259.90 kmol/h, whereas from stage 13 to 20, the flow rate decreased from 259.90 to 256.60 kmol/h. In other words, from all the targeted components, CO_2 is the one component that will determine the optimum number of stages. Due to the small variation in the CO_2 flow rate from stage 13 to 20, the optimum number of stages was determined to be 13.

The next sensitivity analysis consisted in varying the solvent flow rate while keeping the solvent temperature constant, and setting the number of stages to 13. The solvent flow rate range was set from 2000 to 8000 kmol/h. The results obtained are presented in Figure 6.3 (a, b and c).

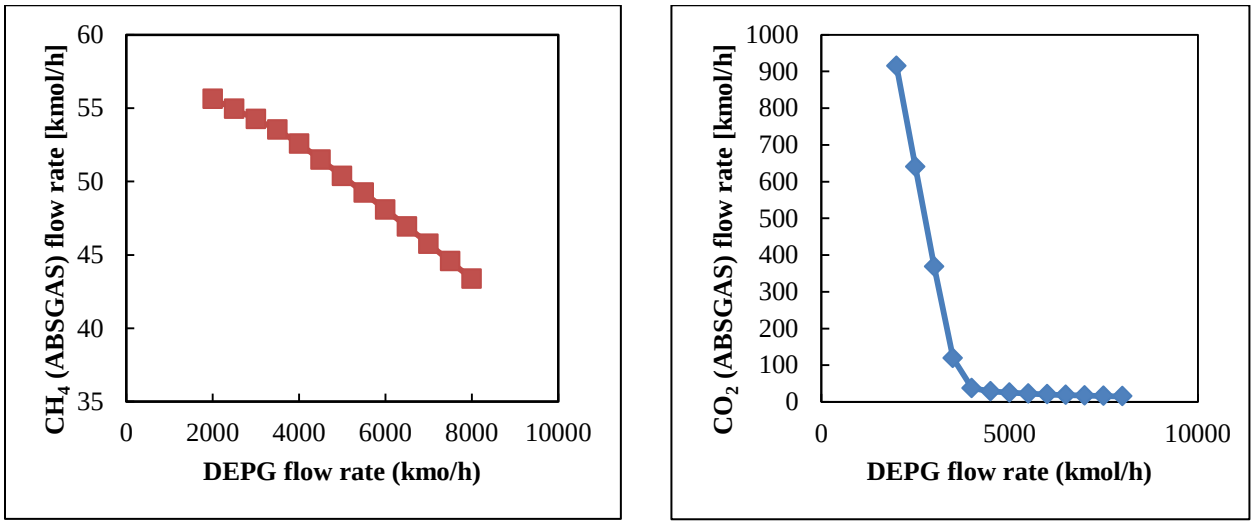

Figure 6.3 (a): Sensitivity analysis relative to the solvent (DEPG) flow rate versus the amount in [kmol/h] of CH_4 (left) and CO_2 (right) emitted into the atmosphere via the ABSGAS stream for the DEPG process.

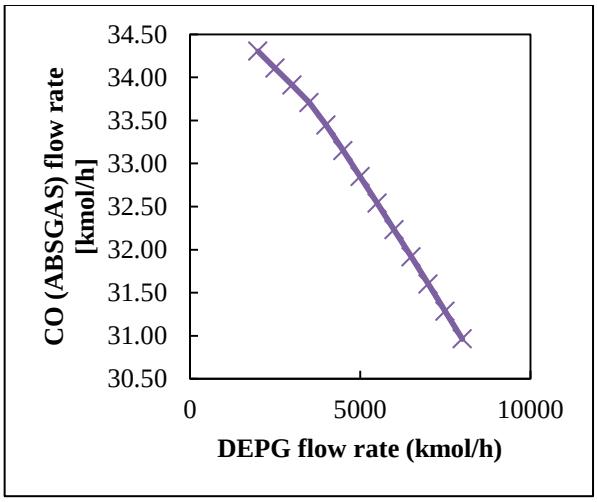

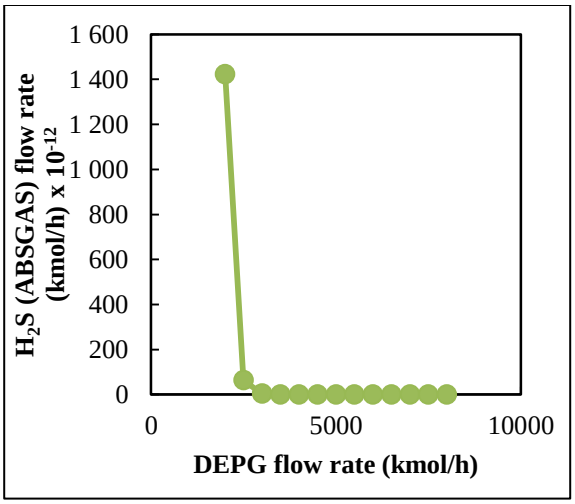

Figure 6.3 (b): Sensitivity analysis relative to the solvent (DEPG) flow rate versus the amount in [kmol/h] of CO (left) and H_2S (right) emitted into the atmosphere via the ABSGAS stream for the DEPG process.

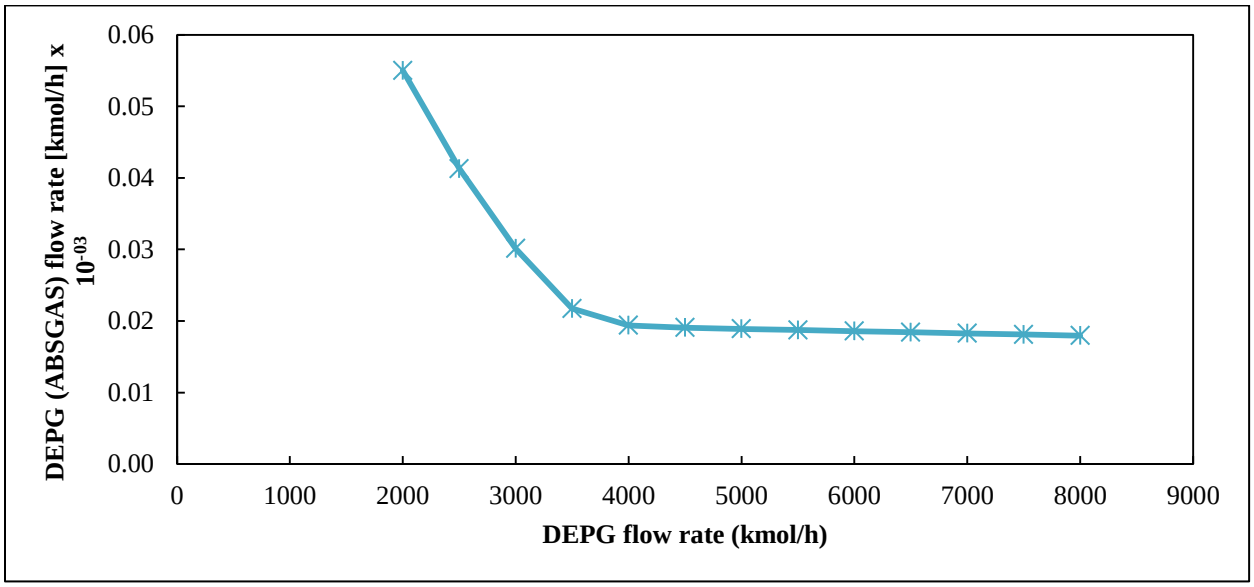

Figure 6.3 (c): Sensitivity analysis relative to the solvent (DEPG) flow rate versus the amount in [kmol/h] of DEPG emitted into the atmosphere via the ABSGAS stream for the DEPG process.

Figure 6.3 (a, b and c) reveals that increasing the solvent flow rate from 2000 to 8000 kmol/h favours the absorption process with varying responses from CO_2, CH_4, H_2S, CO and DEPG in the ABSGAS stream. The CO_2 component stands out as it has the most significant response, its flow rate in the ABSGAS stream varied from 915.10 to 15.000 kmol/h. The flow rates relative to CO and CH_4 varied from 34.300 to 30.960 kmol/h and 55.630 to 43.000 kmol/h, respectively,

whereas trace amounts are observed for H_2S and DEPG. From Figure 6.3, one can see that none of the curves reached a plateau except for CO_2, H_2S and DEPG. This means the addition of more solvent would have resulted in absorption of more gas. However, for economic reasons, it is advised to operate an absorber with the minimum solvent flow rate necessary to absorb the required amount of the treated gas. Consequently, the DEPG flow rate of 8000 kmol/h was considered as the optimum flow rate.

The last variable consisted of the solvent temperature. As discussed in Chapter 2 and 5, solubility of most solvents increases with decreasing temperature. However, one should always keep in mind the operating temperature range for the solvent under investigation. The DEPG is suitable for operation at temperatures ranging from 255.15 to 448.15 K. Hence, a sensitivity analysis on temperature was performed from 260.15 to 272.04 K keeping the solvent flow rate at 8000 kmol/h and the number of stages at 13. The results obtained are graphically presented in Figure 6.4.

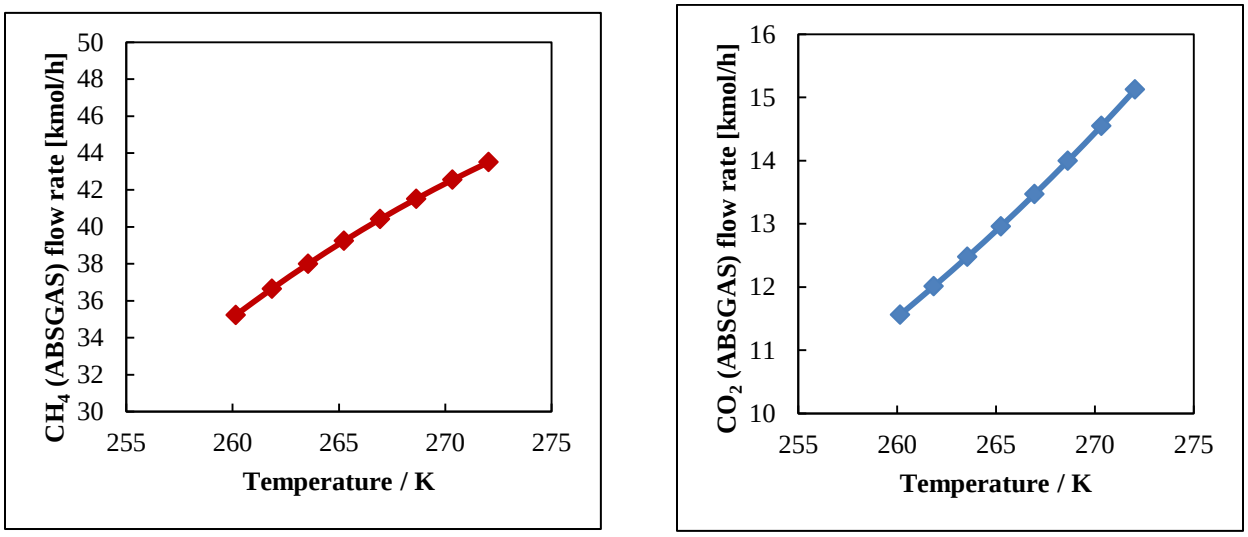

Figure 6.4 (a): Sensitivity analysis relative to the solvent (DEPG) temperature versus the amount in [kmol/h] of CH_4 (left) and CO_2 (right) emitted into the atmosphere via the ABSGAS stream for the DEPG process.

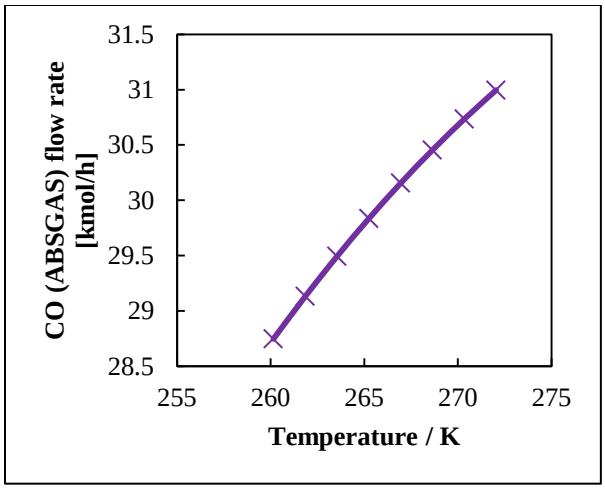

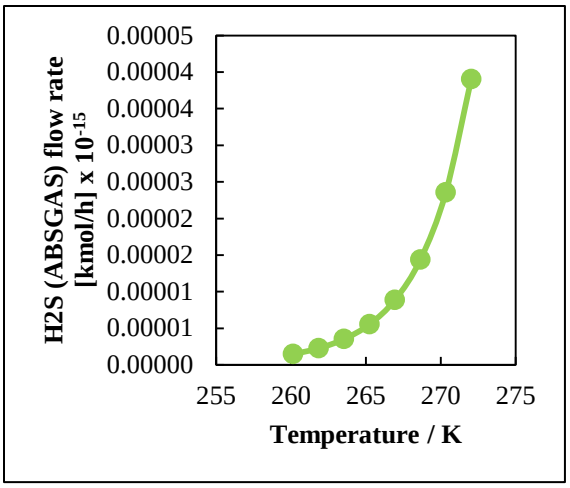

Figure 6.4 (b): Sensitivity analysis relative to the solvent (DEPG) temperature versus the amount in [kmol/h] of CO (left) and H_2S (right) emitted into the atmosphere via the ABSGAS stream for the DEPG process.

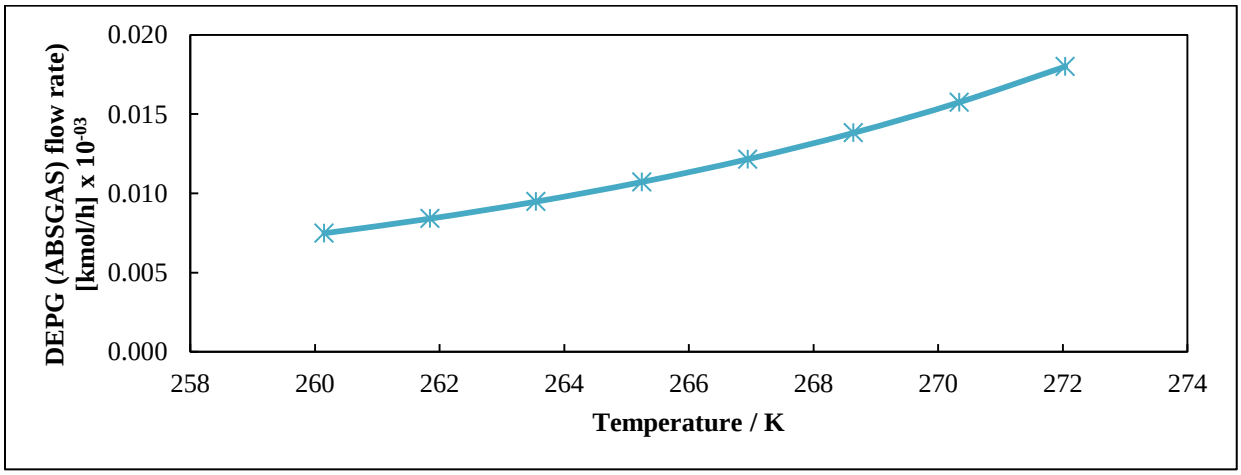

Figure 6.4 (c): Sensitivity analysis relative to the solvent (DEPG) temperature versus the amount in [kmol/h] of DEPG emitted into the atmosphere via the ABSGAS stream for the DEPG process.

Figure 6.4 is in agreement with the anticipated results. The reduction of the solvent (DEPG) temperature increased the absorption capability of DEPG only for CO_2, CH_4 and CO. One should note that significant absorption is mainly observed for CO_2 and CH_4 with their flow rates in the ABSGAS stream decreasing from 15.120 to 11.560 kmol/h, and 43.500 to 35.230 kmol/h, respectively. The components H_2S and DEPG remain indifferent towards the reduction of the solvent temperature with only trace amounts being emitted into the atmosphere. Due to the fact

that the temperature of 260.15 K has further reduced the emission of CO_2 to11.560 kmol/h, corresponding to 0.57 %, this temperature was selected as the optimum temperature.

The optimum conditions resulting from the sensitivity analysis are as follows: 13 stages, solvent flow rate of 8000 kmol/h and solvent temperature of 260.15 K.

An absorption section using DEPG as a physical solvent was thereafter undertaken using the optimum conditions obtained from the sensitivity analysis. For benchmarking purposes, between the DEPG and the C_4F_{10} solvents, the optimum conditions for the DEPG were also used in the gas absorption system based on the C_4F_{10}. The results obtained for both DEPG and C_4F_{10} gas absorption systems are presented in Tables 6.2 and 6.3, respectively.

Table 6.2: Stream results for the absorption process using the DEPG solvent at 260.15 K with the DEPG flow rate of 8000 kmol/hr and the number of stage set to 13

	DEPG	FG	ABSGAS	ABSLIQ	component absorbed (%)	component emitted (%)
Mole Flow kmol/hr						
DEPG	7948.0	0	<0.0010	7948.0	~100	~ 0
CO	0	35.090	28.750	6.3470	18.09	81.91
CO_2	52.410	1967.0	11.560	2008.0	99.43	0.570
H_2	0	2545.0	2293.0	252.40	9.920	90.08
H_2O	0.0320	28.080	<0.0010	28.110	~100	~ 0
N_2	0	3314.0	2873.0	441.30	13.31	86.69
Ar	0	40.190	26.310	13.880	34.54	65.46
CH_4	0	58.410	35.230	23.180	39.68	60.32
NH_3	0	1.3560	trace	1.3560	~100	~ 0
H_2S	0	0.1810	trace	0.1810	~100	~0
Total Flow kmol/hr	8000.0	7989.8	5267.9	10721	—	—
T / K	260.15	293.22	268.4421	274.003	—	—
P / MPa	6.805	6.791	6.771	6.771	—	—
Vapor Frac	0.000	0.997	1.000	0.000	—	—
Liquid Frac	1.000	0.003	0.000	1.000	—	—
Solid Frac	0	0	0	0	—	—
H / kJ/mol	-119.31	-99.486	-2.9590	-161.70	—	—
S / kJ/mol.K	-0.287	-0.027	-0.032	-0.215	—	—
Density kg/m^3	1102.1	68.467	50.120	1074.3	—	—
Average MW	278.45	23.600	16.710	217.14	—	—

Table 6.3: Stream results for the absorption process using the C_4F_{10} solvent at 260.15 K with the C_4F_{10} flow rate of 8000 kmol/hr and the number of stage set to 13

	C_4F_{10}	FG	ABSGAS	ABSLIQ	component absorbed (%)	component emitted (%)
Mole Flow kmol/hr						
C_4F_{10}	8000.0	0	96.909	7903.1	98.79	1.21
CO	0	35.091	21.428	13.663	38.94	61.06
CO_2	0	1966.8	0.2640	1966.5	99.99	0.01
H_2	0	2545.5	2213.0	332.48	13.06	86.94
H_2O	0	28.084	trace	28.084	100	~ 0
N_2	0	3314.2	1702.4	1611.8	48.63	51.37
Ar	0	40.189	0.0140	40.174	99.96	0.04
CH_4	0	58.406	24.985	33.420	57.22	42.78
NH_3	0	1.3580	trace	1.3580	~100	~ 0
H_2S	0	0.1840	trace	0.1840	~100	~ 0
Total Flow kmol/hr	8000.0	7989.8	4059.0	11930	—	—
T / K	260.15	293.24	262.12	271.31	—	—
P / MPa	6.895	6.881	6.860	6.860	—	—
Vapor Frac	0.000	0.997	1.000	0.000	—	—
Liquid Frac	1.000	0.003	0.000	1.000	—	—
Solid Frac	0	0	0	0	—	—
H / kJ/mol	-2199.8	-99.922	-54.403	-1523.5	—	—
S / kJ/mol.K	-0.664	-0.028	-0.047	-0.446	—	—
Density kg/m^3	1795.8	72.810	59.780	1558.5	—	—
Average MW	238.03	23.600	18.780	169.02	—	—

As can be seen from Tables 6.2 and 6.3, there is a 0.003 liquid fraction in the FLUEGAS stream for all the absorption processes. This is due to the presence of water vapour (H_2O) in the flue gas, which is at a pressure and temperature of 6.895 MPa and 260.15 K, respectively. These conditions are believed to conduct a partial condensation of water vapour into the FLUEGAS stream. In addition, the absorber solvent stream contains dissolved CO_2 and H_2O. This was proposed by the engineers at AspenTech. However, it is explained by the fact that a stripping process does not generally produce a pure solvent for recycling but a solvent containing dissolved CO_2 and H_2O. Thus, the absorber solvent stream is generally simulated to the stripping process outlet.

One should also note that the density of C_4F_{10} evaluated in Aspen (2004) at 260.29 K is 1639.7 kg/m^3 whereas that calculated by the Peng-Robinson EoS, in this study and reported in Table 7.3, is 1795.4 kg/m^3. A comparison between the two values reveals the incapability of the PR EoS to accurately calculate the liquid density of the C_4F_{10} component. As stated in Chapter 3, the PR EoS generally suffers from poor liquid density calculations.

Analysis of Tables 6.2 and 6.3 reveals that 99.42 % of CO_2 is absorbed in DEPG, as opposed to approximately 100 % that is absorbed in C_4F_{10}. The same trend is also observed for CH_4 where 57.21 % is absorbed in C_4F_{10} and 39.00 % in DEPG. However, the component CO was poorly absorbed in both the DEPG and C_4F_{10} solvent, with higher absorption observed in C_4F_{10}, whereas H_2S is almost fully absorbed in both solvents with trace amounts emitted into the atmosphere.

In reference to the solvents, less than 0.0010 kmol/h of DEPG is emitted into the atmosphere, versus 96.909 kmol/h of C_4F_{10}, which corresponds to 1.21 % of the C_4F_{10} introduced into the absorber. The C_4F_{10} solvent has also demonstrated higher selectivity for CO_2, H_2S, NH_3 and H_2O as opposed to the remaining components. This can be clearly seen by the amount of CO_2 and H_2S absorbed in the C_4F_{10} solvent.

As can be seen from Table 6.3, the C_4F_{10} solvent process has demonstrated higher absorption capability for gases such as CO, H_2, N_2 and Ar, compared to the DEPG solvent process. This reinforces the work conducted by Battino and Cleve (1966), Wilhelm and Battino (1973), and numerous other literature sources, which state that PFCs have the ability to dissolve oxygen and other gases.

The components NH_3 and H_2O (water vapour) have shown high absorption in both the DEPG and C_4F_{10} solvent processes. One should note that the absorption of H_2O in any solvent is undesirable since it reduces the solvent's purity and therefore its absorption capability. Consequently, the absorbed H_2O in any solvent would require further processing, such as hot regeneration or a glycol unit, to remove it prior to the recycling of the solvent. Moreover, one should bear in mind that throughout this work, H_2O is referred to as water vapour unless otherwise stated.

Although C_4F_{10} has shown higher absorption capability for CO_2, CO, N_2, H_2, H_2O and H_2S than DEPG. Tables 6.2 and 6.3 reveal that 0.01 % (96.909 kmol/hr) of C_4F_{10} is emitted into the atmosphere whereas more than 0.0010 kmol/h of DEPG is emitted into the atmosphere.

As a potential physical solvent, C_4F_{10} should, among other properties, have low vapour pressures under operating conditions to prevent solvent loss. However, Table 6.3 shows that 96.909 kmol//h of C_4F_{10} is emitted into the atmosphere, which is highly undesirable. It is undesirable because it constitutes a significant loss of the solvent and, because of the high global warming potential associated with C_4F_{10}. The principal idea is to use C_4F_{10} as a physical solvent while minimizing its emission into the atmosphere, thereby meeting the environmental regulations.

A sensitivity analysis was thereafter performed on the number of stages of the gas absorption process using the C_4F_{10} solvent to check its effect on the emission of C_4F_{10} into the atmosphere.

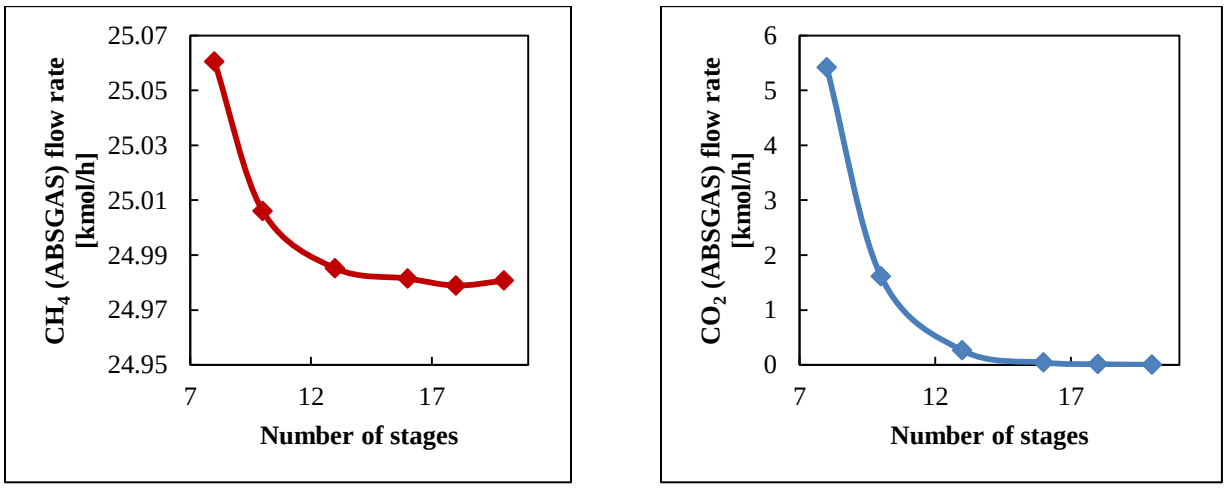

Figure 6.5 (a): Sensitivity analysis relative to the number of stages versus the amount in [kmol/h] of CH_4 (left) and CO_2 (right) emitted into the atmosphere via the ABSGAS stream for the C_4F_{10} process.

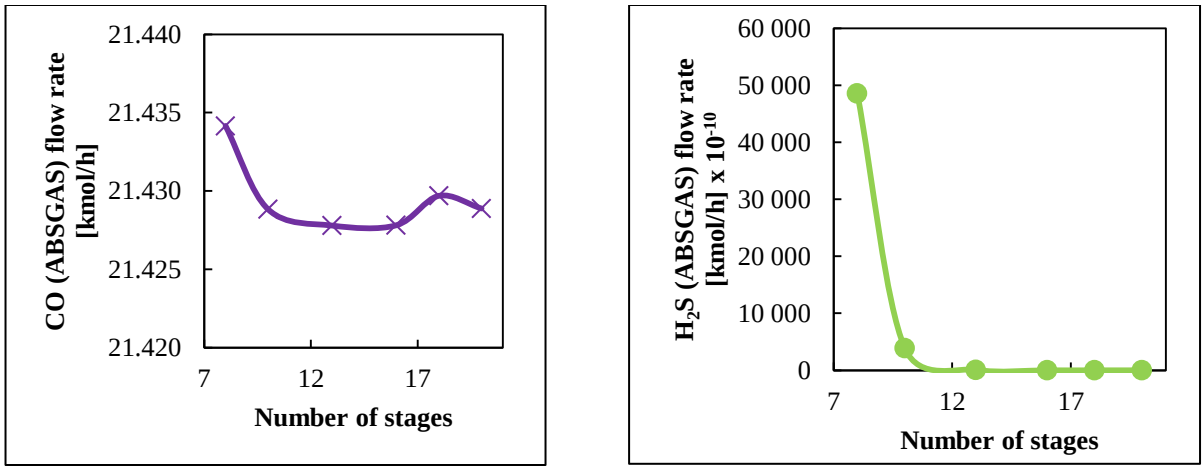

Figure 6.5 (b): Sensitivity analysis relative to the number of stages versus the amount in [kmol/h] of CO (left) and H_2S (right) emitted into the atmosphere via the ABSGAS stream for the C_4F_{10} process.

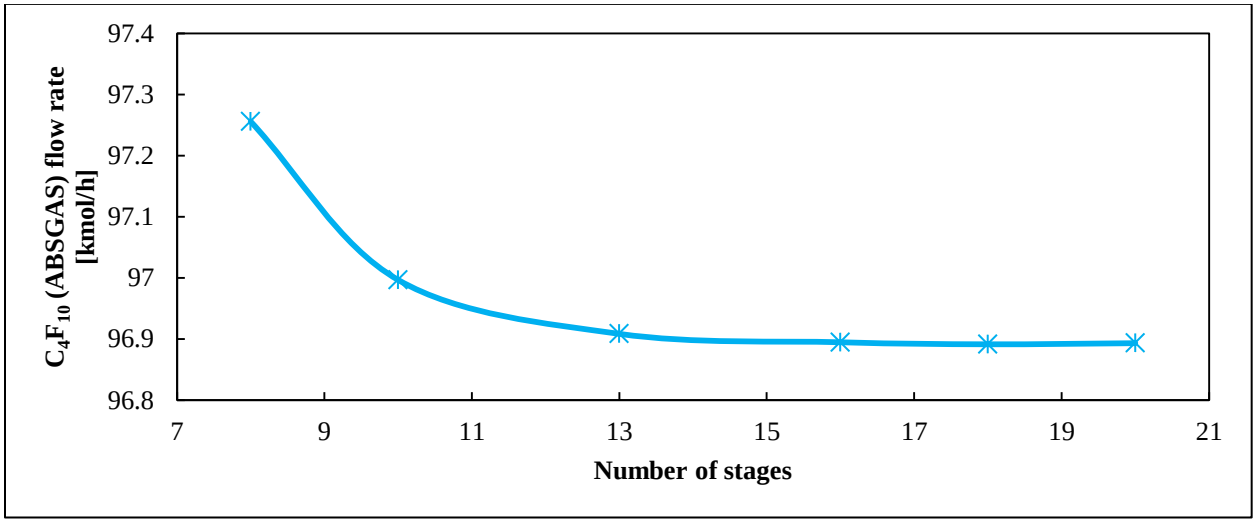

Figure 6.5 (c): Sensitivity analysis relative to the number of stages versus the amount in [kmol/h] of C_4F_{10} emitted into the atmosphere via the ABSGAS stream for the C_4F_{10} process.

As can be seen in Figure 6.5, an increase of stages from 8 to 20 did not have significant effects on all the components except for CO_2 where the flow rate decreased from 5.4100 reaching a plateau at 0.0040 kmol/h. An increase of the number of stages from 8 to 20, resulted in a decrease of the C_4F_{10} flow rate in the ABASGAS stream from 97.260 to 96.890 kmol/h. From Figure 6.5, one can also notice that not much difference is observed from varying the number of stages from 13 to 20, except for CO, as it exhibited a fluctuation in that interval. Hence the number of stage was kept at 13.

Some of the means of remediation of the high vapour pressures for C_4F_{10} could either be the reduction of the absorber operating temperature or the investigation of the carbon chain length of the PFC components. As stated in Chapter 2, the number of carbon atoms in PFCs defines most of their physical properties. The greater the number of carbon atoms, the higher the boiling point, the higher the density, the higher the surface tension, the higher the critical properties, the higher the refractive indices, the higher the viscosity and the lower the vapour pressure.

However, one should keep in mind that the actual operating temperature was chosen in agreement with the operating temperature range for the DEPG solvent. Consequently, the reduction of the operating temperature at a value less than the operating temperature range for current commercial physical solvents should be justified by an outperformance of the C_4F_{10} solvent process against the DEPG solvent processes. The C_4F_{10} outperformance would then compensate the energy usage for refrigeration of the solvent to a lower temperature value.

Since most absorbers operate at low temperature where equilibrium favours absorption, an operating temperature of 220.15 K was, thereafter, chosen for the C_4F_{10} solvent process and, as expected, it yielded better results than the 260.15 K solvent temperature. With the new solvent temperature, 0.19 % of C_4F_{10}, which corresponds to15.420 kmol/h, is emitted into the atmosphere, whereas approximately 100 % of CO_2 is absorbed as, less than 0.001 kmol/h is emitted into the atmosphere. The absorption capability of C_4F_{10} has also increased for CH_4 (95.21 %), CO (43.35 %), N_2 (65.09 %) and H_2 (12.47 %). However, the quantity of Ar, H_2S, NH_3 and H_2O absorbed in the C_4F_{10} solvent remain intact, as in the previous run where only trace amounts were emitted into the atmosphere. These results, reported in Table 6.5, show that the solubility of flue gas components in C_4F_{10} increases with decreasing temperature.

A comparison between the results reported in Tables 6.2 and 6.4 reveals that the amount of C_4F_{10} emitted into the atmosphere at 220.15 K is still higher than the amount of solvent emitted into the atmosphere in the DEPG at 260.15 K.

Table 6.4: Stream results for the absorption process using the C_4F_{10} solvent at 220.15 K with the C_4F_{10} flow rate of 8000 kmol/hr and the number of stages set to 13

	C_4F_{10}	FG	ABSGAS	ABSLIQ	component absorbed (%)	component emitted (%)
Mole Flow kmol/hr						
C_4F_{10}	8000.0	0.000	15.420	7984.6	99.81	0.19
CO	0	35.091	19.881	15.211	43.35	56.65
CO_2	0	1966.8	< 0.001	1966.8	~100	~ 0
H_2	0	2545.5	2228.0	317.55	12.47	87.53
H_2O	0	28.084	trace	28.084	~100	~ 0
N_2	0	3314.2	1157.0	2157.2	65.09	34.91
Ar	0	40.189	trace	40.189	~100	~ 0
CH_4	0	58.406	2.8000	55.605	95.21	4.79
NH_3	0	1.3580	trace	1.3580	~100	~ 0
H_2S	0	0.1840	trace	0.1840	~100	~ 0
Total Flow kmol/hr	8000.0	7989.8	3423.1	12566	—	—
T / K	220.15	293.14	223.41	241.58	—	—
P / MPa	6.895	6.881	6.860	6.860	—	—
Vapor Frac	0.000	0.997	1.000	0.000	—	—
Liquid Frac	1.000	0.003	0.000	1.000	—	—
Solid Frac	0	0	0	0	—	—
H / kJ/mol	-2209.2	-99.922	-12.999	-1466.4	—	—
S / kJ/mol.K	-0.7034	-0.0281	-0.0409	-0.4510	—	—
Density kg/m^3	1906.6	72.810	44.840	1682.1	—	—
Average MW	238.03	23.600	12.030	163.26	—	—

An investigation of the carbon chain-length of the PFC molecule was thereafter undertaken using the perfluorohexane (C_6F_{14}) solvent. The process was run similarly to the C_4F_{10} processes. The run was firstly undertaken with the optimum operating conditions obtained for the DEPG solvent, which can be summarised as follows: 13 stages, solvent flow rate of 8000 kmol/h and solvent temperature of 260.15 K. Thereafter another run was undertaken at 220.15 K keeping the flow rate at 8000 kmol/h and the number of stage at 13. The results obtained are presented in Tables 6.5 and 6.6.

Table 6.5: Stream results for the absorption process using the C_6F_{14} solvent at 260.15 K with the C_6F_{14} flow rate of 8000 kmol/hr and the number of stage set to 13

	C_6F_{14}	FG	ABSGAS	ABSLIQ	component absorbed (%)	component emitted (%)
Mole Flow kmol/hr						
C_6F_{14}	8000.0	0.000	12.244	7987.8	99.85	0.15
CO	0	35.091	21.569	13.522	38.53	61.47
CO_2	0	1966.8	0.0010	1967.0	~100	~0
H_2	0	2545.5	2268.0	277.59	10.91	89.09
H_2O	0	28.084	trace	28.084	~100	~0
N_2	0	3314.2	2668.0	646.29	19.50	80.50
Ar	0	40.189	0.0030	40.186	99.99	0.01
CH_4	0	58.406	11.177	47.228	80.86	19.14
NH_3	0	1.3580	trace	1.3580	~100	~0
H_2S	0	0.1840	0.0010	0.1820	99.24	0.76
Total Flow kmol/hr	8000.0	7989.8	4980.9	11008	—	—
T/ K	260.15	293.24	259.87	270.59	—	—
P/MPa	68.046	67.910	67.706	67.706	—	—
Vapor Frac	0.000	0.997	1.000	0.000	—	—
Liquid Frac	1.000	0.003	0.000	1.000	—	—
Solid Frac	0	0	0	0	—	—
H/ kJ/mol	-3033.4	-99.880	-9.5100	-2272.5	—	—
S/ kJ/mol.K	-0.964	-0.028	-0.036	-0.702	—	—
Density kg/m^3	1820.0	72.810	53.960	1703.5	—	—
Average MW	338.04	23.600	16.910	255.13	—	—

Table 6.6: Stream results for the absorption process using the C_6F_{14} solvent at 220.15 K with the C_6F_{14} flow rate of 8000 kmol/hr and the number of stage set to 13

	C_6F_{14}	FG	ABSGAS	ABSLIQ	component absorbed (%)	component emitted (%)
Mole Flow kmol/hr						
C_6F_{14}	8000.0	0.000	1.1480	7998.9	99.99	0.01
CO	0	35.091	20.192	14.899	42.46	57.54
CO_2	0	1966.8	trace	1966.8	~100	~0
H_2	0	2545.5	2287.8	257.66	10.12	89.88
H_2O	0	28.084	trace	28.084	~100	~0
N_2	0	3314.2	2679.2	635.03	19.16	80.84
Ar	0	40.189	trace	40.189	~100	~0
CH_4	0	58.406	0.1290	58.276	99.78	0.22
NH_3	0	1.3580	trace	1.3580	~100	~0
H_2S	0	0.1840	trace	0.1840	~100	~0
Total Flow kmol/hr	8000.000	7989.820	4988.509	11001.310	–	–
T/ K	220.15	293.24	220.28	239.67	–	–
P/ MPa	6.895	6.881	6.860	6.860	–	–
Vapor Frac	0.000	0.997	1.000	0.000	–	–
Liquid Frac	1.000	0.003	0.000	1.000	–	–
Solid Frac	0	0	0	0	–	–
H/ kJ/mol	-3045.2	-99.880	-3.8580	-2285.2	–	–
S/ kJ/mol.K	-1.0130	-0.0280	-0.0390	-0.735	–	–
Density kg/m^3	1889.1	72.810	62.590	1796.4	–	–
Average MW	338.04	23.600	16.160	255.64	–	–

A comparison between Tables 6.3 and 6.5 shows that 12.244 kmol/h of solvent is emitted into the atmosphere for the C_6F_{14} process, as opposed to 96.909 kmol/h for the C_4F_{10} process. These results are in agreement with what was anticipated, as the longer the carbon chain length in PFCs, the lower the vapor pressure. The absorption for components such as CO_2 and CH_4 also increased using C_6F_{14}, except for N_2 and H_2. The absorption of H_2 and N_2 in C_6F_{14} is less compared to C_4F_{10}. This implies that more H_2 and N_2 were emitted into the atmosphere. The remaining components (Ar, NH_3, CO and H_2S) were equally absorbed in both solvents.

Although 12.244 kmol/h or 0.01 % of C_6F_{14} is emitted into the atmosphere, which is significantly lower, compared to the C_4F_{10} process (96.909 kmol/h), no PFCs should be emitted into the atmosphere to meet the environmental regulations. As for the C_4F_{10} process, the C_6F_{14} process solvent temperature was decreased to 220.15 K in an attempt to reduce its emission into the atmosphere. The results obtained, which are reported in Table 6.6, reveal that the reduction of the solvent temperature resulted not just in lowering the emission of C_6F_{14} into the atmosphere to 0.01 % or 1.1480 kmol/hr, but also in increasing the absorption capability of C_6F_{14} for CO_2 with trace amounts being emitted into the atmosphere. The absorption for CH_4 also increased to 99.78 % whereas that of H_2 and N_2 decreased. One should note that the reduction of the solvent temperature to 220.15 K did not have significant impacts on CO, H_2 and N_2 as can be seen from Tables 6.5 and 6.6.

However, a comparison of the C_6F_{14} with DEPG solvent process shows that 1.1480 kmol/hr is still high, compared to a trace amount of solvents emitted into the atmosphere in the DEPG absorption process. Nevertheless, an increase in the carbon chain length significantly improved the absorption capability of PFCs (C_4F_{10} and C_6F_{14}), for components such as CO_2 and CH_4.

6.2.1.2 *N*-Methyl-2-Pyrrolidone (NMP) and propylene carbonate (PC) versus perfluorobutane (C_4F_{10}) or perfluorohexane (C_6F_{14}) solvents

As for the DEPG absorption process, a sensitivity analysis was performed for parameters such as the number of stages in the absorber, the solvent flow rate and the solvent temperature for the NMP and PC absorption processes. The sensitivity analysis was performed on one of the parameters, while keeping the other two constant. The number of stages ranged from 6 to 20, the solvent flow rate ranged from 2000 to 10000 kmol/h, and the solvent temperature ranged from

260.15 K to 272.04 K. The temperature range was chosen in accordance with the operating temperature of the considered solvent. The optimal parameters obtained from the sensitivity analysis for the NMP and PC solvents were more or less equal as can be seen in Figures 6.6-6.11. Figures 6.6 and 6.7 present graphically the sensitivity analysis pertaining to the number of stages for the NMP and PC absorptions processes, respectively.

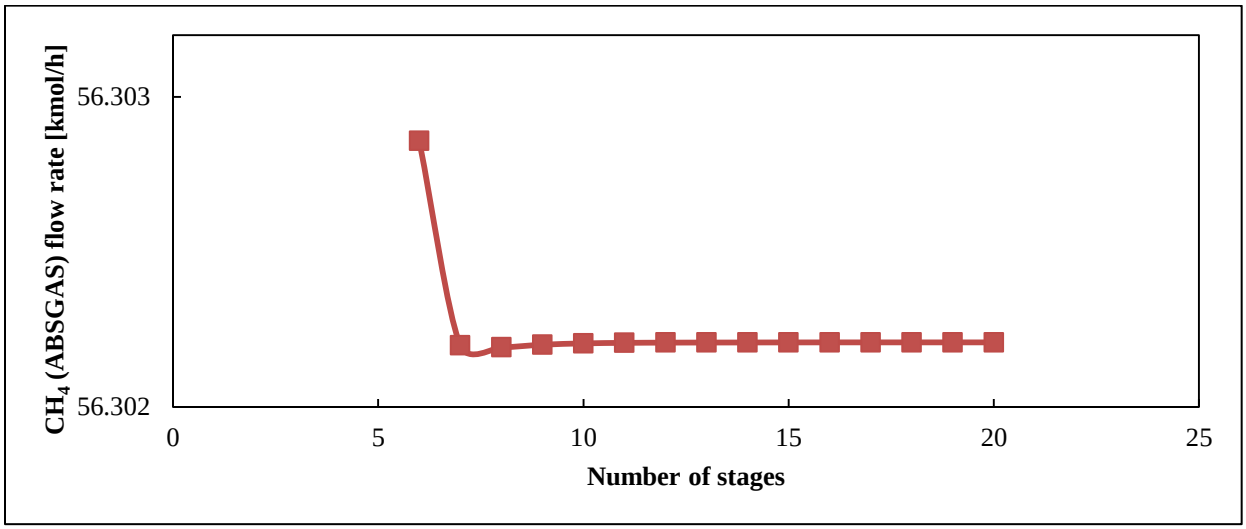

Figure 6.6 (a): Sensitivity analysis relative to the number of stages versus the amount [kmol/h] of CH_4 emitted into the atmosphere via the ABS-GAS stream for the NMP process.

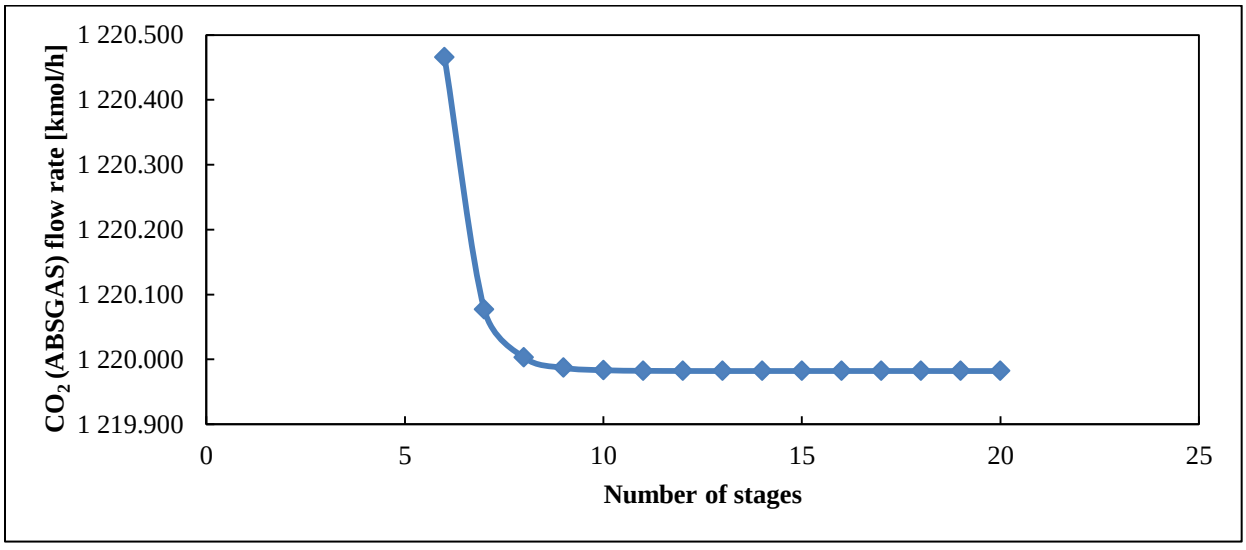

Figure 6.6 (b): Sensitivity analysis relative to the number of stages versus the amount [kmol/h] of CO_2 emitted into the atmosphere via the ABS-GAS stream for the NMP process

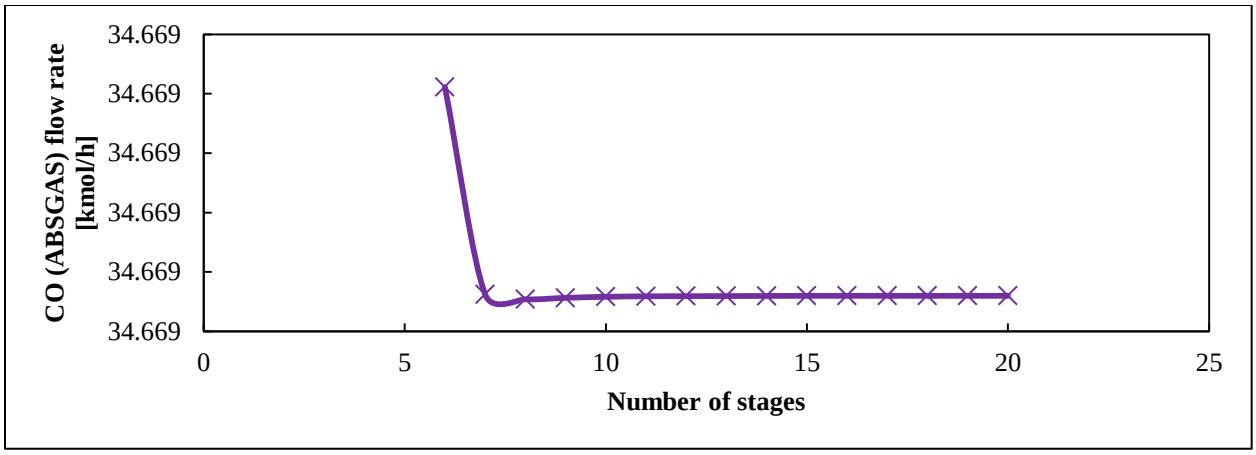

Figure 6.6(c): Sensitivity analysis relative to the number of stages versus the amount [kmol/h] of CO emitted into the atmosphere via the ABS-GAS stream for the NMP process.

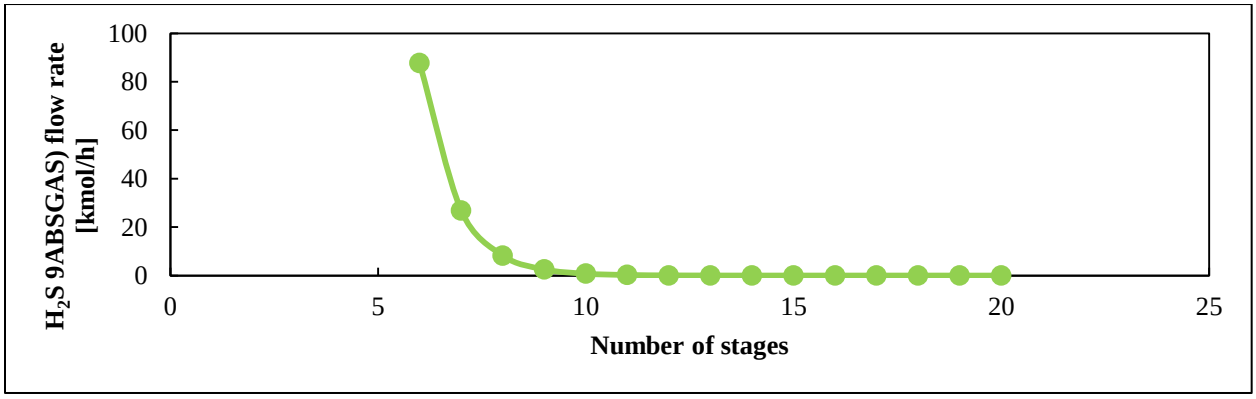

Figure 6.6 (d): Sensitivity analysis relative to the number of stages versus the amount [kmol/h] of H_2S emitted into the atmosphere via the ABS-GAS stream for the NMP process.

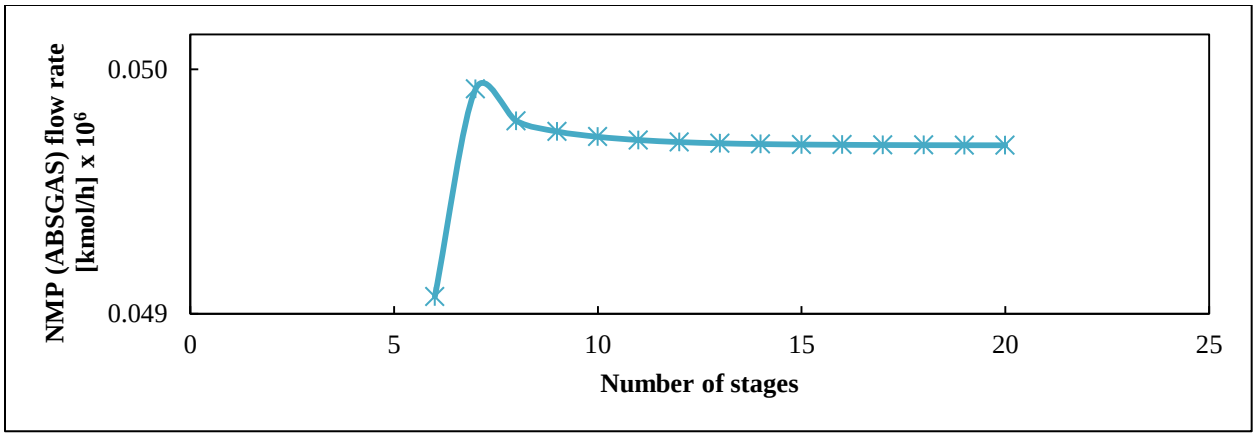

Figure 6.6 (e): Sensitivity analysis relative to the number of stages versus the amount [kmol/h] of NMP emitted into the atmosphere via the ABS-GAS stream for the NMP process.

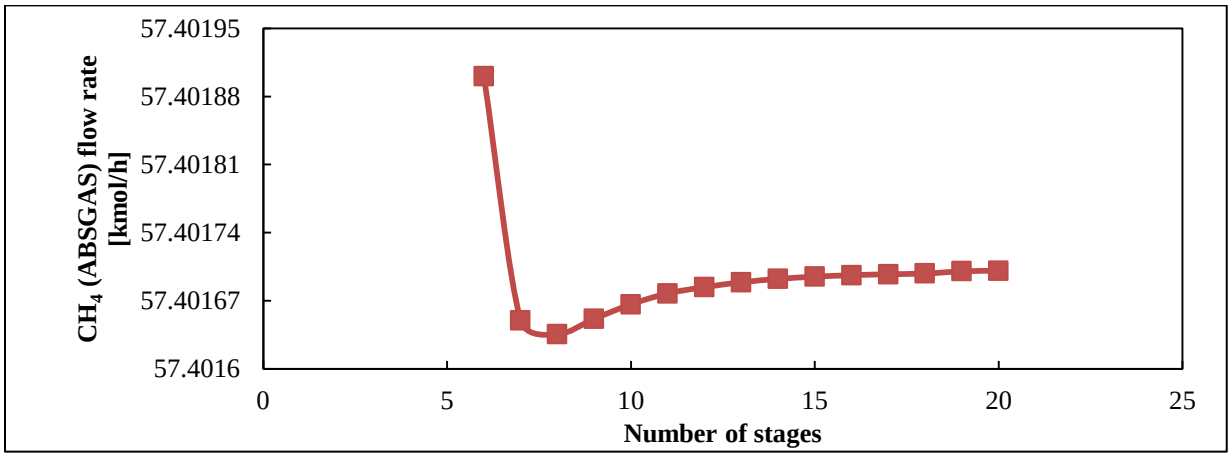

Figure 6.7 (a): Sensitivity analysis relative to the number of stages versus the amount [kmol/h] of CH_4 emitted into the atmosphere via the ABS-GAS stream for the PC process.

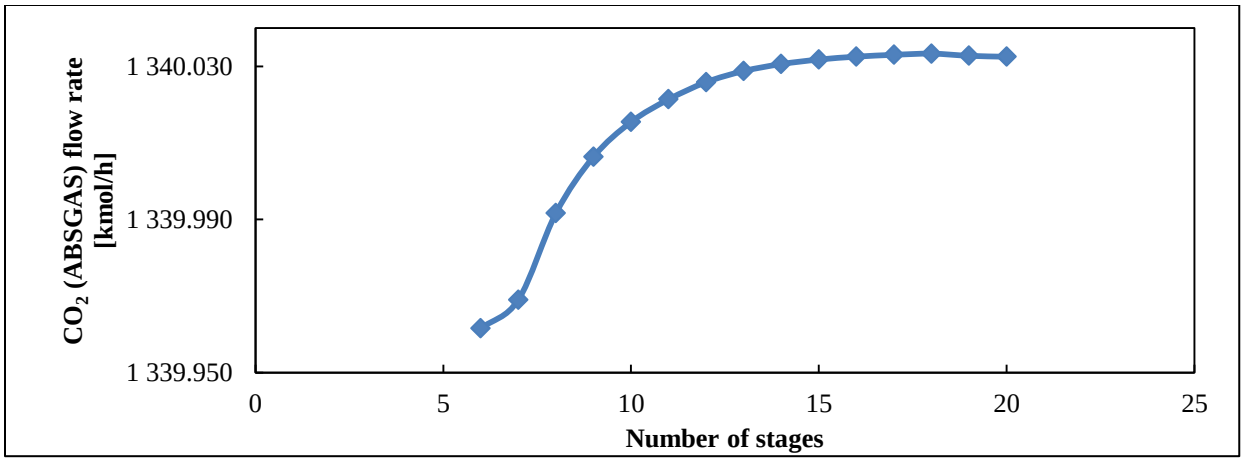

Figure 6.7 (b): Sensitivity analysis relative to the number of stages versus the amount [kmol/h] of CO_2 emitted into the atmosphere via the ABS-GAS stream for the PC process.

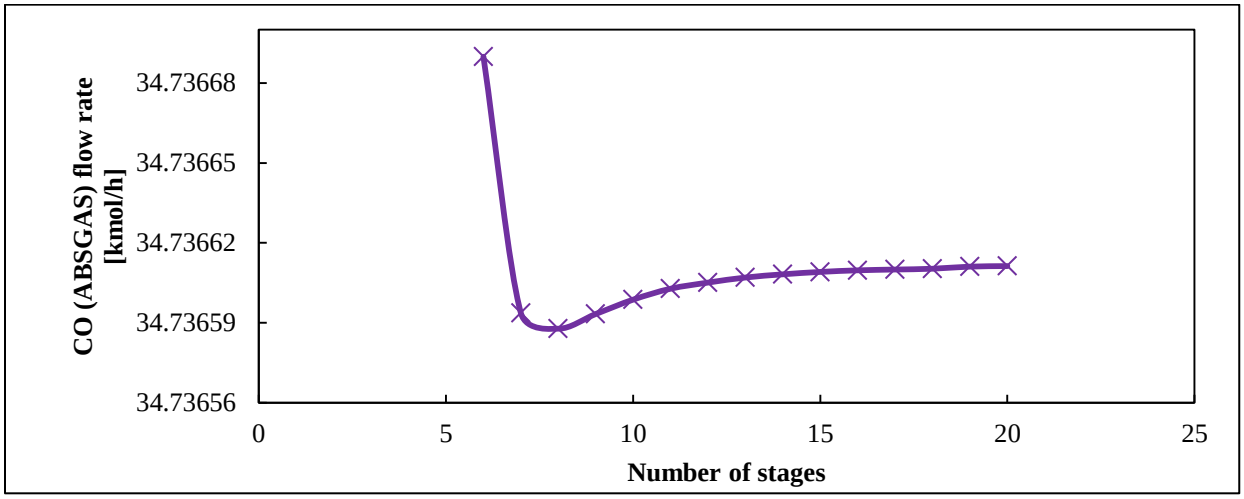

Figure 6.7 (c): Sensitivity analysis relative to the number of stages versus the amount [kmol/h] of CO emitted into the atmosphere via the ABS-GAS stream for the PC process.

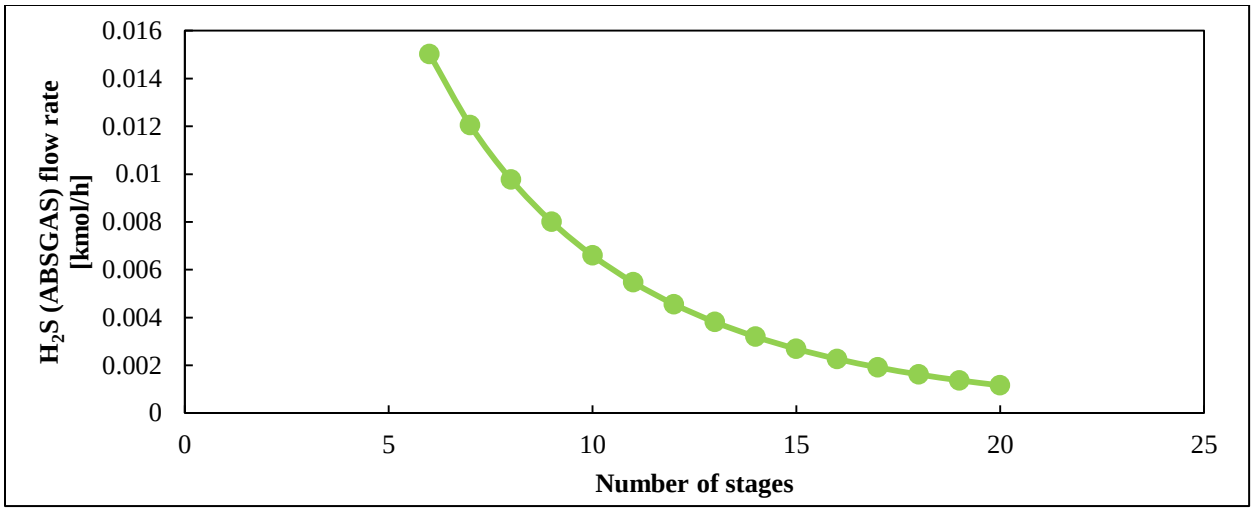

Figure 6.7 (d): Sensitivity analysis relative to the number of stages versus the amount [kmol/h] of H_2S emitted into the atmosphere via the ABS-GAS stream for the PC process.

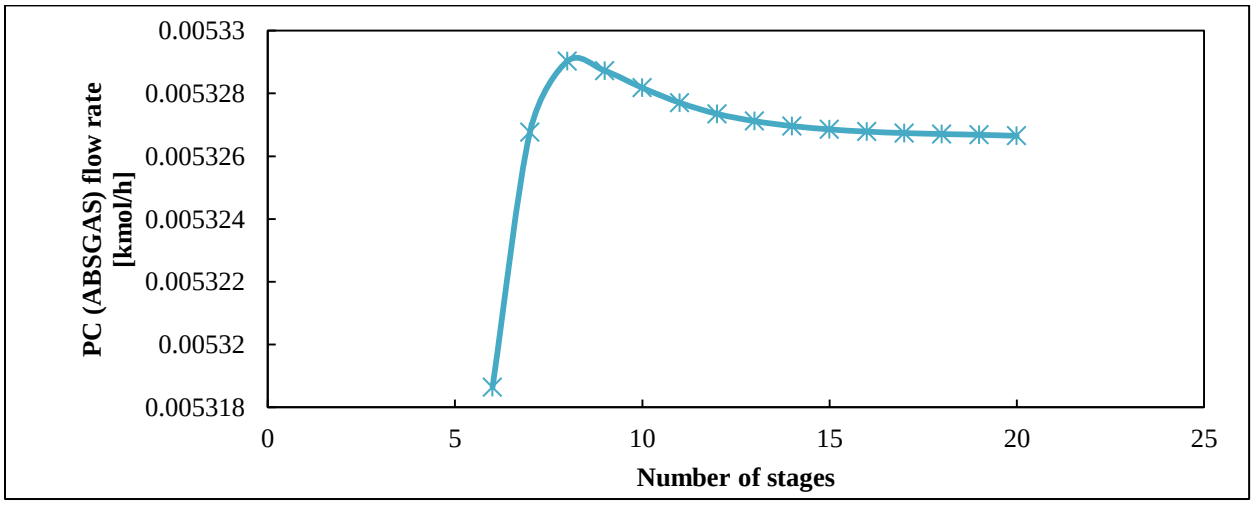

Figure 6.7 (e): Sensitivity analysis relative to the number of stages versus the amount [kmol/h] of PC emitted into the atmosphere via the ABS-GAS stream for the PC process.

Analysis of Figures 6.6 (a, b, c, d and e) reveals that the variation of the number of stages in the NMP absorption process has no significant effect on the flow rate of all the components of interest emitted into the atmosphere from stage 10, except for H_2S where a slight variation is observed. Hence, the optimum number of stages of the NMP absorption process was set to 10.

For the PC absorption process, as can be seen from Figures 6.7 (a, b, c, d and e), the variation of the flow rate, as a function of the number of stages has no effect from stage 15 for all the

components except H_2S. However, the variation in the flow rate of components such as CO_2, CO, CH_4 and PC from stage 10 to stage 15 results in a difference of 0.0160 kmol/h for CO_2, 0.0040 kmol/h for H_2S, less than 0.0010 kmol/h for CO, CH_4 and NMP, respectively. Given the slight variations observed in the flow rate for all components of interest from stage 10 to 15, the optimal number of stages for the PC absorption process was set to 10.

Once the number of stages was set, a sensitivity analysis was performed on the solvent flow rate for both the NMP and PC absorption processes. The solvent flow rate ranged from 2000 to 10000 kmol/h. As can be seen from the sensitivity analysis results pertaining to the DEPG absorption process, the solvent flow rate range for the NMP and PC absorption processes has increased to 10000 kmol/h. This is due to the fact that at 8000 kmol/h none of the components in the NMP and PC absorption processes reached a plateau. However, an increase of the solvents' flow rates to 10000 km/h brought components such as CO_2, NMP and PC close to stabilisation, whereas H_2S reached complete stabilisation. Based on the results obtained, which are graphically presented in Figures 6.8 and 6.9, the optimum flow rate for both the NMP and PC processes was determined to be 10000 kmol/h.

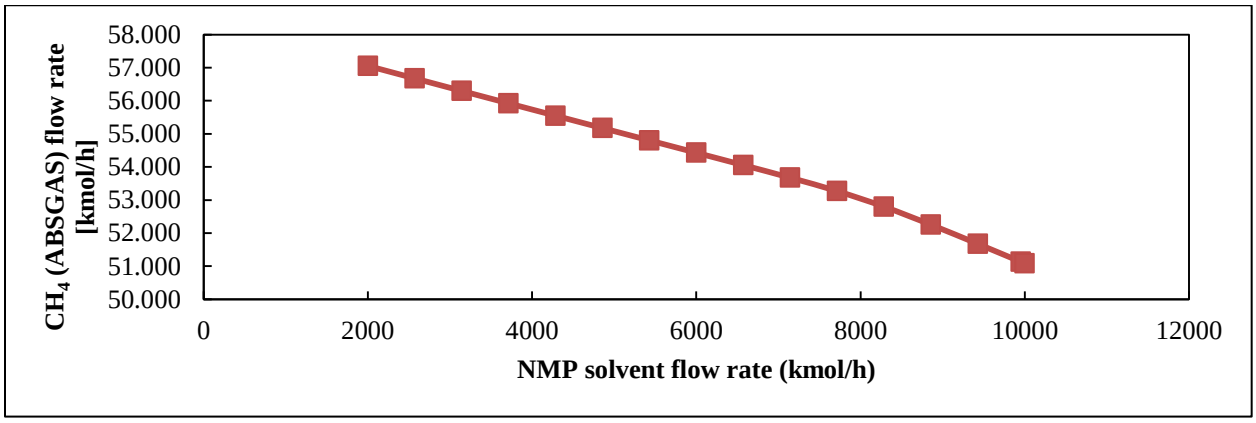

Figure 6.8 (a): Sensitivity analysis relative to the solvent (NMP) flow rate versus the amount [kmol/h] of CH_4 emitted into the atmosphere via the ABS-GAS stream for the NMP process.

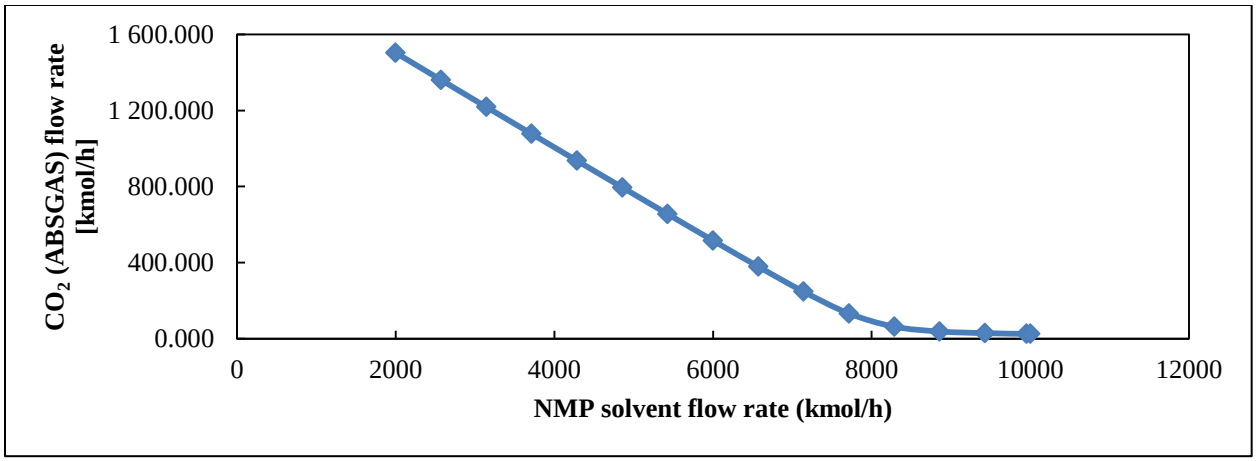

Figure 6.8 (b): Sensitivity analysis relative to the solvent (NMP) flow rate versus the amount [kmol/h] of CO_2 emitted into the atmosphere via the ABS-GAS stream for the NMP process.

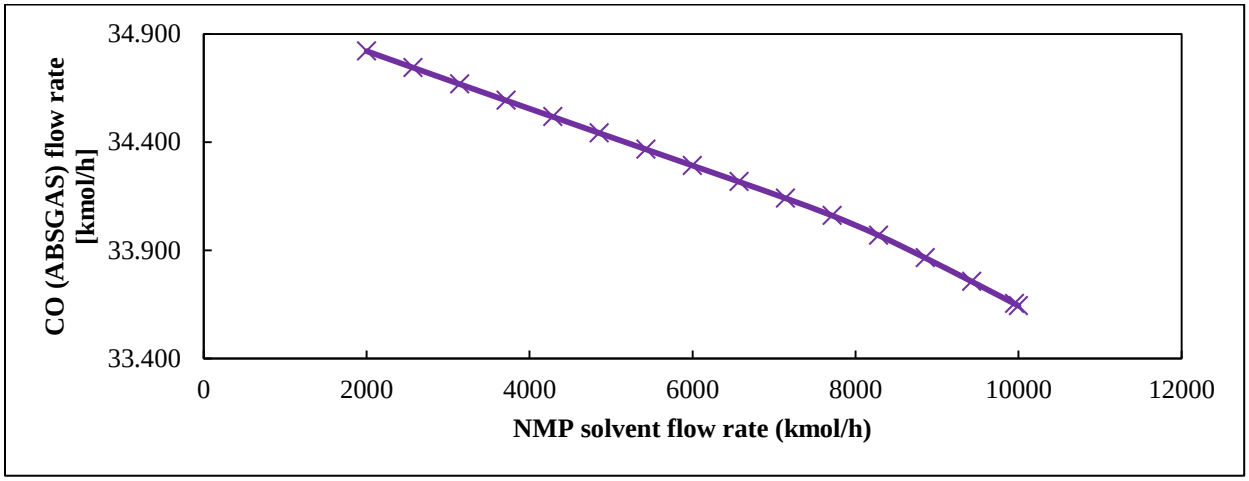

Figure 6.8 (c): Sensitivity analysis relative to the solvent (NMP) flow rate versus the amount [kmol/h] of CO emitted into the atmosphere via the ABS-GAS stream for the NMP process.

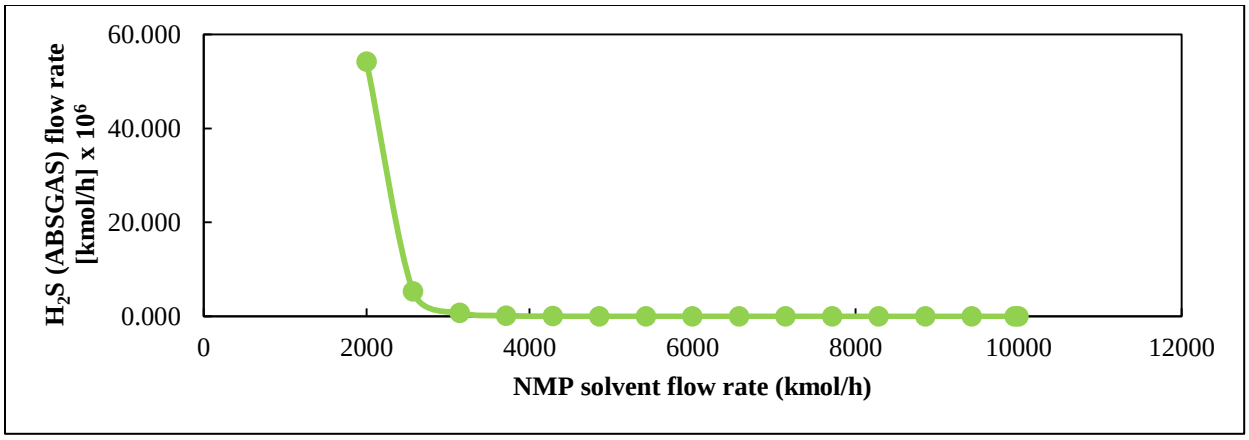

Figure 6.8 (d): Sensitivity analysis relative to the solvent (NMP) flow rate versus the amount [kmol/h] of H_2S emitted into the atmosphere via the ABS-GAS stream for the NMP process.

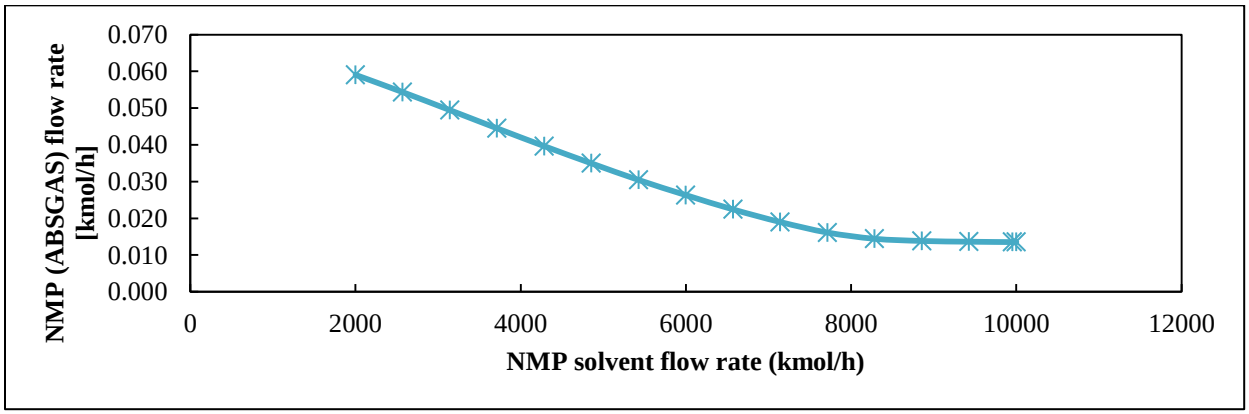

Figure 6.8 (e): Sensitivity analysis relative to the solvent (NMP) flow rate versus the amount [kmol/h] of NMP emitted into the atmosphere via the ABS-GAS stream for the NMP process.

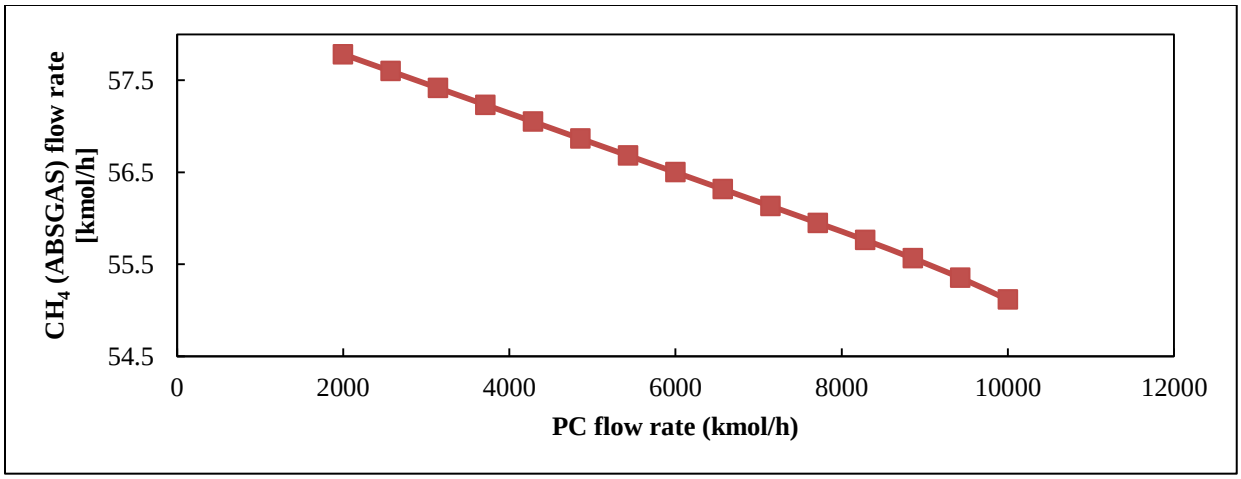

Figure 6.9 (a): Sensitivity analysis relative to the solvent (PC) flow rate versus the amount [kmol/h] of CH_4 emitted into the atmosphere via the ABS-GAS stream for the PC process.

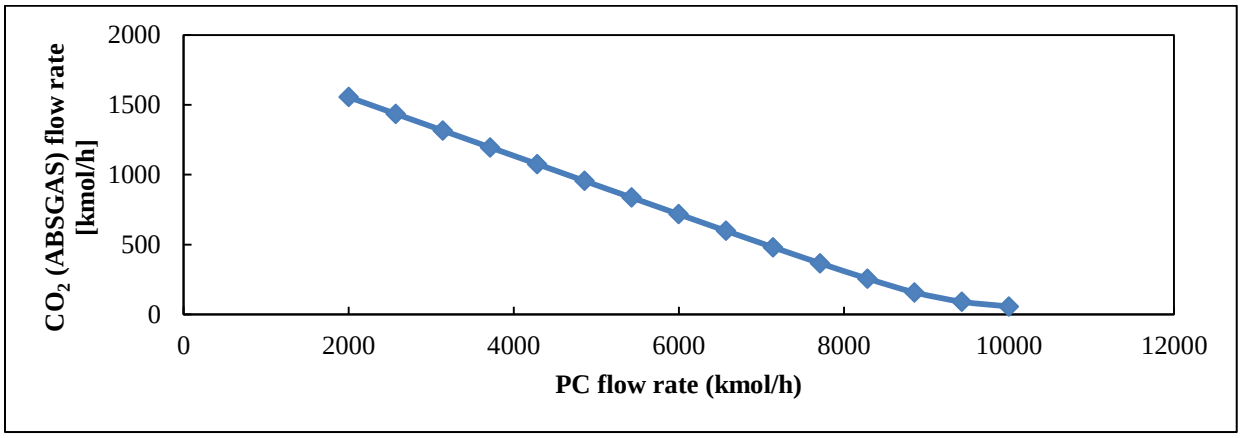

Figure 6.9 (b): Sensitivity analysis relative to the solvent (PC) flow rate versus the amount [kmol/h] of CO_2 emitted into the atmosphere via the ABS-GAS stream for the PC process.

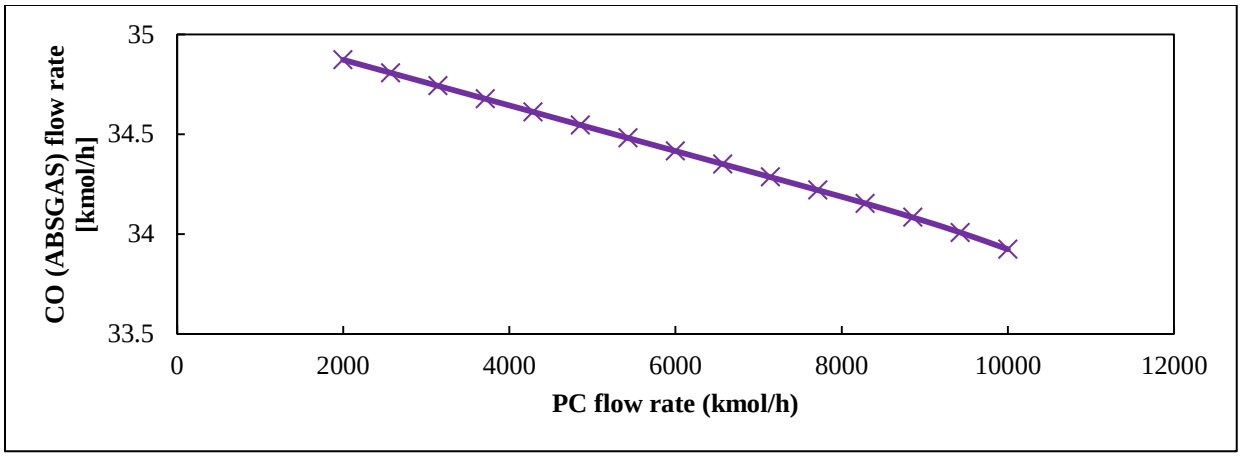

Figure 6.9 (c): Sensitivity analysis relative to the solvent (PC) flow rate versus the amount [kmol/h] of CO emitted into the atmosphere via the ABS-GAS stream for the PC process.

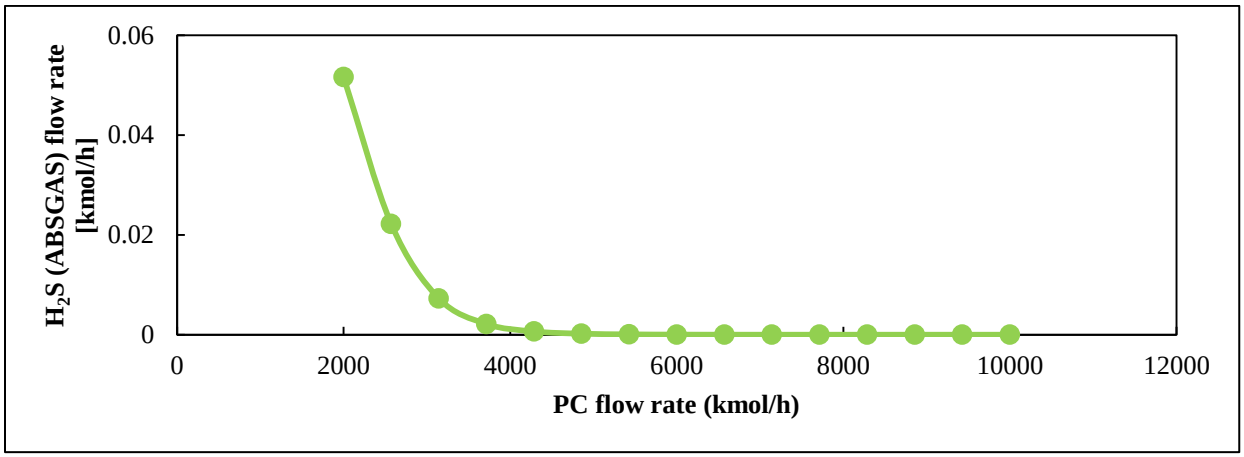

Figure 6.9 (d): Sensitivity analysis relative to the solvent (PC) flow rate versus the amount [kmol/h] of H_2S emitted into the atmosphere via the ABS-GAS stream for the PC process.

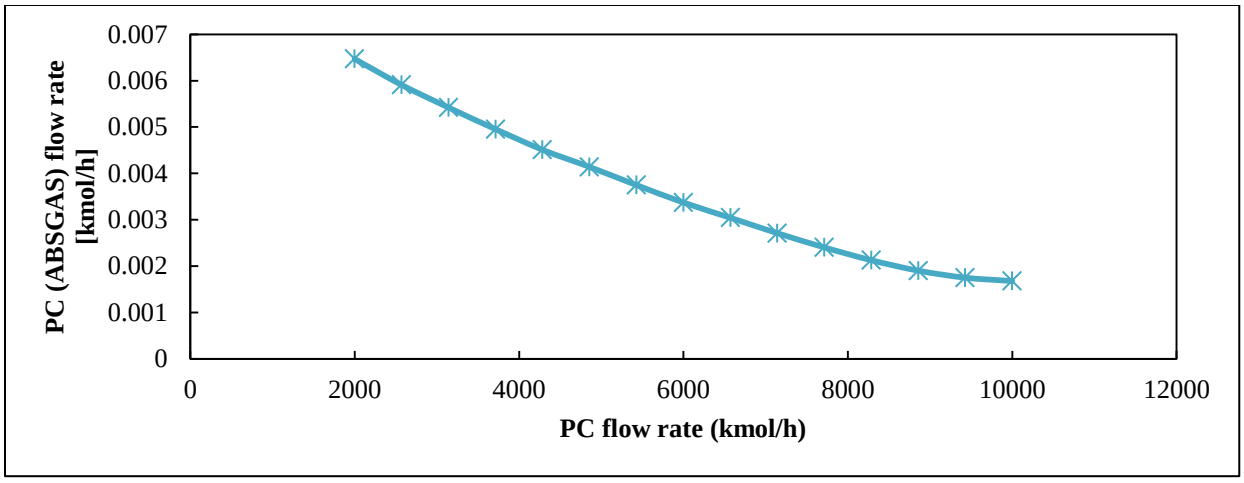

Figure 6.9 (e): Sensitivity analysis relative to the solvent (PC) flow rate versus the amount [kmol/h] of PC emitted into the atmosphere via the ABS-GAS stream for the PC process.

Lastly, a sensitivity analysis was undertaken for solvent temperatures, ranging from 260.15 to 272.04 K, for both the NMP and PC absorption processes. One should note that chilling the PC solvent to 255.15 K would have resulted in condensation of the hydrocarbons (Burr and Lyddon, 2008). Hence, its temperature was set at a minimum of 260.15 K. The results pertaining to the sensitivity analysis for the solvents (NMP and PC) temperatures are graphically presented in Figures 6.10 and 6.11.

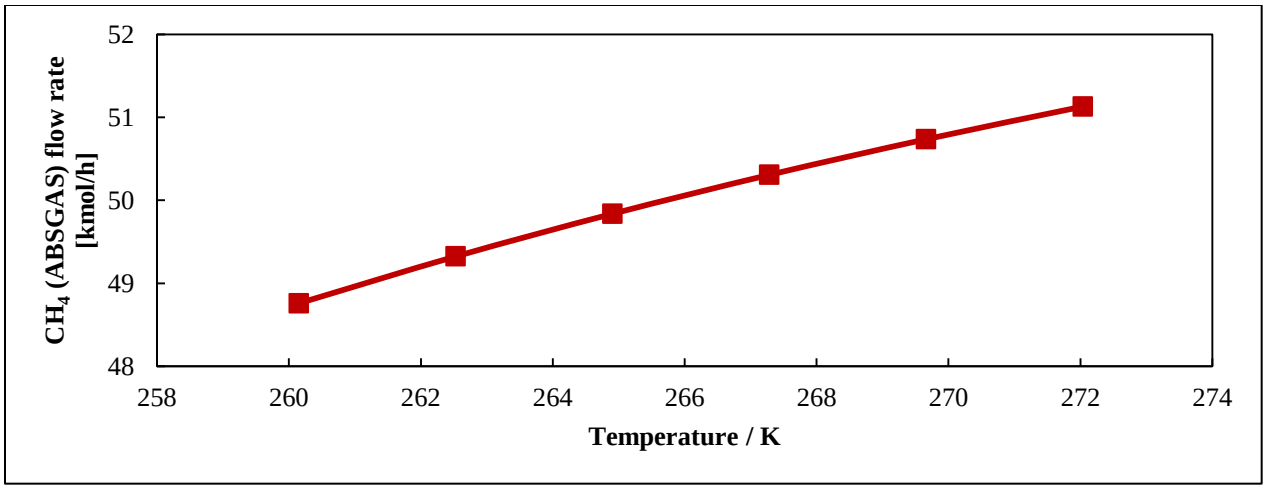

Figure 6.10 (a): Sensitivity analysis relative to the solvent (NMP) temperature versus the amount [kmol/h] of CH_4 emitted into the atmosphere via the ABS-GAS stream for the NMP process.

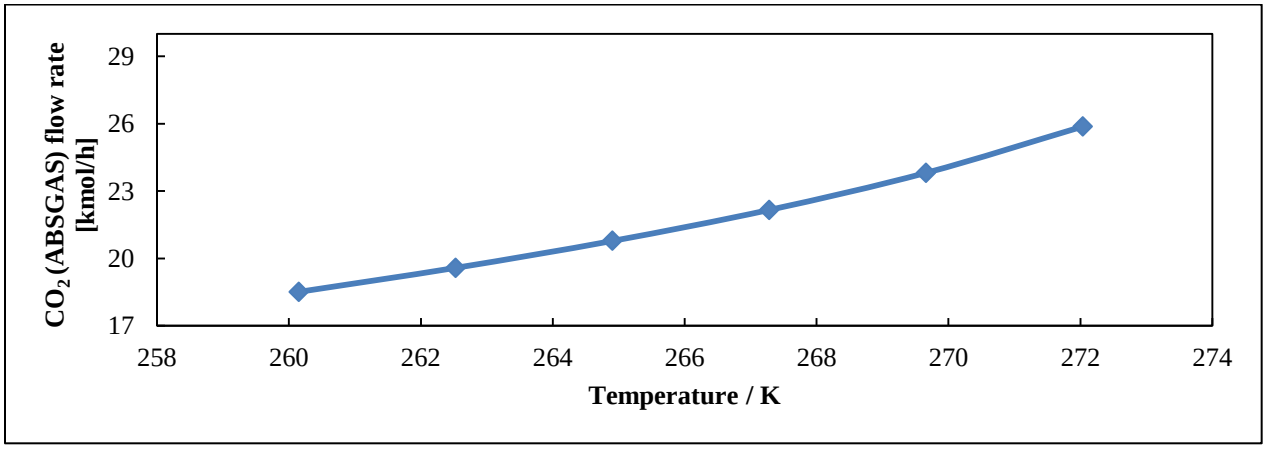

Figure 6.10 (b): Sensitivity analysis relative to the solvent (NMP) temperature versus the amount [kmol/h] of CO_2 emitted into the atmosphere via the ABS-GAS stream for the NMP process.

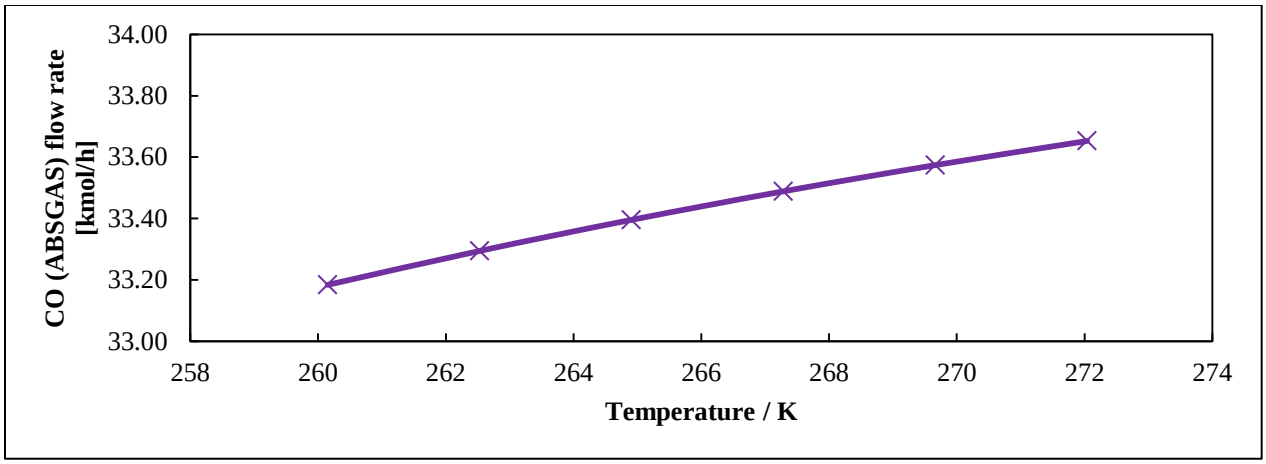

Figure 6.10 (c): Sensitivity analysis relative to the solvent (NMP) temperature versus the amount [kmol/h] of CO emitted into the atmosphere via the ABS-GAS stream for the NMP process.

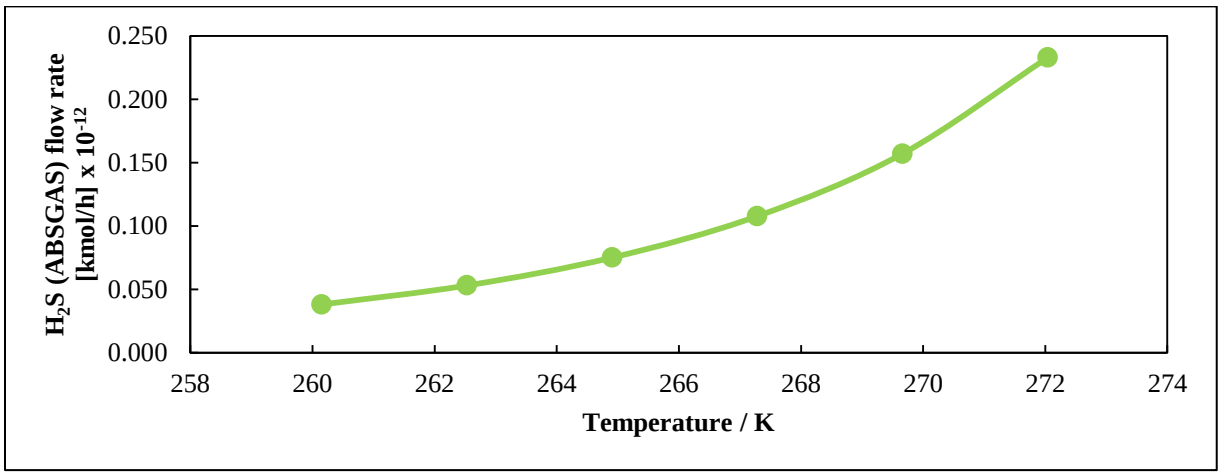

Figure 6.10 (d): Sensitivity analysis relative to the solvent (NMP) temperature versus the amount [kmol/h] of H_2S emitted into the atmosphere via the ABS-GAS stream for the NMP process.

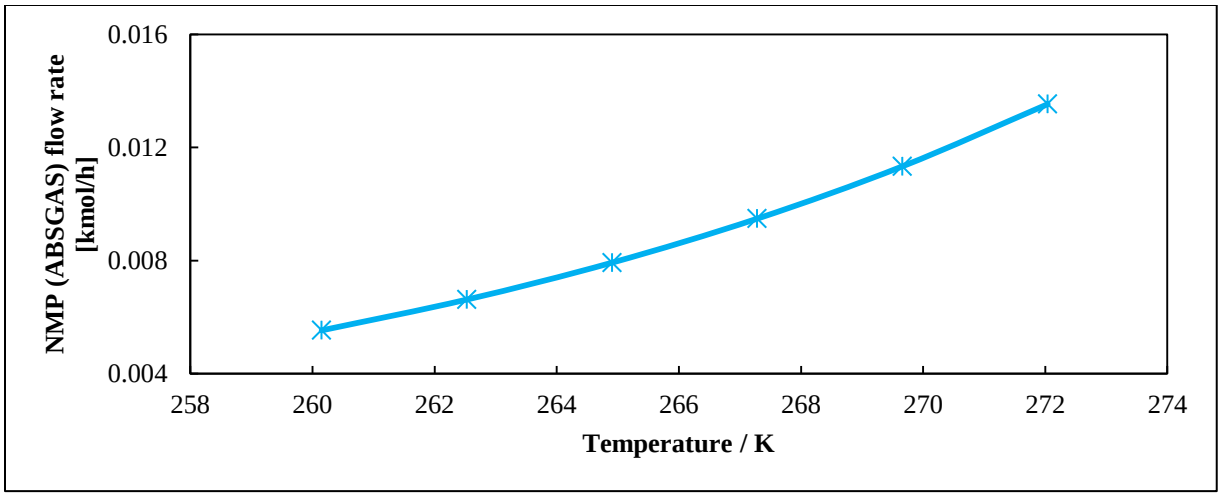

Figure 6.10 (e): Sensitivity analysis relative to the solvent (NMP) temperature versus the amount [kmol/h] of NMP emitted into the atmosphere via the ABS-GAS stream for the NMP process.

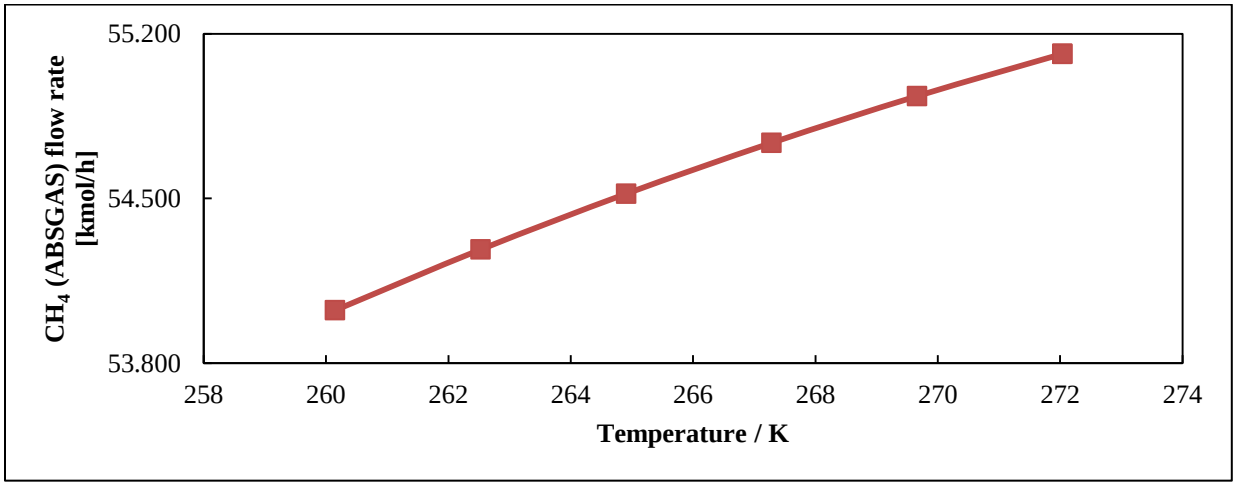

Figure 6.11(a): Sensitivity analysis relative to the solvent (PC) temperature versus the amount [kmol/h] of CH_4 emitted into the atmosphere via the ABS-GAS stream for the PC process.

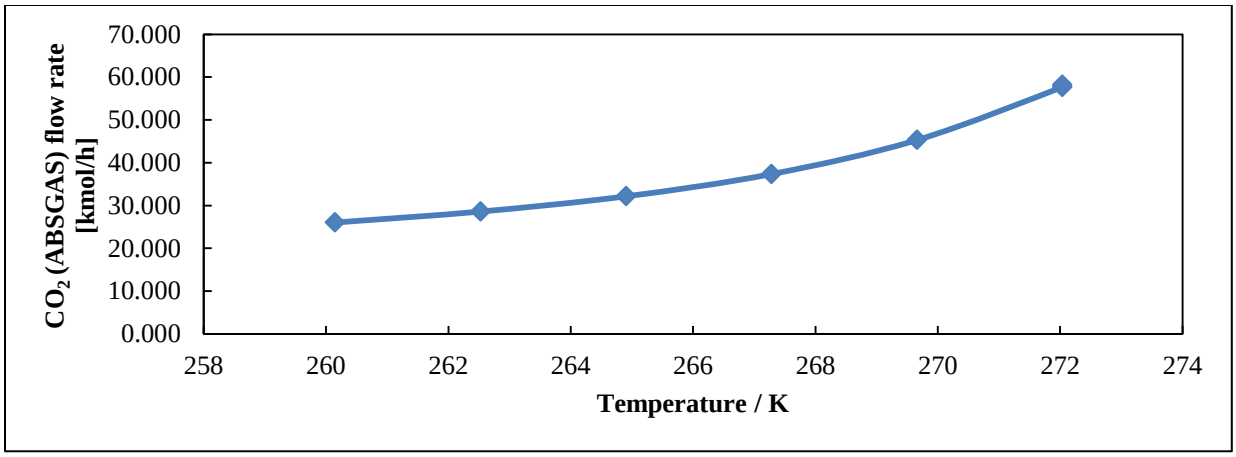

Figure 6.11(b): Sensitivity analysis relative to the solvent (PC) temperature versus the amount [kmol/h] of CO_2 emitted into the atmosphere via the ABS-GAS stream for the PC process.

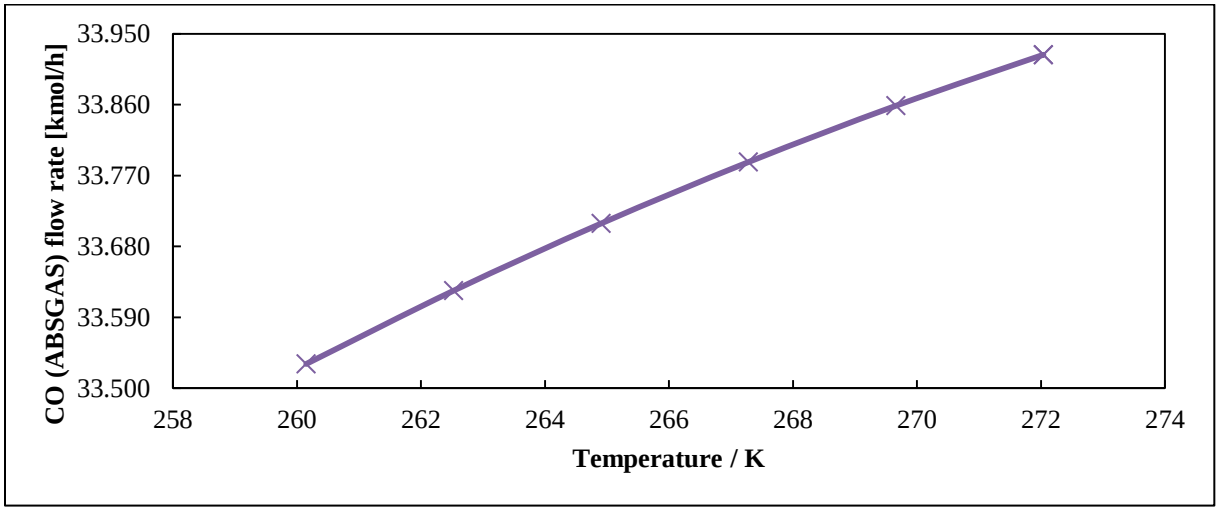

Figure 6.11(c): Sensitivity analysis relative to the solvent (PC) temperature versus the amount [kmol/h] of CO emitted into the atmosphere via the ABS-GAS stream for the PC process.

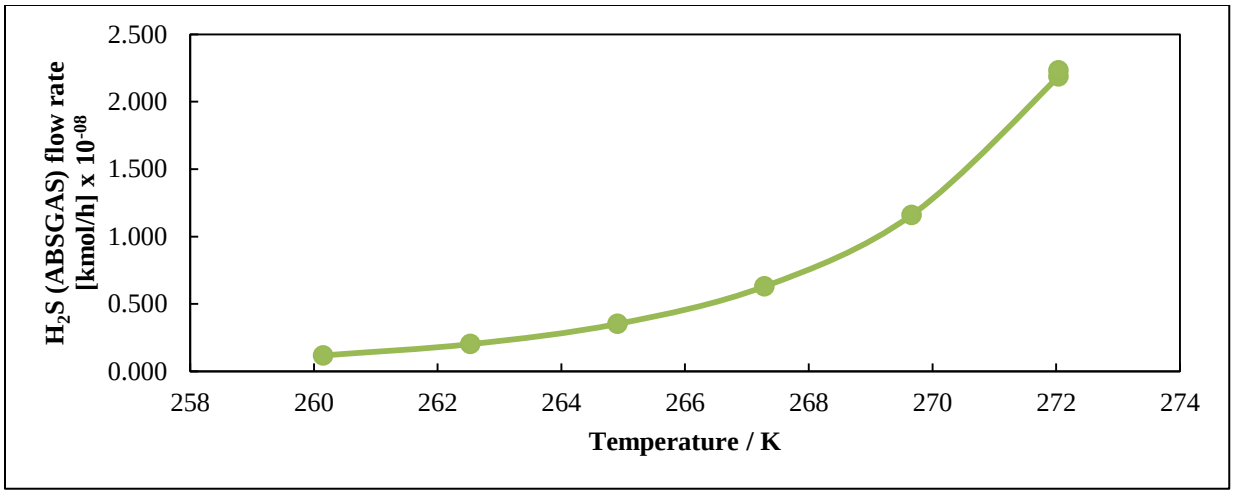

Figure 6.11(d): Sensitivity analysis relative to the solvent (PC) temperature versus the amount [kmol/h] of H_2S emitted into the atmosphere via the ABS-GAS stream for the PC process.

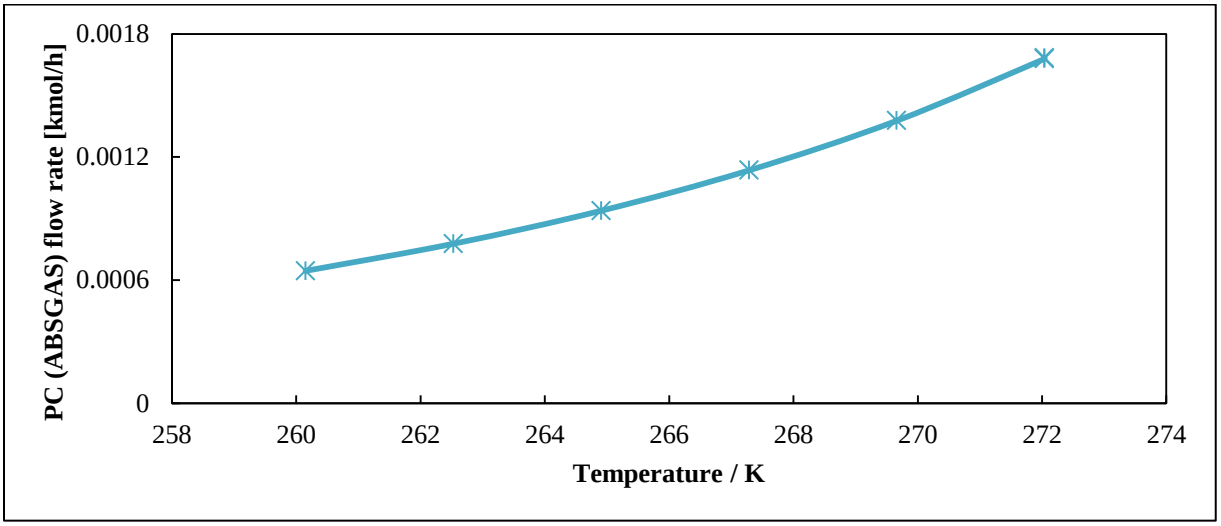

Figure 6.11(e): Sensitivity analysis relative to the solvent (PC) temperature versus the amount [kmol/h] of PC emitted into the atmosphere via the ABS-GAS stream for the PC process.

As for the DEPG absorption process, the reduction of the NPM solvent temperature resulted in more absorption for CO_2 and CH_4, whereas no significant effect was observed for the H_2S and CO. One should also note that more NMP was retained in the liquid phase.

The PC absorption process exhibited quite a similar response to the NMP absorption process regarding the reduction of the PC temperature, where more CO_2 and CH_4 were absorbed as the temperature decreased. As for H_2S and CO no much difference was observed. More retention of

the PC in the liquid phase was also observed as the temperature decreased from 272.04 to 260.15 K.

The results obtained for both the NMP and PC absorption processes exhibited a strong correlation between the solvent temperature and its absorption capability for components such as CO_2 and H_2S. As mentioned earlier, due to the limitation in the operating temperature of both the NMP and PC solvents, a temperature of 260.15 K was determined as optimum.

The optimum conditions resulting from the sensitivity analysis for both the NMP and PC absorption processes are as follows: 10 stages, solvent flow rate of 10000 kmol/h and solvent temperature of 260.15 K.

As for the gas absorption system using the DEPG solvent: gas absorption systems based on either the NMP or PC solvent were undertaken using the optimum conditions obtained from the sensitivity analysis. For benchmarking purpose between the NMP, PC and the C_4F_{10} solvents, the optimum conditions for the NMP and PC solvents were also used in the gas absorption system, based on C_4F_{10}. The results obtained for the NMP, PC and C_4F_{10} gas absorption systems are presented in Tables 6.7 -6.9, respectively.

6.7 Stream results for the absorption process using the NMP solvent at 260.15 K with the NMP flow rate of 10000 kmol/hr and the number of stages set to 10

	NMP	FG	ABSGAS	ABSLIQ	component absorbed (%)	component emitted (%)
Mole Flow kmol/hr						
NMP	9952.0	0.000	0.0060	9952.0	~100	~0
CO	0	35.094	33.184	1.9100	5.44	94.56
CO_2	48.000	1966.8	18.513	1996.3	99.08	0.92
H_2	0	2545.5	2495.9	49.644	1.95	98.05
H_2O	0.0010	28.082	trace	28.083	~100	~0
N_2	0	3314.2	3154.8	159.48	4.81	95.19
Ar	0	40.188	36.327	3.8610	9.61	90.39
CH_4	0	58.409	48.759	9.6500	16.52	83.48
NH_3	0	1.3560	trace	1.3560	~100	~0
H_2S	0	0.1810	trace	0.1810	~100	~0
Total Flow kmol/hr	10000	7989.8	5787.4	12202	—	—
T/ K	260.15	293.22	261.75	278.92	—	—
P/ MPa	6.895	6.881	6.860	6.860	—	—
Vapor Frac	0.000	0.997	1.000	0.000	—	—
Liquid Frac	1.000	0.003	0.000	1.000	—	—
Solid Frac	0	0	0	0	—	—
H/ kJ/mol	-271.95	-99.49	-3.72	-286.24	—	—
S/ kJ/mol.K	-0.607	-0.027	-0.033	-0.498	—	—
Density kg/m^3	1069.8	68.470	51.860	1051.9	—	—
Average MW	98.87	23.60	16.83	88.50	—	—

6.8 Stream results for the absorption process using the PC solvent at 260.15 K with the PC flow rate of 10000 kmol/hr and the number of stages set to 10

	PC	FG	ABSLIQ	ABSGAS	component absorbed (%)	component emitted (%)
Mole Flow kmol/hr						
PC	9952.0	0	9952.0	0.0010	~100	~0
CO	0	35.094	1.5640	33.531	4.46	95.54
CO_2	48.000	1966.8	1988.8	26.021	98.71	1.29
H_2	0	2545.5	48.729	2496.8	1.91	98.09
H_2O	0.0010	28.082	28.083	trace	~100	~0
N_2	0	3314.2	66.402	3247.8	2.00	98.00
Ar	0	40.188	2.3030	37.885	5.73	94.27
CH_4	0	58.409	4.3840	54.025	7.51	92.49
NH_3	0	1.3560	1.3560	trace	~100	~0
H_2S	0	0.1810	0.1810	trace	~100	~0
Total Flow kmol/hr	10000	7989.8	12093	5896.1	—	—
T/ K	260.15	293.22	277.92	262.94	—	—
P/ MPa	6.895	6.881	6.860	6.860	—	—
Vapor Frac	0.000	0.997	0.000	1.000	—	—
Liquid Frac	1.000	0.003	1.000	0.000	—	—
Solid Frac	0	0	0	0	—	—
H/ kJ/mol	-155.22	-23.770	-143.56	-1.0100	—	—
S/ kJ/mol.K	-0.14	-0.01	-0.11	-0.01	—	—
Density kg/m^3	1227.28	68.470	1199.9	52.330	—	—
Average MW	101.81	23.600	91.470	17.040	—	—

6.9 Stream results for the absorption process using the C_4F_{10} solvent at 260.15 K with the C_4F_{10} flow rate of 10000 kmol/hr and the number of stages set to 10

	C_4F_{10}	FG	ABSLIQ	ABSGAS	component absorbed (%)	component emitted (%)
Mole Flow kmol/hr						
C_4F_{10}	10000	0	9915.5	84.496	99.16	0.85
CO	0	35.091	16.656	18.436	47.46	52.54
CO_2	0	1966.8	1966.6	0.1780	99.99	0.01
H_2	0	2545.5	392.35	2153.2	15.41	84.59
H_2O	0	28.084	28.084	trace	~100	~0
N_2	0	3314.2	1990.2	1324.0	60.05	39.95
Ar	0	40.189	40.182	0.0060	99.98	0.02
CH_4	0	58.406	41.724	16.682	71.44	28.56
NH_3	0	1.3580	1.3580	trace	~100	~0
H_2S	0	0.1840	0.1840	trace	~100	~0
Total Flow kmol/hr	10000	7989.8	14393	3597.0	—	—
T/ K	260.15	293.44	269.67	261.81	—	—
P/ MPa	6.895	6.881	6.860	6.860	—	—
Vapor Frac	0.000	0.997	0.000	1.000	—	—
Liquid Frac	1.000	0.003	1.000	0.000	—	—
Solid Frac	0	0	0	0	—	—
H/ kJ/mol	-2199.84	-99.923	-1570.55	-53.413	—	—
S/kJ/mol.K	-0.664	-0.028	-0.463	-0.046	—	—
Density kg/m^3	1795.4	72.808	1577.9	54.969	—	—
Average MW	238.03	23.600	174.15	17.330	—	—

Analysis of Tables 6.7-6.9 reveals that 99.08 % and 98.71 % of CO_2 is absorbed in the NMP and PC solvents, respectively, as opposed to 99.99 % that is absorbed in the C_4F_{10} solvent. The component CH_4 is poorly absorbed in both the NMP and PC absorption processes, whereas 71.44 % is absorbed in the C_4F_{10} absorption process.

As can be seen from Table 6.9, the C_4F_{10} solvent has demonstrated higher absorption for gases such as CO, N_2 and H_2 compared to the NMP and PC processes. This reinforces the work of Battino and Cleve (1996), Wihelm and Battino (1973), and numerous other literature sources, which state that PFCs have the ability to dissolve oxygen and other gases. However, emitting gases such as N_2 and H_2 into the atmosphere is desirable as they pose no harm to the environment and it is also advantageous for the stripping process, as less amounts of N_2 and H_2 will remain for removal.

One should note that the component H_2S is fully absorbed in all the absorption processes. Tables 6.7-6.9 show that trace amounts of H_2S are emitted into the atmosphere via the ABSGAS stream. Components such as NH_3 and H_2O have shown high absorption in all three absorption processes except for Ar which is fully absorbed only in the C_4F_{10} absorption process. However, the absorption of H_2O in any solvent is undesirable, since it reduces the solvent's purity and therefore its absorption capability. Consequently, the absorbed H_2O in any solvent would require further processing, by means of hot regeneration or glycol unit, to remove it prior to the recycling of the solvent. Moreover, one should bear in mind that throughout this work, H_2O is referred to as water vapour unless otherwise stated.

Tables 6.7-6.9 also reveal that co-absorption of CO_2 and H_2S is highly probable to occur in the NMP, PC and C_4F_{10} solvents. Consequently, for current conditions, the three solvents would not be a good option for selective removal of H_2S. Bucklin and Schendel (1984) compared Fluor solvents and Selexol processes, and revealed that Selexol, NMP and Sepasolv are more efficient than PC- if selective removal of H_2S from flue gas containing CO_2 is required. In addition, Bucklin and Schendel (1984) know no cases where PC would be recommended for the removal of H_2S. One should note that selective H_2S removal with deep CO_2 removal requires two absorption and stripping columns (Burr and Lyddon, 2008). H_2S is selectively removed in the first absorption column and CO_2 in the second one.

Although C_4F_{10} has shown higher absorption capability for all the components (CO_2, CO, CH_4, H_2S, Ar, NH_3 and H_2O), Tables 6.7-6.9 reveal that 84.496 kmol/h corresponding to 0.85 % of C_4F_{10} is emitted into the atmosphere whereas 0.0010 and 0.0060 kmol/h of the PC and NMP are emitted into the atmosphere, respectively.

Due to the high global warming potential associated with C_4F_{10}, to be used as a solvent one has to minimise its emission to meet environmental regulations.

Consequently, as previously, the temperature of the C_4F_{10} solvent was reduced to 220.15 K in order to minimize its emission into the atmosphere. The results pertaining to the absorption process are presented in Table 6.10. One should note that solvent flow rate was kept at 10000 kmol/h and the number of stages kept at 10. As can be seen from Table 6.10, the temperature of 220.15 K resulted in increased absorption for most of the components with CO_2 reaching approximately 100 %, as less than 0.001 kmol/h is emitted into the atmosphere. CH_4 and N_2 absorption also increased to 99.06 % and 80.62 %, respectively. However, Ar, H_2S, NH_3 and H_2O remained fully absorbed, as in the previous run, which was undertaken at 260.15 K.

A comparison between the NMP and PC absorption processes, at 260.15 K with the C_4F_{10} absorption process undertaken at 220.15 K, reveals that the amount of C_4F_{10} solvent emitted into the atmosphere is higher than that of NMP and PC solvents, i.e., 15.362 kmol/h for C_4F_{10} as opposed to 0.0060 kmol/h and 0.0010 kmol of NMP and PC, respectively. In an attempt to overcome the high vapour pressure associated with the C_4F_{10} solvent, the C_6F_{14} component was considered, and the absorption process was undertaken, firstly at 260.15 K, while keeping the solvent flow rate equal to that of C_4F_{10} (10000 kmol/h), and the number of stages to 10. Thereafter, the solvent temperature was reduced to 220.15 K in order to analyse the effect of temperature on the absorption process. The results obtained are presented in Tables 6.11 and 6.12.

Table 6.10: Stream results for the absorption process using the C_4F_{10} solvent at 220.15 K with the C_4F_{10} flow rate of 10000 kmol/hr and the number of stages set to 10

	C_4F_{10}	FG	ABSLIQ	ABSGAS	component absorbed (%)	component emitted (%)
Mole Flow kmol/hr						
C_4F_{10}	10000	0	9984.6	15.362	99.85	0.15
CO	0	35.091	18.456	16.636	52.59	47.41
CO_2	0	1966.8	1966.8	< 0.0010	~100	~0
H_2	0	2545.5	369.10	2176.5	14.50	85.50
H_2O	0	28.084	28.084	trace	100	0
N_2	0	3314.2	2671.8	642.39	80.62	19.38
Ar	0	40.189	40.189	trace	~100	~0
CH_4	0	58.406	57.856	0.5490	99.06	0.94
NH_3	0	1.3580	1.3580	trace	~100	~0
H_2S	0	0.1840	0.1840	trace	~100	~0
Total Flow kmol/hr	10000	7989.8	15138	2851.4	–	–
T/ K	220.15	293.24	238.64	222.32	–	–
P/ MPa	6.895	6.881	6.860	6.860	–	–
Vapor Frac	0.000	0.997	0.000	1.000	–	–
Liquid Frac	1.000	0.003	1.000	0.000	–	–
Solid Frac	0	0	0	0	–	–
H/ kJ/mol	-2209.2	-99.920	-1509.3	-14.840	–	–
S/ kJ/mol.K	-0.703	-0.028	-0.468	-0.042	–	–
Density kg/m^3	1906.3	72.810	1704.00	34.380	–	–
Average MW	238.03	23.600	167.94	9.300	–	–

Table 6.11: Stream results for the absorption process using the C_6F_{14} solvent at 260.15 K with the C_6F_{14} flow rate of 10000 kmol/hr and the number of stages set to 10

	C_6F_{14}	FG	ABSGAS	ABSLIQ	compoenent absorbed (%)	component emitted (%)
Mole Flow kmol/hr						
C_6F_{14}	10000	0	11.762	9988.2	99.88	0.12
CO	0	35.091	18.352	16.740	47.70	52.30
CO_2	0	1966.8	0.0030	1966.8	~100	~0
H_2	0	2545.5	2211.7	333.75	13.11	86.89
H_2O	0	28.084	trace	28.084	~100	~0
N_2	0	3314.2	2544.9	769.375	23.21	76.79
Ar	0	40.189	0.0020	40.187	99.99	0.01
CH_4	0	58.406	5.2570	53.149	91.00	9.00
NH_3	0	1.3580	trace	1.3580	~100	~0
H_2S	0	0.1840	0.0010	0.1830	99.69	0.31
Total Flow kmol/hr	10000	7989.8	4792.0	13198	–	–
T/ K	260.15	293.24	259.85	268.70	–	–
P/ MPa	6.895	6.881	6.860	6.860	–	–
Vapor Frac	0.000	0.997	1.000	0.000	–	–
Liquid Frac	1.000	0.003	0.000	1.000	–	–
Solid Frac	0	0	0	0	–	–
H kJ/mol	-3034.7	-99.920	-9.3600	-2356.5	–	–
S kJ/mol.K	-0.964	-0.028	-0.036	-0.732	–	–
Density kg/m^3	1820.00	72.810	54.450	1716.8	–	–
Average MW	338.04	23.600	16.760	264.34	–	–

Table 6.12: Stream results for the absorption process using the C_6F_{14} solvent at 220.15 K with the C_6F_{14} flow rate of 10000 kmol/hr and the number of stages set to 10

	C_6F_{14}	FG	ABSGAS	ABSLIQ	component absorbed (%)	component emitted (%)
Mole Flow kmol/hr						
C_6F_{14}	10000	0	1.1030	9999.0	99.99	0.01
CO	0	35.091	16.556	18.536	52.82	47.18
CO_2	0	1966.8	trace	1966.8	~100	~0
H_2	0	2545.5	2238.7	306.73	12.05	87.95
H_2O	0	28.084	trace	28.084	~100	~0
N_2	0	3314.2	2561.2	753.043	22.72	77.28
Ar	0	40.189	trace	40.189	~100	~0
CH_4	0	58.406	0.0600	58.346	99.90	0.10
NH_3	0	1.3580	trace	1.3580	~100	~0
H_2S	0	0.1840	trace	0.1840	~100	~0
Total Flow kmol/hr	10000	7989.8	4817.7	13172	–	–
T/ K	220.15	293.24	220.28	236.39	–	–
P/ MPa	6.895	6.881	6.860	6.860	–	–
Vapor Frac	0.000	0.997	1.000	0.000	–	–
Liquid Frac	1.000	0.003	0.000	1.000	–	–
Solid Frac	0	0	0	0	–	–
H/ kJ/mol	-3046.5	-99.920	-3.7800	-2372.0	–	–
S/ kJ/mol.K	-1.013	-0.028	-0.039	-0.768	–	–
Density kg/m^3	1889.1	72.810	61.930	1809.3	–	–
Average MW	338.04	23.600	16.000	265.10	–	–

Table 6.11 reveals that the variation of the carbon chain length of PFC compounds by 2, which corresponds to C_6F_{14}, has a significant effect on the amount of solvent emitted into the atmosphere, as the flow rate of C_6F_{14} in the ABSGAS stream decreased to 11.762 kmol/h. One should also note that increased absorption of all the gases is also observed, with 0.0030 kmol/h and 0.0010 kmol/h of CO_2 and H_2S emitted into the atmosphere, respectively.

Table 6.12, which presents the results of the C_6F_{14} absorption process undertaken at 220.15 K, shows that 1.103 kmol/h, corresponding to 0.01 % of C_6F_{14}, is emitted into the atmosphere. This value is significantly low, compared to the 15.362 kmol/h of C_4F_{10} emitted in the atmosphere emanating from the C_4F_{10} absorption process at 220.15 K. However, 1.103 kmol/h of C_6F_{14} is still higher compared to 0.006 kmol/h of NMP and 0.0010 kmol of PC emitted into the atmosphere. The results emanating from the C_6F_{14} absorption process reveal that PFC compounds with longer carbon chains have the potential to behave as ideal physical solvents.

A comparison between Tables 6.4 and 6.10 reveals that the results emanating from the conditions, solvent molar flow of 8000 or 10000 kmol/h, temperature of 220.15 K and number of stages of 10 or 13, are quite similar, except for slight differences in the emission of C_4F_{10}, CO and CH_4. However, given that the major differences reside in the operating conditions, a trade-off was undertaken between 10 versus 13 stages, and 8000 versus 10000 kmol/h of either C_4F_{10} or C_6F_{14}. The conditions of 13 stages and 8000 kmol/h was considered on the basis that less solvent will be used and the expenditure to build a tower with 3 additional stages will be a once off.

In light of the results obtained, one can observe that C_4F_{10} and C_6F_{14} have demonstrated excellent capacity to absorb the targeted flue gas components (CO_2, H_2S, CO and CH_4), thereby partially meeting the design objectives. However, the two PFC solvents have shown poor selectivity for the targeted flue gas components. A comparison between Tables 6.10 and 6.12 show that C_6F_{14} is better than C_4F_{10} in terms of selectivity. Hence, PFC components with longer carbon chains have the potential to be more selective towards the targeted flue gas components.

6.2.2 Solvent regeneration section

As explained in Section 2.2.1, in the solvent regeneration section, the absorbed gases are recovered from the rich solvent by either a sequence reduction of pressure at constant

temperature denoted as a P-Swing option or by a sequence reduction of both pressure and temperature denoted as a P-T-Swing option. However, a stripping column is often added to the design to facilitate a full recovery of the absorbed gases, thereby purifying the regenerated solvent.

In this simulation, the P-T-Swing option could not be used as the absorption process took place at a temperature of 220.15 K and more energy would have required reducing the rich solvent temperature to lower temperature values. Conversely, the P-Swing option was considered where a series of flash drums was initially used for solvent regeneration, and thereafter a stripping column was used to further ameliorate the desorption process. One should note, as absorption is favoured at high pressure and low temperature, the reverse process is favoured at low pressure and high temperature. Therefore, heat in the form of steam was supplied to the stripper to facilitate the desorption process (Sattler and Feindt, 1995).

The reduction of pressure at constant temperature was undertaken in sequences of one, two or three pressure values, depending on the result for each flash drum. Considering the rich solvent (ABS-LIQ) pressure and temperature, for each solvent absorption process, the flash drum pressures were selected in a manner to maintain the solvent in the liquid phase, while recovering the absorbed gases throughout the P-swing option. One should note that the flash drum conditions were different for each solvent absorption process, as they depend solely on the nature of the solvent used and the desired purity.

In this study, the aim was to maintain 100% of the solvent in the liquid phase of each flash drum while stripping off the remaining gases. Consequently, the subsequent sections will focus on the solvent regeneration for the C_4F_{10} and C_6F_{14} absorption processes, respectively.

6.2.2.1 Solvent regeneration for the C_4F_{10} absorption process

For the C_4F_{10} absorption process, a series of three flash drums was initially used, and thereafter a stripping column was added, to complete the desorption process. Figure 6.12 illustrates the solvent regeneration section for the C_4F_{10} absorption process. Appendix G contains the inputs and outputs for the solvent regeneration section relative to the C_4F_{10} absorption process.

The reduction of pressure was undertaken in the sequence of 5.000, 3.500 and 2.000 MPa at a constant temperature of ~ 241.58 K, which is the rich solvent stream (ABS-LIQ) temperature. The sequence reduction of pressure could not be lowered to pressure values below 2.000 MPa, as this would have resulted in a significant loss of C_4F_{10} in the vapour phase. In addition, having the flash drum temperature set at ~ 241.58 K, further reduction of the pressure to the atmospheric value would have resulted in vaporisation of C_4F_{10} and its loss to the vapour phase, as 241.58 K would have been higher than the C_4F_{10} normal boiling point. However, one should note that a straight reduction of pressure from 6.860 to 2.000 MPa would have resulted in having more C_4F_{10} in the vapour phase, which is highly undesirable.

The pressure of 5.000 MPa corresponding to the first flash drum was chosen considering the pressure of the ABS-LIQ stream, which is 6.860 MPa. The pressure reduction in the first flash drum stripped off some of the flue gas components, while maintaining in the liquid phase 99.93 % of the C_4F_{10} solvent introduced into the first flash drum; the second pressure reduction maintained 99.91 % of C_4F_{10} introduced in the second flash drum and the third pressure reduction maintained 99.81 % of C_4F_{10} introduced in the third flash drum.

The result obtained from the P-swing option shows that 0.35 % of C_4F_{10} introduced in the first flash drum is lost at the end of the third flash drum. However, the F3Down stream does not only contain C_4F_{10} but also a significant amount of flue gas components, such as CO, CO_2, N_2, Ar, CH_4, etc. Ideally, the F3Down stream is not deemed to be recycled to the absorber unless it contains mainly C_4F_{10}, with the remaining gases in trace amounts. One should note that a recycled solvent of higher purity will absorb more gas per pass, thereby reducing the solvent recirculation rate.

Consequently, a stripping column was added to the solvent regeneration section. Similar to the absorption column, the RadFrac column was chosen for the design of the stripping column. One should note that a sensitivity analysis was performed on the stripper's number of stages ranging from 10 to 20, and the optimum number of stage was determined to be 16, as it resulted in less emission of C_4F_{10} and stripped off nearly all the gases from C_4F_{10} except for H_2O. The feed stage was also varied from stage 2 to stage 15, and the optimum feed stage was determined to be stage 2. The results emanating from the sensitivity analysis for the number of stages, and feed stage,

relative to the stripper, are presented in Appendix I. One should also note that the stripping column employed a partial vapour condenser and kettle reboiler.

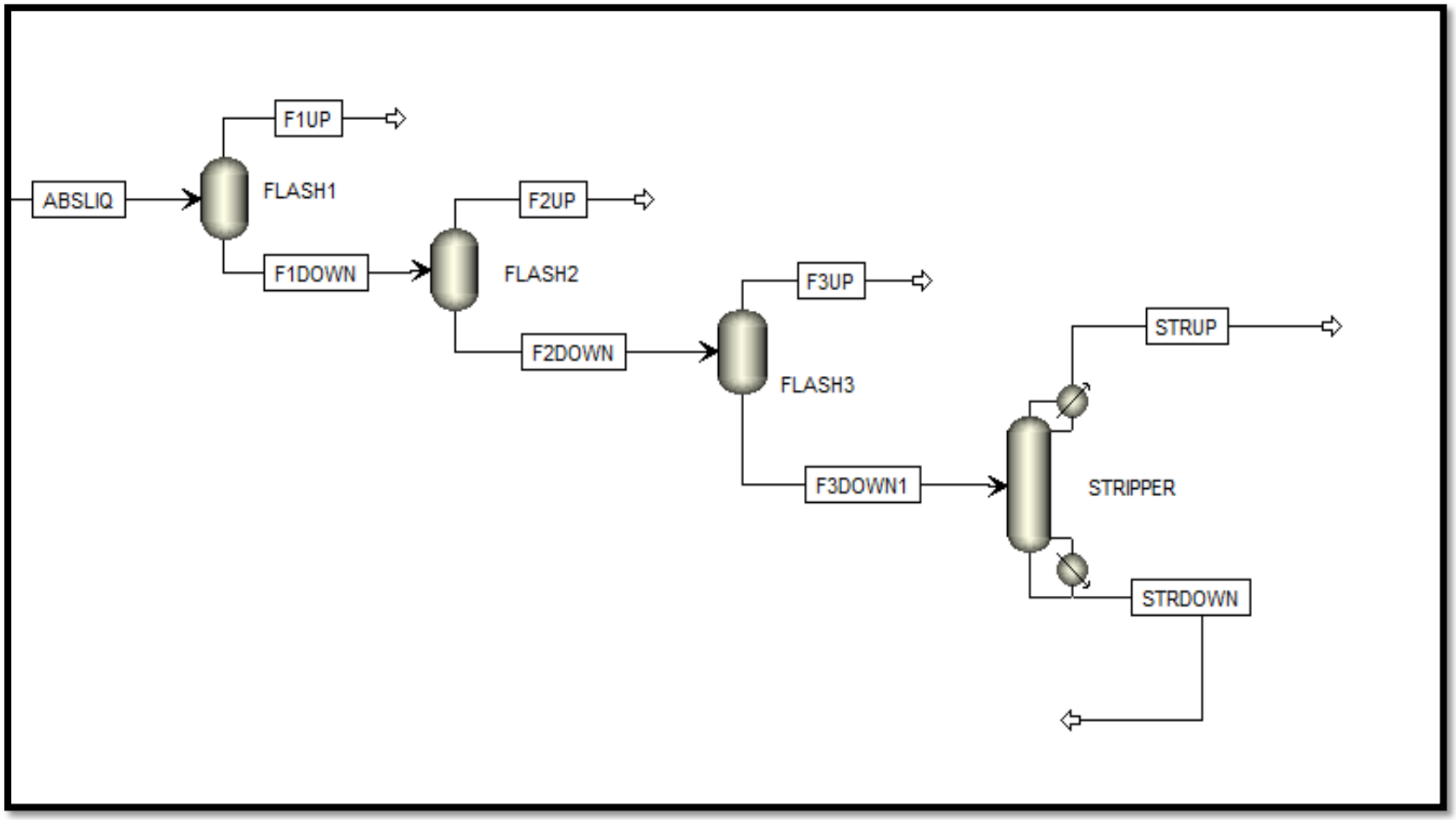

Figure 6.12: Solvent regeneration section for the C_4F_{10} / C_6F_{14} absorption process

The stripping process was undertaken at 1.400 MPa at reflux ratios of 0.1, which was determined by the "Design/Spec/Vary' function of Aspen Plus®. In addition, the optimum feed stage to the stripping column was determined to be 2, resulting in a reboiler heat duty of 75827.43 kW. The Stripping column results show that it is near impossible to strip essentially all the flue gas components from the C_4F_{10} solvent at the considered reflux ratio range. However, one could observe that as the reflux ratio was increased from 0.1 to 2.0, the molar flow of the C_4F_{10} solvent in the stripper overhead did not vary significantly, as it decreased from 22.013 to 22.011 kmol/hr, whilst the molar flow rate of CO_2 in the stripper bottom decreased from 0.002 to less than 0.001 kmol/hr. In other words, at higher reflux ratios, it is probable to have less C_4F_{10} and CO_2 in both the stripper overhead and stripper bottom, respectively. One should also note that flue gas components such as CO, N_2, H_2 and H_2S were significantly stripped off the C_4F_{10} solvent but H_2O exhibited, once again, indifference or insensitivity behaviour towards the stripping process. To rectify the results stemming from the stripper, the bottom stream will have to be further processed before recycling, as current practice suggests. Consequently, the C_4F_{10} solvent could not be recycled to the absorber in this study.

For the entire perfluorobutane gas absorption system operated at 220.15 K, with the solvent molar flow rate of 8000 kmol/hr, which is shown in detail in Figure 7.13, 0.27 % of C_4F_{10} is emitted into the atmosphere.

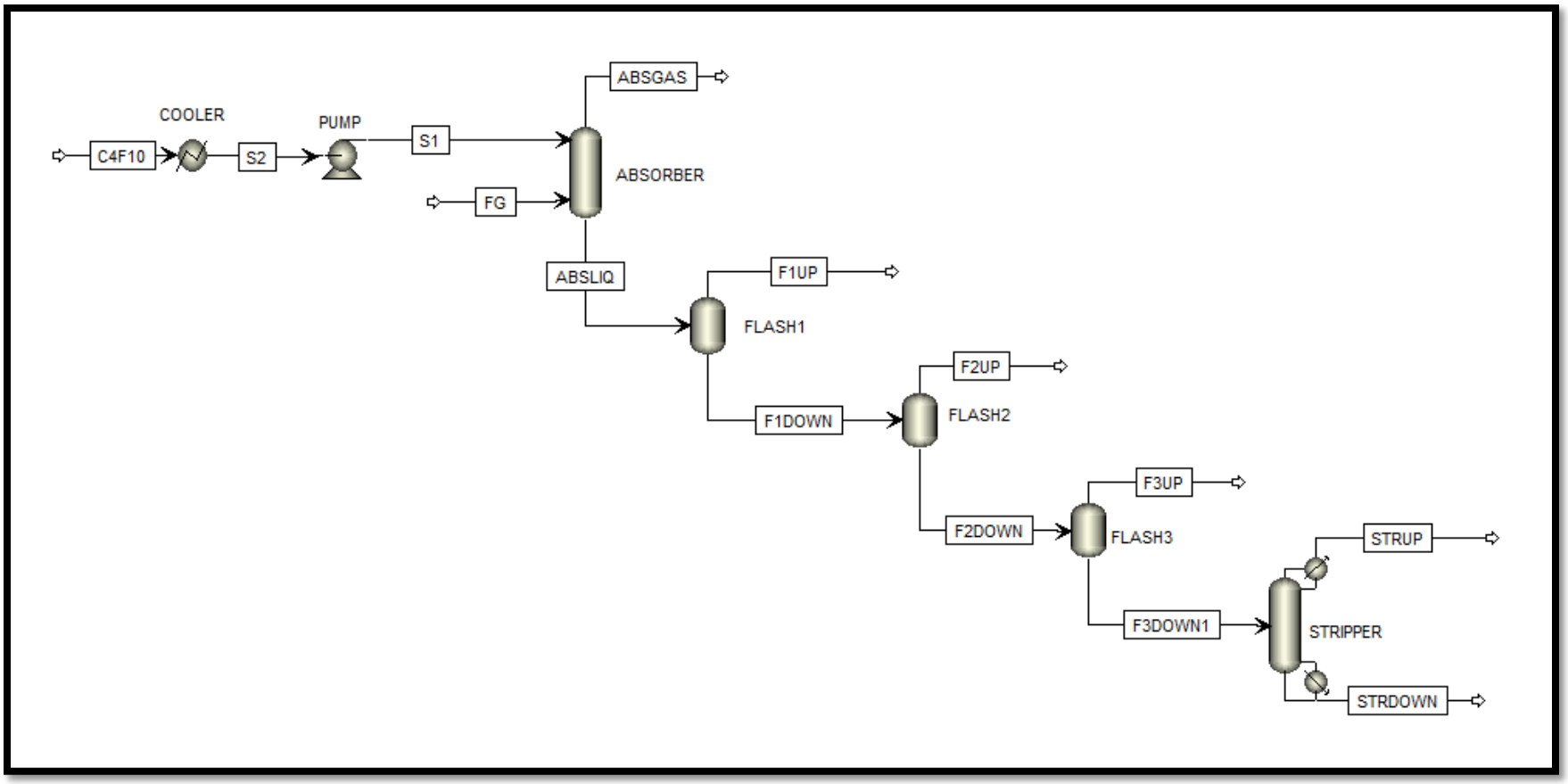

Figure 6.13 Detailed gas absorption system using C_4F_{10} / C_6F_{14} as a physical solvent

6.2.2.2 Solvent regeneration for the C_6F_{14} absorption process

As for the C_4F_{10} absorption process, a series of three flash drums was initially considered and thereafter a stripping column was added. The reduction of pressure at ~ 239.70 K was undertaken in sequences of 5.000, 3.500 and 1.000 MPa. Again, the pressure could not be reduced to values less than 1.000 MPa to prevent vaporisation of the C_6F_{14} solvent. Figure 6.12 illustrating the solvent regeneration section for the C_4F_{10} absorption process was also used for the C_6F_{14} absorption process. Appendix G contains the inputs and outputs for the solvent regeneration section for the C_6F_{14} absorption process.

The results obtained from the P-swing option can be summed up as follows: the three flash drums stripped off some of the flue gas components and maintained in the liquid phase approximately 100 % of C_6F_{14} introduced in each flash drum. However, only 0.169, 0.148 and 0.204 kmol/hr of C_6F_{14} were in the vapour phase of each of the three flash drums, respectively. Although most of the C_6F_{14} was maintained in the liquid phase throughout the flash drums, the bottom product of the third flash drum still had flue gas components in concentrations higher than trace amounts.

Consequently, a stripping column was added to fully recover the solvent. The stripping column was designed similarly to the one in the solvent regeneration for the C_4F_{10} absorption process. A sensitivity analysis was conducted on the number of stages and 16 stages were determined to be optimum. The optimum feed stage to the stripping column, with respect to minimizing the reboiler heat duty, was determined to be 2, resulting in a reboiler heat duty of 159174.1 kW. One should note that no sensitivity analysis was undertaken for the feed stage, the stage 2 was chosen following the results obtained for the C_4F_{10} absorption process. The results stemming from the sensitivity analysis for the number of stages of the stripping column are available in Appendix I.

The stripping process was undertaken at 1.000 MPa at reflux ratio of 0.5. The stripping column results show that most of the flue gas components were stripped off the C_6F_{14} solvent at the reflux ratio considered, except for H_2O. However, variation of the reflux ratio from 0.5 to 5.0 did not have any effect on the molar flow rate of either C_6F_{14} or the flue gas components. Due to the high concentration of H_2O (28.060 kmol/hr) in the bottom product of the stripper, C_6F_{14} could not be recycled to the absorber. Further processing of the stripper bottom product is required before the solvent is recycled. As for the C_4F_{10} process, a glycol

dehydration unit could be used to remove H_2O and thereby purifying the C_6F_{14} solvent before recycling.

One should note that further stripping of the vent stream could be an option but this was not considered in this study due to the fact that it would not have solved the high vapour pressure issue associated with the C_4F_{10} and C_6F_{14} components, but would have increased the capital expenditure of the process.

For the entire perfluorohexane gas absorption system operated at 220.15 K with the solvent molar flow rate of 8000 kmol/hr, which is shown in Figure 6.13, less than 0.01 % of C_6F_{14} corresponding to 0.216 kmol/h, was emitted into the atmosphere.

The results obtained for the C_6F_{14} solvent confirm that PFCs with longer carbon chain length can be better solvents. Consequently, PFC compounds with longer carbon chain length should be investigated.

Gas absorption systems using perfluoroalkanes with longer carbon chains could have been undertaken in this study, but this was not possible due to unavailability of most of their properties, which are required for the design of gas absorption systems. One would normally use predictive models to obtain the required properties. However, this practice becomes tedious and unsuccessful at times, when almost all the properties have to be predicted in the absence of any reference. Critical properties are generally easy to predict as there are various predictive models available for their completion. For properties such as heat of formation and Gibbs free energy of formation for perfluoroalkanes with longer carbon chains, such as $C_{15}F_{32}$, most of the contribution methods available do not cater for the C-F functional group. However, contribution methods such as the modified Dortmund UNIFAC (Gmehling et al., 1998) and Constantinou and Gani (1994) cater for the C-F functional group, but they yield inconsistent results.

As mentioned in Chapter 2, Heintz et al. (2008) investigated carbon capture from fuel gas streams under elevated pressures and temperatures using PFCs ranging from C_{13} to C_{17}. In their study, the PFC solvent used, which is $C_{17}F_{30}$, was regenerated using three flash drums, and no stripping column was involved. The solvent loss observed was attributed to the fact that the absorption and regeneration temperatures were close to the solvent boiling point. However, this challenge could be overcome by undertaking absorption and regeneration at lower temperatures. One should ensure that the viscosity of the solvent at lower temperatures

does not significantly reduce mass transfer between components involved in the gas absorption system.

A comparison between the energy requirements for the C_4F_{10} and C_6F_{14} gas absorption systems was also undertaken. Their results are reported in Table J.1of Appendix J. From this table, one can see that the heat duties for all the units, except for the network required for the coolers relative to C_4F_{10}, are generally less than those for C_6F_{14}. These results are primarily attributed to the physical properties of C_4F_{10} and C_6F_{14}, which are summarised in Chapter 2. Table J.1, in Appendix J, reveals that 89273.8 kW are required to cool C_4F_{10} from 298.15 K to 220.15 K, whereas 54394 kW are required for C_6F_{14} to attain the same temperature from 298.15 K. This is due to the fact that denser components require more energy to cool down. One should note that C_4F_{10} is gaseous whereas C_6F_{14} is liquid at atmospheric conditions.

As mentioned earlier, the greater the number of carbon atoms in PFCs, the higher the viscosity and therefore, the higher the network that a pump would require to achieve high pressure values. This is demonstrated in the network required to pump 8000kmol/hr of C_4F_{10} and C_6F_{14} from nearly atmospheric pressure to 6.895 MPa, where 2207.98 kW is required for the former and 3923.28 kW for the latter.

One should note that the absorbers and flash drums were configured to operate adiabatically for the two gas absorption systems and therefore their heat duties were null.

The heat duties relative to the stripping column reboiler reveal that the energy required for the C_6F_{14} process is approximately double that required for the C_4F_{10} processes. This is due to the fact that C_4F_{10} is lighter than C_6F_{14} and more energy is generally required to heat up heavier components. One should note that the normal boiling point of a component is the temperature at which its vapour pressure is equal to the atmospheric pressure. In addition, the boiling point of any component increases with increased pressure. Consequently, running the stripping column at lower pressures would have required less heat duty for the reboiler but this could not be achieved as more of the PFC solvent would have vaporised.

From the tables, one can see that the condenser duty in the stripping column for the C_6F_{14} process is less than that for C_4F_{10} process. These results are reflective of the heat duties relative to the stripping column reboiler, as the condensation process is the opposite of the vaporisation process, which is driven by the reboiler. In the case where total condensation

occurs in a stripping column, the heat of condensation will numerically be equal to the heat of vaporisation with the opposite sign.

6.3 Preliminary cost estimation for the gas absorption system using either the C_4F_{10} or C_6F_{14} solvents

As mentioned in Chapter 2, innovative technologies are encouraged but the associated high costs of testing and that of commercialization, constitute both a barrier to development and an incentive to stick to old technologies, if they have proven to be satisfactory. Consequently, a preliminary cost estimation for the gas absorption system using either the C_4F_{10} or C_6F_{14} solvents was undertaken using the process economic analyser in Aspen Plus® V8.0.

All the equipment used in the gas absorption systems were assumed to be constructed in stainless steel, as this material is impervious to all the flue gas components and PFCs, components considered in this study (Air Liquide, 2013). The absorption and stripping columns for both the C_4F_{10} and C_6F_{14} gas absorption systems had 13 and 16 stages, respectively.

For each gas absorption system using either the C_4F_{10} or C_6F_{14} solvent, a cooler followed by a pump, or the opposite, was used to attain the conditions of 6.895MPa and 220.15 K. One should note that different units could have been used to attain the same conditions of pressure and temperature for C_4F_{10}, as it was in its gaseous state. For example, a two-stage compressor followed by a cooler could have been used to attain the conditions of 6.895 MPa and 220.15 K for the C_4F_{10} solvent. This method is feasible but it would have required ~ 12921 kW, as opposed to ~ 2660.5 kW required, using a pump. In addition the cost associated with using a two-stage compressor is greater than that of a pump. Consequently, C_4F_{10} was initially cooled to 220.15 K for liquefaction and thereafter pumped to 6.895 MPa.

One should note that the equipment used in the gas absorption systems was mapped using the process economic analyser in Aspen Plus® V8.0. For unit operations such as the absorption and stripping columns, the process economic analyser in Aspen Plus® V8.0 considers the simulation stages as ideal and thereafter applies a default stage efficiency to obtain the real number of stages or trays. The results obtained, relative to the equipment mapping from the absorption and stripping columns for the C_4F_{10} and C_6F_{14} solvents, are listed in Tables 6.13 and 6.14, respectively.

The preliminary costs estimation for the gas absorption system using both the C_4F_{10} and C_6F_{14} solvents are summarised in Tables 6.15 and 6.16. Their equipment and installation costs are reported in Tables 6.17 and 6.18. In Tables 6.19 and 6.20 are list their utility costs.

Preliminary cost estimation was also undertaken for gas absorption systems using the DEPG and NMP solvents, to facilitate a benchmarking of these solvents, against the C_4F_{10} and C_6F_{14} solvents. The cost estimation relative to the DEPG and NMP solvents are presented in Tables 6.21 and 6.22, respectively. One should note that the process flow diagrams for the DEPG and NMP solvents are similar to that of C_6F_{14} solvent.

Table 6.13: Equipment mapped from the absorption and stripping columns for the C_4F_{10} gas absorption system

Name	**ABSORBER-tower**	**STRIPPER-tower**
Remarks 1	Equipment mapped from 'ABSORBER'	Equipment mapped from 'STRIPPER'
Tray type	sieve	sieve
Vessel diameter [m]	2.13	10.97
Vessel tangent to tangent height [m]	15.24	15.85
Number of trays	19	20
Tray spacing [m]	0.61	0.61

Table 6.14: Equipment mapped from the absorption and stripping columns for the C_6F_{14} gas absorption system

Name	**ABSORBER-tower**	**STRIPPER-tower**
Remarks 1	Equipment mapped from 'ABSORBER'	Equipment mapped from 'STRIPPER'
Tray type	sieve	sieve
Vessel diameter [m]	2.13	12.19
Vessel tangent to tangent height [m]	15.24	15.85
Number of trays	19	20
Tray spacing [m]	0.61	0.61

Table 6.15: Preliminary costs summary for the gas absorption system using the C_4F_{10} solvent

Name	Summary
Total Capital Cost [USD]	21,239,600
Total Operating Cost [millions of USD/Year]	52,991,900
Total Raw Materials Cost [millions of USD/Year]	49,066,500
Total Utilities Cost [USD/Year]	22,838,900
Desired Rate of Return [Percent/'Year]	20
Equipment Cost [USD]	5,993,900
Total Installed Cost [USD]	11,353,000

1. Absorption column (No. of stages: 13; solvent flow rate: 8000 kmol/h; solvent temperature: 220.15 K). 2. Stripping column (No. of stages: 16; feed stage: 2; pressure: 1.400 MPa).

Table 6.16: Preliminary costs summary for the gas absorption system using the C_6F_{14} solvent

Name	Summary
Total Capital Cost [USD]	28,970,200
Total Operating Cost [millions of USD/Year]	59,899,400
Total Raw Materials Cost [millions of USD/Year]	55,462,400
Total Utilities Cost [USD/Year]	45,672,700
Desired Rate of Return [Percent/'Year]	20
Equipment Cost [USD]	12,092,100
Total Installed Cost [USD]	18,897,600

1. Absorption column (No. of stages: 13; solvent flow rate: 8000 kmol/h; solvent temperature: 220.15 K). 2. Stripping column (No. of stages: 16; feed stage: 2; pressure: 1.000 MPa).

Table 6.17: Equipment and installation costs of the equipment used in the C_4F_{10} gas absorption system

Equipment	Equipment Cost [USD]	Installed Cost [USD]
ABSORBER-tower	346,800	620,300
COOLER	409,500	690,900
FLASH1-flash vessel	575,600	960,100
FLASH2-flash vessel	450,600	784,100
FLASH3-flash vessel	337,900	621,500
PUMP	504,700	813,600
STRIPPER-condenser	61,400	358,200
STRIPPER-condenser acc	11,700	81,700
STRIPPER-reboiler	361,900	598,500
STRIPPER-reflux pump	5,200	34,900
STRIPPER-tower	2,928,600	5,789,200

Table 6.18: Equipment and installation costs of the equipment used in the C_6F_{14} gas absorption system

Equipment	Equipment Cost [USD]	Installed Cost [USD]
ABSORBER-tower	391,900	714,100
COOLER	669,200	949,500
FLASH1-flash vessel	693,900	1,119,700
FLASH2-flash vessel	558,800	961,100
FLASH3-flash vessel	423,700	758,500
PUMP	652,900	1,181,600
STRIPPER-condenser	186,900	367,900
STRIPPER-condenser acc	17,400	111,700
STRIPPER-reboiler	2,732,100	2,900,300
STRIPPER-reflux pump	7,200	49,400
STRIPPER-tower	5,758,100	9,783,800

Table 6.19: Utility costs relative to the C_4F_{10} absorption process

Utilities					
Name	**Fluid**	**Rate**	**Rate Units**	**Cost per Hour**	**Cost Units**
Electricity	—	2667	kW	206	USD/h
Refrigerant - Propylene	Refrigerant	16820	kg/h	2	USD/h
Refrigerant - Ethane	Refrigerant	664100	kg/h	26	USD/h
Steam at 0.689 MPa	Steam	132000	kg/h	2,370	USD/h

Table 6.20: Utility costs relative to the C_6F_{14} absorption process

Utilities					
Name	**Fluid**	**Rate**	**Rate Units**	**Cost per Hour**	**Cost Units**
Electricity	—	4170	kW	323	USD/h
Refrigerant - Propylene	Refrigerant	57560	kg/h	8	USD/h
Refrigerant - Ethane	Refrigerant	404700	kg/h	16	USD/h
Steam at 0.689 MPa	Steam	270900	kg/h	4862	USD/h

Table 6.21: Preliminary costs summary for the gas absorption system using the DEPG solvent

Name	**Summary**
Total Capital Cost [USD]	25,549,300
Total Operating Cost [millions of USD/Year]	4,583,410
Total Raw Materials Cost [millions of USD/Year]	4,243,890
Total Utilities Cost [USD/Year]	2,137,620
Desired Rate of Return [Percent/Year]	20
Equipment Cost [USD]	8,085,200
Total Installed Cost [USD]	13,950,300

Table 6.22: Preliminary costs summary for the gas absorption system using the NMP solvent

Name	**Summary**
Total Capital Cost [USD]	16,789,300
Total Operating Cost [millions of USD/Year]	613,405
Total Raw Materials Cost [millions of USD/Year]	567,965
Total Utilities Cost [USD/Year]	846,493
Desired Rate of Return [Percent/'Year]	20
Equipment Cost [USD]	5,059,800
Total Installed Cost [USD]	8,125,600

Tables 6.13 and 6.14 reveal that the real number of trays for the absorption and stripping columns in the C_4F_{10} and C_6F_{14} gas absorption systems has been determined to be 19 and 20, respectively. Considering the overall efficiency, which is defined in Eq. (6.1), the efficiency in the absorber and stripper was calculated to be 68.42 % and 70.00 %, respectively. One should note that in a stripping column, the top and bottom stages are not counted as part of the total number of stages.

$$E = \frac{N_t}{N_r} \tag{6.1}$$

where N_r is the number of real or physical trays, N_t is the number of theoretical trays and E is the tray efficiency.

Analysis of Tables 6.15-6.18 shows that the preliminary cost summary for the two gas absorption systems, using C_4F_{10} and C_6F_{14} are higher, compared to the gas absorption systems based on current commercial physical solvents such as DEPG and NMP. The elevated costs are primarily associated with the physical properties and the high costs of the C_4F_{10} and C_6F_{14} solvents. Their prices were found to be 2940 USD/kg and 2340 USD/kg for C_4F_{10} and C_6F_{14}, respectively, from SynQuest laboratories, whilst the prices of DEPG and NMP were found to be 578 USD/l and 125 USD/l, respectively from Sigma-Aldrich.

However, one should note that the prices for PFCs depend on their availability. For example, most of companies have stopped manufacturing C_4F_{10} and consequently, its market price has increased. Although, the price of C_4F_{10} is higher than that of C_6F_{14}, Tables 6.15 and 70.16 reveal that the preliminary cost summary for the gas absorption system using C_4F_{10} is lower

than for C_6F_{14}. This is mainly justified by the characteristics of the PFC components, where the carbon chain length dictates their physical properties. Therefore, C_6F_{14} has higher vapour pressures, higher densities, higher viscosities, etc. compared to C_4F_{10}.

One should note that only two PFC components were used in this study and therefore no trend could be observed, as trend estimation requires at least three components. However, the work of Heintz et al. (2008) which investigated the use of $C_{13}F_{22}$, $C_{14}F_{24}$ and $C_{17}F_{30}$ as novel physical solvents for CO_2 capture from fuel gas streams under elevated pressures and temperatures, demonstrated that the longer the carbon chain length, the better the solvent, but no cost estimation was undertaken. Consequently, a trend could be predicted in this study based on the work of Heintz et al. (2008). The costs relative to the PFC solvents can then be reduced using a higher carbon chain length PFC, as less amounts will be required to absorb more flue gas components.

In addition, the Government Department of Science and Technology in South Africa has recently launched a programme called the Flurochemical Expansion Initiative (FEI) which aims at the beneficiation of fluorspar, a mineral of which South Africa possesses the largest reserve in the world, followed by China. Chemicals at the end of the value chain include Teflon, lithium fluoride, perfluorocarbons to name just a few. The local manufacturing of the PFC components can significantly reduce the price of the solvent and consequently, the costs for the gas absorption systems, if blended PFC components can be used, as their separation requirements are generally relaxed.

7

CHAPTER SEVEN

CONCLUSIONS AND RECOMMENDATIONS

7.1 Conclusions

This study forms part of an on-going research programme initiated to investigate the use of perfluorocarbons as potential physical solvents for flue gas cleaning. As part of the investigation, two perfluorocarbons were considered in this study, perfluorobutane and perfluorohexane. The flue gas emanated from the gasification of Illinois No. 6 bituminous coal was of particular interest as it was available at high pressure, and consequently, was suitable for physical absorption processes. Accurate phase equilibrium data are vital to undertake process design and simulations. However, for a preliminary design, predicted data are acceptable. One should note that phase equilibrium data, such as vapour-liquid equilibrium (VLE) for systems involving perfluorocarbons, range from rare to non-existent in the open literature.

An experimental programme was therefore devised to undertake phase equilibrium data measurements for systems involving perfluorobutane or perfluorohexane with common flue gas components. The measurements were undertaken using two experimental apparatuses based on the static analytic method. The apparatuses used are described by Laugier et al. (1986) and Narasigadu (2011), respectively.

The VLE data of El Ahmar et al. (2011), for the ethane (1) + perfluorobutane (2) system at 308.24 K, was chosen as a test system to demonstrate the capability of the experimental apparatus by Narasigadu (2011) to reproduce accurate VLE data and, thus, check the accuracy of the experimental procedure. The results obtained were satisfactory as all the experimental VLE data agreed well with the literature data.

Isothermal VLE data for 11novel binary systems were thereafter successfully measured at three temperatures (293, 313 and 333) K. The experimental apparatus described by Laugier et al. (1986) was used to measure 6 novel binary systems, including:

- perfluorobutane + (carbon monoxide, hydrogen sulphide, nitric oxide and methane)
- Perfluorohexane + (carbon monoxide and hydrogen sulphide)

The experimental apparatus described by Narasigadu (2011) was used to measure the remaining novel systems, which include:

- Perfluorobutane + (oxygen, nitrogen and hydrogen)
- Perfluorohexane + (methane and ethane)

The experimental VLE data for all the systems were modelled via the direct method using various combinations of thermodynamic models. These include: the Peng-Robinson or the Soave-Redlich-Kwong EoS, incorporating the Mathias-Copeman or Stryjek-Vera alpha function, with the Wong-Sandler, Huron-Vidal, predictive Soave-Redlich-Kwong, modified Huron-Vidal 1 or 2 mixing rule, utilizing the non-random two liquid activity coefficient model. The combined thermodynamic models did not uniformly represent the experimental VLE data for all the systems, as some provided better fits than the others.

Due to the fact that C_4F_{10} and C_6F_{14} did not meet the 'ideal solvent' criteria, design of gas absorption systems using the two perfluorocarbons was undertaken, for illustration purpose, using the results from the measured VLE data.

For design purposes, Aspen Plus® requires that a single combination of thermodynamic models, in the form of property method, be selected to represent all the systems involved in the design. Thus, the Peng-Robinson EoS incorporating the Mathias-Copeman alpha function, and the Wong-Sandler mixing rule utilizing the non-random two liquid activity coefficient model, abbreviated as PR-MC-WS-NRTL, was selected, as it outperformed the other models in representing all the systems under investigation.

In order to fully describe the gas absorption systems using either the perfluorobutane or perfluorohexane as physical solvents, VLE data for binary systems that could not be measured were predicted in Aspen Plus®, using the predictive Soave-Redlich-Kwong (PSRK) property method, incorporating either the modified UNIversal Functional Activity Coefficient (UNIFAC) (Dortmund), or Conduct-like Screening Model-Segment Activity Coefficient

(COSMO-SAC) models. These models were validated against existing literature data and were proven satisfactory in predicting VLE data of interest to this study.

The RadFrac column model using the equilibrium method was selected for the design of the absorption and stripping columns. The optimum operating conditions were determined, by means of sensitivity analysis, to be 10 or 13 stages, 260.15 K, 6.890 MPa and 8000 or 10000 kmol/h.

The absorption results relative to the perfluorobutane and perfluorohexane were benchmarked against those for the dimethyl ethers of polyethylene glycol (DEPG), N-methyl-2-pyrrolidone (NMP) and propylene carbonate (PC) solvents. It was found that the perfluorocarbon solvents have high absorption capacity for the flue gas of interest (CO_2, H_2S, CH_4 and CO), increasing with the carbon chain length, but exhibited poor selectivity for these gases. In addition, their associated high vapour pressures constitute a major drawback as 84.496 kmol/h of C_4F_{10} and 11.762 kmol/h of C_6F_{14} were emitted into the atmosphere at the optimum conditions. On the contrary their DEPG, NMP and PC counterparts exhibited less gas absorption capacity for the flue gas of interest, but their emissions into the atmosphere ranged from less than 0.001 to 0.006 kmol/h, respectively.

The reduction of the operating temperature to 220.15 K for the perfluorocarbon absorption processes resulted, generally, in higher absorption capacity of the flue gas of interest, but their emissions into the atmosphere were still greater than those of DEPG, NMP and PC absorption processes.

A solvent regeneration section containing a series of three flash drums, coupled with a stripping column, was added to both the perfluorobutane and perfluorohexane absorption processes for conditions that provided better results. It was found that for both perfluorocarbon solvents, the flash drums alone were not sufficient for complete solvent regeneration. Consequently, a stripping column equipped with 16 stages was added for each gas absorption process, and operated at 2.000 and 1.000 MPa, respectively. However, the perfluorocarbon solvents could not be recycled as it was essentially impossible to strip off water vapour in the two gas absorption systems. Further processing such as using a glycol unit would be required before the recycling took place.

The energy requirement for the perfluorobutane and perfluorohexane gas absorption systems revealed that more energy is required for the latter and this was attributed to the physical properties relative to the C_4F_{10} and C_6F_{14} solvents.

Preliminary cost estimations for the two gas absorption systems were undertaken, and revealed that the total operating costs for both the perfluorobutane and perfluorohexane gas absorption systems were exorbitant, with the former being higher. These elevated costs were primarily attributed to the solvent market prices. This could be overcome by using blended PFC solvents as their separation requirements during the manufacturing process are generally not strict.

The two perfluorocarbons investigated in this study as potential physical solvents for flue gas cleaning follow the trend similar to the work of Heintz et al. (2008) which demonstrated that the longer the carbon chain of perfluorocarbons, the better the solvent in terms of the overall performance. Consequently, longer carbon chain perfluorocarbons are recommended for further investigation.

7.2 Recommendations

The modifications to both the experimental apparati of Laugier et al. (1986) and Narasigadu (2011) to ameliorate measurements of phase equilibrium data are suggested. Other recommendations include further measurements of phase equilibrium data to accurately describe the behaviour of the systems investigated in this study.

Measurements of phase equilibrium data in the vicinity of the critical region have been quasi-impossible using the apparatus of Laugier et al. (1986) and Narasigadu (2011). In addition analysis of multiple phases was near impossible. This is explained by the use of an opaque bath in which the equilibrium cell is fully immersed. One had to periodically remove the equilibrium cell from the bath to observe the state of phases in equilibrium. Oftentimes, the change of environment affected the equilibrium cell conditions, and consequently leading to uncertain analysis. A solution could be the use of a transparent bath or a ROLSI sampler with two capillaries, one position in the vapour phase and the other in the liquid phase.

Some of the phase equilibrium data could not be measured and therefore were predicted using either the modified UNIFAC (Dortmund) or PSRK/COSMO-SAC model. This is acceptable in the preliminary stage of a design process. However, in the final stage of the design and for a better description of the components involved in the gas absorption systems using

perfluorobutane or perfluorohexane, experimental phase equilibrium data should be considered.

The perfluorocarbons with longer carbon chains should also be investigated as suggested by the results obtained in this study. Due to the global warming potential and high vapour pressures associated with perfluorocarbon compounds, one should ensure that, as physical solvents, their emission into the atmosphere comply with the environmental regulations. Perfluorocarbons with longer carbon chain have the potential to have lower vapor pressure, however, the longer the carbon chain, the higher the viscosity. Thus, one has to ensure that the viscosity of the selected PFC compound does not interfere with easy mass transfer between the solvent and the solute. One should also consider that at lower temperatures, viscosity of PFC compounds is higher.

A thorough recommendation regarding the use of PFCs as physical solvents will be provided once the investigation on the PFCs with longer carbon chains has been undertaken.

REFERENCES

Abrams, D. S. and Prausnitz, J. M., (1975), "Statistical Thermodynamics of Liquid Mixtures: A New Expression for the Excess Gibbs Energy of Partly or Completely Miscible Systems", *American Institute of Chemical Engineers Journal*, Vol. 21(1), pp. 116-128.

Ahlers,J.,(2003),Thesis: "Entwicklung einer universellen Gruppenbeitragszustandsgleichung" Carl-von-Ossietzky-Universität Oldenburg, 1-144.

Air Liquide, (2013), "Material Safety Data Sheet" Encyclopedia. www.encyclopedia.airliquide.com.

Arshad, M. W., (2009), "CO_2 capture using Ionic Liquids", Department of Chemical and Biochemical Engineering Technical University of Denmark. Accessed 28/3/2011.

Aspen Plus, (2004), "Physical Properties and Methods", Cambridge, M A: Aspen Technology Incorporation.

AspenTech. Aspen Plus V8.0 (27.0.36), (2012).

Battino, R. and Cleve, H. L., (1966), "Solubility of Gases in Liquids", *Chemical Reviews*, Vol. 66 (4), pp. 395-463.

Breeze, P., (2014), "Coal-Fired Generation", Elsevier, San Diego, CA, USA.

Bruce, E. S. and Tatlow, J. C., (1994), "Organofluorine Chemistry: Principles and Commercial Applications", New York: Plenum Press.

Buckingham, P. A., (1961), "Fluor Solvent Process Demonstrated in EPNG Plant", paper presented at NGAA Regional Meeting, Odessa, TX, May.

Buckingham, P. A., (1964), "Fluor Solvent Process Plants: How They Are Working", *Hydrocarbon Processing*, Vol. 43, April, pp. 113-116.

Bucklin, R. W. and Schendel, R. L., (1985), "Comparison of Physical Solvents Used for Gas processing in Acid and Sour Gas Treating processes", S. A. Newman, editor, Gulf Publishing Co., Houston, TX, pp. 42-79.

Bullin, J. A., (2003), "Why Not Optimize Your Amine Sweetening Unit", Paper presented at the 20th GPA Europe Annual Conference, Heidelberg, Germany.

Burr, B. and Lyddon, L., (2008), "A Comparison of Physical Solvents for Acid Gas Removal", Paper presented at the 87th GPA Annual Convention, Grapevine, TX.

Chien-Bin, S., (2011), PhD dissertation: Experimental Thermodynamic Measurements of Biofuel-related Associating Compounds and Modeling using the PC-SAFT Equation of State, MINES ParisTech, Fontainebleau, France.

Chiyen, K. J., (2010), MSc dissertation: Modification and Commissioning of A Static High Pressure Apparatus and Phase Equilibria Measurements for Fluorinated Hydrocarbons, University of KwaZulu-Natal, Durban, South Africa.

Constantinou, L. and Gani, R., (1994), "New contribution method for estimating properties of pure compounds", *American Institute of Chemical Engineering Journal*., Vol. 40, pp. 1697-1710.

Coquelet, C, (2003), "Etude des Fluides Frigorigènes. Mesures et Modélisations", Thèse de doctorat, Ecole des Mines de Paris, France.

Coquelet, C. and Richon, D., (2009), "Experimental Determination of Phase Diagram and Modeling: Application to Refrigerant Mixtures", *International Journal of Refrigeration*, Vol. 32, pp. 1604-1614.

Costa Gomes, M. F., Padua, A. A. H., (2003), "Interactions of carbon dioxide with liquid fluorocarbons", *Journal of Physical Chemistry B*, Vol. 107 (50), pp. 14020-14024.

Cussler, E. L., (2009), "Diffusion Mass Transfer in Fluid Systems", Cambridge University Press. New York.

Dahl, S. and Michelsen, M.L., (1990), "High-pressure vapour-liquid equilibrium with a UNIFAC based equation of state", *American Institute of Chemical Engineers Journal.*, Vol. 36, pp. 1829-1836.

Danner, R. P. and Gess, M. A., (1990), "A Data Base Standard for the Evaluation of Vapor-Liquid-Equilibrium Models", *Fluid Phase Equilibria*, Vol. 56, pp. 285-301.

Daubert, T. E., Sibul, H. M., Stebbins, C. and Kendall, R., (1990), "Policies and procedures Documenting Compilation, Prediction, and Correlation for DIPPR Data Compilation Project", *American Institute of Chemical Engineering Symposium*, Vol. 86, pp. 62-92.

Davidson, J., (2007), "Performance and costs of power plants with capture and storage of CO_2", *Energy* Vol.32, pp. 1163-1176.

Derr, E.L. and Deal, C.H., (1969) "Analytical solutions of groups: Correlation of activity Coefficients through structural group parameters", *Institution of Chemical Engineering Symposium Series,* Vol. 3, pp. 40-53.

Dias, A. M. A., Boifàcio, R. P., Marrucho, I. M., Pàdua, A. A. H., and Costa Gomes, M. F., (2003), "Solubility of oxygen in n-hexane and in n-perfluorohexane. Experimental determination and prediction by molecular simulation", *Physical Chemistry Chemical Physics B,* Vol. *5(3),* pp. *543-549.*

Doctor, R. D., Molburg, J. C., Thimmapuram, P. R., Berry, G. F. and Livengood, C. D., Energy Systems Division, Argonne National Laboratory, Argonne Illinois, (1994), "Gasification Combined Cycle: Carbon Dioxide Recovery, Transport and Disposal", ANL/ESD-24, work sponsored by United States Department of Energy, September 1994.

Dunlap, R. D., Murphy, C. J. and Bedford, R. G., (1958), "Some Physical Properties of Perfluoro-*n*-hexane", *Journal of the American Chemical Society,* Vol. 80, pp. 83-85.

El Ahmar, E., Valtz, A., Naidoo, P., Coquelet, C., and Ramjugernath, D., (2010), "Isothermal Vapour-Liquid Equilibrium Data for the Perfluorobutane (R610) + Ethane System at Temperatures from (263 to 353) K*", Journal of Chemical Engineering Data*, Vol. (56), pp. 1918-1924.

European Commission (2012), "F-Gas emissions to be cut by two-thirds by 2030 in the EU", www.ec.europa.eu/clima/policies/f-gas/index_en.htm.

European Commission (2014), "Final Communication from the Commission to the European Parliament and the Council, Brussels GNG 451.

Felder, R. M. and Rousseau, R. W., (2005), "Elementary Principles of Chemical Processes", 3rd edition, Wiley.

Fournier, J. A., Congtin, L. P., and Robert, K. B., (2011), "Microwave spectroscopy and characterization of the helical conformer of perfluorohexane" ARKIVOC 2011 (v) 5-11.

Fredenslund, Aa., Gmehling, J. and Rasmussen, P., (1977), "Vapor-Liquid Equilibria using UNIFAC. A Group Contribution Method", Elsevier, Amsterdam.

Fredenslund, A., Jones, R. L. and Prausnitz, J. M., (1975), "Group-Contribution Estimation of Activity Coefficients in Nonideal Liquid Mixtures", *American Institute of Chemical Engineering Journal*, Vol. 21 (6), pp. 1086-1099.

Freireich, E. and Tennyson, R. N., (1977), "Increased Natu

ral Gas Recovery from Physical Solvent Gas Treating Systems", *Processing Gas Conditioning Conference*, University of Oklahoma, Norman, OK, March 7-9.

Gale, J., Bachu, S., Bolland, O., Xue, Z., (2007), "To store or not to store", *International Journal of Greenhouse Gas Control*, Vol. 1, p. 1.

Gielen D., (2003), "The energy policy consequences of future CO2 capture and sequestration technologies", International Energy Agency, France.

Gmehling, J., Jiding, L. and Fischer, K., (1997), "Further Development of the PSRK model for the Prediction of Gas Solubilities and Vapor-Liquid Equilibria at Low and High Pressures II", *Fluid Phase Equilibria,* Vol. 141, pp. 113-127.

Guilbot, P., Valtz, A., Legendre, H. and Richon D., (2000), "Rapid On-Line Sampler-Injector: A Reliable Tool for HT-HP Sampling and On-Line GC Analysis", *Analysis,* Vol. 28(5), pp. 426-431.

Hansen, H. K., Rasmussen, P., Fredenslund, A., Schiller, M. and Gmehling, J., (1991), "Vapor-Liquid Equilibria by UNIFAC Group Contribution. 5. Revision and Extension", *Industrial & Engineering Chemistry Research*, Vol. 30 (10), p.2352.

Hansen, J. E. and Sato, M., (2012), "Paleoclimate Implications for Human-made Climate Change. *In Climate Change: Inferences from Paleoclimate and Regional Aspects*. Editions Springer, 21-48, doi:10.1007/978-3-7091-0973-1_2.

Hegwer, A. M. and Harris, R. A., (1970), "Selexol Solves High H_2S/CO_2 Problem" *Hydrocarbon Processing*, Vol. 49 (4), pp. 103-104.

Heintz, Y. H., Sehabiague, L., Morsi, B. I., Jones, K. L., and Pennline, H. W., (2008), "Novel Physical Solvents for Selective CO_2 Capture from Fuel Gas Streams at Elevated Pressures and Temperatures". *Energy & Fuels*, Vol. 22, pp. 3824-3837.

Herington, E. F. G., (1947), "A Thermodynamic Test for the Internal Consistency of Experimental Data on Volatility Ratios", *Nature*, Vol. 160, pp. 610-611.

Hildebrand, J. H., Prausnitz, J. M., and Scott, R. L., (1970), "Regular and Related Solutions", Van Nostrand Reinhold Co., New York.

Hochgesand, G., (1970), "Rectisol and Purisol", *European and Japanese Chemical Industries Symposium*, Vol. 62, pp. 37-43.

Holderbaum, T. and Gmehling, J., (1991), "PSRK: A Group Contribution Equation of State based on UNIFAC", *Fluid Phase Equilibria*, Vol.70, pp. 251-265.

Houghman Gareth, (2002), "Fluoropolymers: Properties". Kluwer Academic/Plenum Publishers, New York.

Huron, M-J., and Vidal, J., (1979) "New Mixing Rules in Simple Equations of State for Representing Vapour-Liquid Equilibria of Strongly Non-Ideal Mixtures," *Fluid Phase Equilibria*, Vol. 3, pp. 255-271.

Intergovernmental Panel on Climate Change, (2005), "Safeguarding the ozone layer and the global climate system: Issues related to HFCs and PFCs". IPCC/TEAP Special Report, UNFCCC/SBSTA 22, Bonn, Germany.

Intergovernmental Panel on Climate Change, (2011), "IPCC Special Report on Renewable Energy Sources and Climate Change Mitigation-Summary for Policymakers", Approved at the 11th Session of Working group III of the IPCC, Abu Dhabi, United Emirates, 5-8 May.

Intergovernmental Panel on Climate Change, (2013), "Climate Change 2013, The Physical Sciences Basis–Summary for Policy Makers", IPCC, http://www.climatechange2013.org.

Jiding, L., Fischer, K. and Gmehling, J., (1998), "Prediction of Vapor-Liquid Equilibria for Asymmetric Systems at Low and High Pressures with the PSRK Model", *Fluid Phase Equilibria*, Vol. 143, pp. 71-82.

Judd, D. K., (1978), “Selexol Unit Saves Energy”, *Hydrocarbon Processing*, Vol. 57, No. 4, April, pp.122-124.

Keller, J. and Staudt, R., (2005), “Gas Adsorption Equilibria: Experimental Methods and Adsorption isotherms”, Springer, Germany.

Klamt, A., (1995), “Conductor-Like Screening Model for Real Solvents: A New Approach to the Quantitative Calculation of Solvation Phenomena”, *Journal of Physical Chemistry,* Vol. 99, pp. 2224-2235.

Kleiber, M., (1995), “An extension to the UNIFAC Group Assignment for Prediction of Vapor-Liquid Equilibria of Mixtures Containing Refrigerants”, *Fluid Phase Equilibria,* Vol. 107, p. 161.

Kohl, A. L. and Riesenfeld, F. C., (1985), “Gas Purification”, 4th Ed., Gulf Publishing, Houston Texas.

Kohl, A. and Nielson, R., (1997), “Gas Purification”. 5th Ed., Gulf Professional Publishing.

Kontogeorgis, G. M. and Folas, G. G., (2010), “Thermodynamic Models for Industrial Applications: from classical and advanced mixing rules to association theories”. John Wiley & son Ltd., United Kingdom.

Korens, N., Simbeck, D. R., Wilhelm, D. J., Longanabach, J. R., Stiegel, G. J., (2002), “Process screening analysis of alternative gas treating and sulfur removal for gasification: Revised final report. SFA Pacific, Inc., Mountain View, CA; U.S. Department of Energy, National Energy Technology Laboratory, Pittsburg, PA; Task Order 739656-00100.

Kriebel, M., (1989), “Ullman’s Encyclopedia of Industrial Chemistry”. *Gas Production*, VCH Verlagsgeselschaft mbH. Weunheim, pp. 253-258.

Lam, M. K. and Mohamed, A. R., (2012), “Current status and challenges on microalgae-based carbon capture”, *International Journal of Greenhouse Control*, Vol. 10, pp. 456-469.

Larsen, B., Rasmussen, P. and Fredenslund, A., (1987), “A Modified Group-Contribution Method for Prediction of Phase Equilibria and Heats of Mixing”, *Industrial & Engineering Chemistry Research,* Vol. 26, p. 2274.

Laugier, S. and Richon, D., (1986), "New Apparatus to Perform Fast Determinations of Mixtures Vapour-Liquid Equilibria up to 10 MPa and 423 K. *Review of Scientific Instrument* Vol. 57, pp. 469-472.

Lei, Z., Li, C., and Chen, B., (2003), "Extractive Distillation: A review". *Separation and purification reviews*, Vol. 32 (2), pp. 121-213.

Letcher, T. M., (2007), "Thermodynamics, Solubility and Environmental Issues", Elsevier Science & Technology Books.

Lewis, G. N., (1980), "The osmotic pressure of concentrated solutions, and the laws of the perfect solution*," Journal of American Chemical Society*, Vol. 30, pp. 668-683.

Li, J. R., Ma, Y., McCarthy, M. C., Sculley, J., Yu, J., Jeong, H. K., Balbuena, P. B. and Zhou, H. C., (2011), "carbon Dioxide Capture-Related Gas Adsorption and Separation in Metal-Organic Frameworks". *Coordination Chemistry Reviews*, Vol. 255, pp. 1791-1823.

Lide, D. R., (1998), "*Handbook of Chemistry and Physics*", 85th edition, CRC Press: Boca Raton.

Lin, S. T. and Sandler, S. I., (2002), "A Priori Phase Equilibrium from a Segment Contribution Solvation Model". *Industrial & Engineering Chemistry*. Vol. 41, p. 899.

Lowry, T. H. and Richardson, K. S., (1987), "Mechanism and Theory in Organic Chemistry" 3rd edition, Harper Collins, Illinois, U.S.A.

Lurgi, O. G. C. GmbH, (1978), "Purisol for Gas Treating", Brochure 1163/6.78.

Lurgi O. G. C. GmbH, (1988), "Purisol". *Hydrocarbon Processing, 1988 Gas Process Handbook*, April, p. 69.

Lurgi O. G. C. GmbH, (1996), "Purisol". *Hydrocarbon Processing. Gas Processes*, Vol. 96, p. 133.

Lurgi, O. G. C. GmbH and Linde, A. G., (1996), "Rectisol". *Hydrocarbon Processing. Gas Processes*, Vol. 96, p. 134.

Luyben, W. L., (2006), "Distillation Design and Control using ASPEN simulation", John Wiley & Sons, Inc., Hoboken, New Jersey.

Marina, J. M. and Tassios, D. P., (1973), "Effective Local compositions in Phase Equilibrium Correlations", *Industrial & Engineering Chemistry Process Design and Development*, Vol. 12 (1), pp. 67-71.

Martin, J. J., (1979), "Cubic Equations of State – Which?", *Industrial and Engineering Chemistry Fundamentals*, Vol. 18(2), pp. 81-97.

Mathias, P. M., Reddy, S., Smith, A. and Afshar, K., (2013), "A Guide to Evaluate Solvents and Processes for Post-Combustion CO_2 Capture", *Energy Procedia*, Vol. 37, pp. 1863-1870.

Mathias, P. M. and Copeman, T. W., (1983), "Extension of the Peng-Robinson Equation of State to Complex Mixtures: Evaluation of the Various Forms of the Local Composition Concept". *Fluid Phase Equilibria*, Vol. 13, pp. 91.

Michelsen, M. L., (1990b), "A Modified Huron Vidal mixing rule for cubic equations of state". *Fluid Phase Equilibria*, Vol. 60, pp. 15-26.

Muzenda, E., (2013), "From UNIQUAC to Modified UNIFAC Dortmund: A Discussion". 3rd International Conference on Medical Sciences and Chemical Engineering (ICMSCE), December 25-26, Bangkok (Thailand).

Naidoo, P., (2004), PhD Dissertation: High-Pressure Vapor-Liquid Equilibrium Studies, University of Kwa-Zulu Natal, Durban, South Africa.

Narasigadu, C., (2011), PhD Dissertation: Design of Static Micro-Cell for Phase equilibrium Measurements (Measurements and Modelling), University of KwaZulu-Natal, Durban, South Africa.

Nelson, M. W., (2012), PhD Dissertation: Separation of Trichlorosilane: Measurement, Modeling and Simulation, University of KwaZulu-Natal, Durban, South Africa.

Orbey, H., Sandler, S. I. and Wong, D. S. H., (1993), "Accurate equation of state predictions at high temperatures and pressures using the existing UNIFAC model. *Fluid Phase Equilibria*, Vol. 85, pp. 41-54.

Peng, D. Y. and Robinson, D. B., (1976), "A New Two Constant Equation of State", *Industrial and Engineering Chemistry Fundamentals*, Vol. 15(1), pp. 59-64.

Perry, R. H. and Chilton, C. H., (1973), "Chemical Engineer's Handbook" 5th Ed., McGraw-Hill, New York.

Prausnitz, J. M., Anderson, T. F., Grens, E. A., Eckert, C. A., Hseih, R. and O'Connell, J. P., (1980), "Computer Calculations for Multicomponent Vapour-Liquid and Liquid-Liquid Equilibria", Prentice-Hall, Englewood Cliffs, New Jersey.

Prausnitz, J. M., Lichtenthaler, R. N. and de Azevedo, E. G., (1999), "Molecular Thermodynamics of Fluid-Phase Equilibria", 3rd edition, Prentice-Hall, Upper Saddle River, New Jersey.

Raal, J. D., Jeffery, G. and Tonkin, T.G., (1980) *Chemical Engineering Research Group Report:* 331, CSIR, Pretoria.

Raal, J. D. and Mühlbauer, A. L., (1998), "Phase Equilibria: Measurement and computation", Taylor and Francis, Bristol, PA.

Rackley, S. A., (2010), "Carbon Capture and Storage". Elsevier.

Ramjugernath, D., (2000), PhD Dissertation: High Pressure Phase Equilibrium Studies, University of Natal, Durban, South Africa.

Ramjugernath, D., Valtz, A., Coquelet, C. and Richon, D. (2009), "Isothermal Vapor-Liquid Equilibrium Data for the Hexafluoroethane (R116) + Propane System at Temperatures from (263 to 323) K", *Journal of Chemical Engineering Data*, Vol. 54, pp.1292-1296.

Ranke, G. and Mohr, V. H., (1985), "The Rectisol Wash-New Developments in Acid Gas Removal from Synthesis Gas", in *Acid and Sour Gas Treating Processes*, S. A. Newman, editor, Gulf Publishing Company, Houston, TX, pp. 80-111.

Rao, A. B. and Rubin, E.S., (2002). "A TECHNICAL, Economic And Environmental Assessment of Amine-based Carbon Capture Technology for Power Plant Greenhouse Gas Control". Environmental Science &Technology, Vol. 36 (20), pp. 4467-4475.

Redlich, O. and Kister, A. T., (1948), "Thermodynamics of Nonelectrolyte Solutions. Algebraic Representation of Thermodynamic Properties and the Classification of Solutions", *Journal of Industrial and Engineering Chemistry*, Vol. 40, pp. 345-348.

Redlich, O. and Kwong, J. N. S., (1949), "On the Thermodynamics of Solutions. V. An Equation of State. Fugacities of Gaseous Solutions", *Chemical Reviews*, Vol. 44, pp. 233-244.

Reid, R. C. and Praustnitz, J. M., (1987), "The Properties of Gases and Liquids", McGraw-Hill Book: New York, NY, USA.

Regulation (EC) "No 842/2006 of the European Parliament and the Council of 17 May 2006 on certain fluorinated greenhouse gases" Official Journal of the European Union, L 161/1.

Renon, H. and Prausnitz, J. M., (1968), "Local Compositions in Thermodynamic Excess Functions for Liquid Mixtures", *American Institute of Chemical Engineers Journal*, Vol. 14(1), pp. 135-144.

Sandler, S. I., (1997), "Chemical and Engineering Thermodynamics", 3rd edition, New York, John Wiley & sons, Inc.

Sekiya, A., & Misaki, S., (2000), "The potential of hydrofluoroethers to replace CFCs, HCFCs and PFCs". *Journal of Fluorine Chemistry*, Vol. *101*, pp. 215–221.

Smart, B. R. E. and Tatlow, J. C., (1994), "Organofluorine Chemistry. Principles and Commercial Applications. Plenum, New York.

Smith, J. M., Van Ness, H. C., and Abott, M. M., (2005), "Introduction to Chemical Engineering Thermodynamics", 6th edition, McGraw-Hill, New York.

Sinnott, R. K., (2005), "Chemical Engineering Design", Coulson and Richardson's Chemical Engineering, Vol. 6, 4th Ed., Elsevier.

Soave, G., (1972), "Equilibrium Constants from a Modified Redlich-Kwong Equation of State", *Chemical Engineering Science*, Vol. 27(6), pp. 1197-1203.

Speight, J. G., (1993), "Gas processing: Environmental Aspects and Methods", Butterworth Heinemann, Oxford, England.

Speight, J. G., (1999), "The Chemistry and Technology of Petroleum", 3rd Ed., Marcel Dekker Inc., New York.

Spiess, B. D., (2010), "Basic mechanisms of gas transport and past research using perfluorocarbons", Driving and Hyperbaric Medicine, Vol. 40 (1), pp. 23-28.

Stryjek, S. and Vera, J. H., (1986), "An improved Peng-Robinson Equation of State for Pure Compounds and Mixtures". *Canadian Journal of Chemical Engineering*, Vol. 64, pp. 323-333.

Sweny, J. W., (1973), "The SELEXOL process in Fuel Gas Treating". Paper presented at 165th National meeting of the American Chemical Society, Division of Fuel Chemistry, Dallas, TX, April 8-12.

Sweny, J. W., (1980), "High CO_2-High H2S Removal with Selexol Solvent", paper presented at 59th Annual GPA Convention, Houston, Tx, March 17-19.

Swinton, S. L., (1978), "Chemical Thermodynamics", *The Chemical Society*, Volume 2.

Tang, D., Han, W., Li, P., Miao, X. and Zhong, J., (2011), "Biofixation and fatty acid composition of *Scenedesmus obliquus and Chlorella pyrenoidosa* in response to different CO2 levels. *Bioresource Technology*, Vol. 102, pp. 3071-3076.

Tassios, D. P., (1969), "Choosing Solvents for Extractive Distillation", *Chemical Engineering*, Vol. 118.

Taylor, B. N., Mohr, P. J. and Douma, M., (2007), "The NIST Reference on Constants, Units, and Uncertainty", available online from: www.physics.nist.gov/cuu/index.html.

Texaco Chemical company, (1960), "Technical Bulletin on propylene Carbonate" January.

Tochigi, K., Namae, T., Suga, T., Matsuda, H., Kurihara, K., Carolina dos Ramos, M. and McCabe, C., (2010), "Measurement and Prediction of High-Pressure Vapour-Liquid Equilibria for Binary Mixtures of Carbon Dioxide + n-Octane, Methanol, Ethanol, and Perfluorohexane". *Journal of Supercritical Fluids*, Vol. 55, pp. 682-689.

Tshibangu, M. M., (2010), MSc dissertation: High Pressure Vapour-Liquid equilibrium Data of Fluorochemical Systems for Various Temperatures Using a New Static Apparatus, University of KwaZulu-Natal, Durban, South Africa.

Tshibangu, M. M., Valtz, A., Narasigadu, C. Coquelet, C. and Ramjugernath, D., (2014a), "Vapor-Liquid Equilibrium (VLE) Data and Thermodynamic Modeling for Binary Systems Containing Perfluorobutane (R610) with Carbon Monoxide or Nitric Oxide at (293, 313 and 333) K", *Journal of Chemical Engineering Data*, Vol. 59(2), pp. 346-354.

Tshibangu, M. M., Valtz, A., Narasigadu, C. Coquelet, C. and Ramjugernath, D., (2014b), "Isothermal Vapor-Liquid Equilibrium Data and Thermodynamic Modeling for Binary Systems of Perfluorobutane (R610) + (Methane or Hydrogen Sulphide) at (293, 313, and 333) K", *Journal of Chemical Engineering Data*, Vol. 59 (9), pp. 2865-2871.

Tsonopoulos, C. and Heidman, J. L., (1986), "High Pressure Vapour-Liquid Equilibria with Cubic Equation of State", *Fluid Phase Equilibria*, 29, 391-414.

Twu, C. H., Bluck, J. R., Coon, J. E. and Cunningham, J. R., (1991), "A Cubic Equation of State with a New Alpha Function and a New Mixing Rule", *Fluid Phase Equilibria*, Vol. 69, pp. 33-50.

United Nations Conference on Sustainable Development, Rio de Janeiro, Brzail 20-22 June 2012.

Valentine, J. P., (1974), "New Solvent Process Purifies Crude, Coal Acid Gases*" Oil & Gas J*., Vol. 72, No. 76, pp. 60-62.

Valtz, A., Coquelet, C., Baba-Ahmed, A. and Richon, D., (2002), "Vapor-Liquid Equilibrium data for the Propane + 1,1,1,2,3,3,3-heptafluoropropane (R227ea) system at temperatures from 293.16 to 353.18 K and Pressures up to 3.4 MPa", *Fluid Phase Equilibria*, Vol. 202(1), pp. 29-47.

Valtz, A., Courtial, X., Johansson, E., Coquelet, C, and Ramjugernath, D., (2011), "Isothermal vapour-liquid equilibrium data for the carbon dioxide (744) + decafluorobutane (R610) system at temperatures from 263 to 353 K*". Fluid Phase Equilibria*, Vol. 304(1-2), pp. 44-51.

Van der Waals, J. D., (1873), "On the Continuity of the Gaseous and Liquid States" Doctoral dissertation). Universiteit Leiden.

Van Deraerschot, R. and Valentine, J. P., (1976), "The SELEXOL Solvent Process for Selective Removal of Sulphur Compounds", paper presented at 2nd International Conference on the Control of Gaseous Sulphur and Nitrogen Emission, Salford University, England, April 6-8.

Van Ness, H. C., Byer, S. M. and Gibbs, R. E., (1973), "Vapor-Liquid Equilibrium: Part I. An Appraisal of Data Reduction Methods", *American Institute of Chemical Engineers Journal*, Vol. 19(2), pp. 238-244.

Van Ness, H. C., (1995), "Thermodynamics in the Treatment of Vapor/Liquid Equilibrium (VLE) Data", *Pure and Applied Chemistry*, Vol. 67(6), pp. 859-872.

Vidal, J., (1978), "Mixing rules and excess properties in cubic equations of state." *Chemical Engineering Science,* 38:787-791.

Walas, S. M., (1985), "Phase Equilibrium in Chemical Engineering", Butterworth, Boston.

Wei, Y. S. and Sadus, R. J., (2000), "Equations of State for the Calculation of Fluid Phase Equilibria", *American Institute of Chemical Engineers Journal*, 46, 169-196.

Weidlich, U. and Gmehling, J., (1987), "A Modified UNIFAC Model1. Prediction of VLE, h^E and γ^{∞}". *Industrial & Engineering Chemistry Research*, Vol. 26, pp. 1372-1381.

Wertheim, M. S., (1984a), "Fluids with highly directional attractive forces: I. Statistical thermodynamics", *Journal of Statistical Physics*, 35, 19.

Wertheim, M. S., (1984b), "Fluids with highly directional attractive forces: II. Thermodynamic perturbation theory and integral equations", *Journal of Statistical Physics*, 35, 35.

White, C. M., Strazibar, B. R., Granite, E. J. and Hoffman, J. S., (2003), Performances and cost analysis for CO_2 capture from large stationary sources and sequestration in geological formations-coalbds and deep saline aquifers, *Journal of the Air & Waste Management Association*, Vol. 53, pp. 645-715.

Wilhelm, E. and Battino, R., (1973), "Thermodynamic Functions of the Solubility of Gases in Liquids at 25 ˚C. *Chemical Reviews*, Vol. 73 (1), pp. 1-10.

Wilson, G. M., (1964), "Vapour-Liquid Equilibrium. XI. A new Expression for the Excess Free Energy of Mixing", *Journal of the American Chemical Society*, Vol. 86, pp. 127-130.

Wong, D. S. H. and Sandler, S. I. (1992), "A Theoretically Correct Mixing Rule for Cubic Equation of State", *American Institute of Chemical Engineers Journal*, Vol. 38, pp. 671-680.

World Coal Association, (2012), “Coal facts 2012. Where is coal found?”, London, UK.

Yusuf, C., (2007), “Biodiesel from microalgae”, Biotechnical Advances.Vol. 25, pp. 294-306.

APPENDICES

Appendix A

This study focuses on the selective removal of CO_2, H_2S, CH_4 and CO using perfluorocarbons as potential physical solvents. However, the additional gases are listed in Table A.1 for future reference as this study forms part of an on-going research programme devised to investigate the use fluorochemicals as enhancing agent in separation processes.

Table A.1: Common flue gas components and their applications (Speight, 2002)

Component	Industrial application
Methane	• In a controlled-oxidation process, methane is used as a raw material in the production of acetylene. • Production of olefins on a large scale.
Ethane	• Production of aromatics by pyrolysis. • Ethane reacts with bromine to form substitution compounds such as: bromoethane and hydrogen bromide. • Important ethane derivatives, by successive oxidation, are ethyl alcohol, acetaldehyde, and acid acetic.
Carbon dioxide	• Refrigerant and inert blanket. • Enhanced oil recovery. • Chemical manufacture (especially soda ash), fire extinguishers, and pH control of waste water. • Fumigant for stored grain as a replacement for ethylene di-bromide.
Carbon monoxide	• Raw material in the production of methanol and other alcohols of hydrocarbons. • In the production of di-isocynate and ethyl acrylate.
Nitric Oxide	• In critical care to promote capillary and pulmonary dilation to treat pulmonary hypertension in neonatal patients post meconium aspiration and related to birth defects.

Table A: Continued

Hydrogen sulphide	• Production of elemental sulfur, sulfuric acid, tri-organic compounds, sodium sulfide, sodium hydrosulfide, etc. • In metallurgy to precipitate copper, nickel and cobalt sulfides from ores.
Oxygen	• Metals manufacturing, chemicals manufacturing, oxidation processes and partial oxidation processes. • Miscellaneous uses include sewage treatment, aeration, pulp and paper bleaching, and missile fuel • Chemical manufacture use includes the formation of ethylene oxide, acrylic acid, propylene oxide, and vinyl acetate.
Nitrogen	• Ammonia synthesis • Oil enhanced recovery where it maintains pressure in oil fields so that a vacuum is not formed underground when natural gas and oil are pumped out. • Blanket atmospheres, food preservation, aerospace, cryogenics, metals processing, and electronic manufacturing.
Ammonia	• Manufacture for fertilizers, manufacture of other nitrogen-containing compounds used for fertilizer or, to a lesser extent, explosives, plastics, and fibres.
Sulfur dioxide	• For refrigeration • Raw material for the production of sulphuric acid • Bleach agent in the textile and food industries • Controls fermentation in the making of wine • In sulphite process for paper pulp • As a liquid solvent in petroleum refining • As raw material in many plants in place of sulphites, bisulphites, or hydrosulphites. • As disinfectants for wooden kegs.

Appendix B

B.1 The UNIversal quasi-chemical Functional-group Activity Coefficient (UNIFAC) model

The UNIFAC model is an activity coefficient model like the non-random two-liquid (NRTL) or the UNIversal QUAsi-Chemical (UNIQUAC). However, it is based on group contributions rather than molecular contributions. Basically, it assumes that the interactions between two molecules emanates from that of functional groups that compose them. The advantage of this concept is evident, since one needs to know just the interactions between functional groups to predict interactions between any molecules. One should note the primary function of a group contribution method is to predict phase equilibrium data for systems of which no experimental data exists, using the existing phase equilibrium data.

The UNIFAC model is a widely used group contribution activity coefficient model based on the (UNIQAC) model and is discussed in detail in the monograph of Fredenslund et al. (1977). The UNIFAC model was initially proposed by Fredenslund et al. (1975).

The basic equations of the original UNIFAC model for the activity coefficient of component *i* can be summarized as follows:

$$\ln \gamma_i = \ln \gamma_i^{comb} + \ln \gamma_i^{res} \tag{B.1}$$

Where the combinatorial (*comb*) contribution (which describes the excess Gibbs energy arising due to differences in molecular size and shape) and residual (*res*) term (which describes the excess Gibbs energy differences due to molecular interactions) are given by the following equations:

$$\ln \gamma_i^{comb} = \ln\left(\frac{\Phi_i}{x_i}\right) + 1 - \left(\frac{\Phi_i}{x_i}\right) - \frac{Z}{2} q_i \left(\ln \frac{\Phi_i}{\theta_i} + 1 - \frac{\Phi_i}{\theta_i}\right) \tag{B.2}$$

$$\ln \gamma_i^{res} = \sum_k \nu_k^{(i)} \left(\ln \Gamma_k - \ln \Gamma_k^{(i)}\right) \tag{B.3}$$

In Eq. (B.2): the molecular volume (Φ_i) and surface fractions (θ_i) are expressed as follows:

$$\Phi_i = \frac{x_i r_i}{\sum_j^{nc} x_j r_j} \quad \text{(B.4)} \qquad \text{and} \qquad \theta_i = \frac{x_i \frac{z}{2} q_i}{\sum_j^{nc} x_j \frac{z}{2} q_j} \quad \text{(B.5)}$$

where nc is the number of components in the mixture; the coordination number z is set to 10; the pure-component parameters r_i and q_i are evaluated from the group volume and area parameters as follows:

$$r_i = \sum_k^{ng} v_{ki} R_k \quad \text{(B.6) and} \quad q_i = \sum_k^{ng} v_{ki} Q_k \qquad \text{(B.7)}$$

where v_{ki} is the number of groups of type k in molecule i, and ng is the number of groups in the mixture.

In Eq. (B.3): Γ_k is the residual activity coefficient of the group (k), and Γ_k^i is the residual activity coefficient of group (k) in a reference solution which contains only molecules of type (i). The group residual activity coefficients Γ_k and Γ_k^i are calculated as follows:

$$\ln \Gamma_k = Q_k \left(1 - \ln \sum_m^{ng} \theta_m \tau_{mk} - \sum_m^{ng} \left(\frac{\theta_m \Psi_{km}}{\sum_n^{ng} \theta_n \Psi_{nm}} \right) \right) \qquad \text{(B.8)}$$

with

$$\theta_k = \frac{X_k \frac{z}{2} Q_k}{\sum_m^{ng} X_m \frac{z}{2} Q_m} \qquad \text{(B.9)}$$

The group interaction parameter (Ψ_{mn}) is given by:

$$\Psi_{mn} = \exp - \left[\frac{U_{mn} - U_{nn}}{RT} \right] = \exp = \left(\frac{a_{mn}}{T} \right) \qquad \text{B.10)}$$

The interaction parameters a_{mn} are assumed to be temperature-independent and are obtained by correlation of the experimental VLE data and thereafter listed in the parameter tables of UNIFAC.

The UNIFAC model is generally accepted as an accurate predictive model for the calculation of activity coefficients for various mixtures. Consequently, this has led to its implementation in several process simulators and its use in the industry. However, Fredenslund and Rasmussen (1985), Malanowski and Anderko (1992) and Fredenslund and Sørenson (1994) have reported a number of limitations and weaknesses associated with the UNIFAC model, which can be summarized as follows:

- ***Activity coefficient approach***. It is based on the so-called gamma-phi approach, which usually assumes the ideality of the vapour phase and therefore limits its application to low or moderate pressures, i.e., in the region 10-15 atm.
- ***Solution of groups approach***. Since the UNIFAC model is based on the solution of groups, it assumes that the behaviour of a structural group is independent of its nearby environment. Consequently, the model fails to distinguish between isomers.
- ***The UNIFAC functional group.*** The parameters employed in UNIFAC are obtained from the correlation of experimental vapour-liquid equilibrium (VLE) data. However, it has been demonstrated that, although, the existence of these parameters, the UNIFAC model fails to predict liquid-liquid equilibrium (LLE) data accurately. In addition, the use of temperature-independent parameters restricts the model to a temperature ranging from 275 to 425 K, which is in contrast with the activity coefficient defined as function of temperature.
- ***Experimental data.*** The prediction of data using the UNIFAC model depends solely on the availability and accuracy of the experimental data. Due to the absence of data in the dilute region of a mixture, the model fails to predict with accuracy values of activity coefficient at infinite dilution.

Since the publication of the original UNIFAC model and in order to address its limitations, numerous modifications have been proposed. Table B.1 lists some of the most important UNIFAC variants (Kontogeorgis and Folas, 2010).

Table B.1: Some of the most important UNIFAC variants

UNIFAC variant	**Reference**	**Temperature-dependency/ parameters**	**Data used**	**Comment**
Original-VLE	Fredenslund et al. (1975) Hansen et al. (1991)	Temperature-independent	VLE	Recommended over narrow temperature ranges
Original LLE	Magnusen et al. (1981)	Temperature-independent	LLE	Recommended over narrow temperature range, around room temperature
'Linear' UNIFAC	Hansen et al. (1992)	Linearly dependent on temperature: $a_{mn} = a_{mn,1} + a_{mn,2}(T - T_0)$	VLE	Parameters not published in the 'open' literature but available via a report from IVC-SEP, Institut for Kemiteknik, Technical University of Denmark
Modified UNIFAC (Lyngby)	Larsen et al. (1987)	Logarithmic dependency: $a_{mn} = a_{mn,0} + a_{mn,1}(T - T_0) + a_{mn,2}\left(T \ln \frac{T_0}{T} + T - T_0\right)$	VLE, H^E	Modified combinatorial term

Table B.1: Continued

UNIFAC variant	**Reference**	**Temperature-dependency /parameters**	**Data used**	**Comment**
Modified UNIFAC (Dortmund)	Weidlich and Gmehling (1987) Gmehling and coworkers (1993, 2002, 2003)	$a_{mn} = a_{mn,0} + a_{mn,1}T + a_{mn,2}T^2$	VLE, HE, Activity coefficients at infinite dilution	Modified combinatorial term. Fitted the *r* and *q* parameters.
Water-UNIFAC	Chen et al. (1993)	Temperature-independent	VLE, Activity coefficients at infinite dilution and water data	Used for octanol-water partition coefficient calculations
Water-UNIFAC	Hooper et al. (1988)	$a_{mn} = a_{mn,0} + a_{mn,1}T + a_{mn,2}T^2$		Suitable for water-hydrocarbon systems
Second order or KT-UNIFAC	Kang et al. (2002)			Changes in equations and new first and second order group parameter tables

As can be seen from Table B.1, the major changes include the combinatorial and residual terms as well as the introduction of temperature-dependent interaction parameters. The modified UNIFAC (Dortmund) produces more reliable results for the activity coefficients at infinite dilution as opposed to the modified UNIFAC (Lyngby). The introduction of the temperature-dependent interaction parameters has improved results for the calculation of enthalpies of mixing. One should note that none of the modified UNIFAC models presented were able to predict, with satisfaction, the activity coefficients at infinite dilution for strongly non-ideal water-containing mixtures (Muzenda, 2013).

Like the original UNIFAC, the modified UNIFAC (Dortmund) fails to calculate excess enthalpies for alkane/alkane systems (Weidlich and Gmehling, 1987).

One should note that, only the modified UNIFAC (Dortmund) model was used in this study.

B.2 Conductor-like Screening Model (COSMO) based activity coefficient models

As an alternative approach to the classical predictive models based on group contribution methods such as the UNIFAC or modified UNIFAC models, the COSMO-based models are used to characterise molecular interactions and account for the liquid phase non-ideality. These methods are based on quantum mechanics (QM) and do not use arbitrarily defined functional groups. Consequently, their predictions are less dependent on fitting to experimental data. One should note the COSMO-based models use the results obtained from the COSMO calculation, wherein a molecule is transferred from a vacuum to a perfect conductor and thereafter dissolves it into an infinite conducting medium. Details relative to COSMO are available in the work of Klamt and Schüürmann (1993).

However, there are various COSMO-based models available. Two such models are the conductor-like screening models–real solvation (COSMO-RS) originally developed by Klamt (1995), and the conductor-like screening models–segment activity coefficient (COSMO-SAC) originally developed by Lin and Sandler (2002) based on the framework of COSMO-RS. In spite of their differences, COSMO-RS and COSMO-SAC present similarities in the calculation of the solvation free energy. The first variant of COSMO-SAC aimed at predicting activity coefficients. Thereafter another variant was proposed to predict vapour pressures and heats of vaporisation by including a dispersion term using mean field theory. Wang and Sandler (2007) developed a refined COSMO-SAC (2007) by combining previous approaches to predict thermodynamic properties of both mixtures and pure-components.

Hsieh et al. (2010) proposed COSMO-SAC (2010) to improve the prediction of phase equilibrium data. Later, Ruichang et al. (2014) proposed the revised COSMO-SAC denoted as COSMO-SAC (2013), which was validated by comparison with the refined COSMO-SAC (2007) and (2010) for the prediction of the thermodynamic properties of both mixtures (vapor-liquid equilibrium data, activity coefficients and partition coefficients) and pure-components (vapor pressures, heats of vaporization and normal boiling points). However, in this study, only the original COSMO-SAC developed by Lin and Sandler (2002) was used as it was the latest model available in Aspen Plus V 8.0. One should note that, in this study, Aspen Plus V8.0 was used for regressing the phase equilibrium data and design purpose.

B.2.1 COSMO-SAC model

The COSMO-SAC model as originally proposed by Lin and Sandler (2002) uses the QM-COSMO solvation calculation to represent the charge distribution of the molecules, and the statistical analysis to determine the chemical potential of pure components or mixtures. One should note that to determine the activity coefficient, the sigma profiles and the van der Waals surface and volume are required. Consequently, this makes COSMO-SAC a predictive model.

COSMO-SAC uses information from the COSMO calculation to produce sigma profiles, which are the principal molecule-specific inputs for the COSMO-based models. A sigma profile is a molecular-specific distribution of the surface-charge density, which enables the application of the solvation-thermodynamic models to predict phase equilibria and other properties. The sigma profiles used in this study were taken from the consortium version of the Dortmund Data Bank and are graphically presented in Figure B.1.

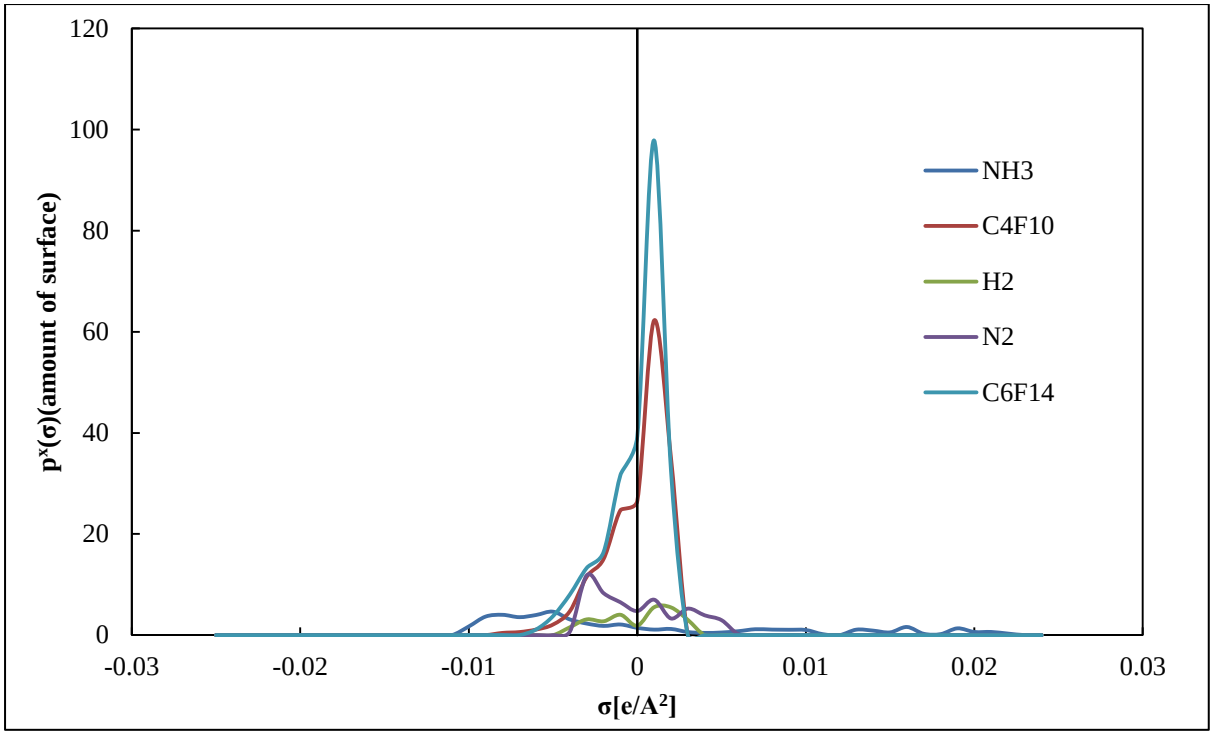

Figure B.1: COSMO-SAC sigma profiles for ammonia, perfluorobutane, hydrogen, nitrogen and perfluorohexane.

In Aspen Plus, the COSMO-SAC model calculates the liquid activity coefficient of component i as follows:

$$\ln \gamma_i = \frac{A_i}{a_{eff}} \sum_{\sigma_m} p_i(\sigma_m)\left[\ln \Gamma_S(\sigma_m) - \ln \Gamma_i(\sigma_m)\right] + \ln \gamma_i^{SG} \tag{B.11}$$

With

$$\ln \Gamma_S(\sigma_m) = -\ln\left\{\sum_{\sigma_n} p_S(\sigma_n)\Gamma_S(\sigma_n)\exp\left[\frac{-\Delta W(\sigma_m,\sigma_n)}{kT}\right]\right\} \tag{B.12}$$

$$\ln \Gamma_i(\sigma_m) = -\left\{\sum_{\sigma_n} p_i(\sigma_n)\Gamma_i(\sigma_n)\exp\left[\frac{-\Delta W(\sigma_m,\sigma_n)}{kT}\right]\right\} \tag{B.13}$$

$$p_i(\sigma) = \frac{A_i(\sigma)}{A_i} \tag{B.14}$$

$$p_S(\sigma) = \frac{\sum_i x_i A_i p_i(\sigma)}{\sum_i x_i A_i} \tag{B.15}$$

$$A_i = \sum_\sigma A_i(\sigma) \tag{B.16}$$

$$\Delta W(\sigma_m, \sigma_n) = \frac{\alpha'}{2}(\sigma_m, \sigma_n)^2 + \Delta W^{HB}(\sigma_m, \sigma_n) \tag{B.17}$$

$$\ln \gamma_i^{SG} = \ln \frac{\phi_i}{x_i} + \frac{z}{2} q_i \ln \frac{\theta_i}{\phi_i} + l_i - \frac{\phi_i}{x_i} \sum_j x_j l_j \tag{B.18}$$

$$\theta_i = \frac{x_i q_i}{\sum_j x_j q_j} \tag{B.19}$$

$$\phi_i = \frac{x_i r_i}{\sum_j x_j r_j} \tag{B.20}$$

$$l_i = \frac{z}{2}(r_i - q_i) - (r_i - 1) \tag{B.21}$$

$$r_i = \frac{V_i}{V_{eff}} \tag{B.22}$$

$$q_i = \frac{A_i}{A_{eff}} \tag{B.23}$$

where from Eq. B.11 – B23:

γ_i is the activity coefficient of component i;

γ_i^{SG} is the Staverman-Guggenheim model for the combinatorial contribution of γ_i;

$\Gamma_i(\sigma_m)$ is the segment activity coefficient of segment σ_m in component i;

$\Gamma_S(\sigma_m)$ is the segment activity coefficient of segment σ_m in solvent mixture;

$p_i(\sigma_m)$ is the sigma profile of component i;

$p_i(\sigma_m)$ is the sigma profile of solvent mixture;

σ is the surface charge density;

$\Delta W(\sigma_m, \sigma_n)$ is the exchange energy between segments σ_m and σ_n;

$\Delta W^{HB}(\sigma_m, \sigma_n)$ is the hydrogen-bonding contribution to exchange energy between segments; σ_m and σ_n

z is the coordination number, 10;

V_i is the molecular volume of component i;

A_i is the molecular surface area of component i;

a_{eff} is the standard segment surface area, 7.50 Å^2;

V_{eff} is the standard component volume, 66.69 Å^2;

A_{eff} is the standard component surface area, 79.53 Å^2;

α' is the misfit energy constant.

For each pure component, the COMO-SAC model has six input parameters, one component volume parameter and five molecular component sigma profile parameters of which each parameter can store up to twelve points of sigma profile values. One should note that all six parameters are obtained from the COSMO calculation.

Appendix C

TCD calibrations

Ethane (1) + perfluorobutane (2) system

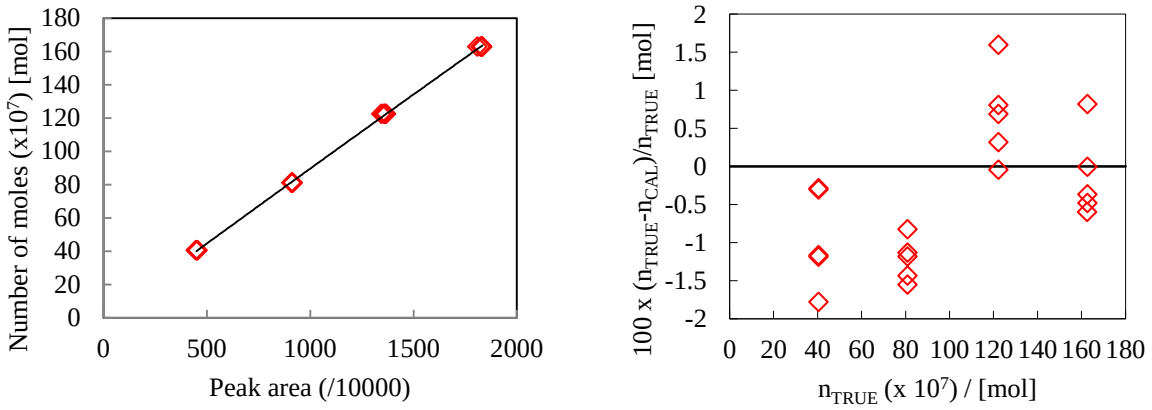

Figure C.1: [*left*] TCD calibration results using the direct injection method for: ◊, perfluorobutane using a gas-tight 500 µl syringe [*right*] Deviation in the number of moles using a second polynomial; n_{TRUE} is the actual number of moles calculated from the volume injected into the GC, n_{CAL} is the number of moles calculated from the correlation polynomial.

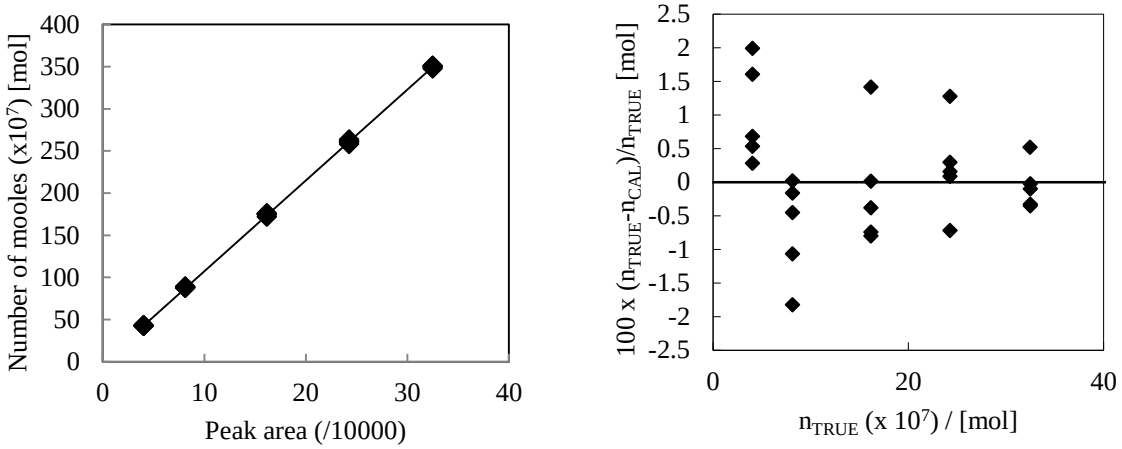

Figure C.2: [*left*] TCD calibration results using the direct injection method for: ♦, perfluorobutane using a gas-tight 100 µl syringe [*right*] Deviation in the number of moles using a second polynomial; n_{TRUE} is the actual number of moles calculated from the volume injected into the GC, n_{CAL} is the number of moles calculated from the correlation polynomial.

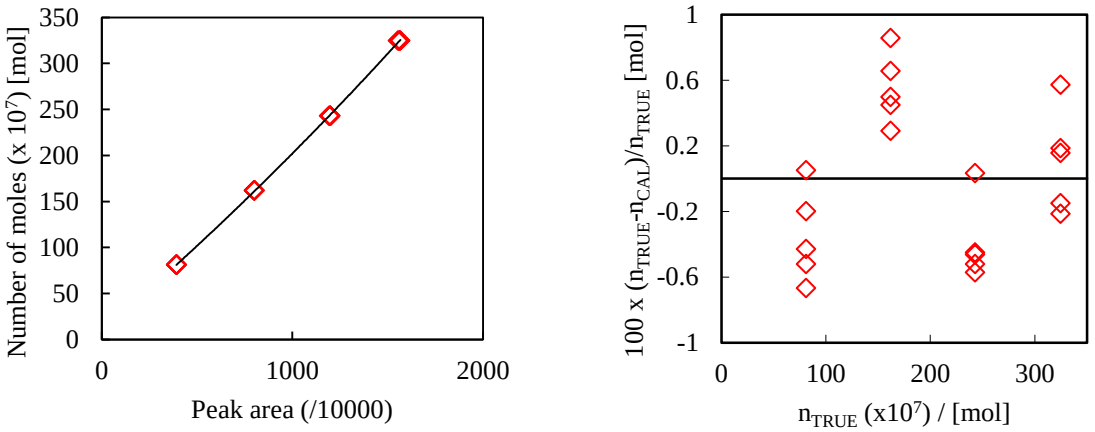

Figure C.3: : [*left*] TCD calibration results using the direct injection method for: ◊, ethane using a gas-tight 1000 µl syringe [*right*] Deviation in the number of moles using a second polynomial; n_{TRUE} is the actual number of moles calculated from the volume injected into the GC, n_{CAL} is the number of moles calculated from the correlation polynomial.

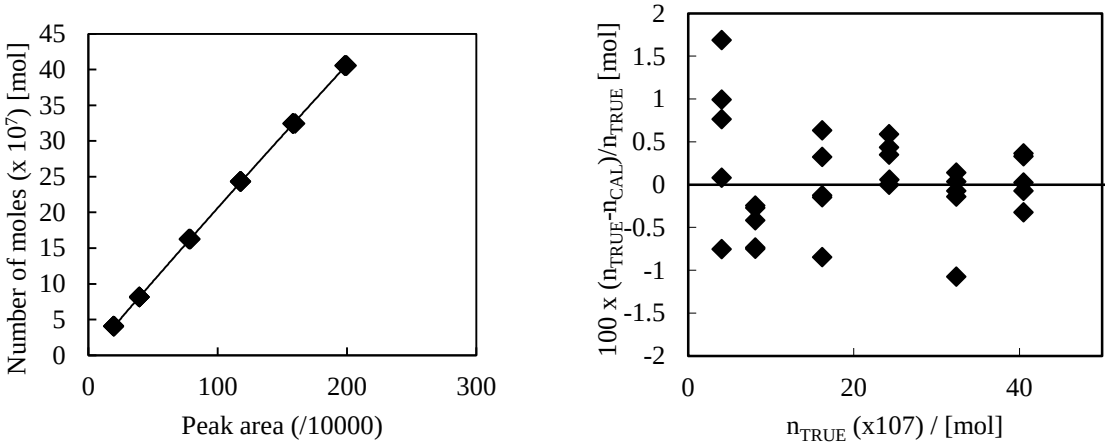

Figure C.4: : [*left*] TCD calibration results using the direct injection method for: ♦, ethane using a gas-tight 1000 µl syringe [*right*] Deviation in the number of moles using a second polynomial; n_{TRUE} is the actual number of moles calculated from the volume injected into the GC, n_{CAL} is the number of moles calculated from the correlation polynomial.

Oxygen (1) +perfluorobutane (2) system

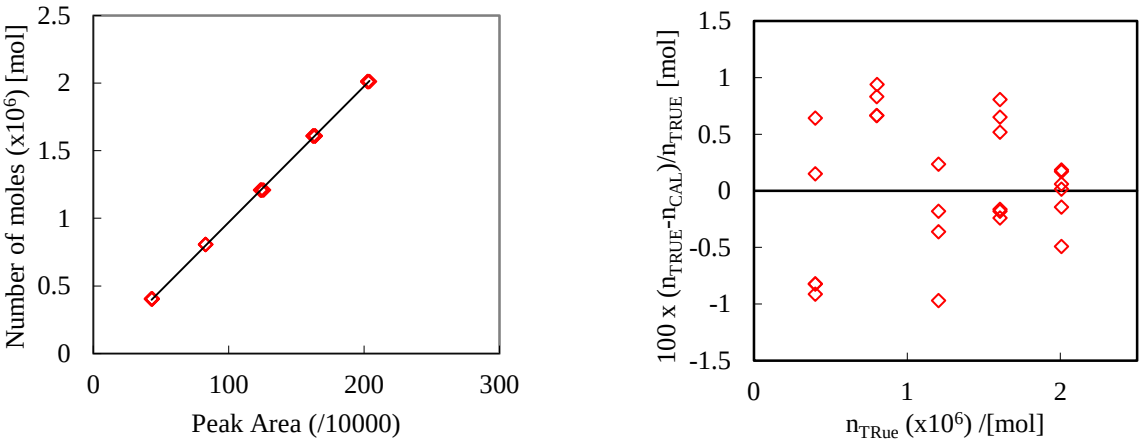

Figure C.5 : [*left*] TCD calibration results using the direct injection method for: ◊, oxygen using a gas-tight 100 µl syringe [*right*] Deviation in the number of moles using a second polynomial; n_{TRUE} is the actual number of moles calculated from the volume injected into the GC, n_{CAL} is the number of moles calculated from the correlation polynomial.

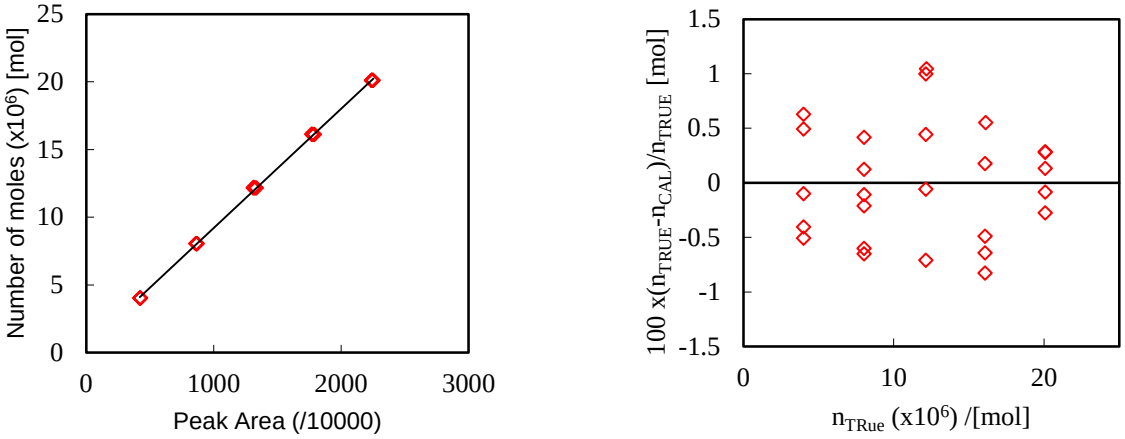

Figure C.6 : [*left*] TCD calibration results using the direct injection method for: ◊, oxygen using a gas-tight 500 µl syringe [*right*] Deviation in the number of moles using a second polynomial; n_{TRUE} is the actual number of moles calculated from the volume injected into the GC, n_{CAL} is the number of moles calculated from the correlation polynomial.

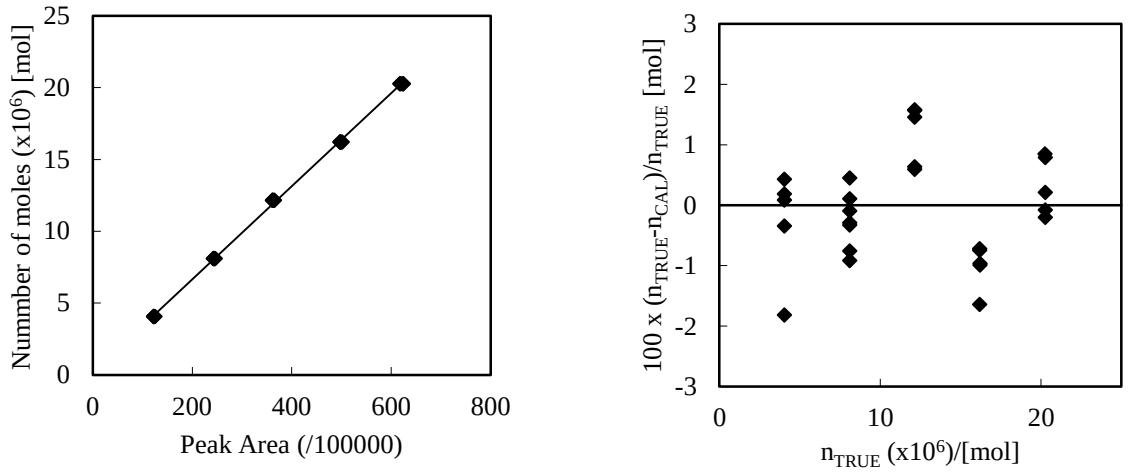

Figure C.7 : [*left*] TCD calibration results using the direct injection method for: ♦, perfluorobutane using a gas-tight 500 µl syringe [*right*] Deviation in the number of moles using a second polynomial; n_{TRUE} is the actual number of moles calculated from the volume injected into the GC, n_{CAL} is the number of moles calculated from the correlation polynomial.

Nitrogen (1) + perfluorobutane (2) system

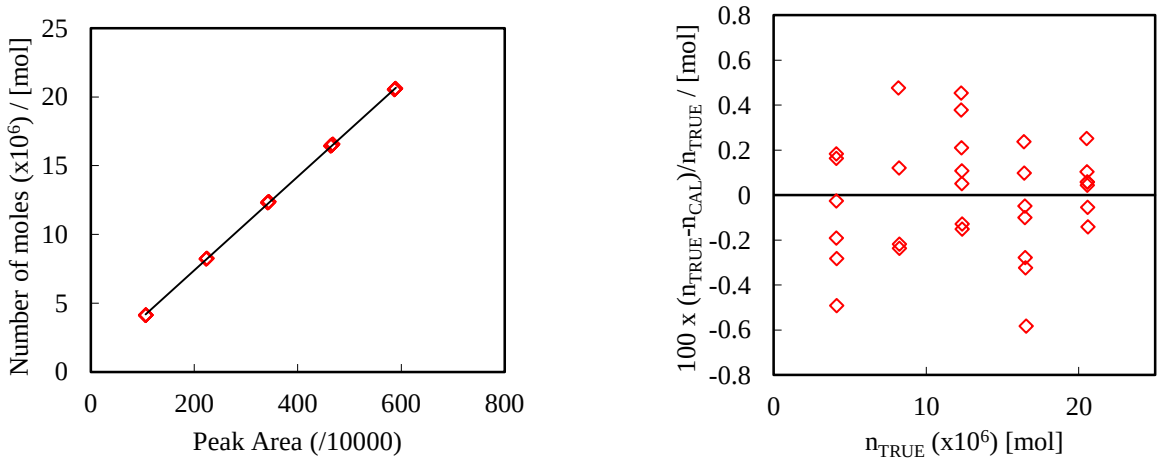

Figure C.8 : [*left*] TCD calibration results using the direct injection method for: ◊, nitrogen using a gas-tight 500 µl syringe [*right*] Deviation in the number of moles using a second polynomial; n_{TRUE} is the actual number of moles calculated from the volume injected into the GC, n_{CAL} is the number of moles calculated from the correlation polynomial.

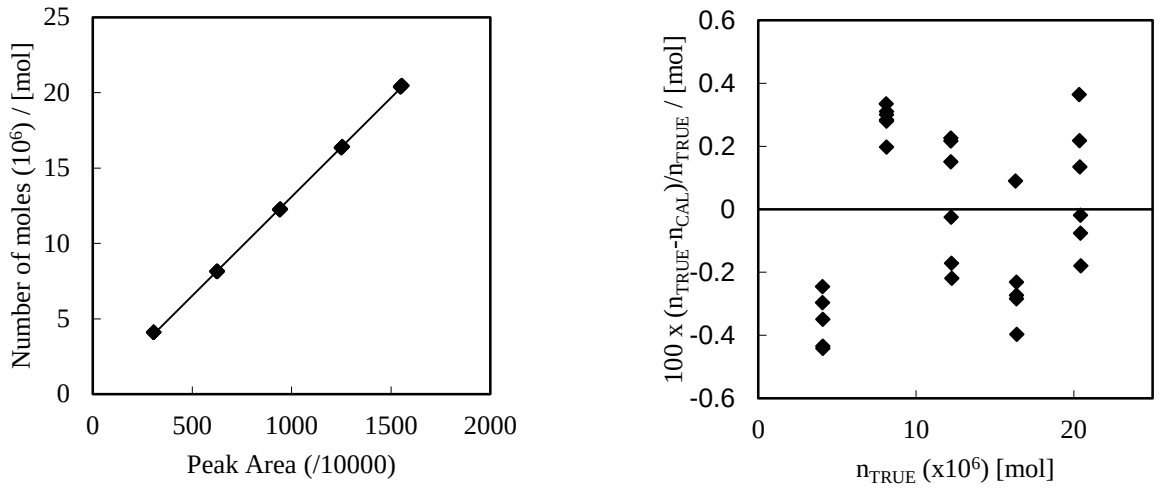

Figure C.9 : [*left*] TCD calibration results using the direct injection method for: ♦, perfluorobutane using a gas-tight 500 µl syringe [*right*] Deviation in the number of moles using a second polynomial; n_{TRUE} is the actual number of moles calculated from the volume injected into the GC, n_{CAL} is the number of moles calculated from the correlation polynomial.

Hydrogen (1) + perfluorobutane (2) system

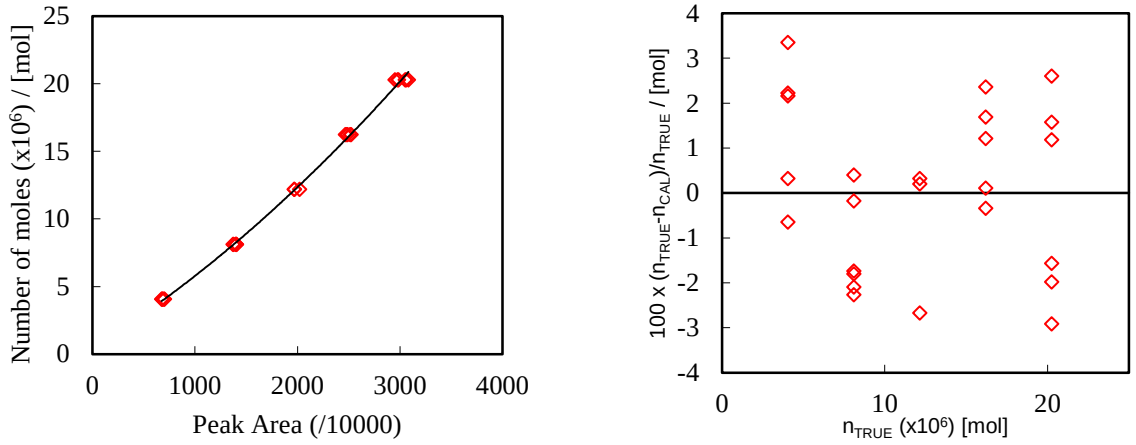

Figure C.10 : [*left*] TCD calibration results using the direct injection method for: ◊, hydrogen using a gas-tight 500 µl syringe [*right*] Deviation in the number of moles using a second polynomial; n_{TRUE} is the actual number of moles calculated from the volume injected into the GC, n_{CAL} is the number of moles calculated from the correlation polynomial.

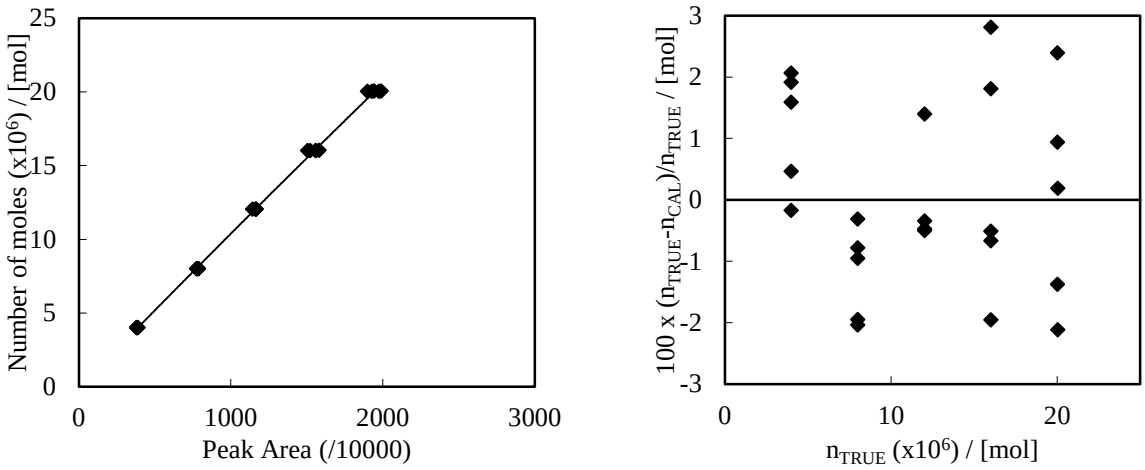

Figure C.11 : [*left*] TCD calibration results using the direct injection method for: ♦, perfluorobutane using a gas-tight 500 µl syringe [*right*] Deviation in the number of moles using a second polynomial; n_{TRUE} is the actual number of moles calculated from the volume injected into the GC, n_{CAL} is the number of moles calculated from the correlation polynomial.

Carbon monoxide (1) + perfluorobutane (2) system

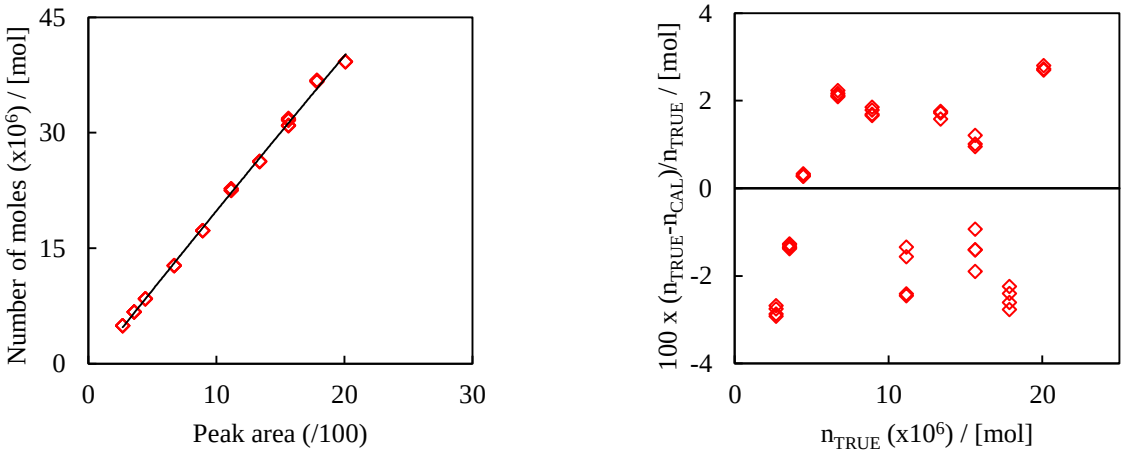

Figure C.12: [*left*] TCD calibration results using the direct injection method for: ◊, carbon monoxide using two gas-tight 100 and 500 µl syringes [*right*] Deviation in the number of moles using a second polynomial; n_{TRUE} is the actual number of moles calculated from the volume injected into the GC, n_{CAL} is the number of moles calculated from the correlation polynomial.

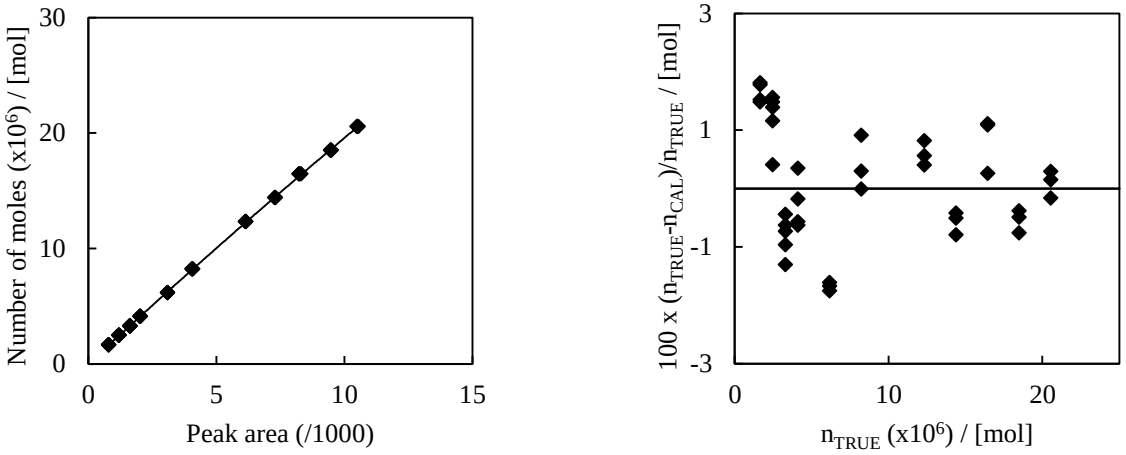

Figure C.13 : [*left*] TCD calibration results using the direct injection method for: ♦, perfluorobutane using a gas-tight 500 µl syringe [*right*] Deviation in the number of moles using a second polynomial; n_{TRUE} is the actual number of moles calculated from the volume injected into the GC, n_{CAL} is the number of moles calculated from the correlation polynomial

Nitric oxide (1) + perfluorobutane (2) system

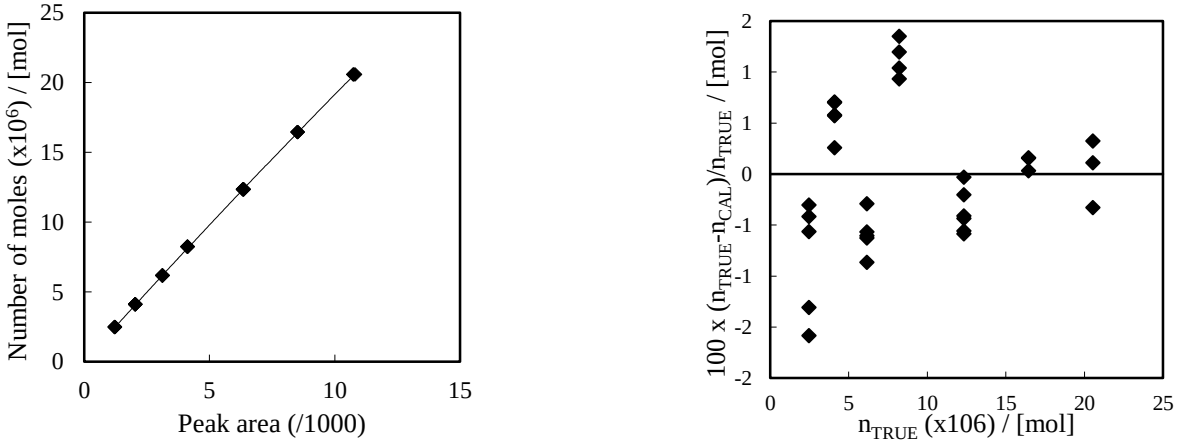

Figure C.14 : [*left*] TCD calibration results using the direct injection method for: ♦, perfluorobutane using a gas-tight 500 µl syringe [*right*] Deviation in the number of moles using a second polynomial; n_{TRUE} is the actual number of moles calculated from the volume injected into the GC, n_{CAL} is the number of moles calculated from the correlation polynomial

Hydrogen sulphide (1) + perfluorobutane (2) system

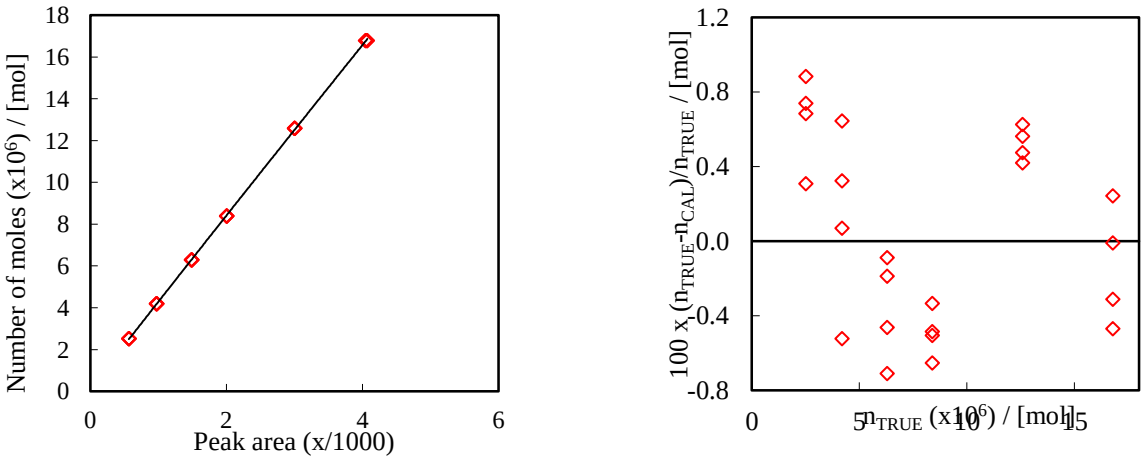

Figure C.15: [*left*] TCD calibration results using the direct injection method for: ◊, hydrogen sulphide using two gas-tight 100 and 500 µl syringes [*right*] Deviation in the number of moles using a second polynomial; n_{TRUE} is the actual number of moles calculated from the volume injected into the GC, n_{CAL} is the number of moles calculated from the correlation polynomial.

Please note that the TCD calibration for perfluorohexane in Figure B.17 was also used for the hydrogen sulphide (1) + perfluorobutane (2) system.

Ethane (1) + perfluorohexane (2) system

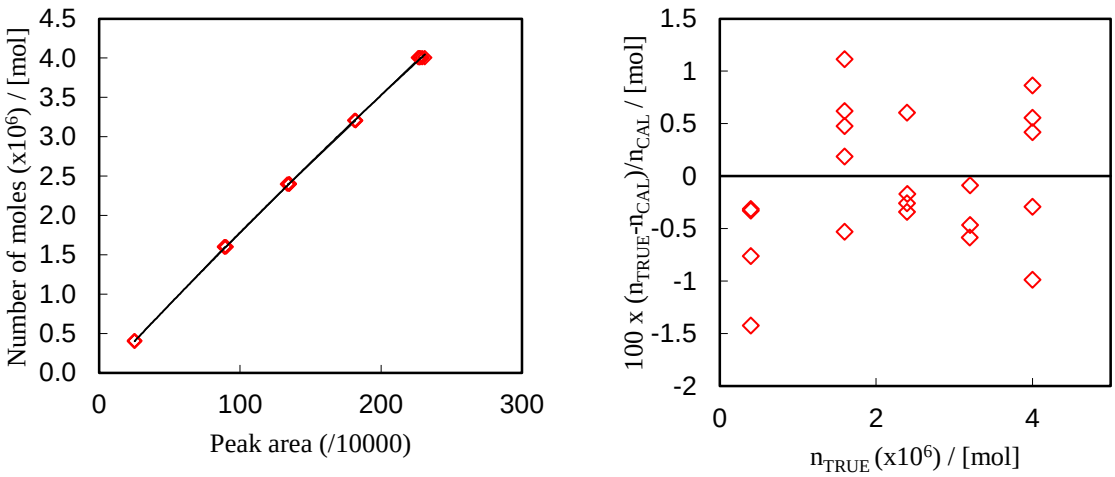

Figure C.16 : [*left*] TCD calibration results using the direct injection method for: ◊, ethane using a gas-tight 100 µl syringe [*right*] Deviation in the number of moles using a second polynomial; n_{TRUE} is the actual number of moles calculated from the volume injected into the GC, n_{CAL} is the number of moles calculated from the correlation polynomial.

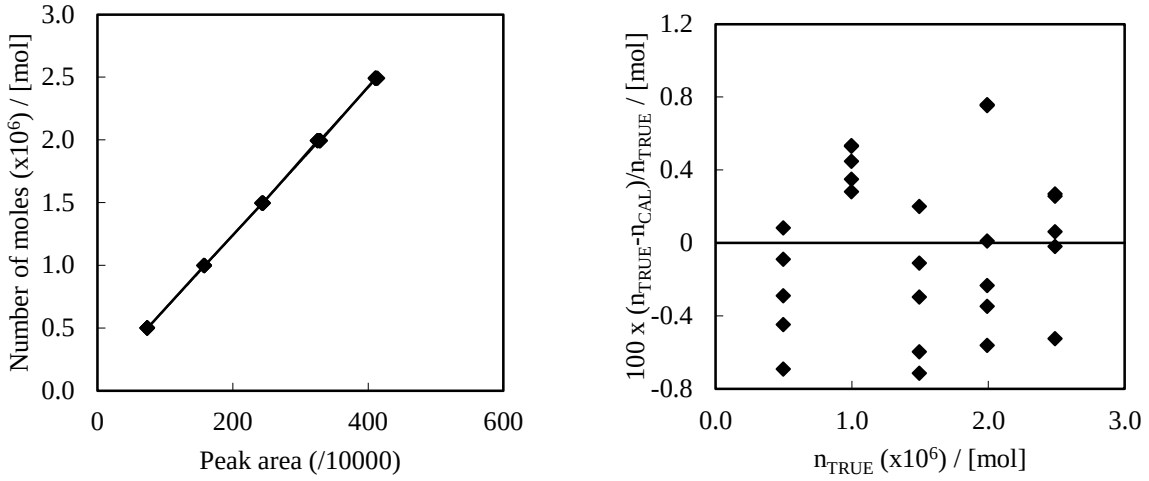

Figure C.17 : [*left*] TCD calibration results using the direct injection method for: ♦, perfluorohexane using a gas-tight 0.6 µl syringe [*right*] Deviation in the number of moles using a second polynomial; n_{TRUE} is the actual number of moles calculated from the volume injected into the GC, n_{CAL} is the number of moles calculated from the correlation polynomial.

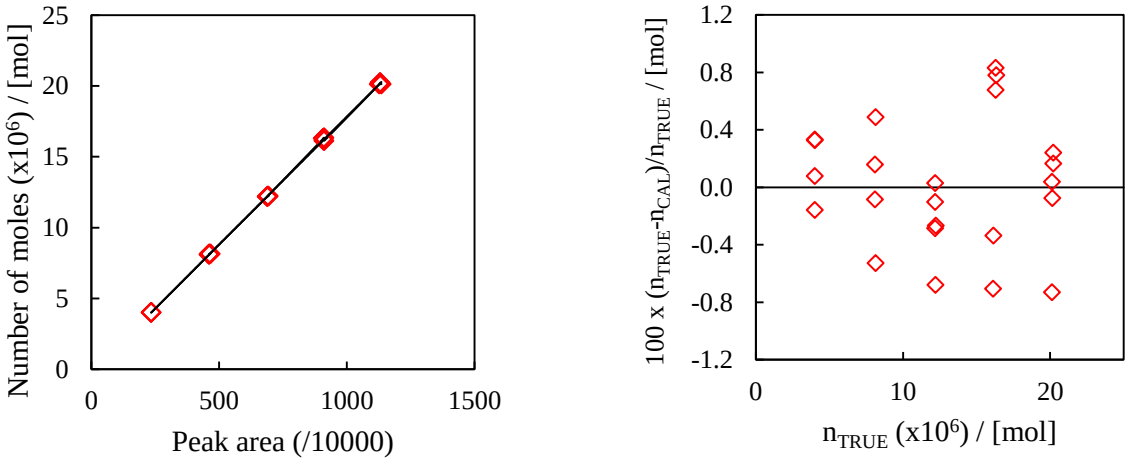

Figure C.18 : [*left*] TCD calibration results using the direct injection method for: ◊, ethane using a gas-tight 500 µl syringe [*right*] Deviation in the number of moles using a second polynomial; n_{TRUE} is the actual number of moles calculated from the volume injected into the GC, n_{CAL} is the number of moles calculated from the correlation polynomial.

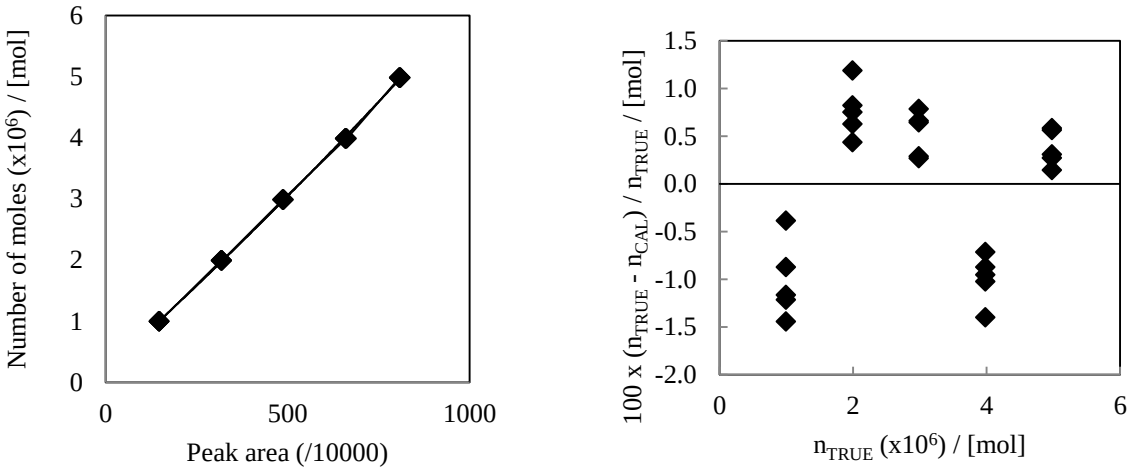

Figure C.19 : [*left*] TCD calibration results using the direct injection method for: ♦, perfluorohexane using a gas-tight 1 µl syringe [*right*] Deviation in the number of moles using a second polynomial; n_{TRUE} is the actual number of moles calculated from the volume injected into the GC, n_{CAL} is the number of moles calculated from the correlation polynomial.

Methane (1) + perfluorohexane (2) system

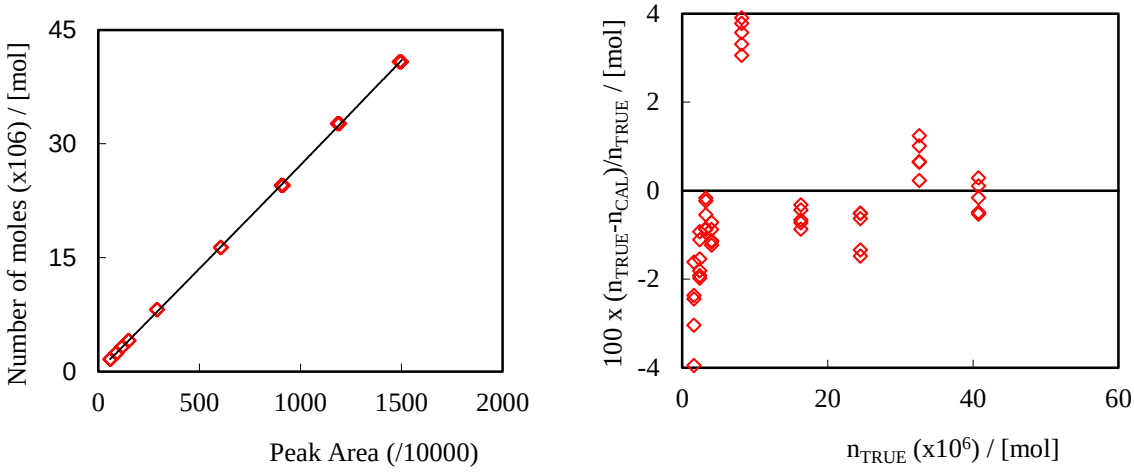

Figure C.20: [*left*] TCD calibration results using the direct injection method for: ◊, methane using two gas-tight 100 and 500 µl syringes [*right*] Deviation in the number of moles using a second polynomial; n_{TRUE} is the actual number of moles calculated from the volume injected into the GC, n_{CAL} is the number of moles calculated from the correlation polynomial.

Please note that the TCD calibration for perfluorohexane in Figure B.14 was also used for the methane (1) + perfluorohexane (2) system.

Table C.1 Correlation polynomial using the LINEST function

Chemical	[a] $\Delta n/n$ (max) [%]	Volume (µl)	Correlation
C_2H_6	2	500	$n_{CAL} = 1.612 \times 10^{-20} A_i^2 + 1.765 \times 10^{-12} A_i$
C_4F_{10}	2.5	100	$n_{CAL} = 2.221 \times 10^{-21} A_i^2 + 9.195 \times 10^{-13} A_i$
C_2H_6	1	1000	$n_{CAL} = -3.324 \times 10^{-20} A_i^2 + 2.107 \times 10^{-12} A_i$
C_4F_{10}	2	500	$n_{CAL} = -3.069 \times 10^{-22} A_i^2 + 8.953 \times 10^{-13} A_i$
O_2	1.5	100	$n_{CAL} = 8.325 \times 10^{-21} A_i^2 + 9.842 \times 10^{-13} A_i$
O_2	1.5	500	$n_{CAL} = -2.208 \times 10^{-21} A_i^2 + 9.411 \times 10^{-13} A_i$
C_4F_{10}	3	500	$n_{CAL} = -2.849 \times 10^{-22} A_i^2 + 3.452 \times 10^{-13} A_i$
N_2	0.8	500	$n_{CAL} = -2.287 \times 10^{-20} A_i^2 + 3.570 \times 10^{-12} A_i$
C_4F_{10}	0.6	500	$n_{CAL} = 4.963 \times 10^{-21} A_i^2 + 1.219 \times 10^{-12} A_i$
H_2	4	500	$n_{CAL} = 6.266 \times 10^{-21} A_i^2 + 4.684 \times 10^{-13} A_i$
C_4F_{10}	3	500	$n_{CAL} = -1.490 \times 10^{-21} A_i^2 + 1.063 \times 10^{-12} A_i$
CO	4	100 and 500	$n_{CAL} = 7.704 \times 10^{-15} A_i^2 + 4.858 \times 10^{-09} A_i$
C_4F_{10}	3	500	$n_{CAL} = -9.433 \times 10^{-15} A_i^2 + 2.052 \times 10^{-09} A_i$
NO	1	500	$n_{CAL} = -3.942 \times 10^{-14} A_i^2 + 4.566 \times 10^{-09} A_i$
C_4F_{10}	2	500	$n_{CAL} = -8.367 \times 10^{-15} A_i^2 + 1.990 \times 10^{-09} A_i$
H_2S	1.2	500	$n_{CAL} = -1.463 \times 10^{-14} A_i^2 + 4.168 \times 10^{-09} A_i$
C_4F_{10}	2	500	$n_{CAL} = -8.367 \times 10^{-14} A_i^2 + 1.990 \times 10^{-09} A_i$
CH_4	1	500	$n_{CAL} = -3.942 \times 10^{-14} A_i^2 + 4.566 \times 10^{-09} A_i$
C_4F_{10}	2	500	$n_{CAL} = -9.371 \times 10^{-15} A_i^2 + 1.992 \times 10^{-09} A_i$
C_2H_6	2	100	$n_{CAL} = -5.769 \times 10^{-20} A_i^2 + 1.915 \times 10^{-12} A_i$
C_6F_{14}	1.2	0.6	$n_{CAL} = 1.266 \times 10^{-14} A_i^2 + 5.824 \times 10^{-09} A_i$
C_2H_6	1.2	500	$n_{CAL} = -1.645 \times 10^{-22} A_i^2 + 1.808 \times 10^{-12} A_i$
C_6F_{14}	2	1	$n_{CAL} = 6.410 \times 10^{-21} A_i^2 + 5.368 \times 10^{-13} A_i$
CH_4	4	100 and 500	$n_{CAL} = 3.034 \times 10^{-21} A_i^2 + 2.683 \times 10^{-12} A_i$
C_6F_{14}	2	500	$n_{CAL} = 6.410 \times 10^{-21} A_i^2 + 5.368 \times 10^{-13} A_i$
H_2S	1.5	500	$n_{CAL} = -3.710 \times 10^{-14} A_i^2 + 6.144 \times 10^{-09} A_i$
C_6F_{14}	0.8	500	$n_{CAL} = 6.663 \times 10^{-15} A_i^2 + 1.986 \times 10^{-09} A_i$
CO	1.5	500	$n_{CAL} = 5.183 \times 10^{-14} A_i^2 + 7.735 \times 10^{-09} A_i$
C_6F_{14}	0.8	500	$n_{CAL} = 6.663 \times 10^{-15} A_i^2 + 1.986 \times 10^{-09} A_i$

[a] $\Delta n / n$ *(max)* is the maximum average relative error induced by the correlation.

Appendix D

Table D.1: Critical properties and acentric factor for all the components used in this study (DDB, 2014)

Name	Formula	CAS Number	V_C [Cm^3/mol]	T_C [K]	P_C [MPa]	ω
Perfluorohexane	C_6F_{14}	355-42-0	560	451.70	1.905	0.494
Perfluorobutane	C_4F_{10}	355-25-9	372	385.84	2.289	0.371
Carbon monoxide	CO	630-08-0	93.1	132.90	3.475	0.049
Nitrogen oxide	NO	10102-43-9	58.0	180.00	6.480	0.588
Methane	CH_4	74-82-8	99.0	190.60	4.600	0.008
Hydrogen sulphide	H_2S	7783-06-4	98.5	372.80	8.937	0.100
Argon	Ar	7440-37-1	74.9	150.80	4.874	-0.004
Ammonia	NH_3	7664-41-7	72.5	405.60	11.28	0.250
Carbon dioxide	CO_2	124-38-9	94.0	304.20	7.376	0.225
Ethane	C_2H_6	74-84-0	148	305.40	4.884	0.098
Oxygen	O_2	7782-44-7	73.4	154.60	5.046	0.021
Nitrogen	N_2	7727-37-9	89.5	126.20	3.394	0.040
Hydrogen	H_2	1333-74-0	65.0	33.200	1.297	-0.220
Water	H_2O	7732-18-5	56.0	647.30	22.05	0.344

One should note that the critical property and acentric factor values in Table D.1 are slightly different from those in the publications related to this work. The differences are due to the fact that the critical properties and acentric factor for the components in Table D.1 are not coherent in the literature although cited as from the Dortmund Data Bank (DDB). To resolve the issue of incoherence, the critical property and acentric factor values in Table D.1, were taken directly from the 2014 version of DDB. One should note that the differences between the critical properties and acentric factor, both in the publications and Table D.1 are insignificant that no change was observed in the modelling results.

Appendix E

Worked example illustrating the estimation of uncertainties

In this section, the procedure for estimating the experimental uncertainties is illustrated using the VLE data measured for the O_2 (1) + C_4F_{10} (2) system at 293.15 K.

Calibration

Two sources of uncertainties related to the temperature and pressure calibrations are generally identified: the first uncertainty stems from either the standard pressure transducer or the standard temperature probe and the second stems from the calibration polynomial.

In this study, the uncertainties stemming from both the standard pressure transducer and standard temperature probe were estimated to be: ± 0.02, whilst the uncertainties emanating from the calibration polynomials for both temperature and pressure were estimated to be within ± 0.03 K and ± 2 kPa, respectively.

If one associates a rectangular distribution to each of the above uncertainties, then the following are obtained:

$$u_{ref}(T) = \frac{0.02}{\sqrt{3}} = 0.012\,\mathrm{K}$$

$$u_{corr}(T) = \frac{0.025}{\sqrt{3}} = 0.014\,\mathrm{K}$$

$$u_{calib}(T) = \sqrt{u_{ref}(T)^2 + u_{corr}(T)^2}$$

$$u_{ref}(P) = \frac{0.02}{\sqrt{3}} = 0.012\,\mathrm{kPa}$$

$$u_{corr} = \frac{2}{\sqrt{3}} = 1.155\,\mathrm{kPa}$$

$$u_{calib}(P) = \sqrt{u_{ref}(P)^2 + u_{corr}(P)}^2$$

Molar composition

One should note that the two components making up the binary systems are both gaseous at room temperature, therefore the ideal gas equation was used in the calculation of the number of moles.

From Eq. (6.11):

$$u_{ig}(n_1) = n_1\sqrt{\left(\frac{u(P)}{P}\right)^2 + \left(\frac{u(V)}{V}\right)^2 + \left(\frac{u(T)}{T}\right)^2}$$

The error associated with the WIKA CPT600 standard pressure transducer is estimated as 0.02 kPa. The Pt-100 temperature probes were calibrated together with other probes, and therefore contain an error stemmed from the standard temperature probe (± 0.02 K as indicated above) and from its own calibration polynomial. The error emanating from the calibration polynomial was estimated to be 0.025 K. The following is thus obtained:

$$u(P) = \frac{0.02}{\sqrt{3}} = 0.012\,\text{kPa}$$

$$u(T) = \sqrt{u_{ref}(T)^2 + u_{corr}(T)^2} = \sqrt{\left(\frac{0.02}{\sqrt{3}}\right)^2 + \left(\frac{0.025}{\sqrt{3}}\right)^2} = 0.02\,\text{K}$$

Since the uncertainty related to the syringe is difficult to quantify, an error of 2% is considered for each volume reading, the following is obtained:

$$u(V) = \frac{0.02 \times V}{\sqrt{3}} = 0.012V$$

One should note that the calibrations were undertaken at atmospheric conditions which were approximately constant (T~298.15 and P~101kPa).

After substitution of the above results,

$$u_{ig}(n_1) = n_1\sqrt{\left(\frac{0.012}{101}\right)^2 + \left(\frac{0.12V}{V}\right)^2 + \left(\frac{0.02}{298.15}\right)^2} = 0.012n_1$$

The calibration polynomials for oxygen and perfluorobutane are given by the following.

$$n_{cal}(oxygen) = -2.21E-21S^2 + 9.41E-13S \text{ where } \left|n_{1,true} - n_{1,calc}\right|_{\max} = 1.34E-07 \text{ mols.}$$

$$n_{cal}(C_4F_{10}) = -2.85E-22S^2 + 3.45E-13S \text{ where } \left|n_{1,true} - n_{1,calc}\right|_{\max} = 2.65E-07 \text{ mols}$$

Considering a type B evaluation with rectangular distribution, the following is thus obtained.

$$u_{corr}(n_1, oxygen) = \frac{1.34E-07}{\sqrt{3}} = 7.71E-08 \text{ mols}$$

$$u_{corr}(n_1, C_4F_{10}) = \frac{2.65E-07}{\sqrt{3}} = 1.53E-07 \text{ mols}$$

Experimental

For illustration purpose, the first equilibrium state is considered for the O2 (1) + C4F10 (2) system VLE data measured at 293.15 K listed in Table E.1. One should note that 14 samples were taken of which 7 were for the liquid phase and the remaining 7 for the vapour phase. The error in repeatability from the average values can be calculated as follows.

$$u_{rep}(T) = \sqrt{\frac{1}{12 \times 11}\left[(292.79 - 292.78)^2 + ... + (292.77 - 292.78)^2\right]} = 0.003 \text{ K}$$

In the same manner, the error in the repeatability from the average values for pressure was obtained.

$$u_{rep}(P) = 1.233 \text{ kPa}$$

The combined standard uncertainty for temperature and pressure are thus obtained as follows.

$$u_c(T) = \pm\sqrt{u_{ref}(T)^2 + u_{corr}(T)^2 + u_{rep}(T)^2} = \pm\sqrt{0.01^2 + 0.01^2 + 0.003^2} = \pm 0.02 \text{ K}$$

$$u_c(P) = \pm\sqrt{u_{corr}(P)^2 + u_{rep}(P)^2} = \pm\sqrt{1.15^2 + 1.233^2} = \pm 1.689 \text{ kPa}$$

Table E.1: Experimental data of the first equilibrium condition for the O_2 (1) + C_4F_{10} (2) system at 292.78 K

vapour samples				
T / K	P/kPa	n_1 (mols)	n_2 (mols)	y_1
292.79	12871.320	6.63E-06	7.50E-07	0.898
292.79	12871.320	6.55E-06	7.47E-07	0.898
292.79	12871.320	6.55E-06	7.44E-07	0.898
292.79	12871.320	6.54E-06	7.43E-07	0.898
292.79	12871.320	6.53E-06	7.41E-07	0.898

liquid samples				
T / K	P/kPa	n_1 (mols)	n_2 (mols)	x_1
292.77	12863.924	3.05E-06	2.65E-06	0.535
292.77	12863.924	2.97E-06	2.64E-06	0.529
292.77	12863.924	2.97E-06	2.64E-06	0.529
292.77	12863.924	2.97E-06	2.65E-06	0.529
292.77	12863.924	2.97E-06	2.63E-06	0.531

Average T/K	Average P / kPa	Average x_1	Average y_1
292.78	12867.622	0.898	0.530

For molecular composition, consider the first line in Table 1,

$$u_{ig}(n_1) = 0.012 n_1 = 0.012 \times 6.63E-06 = 7.957E-08 \text{ mols}$$

$$u(n_1) = \sqrt{u_{ig}(n_1)^2 + u_{corr}(n_1)^2} = \sqrt{7.957E-08^2 + 7.710E-08^2} = 1.101E-07 \text{ mols}$$

In the same way as for $u(n_1)$, $u(n_2)$ is calculated to be 1.535E-07 mols.

$u_{calib}(x_1)$ is then calculated using Eq. (6.8):

$$u_{calib}(x_1) = \sqrt{\left(\frac{x_2}{n_1+n_2}u(n_1)\right)^2 + \left(\frac{x_1}{n_1+n_2}u(n_2)\right)^2}$$

$$= \sqrt{\left(\frac{(1-0.535)}{3.053E-06+2.651E-06}8.537E-08\right)^2 + \left(\frac{(0.535)}{3.053E-06+2.651E-06}1.565E-07\right)^2}$$

$$= 0.016$$

The remaining results are shown in Table E.2.

Table E.2: Calculation of the uncertainties on molar composition taking into account the errors in the calibration procedure for both the liquid and vapour samples.

n_1 (mols)	n_2 (mols)	y_1	$u(n_1)$	$u(n_2)$	u_{calib} (y_1)
6.63E-06	7.50E-07	0.898	1.1080E-07	1.53483E-07	0.019
6.55E-06	7.47E-07	0.898	1.1010E-07	1.53481E-07	0.019
6.55E-06	7.44E-07	0.898	1.1008E-07	1.53479E-07	0.019
6.54E-06	7.43E-07	0.898	1.1000E-07	1.53478E-07	0.019
6.53E-06	7.41E-07	0.898	1.1000E-07	1.53477E-07	0.019

n_1 (mols)	n_2 (mols)	x_1	$u(n_1)$	$u(n_2)$	u_{calib} (x_1)
3.05E-06	2.65E-06	0.535	8.5374E-08	1.5649E-07	0.016
2.97E-06	2.64E-06	0.529	8.4934E-08	1.5647E-07	0.016
2.97E-06	2.64E-06	0.529	8.4941E-08	1.5647E-07	0.016
2.97E-06	2.65E-06	0.529	8.4955E-08	1.5648E-07	0.016
2.97E-06	2.63E-06	0.531	8.4938E-08	1.5643E-07	0.016

Average u_{calib} (x_1)	Average u_{calib} (y_1)
0.016	0.019

One should note that the uncertainties stemming from repeated measurements are negligible and therefore:

$$u_c(x_1) = \pm\sqrt{\bar{u}_{calib}(x_1)^2} = \pm 0.016$$

The final uncertainties considering a coverage factor (k = 2) for temperature (T), pressure (P) and compositions (x and y) can be written as:

$$T = (292.78 \pm 0.04)\ \text{K}$$

$$P = (12.868 \pm 0.003)\ \text{MPa}$$

$$x = 0.898 \pm 0.032$$

$$y = 0.530 \pm 0.038$$

The combined standard uncertainty in the relative volatility was calculated using Eq. 6.14, which is expressed as:

$$u(\alpha_{ij}) = \alpha_{ij}\sqrt{\left(\frac{u(x_i)}{x_i x_j}\right)^2 + \left(\frac{u(y_i)}{y_i y_j}\right)^2} \tag{5.15}$$

where $u(x_i)$ and $u(y_i)$ are the standard uncertainties for the liquid and vapor mole fraction, respectively. α_{ij} is the relative volatility defined in Eq. (5.24) as:

$$\alpha_{ij} = \frac{y_1 / x_1}{1 - y_1 / 1 - x_1} \tag{5.24}$$

One should note that the unknowns in Eq. 5.15, except for the relative volatility, were calculated and reported in Table E.2. Hence, the uncertainties in the relative volatility for the O_2 + C_4F_{10} system at 293.41 K are presented in Table E.3.

Table E.3 Uncertainty calculations in the relative volatility for the O_2 + C_4F_{10} system at 293.41 K.

y_1	y_2	x_1	x_2	α_{12}	$u_c(x_1)$	$u_c(y_1)$	$u(\alpha_{12})$	$U(\alpha_{12})$	residual %
0.842	0.158	0.089	0.911	54.183	0.013	0.025	7.369	14.74	27.20
0.916	0.084	0.396	0.604	16.639	0.009	0.011	0.219	0.437	2.63
0.909	0.091	0.469	0.531	11.333	0.010	0.012	0.132	0.265	2.33
0.898	0.102	0.530	0.470	7.795	0.016	0.019	0.114	0.228	2.93
0.875	0.125	0.610	0.390	4.461	0.015	0.027	0.047	0.094	2.10
0.819	0.181	0.723	0.277	1.730	0.027	0.040	0.024	0.047	2.74
0.849	0.151	0.655	0.345	2.954	0.027	0.041	0.048	0.095	3.22
0.890	0.110	0.173	0.827	38.965	0.007	0.012	1.389	2.779	7.13
0.917	0.083	0.292	0.708	26.763	0.008	0.012	0.546	1.091	4.08
0.912	0.088	0.239	0.761	32.791	0.007	0.016	0.740	1.480	4.51
0.918	0.082	0.347	0.653	20.980	0.014	0.008	0.559	1.117	5.32
									Average residual 5.84 %

Appendix F

Modelling of the predicted data (PSRK/COSMO-SAC or modified UNIFAC-Dortmund) using the PR-MC-WS-NRTL model.

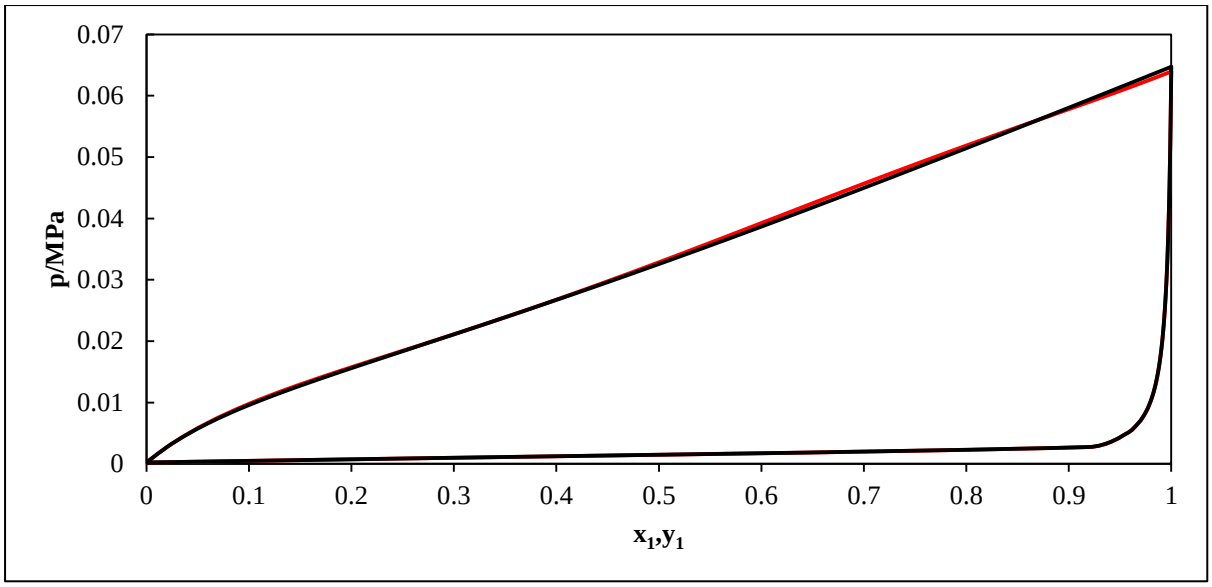

Figure F.1**:** Phase diagram (P-x-y) for the C_4F_{10} (1) + H_2O (2) system at 260.15 K; Predicted data using modified UNIFAC (Dortmund): —; Modelled data using PR-MC-WS-NRTL: —.

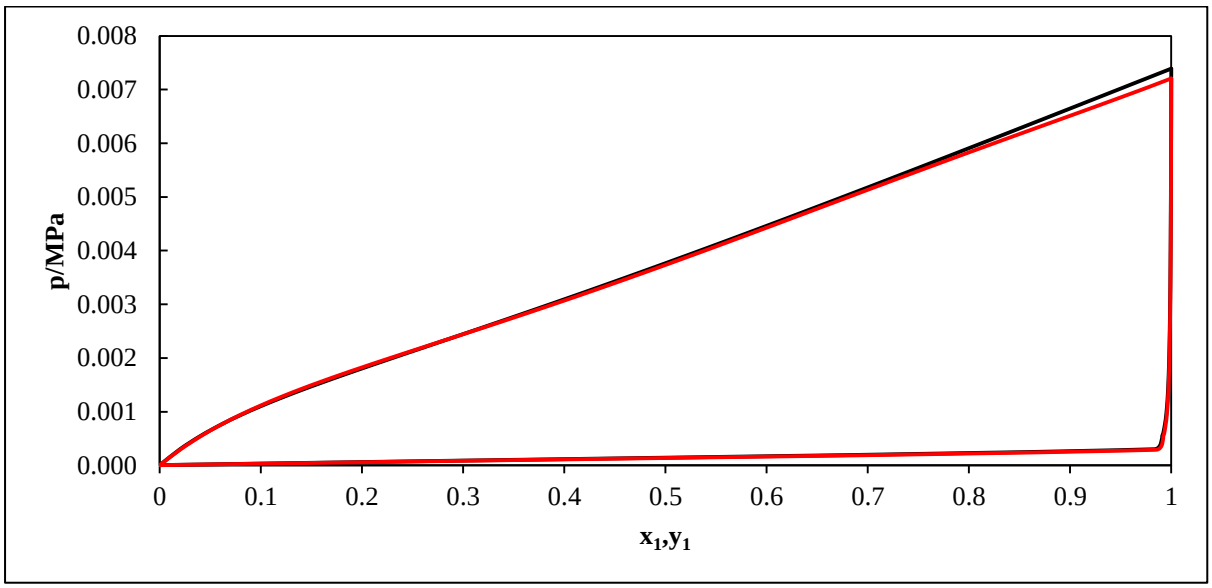

Figure F.2**:** Phase diagram (P-x-y) for the C_4F_{10} (1) + H_2O (2) system at 220.15 K; Predicted data using modified UNIFAC (Dortmund): —; Modelled data using PR-MC-WS-NRTL: —.

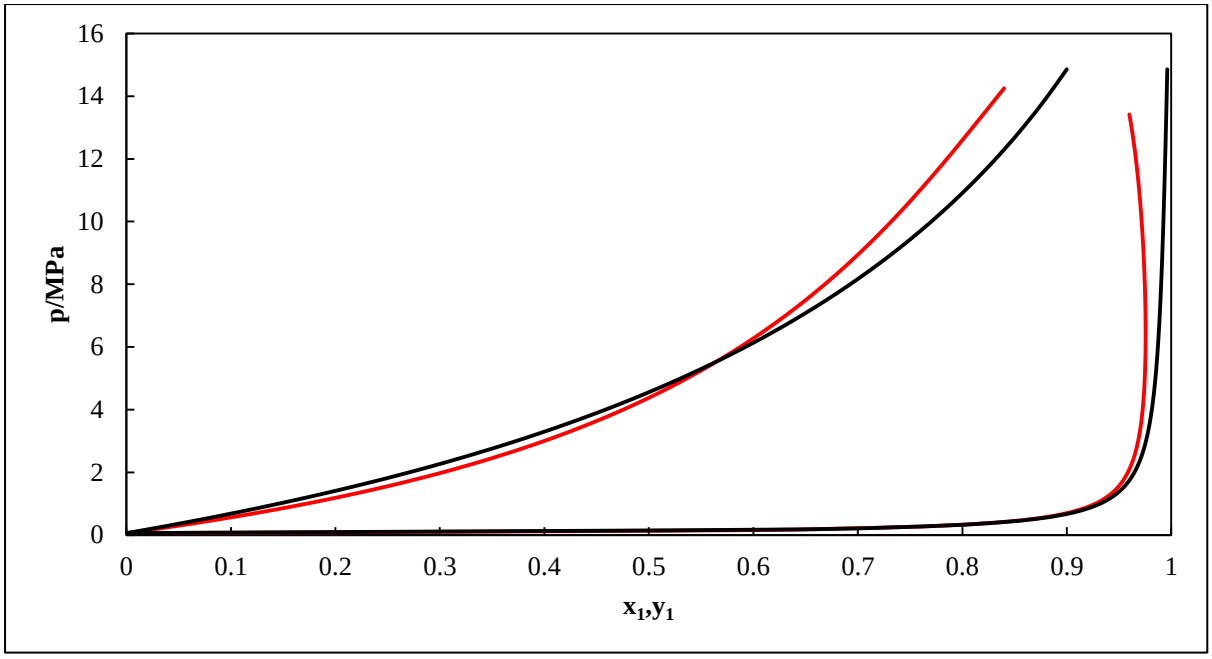

Figure F.3**:** Phase diagram (P-x-y) for the Ar (1) + C_4F_{10} (2) system at 260.15 K; Predicted data using modified UNIFAC (Dortmund): —; Modelled data using PR-MC-WS-NRTL: —.

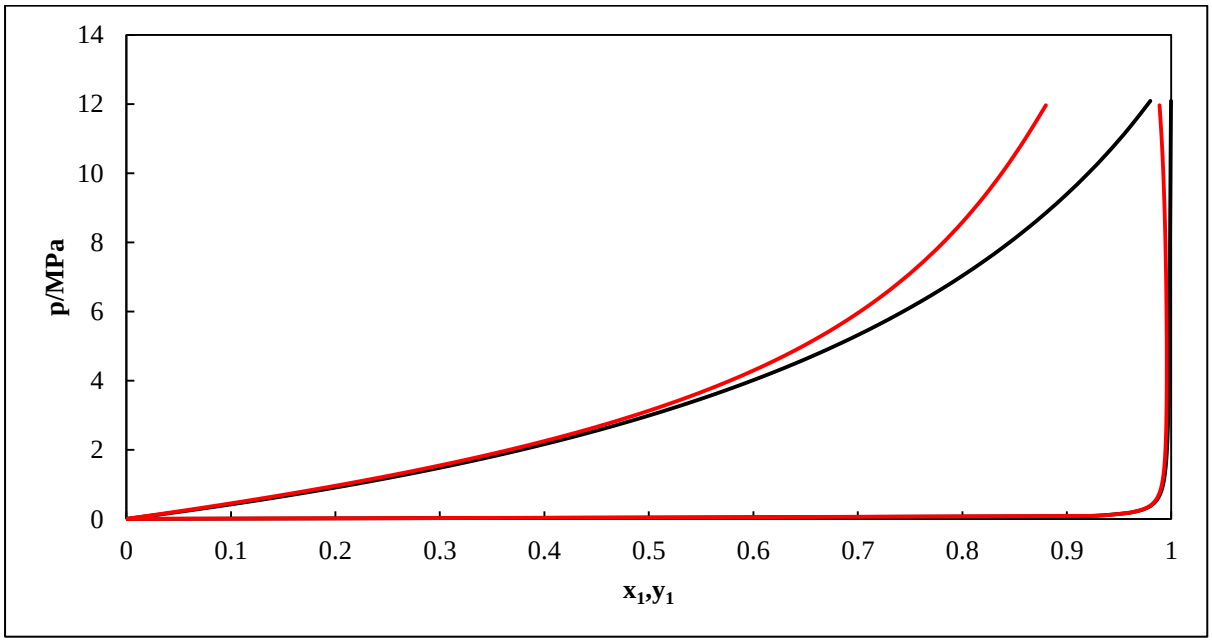

Figure F.4**:** Phase diagram (P-x-y) for the Ar (1) + C_4F_{10} (2) system at 220.15 K; Predicted data using modified UNIFAC (Dortmund): —; Modelled data using PR-MC-WS-NRTL: —.

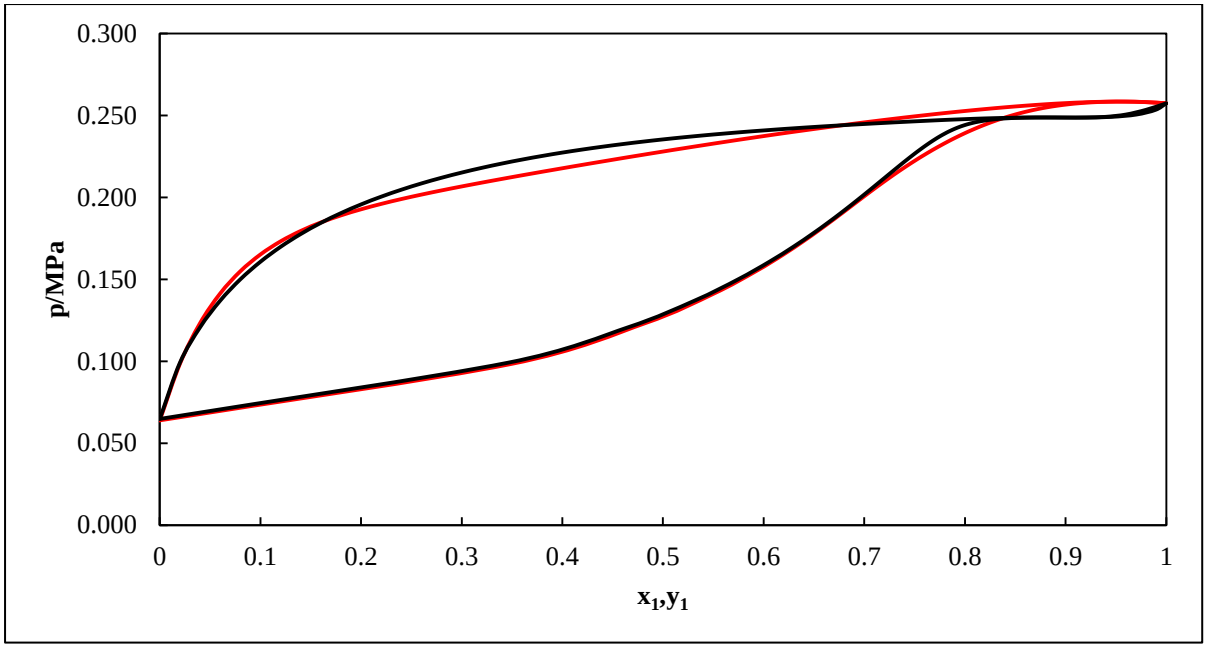

Figure F.5**:** Phase diagram (P-x-y) for the NH_3 (1) + C_4F_{10} (2) system at 260.15K; Predicted data using PSRK/COSMO-SAC: —; Modelled data using PR-MC-WS-NRTL: —.

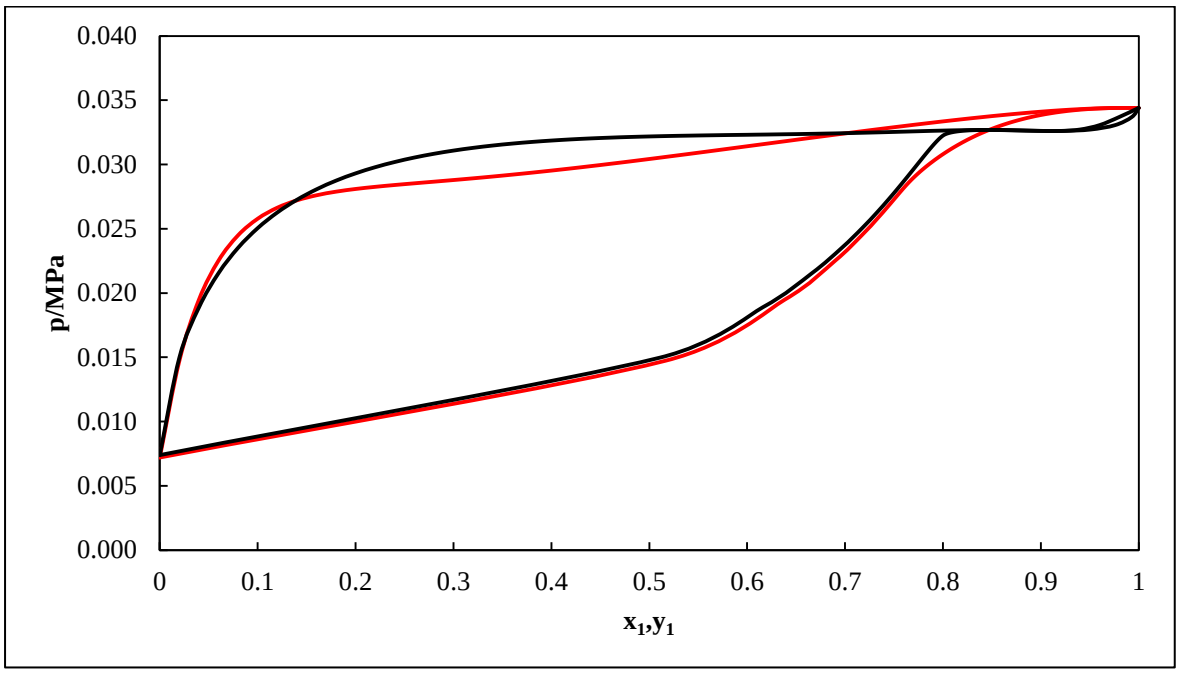

Figure F.6: Phase diagram (P-x-y) for the NH_3 (1) + C_4F_{10} (2) system at 220.15 K; Predicted data using PSRK/COSMO-SAC: —; Modelled data using PR-MC-WS-NRTL: —.

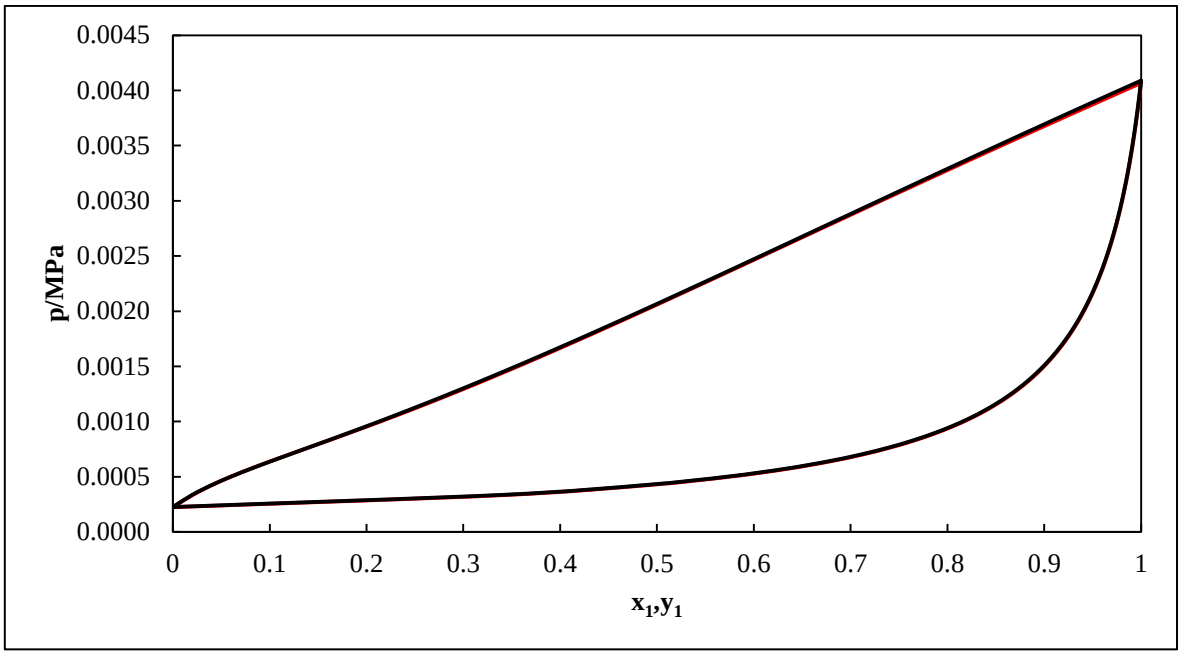

Figure F.7: Phase diagram (P-x-y) for the C_6F_{14} (1) + H_2O (2) system at 260.15 K; Predicted data using modified UNIFAC (Dortmund): —; Modelled data using PR-MC-WS-NRTL: —.

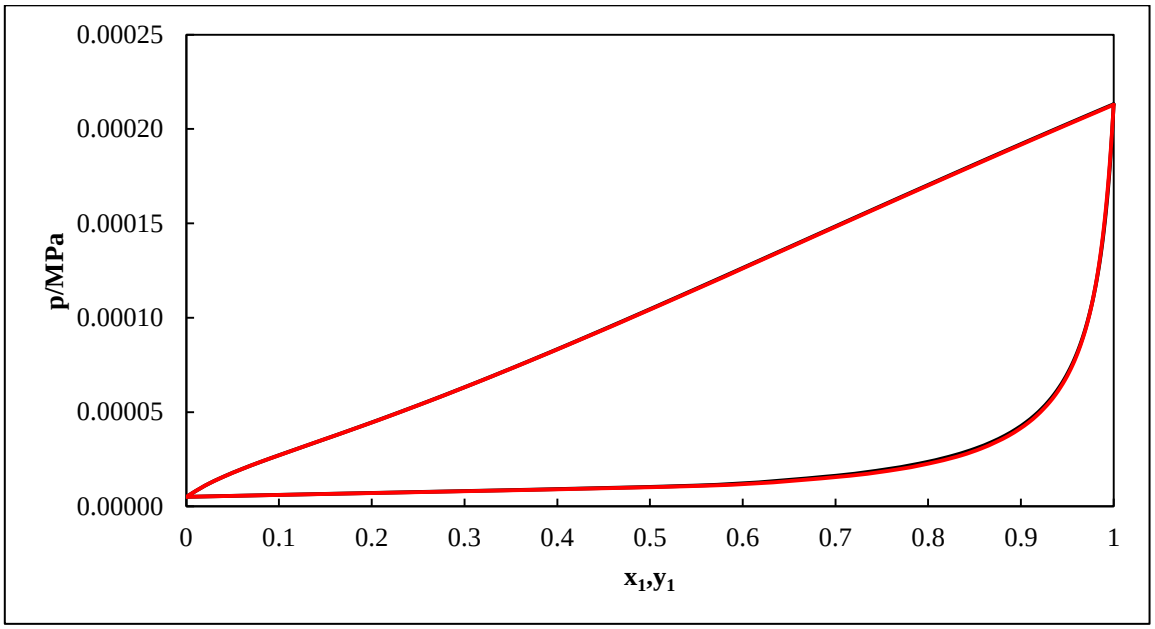

Figure F.8: Phase diagram (P-x-y) for the C_6F_{14} (1) + H_2O (2) system at 220.15 K; Predicted data using modified UNIFAC (Dortmund): —; Modelled data using PR-MC-WS-NRTL: —.

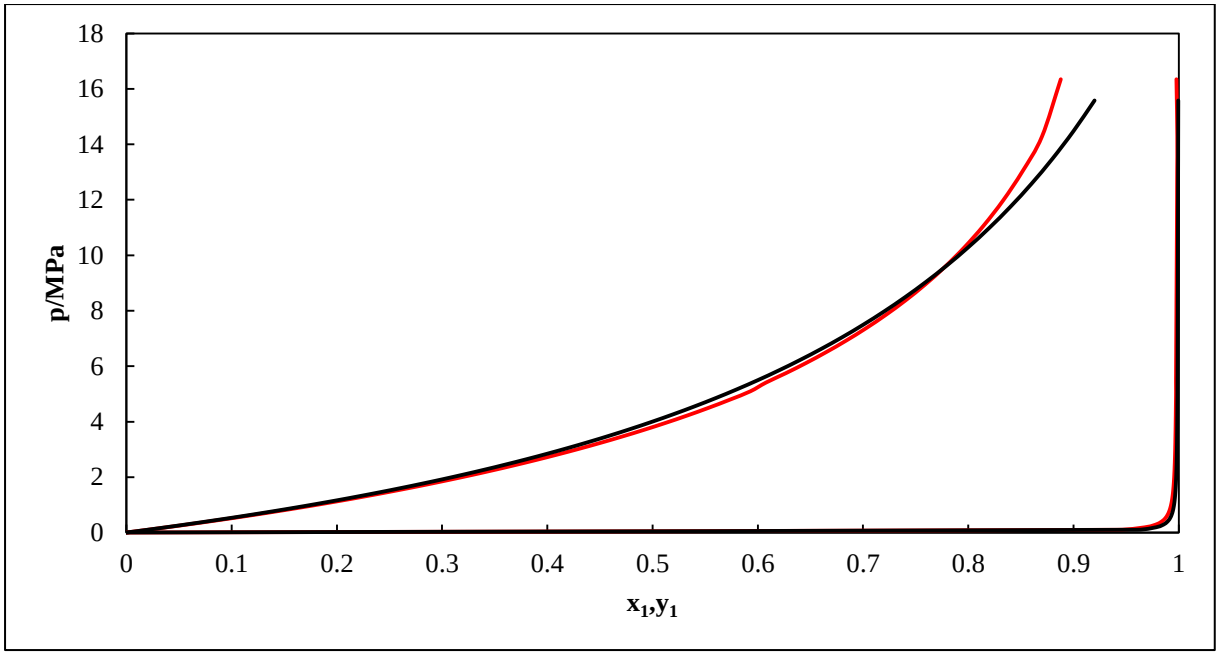

Figure F.9: Phase diagram (P-x-y) for the Ar (1) + C_6F_{14} (2) system at 260.15 K; Predicted data using modified UNIFAC (Dortmund): —; Modelled data using PR-MC-WS-NRTL: —.

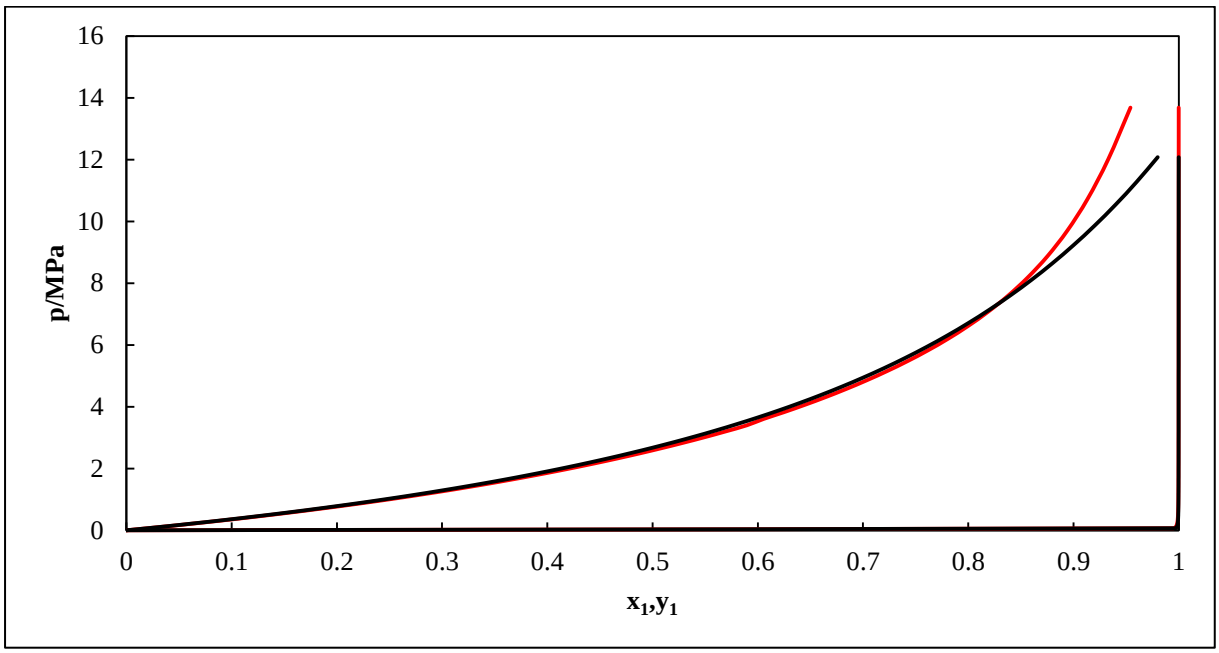

Figure F.10: Phase diagram (P-x-y) for the Ar (1) + C_6F_{14} (2) system at 220.15 K; Predicted data using modified UNIFAC (Dortmund): —; Modelled data using PR-MC-WS-NRTL: —.

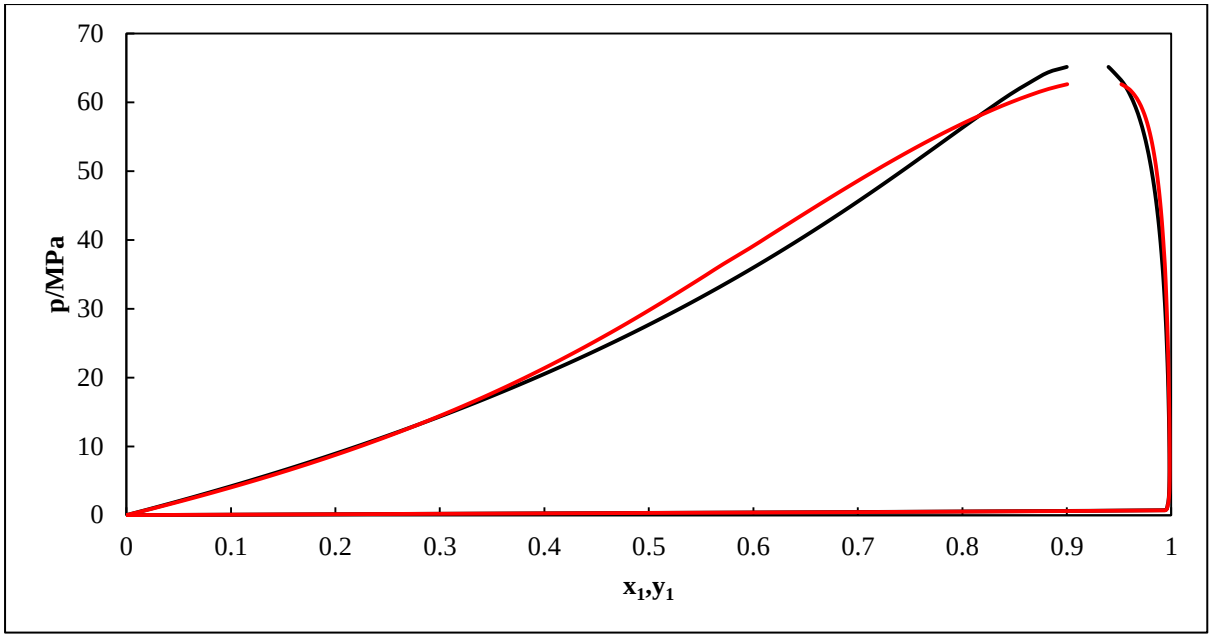

Figure F.11: Phase diagram (P-x-y) for the H_2 (1) + C_6F_{14} (2) system at 260.15 K; Predicted data using PSRK/COSMO-SAC: —; Modelled data using PR-MC-WS-NRTL: —.

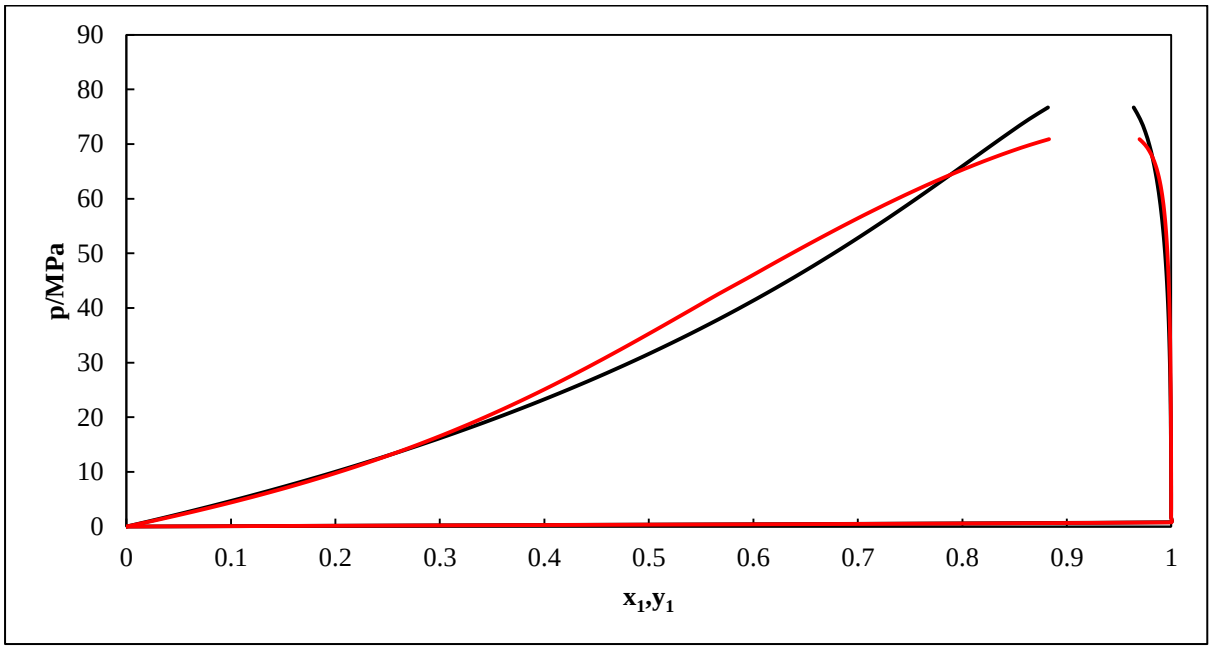

Figure F.12: Phase diagram (P-x-y) for the H_2 (1) + C_6F_{14} (2) system at 220.15 K; Predicted data using PSRK/COSMO-SAC: —; Modelled data using PR-MC-WS-NRTL: —.

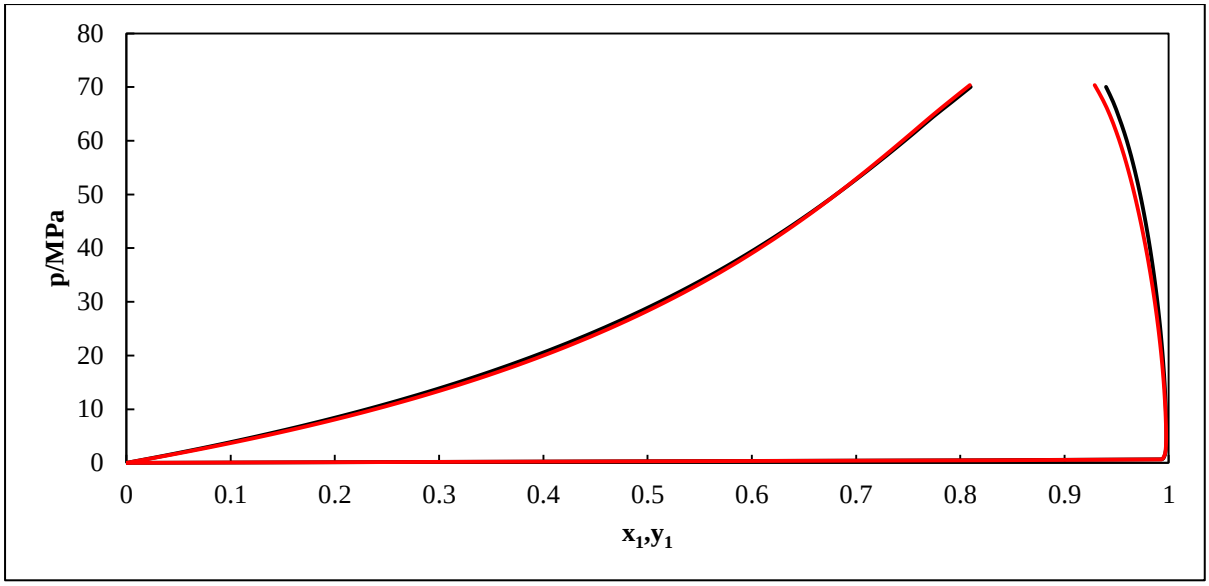

Figure F.13: Phase diagram (P-x-y) for the N_2 (1) + C_6F_{14} (2) system at 260.15 K; Predicted data using PSRK/COSMO-SAC:—; Modelled data using PR-MC-WS-NRTL: —.

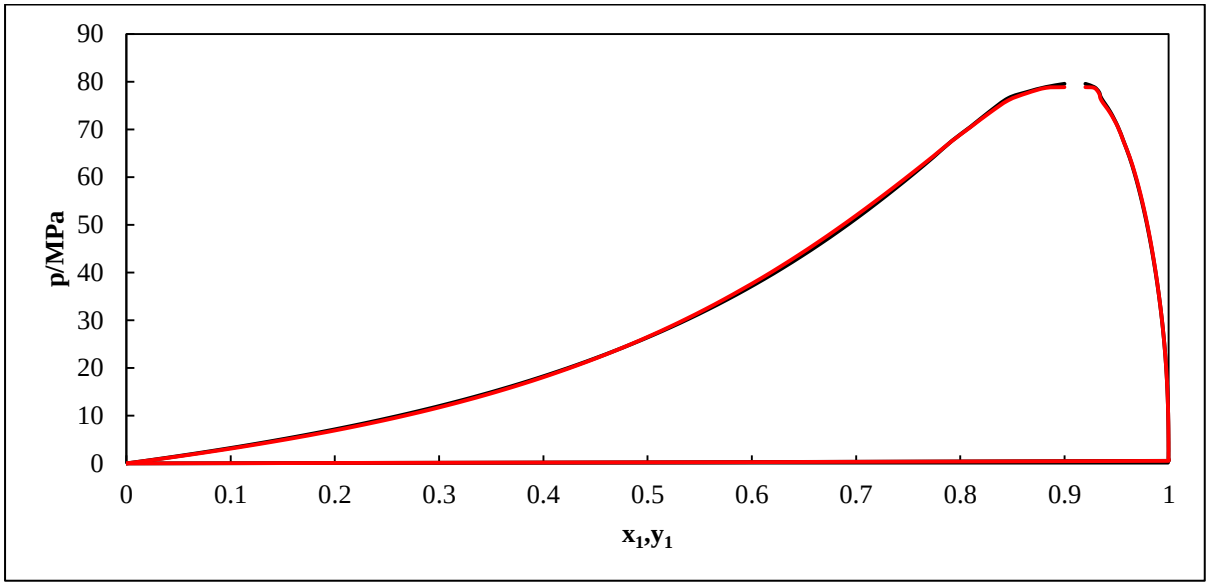

Figure F.14: Phase diagram (P-x-y) for the N_2 (1) + C_6F_{14} (2) system at 220.15 K; Predicted data using PSRK/COSMO-SAC:—; Modelled data using PR-MC-WS-NRTL: —.

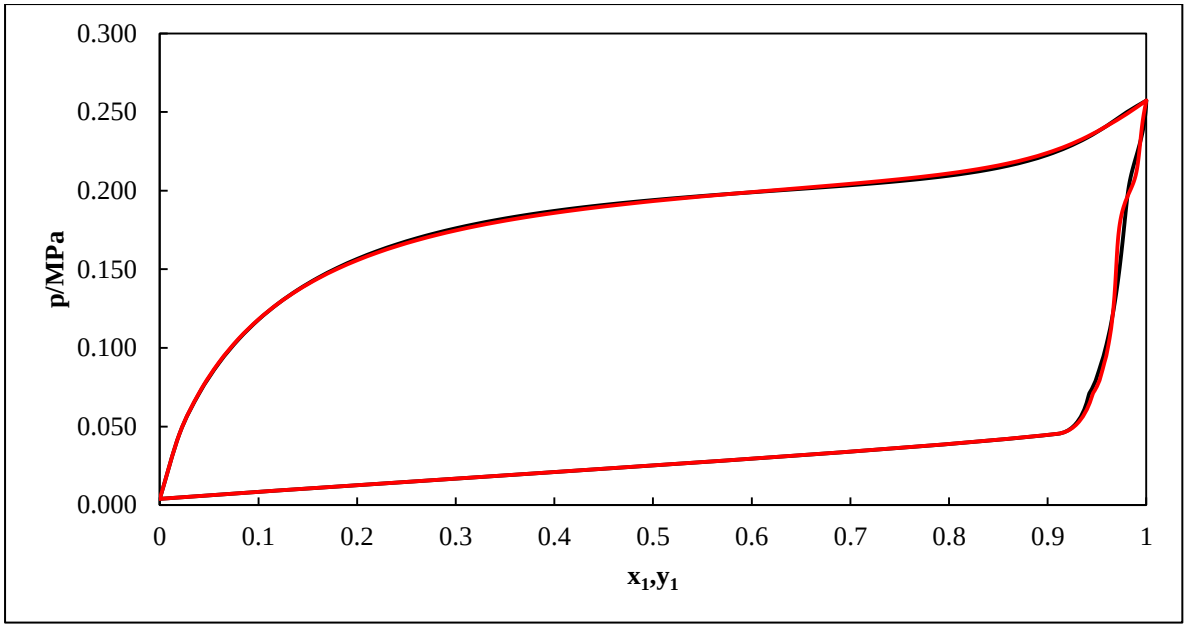

Figure F.15: Phase diagram (P-x-y) for the NH_3 (1) + C_6F_{14} (2) system at 260.15 K; Predicted data using PSRK/COSMO-SAC; —. Modelled data using PR-MC-WS-NRTL: —.

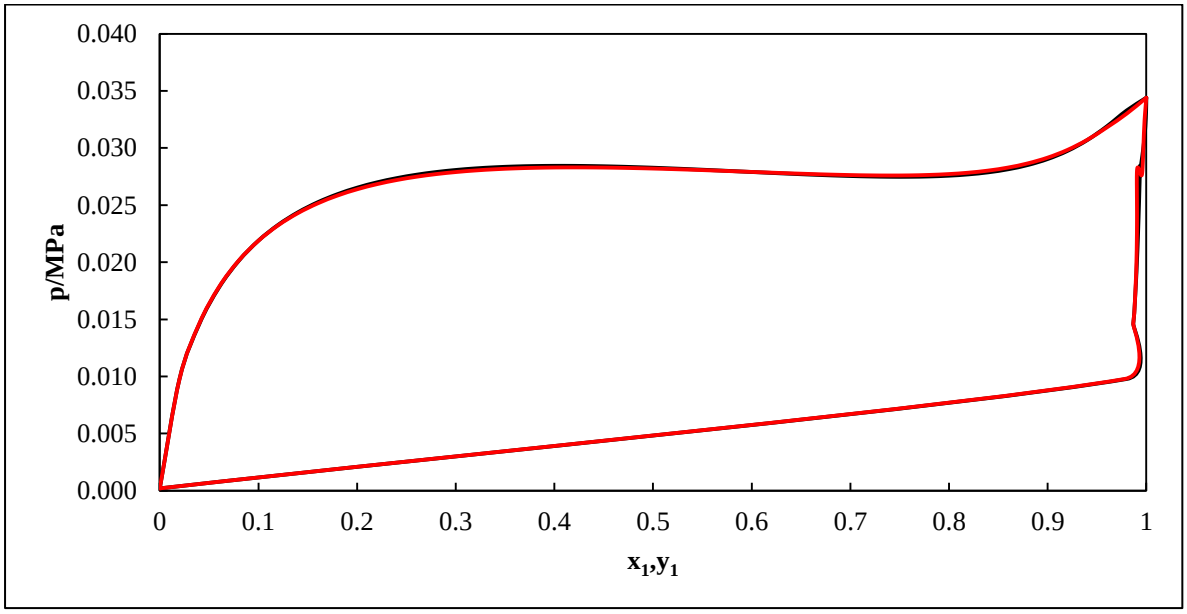

Figure F.16: Phase diagram (P-x-y) for the NH_3 (1) + C_6F_{14} (2) system at 220.15 K; Predicted data using PSRK/COSMO-SAC: —; Modelled data using PR-MC-WS-NRTL: —.

Appendix G

Table G.1: Regeneration section for the C_4F_{10} solvent: Stream results

	FLASH DRUMS						STRIPPER	
	F1DOWN	F1UP	F2DOWN	F2UP	F3DOWN	F3UP	STRDOWN	STRUP
Mole Flow kmol/hr								
CO	1903.9	62.845	1823.9	80.050	1640.7	183.22	0.0020	1640.7
CO_2	12.103	3.1080	8.7780	3.3250	4.2600	4.5180	trace	4.2600
C_4F_{10}	7978.7	5.8930	7971.7	7.0180	7956.7	14.934	7934.7	22.013
N_2	1835.8	321.45	1463.5	372.27	866.03	597.45	trace	866.03
Ar	39.335	0.8540	38.194	1.1410	35.543	2.6510	trace	35.543
CH_4	49.589	6.0170	42.327	7.2620	28.996	13.331	trace	28.996
H_2	161.07	156.48	63.524	97.544	11.026	52.499	trace	11.026
H_2O	28.084	trace	28.084	trace	28.084	trace	28.084	trace
H_3N	1.3480	0.0100	1.3360	0.0120	1.3050	0.0310	trace	1.3050
H_2S	0.1810	0.0030	0.1780	0.0030	0.1700	0.0080	trace	0.1700
Total Flow kmol/hr	12010	556.66	11441	568.63	10572	868.64	7962.8	2610.0
T/ K	241.58	241.58	241.58	241.58	241.58	241.58	361.85	232.42
P/ MPa	5.000	5.000	3.500	3.500	2.000	2.000	1.400	1.400

Table G.1: Continued

	FLASH DRUMS						STRIPPER	
	F1DOWN	F1UP	F2DOWN	F2UP	F3DOWN	F3UP	STRDOWN	STRUP
Vapor Frac	0	1	0	1	0	1	0	1
Liquid Frac	1	0	1	0	1	0	1	0
Solid Frac	0	0	0	0	0	0	0	0
Enthalpy kJ/mol	-1530.3	-71.275	-1602.0	-86.144	-1723.0	-124.29	-2166.0	-269.51
Entropy kJ/mol-K	-0.469	-0.038	-0.489	-0.037	-0.524	-0.035	-0.575	-0.029
Density kg/m^3	10.007	2.7216	9.7054	1.8964	9.2433	1.0684	4.8574	0.8240
Average MW	169.69	24.620	176.71	28.270	188.50	33.280	237.25	39.750

Table G.2: Regeneration section for the C_6F_{14} solvent: Stream results

	FLASH DRUMS						STRIPPER	
	F1DOWN	F1UP	F2DOWN	F2UP	F3DOWN	F3UP	STRDOWN	STRUP
Mole Flow kmol/hr								
CO	13.241	1.6590	11.478	1.7630	8.8100	2.6680	trace	8.8100
CO_2	1948.3	18.447	1928.5	19.880	1894.5	33.989	<0.0010	1894.462
H_2	167.82	89.839	100.24	67.585	42.329	57.908	trace	42.329
H_2O	28.084	0	28.084	0	28.084	0	28.084	0.000
N_2	499.77	135.27	374.53	125.24	224.81	149.72	trace	224.81
Ar	39.878	0.3110	39.502	0.3750	38.782	0.7200	trace	38.782
CH_4	56.132	2.1450	53.620	2.5120	49.088	4.5320	trace	49.088
NH_3	1.3520	0.0060	1.3450	0.0070	1.3340	0.0110	trace	1.3340
H_2S	0.1810	0.0030	0.1780	0.0030	0.1730	0.0050	trace	0.1730
C_6F_{14}	7998.7	0.1690	7998.5	0.1480	7998.3	0.2040	7998.1	0.2150
Total Flow kmol/hr	10753	247.84	10536	217.51	10286	249.76	8026.2	2260.0
T/ K	239.70	239.70	239.70	239.70	239.70	239.70	418.12	230.72
P/ MPa	5.000	5.000	3.500	3.500	2.000	2.000	1.000	1.000

Table G.2: Continued

	FLASH DRUMS						STRIPPER	
	F1DOWN	F1UP	F2DOWN	F2UP	F3DOWN	F3UP	STRDOWN	STRUP
Vapor Frac	0	1	0	1	0	1	0	1
Liquid Frac	1	0	1	0	1	0	1	0
Solid Frac	0	0	0	0	0	0	0	0
Enthalpy kJ/mol	-2337.2	-34.871	-2384.7	-41.918	-2441.2	-60.574	-2967.5	-334.97
Entropy kJ/mol.K	-0.751	-0.033	-0.765	-0.029	-0.782	-0.024	-0.790	-0.024
Density kg/m^3	6.907	2.661	6.802	1.854	6.682	1.049	3.244	0.585
Average MW	261.07	19.903	266.01	21.490	271.89	24.232	336.92	40.904

Appendix H

Extrapolation of the experimental VLE data to 260.15 and 220.15 K

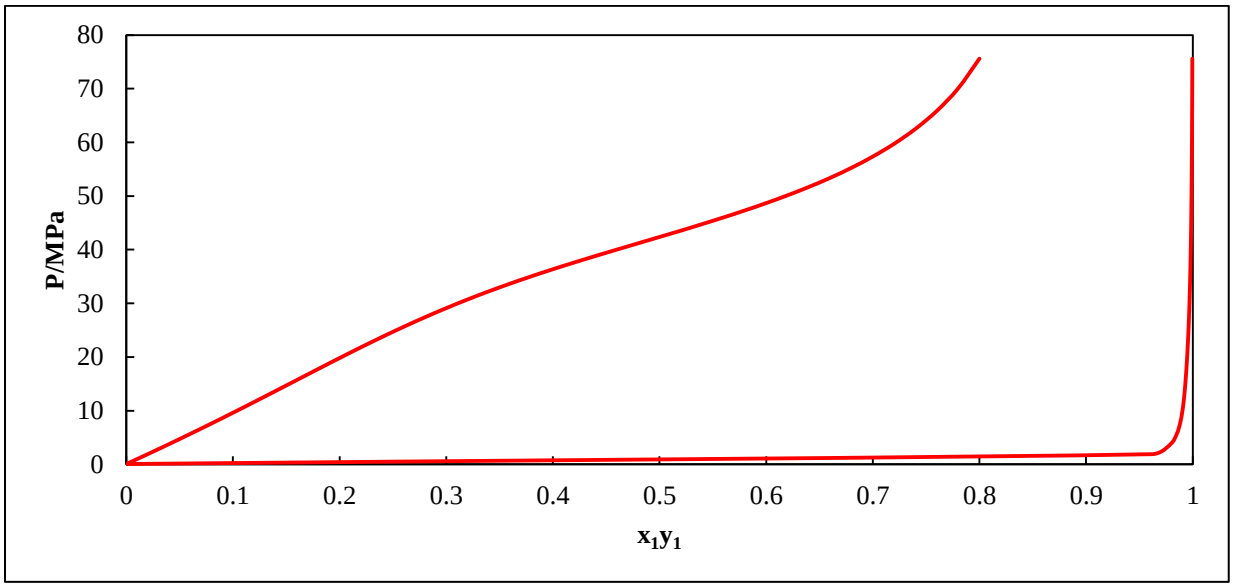

Figure H.1**:** Phase diagram (P-x-y) for the H_2 (1) + C_4F_{10} (2) system extrapolated to 260.15 K Using the PR-MC-WS-NRTL model.

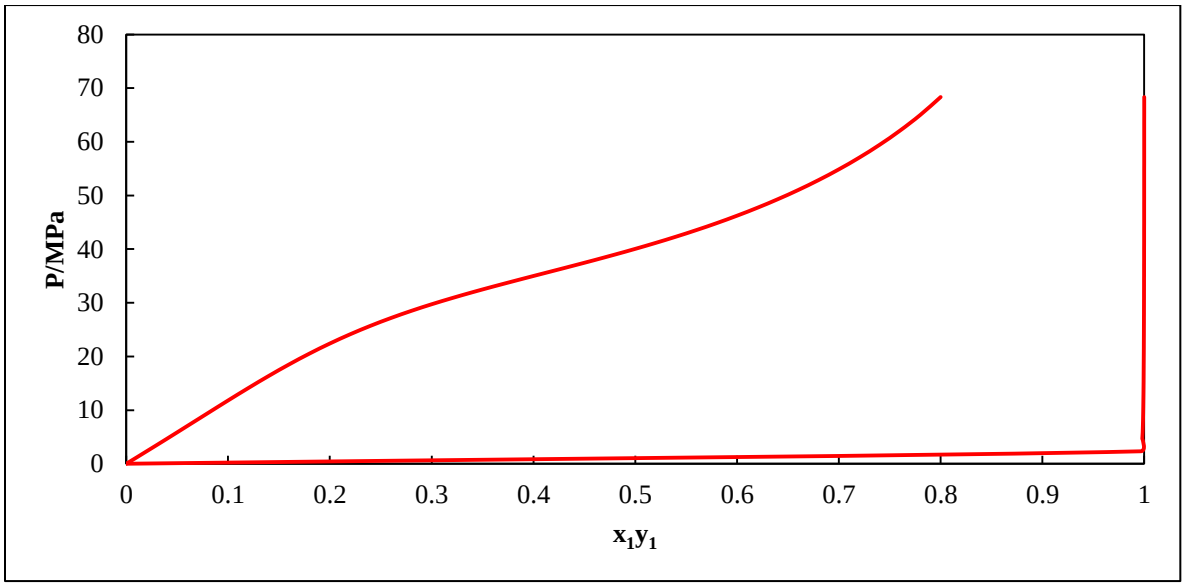

Figure H.2: Phase diagram (P-x-y) for the H_2 (1) + C_4F_{10} (2) system extrapolated to 220.15 K Using the PR-MC-WS-NRTL model.

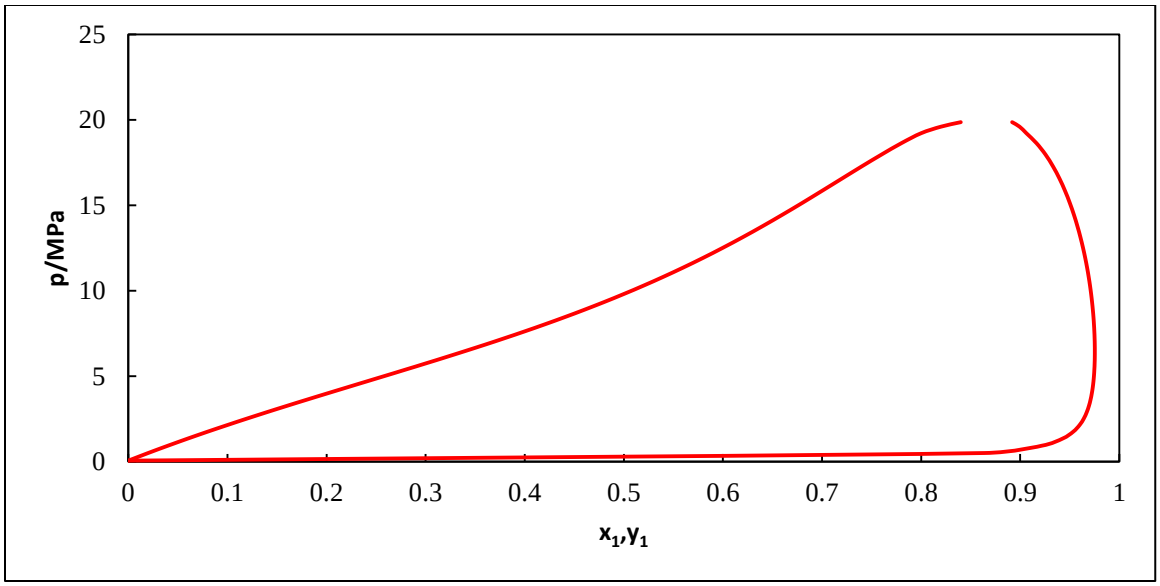

Figure H.3: Phase diagram (P-x-y) for the CH_4 (1) + C_4F_{10} (2) system extrapolated to 260.15 K Using the PR-MCWS-NRTL model.

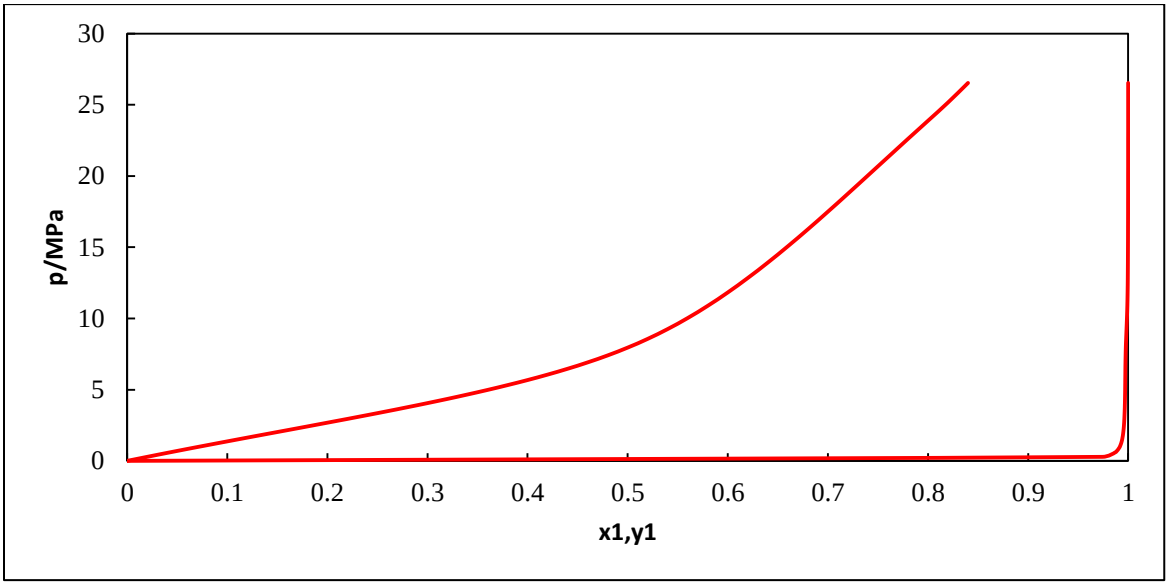

Figure H.4: Phase diagram (P-x-y) for the CH_4 (1) + C_4F_{10} (2) system extrapolated to 220.15 K Using the PR-MC-WS-NRTL model.

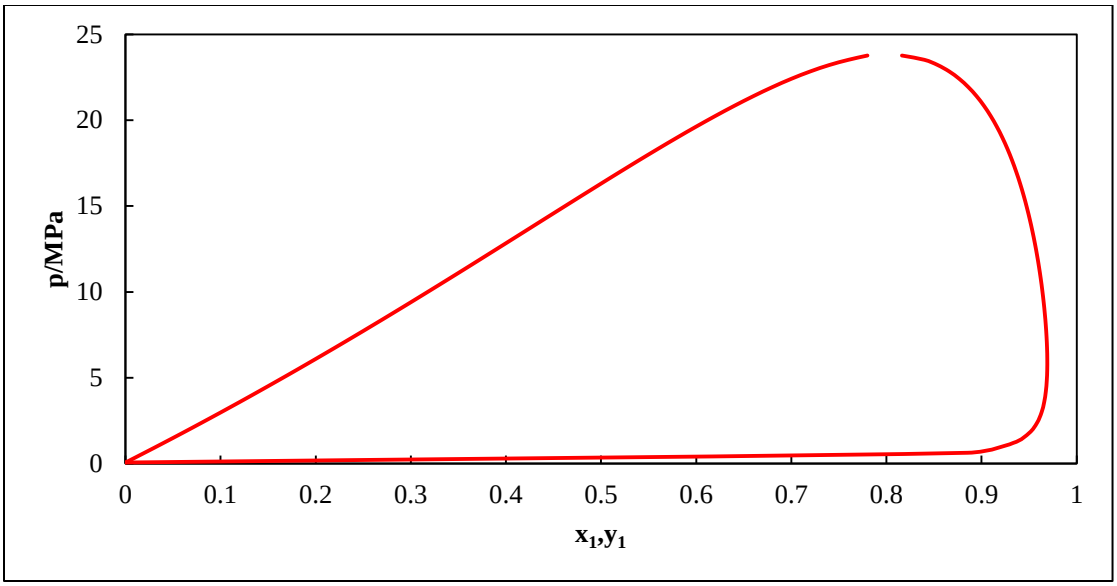

Figure H.5: Phase diagram (P-x-y) for the CO (1) + C_4F_{10} (2) system extrapolated to 260.15 K Using the PR-MC-WS-NRTL model.

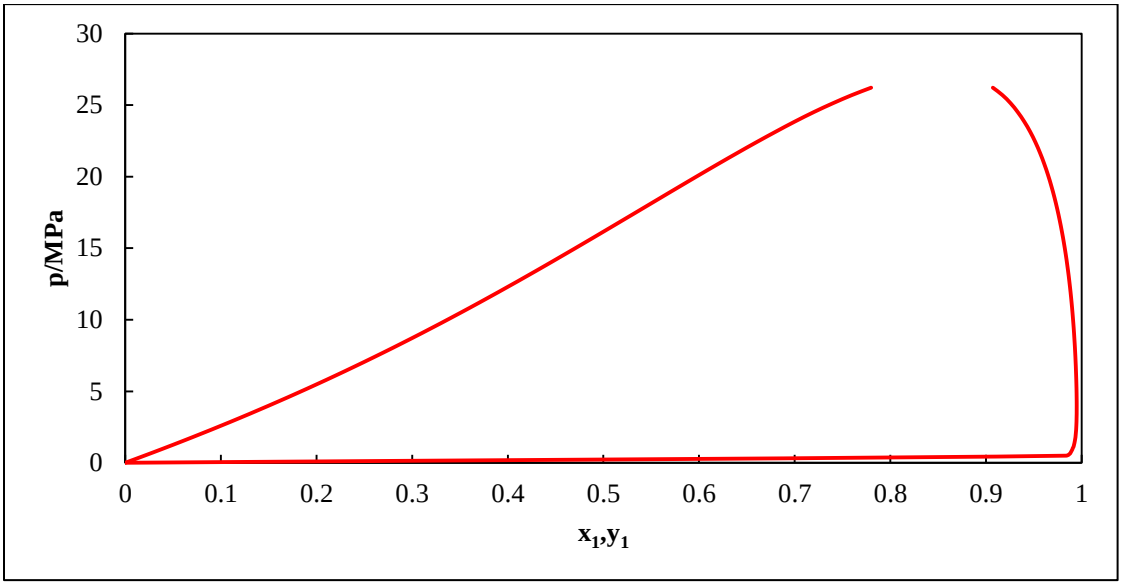

Figure H.6: Phase diagram (P-x-y) for the CO (1) + C_4F_{10} (2) system extrapolated to 220.15 K Using the PR-MC-WS-NRTL model.

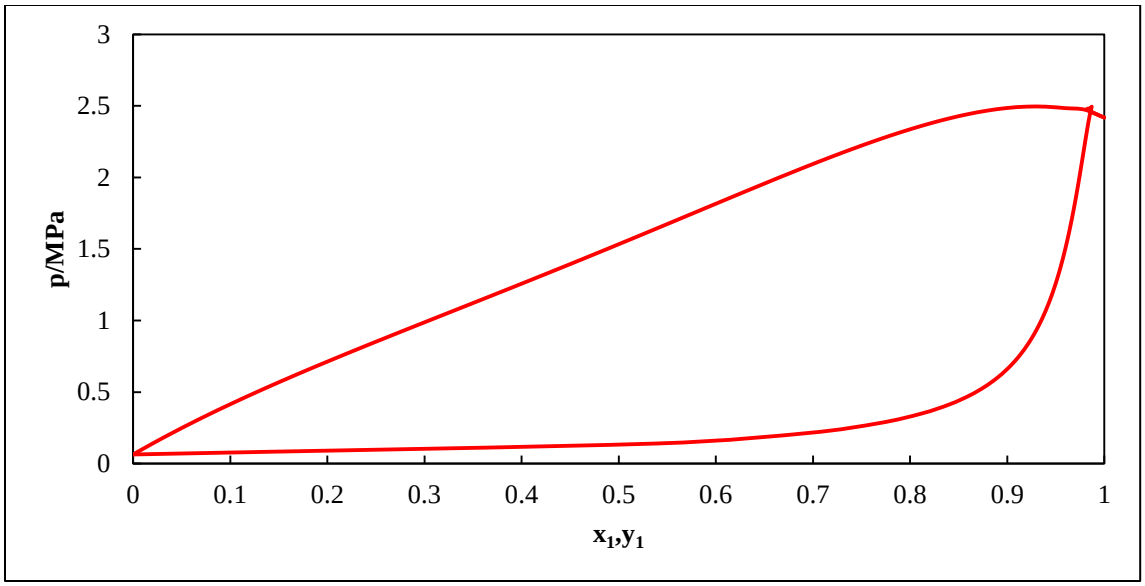

Figure H.7: Phase diagram (P-x-y) for the CO_2 (1) + C_4F_{10} (2) system extrapolated to 260.15 K Using the PR-MC-WS-NRTL model.

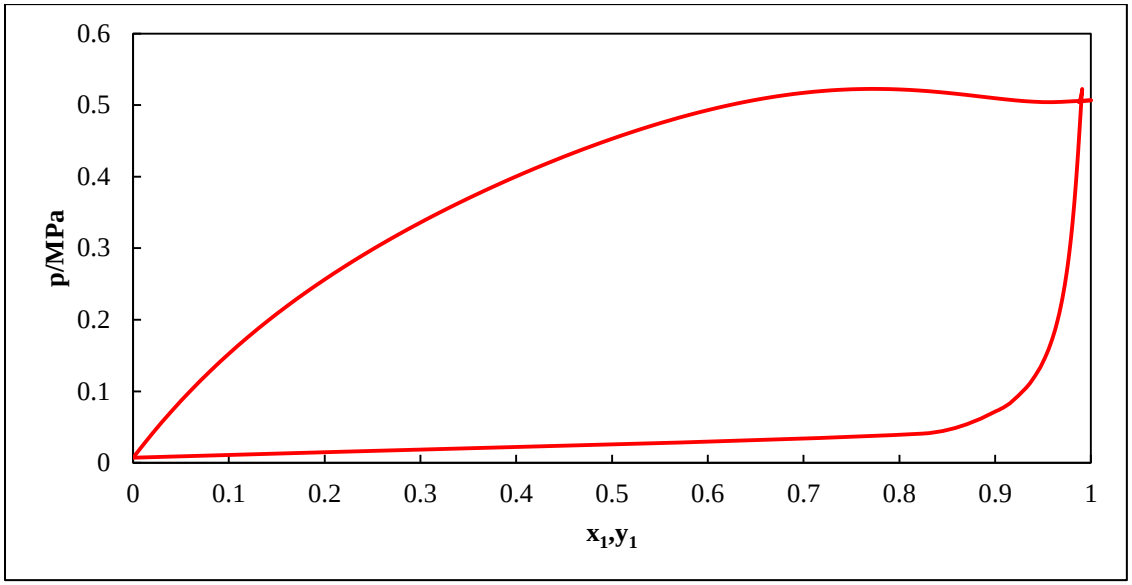

Figure H.8: Phase diagram (P-x-y) for the CO_2 (1) + C_4F_{10} (2) system extrapolated to 220.15 K Using the PR-MC-WS-NRTL model.

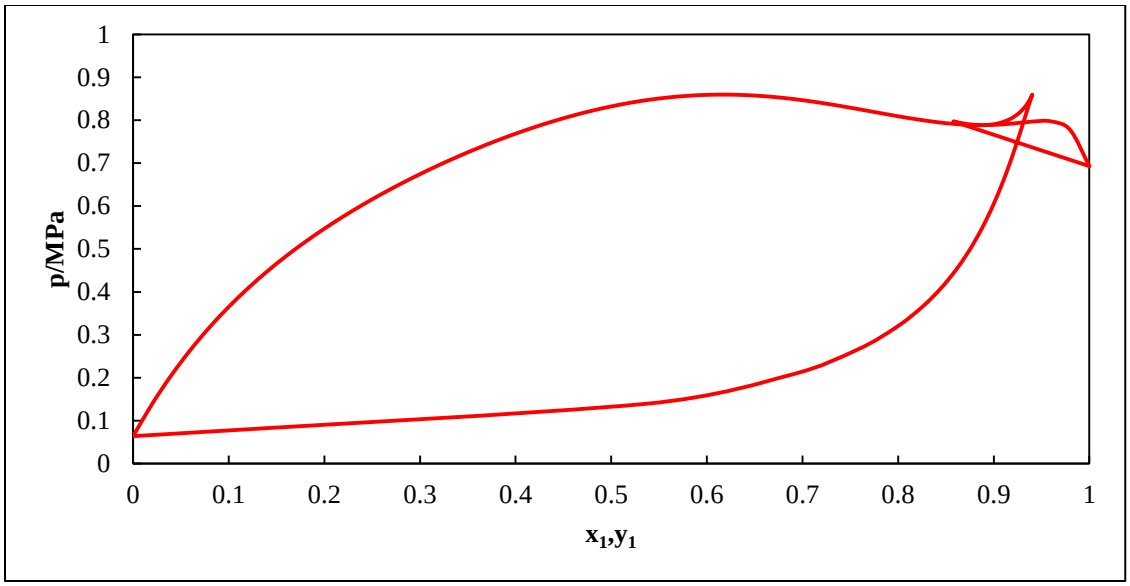

Figure H.9: Phase diagram (P-x-y) for the H_2S (1) + C_4F_{10} (2) system extrapolated to 260.15 K Using the PR-MC-WS-NRTL model.

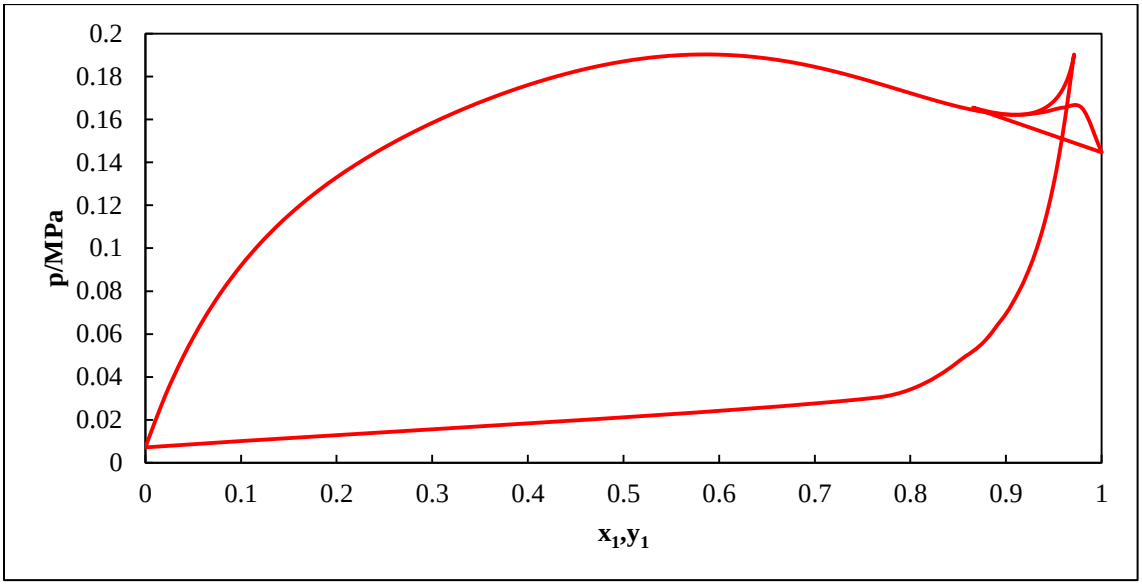

Figure H.10: Phase diagram (P-x-y) for the H_2S (1) + C_4F_{10} (2) system extrapolated to 220.15 K Using the PR-MC-WS-NRTL model.

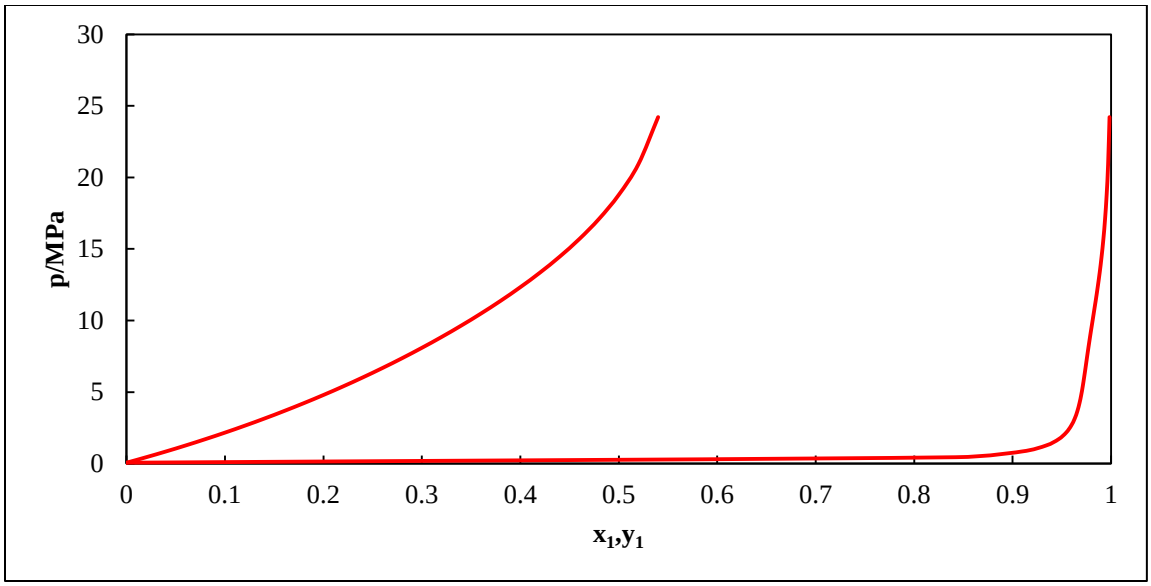

Figure H.11: Phase diagram (P-x-y) for the N_2 (1) + C_4F_{10} (2) system extrapolated to 260.15 K Using the PR-MC-WS-NRTL model.

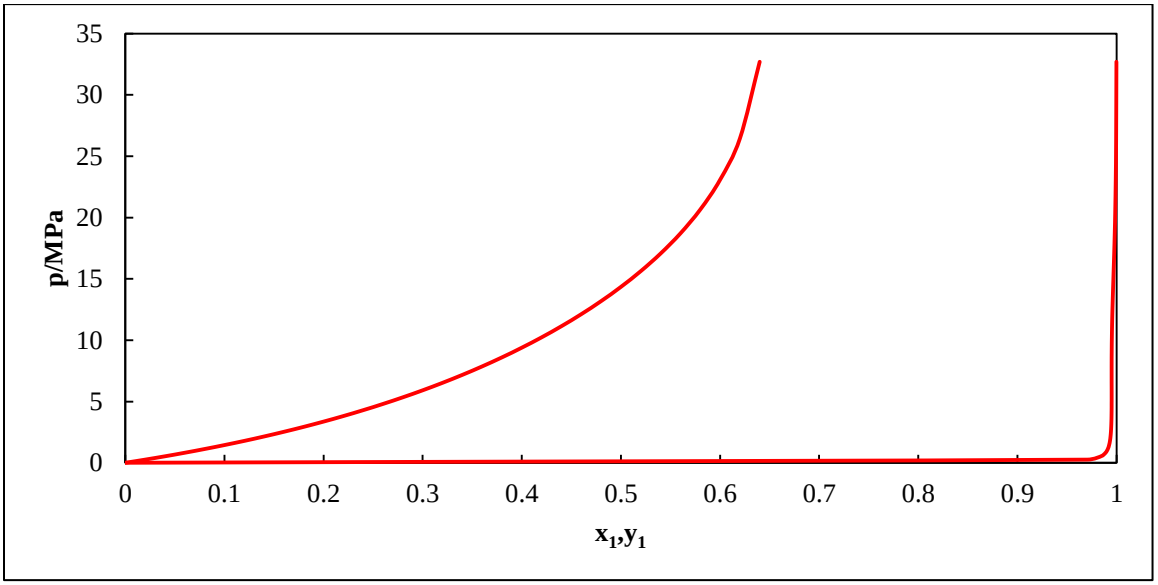

Figure H.12: Phase diagram (P-x-y) for the N_2 (1) + C_4F_{10} (2) system extrapolated to 220.15 K Using the PR-MC-WS-NRTL model.

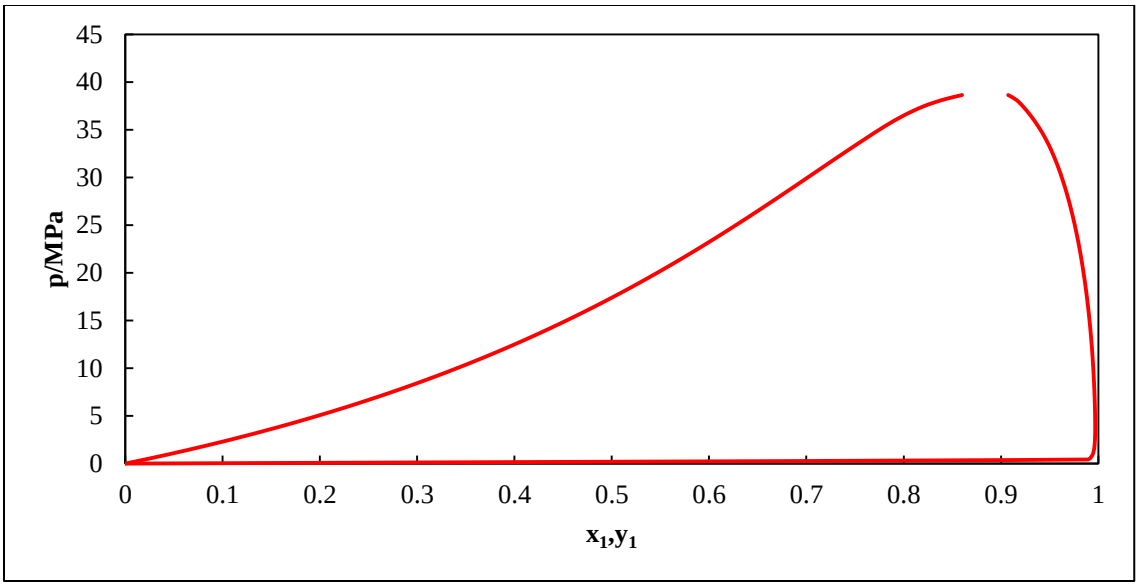

Figure H.13: Phase diagram (P-x-y) for the CO (1) + C_6F_{14} (2) system extrapolated to 260.15 K Using the PR-MC-WS-NRTL model.

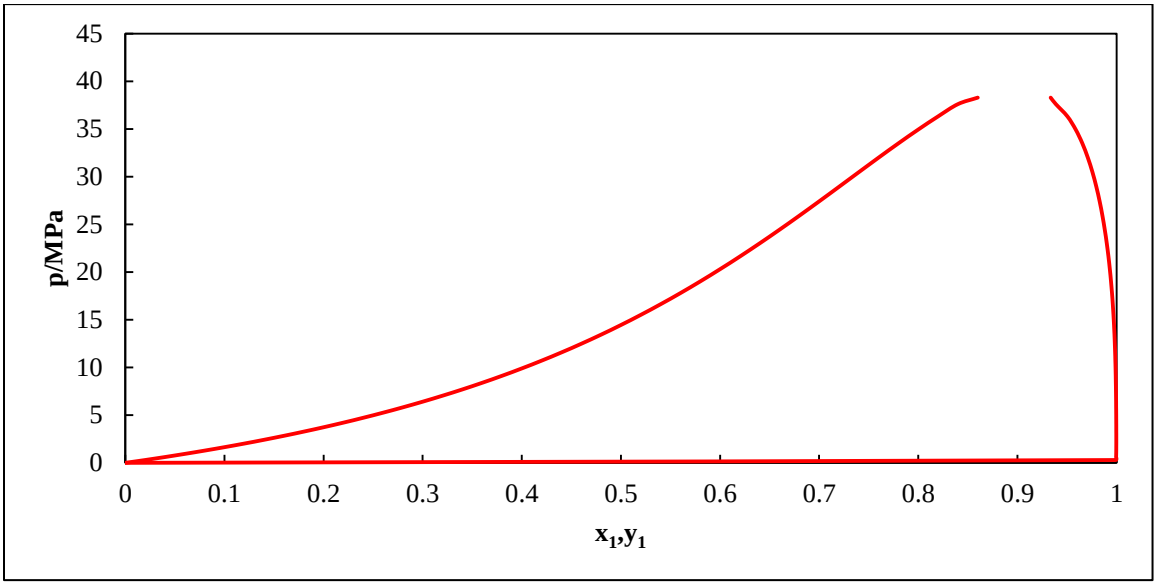

Figure H.14: Phase diagram (P-x-y) for the CO (1) + C_6F_{14} (2) system extrapolated to 220.15 K Using the PR-MC-WS-NRTL model.

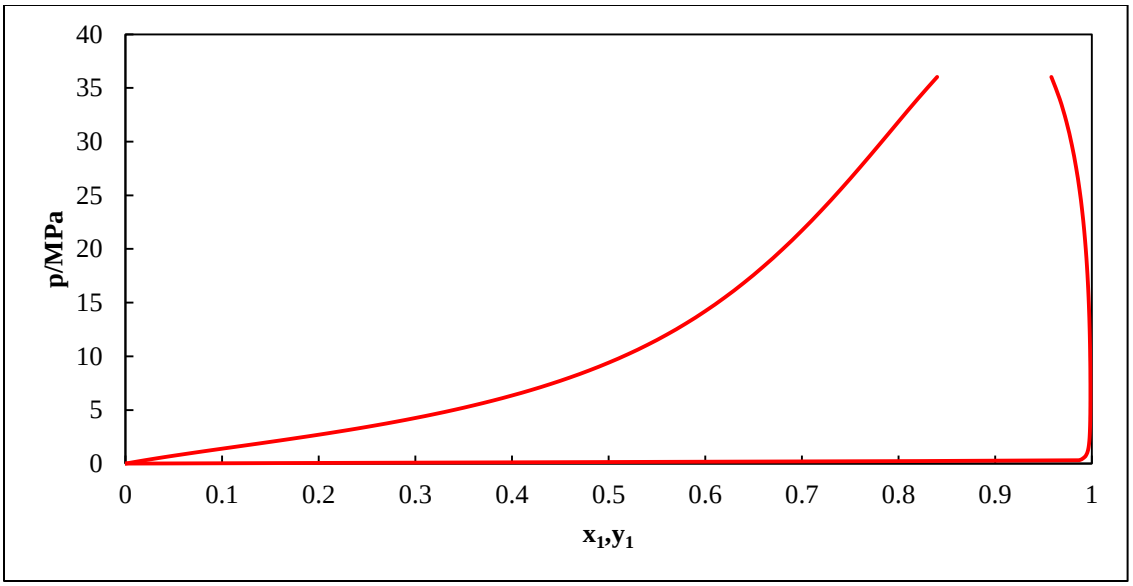

Figure H.15: Phase diagram (P-x-y) for the CH_4 (1) + C_6F_{14} (2) system extrapolated to 260.15 K Using the PR-MC-WS-NRTL model.

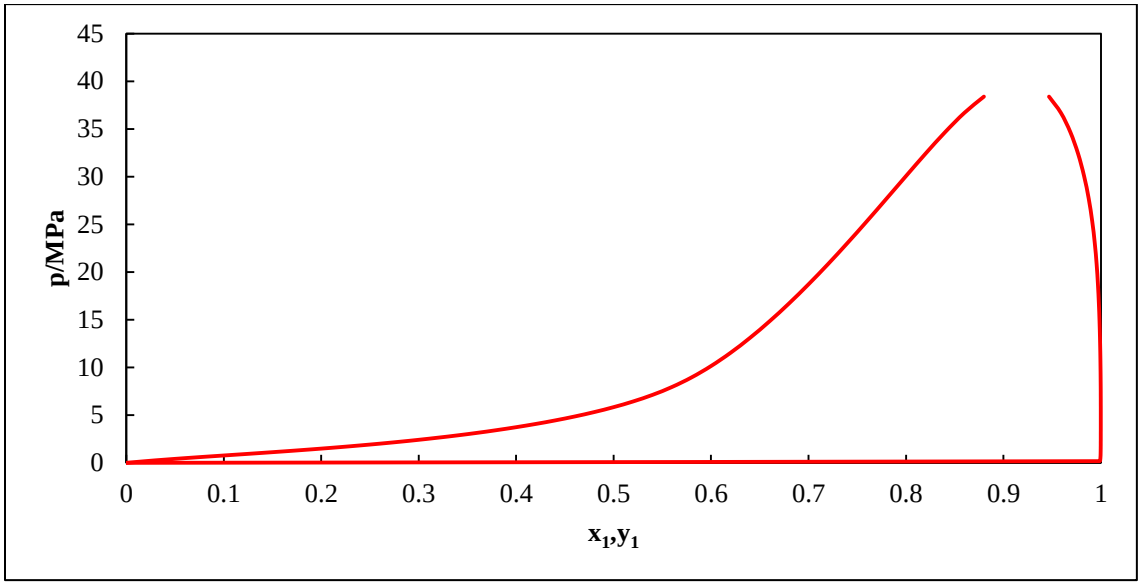

Figure H.16: Phase diagram (P-x-y) for the CH_4 (1) + C_6F_{14} (2) system extrapolated to 220.15 K Using the PR-MC-WS-NRTL model.

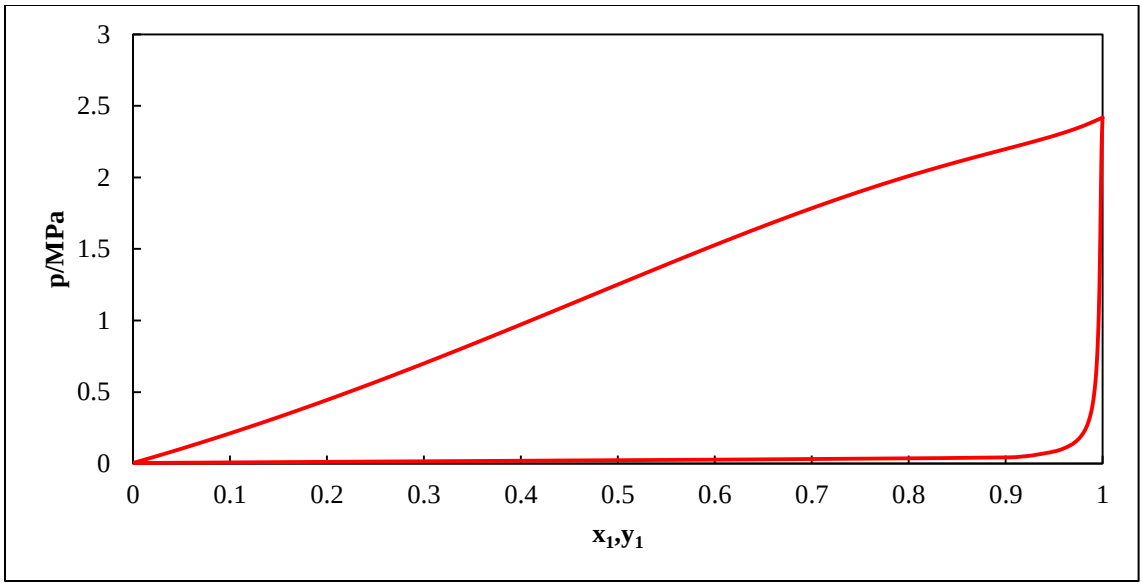

Figure H.17: Phase diagram (P-x-y) for the CO_2 (1) + C_6F_{14} (2) system extrapolated to 260.15 K Using the PR-MC-WS-NRTL model.

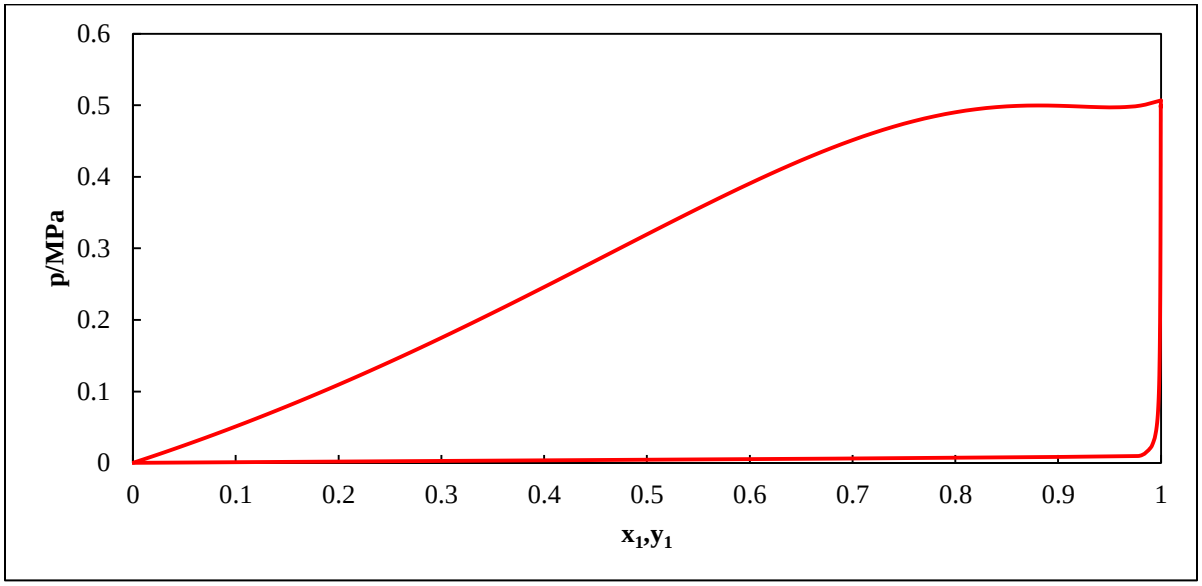

Figure H.18: Phase diagram (P-x-y) for the CO_2 (1) + C_6F_{14} (2) system extrapolated to 220.15 K Using the PR-MC-WS-NRTL model.

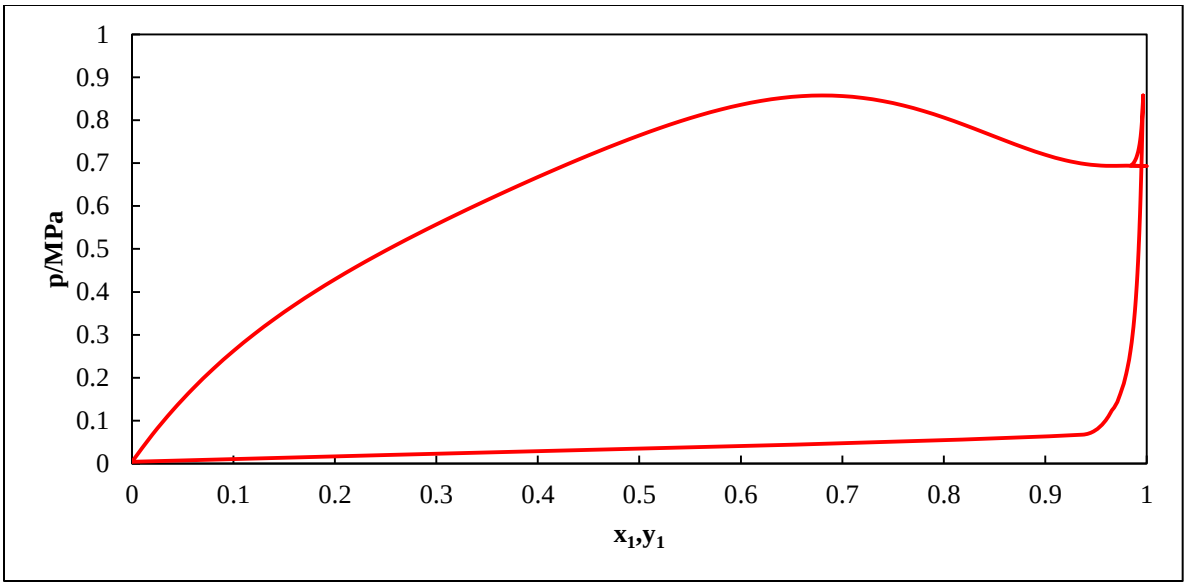

Figure H.19: Phase diagram (P-x-y) for the H_2S (1) + C_6F_{14} (2) system extrapolated to 260.15 K Using the PR-MC-WS-NRTL model.

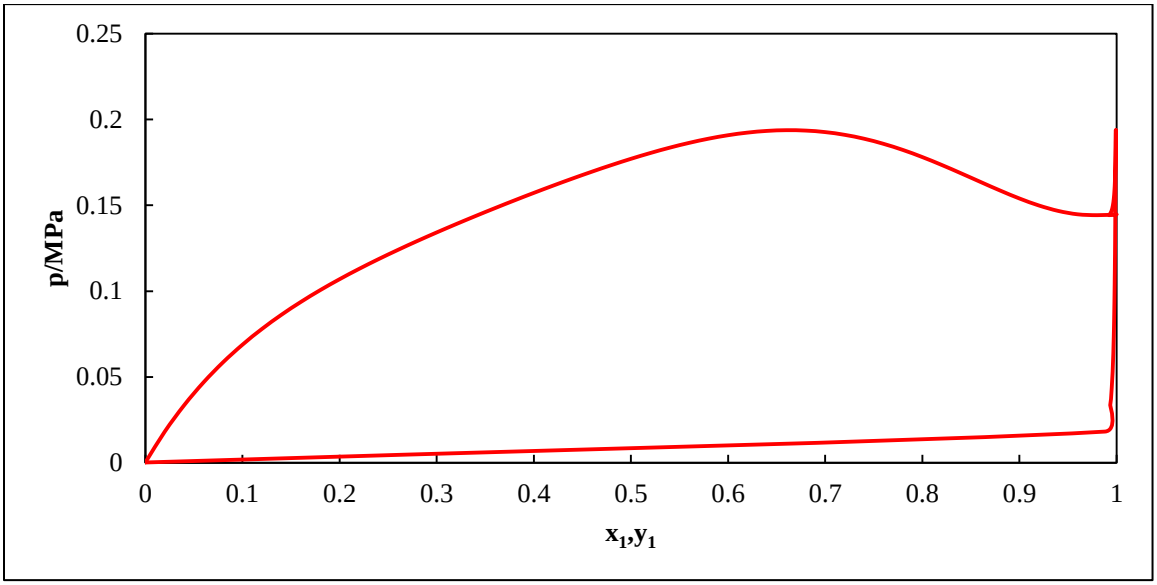

Figure H.20: Phase diagram (P-x-y) for the H_2S (1) + C_6F_{14} (2) system extrapolated to 220.15 K using the PR-MC-WS-NRTL model.

Appendix I

Sensitivity analysis results relative to the stripping column

Table I.1: Sensitivity analysis relative to the number of stages of the stripping column for the C_4F_{10} process

	Stripper overhead				
No. Stages	CO_2	CH_4	CO	H_2S	C_4F_{10}
10	1639.285	28.996	4.260	11.026	23.418
12	1640.443	28.996	4.260	11.026	22.235
14	1640.633	28.996	4.260	11.026	22.036
16	1640.655	28.996	4.260	11.026	22.013
18	1640.657	28.996	4.260	11.026	22.011
20	1640.657	28.996	4.260	11.026	22.011

Table I.2: Sensitivity analysis relative to the feed stage of the stripping column for the C_4F_{10} process

	Stripper overhead				
Feed stage	CO_2	CH_4	CO	H_2S	C_4F_{10}
2	1640.655	28.996	4.26	11.026	22.013
4	1640.653	28.996	4.26	11.026	22.016
6	1640.612	28.996	4.26	11.026	22.057
8	1640.195	28.996	4.26	11.026	22.476
10	1636.489	28.996	4.26	11.026	26.203
12	1611.135	28.996	4.26	11.026	51.757

Table I.3: Sensitivity analysis relative to the number of stages of the stripping column for the C_6F_{14} process

	Stripper overhead				
No. Stages	CO_2	CH_4	CO	H_2S	C_6F_{14}
8	1890.990	49.087	8.8090	0.173	3.689
10	1894.042	49.088	8.8100	0.173	0.635
12	1894.407	49.088	8.8100	0.173	0.271
14	1894.457	49.088	8.8100	0.173	0.221
16	1894.462	49.088	8.8100	0.173	0.216
18	1894.461	49.088	8.8100	0.173	0.215

Appendix J

Table J.1: Heat duties for the equipment used in the gas absorption systems

	Solvent	
	C_4F_{10}	C_6F_{14}
Cooler (heat duty in kW)	89,273.80	54,394.00
Pump (network required in kW)	2,207.89	3,923.28
Stripper reboiler (heat duty in kW)	75,827.40	155,581.00
Stripper condenser (heat duty in kW)	1,869.35	6,395.30